

# ATMOSPHERIC FORECASTING

Final Report # SAIC-00/1037

October 16, 2000



**Science Applications International Corporation**

*An Employee-Owned Company*

**DISTRIBUTION STATEMENT A**  
Approved for Public Release  
Distribution Unlimited

20001107 116

**DTIC QUALITY INSPECTED 4**

1710 Goodridge Drive, P.O. Box 1303, McLean, Virginia 22102 (703) 821-4300

Other SAIC Offices: Albuquerque, Boston, Colorado Springs, Dayton, Huntsville, Las Vegas, Los Angeles, Oak Ridge, Orlando, Palo Alto, San Diego, Seattle, and Tucson

# **ATMOSPHERIC FORECASTING**

**Final Report # SAIC-00/1037**

**Contract # N00014-93-C-2214**

**Prepared by**

**Ellis Hyman**

**with**

**Roger Shi, Mark Czarnaski,**

**and**

**Sethu Raman (North Carolina State University)**

**Science Applications International Corporation**

**1710 SAIC Drive**

**McLean, VA 22102**

**Submitted to**

**Dr. John Hornstein**

**Remote Sensing Physics Branch**

**Naval Research Laboratory**

**4555 Overlook Avenue, S.W.**

**Washington, DC 20375**

**October 16, 2000**



## **I. Introduction**

This report is the final report for the Science Applications International Corporation (SAIC) contract# N00014-93-C-2214, SAIC project# 01-0157-13-7020, titled "Atmospheric Forecasting," and covers the period of the contract: September 30, 1993 to June 30, 2000. The work performed by SAIC and its subcontractor, North Carolina State University (NCSU), was in support of the goals of the Remote Sensing Division of the Naval Research Laboratory (NRL). The SAIC Principal Investigator was Dr. Ellis Hyman and the technical effort was performed by Dr. Roger Shi and Mr. Mark Czarnaski of SAIC and by Dr. Sethu Raman of NCSU. The effort by Dr. Shi was performed at NRL in collaboration with NRL scientists and is reported in Section II. In Section III we describe the work performed by Mr. Czarnaski in the calibration of the NRL optical remote sensing facility. Finally, in Section IV we outline the work performed by our subcontractor NCSU, directed by Dr. Raman.

## **II. Mesoscale Simulations of Weather Systems Tracking**

### **A. IMPACT OF ASSIMILATIONS OF DROPWINDSONDE DATA AND SSM/I RAIN RATES ON NUMERICAL PREDICTION OF TROPICAL CYCLONES**

Numerical experiments were conducted to assess the impact of Omega-dropwindsonde (ODW) data and Special Sensor Microwave/Imager (SSM/I) rain rates in the analysis and prediction of Hurricane Florence (1988). The ODW data were used to enhance the initial analysis that was based on the National Meteorological Center/Regional Analysis and Forecast System (NCEP/RAFS) 2.5° analysis at 0000 UTC 9 September 1988. The SSM/I rain rates at 0000 and 1200 UTC 9 September 1988 were assimilated into the Naval Research Laboratory's limited-area model during model integration.

Four numerical simulations were performed to assess the impact of ODW data and SSM/I rain rates on numerical forecasts of Hurricane Florence (1988). A nested three-pass Barnes scheme objective analysis was used to enhance the NCEP/RAFS 2.5° analysis because of the relative high resolution of the ODW data near the center of Florence. The NCEP/RAFS 2.5° analysis and the ODW enhanced analysis were then used as the initial conditions for the numerical prediction experiments. We found that the forecast error of the intensity was reduced from 14 to 4 mb with the assimilation of the ODW data. It is also clear that the ODW data reduced the forecast error of the landfall time in the control experiment by 5 hours (down from 9 to 4 hours), and the landfall location error by 95% (down from 294 to 15 km). The impact of the ODW data was more pronounced in the first 24 hours of the integration and gradually decreased beyond 24 hours. This result is in agreement with Franklin and DeMaria (1992), in which a barotropic, nested, spectral hurricane track forecasting model was used to determine the impact of the ODW data. The advantage of using a three-dimensional primitive equation model with the inclusion of baroclinic and physical processes, as in this study, is that the model can simulate the hurricane structure in more detail (DeMaria et al., 1992). However, a major limitation of the ODW observations is that they do not provide information above 400 mb because of the altitude limitations of the NOAA WP-3D,

while satellite-derived winds can provide some upper-level information (Velden et al., 1992). Detailed observations of the three-dimensional structure of the upper levels of tropical cyclones are extremely scarce. Dropsonde data collected from 200 mb to the surface by the recent TCM-90 experiment (Elsberry and Abbey, 1991) may be proven to be very useful in depicting the upper-level structure of tropical cyclones (Merrill and Velden, 1995).

The rainfall rates retrieved from the SSM/I data at 0000 UTC and 1200 UTC 9 September 1988 were assimilated into the NRL limited-area model initialized with the NCEP/RAFS 2.5° analysis (Exp. Control+SSMI) and the ODW enhanced analysis (Exp. ODW+SSMI). Results indicate that the assimilation of the SSM/I rain rates (Exp. Control+SSMI) reduced the 24-hour forecast errors in the landfall location in the control experiment by about 43% (down from 294 to 169 km), and the landfall time by 5 hours (down from 9 to 4 hours). At mean time, the 24-hour minimum SLP and maximum surface wind speed forecasts were also improved by 5 mb and 10.1 ms<sup>-1</sup>, respectively. This study suggests that the assimilation of SSM/I rain rates can improve the track and intensity forecasts of tropical cyclones, especially when the ODW data are not available to the operational analysis. The benefit of the assimilation of SSM/I rain rates was limited when the simultaneous ODW data had already been assimilated into the initial condition, and vice versa. The landfall time error was reduced from 4 to 0 hour, and there was an improvement on the predicted storm track when the SSM/I rain rates were assimilated. The intensity forecast was also improved with the 24-hour minimum SLP forecast error reduced by 2 mb. There is no question that the combination of the ODW data and SSM/I rain rates provided the best simulation at 24 hours in this study. Results from this study agree with the assessment of Chang and Holt (1994) regarding the positive impact of assimilating SSM/I rain rates on the numerical predictions. This study suggests that operational forecasts can benefit from the assimilation of ODW and SSM/I data into numerical models for the prediction of the intensity and track of tropical cyclones. The increase of the track forecast accuracy will allow forecasters to reduce the overwarned area in the warning process and result in reducing the preparation costs incurred by the public in coastal areas (Sheet, 1990; Franklin, et al. 1991). In any case

study, the question arises whether or not the behavior shown is relevant to a large group of tropical cyclones. More studies need to be performed to further explore the value of both ODW and SSM/I data for the numerical forecast of tropical cyclones, especially when the ODW data collected from 200 mb to the surface become available from the AOML/HRD. The upper tropospheric influence on the intensity and track change of tropical cyclones has long been recognized.

Additional details can be found in a published paper by Shi, et al. (1996) in *Monthly Weather Review*. A reprint of this paper is included in this report as Appendix A.

#### B. INTERACTION BETWEEN HURRICANE FLORENCE (1988) AND AN UPPER-TROPOSPHERIC WESTERLY TROUGH

The Naval Research Laboratory's limited-area numerical prediction system, a version of the Navy Operational Regional Atmospheric Prediction System (NORAPS), was used to investigate the interaction between Hurricane Florence (1988) and its upper-tropospheric environment. The model was initialized with the NCEP/RAFS 2.5° analysis at 0000 UTC 9 September 1988, enhanced by a set of Omega Dropwindsonde (ODW) data through a three-pass nested-grid objective analysis.

In this study, model simulated results were analyzed to reveal the detailed structure of the outflow layer of Florence and a numerical experiment was performed to study the interactions between the outflow layer of Florence and the upper level westerlies. Diagnosis of the 200 mb level structure of Exp. ODW at 12 hour showed that the outflow layer was highly asymmetric, especially beyond three degrees radius, with an outflow jet originating at approximately three degrees north of the storm center. The outflow jet was elongated with a length of roughly 2500 km and a width of 500 km. Further diagnosis of the 12 hour wind and RH in the outflow jet at the entrance and exit regions of the outflow showed that there was a thermally-direct, circum-jet secondary circulation in the entrance region and a reversed thermally indirect one in the exit region. The secondary circulation had an outward branch above the jet, an inward branch below the jet (near 400 mb), an ascending branch in the anticyclonic shear side and a

descending branch in the cyclonic shear side of the outflow jet. The inward branch below the outflow jet in the entrance region of the outflow jet, however, was less apparent in this study than the one shown in Shi, et al. (1990).

Because of the complexity due to the existence of other synoptic systems, including the coastal front along the U. S. East Coast, it was difficult to isolate a well-defined secondary circulation. In general, the structure of the outflow layer of the simulated Florence was qualitatively similar to the idealized model study in Shi et al. (1990). In their composite study, Chen and Chou (1994) also found a similar jet streak associated with the evolution of upper tropospheric cold vortices over the western North Pacific during the warm season. They suggested the existence of the circum-jet thermally direct (indirect) secondary circulation in the entrance (exit) region of the jet streak, based on the cloud distribution. This is also consistent with Molinari and Vollaro (1989) in which they speculated that the frontogenetical forcing in the confluence region between the cold trough and the warm hurricane outflow may have enhanced the outflow ahead of the trough via thermal wind adjustment. At 24 hour, the westerly jet moved northeastward and was located over Virginia and far away from Florence. However, Florence's center also moved northward and into a region below the south end of the westerly trough. This resulted in the increase of vertical wind shear, the reduction of outflow and consequently the weakening of the intensity of Florence. At this moment, Florence was about to make landfall. This result is similar to the case described by Holland and Merrill (1984) where Hurricane Kerry began to decay after the cutoff of the poleward outflow channel.

Calculation of the storm-relative angular momentum budget at 12 hour demonstrated that the angular momentum balance was primarily maintained by the Coriolis torque and horizontal transports. It also revealed that the contribution by the horizontal import of eddy cyclonic angular momentum was the dominant feature at large radii, in agreement with the observational study by Molinari and Vollaro (1989). This result again underscored the dominance of the outflow jet in the outflow layer and the highly asymmetric nature of the outflow layer of tropical cyclones (Black and Anthes,

1971).

The most interesting numerical experiment to elucidate the interactions between Hurricane Florence (1988) and its environment is the one in which the approaching westerly UTT was very much weakened (Exp. ODW+WTR). In this numerical experiment, the weakened westerly UTT resulted in a reduction of the maximum speed of the outflow jet of Florence by  $6.4 \text{ ms}^{-1}$  (or about 15%) at 12 hour. The weakened trough and outflow jet of Florence was responsible for a 2-mb minimum SLP increase and a  $5.0 \text{ ms}^{-1}$  or 13% maximum surface wind reduction. This study also showed that the weakened outflow jet also resulted in weaker convections in the core region in the 10 to 15 hour window, 8 to 13 hours before the model storm reached its maximum intensity. Diagnosis of the 200 mb RH field of this experiment indicated a weaker outflow, a weaker and broader thermally direct circulation in the entrance region, and the absence of the thermally indirect circulation in the exit region because of a weaker approaching westerly UTT. The weakened upper-level westerly trough was also responsible for the reduction of inward cyclonic eddy AMF in this numerical experiment. This result suggested that the large inward flux of cyclonic eddy angular momentum produced by the passage of an upper-level westerly trough was important to the intensification of Florence's inner core convection between 1000 and 1500 UTC September 9 and therefore the deepening of the minimum SLP between 1200 and 2400 UTC September 9. This result also coincided with the cooling of up to  $4^\circ \text{ K day}^{-1}$  by the eddy heat flux, likely induced by the passage of the upper-level westerly trough at large radii in the upper troposphere, at 15h in Exp. ODW, while only  $2^\circ \text{ K day}^{-1}$  in Exp. ODW+WTR, suggesting the interaction between the upper-level westerly trough and Florence. This result is consistent with the estimate shown in Molinari and Vollaro (1990).

On the other hand, the strong vertical shear associated with the upper level westerly trough might prevent Florence from further intensifying. Merrill (1988 a and b) suggested that the upper level environmental interactions with tropical cyclones, in general, contribute negatively to intensity changes. His conclusion was based upon two observations: 1) maximum intensity of tropical cyclones are limited by the potential

which the sea surface temperature can provide (Emanuel, 1986), and tropical cyclones rarely reach to their potential maximum intensity; 2) increasing vertical shear is usually accompanied with the approaching of the upper level westerly trough and works against the intensification of tropical cyclones. In Florence, however, because it made landfall three hours after it reached maximum intensity, it was difficult to fully determine whether or not the vertical shear associating with the approaching upper-level westerly trough had any negative effect on the intensification. Nevertheless, the result from this numerical experiment suggested that the upper level westerly trough's contribution was important to the intensification of Florence and the timing and relative position of an approaching westerly UTT and a tropical cyclone is critical for the intensification and decay of a tropical cyclone.

Even though the model simulated outflow structure of Hurricane Florence is very consistent dynamically and thermodynamically, it remains to be directly verified with observations. Detailed observations of the three-dimensional structure of the outflow layer of tropical cyclones are extremely scarce. The ODW observations used in this study do not provide information above 400 mb, limited by the operational altitude of NOAA WP-3D aircraft that deployed them. Dropsonde data collected from 200 mb to surface in TCM-90 and 92 experiments (Elsberry and Abbey, 1991; Dunnavan et al., 1993) may be very useful in the study of the interactions between the upper level environment and tropical cyclones. Because Florence made landfall at 0200 UTC 10 September, three hours after it reached its maximum intensity, the window of opportunity for studying interactions between Florence and the upper level westerly trough is very short (less than a day). Therefore, it is rather difficult to study the full extent of the interactions. A real case study of the interactions between a tropical cyclone and the upper level environment over an open ocean would be valuable for this purpose, where the timing and relative position of an UTT and a tropical cyclone can be more conveniently analyzed.



Additional details can be found in a published paper by Shi, et al. (1997) in *JOURNAL OF THE ATMOSPHERIC SCIENCES*. A reprint of this paper is included in this report as Appendix B.

### C. SIMULATIONS OF HURRICANE HUGO (1989)

Hurricane Hugo of 1989 developed from low latitude easterlies and was found by reconnaissance aircraft to have a minimum SLP of 918 hPa with a maximum surface sustained wind speed of  $72 \text{ ms}^{-1}$  on 15 September. While maintaining its strength as Categories 4 and 5, it traveled along the edge of the subtropical high pressure, leaving vast destruction for several Caribbean islands along its path, and finally made landfall at 04 UTC 22 September just north of Charleston, South Carolina. Prior to landfall, Hugo, reintensified over the Gulf Stream and with a sustained surface wind of  $60 \text{ ms}^{-1}$  and a large translational speed, was responsible for the significant storm surf and severe damage along the South Carolina coastline. More detailed description of the intensity changes and storm structure of Hurricane Hugo can be found in Alliss et al. (1992).

On 19 September, when the center of Hugo was just north of Puerto Rico, the upper level flow patterns featured a deep N-S oriented westerly trough centered along Lake Erie to northern Florida. This upper-level trough became a cold core cutoff low-pressure system, which was located over the Florida panhandle at 00 UTC 20 September and was discernible only above the 500 mb level. During the next two days, as Hugo accelerated toward the northwest, it seems to have significant interaction with the cutoff low. At the 200 hPa level, the outflow jet of Hugo was located between the cutoff low and the subtropical high, a "geostrophically correct" location. Based on the NCEP/RAFS 500 hPa analyses, the cutoff low first moved south and then drifted toward southwest after 21 September, suggesting an upper level Fujiwhara effect.

The limited-area model used for the investigation is the Naval Research Laboratory model, similar to the Navy Operational Regional Atmosphere Prediction System (NORAPS). Various aspects of the model have been reported in Madala, et al.



(1987), Chang, et al. (1989), Holt, et al. (1990) and Shi, et al. (1997). The model is a three-dimensional, hydrostatic, finite difference model with a multi-level 1.5 order closure boundary layer, Kuo's cumulus parameterization and a simplified radiation treatment. For this study, the horizontal resolution is 1/3 degree latitude and 1/2 degree longitude and there are 22  $\sigma$ -levels in the vertical. The model domain covers an area from 100 to 50 W and 10 to 50 N. The sea surface temperature (SST) is obtained from the Ocean Thermal Interpolation System (OTIS) of U. S. Navy Fleet Numerical Meteorology and Ocean Center (FNMOC). The boundary conditions used in the integration are the interpolated values from NCEP/RAFS analyses. A vertical normal mode initialization (Sashegyi and Madala, 1993) is used to balance the initial analysis.

The experimental design strategy is fairly standard and follows that in Shi, et al. (1997). Because the NCEP/RAFS analyses were archived at a 2.5 degree latitude resolution, a detailed and dynamically consistent structure of Hurricane Hugo and its outflow cannot be inferred. The model was integrated for 72 hours from the NCEP/RAFS analysis valid for 00 UTC 20 September. In this integration, the thermal and dynamic structure and the behavior of Hurricane Hugo and the environment were closely reproduced with higher resolution. This integration was thus considered the control experiment and used for comparison with an additional variational numerical experiment. In the variational experiment (Exp. 1), the initial analysis at 00 UTC 20 September was altered. The upper level cutoff low above the southeastern United States was removed (debugged) during the alteration.

A procedure was used to remove the upper level cutoff low from the initial analysis. First, the mean wind and mean temperature within a circular area with a radius of 800 km centered around the location of the minimum SLP were computed for each pressure analysis level. The analyzed wind and the temperature within the circle were then replaced with the mean values to remove the cutoff low structure. A nine point smoothing was then applied 10 times over the circular area to achieve the desired field. The replacement and smoothing were carried out from the 500 mb to 50 mb level.

In the control experiment, Hurricane Hugo quickly developed from the initial weak tropical storm an intense tropical disturbance with well defined cyclonic circulation and a characteristic warm core up to 300 hPa. Starting from a minimum SLP of 1005 hPa, the central SLP reached 985 at 24 h and 929 hPa (see Fig. II-1) with a maximum wind speed near  $70 \text{ ms}^{-1}$  at 46 h just prior to landfall. The landfall in the control experiment occurred at 50 h, merely two hours early as compared to the actual landfall time at 04 UTC 22 September (see Fig. II-2). The simulated track stayed very close to the observed track, making landfall at approximately one grid point northeast of Charleston, SC. At 36 h, the simulated Hugo came to within 10 degrees longitude --- a commonly accepted distance for the onset of the Fujiwhara effect, to the east of the cutoff low at 36 h. Just prior to the landfall at 48 h (Fig. II-2), the simulated hurricane moved to a more northern latitude than the upper level low. A close examination of the 500mb height and wind field plots of the control experiment between 36 and 60h shows that a counterclockwise rotation appeared to have occurred between the two low centers at the 500 mb level. Similar counterclockwise rotation between the two low centers at the 500 mb level had not occurred in Exp. 1, because of the removal of the cutoff low above the southeastern United States. Figure II-2 shows that the track of the simulated Hugo stayed about two degrees southwest of the track of the control experiment (see Fig. II-2). Past studies have documented that the Fujiwhara effect is a result of an interaction between a tropical cyclone and a low pressure system in the lower level when these two systems are located within 10 degrees of each other. This study reveals that this effect occurs not only in the lower level but also in the upper level.

#### D. A TWO-MONTH MESOSCALE REANALYSIS

Working with the scientists of the Marine Meteorology Division of the Naval Research Laboratory (NRL), we have performed a mesoscale reanalysis to support the study of Gulf War Illness. Realistic and quantitatively accurate atmospheric conditions are needed to drive dispersion models that can predict the transport and dispersion of chemical and biological agents that may have affected U. S. and other coalition troops in the hours and days following the demolition of chemical and biological weapons in Iraq

during the Desert Storm Operation between 15 January and 15 March 1991. The reanalysis was conducted with the Navy's global and mesoscale analysis and prediction systems: the Navy Operational Global Atmospheric Prediction System (NOGAPS) and the Coupled Ocean/Atmosphere Mesoscale Prediction System (COAMPS). A comprehensive set of observations has been collected and used in the reanalysis, including unclassified and declassified surface reports, ship and buoy reports, observations from rawinsonde, and retrievals from civilian and military satellites. The atmospheric conditions for the entire globe have been reconstructed using the global system at the effective spatial resolution of 0.75 degrees. The atmospheric conditions over southern Iraq, Kuwait, and northern Saudi Arabia have been reconstructed using the mesoscale system at the spatial resolutions of 45, 15 and 5 km.

The reanalysis was first started with the older version of NOGAPS and COAMPS in 1997. Intermittent reanalyses for Khamisiyah, Al Muthana and other cases were produced. In each case, the reanalyses were performed only for a 3-4 day period. In 1998, when the improved version of NOGAPS and COAMPS with 1-km land use data became available, it was determined that reanalyses- covering the entire 1991 Gulf War between 15 January and 15 March 1991 are needed. After the 2-month reanalyses were performed, results were statistically compared with the reanalyses performed by the older version of NOGAPS and COAMPS. The comparison (Table II-1) shows that the root mean square error (RMSE), bias and absolute error of the 12h forecast fields are much reduced with the improved version of NOGAPS and COAMPS.

RMSE and bias of the analysis and 12h forecast fields from the 2-month reanalysis were also compared with other major models (see Tables II-2-5). Results from other major models were adopted from White, et al. (1999). As shown in these tables, our reanalysis results are statistically better than or comparable to other major models' results, especially for the analysis fields. This comparison highly endorses the superiority of the data assimilation system used in NOGAPS and COAMPS. One of the major challenges of this 2-month reanalysis was the processing and archiving of 200+ GB model generated reanalysis data. This was a very time consuming job. Nevertheless, the

200+ GB, 2-month re-analyzed meteorological fields were archived into 8mm magnetic tapes and delivered to dispersion modelers for computation of concentration and dosage of the released chemical agents for epidemiological analysis.

The synoptic conditions during the 2-month period were typical of the transitional period after a Shamal and controlled by eastward propagating small-amplitude troughs and ridges. On the mesoscale, the conditions over the Tigris-Euphrates valley were further modulated by the diurnal variation in the local circulations between land, the Persian Gulf, and the Zagros mountains. Figure II-1 shows the daytime and nocturnal 2-month mean wind at 10m height in the region. At 12Z, the dominated features were the Shamal in the Persian Gulf and southwesterlies over Zagros. Sea breezes were also apparent near the coast of the Persian Gulf during daytime hours. At 00Z, the dominated features were drainage flows coming down from Zagros toward Iraq and the Shamal still in the Persian Gulf. However, sea breezes had turned into land breezes during nocturnal hours. In general, winds in the Tigris-Euphrates valley were weak. Figure II-2 shows the 2-month mean wind at 10m height near the two lakes (Buhayrat ath Tharthar and Bahr al Milh Lakes) in central Iraq. There were divergent flows coming out of the lakes (lake breeze) during daytime hours and convergent flows going into the lakes (land breeze) during nocturnal hours. This diurnal change of wind patterns should have strong impact on the transport and dispersion of chemical and biological agents that may have affected U. S. and other coalition troops, since a few demolitions of chemical and biological weapons were near the lakes.

A technical paper based on this study is in preparation and will be submitted to a major journal shortly.

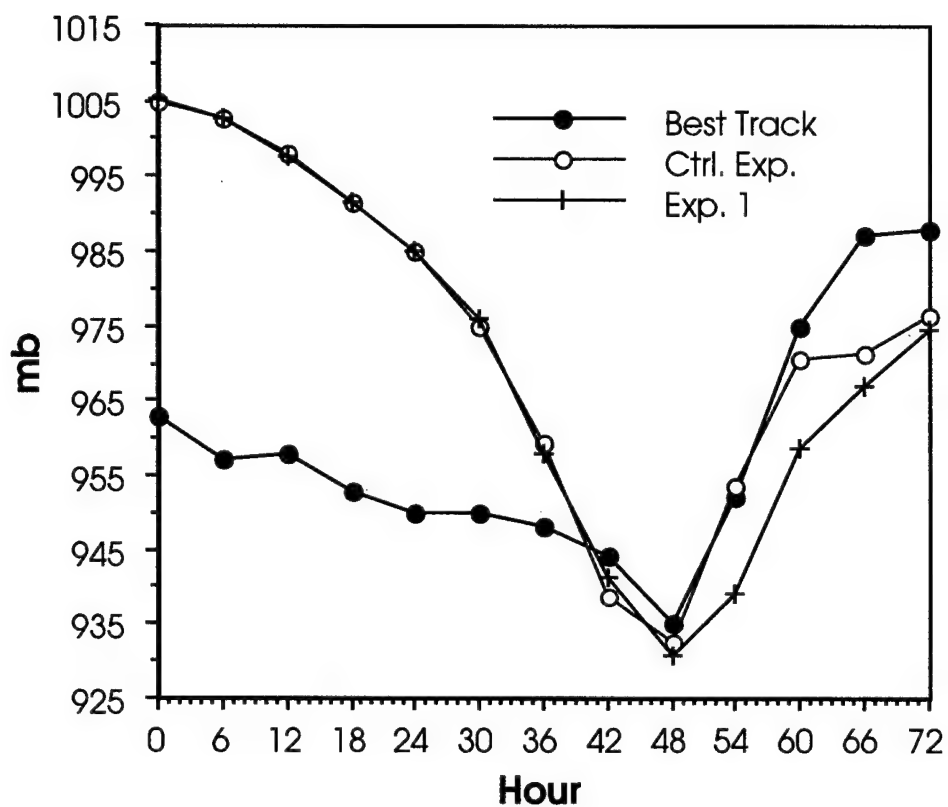


Figure II-1 Hourly change of the minimum mean sea level pressure of the observed and simulated Hurricane Hugo (1989).

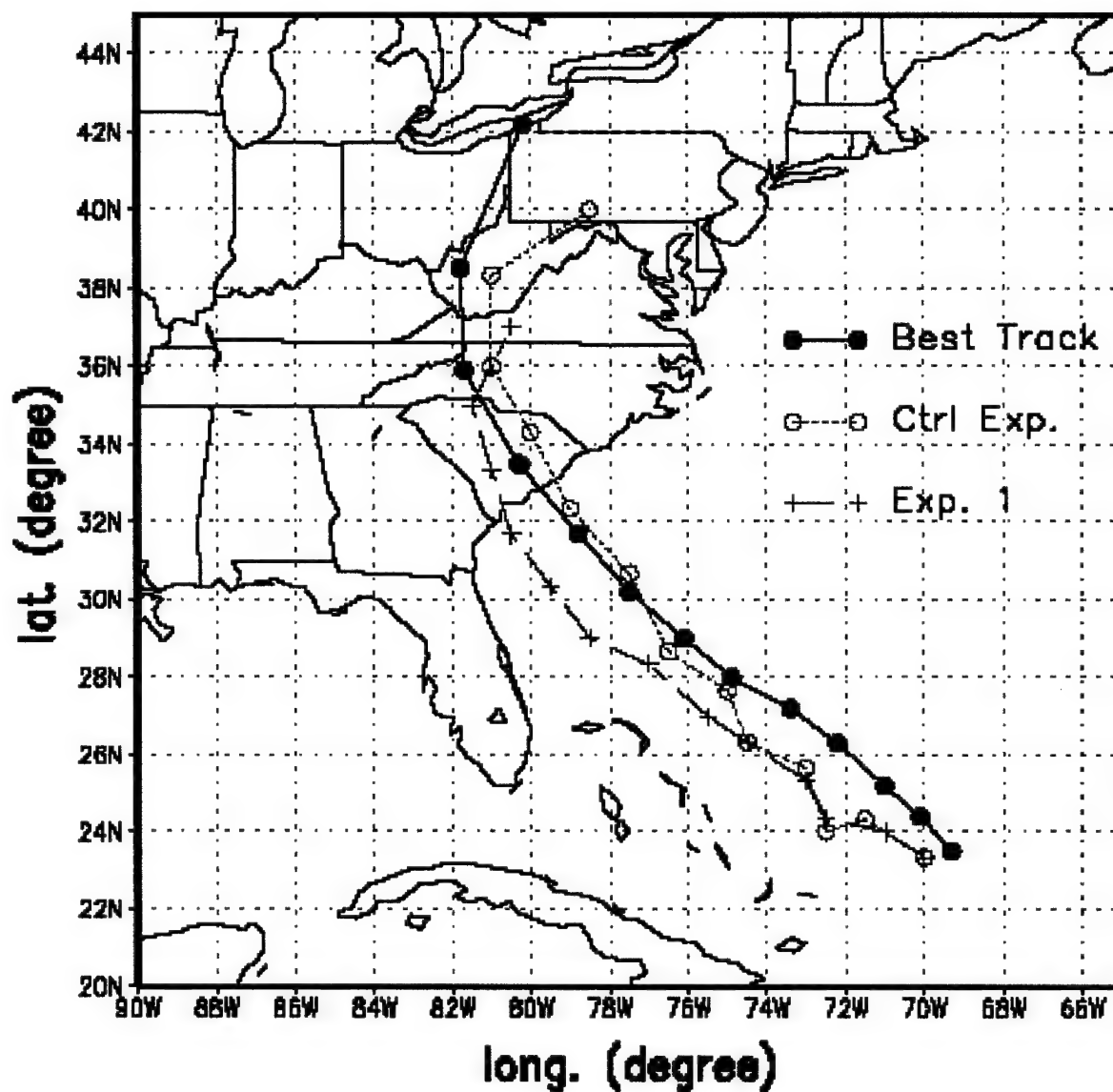
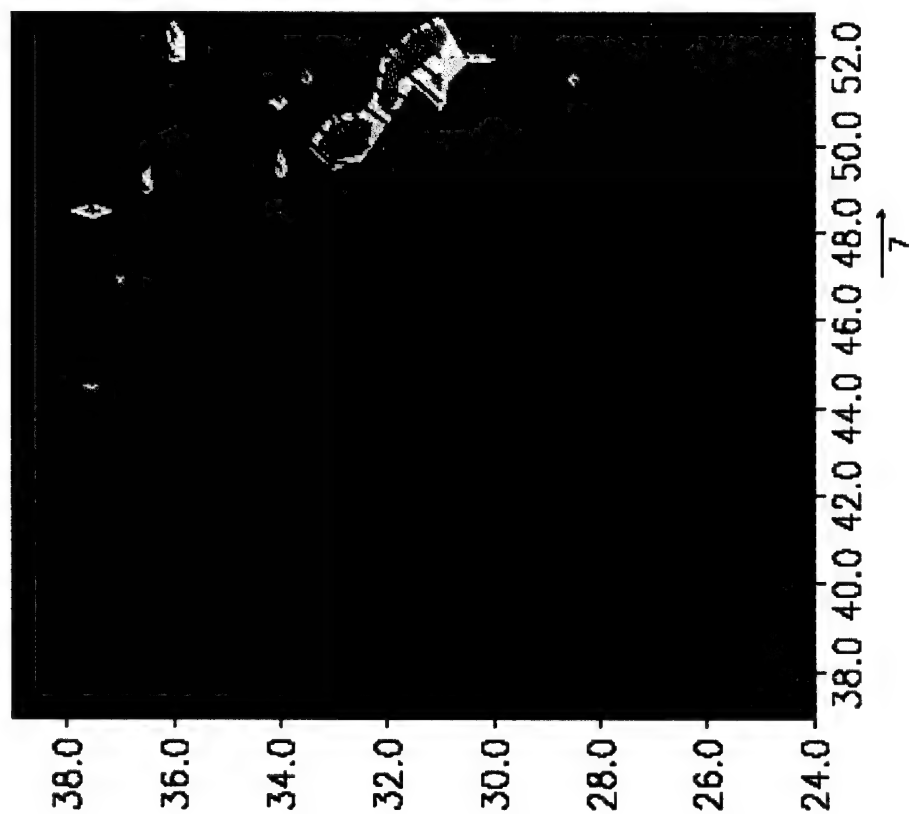


Figure II-2 The observed and simulated tracks of Hurricane Hugo (1989).

00Z



12Z

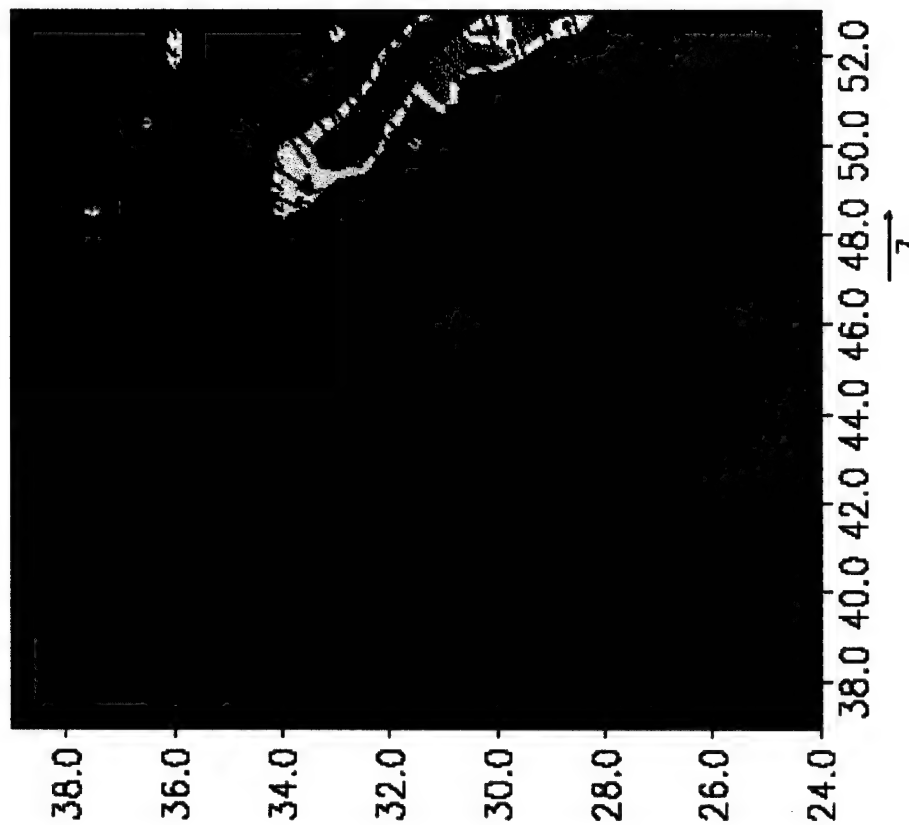
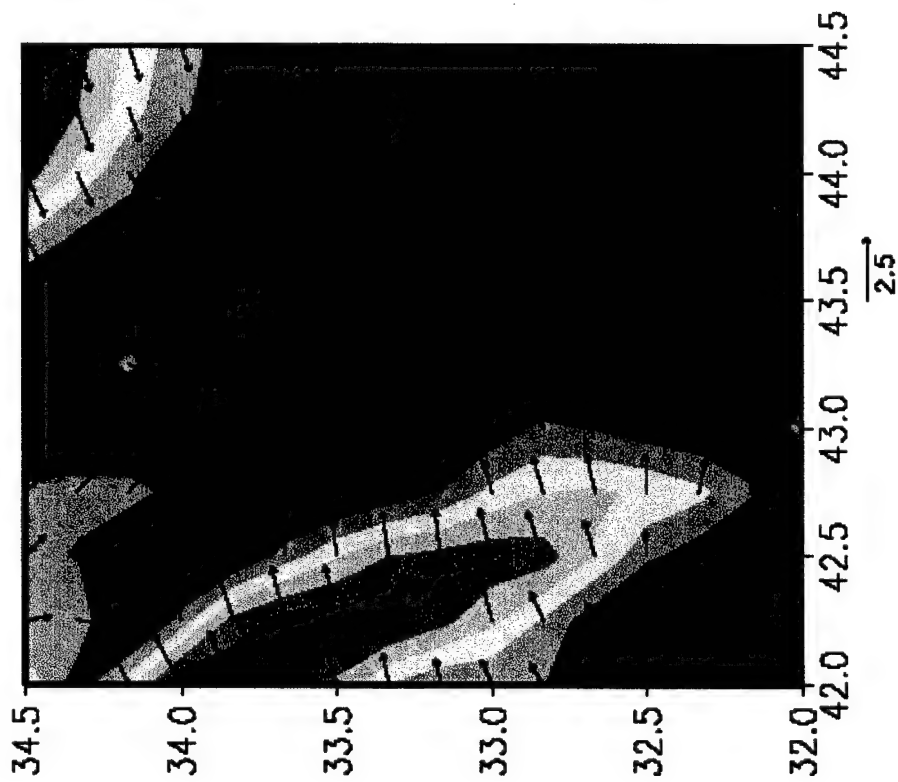


Figure II- 3. 2-month 10m mean wind (m/s) calculated from the 2-month reanalysis data.

00Z



12Z

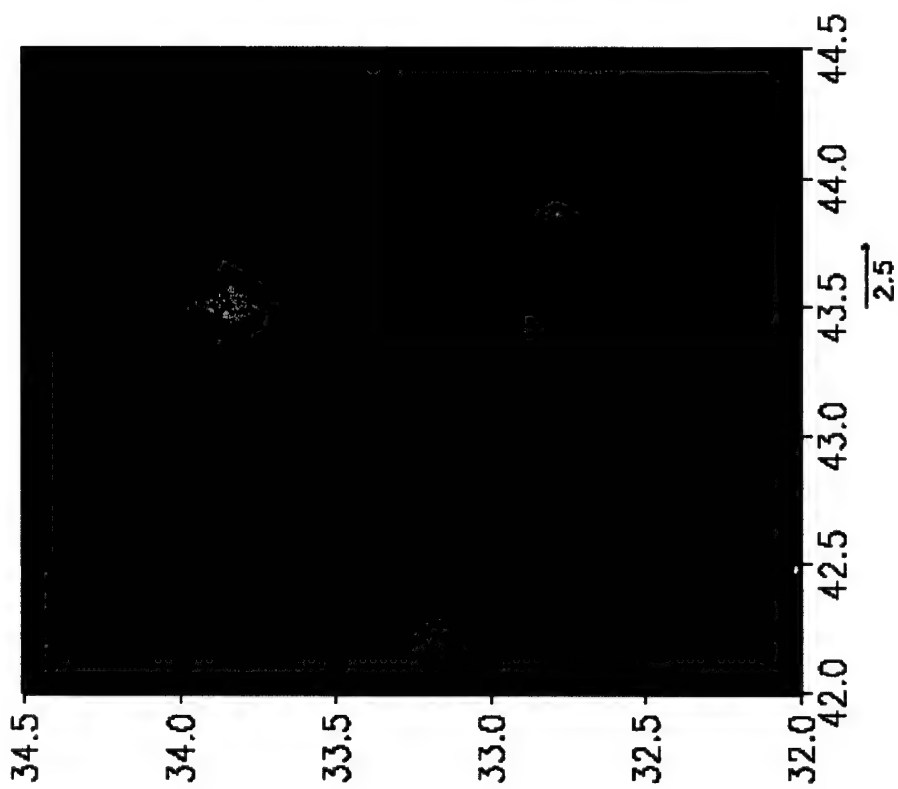


Figure II-4. Same as Figure II-1 except for the region near central Iraq.



	RMSE		Bias		Abs err	
Wind speed (m/s)	old	new	old	new	old	new
1000 < Z < 850 mb	5.20	3.32	0.53	-1.15	4.28	2.44
850 < Z < 500 mb	7.98	3.16	2.67	-0.20	6.44	2.42
Wind direction (degree)						
1000 < Z < 850 mb	81.05	59.03	42.82	9.69	63.58	46.04
850 < Z < 500 mb	62.02	36.86	13.71	2.22	47.30	22.88
Temperature (°C)						
1000 < Z < 850 mb	4.19	1.29	1.17	0.12	3.52	0.96
850 < Z < 500 mb	3.86	1.29	0.51	0.23	3.11	1.01
RH (%)						
1000 < Z < 850 mb	36.83	17.35	-5.03	1.42	28.13	14.13
850 < Z < 500 mb	34.30	21.29	3.27	4.23	25.11	16.16

Table II-1 The comparison between the reanalysis using the old Navy's models and the reanalysis using the new ones for the Al Muthana case between 02/08/1991 00Z and 02/10/1991 12Z.

Geopotential Height (m)										
	ETA	NGM	MRF	MESO	MM5	ULAM	COAMPS			
300 mb	15.00	18.31	18.67	15.32	23.24	17.94	9.44			
500 mb	9.07	11.09	12.56	9.45	17.31	14.84	7.57			
700 mb	6.02	8.79	9.66	6.83	12.16	15.15	5.67			
Temperature (°C)										
	ETA	NGM	MRF	MESO	MM5	ULAM	COAMPS			
300 mb	1.27	1.40	1.16	1.37	1.16	1.31	0.98			
500 mb	1.18	1.22	1.09	0.99	1.04	1.19	0.78			
700 mb	1.64	1.34	1.28	2.08	1.57	1.39	0.90			
Wind (m/s)										
	ETA	NGM	MRF	MESO	MM5	ULAM	COAMPS			
300 mb	3.80	4.75	5.90	3.63	4.04	4.46	3.06			
500 mb	3.21	4.18	4.65	3.04	3.30	3.90	2.33			
700 mb	2.70	3.90	4.02	2.32	2.89	3.07	2.19			
Relative Humidity (%)										
	ETA	NGM	MRF	MESO	MM5	ULAM	COAMPS			
300 mb	16.16	18.51	19.72	21.21	12.04	14.02	12.40			
500 mb	11.62	9.17	14.28	10.75	11.67	12.78	15.20			
700 mb	9.16	8.41	14.07	9.70	10.20	10.53	18.46			
Resolution	48km	83km	~100km	29km	27km	30km	15km			

Table II-2 RMSE of analysis fields among COAMPS and other major models. Other model data adopted from White et al. (Wea. Forecasting, 1999). Red color indicates the best result in each row.

		Geopotential Height (m)								
		ETA	NGM	MRF	MESO	MM5	ULAM			
								COAMPS		
300 mb		21.78	24.79	22.96	19.73	23.55	26.65	19.75		
500 mb		17.50	21.05	19.05	15.44	19.27	19.01	17.43		
700 mb		15.21	17.92	14.81	13.91	16.44	19.35	14.90		
<b>Temperature (°C)</b>										
	ETA	NGM	MRF	MESO	MM5	ULAM				
300 mb	1.64	1.95	1.78	1.63	1.85	2.17		COAMPS	1.93	
500 mb	1.49	1.70	1.52	1.41	1.57	1.69			1.47	
700 mb	1.63	1.64	1.42	1.52	1.68	1.93			1.59	
<b>Wind (m/s)</b>										
	ETA	NGM	MRF	MESO	MM5	ULAM				
300 mb	8.13	8.62	8.15	7.68	7.94	8.13		COAMPS	6.37	
500 mb	6.05	6.48	6.14	6.12	6.61	6.69			4.76	
700 mb	5.55	5.85	5.39	5.46	6.23	6.85			4.02	
<b>Relative Humidity (%)</b>										
	ETA	NGM	MRF	MESO	MM5	ULAM				
300 mb	18.72	27.30	22.90	16.69	14.57	18.87		COAMPS	32.34	
500 mb	19.56	24.51	19.11	19.41	21.06	22.27			26.21	
700 mb	18.30	22.11	18.98	17.73	19.64	22.60			25.66	
<b>Resolution</b>	<b>48km</b>	<b>83km</b>	<b>~100km</b>	<b>29km</b>	<b>27km</b>	<b>30km</b>	<b>15km</b>			

Table II-3 Same as Table 2 except for RMSE of the 12h forecast fields.

Geopotential Height (m)								
	ETA	NGM	MRF	MESO	MM5	ULAM	COAMPS	
300 mb	-6.54	-8.80	-2.96	-5.94	-16.64	1.25	-0.83	
500 mb	-3.9	-3.26	-4.05	-3.58	-10.83	-3.25	-0.51	
700 mb	-1.17	-0.54	-2.15	-0.87	-5.95	-5.33	-0.41	
Temperature (°C)								
	ETA	NGM	MRF	MESO	MM5	ULAM	COAMPS	
300 mb	-0.67	-0.48	0.10	-0.57	-0.30	0.11	-0.12	
500 mb	-0.60	-0.53	0.02	-0.47	-0.51	-0.20	-0.10	
700 mb	-1.22	-0.62	0.12	1.55	-1.08	-0.74	-0.02	
Wind (m/s)								
	ETA	NGM	MRF	MESO	MM5	ULAM	COAMPS	
300 mb	0.70	0.86	0.90	0.72	0.74	0.88	-0.25	
500 mb	0.62	0.86	0.74	0.56	0.60	0.75	-0.13	
700 mb	0.74	1.24	1.05	0.59	0.82	0.89	-0.11	
Relative Humidity (%)								
	ETA	NGM	MRF	MESO	MM5	ULAM	COAMPS	
300 mb	-0.67	3.33	12.88	13.72	2.54	-2.65	3.23	
500 mb	0.72	-0.37	-1.65	1.27	-1.55	0.69	0.08	
700 mb	2.45	0.06	0.39	4.19	1.28	1.73	-3.42	
Resolution	48km	83km	~100km	29km	27km	30km	15km	

Table II-4 Same as Table 2 except for Bias of the analysis fields.

		Geopotential Height (m)							
		ETA	NGM	MRF	MESO	MM5	ULAM	COAMPS	
300 mb		3.69	-5.30	-4.01	3.83	2.92	12.90	-6.54	
500 mb		4.02	-5.50	-8.70	1.87	3.09	-0.35	-7.03	
700 mb		6.16	-3.94	-6.71	3.53	6.55	-9.96	-5.76	
Temperature (°C)									
		ETA	NGM	MRF	MESO	MM5	ULAM	COAMPS	
300 mb		0.24	0.53	0.93	0.28	0.68	1.19	-0.28	
500 mb		-0.30	-0.27	0.06	-0.14	-0.15	0.41	-0.23	
700 mb		-0.70	-0.26	-0.05	-0.49	-0.55	0.85	0.05	
Wind (m/s)									
		ETA	NGM	MRF	MESO	MM5	ULAM	COAMPS	
300 mb		1.32	1.95	2.20	1.28	1.72	1.95	-0.60	
500 mb		1.06	1.09	1.21	1.09	1.70	1.54	-0.04	
700 mb		1.49	1.43	1.34	1.22	1.55	2.03	0.02	
Relative Humidity (%)									
		ETA	NGM	MRF	MESO	MM5	ULAM	COAMPS	
300 mb		-6.30	11.90	15.57	8.08	2.44	-2.05	18.32	
500 mb		0.80	2.78	2.61	1.66	-0.72	-2.75	4.52	
700 mb		1.98	0.40	1.31	1.10	-0.84	5.05	-3.21	
Resolution	48km	83km	~100km	29km	27km	30km	15km		

Table II-5 Same as Table 2 except for Bias of the 12h forecast fields.

## E. REFERENCES

- Alliss, R. J., S. Raman and S. Chang, 1992: Special Sensor Microwave/Imager (SSM/I) Observation of Hurricane Hugo (1989), *Mon. Wea. Rev.*, **120**, 2723-2737.
- Black, P. G. and R.A. Anthes, 1971: On the asymmetric structure of the tropical cyclone outflow layer. *J. Atmos. Sci.*, **28**, 1348-1366.
- Chang, S. W., K. Brehme, R. V. Madala and K. D. Sashegyi, 1989: A numerical study of the east coast snowstorm of 10-12 February 1983. *Mon. Wea. Rev.*, **117**, 1768-1778.
- and T. R. Holt, 1994: Impact of assimilating SSM/I rainfall rates on numerical prediction of winter cyclones. *Mon. Wea. Rev.*, **122**, 151-164.
- Chen, G. T.-J. and L.-F. Chou, 1994: An investigation of cold vortices in the upper troposphere over the western north Pacific during the warm season. *Mon. Wea. Rev.*, **122**, 1436-1448.
- DeMaria, M., S. D. Aberson and K. V. Ooyama, 1992: A nested spectral model for hurricane track forecasting. *Mon. Wea. Rev.*, **120**, 1628-1643.
- Dunnavan, G. M., R. L. Elsberry, P. A. Harr, E. J. McKinley and M. A. Boothe, 1993: Overview of the tropical cyclone motion - 92 (TCM-92) mini-field experiment. Preprints, 20th Conference Hurricanes and Tropical Meteorology, San Antonio, Texas, Amer. Meteor. Soc., 1-6.
- Elsberry, R. L. and R. F. Abbey, Jr., 1991: Overview of the tropical cyclone motion (TCM-90) field experiment. Preprints, 19th Conference Hurricanes and Tropical Meteorology, Miami, Amer. Meteor. Soc., 1-6.
- Emanuel, K. A., 1986: An air-sea interaction theory for tropical cyclones. Part I: Steady - state maintenance. *J. Atmos. Sci.*, **43**, 585-604.
- Franklin, J. L., M. DeMaria and C. S. Velden, 1991: The impact of Omega Dropwindsonde and satellite data on hurricane track forecasts. Preprints, 19th Conference on Hurricanes and Tropical Meteorology, *Miami*, Amer. Meteor. Soc., 87-92.
- and M. DeMaria, 1992: The impact of Omega Dropwindsonde Observations on barotropic hurricane track forecasts. *Mon. Wea. Rev.*, **120**, 381-391. *Mon. Wea. Rev.*, **121**, 2433-2451.

- Holt, T, S. W. Chang and S. Raman, 1990: A numerical study of the coastal cyclogenesis in GALE IOP 2: Sensitivity to PBL parameterizations. *Mon. Wea. Rev.*, **118**, 234-257.
- Holland, G. J. and R. T. Merrill, 1984: On the dynamics of tropical cyclone structural changes. *Quart. J. R. Met. Soc.*, **110**, 723-745.
- Madala, R. V., S. W. Chang, U. C. Mohanty, S. C. Madan, R. K., Paliwal, V. B. Sarin, T. Holt and S. Raman, 1987: Description of the naval research laboratory limited-area dynamical Weather prediction model . NRL Technical Report No. 5992, Washington, D.C., 131pp.
- Merrill, R. T., 1988a: Characteristics of the upper-tropospheric environmental flow around hurricanes, *J. Atmos. Sci.*, **45**, 1665-1677.
- , 1988b: Environmental influences on hurricane intensification. *J. Atmos. Sci.*, **45**, 1678-1687.
- and C. S. Velden, 1996: A three-dimensional analysis of the outflow layer of supertyphoon Flo (1990). *Mon. Wea. Rev.* **124**, 47-63.
- Molinari, J. and D. Vollaro, 1989: External influences on hurricane intensity. Part I: Outflow layer eddy angular momentum fluxes. *J. Atmos. Sci.*, **46**, 1093-1105.
- and -----, 1990: External influences on hurricane intensity. Part II: Vertical structure and response of the hurricane vortex. *J. Atmos. Sci.*, **47**, 1902-1918.
- Sheet, R. C., 1990: The National Hurricane Center-past, present, and future. *Wea. Forecasting*, **5**, 185-232.
- Sashegyi, K. D. and R. V. Madala, 1993: Application of vertical-mode initialization to a limited-area model in flux form. *Mon. Wea. Rev.*, **121**, 207-220.
- Shi, J. J., S. W. Chang and S. Raman, 1990: A numerical study of the outflow layer of tropical cyclones. *Mon. Wea. Rev.*, **118**, 2042-2055.
- , S. W. Chang and S. Raman, 1996: Impact of assimilations of dropwindsonde data and SSM/I rain rates on numerical predictions of Hurricane Florence (1988). *Mon. Wea. Rev.* **124**, 1435-1448.
- , S. W. Chang and S. Raman, 1997: Interaction between Hurricane Florence (1988) and an upper-tropospheric westerly trough. *J. Atmos. Sci.*, **54**, 1231-1247.

- Velden, C. S., C. M. Hayden, W. P. Menzel, J. L. Franklin and J. S. Lynch, 1992: The impact of satellite-derived winds and numerical hurricane track forecasting. *Wea. Forecasting*, **7**, 107-118.
- White, B. G., J. Paegle, W. J. Steenburgh, J. D. Horel, R. T. Swanson, L. K. Cook, D. J. Onton and J. G. Miles, 1999: Short-term forecast validation of six models. *Wea. Forecasting*, **14**, 84-108.



### **III. Optical Remote Sensing Calibration Facility (ORSCF) Calibration Report**

**Introduction:** The following is a report of the calibration status to date of the Optical Remote Sensing Calibration Facility (ORSCF) calibration plan. The measurement plan covers the operation and maintenance procedures to monitor the high use calibration equipment and standards. The ORSCF plan initiated in April of 1997 continues to evolve with version 3.0 presented.

The current physical space plan is shown in Fig. III-1. The layout of the Optronics Laboratories, Inc., measurement equipment has been optimized to facilitate an increased demand on the integrating sphere calibrations and to accommodate multiple CCD camera and spectrometer setups. The new plan layout allows for one 4' x 6' optics table and half of the adjoining 4' x 8' table near the integrating sphere to be available for camera and field instrument testing and calibrations.

To date 88 measurement exercises have been conducted in the ORSCF with the calibration log listed in Appendix C. To summarize, the measurements have included: 46 OL measurement system; 15 reflectance targets; 8 PHILLS; 5 ASD; 2 GER; 3 filter set transmittance; 1 Red Stick; 1 Lumitex Fiber Optic Source; 1 Spectral Goggles; 1 PRS3 calibration source; 1 Labsphere mapping; 1 SeaWiFS; 1 Transfer Radiometer; and 3 imaging spectrometers.

Tabulated in the current calibration plan/status report and included in Appendix D are the past calibration schedules, test unit measurement data, and comparison analysis to date for review. As shown in Table III-1, the schedule for each of the five ORSCF test units has been updated to reflect the measurements conducted over the past year. The plan for each test unit follows with the equipment listed along with their identified calibration accuracy, manufacturer recommended calibration interval, and dates measured to present.

In Table III-2 the planned calibration schedule for the upcoming 1999-2000 measurement years is shown. The measurement schedule has been changed and updated to coincide with the NRL fiscal calendar.

**Calibration Data:** The calibration data is acquired and stored on the ORSCF Lab PC computer with data backups to the Iomega Zip drive performed at the end of each data set.

**Data Analysis:** Data analysis has consisted of comparisons of the measurement data to the corresponding calibration and previous measurement data.

**Results:** Comparisons have been generated from the results of the test unit calibrations performed as requested. Currently the results on measurements performed in the ORSCF Lab have been within the Optronics Laboratories and Labsphere operational specifications for the identified test unit equipment.

#### **Y2K: NRL ORSCF Y2K**

The following ORSCF Laboratory equipment had been identified as possibly being affected by year 2000 roll-over and had undergone testing for compliance with the result reported.

##### OL65A Optronic Laboratories Programmable Current Source

Real time clock—hr/min/day/month/year roll over test passed

##### OL83A Optronic Laboratories Programmable Current Source

Real time clock—hr/min/day/month/year roll over test passed

##### ORSCF Lab 486 PC

Y2K test consisted of setting the date on the Lab PC forward into the year 2000, shutting the system down in the normal mode, powering it off, and then rebooting the system. A W95 software roll over test was also conducted. This test consisted of setting the system clock forward to December 31, 1999 at 11:58:00 PM and letting the clock roll over into the New Year. Then shutting the system down and cold booting.

The Lab PC operated normally after manually setting the date forward and rolling the clock over while running W95 software.

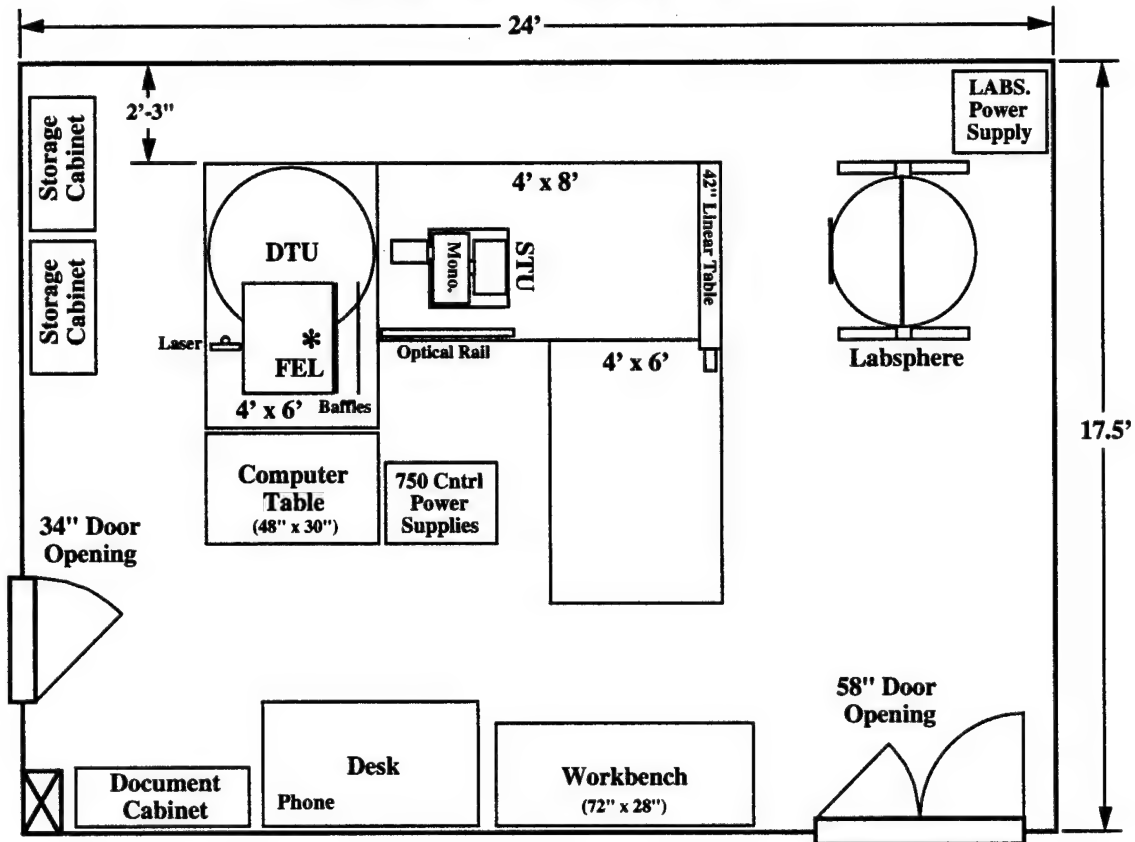
### OL 750 Measurement Software

The measurement software uses two digits supplied by the operating system for date stamps on data files. Y2K test consisted of setting the date on the Lab PC forward into the year 2000 and running the software in its normal mode. Measurement data was recorded, saved, and reloaded with correct date stamp.

**Recommendations:** The following recommendations are presented for the measurements covering the 1999-2000 calibrations' schedule in the ORSCF.

1. The re-calibration of FEL-M F-400 as per 3 year ITU interval.
2. The purchase from Optronics Laboratories, Inc. of an FEL-C Spectral Irradiance Lamp Standard with calibration covering the 300-2500nm wavelength ranges or the re-calibration of one existing FEL-M (F-400) out to 2500nm.
3. Upgrading the existing 100MHz 486 ORSCF Lab PC and system software.
4. Returning the FEL OL 83A Programmable Current Source for re-calibration and fuse holder upgrade (see quote).
5. Modification to the existing DTU plaque holder to accommodate plaques up to 18" square.
6. The purchase of data acquisition equipment to monitor room temperature and humidity as a function of time.
7. The purchase of high intensity IR lamp source.
8. Telephone line to be moved to laboratory desk as per physical plan.

**Optical Remote Sensing Calibration Facility**  
 NRL Physical Space - Rm. 214, Bldg. 2



Revised: 07/16/1999

**Figure III-1: Optical Remote Sensing Calibration Facility physical space.**

Table III-1

ORSCF Test Unit Calibrations (1998-99)													
Measurement		Month (X-completed)											
Test Unit	Items	O	N	D	J	F	M	A	M	J	J	A	S
ITU	F-399 F-400										X X		
STU	Mono. HI Source Detector s							X		X			X
									X				
RTU	FEL xfer Sphere Mappin g										X X		
DTU	Plaques	X	X	X	X						X		
OTU	Slit												

Table III-2

ORSCF Test Unit Calibration Schedule (1999-2000)													
Measurement		Month (X-completed)											
Test Unit	Items	O	N	D	J	F	M	A	M	J	J	A	S
ITU	F-399 F-400	▽ ▽			▽			▽ ▽			▽		
STU	Mono. HI Source Detector s	▽ ▽	▽		▽ ▽ ▽		▽	▽ ▽ ▽	▽		▽ ▽ ▽		▽
RTU	FEL xfer Sphere Mappin g	▽		▽		▽		▽		▽		▽ ▽ ▽	
DTU	Plaques		▽						▽				
OTU	Slit						▽						▽

## **1.0 ITU-Irradiance Test Unit**

### **FEL Standards of Spectral Irradiance**

Calibration:  $\pm 1\%$

Interval: period of 50 hours of use or 1 year which ever occurs first

**OL FEL-M Standard (S/N: F-399)—to date lamp hour total: 25.4 hrs**

Interval: yearly

Calibrated: 02-28-1996 (OL)

Measured: 03-14-96 (RY), 06-04-96  
04-28-97, 07-28-97, 10-30-97  
01-12-98, 04-02-98, 07-16-98  
07-22-99

**OL FEL-M Standard (S/N: F-400)—to date lamp hour total: 4.8 hrs**

Interval: yearly

Calibrated: 02-28-1996 (OL)

Measured: 03-14-96 (RY),  
04-28-97, 10-30-97  
04-02-98  
07-29-99

### **OL 83A Programmable DC Current Source (S/N: 96113052)**

Interval: recommended once a year

Calibrated: 02-01-1996 (OL)

Procedure: Refer to Irradiance Test Unit manual Section 3, pages 12-16

Cal-plan: The OL FEL-M Standard Lamp (S/N: F-399) will be used for all instrument irradiance calibrations performed by ORSCF. Quarterly measurement of the F-399 standard with comparisons to the F-400 standard conducted semi-annually. Irradiance will be measured at 50cm for each FEL-M lamp using the ORSCF STU configured with a 1.25mm entrance slit and 1.5mm exit aperture, IS-670 6 inch integrating sphere at the monochromator entrance port, Si PMT detector and lens collimator at the exit port. Data records will be acquired in the 300-1100nm range at 10nm increments. The STU system will be calibrated using the corresponding FEL-M standard and three measurements made using that calibration.

The Optronics Laboratories, Inc. FEL-M F-300 standard of spectral irradiance is considered the ORSCF standard and all other calibrations are correlated to its calibration. The OL FEL-M F-400 standard will be calibrated at Optronics Laboratories, Inc. or NIST once every 3 years.

## 2.0 STU-Spectral Test Unit

### OL 740-20A High Intensity Source

Interval: quarterly (ORSCF)  
 Measured: 06-04-96  
 04-25-97, 07-28-97, 10-30-97  
 01-12-98, 04-02-98, 07-16-98

High Intensity Source (S/N: 96300272)—to date lamp hour total: **326.1 hrs**

### OL 65A Programmable DC Current Source (S/N: 96108073)

Interval: recommended once a year  
 Calibrated: 01-15-1996 (OL)  
 Procedure: Refer to Irradiance Test Unit manual Section 3, pages 12-16

### OL 750-M-S Single Tri-grating Monochromator (S/N: 96409045)

$\lambda$  Accuracy:  $\pm 0.05\%$   
 Interval: every two months (ORSCF)  
 Measured: 03-14-96 (RY), 11-22-96  
 05-08-97, 05-29-97, 07-28-97, 09-18-97, 11-19-97  
 01-07-98, 03-05-98, 05-07-98, 07-15-98, 09-30-98  
 04-22-99, 06-04-99  
 Optimized Grating: 02-04-1997, 11-19-97

OL 750-M-S Monochromator Measurements									
Date	Wavelength (nm) Accuracy (%) *extrapolated								
	300*	400	500	600	700	800	900	1000	1100*
11-22-96		0.10	0.05	0.06	0.09	0.08	0.08	0.07	0.06
05-08-97	0.05	0.12	0.06	0.05	0.04	0.04	0.03	0.03	0.02
05-29-97	0.08	0.05	0.04	0.04	0.03	0.03	0.03	0.03	0.03
07-28-97	0.08	0.10	0.04	0.04	0.03	0.02	0.02	0.01	0.01
09-18-97	0.080	0.050	0.095	0.055	0.060	0.065	0.040	0.020	0.040
11-19a-97	0.090	0.100	0.095	0.080	0.070	0.080	0.050	0.050	0.045
11-19b-97	0.030	0.035	0.025	0.020	0.030	0.030	0.015	0.015	0.015
01-07-98	0.035	0.035	0.045	0.025	0.035	0.030	0.015	0.015	0.020
03-05-98	0.035	0.010	0.065	0.050	0.050	0.030	0.035	0.015	0.040
05-07-98	0.008	0.012	0.060	0.019	0.002	0.018	0.011	0.002	0.012
07-15-98	0.070	0.076	0.030	0.029	0.010	0.010	0.026	0.021	0.014
09-30-98	0.006	0.036	0.032	0.019	0.021	0.020	0.006	0.005	0.012
04-22-99	0.012	0.016	0.002	0.005	0.010	0.050	0.012	0.006	0.013
06-04-99	0.020	0.028	0.041	0.020	0.026	0.054	0.029	0.008	0.014
09-17-99	0.015	0.030	0.020	0.040	0.018	0.015	0.012	0.011	0.008

**OL HSD-300 Silicon Detector Module (S/N: 96101054/96100051)**

Interval: yearly  
Calibrated: 02-27-1996  
Measured: 03-15-96 (RY), 05-02-96  
07-30-97, 10-30-97,  
01-07-98, 04-02-98, 07-17-98  
05-14-99

**OL HSD-340 PbS Detector Module (S/N: 96100024/96100048)**

Interval: yearly  
Calibrated: 02-27-1996  
Measured: 03-15-96 (RY), 05-03-96  
07-30-97, 10-30-97  
01-07-98, 04-02-98, 07-17-98  
05-14-99

Cal-plan: The spectral irradiance of high intensity source will be measured quarterly and compared to the FEL-M standards for output stability.

Every two months monochromator calibration to Hg, He, and Ar gas line sources. The STU will be calibrated over the 300-1100nm range with the gas line emission sources oriented horizontally and placed at a distance of 30cm. Each gas emission source investigation will be conducted with the STU software configured for transmittance measurement, the monochromator set for the smallest bandwidth (0.125mm entrance and exit slits), and the corresponding preset file loaded for the gas lines of interest.

Based on the results of monochromator calibration, a grating factor and alignment optimization may also be performed, and the system recalibrated.

The Silicon and PbS High Sensitivity Detector calibrations will be verified quarterly. The detector spectral response will be measured with the STU configure with 1.25mm entrance slit and 1.5mm exit aperture. The Silicon detector will be recorded over the 300-1100nm range in 10nm increments. The PbS detector will be measured from 1125-3000nm in 25nm increments. In each case a STU system calibration will be performed using the corresponding standard and three consecutive measurements performed using that calibration.



### 3.0 RTU-Radiance Test Unit

#### Labsphere Unisource 4000 Integrating Sphere

Interval: every two months (ORSCF)  
Calibrated: 03-08-1996 (OL)  
Measured: 03-15-96 (RY), 08-19-96  
04-29-97, 06-26-97, 08-19-97, 10-16-97, 12-17-97  
02-26-98, 04-07-98, 6-12-98, 08-24-98  
07-22-99

To date lamp hours: A 0275:13:57  
B 0147:27:29  
C 0216:14:59  
D 0354:57:17  
E 0178:35:33  
F 0254:39:26  
G 0148:25:15  
H 0223:59:07  
I 0314:16:44  
J 0197:51:05

#### Labsphere LPS-200-H Power Supplies A-J

Interval: yearly  
Calibrated: 02-20-1996 (Labsphere)

Cal-plan: 1, 2, 4, 6, 8, and 10 lamp radiance measurements of the Labsphere every two months. The identified PHILLS calibration combinations for the appropriate lamp levels: 10 lamps (A-J on); 8 lamps (B&G off); 6 lamps (E&J off); 4 lamps (C&H off); 2 lamps (A&F off); 1 lamp (I off). The sphere radiance over the 300-2500nm range at 10nm increments will be performed at a distance of 1 meter using the STU configured with 1.5mm entrance aperture, 1.25mm exit slit, and the OL 730-9Q Reflex Telescope. The measurement sequence will consist of a system calibration performed using the Labsphere standard and a radiance for 10, 8, 6, 4, 2, and 1 lamp levels with an initial 30 sphere warm-up and 10 minute stabilization interval between lamp settings.

Mapping of the Labsphere will be performed once a year at the 10 lamp radiance level. The STU equipped with a fiber optic (Optronics Laboratories, Inc. Model 730-7IR Quartz Fiber Optic Probe) or the NRL Analytical Spectral Devices (ASD) Dual Field Spec at a distance of 1 meter the entrance port will be used to map the Labsphere. Translation in the x-direction will be accomplished using the 40 inch Aerotech linear position table, and motion in the y-direction achieved by a 4 inch travel vertical positioning assembly (Model ATS02010-U-02B-1-99/). Radiance measurements at 900nm conducted in 1 inch steps in the x and y directions, for a total of 145 sampled

points. Spectral radiance in the range of 300-2500nm at 25nm increments will be recorded in 2 inch steps in the x and y directions, for a total of 25 points as shown in Fig. III-2. To test the mapping procedures, preliminary measurements will be recorded using the NRL Analytical Spectral Devices (ASD) Dual Field Spec.

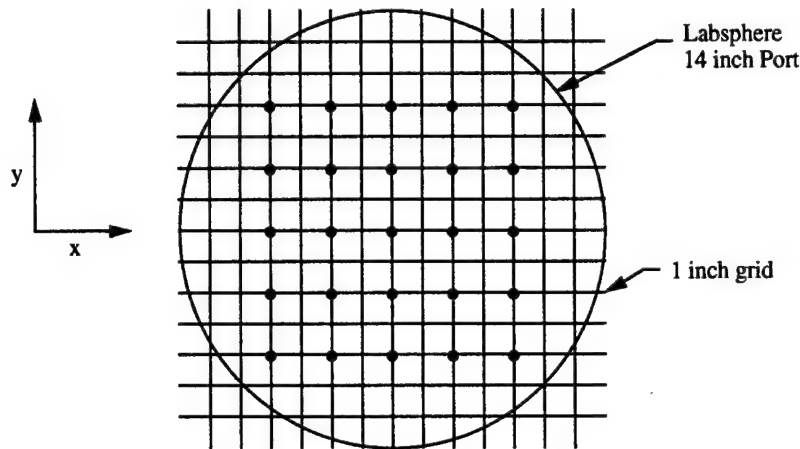


**Figure III-2: The Labsphere Unisource 4000 mapping coordinates.**

A FEL transfer calibration will be conducted once a year and coincide with the radiance and mapping measurements. The following two approaches will be performed during the preliminary calibration with one method being down selected as the procedure for future measurements.

1. The transfer calibration will consist of a FEL-M standard irradiance measurement performed at 50cm using the ORSCF STU configured with a 1.25mm entrance slit and 1.5mm exit aperture, IS-670 6 inch integrating sphere at the monochromator entrance port, Si PMT detector and lens collimator at the exit port. Irradiance will be measured in the 300-1100nm range at 10nm increments. The STU system will be calibrated using the corresponding FEL-M standard and one measurement made using that calibration. The Labsphere Unisource 4000 will then be measured at 1 meter with the STU under the same configuration and calibrated using the FEL-M irradiance transfer. The measurement will consist of 10 lamp intensity over 300-1100nm range in 10nm increments. The Labsphere Unisource 4000 radiance will be calculated via the measurement equation:

$$L_{(\lambda)} = E_{l(\lambda)} (I_s(\lambda) / I_l(\lambda)) \frac{r^2 + R^2 + d^2}{\pi R^2}$$

$L_{(\lambda)}$  is the near normal radiance of the Labsphere;  
 $E_{l(\lambda)}$  is irradiance of the FEL-M lamp;

$I_l(\lambda)$ ,  $I_s(\lambda)$  is the detector outputs when viewing the irradiance of lamp and sphere, respectively;  
 $r$ ,  $R$  is the aperture radii of small integrating sphere and Labsphere source;  
 $d$  is the distance between the aperture of the Labsphere source and the small integrating sphere.

2. The calibration will consist of a radiance measurement of an FEL-M standard of spectral irradiance from a spectralon plaque place at a distance of 50cm and an angle of 45 degrees. The plaque will be viewed at 1 meter by the ORSCF STU configured with 1.5mm entrance aperture, 1.25mm exit slit, and the OL 730-9Q Reflex Telescope. The FEL-M radiance will be measure via the spectralon BRDF over 300-2500nm range in 10nm increments. The Labsphere Unisource 4000 will then be measured at 1 meter with the STU under the same configuration and calibrated using the FEL-M irradiance transfer. The measurement will consist of 10 lamp radiance over 300-2500nm range in 10nm increments.

#### **4.0 DTU-Diffuse-Reflectance Test Unit**

##### **OL 55RS Reflectance Standard (S/N: 96100001)**

Interval: yearly  
 Measured: 03-15-96 (RY), 09-05-96  
 02-11-97, 05-30-97, 11-26-97  
 02-12-98, 5-29-98, 06-03-98, 06-10-98, 11-10-98, 12-11-98  
 01-29-99, 07-15-99

##### **Labsphere Spectral Reflectance Target (SRT-SP-100) 10" x 10" White/Grey**

Calibrated: 04-25-1996 (Labsphere)  
 Measured: 09-05-96  
 05-30-97, 11-26-97  
 06-10-98

##### **Labsphere Spectral Reflectance Target (SRT-99-100) 10" x 10" White**

Calibrated: 04-26-1996 (Labsphere)  
 Measured: 09-05-96  
 05-30-97, 11-26-97  
 06-10-98

##### **Labsphere Spectral Reflectance Target (CSTM-SRT-10-100) 10" x 10" Grey**

Calibrated: 10-29-1998 (Labsphere)  
 Measured: 11-10-98, 12-11-98

Cal-plan: Semi-annually and as required by NRL, TEC, and SITAC deployment of reflectance targets. The plaques will be interrogated using the OL 750

Measurement System over the 300-1100nm range in 5nm increments, and over the 1125-2500nm range in 25nm increments. The STU will be configured with the high intensity source, 1.25mm entrance slit, 1.5mm exit aperture, and the mirror collimating optics module. The measurement system will be calibrated using appropriate standard and nadir reflectance will be recorded for viewing angle of 15°, 30°, and 45°.

## **5.0 OTU-Optical Transfer-Function Test Unit**

### **4.0 Inch Adjustable Optical Slit Assembly**

Calibrated: yearly  
Measured: 03-15-96 (RY)  
09-23-97  
03-11-98

Cal-plan: Semi-annually calibration of the adjustable optical slit assembly. The optical slit calibration will consists of measuring the fringe pattern, a three point measurement across the slit at 0.5 inches from the top, the center, and 0.5 inches from the bottom, and a dial calibration of the micrometer.

#### **IV. Mesoscale Research Contributions From North Carolina State University**

The research that was performed by NCSU under this project during this period consisted of:

1. Diabatic initialization of the NRL/NCSU model and application to a mid-latitude and a tropical region.
2. Use of multi variate analysis for initialization.
3. Simulation of an extra-tropical cyclone using ERICA data.
4. Assimilation of surface data for mesoscale weather forecasting.
5. Simulation of monsoon boundary layer processes.
6. Non-hydrostatic mesoscale modeling.
7. Interaction of a hurricane with an upper tropospheric trough.
8. Assimilation of dropwindsondes in a mesoscale model.
9. Evaluation of cumulus parameterizations for use in mesoscale modeling.

Results from this research were published in fifteen refereed scientific papers in international journals. Also, five Ph.D. dissertations and one M.S.thesis were based on this research. Important findings are listed below:

- Diabatic initialization improves the mesoscale weather forecast in mid-latitudes and in the tropics.
- Initialization using the Bratseth scheme of multivariate analysis provides another improvement to a mesoscale weather forecast.
- The NRL/NCSU model was able to predict the structure and movement of the ERICA (Extra Tropical Rapid Intensification of Cyclones in the Atlantic) IOP 4 cyclone. Results agreed with SSM/I observations of rainfall.
- An assimilation technique for surface data was developed and tested for a GALE case. This assimilation again improves the forecast.
- The NRL/NCSU model is able to perform well in the tropics and is able to predict monsoon boundary layer processes well. This includes the Somali jet over the Arabian Sea and the monsoon trough in north India.
- A non-hydrostatic model (a prior version of COAMPS) was tested for the case of mesoscale convection induced by sea breezes in Florida.
- Large scale processes associated with an upper tropospheric trough interact with the outflow jet and influence the structure and track of a tropical cyclone. Hurricane Florence (1988) was used for this study.
- Including additional data such as dropwindsondes improved the forecast of the intensity and track of tropical cyclones. However, the assimilation is to be done selectively for best results. Hurricane Florence (1988) was used for this study.
- Betts-Miller cumulus parameterization does well in monsoon weather forecasting.

The above research is described in further detail in a number of publications that are included in Appendices as follows:

Appendix E - Ruggiero, F.H.\*, K.D. Sashegyi, R.V. Madala and S. Raman, 1996: Diabatic Initialization of Stratiform Precipitation for a Mesoscale Model, *J. Applied Meteorology*, 35, 1111-1128.

Appendix F - Ruggiero, F.H.\*, K.D. Sashegyi, R.V. Madala and S. Raman, 1996: The Use of Surface Observations in Four-Dimensional Data Assimilation in a Mesoscale Model, *Monthly Weather Review*, 124, 1018-1033.

Appendix G - Alapaty, K., S. Raman, R.V. Madala and U.C. Mohanty, 1994: Monsoon rainfall simulations with the Kuo and Betts-Miller schemes, *Meteorology and Atmospheric Physics*, 53, 33-49.

Appendix H - Alapaty, K., S. Raman and R.V. Madala, 1994: Simulation of monsoon boundary layer processes using a regional scale nested grid model, *Boundary-Layer Meteorology*, 67, 407-426.

Appendix I - Alapaty, K., R.V. Madala, S. Raman and J.J. Baik, 1994: Numerical simulation of orographic-convective rainfall with Kuo and Betts-Miller cumulus parameterization schemes, *J. of Meteor. Soc. of Japan*, 72, 123-137.

Appendix J - Alapaty, K., R.V. Madala and S. Raman, 1993: Sensitivity of monsoon rainfall predictions to initialization procedures, *Atmospheric Research*, 30, 157-170.

Appendix K - Sashegyi, K.D., D.E. Harms, R.V. Madala and S. Raman 1993: Application of the Bratseth scheme for the analysis of GALE data using a mesoscale model, *Monthly Weather Review*, 121, 3184-3190.

Appendix L - Harms, D.E., R.V. Madala, S. Raman and K. Sashegyi 1993: Diabatic initialization tests using the Naval Research Laboratory limited-area numerical weather prediction model, *Monthly Weather Review*, 121, 3184-3190.

Appendix M - Xu, L., R.V. Madala, and S. Raman 1997: A study of the effect of the Gulf Stream and the Appalachian Mountains on Carolina coastal frontogenesis using a nonlinear numerical model, *Nonlinear Studies*, 4, 53-68.

## **Appendix A**

### **Impact of Assimilations of Dropwindsonde Data and SSM/I Rain Rates on Numerical Predictions of Hurricane Florence (1988)**

## Impact of Assimilations of Dropwindsonde Data and SSM/I Rain Rates on Numerical Predictions of Hurricane Florence (1988)

JAINN JONG SHI

*Science Applications International Corporation, McLean, Virginia*

SIMON CHANG

*Naval Research Laboratory, Monterey, California*

SETHU RAMAN

*Department of Marine, Earth and Atmospheric Sciences, North Carolina State University at Raleigh, Raleigh, North Carolina*

(Manuscript received 27 June 1995, in final form 20 November 1995)

### ABSTRACT

Numerical experiments were conducted to assess the impact of Omega dropwindsonde (ODW) data and Special Sensor Microwave/Imager (SSM/I) rain rates in the analysis and prediction of Hurricane Florence (1988). The ODW data were used to enhance the initial analysis that was based on the National Meteorological Center/Regional Analysis and Forecast System (NMC/RAFS) 2.5° analysis at 0000 UTC 9 September 1988. The SSM/I rain rates at 0000 and 1200 UTC 9 September 1988 were assimilated into the Naval Research Laboratory's limited-area model during model integration.

Results show that the numerical prediction with the ODW-enhanced initial analysis was superior to the control without ODW data. The 24-h intensity forecast error is reduced by about 75%, landfall location by about 95% (reduced from 294 to 15 km), and landfall time by about 5 h (from 9 to 4 h) when the ODW data were included. Results also reveal that the assimilation of SSM/I-retrieved rain rates reduce the critical landfall location forecast error by about 43% (from 294 to 169 km) and the landfall time forecast error by about 7 h (from 9 to 2 h) when the NMC/RAFS 2.5° initial analysis was not enhanced by the ODW data. The assimilation of SSM/I rain rates further improved the forecast error of the landfall time by 4 h (from 4 to 0 h) when the ODW data were used. This study concludes that numerical predictions of tropical cyclone can benefit from assimilations of ODW data and SSM/I-retrieved rain rates.

### 1. Introduction

The current conventional observation networks and assimilation scheme cannot routinely define tropical cyclone structure and reliable steering flows (Bender et al. 1991; Lord 1991; Davidson and Puri 1992). The accurate description of the initial conditions in numerical simulations of the tropical cyclone usually suffers from two main deficiencies. The first is the lack of observational data over tropical oceans. This is an important factor limiting the improvement of numerical model simulations and the accuracy of hurricane track forecasts (Neumann 1981). A reasonably good density and accuracy of observations are required to initialize hurricane models (Anthes 1982). The second is that prediction models do not accurately reproduce the tem-

poral and spatial distribution of latent heating (up to  $300 \text{ K day}^{-1}$ ), which is the major energy source to drive a hurricane circulation and determine its intensity.

Franklin and DeMaria (1992) demonstrated that the Omega dropwindsonde (ODW) data collected during the 1982–89 synoptic flow experiments resulted in highly consistent reductions in track forecast errors in a barotropic track forecast model. In addition, they demonstrated the ability of utilizing all the data available with a scale-controlled objective analysis described by Ooyama (1987). Their results suggest that the collection of the ODW data in the hurricane environment can be a viable, cost-effective means of improving operational hurricane forecasts. Furthermore, Franklin et al. (1993) used the ODW data in a nested objective analysis scheme following Ooyama (1987) and DeMaria et al. (1992) to determine the kinematic structure of Hurricane Gloria (1985). They asserted that the nested analyses of Hurricane Gloria, based on the ODW and Doppler radar data, were the most complete kinematic analyses of a single hurricane constructed to date.

Corresponding author address: Dr. Jaiinn Jong Shi, Naval Research Laboratory, Code 7335, 4555 Overlook Ave., SW, Washington, DC 20375.  
E-mail: shi@metcomp.nrl.navy.mil



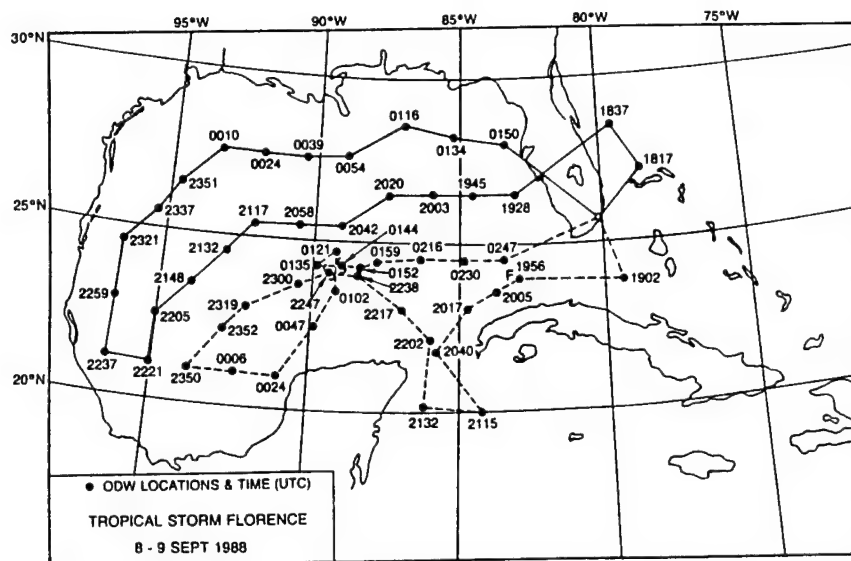


FIG. 1. Location and time (UTC) of the Omega dropwindsonde data collected during the AOML/HRD synoptic flow experiment on 8-9 September 1988.

Despite numerous research efforts, the lack of an accurate reproduction of the temporal and spatial distribution of latent heating remains a major factor contributing to the poor performance in numerical tropical cyclone prediction. Diabatic heat sources, which include latent heating, are generally poorly observed and seldom assimilated in the initial conditions, especially for tropical cyclones (Davidson and Puri 1992). Model forecasted latent heating may not occur in the right place at the right time if the latent heat sources are improperly defined in the initial conditions. Horizontal divergence and moisture fields, crucial variables toward determining the latent heating, are usually poorly analyzed in objective analyses, resulting in the delay of the onset of precipitation or the so-called spinup problem (Chang and Holt 1994). Efforts have been made to assimilate the observed or satellite-retrieved rain rates into numerical models in the past. Molinari (1982) successfully assimilated a relatively small area of radar-observed rain rates into a numerical model to improve the simulation of a hurricane. Idealized rain rates were incorporated into a mesoscale hurricane model by using dynamic initialization (Fiorino and Warner 1981). Chang and Holt (1994) assimilated the Special Sensor Microwave/Imager (SSM/I) rain rates into a limited-area numerical model to simulate a rapidly moving and intensifying extratropical marine cyclone. Their results showed that the assimilation of the SSM/I rain rates cut the intensity forecast error by 50%. These studies have demonstrated that the assimilation of the observed rain rates may have a positive impact on the numerical prediction of tropical and extratropical cyclones.

The primary objective of this study is to investigate the impact of ODW data and the SSM/I rain rates on

a numerical prediction of Hurricane Florence (1988). To accomplish this, a research version of the Navy Operational Regional Atmospheric Prediction System (NORAPS) of the Naval Research Laboratory (NRL), which includes an objective analysis, a vertical-mode initialization (VMI) and a limited-area numerical model, will be used.

## 2. Data sources

The data used for this study were acquired from three different sources: 1) the National Meteorological Center/Regional Analysis and Forecasting System (NMC/RAFS, the NMC is now referred to as the National Centers for Environmental Prediction) 2.5° analyses at 0000 UTC 9 September 1988; 2) the Omega dropwindsonde (ODW) data collected during a synoptic flow experiment (1988) from the Hurricane Research Division (HRD) of the Atlantic Oceanographic and Meteorological Laboratory (AOML) of the National Oceanic and Atmospheric Administration (NOAA); 3) the SSM/I data from the NRL archives. The NMC/RAFS 2.5° analyses were used as the first guess (background data) in the nested-grid analysis scheme that will be discussed in section 5. The ODW data were used to enhance the NMC/RAFS 2.5° analyses. The SSM/I rain rates were assimilated into the numerical model as observational rain rates in the model simulations. The SSM/I data were used for both assimilation and the verification.

Since 1982, synoptic flow experiments have been conducted by the AOML/HRD. The experiments are designed to determine the three-dimensional structure of tropical cyclones below approximately 400 mb from roughly 1000 km of the storm's center out (Kaplan and

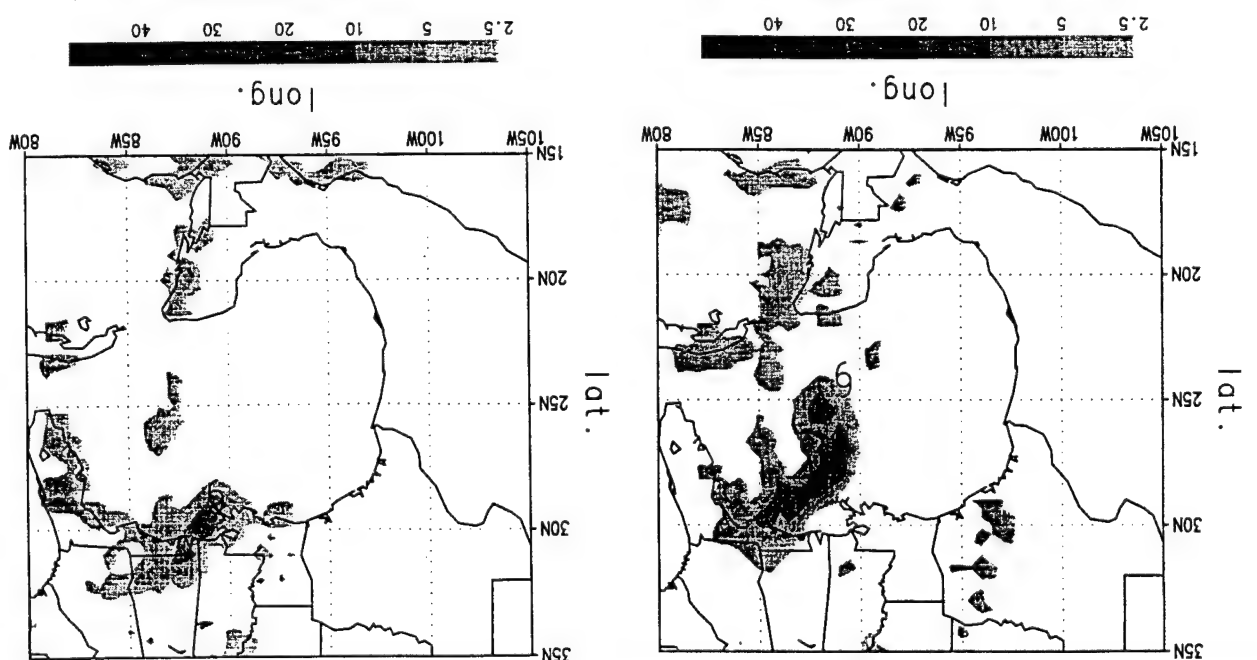


FIG. 4. Same as Fig. 3 except for 1200 UTC 9 September.

FIG. 5. Same as Fig. 3 except for 0000 UTC 10 September.

Mexico on 7 September. The frontal cloud band had previously been associated with a cold front, which entered the Gulf of Mexico from the northeast several days earlier. Florence was classified as a tropical depression with a maximum wind speed of 25 kt and a central pressure of 1000 mb at 0000 UTC 7 September. The depression quickly intensified into a tropical storm with a maximum wind speed of 40 kt and a central pressure of 998 mb at 1800 UTC 7 September. It moved eastward in the following 24 h and then turned northward on 8 September. The SSM/I rain rates at 0000 UTC 9 September (Fig. 3) show that the maxi-

Date	Time (UTC)	Position	Pressure (mb)	Wind (m s <sup>-1</sup> )	Stage
7 Sep	0600	22.8°N, 92.0°W	1000	12.9	Tropical depression
	1200	22.8°N, 91.2°W	998	15.4	Tropical depression
8 Sep	1800	22.7°N, 90.2°W	996	20.6	Tropical storm
	0000	22.6°N, 89.6°W	993	23.1	Tropical storm
	0600	22.7°N, 89.8°W	990	23.1	Tropical storm
	1200	23.1°N, 89.7°W	990	23.1	Tropical storm
9 Sep	1800	23.4°N, 89.5°W	992	23.1	Tropical storm
	0000	24.2°N, 89.2°W	992	25.7	Tropical storm
	0600	25.0°N, 89.2°W	991	25.7	Tropical storm
	1200	26.1°N, 89.2°W	988	28.3	Tropical storm
10 Sep	1800	27.4°N, 89.2°W	985	33.4	Hurricane
	0000	28.7°N, 89.3°W	983	36.0	Hurricane
	0600	29.7°N, 89.7°W	988	30.9	Tropical storm
	1200	30.7°N, 90.7°W	998	15.4	Tropical depression
11 Sep	1800	31.8°N, 91.5°W	1003	10.3	Tropical depression
	0000	32.4°N, 92.3°W	1007	7.7	Tropical depression
	0600	32.7°N, 93.3°W	1009	7.7	Tropical depression
	1200	33.0°N, 94.5°W	1010	7.7	Tropical depression
9 Sep	2300	28.5°N, 89.3°W	982	36.0	Minimum pressure
	0200	29.1°N, 89.3°W	984	36.0	Landfall

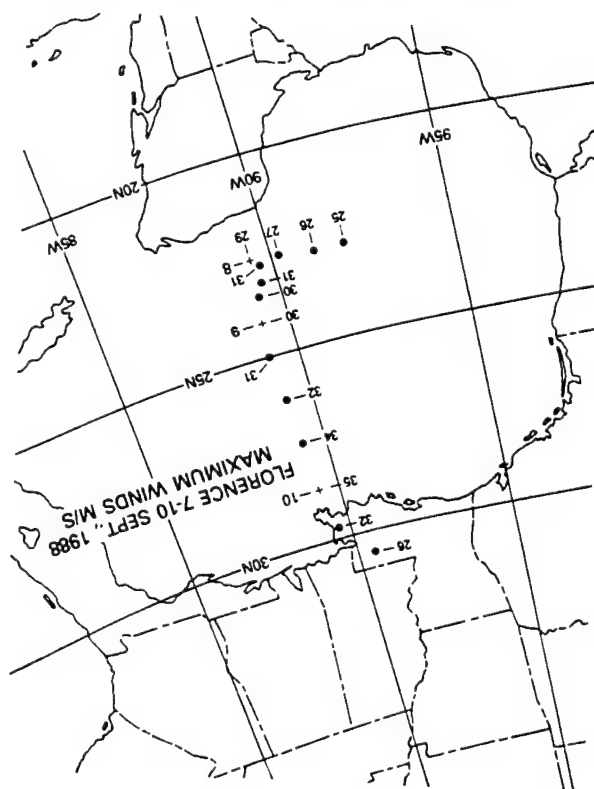
TABLE 1. Best track record of Hurricane Florence (1988), obtained from the National Hurricane Center (NHC) in Miami, Florida.

quency, linearly polarized, passive radiometric system that measures upwelling microwave radiation from the atmosphere and the surface of the earth at 19.3, 22.0, 37.0, and 85.5 GHz (Hollinger 1989 and 1991; Ferriday and Avery 1994). Recent studies (Velden et al. 1989; Rodgers et al. 1991; Alliss et al. 1992, 1993; Chang et al. 1993; Rodgers et al. 1994; Chang and Holt 1994; Rao and MacArthur 1994) have validated the usefulness of the meteorological parameters derived from the SSM/I brightness temperature data for observational and numerical studies. Goerss and Phoebus (1992) reported the operational use of SSM/I wind speed in the Navy Operational Global Atmospheric System (NOGAPS). Chang et al. (1993) found that the SSM/I-retrieved precipitation patterns are very useful in subjective analysis over data-sparse oceans. The SSM/I rain rates used in this study were derived from three SSM/I passes over Florence at 0000 UTC and 1200 UTC 9 September and 0000 UTC 10 September 1988, based on the algorithm described in Hollinger (1991).

### 3. Synoptic review of Hurricane Florence (1988)

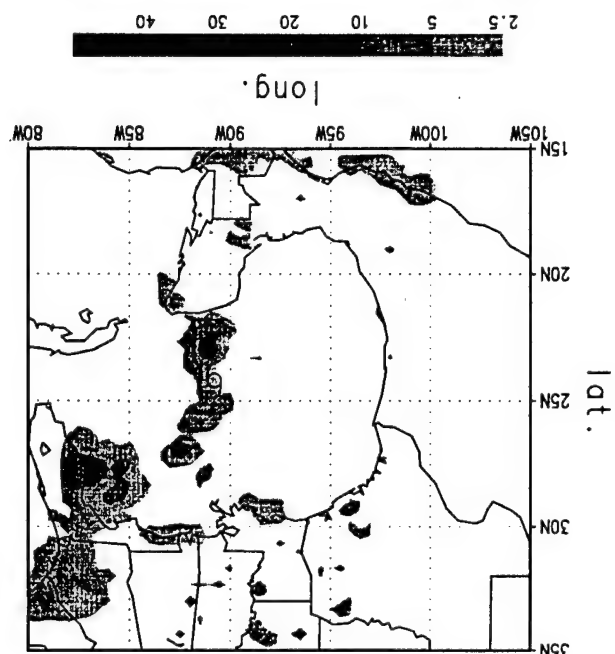
Figure 2, adapted from Rodgers et al. (1991), shows Florence's position and intensity (maximum wind in meters per second) every 6 h between 0600 UTC 7 September and 1200 UTC 10 September 1988. Hurricane Florence's circulation developed from a quasi-stationary frontal cloud band in the south-central Gulf of

FIG. 2. Position and intensity (maximum winds in meters per second) of Hurricane Florence (7–10 September) every 6 h. Crosses from Rodgers et al. (1991).



Franklin 1991; Franklin et al. 1991; Franklin and DeMaria 1992). During each field experiment, a set of ODW sondes were deployed from NOAA WP-3D aircraft flights at the level near 400 mb over the region surrounding the targeted tropical storm. A total of 51 ODW datasets were obtained from two NOAA WP-3D aircrafts during the synoptic flow experiment on 8–9 September 1988. These data make a better description of the initial conditions for the numerical simulation of Florence possible. Figure 1 shows the two flight routes and the location and release time of each ODW deployment in the synoptic flow experiment. The release times started at 1817 UTC 8 September 1988 and ended at 0247 UTC 9 September 1988. Each ODW record consisted of the time and location of launch (longitude and latitude), and the sounding data were recorded every 10 mb from the flight level (ranging from 374 to 528 mb) to the surface. The sounding data included pressure, temperature, relative humidity, geopotential height, wind direction, wind speed, and wind uncertainty. The wind data were missing in the lowest few levels near the surface in every ODW record. Onboard Defense Meteorological Satellite Program (DMSP) satellites, SSM/I is a seven-channel, four-fire-

FIG. 3. SSM/I-retrieved rain rates ( $\text{mm h}^{-1}$ ) at 0000 UTC 9 September. The hurricane symbol depicts the location of Florence's center.



(MCSST) data derived from AVHRR (Advanced Very High Resolution Radiometer) imagery. This MCSST product is a weekly composite at a horizontal resolution of approximately 18 km. The model uses a modified Kuo scheme for cumulus convection (Kuo 1965; Anthes 1977). The large-scale precipitation occurs when there is a supersaturated layer in the model. The excess moisture is condensed out isobarically with the released latent heat warming the air, leaving the layer saturated. Model physics also includes horizontal diffusion and dry convection adjustment.

### 5. Assimilation of the ODW data

The ODW data were used to enhance the NMC/RAFS 2.5° analyses at 0000 UTC 9 September. In a previous treatment of the ODW data for Florence, Kaplan and Franklin (1991) used a nested objective analysis scheme (Ooyama 1987), which employs a two-dimensional, least squares fitting algorithm with a derivative

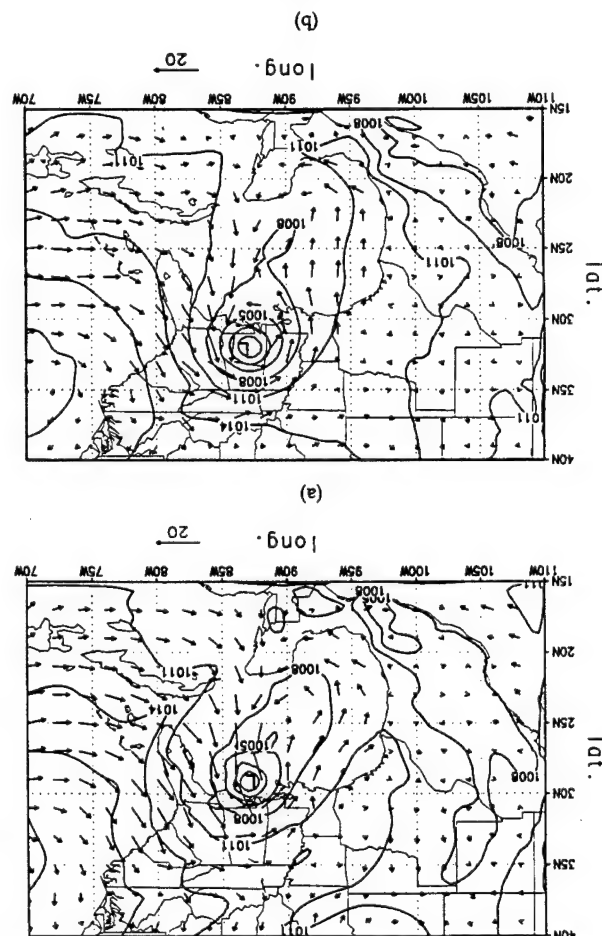


FIG. 9. Same as Fig. 7 except for the NMC/RAFS 2.5° analysis at (a) 1200 UTC 9 September and (b) 0000 UTC 10 September.

field and induces smaller changes to the initial mass and wind fields as compared to static initialization schemes.

The limited-area prognostic model is a three-dimensional, hydrostatic, primitive equation model incorporating a split-explicit time integration scheme (Madala et al. 1981). Details of the model are described in Madala et al. (1987), Chang et al. (1989), and Holt et al. (1990). The version of the model used in this study has 23 layers in the vertical. A terrain following  $\sigma (=P/P_s)$  vertical coordinate and time-dependent lateral boundary conditions are utilized, where  $P$  is the pressure and  $P_s$  the surface pressure. Topography used in this model is derived from the United States Navy global 10' elevation data. The model domain covers 15°–45°N, 110°–65°W including most of the continental United States and all the Gulf of Mexico, with horizontal resolutions of  $1/2^\circ$  and  $1/3^\circ$  in longitude and latitude directions, respectively.

The sea surface temperature analysis is obtained from the multichannel sea surface temperature

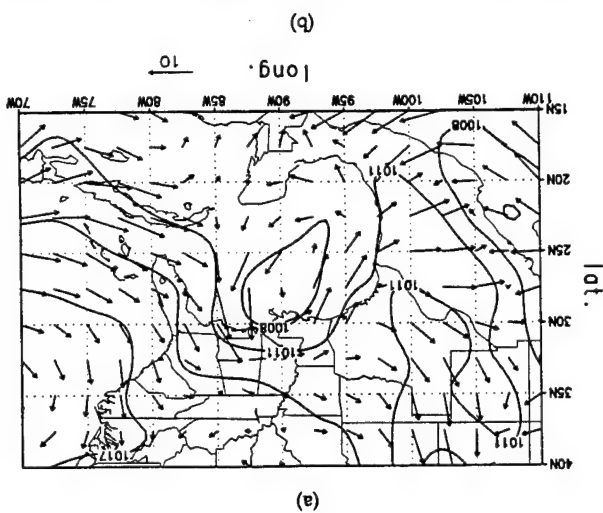


FIG. 10. Sea level pressures (mb) and 1000-mb winds ( $m s^{-1}$ ) from the control experiment at (a) 12 h and (b) 24 h, valid at 1200 UTC 9 September and 0000 UTC 10 September, respectively.

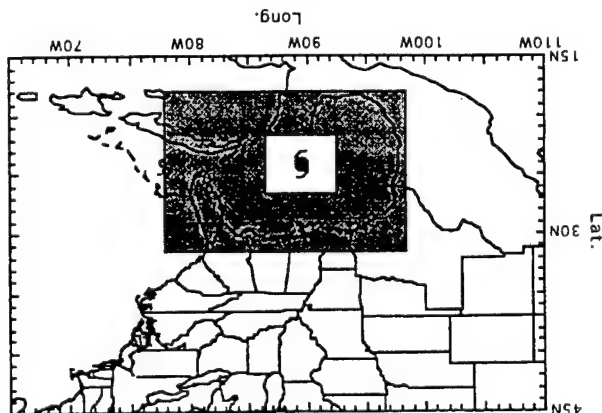


FIG. 6. Analysis domain for the nested three-pass objective analysis. Shaded area is for the first and second pass. Plain area inside the shaded area is for the third pass. The hurricane symbol depicts the location of Florence's center at 0000 UTC 9 September.

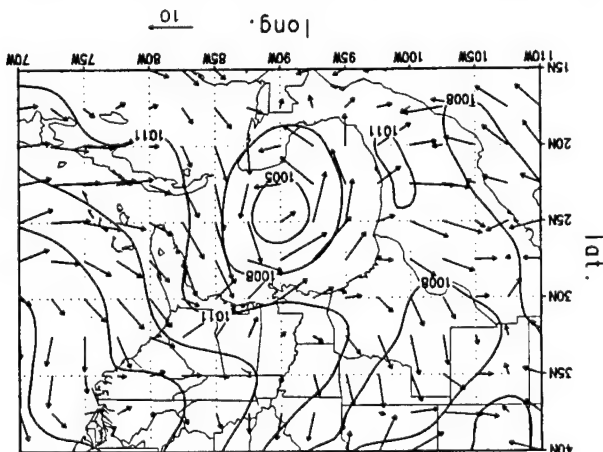


FIG. 7. Sea level pressures (mb) and 1000-mb winds ( $\text{m s}^{-1}$ ) from the NMC/RAFS 2.5° analysis at 0000 UTC 9 September.

#### 4. Regional analysis and forecast system

The research version of the NORAPS/NRL employed in this study includes a data assimilation system, a VMI, and a limited-area numerical model. The data assimilation includes two steps. The first step is a data preparation and quality control scheme and the second step is an objective analysis scheme. The data quality control consists of a "gross" check and a "buddy" check following DiMego (1988). Two different objective analysis schemes are available for the NRL model—a three-pass nested-grid Barnes scheme and a single-grid multivariate, successive correction objective scheme using the Bratseth method (Sashegyi et al. 1993). In this study, the three-pass nested-grid Barnes scheme was used. The vertical-mode initialization of NRL is described in Sashegyi and Madala (1993). This VMI scheme produces a balanced vertical motion

span of Florence's circulation lasted only for about 4 days. According to the best track data from the National Hurricane Center (NHC), Florence attained hurricane force for only 12 h, between 1200 UTC 9 September and 0600 UTC 10 September (Table 1). Estimated from the Air Force reconnaissance flight data, the highest sustained surface wind was  $36 \text{ m s}^{-1}$  and the lowest surface pressure 982 mb, occurring at 2300 UTC 9 September, just 3 h before landfall. Rainfall totals of up to 100 mm were observed along the path of the storm (Lawrence and Gross 1989). Florence caused the water level to rise from 1 to 2 m above normal along the southeast Louisiana and Mississippi coast just east of where the center moved ashore.

According to the best track data from the National Hurricane Center (NHC), Florence attained hurricane force for only 12 h, between 1200 UTC 9 September and 0600 UTC 10 September (Table 1). Estimated from the Air Force reconnaissance flight data, the highest sustained surface wind was  $36 \text{ m s}^{-1}$  and the lowest surface pressure 982 mb, occurring at 2300 UTC 9 September, just 3 h before landfall. Rainfall totals of up to 100 mm were observed along the path of the storm (Lawrence and Gross 1989). Florence caused the water level to rise from 1 to 2 m above normal along the southeast Louisiana and Mississippi coast just east of where the center moved ashore.

FIG. 8. Sea level pressures (mb) and 1000-mb winds ( $\text{m s}^{-1}$ ) from the ODW enhanced analysis at 0000 UTC 9 September.

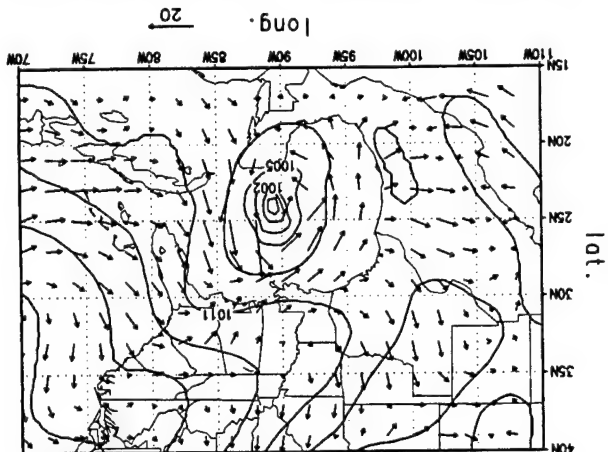


TABLE 2. Minimum SLP (mb), maximum wind speed ( $\text{m s}^{-1}$ ), and location of storm center from the best track record, the control experiment, and experiment ODW.

	0 h	6 h	12 h	18 h	24 h
Minimum sea level pressure (mb)					
Best track record	992	991	988	985	983
Control	1006	1003	996	995	997
ODW	1005	1001	997	988	987
Maximum surface wind speed ( $\text{m s}^{-1}$ )					
Best track record	25.7	25.7	28.3	33.4	36.0
Control	14.1	23.7	33.6	28.6	22.2
ODW	28.4	24.4	30.4	35.8	38.8
Location of storm center					
Best track record	24.2°N, 89.2°W	25.2°N, 89.2°W	26.1°N, 89.2°W	27.4°N, 89.2°W	28.7°N, 89.3°W
Control	24.9°N, 89.9°W	27.3°N, 87.1°W	29.1°N, 87.1°W	30.7°N, 86.8°W	32.1°N, 86.7°W
ODW	24.3°N, 89.4°W	25.6°N, 88.6°W	27.1°N, 88.8°W	28.5°N, 89.1°W	29.6°N, 89.3°W

constraint term, to analyze the ODW data. The derivative constraint term functions as a spatial low-pass filter on the analyzed field. In the present study, a three-pass nested-grid Barnes scheme was used. A time domain of 6 h from 2100 UTC 8 September to 0300 UTC 9 September was imposed to filter out the ODW data outside this time domain. The choice of a 6-h time domain centered at 0000 UTC 9 September was simply based on a 3-h data cutoff time commonly used in many operation forecasting centers.

The NMC/RAFS 2.5° analyses were bicubically interpolated to the model's grid as shown in Fig. 6, and used as the first guess. The first guess data were then bilinearly interpolated to the ODW data locations. The three-pass nested-grid Barnes scheme was employed to analyze the corrections that resulted from subtracting the interpolated first guess data from the ODW data. The analyzed corrections were then added back to the first guess at each grid point. The first two passes of the Barnes scheme were done in the shaded area including the plain area inside the shaded area, while the third pass was done only in the plain area (Fig. 6) using the analyzed results from the first two passes as the background data. The horizontal resolution was  $1/2^\circ$  in the first two passes and  $1/6^\circ$  in the third pass. The selection of the two resolutions for the three passes in the objective analysis was to match the varying ODW data resolutions over the Gulf of Mexico area (Fig. 1). The details and results of the ODW enhanced analyses for Hurricane Florence (1988) were documented in Shi et al. (1991) and Shi (1993). Figures 7 and 8 show the sea level pressures and 1000-mb isotaches from the NMC/RAFS 2.5° and the ODW enhanced analyses at 0000 UTC 9 September, respectively. It is apparent that the ODW enhanced analyses provide a more realistic depiction of Florence. Both the NMC/RAFS 2.5° and the ODW enhanced analyses were initialized by the

VMI and used as the initial data for the model integration of the various numerical experiments.

## 6. Assimilation of the SSM/I rain rates

As mentioned earlier, a modified Kuo scheme is used in the numerical model for cumulus convection. Following the discussion in Chang and Holt (1994), the convective latent heating at a grid point in the model with the modified Kuo convective scheme is

$$\frac{\delta T}{\delta t} = \frac{bgLM_i(T_c - T)}{C_p P_s \int_{\sigma} (T_c - T) d\sigma}, \quad \text{if } M_i > 0, \quad (1)$$

where  $b$  is a partitioning parameter set equal to the vertical mean relative humidity;  $T_c$ , the cloud temperature;  $L$ , the specific latent heat;  $C_p$ , the specific heat at constant pressure of air; and  $P_s$ , the surface pressure. Here,  $M_i$  is the total moisture convergence defined as

$$M_i = \frac{P_s}{g} \int_{\sigma} -\nabla \cdot \mathbf{V} q d\sigma, \quad (2)$$

where  $q$  is the specific humidity. The rain rate  $\delta R / \delta t$  ( $\text{cm s}^{-1}$ ) in the model, which is related to the vertically integrated heating rate, is then defined at each grid point as

$$\frac{\delta R}{\delta t} = \frac{P_s C_p}{g \rho_w L} \int_{\sigma} \frac{\delta T}{\delta t} d\sigma, \quad (3)$$

where  $\rho_w$  is the density of liquid water. In the assimilation experiments presented here, the left-hand side of (3) was replaced by the SSM/I-retrieved rain rates in the area inside the SSM/I swath within the assimilation windows. The assimilation window was between 0 and 3 h of the integration for the SSM/I overpass at 0000



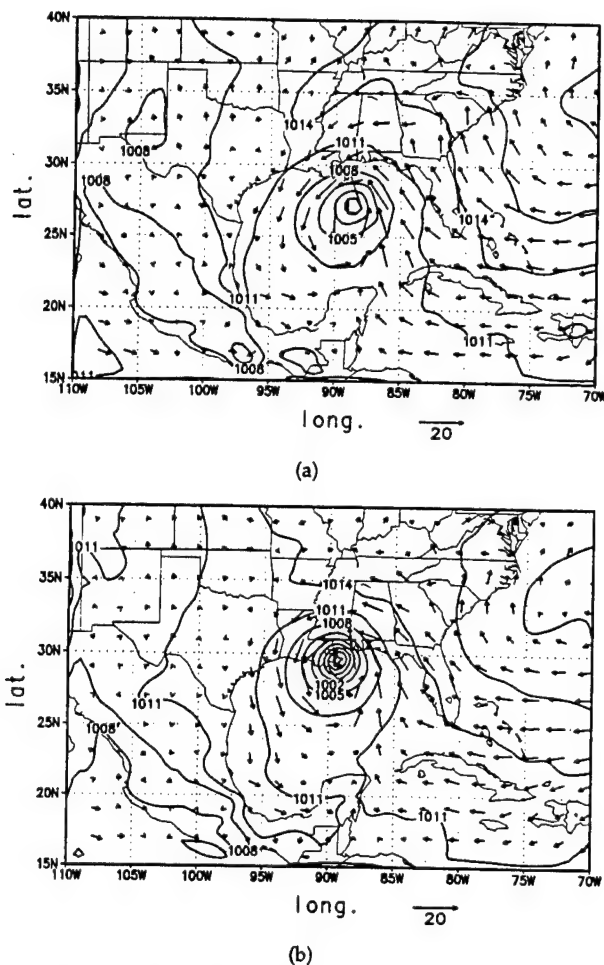


FIG. 11. Same as Fig. 10 except for experiment ODW.

UTC 9 September and 9–15 h for the SSM/I overpass at 1200 UTC 9 September. The rain rates outside the SSM/I swath were not changed.

## 7. Simulation results

To assess the impact of the ODW and the SSM/I rain rate data on the numerical simulation of Hurricane Florence (1988), model integrations using different initial data were conducted. All the model runs were started at 0000 UTC 9 September and integrated for 48 h. The first numerical simulation (the control experiment) used the NMC/RAFS 2.5° analyses at 0000 UTC 9 September as the initial condition, while the second experiment (experiment ODW) used the ODW enhanced analyses as the initial condition. The third (experiment control + SSMI) and the fourth (experiment ODW + SSMI) experiments were the same as the first and the second experiments, respectively, except that the SSM/I rain rates were assimilated into the model during the integration by using the approach described in the previous section. The last two experiments

were designed to study the impact of the SSM/I rain rates on the numerical simulation.

### a. Intensity

Figure 10 shows the sea level pressures (SLPs) and the 1000-mb wind vectors at 12 and 24 h from the control experiment valid at 1200 UTC 9 September and 0000 UTC 10 September. For comparison, Fig. 9 shows the NMC/RAFS 2.5° analyses at 1200 UTC 9 September and 0000 10 September. The minimum SLPs of the control experiment were 996 and 997 mb at 12 and 24 h, respectively. Compared with the best track record shown in Table 1 and the NMC/RAFS 2.5° analyses (Fig. 9), the simulated storm in the control experiment moved northward faster than the best track record and was much weaker than the best track record by an average of greater than 10 mb, but stronger than the storm depicted in the NMC/RAFS 2.5° analyses. The maximum surface wind speeds in the control experiment were 33.6 and 22.2  $\text{m s}^{-1}$  at 12 and 24 h, respectively (Table 2). The simulated storm at 24 h in the control experiment had a min-

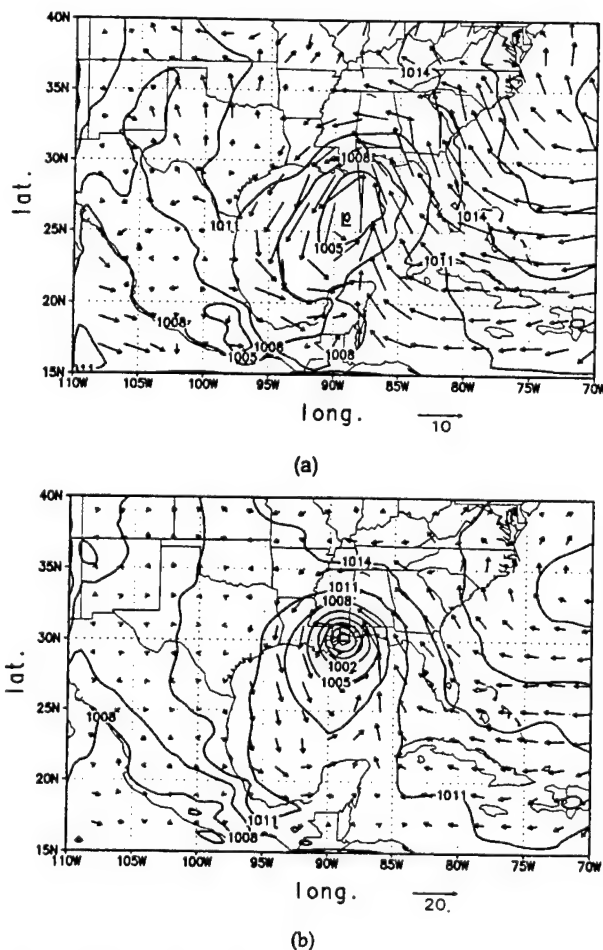


FIG. 12. Same as Fig. 10 except for experiment control + SSMI.

TABLE 3. Minimum SLP (mb), maximum wind speed ( $\text{m s}^{-1}$ ), and location of storm center from the best track record and experiments control + SSMI and ODW + SSMI.

	0 h	6 h	12 h	18 h	24 h
Minimum sea level pressure (mb)					
Best track record	992	991	988	985	983
Control + SSMI	1006	1004	1002	999	992
ODW + SSMI	1005	1003	999	992	985
Maximum surface wind speed ( $\text{m s}^{-1}$ )					
Best track record	25.7	25.7	28.3	33.4	36.0
Control + SSMI	14.1	20.3	23.1	29.3	32.3
ODW + SSMI	28.4	20.0	24.2	34.5	38.3
Location of storm center					
Best track record	24.2°N, 89.2°W	25.2°N, 89.2°W	26.1°N, 89.2°W	27.4°N, 89.2°W	28.7°N, 89.3°W
Control + SSMI	24.9°N, 89.9°W	25.3°N, 89.0°W	25.9°N, 89.1°W	27.4°N, 88.5°W	30.6°N, 88.9°W
ODW + SSMI	24.3°N, 89.4°W	25.5°N, 89.1°W	26.5°N, 89.4°W	27.5°N, 89.2°W	29.0°N, 89.6°W

imum SLP 14 mb higher and a maximum surface wind speed  $13.8 \text{ m s}^{-1}$  lower than what the best track indicated, a rather poor intensity forecast.

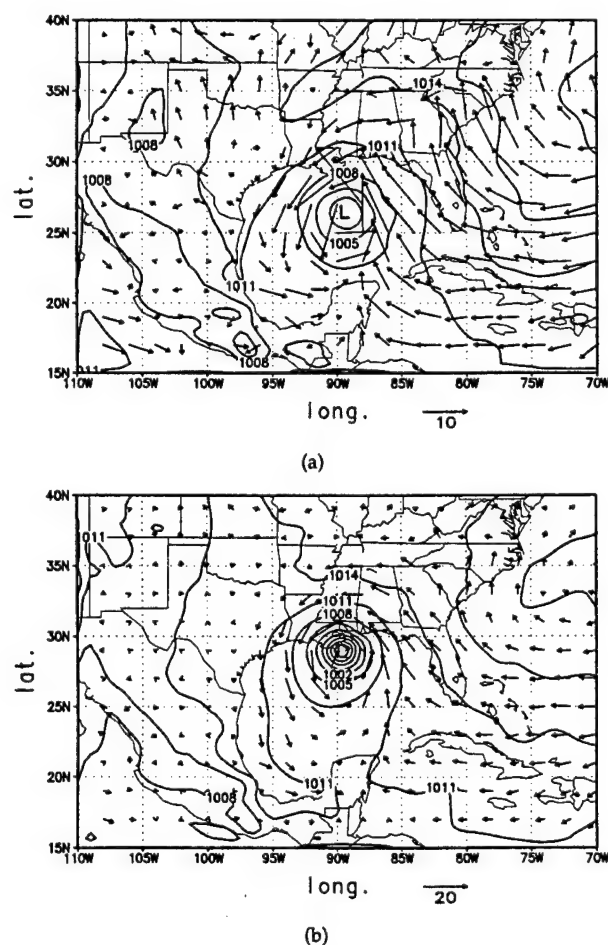


FIG. 13. Same as Fig. 10 except for experiment ODW + SSMI.

Experiment ODW was initialized on the ODW enhanced analysis, with the SLPs and the 1000-mb wind vectors at 12 and 24 h shown in Fig. 11. The minimum SLPs of the storm in experiment ODW were 997 and 987 mb at 12 and 24 h, respectively. The maximum surface wind speeds of the simulated storm in experiment ODW were  $30.4$  and  $38.8 \text{ m s}^{-1}$  at 12 and 24 h, respectively (Table 2). It is apparent that the intensity of the simulated storm in experiment ODW was stronger in comparison to the control experiment (Fig. 10) and in the NMC/RAFS  $2.5^\circ$  analyses (Fig. 9). The minimum SLP and maximum surface wind speed of experiment ODW at 24 h valid at 0000 UTC 10 September was about 4 mb weaker and  $2.8 \text{ m s}^{-1}$  stronger than the best track verification. The assimilation of the ODW data into the initial data has thus improved the intensity forecast relative to the control experiment by 10 mb for the minimum SLP and  $11 \text{ m s}^{-1}$  for the maximum surface wind speed at 24 h.

Figure 12 shows the SLPs and the 1000-mb wind vectors in experiment control + SSMI at 12 and 24 h. The minimum SLPs of the simulated storm in experiment control + SSMI were 1002 and 992 mb at 12 and 24 h, respectively (Table 3). The maximum surface wind speed of experiment control + SSMI at 12 and 24 h were  $23.1$  and  $32.3 \text{ m s}^{-1}$ , respectively (Table 3). Compared to the control experiment, the 24-h minimum SLP and maximum wind speed forecast in experiment control + SSMI valid at 0000 UTC September 10 were superior by 5 mb and  $10.1 \text{ m s}^{-1}$ , respectively, relative to the best track record.

Figure 13 shows the SLPs and the 1000-mb wind vectors in experiment ODW + SSMI at 12 and 24 h. The minimum SLPs at 12 and 24 h were 999 and 985 mb, respectively, and the corresponding maximum wind speeds were  $24.2$  and  $38.3 \text{ m s}^{-1}$ , respectively (Table 3). Comparing the results from experiment ODW and ODW + SSMI (Tables 2 and 3) with the



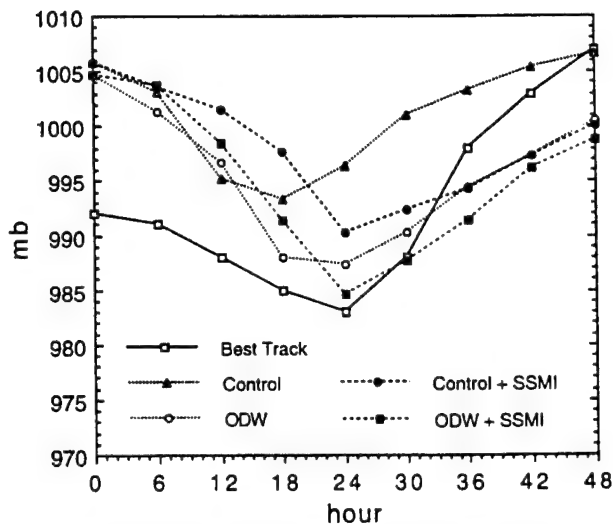


FIG. 14. Evolution of minimum sea level pressure of Florence with time in the best track record, the control experiment, and experiments control + SSMI, ODW, and ODW + SSMI.

best track record, the assimilation of the SSM/I rain rates in experiment ODW + SSMI has improved the 24-h prediction of the minimum SLP by 2 mb (down

from 987 mb in experiment ODW to 985 mb), and the maximum wind speed by  $0.5 \text{ m s}^{-1}$ . Although the assimilation of the SSM/I rain rates did not improve much over experiment ODW, it provided the best 24-h intensity forecast among all four model simulations. Figure 14 shows the evolution of the minimum SLP with time from the best track and all four experiments. It is obvious that experiment ODW + SSMI produced the best minimum SLP forecast at 24 h and the control experiment produced the worst. This study shows that both the ODW data and SSM/I rain rates made positive impacts on the numerical prediction of the intensity of Hurricane Florence (1988) at 12–30 h. At 48 h, however, the impact of the assimilation of both the ODW data and SSM/I rain rates diminished enough that the difference is not discernible. This also suggests that an update cycle with more frequent data assimilations is important for accurate numerical predictions.

#### b. Track

The 48-h tracks from the best track and all four experiments (Fig. 15) show that the simulated storm in the control experiment moved faster than the observation. The simulated storm in the control experiment

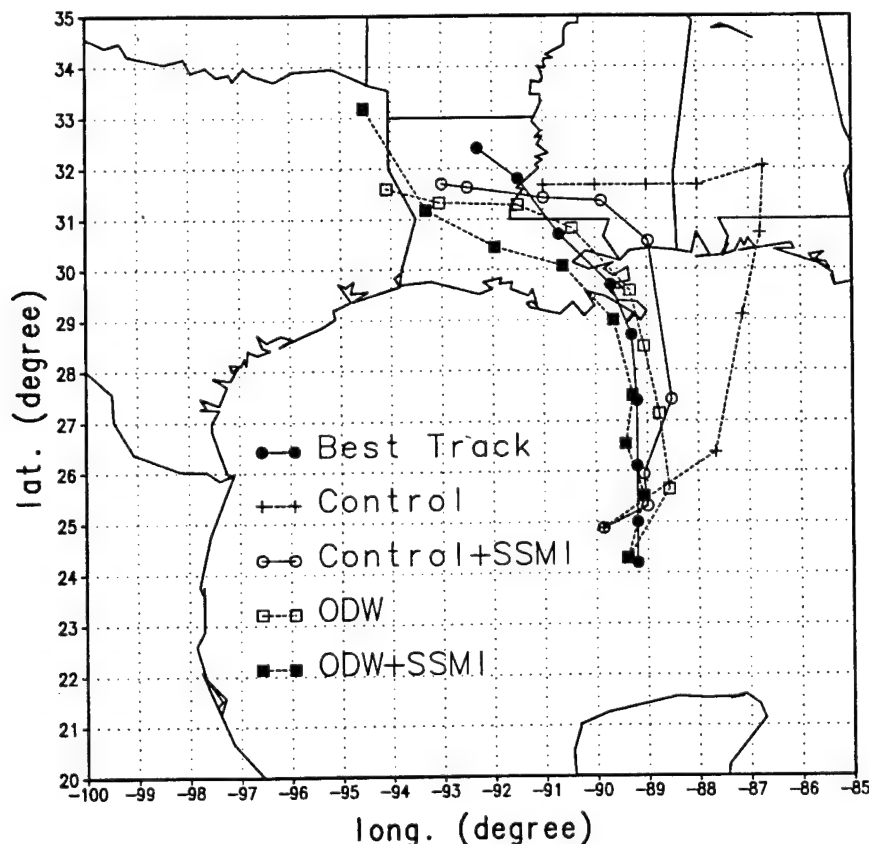


FIG. 15. Tracks of Florence in the best track record, control experiment, and experiments ODW, control + SSMI, and ODW + SSMI.

made landfall at 1700 UTC 9 September 1988, about 9 h (Table 4) earlier than the landfall time in the best track. The forecast landfall location was about 294 km northeast of the location in the best track. The track forecast in the control experiment is poor, mainly because the NMC/RAFS 2.5° analysis failed to resolve the storm properly and to provide the accurate environmental steering force. As listed in Table 4, it shows that the forecast storm in experiment control + SSMI made landfall only 2 h earlier than the landfall time in the best track and at a location about 169 km north of the location in the best track. This is an improvement of about 7 h in landfall time and 43% in landfall location over the control experiment. In experiment ODW, the landfall time was 4 h earlier than the actual landfall and the landfall location was about 15 km southeast of the actual landfall location. In experiment ODW + SSMI, the landfall time was exactly predicted and the landfall location was about 69 km northwest of the actual landfall location. While experiment ODW predicted the best landfall location, experiment ODW + SSMI produced the exact landfall time.

Among the four predicted tracks in Fig. 15, it is apparent that experiment ODW + SSMI produced the best forecast of the track of Hurricane Florence (1988). Because the initial storm location in the ODW enhanced analysis was better than in the NMC/RAFS 2.5° analysis, and the better wind analysis provided by the ODW data resulted in more accurate environmental steering, the predicted tracks in experiments ODW and ODW + SSMI were better than those in the control experiment and experiment control + SSMI. Figure 15 also shows that the storms in experiments control + SSMI and ODW + SSMI moved slower than those in the control experiment and experiment ODW. It is believed that the more accurate latent heating furnished by the SSM/I data effectively slowed down the movement of the predicted storms. It leaves no doubt that both ODW data and SSM/I rain rates have positive impact on the track forecast of Hurricane Florence (1988). However, the ODW data are relatively rare observations that require a nonordinary effort to collect them, while the SSM/I supplies near-real time and up to six observations per day depending on the latitude.

The track improvement shown in experiment Control + SSMI is significant. The predicted storm tracks in the second 24 h were less accurate than those in the first 24 h. This again underscores that an update cycle with more frequent data assimilations is needed.

### c. Precipitation pattern

The simulated rain rates at 24 h from the different experiments were compared to the verifying SSM/I rain rates at 0000 UTC 10 September 1988 (Fig. 5) to verify the model simulations and to investigate the impact of assimilations. At 24 h valid at 0000 UTC September 10, the heaviest rain rates ( $>20 \text{ mm h}^{-1}$ ) in the control experiment (Fig. 16) were located far inland in Georgia with the heavy rain-rate region stretching southward into the Gulf of Mexico. The heaviest SSM/I-observed rain rates ( $>15 \text{ mm h}^{-1}$ ) were located near New Orleans (see Fig. 5) at 0000 UTC September 10. It is apparent that the control experiment misplaced the precipitation of Florence mainly because of the poor location forecast. The heaviest forecasted rainfall ( $>40 \text{ mm h}^{-1}$ ) in experiment ODW at 24 h was located just off the coast of Mississippi in a northeast-southwest oriented rain band (see Fig. 17). The heavy rain-rate region started at the border of Alabama and Georgia and extended southwestward into the Gulf of Mexico off the Louisiana coast. The rainfall pattern in experiment ODW had the same northeast to southwest orientation as in the SSM/I rain rates (Fig. 5), except the SSM/I retrieval had a much lighter maximum rain rate ( $>15 \text{ mm h}^{-1}$ ). Previous studies have shown that the SSM/I rain rates are a good analysis tool for hurricanes (Rodgers et al. 1991; Alliss et al. 1992, 1993) and midlatitude marine cyclone studies (Chang et al. 1993). As pointed out in (Chang and Holt 1994), SSM/I rain-rate retrieval is invaluable in identifying the precipitation patterns in spite of the uncertainties in rain-rate estimates. This study has shown that the forecast rain patterns at 24 h in experiment ODW agreed well with the verifying SSM/I rain patterns.

With the assimilation of the SSM/I rain rates, the simulated rain rates in experiment control + SSMI (Fig. 18) at 24 h showed that the heaviest rain rates

TABLE 4. Landfall times and locations from the best track record, the control experiment, and experiments control + SSMI, ODW, and ODW + SSMI. The landfall locations relative to the location shown in the best track record are also listed.

	Landfall time	Landfall location	
		Lat./Long.	Relative location to best track
Best track record	0200 UTC 10 Sep 93	29.1°N, 89.3°W	
Control experiment	1700 UTC 9 Sep 93	30.5°N, 86.7°W	294 km northeast
Exp. control + SSMI	0000 UTC 10 Sep 93	30.6°N, 88.9°W	169 km north
Exp. ODW	2200 UTC 9 Sep 93	29.0°N, 89.2°W	15 km southeast
Exp. ODW + SSMI	0200 UTC 10 Sep 93	29.2°N, 89.9°W	69 km northwest

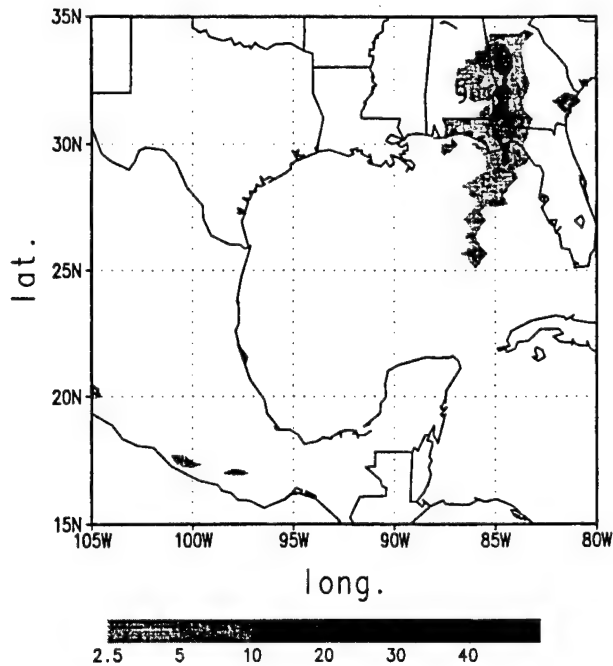


FIG. 16. Predicted rain rate ( $\text{mm h}^{-1}$ ) of the control experiment at 24 h valid at 0000 UTC 10 September. The hurricane symbol depicts the location of the predicted storm center.

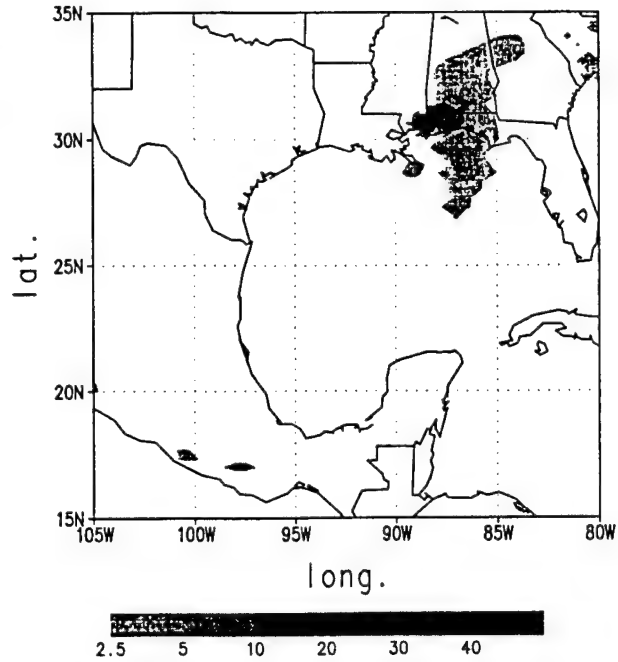


FIG. 18. Same as Fig. 16 except for experiment control + SSMI.

( $>40 \text{ mm h}^{-1}$ ) were located at southern Alabama and Mississippi near the coast and extended from central Alabama into the Gulf of Mexico. Comparison of Figs. 18 and 5 reveals that the simulated rain rates did not

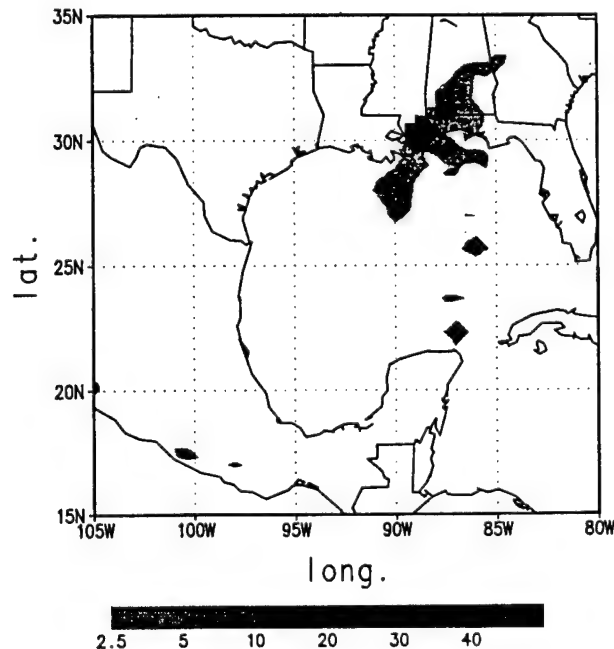


FIG. 17. Same as Fig. 16 except for experiment ODW.

agree well with the verifying SSM/I rain rates in pattern and intensity, but had improved on the poorly forecasted rain rates in the control experiment. The simulated rain rates in experiment ODW + SSMI at 24 h are shown in Fig. 19. The heaviest rain rates ( $>30 \text{ mm h}^{-1}$ ) were located just east of New Orleans and north of the Mississippi River delta. The pattern of the forecasted rain rates in this experiment was similar to the one in experiment ODW and the verifying SSM/I rain rates. However, the maximum intensity of the simulated rain rates was weaker than the maximum intensity ( $>40 \text{ mm h}^{-1}$ ) in experiment ODW.

## 8. Summary and discussion

Four numerical simulations were performed to assess the impact of ODW data and SSM/I rain rates on numerical forecasts of Hurricane Florence (1988). A nested three-pass Barnes scheme objective analysis was used to enhance the NMC/RAFS  $2.5^\circ$  analysis because of the relative high resolution of the ODW data near the center of Florence. The NMC/RAFS  $2.5^\circ$  analysis and the ODW enhanced analysis were then used as the initial conditions for the numerical prediction experiments. We found that the forecast error of the intensity was reduced from 14 to 4 mb with the assimilation of the ODW data. It is also clear from Table 4 that the ODW data reduced the forecast error of the landfall time in the control experiment by 5 h (down from 9 to 4 h), and the landfall location error by 95% (down from 294 to 15 km). The impact of the ODW data was

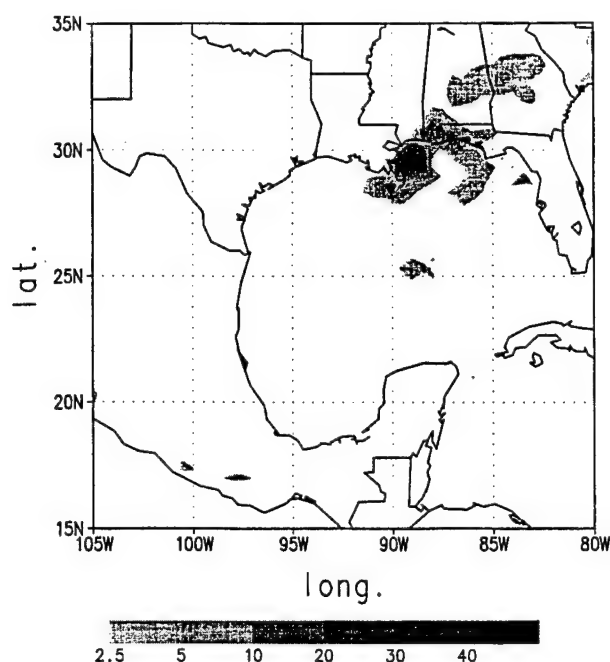


FIG. 19. Same as Fig. 16 except for experiment ODW + SSMI.

more pronounced in the first 24 h of the integration (Figs. 14 and 15) and gradually decreased beyond 24 h. This result is in agreement with Franklin and DeMaria (1992), in which a barotropic, nested, spectral hurricane track forecasting model was used to determine the impact of the ODW data. The advantage of using a three-dimensional primitive equation model with the inclusion of baroclinic and physical processes, as in this study, is that the model can simulate the hurricane structure in more detail (DeMaria et al. 1992). However, a major limitation of the ODW observations is that they do not provide information above 400 mb because of the altitude limitations of the NOAA WP-3D. While satellite-derived winds can provide some upper-level information (Velden et al. 1992), detailed observations of the three-dimensional structure of the upper levels of tropical cyclones are extremely scarce. Dropsonde data collected from 200 mb to the surface by the recent TCM-90 experiment (Elsberry and Abbey 1991) may be proven to be very useful in depicting the upper-level structure of tropical cyclones (Merrill and Velden 1996).

The rainfall rates retrieved from the SSM/I data at 0000 UTC and 1200 UTC 9 September 1988 were assimilated into the NRL limited-area model initialized with the NMC/RAFS 2.5° analysis (experiment control + SSMI) and the ODW enhanced analysis (experiment ODW + SSMI). Results indicate that the assimilation of the SSM/I rain rates (experiment control + SSMI) reduced the 24-h forecast errors in the landfall location in the control experiment by about 43% (down from 294 to 169 km), and the landfall time by 5 h (down

from 9 to 4 h). At mean time, the 24-h minimum SLP and maximum surface wind speed forecasts were also improved by 5 mb and  $10.1 \text{ m s}^{-1}$ , respectively. This study suggests that the assimilation of SSM/I rain rates can improve the track and intensity forecasts of tropical cyclones, especially when the ODW data are not available to the operational analysis. The benefit of the assimilation of SSM/I rain rates was limited when the simultaneous ODW data had already been assimilated into the initial condition, and vice versa. The landfall time error was reduced from 4 to 0 h, and there was an improvement on the predicted storm track when the SSM/I rain rates were assimilated. The intensity forecast was also improved with the 24-h minimum SLP forecast error reduced by 2 mb. There is no question that the combination of the ODW data and SSM/I rain rates provided the best simulation at 24 h in this study. Results from this study agree with the assessment of Chang and Holt (1994) regarding the positive impact of assimilating SSM/I rain rates on the numerical predictions. This study suggests that operational forecasts can benefit from the assimilation of ODW and SSM/I data into numerical models for the prediction of the intensity and track of tropical cyclones. The increase of the track forecast accuracy will allow forecasters to reduce the overwarned area in the warning process and result in reducing the preparation costs incurred by the public in coastal areas (Sheet 1990; Franklin et al. 1991). In any case study, the question arises whether or not the behavior shown is relevant to a large group of tropical cyclones. More studies need to be performed to further explore the value of both ODW and SSM/I data for the numerical forecast of tropical cyclones, especially when the ODW data collected from 200 mb to the surface become available from the AOML/HRD. The upper-tropospheric influence to the intensity and track change of tropical cyclones has long been recognized.

**Acknowledgments.** The authors wish to thank Dr. Keith Sashegyi of NRL for providing the help on NRL's data analysis system, Mr. Glenn Sandlin of NRL for providing the SSM/I imagery data, and Mr. Randy Alliss of North Carolina State University for processing the SSM/I imagery data for us. We also want to extend our appreciation to Dr. James Franklin of the AOML/HRD for providing the ODW data to the research community. The research was supported by the NRL basic research program.

#### REFERENCES

- Alliss, R. J., S. Raman, and S. Chang, 1992: Special Sensor Microwave/Imager (SSM/I) observation of Hurricane Hugo (1989). *Mon. Wea. Rev.*, **120**, 2723–2737.
- , G. D. Sandlin, S. W. Chang, and S. Raman, 1993: Application of SSM/I data in the analysis of Hurricane Florence (1988). *J. Appl. Meteor.*, **32**, 1581–1591.
- Anthes, R. A., 1977: A cumulus parameterization scheme utilizing a one-dimensional cloud model. *Mon. Wea. Rev.*, **105**, 270–286.

- , 1982: *Tropical Cyclones: Their Evolution, Structure and Effects*. Vol. 19, American Meteorological Society, 208 pp.
- Bender, M. A., R. J. Ross, Y. Kurihara, and R. E. Tuleya, 1991: Improvements in tropical cyclone track and intensity forecasts using a bogus vortex. Preprints, *19th Conf. on Hurricanes and Tropical Meteorology*, Miami, FL, Amer. Meteor. Soc., 324–325.
- Chang, S. W., and T. R. Holt, 1994: Impact of assimilating SSM/I rainfall rates on numerical prediction of winter cyclones. *Mon. Wea. Rev.*, **122**, 151–164.
- , K. Brehme, R. V. Madala, and K. D. Sashegyi, 1989: A numerical study of the east coast snowstorm of 10–12 February 1983. *Mon. Wea. Rev.*, **117**, 1768–1778.
- , R. J. Alliss, S. Raman, and J. J. Shi, 1993: SSM/I observations of ERICA/IOP 4 marine cyclone: A comparison with in situ observations and model simulation. *Mon. Wea. Rev.*, **121**, 2452–2464.
- Davidson, N. E., and K. Puri, 1992: Tropical prediction using dynamic nudging, satellite-defined convective heat sources, and a cyclone bogus. *Mon. Wea. Rev.*, **120**, 2501–2522.
- DeMaria, M., S. D. Abernson, and K. V. Ooyama, 1992: A nested spectral model for hurricane track forecasting. *Mon. Wea. Rev.*, **120**, 1628–1643.
- DiMego, G., 1988: The National Meteorological Center regional analysis system. *Mon. Wea. Rev.*, **116**, 977–1000.
- Elsberry, R. L., and R. F. Abbey Jr., 1991: Overview of the tropical cyclone motion (TCM-90) field experiment. Preprints, *19th Conf. on Hurricanes and Tropical Meteorology*, Miami, FL, Amer. Meteor. Soc., 1–6.
- Ferriday, J. G., and S. K. Avery, 1994: Passive microwave remote sensing of rainfall with SSM/I: Algorithm development and implementation. *J. Appl. Meteor.*, **33**, 1587–1596.
- Fiorino, M., and T. T. Warner, 1981: Incorporating surface winds and rainfall rates into the initialization of a mesoscale hurricane model. *Mon. Wea. Rev.*, **109**, 1914–1929.
- Franklin, J. L., and M. DeMaria, 1992: The impact of Omega dropwindsonde observations on barotropic hurricane track forecasts. *Mon. Wea. Rev.*, **120**, 381–391.
- , and C. S. Velden, 1991: The impact of Omega Dropwindsonde and satellite data on hurricane track forecasts. Preprints, *19th Conf. on Hurricanes and Tropical Meteorology*, Miami, FL, Amer. Meteor. Soc., 87–92.
- , S. J. Lord, S. E. Feuer, and F. D. Marks Jr., 1993: The kinematic structure of Hurricane Gloria (1985) determined from nested analyses dropwindsonde and Doppler radar data. *Mon. Wea. Rev.*, **121**, 2433–2451.
- Goerss, J., and P. Phoebus, 1992: The Navy's operational atmospheric analysis. *Wea. Forecasting*, **7**, 232–249.
- Hollinger, J. P., 1989: DMSP Special Sensor Microwave/Imager calibration. Final Rep. Vol. I, 176 pp. [Available from the author at Naval Research Laboratory, Washington, DC 20375.]
- , 1991: DMSP Special Sensor Microwave/Imager calibration. Final Rep. Vol. II, 277 pp. [Available from the author at Naval Research Laboratory, Washington, DC 20375.]
- Holt, T., S. W. Chang, and S. Raman, 1990: A numerical study of the coastal cyclogenesis in GALE IOP 2: Sensitivity to PBL parameterizations. *Mon. Wea. Rev.*, **118**, 234–257.
- Kaplan, J., and J. L. Franklin, 1991: The relationship between the motion of tropical storm Florence (1988) and its environmental flow. Preprints, *19th Conf. on Hurricanes and Tropical Meteorology*, Miami, FL, Amer. Meteor. Soc., 93–97.
- Kuo, H. L., 1965: On formation and intensification of tropical cyclones through latent heat release by cumulus convection. *J. Atmos. Sci.*, **22**, 40–63.
- Lawrence, M. B., and J. M. Gross, 1989: Atlantic hurricane season of 1988. *Mon. Wea. Rev.*, **117**, 2248–2259.
- Lord, S. J., 1991: A bogus system for vortex circulations in the National Meteorological Center global forecast model. Preprints, *19th Conf. on Hurricanes and Tropical Meteorology*, Miami, FL, Amer. Meteor. Soc., 328–330.
- Madala, R. V., 1981: Efficient time integration schemes for atmospheric and ocean models. *Finite Difference Techniques for Vectorized Fluid Dynamic Calculations*, Springer-Verlag, 56–74.
- , S. W. Chang, U. C. Mohanty, S. C. Madan, R. K. Paliwal, V. B. Sarin, T. Holt, and S. Raman, 1987: Description of the Naval research laboratory limited-area dynamical Weather prediction model. NRL Tech. Rep. 5992, 131 pp. [NTIS A182780.]
- Merrill, R. T., and C. S. Velden, 1996: A three-dimensional analysis of the outflow layer of Supertyphoon Flo (1990). *Mon. Wea. Rev.*, **124**, 47–63.
- Molinari, J., 1982: Numerical hurricane prediction using remotely-sensed rainfall rates. *Mon. Wea. Rev.*, **110**, 553–571.
- Neumann, C. J., 1981: Trends in forecasting the tracks of Atlantic tropical cyclones. *Bull. Amer. Meteor. Soc.*, **62**, 1473–1485.
- Ooyama, K. V., 1987: Scale controlled objective analysis. *Mon. Wea. Rev.*, **115**, 2479–2506.
- Rao, G. V., and P. D. MacArthur, 1994: The SSM/I estimated rainfall amounts of tropical cyclones and their potential in predicting the cyclone intensity changes. *Mon. Wea. Rev.*, **122**, 1568–1574.
- Rodgers, E. B., S. W. Chang, J. Stout, J. Steranka, and J. J. Shi, 1991: Satellite observations of variations in tropical cyclone convection caused by upper-tropospheric troughs. *J. Appl. Meteor.*, **30**, 1163–1184.
- , —, and H. F. Pierce, 1994: A satellite observational and numerical study of precipitation characteristics in western North Atlantic tropical cyclones. *J. Appl. Meteor.*, **33**, 129–139.
- Sashegyi, K. D., and R. V. Madala, 1993: Application of vertical-mode initialization to a limited-area model in flux form. *Mon. Wea. Rev.*, **121**, 207–220.
- , D. E. Harms, R. V. Madala, and S. Raman, 1993: Application of Bratseth scheme for the analysis of GALE data using a meso-scale model. *Mon. Wea. Rev.*, **121**, 2331–2350.
- Sheet, R. C., 1990: The National Hurricane Center—Past, present, and future. *Wea. Forecasting*, **5**, 185–232.
- Shi, J. J., 1993: Numerical investigation of the interaction between Hurricane Florence (1988) and its upper-level environment. Ph.D. dissertation, North Carolina State University at Raleigh, 206 pp.
- , S. W. Chang, K. D. Sashegyi, and S. Raman, 1991: Enhancement of objective analysis of Hurricane Florence (1988) with dropsonde data. Preprints, *19th Conf. on Hurricanes and Tropical Meteorology*, Miami, FL, Amer. Meteor. Soc., 335–337.
- Velden, C. S., W. S. Olsen, and B. A. Roth, 1989: Tropical cyclone center-fixing using SSM/I data. *Proc. Fourth Conf. on Satellite Meteorology and Oceanography*, San Diego, CA, Amer. Meteor. Soc., J36–J39.
- , C. M. Hayden, W. P. Menzel, J. L. Franklin, and J. S. Lynch, 1992: The impact of satellite-derived winds and numerical hurricane track forecasting. *Wea. Forecasting*, **7**, 107–118.

## **Appendix B**

### **Interaction Between Hurricane Florence (1988) and an Upper-Tropospheric Westerly Trough**

## Interaction between Hurricane Florence (1988) and an Upper-Tropospheric Westerly Trough

JAINN JONG SHI

*Science Applications International Corporation, McLean, Virginia*

SIMON CHANG

*Naval Research Laboratory, Monterey, California*

SETHU RAMAN

*Department of Marine, Earth and Atmospheric Sciences, North Carolina State University, Raleigh, North Carolina*

(Manuscript received 7 August 1995, in final form 18 October 1996)

### ABSTRACT

The Naval Research Laboratory's limited-area numerical prediction system, a version of Navy Operational Regional Atmospheric Prediction System, was used to investigate the interaction between Hurricane Florence (1988) and its upper-tropospheric environment. The model was initialized with the National Meteorological Center (now the National Centers for Environmental Prediction)/Regional Analysis and Forecasting Systems 2.5° analysis at 0000 UTC 9 September 1988, enhanced by a set of Omega dropwindsonde data through a three-pass nested-grid objective analysis.

Diagnosis of the 200-mb level structure of the 12-h forecast valid for 1200 UTC 9 September 1988 showed that the outflow layer was highly asymmetric with an outflow jet originating at approximately 3° north of the storm. In agreement with the result of an idealized simulation (Shi et al. 1990), there was a thermally direct, circum-jet secondary circulation in the jet entrance region and a thermally indirect one in a reversed direction in the jet exit region. In several previous studies, it was postulated that an approaching westerly jet had modulated the convection and intensity variations of Florence. In a variational numerical experiment in this study, the approaching westerly jet was flattened out by repeatedly setting the jet-level meridional wind component and zonal temperature perturbations to zero in the normal mode initialization procedure. Compared with the control experiment, the variational experiment showed that the sudden burst of Florence's inner core convection was highly correlated with the approaching upper-tropospheric westerly jet. These experiments also suggested that the approaching upper-tropospheric westerly jet was crucial to the intensification of Florence's inner core convection between 1000 and 1500 UTC 9 September, which occurred prior to the deepening of the minimum sea level pressure (from 997 to 987 mb) between 1200 UTC 9 September and 0000 UTC 10 September.

Many earlier studies have attempted an explanation for the effect on tropical cyclones of upper-tropospheric forcings from the eddy angular momentum approach. The result of this study provides an alternative but complementary mechanism of the interaction between an upper-level westerly trough and a tropical cyclone.

### 1. Introduction

Numerous observational and numerical modeling studies during the past 40 years have tremendously increased our understanding of tropical cyclones. The adoption of satellite data also helps forecasters and researchers to track the movement and intensity of tropical cyclones. Still, compared to the understanding of mid-latitude weather systems, most of the structure and behavior of tropical cyclones are still not fully understood,

mainly because of the insufficient observational data over the vast tropical ocean. Past studies (Black and Anthes 1971; Sadler 1976, 1978; Frank 1977b; Tuleya and Kurihara 1981; Pfeffer and Challa 1981; Merrill 1984; Holland and Merrill 1984; Chen and Gray 1984; Ooyama 1987; Merrill, 1988a,b; Molinari and Vollaro 1989, 1990; Kaplan and Franklin, 1991; Shi et al. 1990; Rodgers et al. 1991; DeMaria et al. 1993) have demonstrated that the movement and growth of tropical cyclones are affected by the interaction between the outflow layer of tropical cyclones and its environmental flows. For example, Holland and Merrill (1984) pointed out that the strong cyclonic vorticity in the lower and middle troposphere in an intense tropical cyclone becomes more stable and likely more resistant to envi-

---

Corresponding author address: Dr. Jaijn Jong Shi, Naval Research Laboratory, 4555 Overlook Ave., SW, Code 7225, Washington, DC 20375-5000.  
E-mail: shi@metcomp.nrl.navy.mil



ronmental forcing, whereas the upper-tropospheric anticyclonic, asymmetric outflow is not as stable inertially (Black and Anthes 1971), and therefore is less resistant to the environmental forcing. Thus, the movement and intensity of an intense tropical cyclone would probably respond more rapidly to upper-tropospheric forcings. An improved understanding of the structure of the outflow layer of tropical cyclones may be important in predicting tropical cyclone intensification and motion.

Real data analysis of the outflow layer of the tropical cyclone is almost impossible because of the sparsity of the observational data over the tropical ocean. Even when some observational data are available, the studies still suffer from not having frequent enough data to construct a chain of events or to establish a cause-effect relationship. Much of our knowledge has come from composite studies (Black and Anthes 1971; Sadler 1976, 1978; McBride 1981; Chen and Gray 1984; Merrill 1988a,b; DeMaria et al. 1993), a few case studies (Molinari and Vollaro 1989, 1990; Kaplan and Franklin 1991; Rodgers et al. 1991), or some idealized model studies (Tuleya and Kurihara 1981; Pfeffer and Challa 1981; Ooyama 1987; Shi et al. 1990). Based on these studies, our knowledge of the structure of the outflow layer of tropical cyclones and the plausible mechanism through which the interaction with the upper troposphere occurs are summarized as follows.

#### *a. Structure of the outflow layer of tropical cyclones*

The outflow layer of the tropical cyclone is comparatively shallow, generally confined between 100 and 300 mb (Frank 1977a). The asymmetric outflow of the tropical cyclone is characterized by outflow jets. Chen and Gray (1984) asserted that the outflow jets help to remove mass from the central region and transport the warm and dry air to outer regions, maintaining the convective instability in the inner core region. Merrill (1984) observed that the outflow from a hurricane concentrates into one or two outflow maxima or channels. The wind maximum in the outflow layer can normally be found to the north or northwest of the storm center in the Northern Hemisphere. He noted that the appearance of outflow channels is similar to that of the "jet streaks," that are commonly observed in association with the mid-latitude troughs. He also speculated that the upper-tropospheric, baroclinic processes may be important in the hurricane outflow jet streak, and there may be a possible secondary circulation around the outflow layer, similar to the jet streak in midlatitudes. Ooyama (1987) was able to generate the asymmetric outflow in various environmental flows in a simple two dimensional (in the  $x$  and  $y$  directions) model of the outflow layer using shallow water equations with a prescribed updraft carrying mass and momentum. Previous numerical study by Shi et al. (1990) demonstrated the existence of a circum-jet secondary circulation at the entrance region of the outflow jet. The circum-jet secondary circulation

at the entrance region is thermally direct with the ascending branch located on the anticyclonic shear side, and the descending branch located at the cyclonic shear side of the outflow jet. Molinari and Vollaro (1989) also speculated that the upward motion constantly occurs at radii inside the outflow maximum. In a composite study, Merrill (1988a) found that the upper-tropospheric circulation associated with a hurricane is clearly visible on the synoptic scale with a substantial asymmetric component of both radial and tangential winds. However, he also stated that the outward branch of the hurricane's secondary circulation, found in the outflow layer between 100 and 300 mb, may not be all originated from the hurricane.

#### *b. Angular momentum transport in the outflow layer*

Pfeffer (1958) proposed that eddy angular momentum is transferred into the core of the hurricane with a net positive (cyclonic) contribution to the angular momentum budget. Black and Anthes (1971) found an anticyclonic eddy to the right and a cyclonic eddy to the left of the storm motion, which transport a significant amount of negative (positive) relative angular momentum outward (inward). Anthes (1974) further demonstrated that the outflow layer of actual storms exhibits a great degree of asymmetry as indicated by a sizable horizontal eddy angular momentum flux. He also noted that a large import of angular momentum is required to offset frictional loss to the sea. To further augment this point, intense and well-organized inward eddy angular momentum flux was found in developing Atlantic hurricanes, and weak and poorly organized flux was found in nondeveloping disturbances by Pfeffer and Challa (1981). In their model study, they showed that a weak disturbance is not capable of developing into a hurricane solely by the Ekman pumping and cooperative instability without the help of the observed convergence of eddy momentum flux.

Holland (1983), in his composite study, found that the azimuthal eddy transport of angular momentum is effective at large radii in the outflow layer for a developed cyclone, while the mean transverse circulation dominates the inner region. Using a 5-year composite of Atlantic hurricanes, Merrill (1988a) found sizable eddy import of angular momentum in the outflow layer. However, he also quickly pointed out that there is no clear relationship between eddy angular momentum flux and intensity changes of hurricanes. He speculated that any benefits to the hurricane from the eddy angular momentum flux will be offset by the increasing vertical shear. Molinari and Vollaro (1989) analyzed the outflow layer winds of Hurricane Elena (1985) during its life cycle at 12-h intervals for six days. They found that the azimuthal eddy angular momentum flux at large radii was important to the intensification of Elena. They also suggested that operational forecasts of tropical cyclones could benefit from the calculations of eddy momentum



flux because they measured the integrated effect in the storm environment, regardless of the complexity of the interactions. DeMaria et al. (1993) calculated the eddy flux convergence (EFC) of relative angular momentum for the named tropical cyclones during the 1989–91 Atlantic hurricane seasons. They found that a period of enhanced EFC within 1500 km of the storm center occurred about every 5 days due to the interaction with upper-level troughs. In addition, storms intensified just after the period of enhanced EFC in about one-third of the cases. For those cases where the storm did not intensify just after the period of enhanced EFC, either the vertical shear increased, the storm moved over cold water, or it became extratropical. They also mentioned that a statistically significant relationship (at the 95% level) was found between the EFC within 600 km of the storm center and the intensity change during the next 48 hours.

### *c. Influence of the environment on the outflow layer*

In the past two decades, there were many observational studies (e.g. Sadler 1976, 1978; Steranka et al. 1986; Rodgers et al. 1986; Merrill 1988a,b; Molinari and Vollaro 1989, 1990; Shi et al. 1990; Rodgers et al. 1991) that linked the behavior of tropical cyclones to the strength and position of upper-tropospheric troughs and ridges (UTTs and UTRs). Sadler showed that in general as a UTT (UTR) aligns vertically with the underlying tropical cyclone, the tropical cyclone weakens (intensifies). However, the relationship between UTTs (UTRs) and tropical cyclones is not simple and straightforward. For example, Chen and Gray (1984) suggested that the outflow jets are formed by the coupling of the storm's outflow with upper- and midtropospheric troughs. Rodgers et al. (1986) also observed this phenomenon. An outflow channel to the west lies has long been recognized as a requirement for tropical storm development. Sadler (1976) suggested that the multidirectional outflow channels to the large-scale circulation of the upper troposphere serve to remove the excess heat in the tropical cyclone's central region. Thus, a tropical cyclone is likely to intensify if it is surrounded by concentrated air currents to the east of an upper-tropospheric trough or by a strong equatorial outflow channel. Sadler (1978) further elaborated that the strengthening of an outflow channel can extend inward towards the storm center and act as a link to the cyclone's deep convection near the storm center. Holland and Merrill (1984) used observations in the Australian southwest Pacific region with an axisymmetric diagnostic model to study the dynamics of tropical cyclone structural changes. They found that a poleward outflow jet was formed by a coupling between the tropical cyclone and passing disturbances in the subtropical westerlies. They further identified that a dominant feature of the interaction was the strong poleward outflow into the divergent region ahead of an approaching westerly trough. An important conclusion of their research was

that upper-tropospheric interactions between tropical cyclones and their environments can directly affect intensity change.

Recent study of satellite-measured total ozone amount by Rodgers et al. (1986) suggested that the enhancement of the inner-core convection of a tropical cyclone can be related to the upper-tropospheric environment forcing. They found that an increase in the inner-core convection in Hurricane Irene (1980) was preceded by the formation of an outflow channel. When the strength of the outflow channel decreased, the inner-core convection weakened abruptly. They also found that there was a 33-h lag between the changes in the inner-core convection and Irene's intensity changes. Based on the satellite-derived tracers (e.g., cirrus clouds, water vapor, and ozone), Rodgers et al. (1991) suggested that the intensification of Hurricane Florence was caused by the approaching of the upper-tropospheric trough from the west. They also indicated that the development of the second convective cell north of Florence's center may have been initiated by the ascending branch of the circum-jet secondary circulation at entrance region of the outflow jet of Florence enhanced by an approaching westerly UTT.

The numerical experiments by Shi et al. (1990) also showed that an accelerated outflow jet helps to increase the mass divergence in the outflow layer. Molinari and Vollaro (1989) pointed out that Hurricane Elena had a major secondary intensification associated with a large inward cyclonic eddy momentum flux produced by the passage of a middle-latitude trough north of the hurricane. Most of the past results suggest that interactions with a UTT or an upper-level westerly trough can modulate the intensification. In contrast, Merrill (1988b) argued that the environmental interactions with tropical cyclones must, in general, contribute negatively to intensity change because real tropical cyclones seldom attain the intensity allowable under theoretical constraints as described in Emanuel (1986). He asserted that interaction with an upper-level westerly trough that stimulates intensification is not apparent, because such encounters often end with tropical cyclones coming under increasing westerly shear, resulting in the filling of tropical cyclones.

The study is an attempt to substantiate the effect of interactions between tropical cyclones and UTTs in a numerical study of Hurricane Florence. The strategy is first to simulate the detailed structure of the outflow layer of Florence, and then to numerically investigate the interactions between Florence and upper-level environmental forcings. The Omega dropwindsonde (ODW)-enhanced National Meteorological Center (now the National Centers for Environmental Prediction)/Regional Analysis and Forecasting System (NMC/RAFS) 2.5° analyses (Shi et al. 1991, 1996) will be used as the initial condition for the numerical model simulations. The sensitivity of the outflow layer and the intensity of

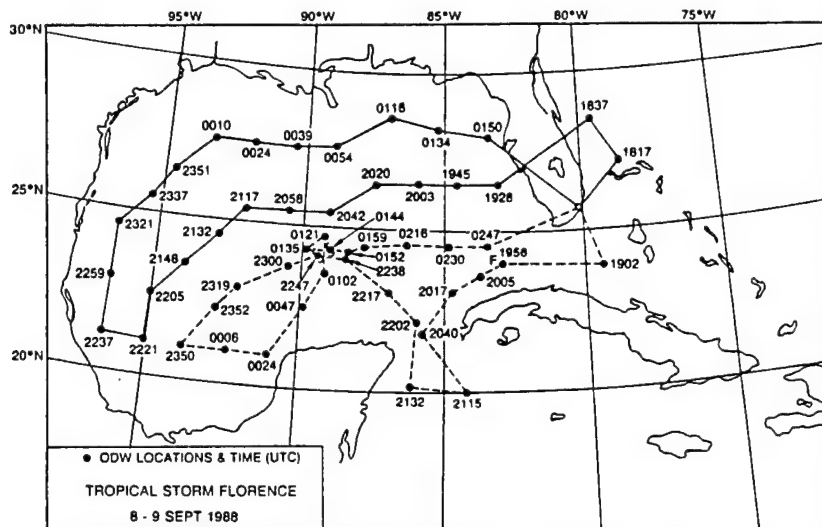


FIG. 1. Location and time (UTC) of the Omega dropwindsonde data collected during a synoptic flow experiment on 8–9 September 1988.

Florence to a westerly UTT will be examined by a series of numerical experiments.

## 2. Analyses

The analyses used for this numerical study were acquired from two different sources. The basic analyses were the NMC/RAFS 2.5° analyses at 0000 UTC 9 September 1988. These analyses were enhanced by the ODW data acquired from the Hurricane Research Division of the Atlantic Oceanographic and Meteorological Laboratory (AOML/HRD) of the National Oceanic and Atmospheric Administration (NOAA). Since 1982, “synoptic flow experiments” have been conducted by the AOML/HRD. The experiments are designed to determine the three-dimensional structure of tropical cyclones below ~400 mb within roughly 1000 km of the storm’s center (Kaplan and Franklin 1991; Franklin et al. 1991; Franklin and DeMaria 1992). During each synoptic flow experiment, a set of ODWs were deployed from NOAA WP-3D aircraft near 400 mb over the region surrounding the targeted tropical storm.

As described in Shi et al. (1996), a total of 51 ODW data were obtained from two NOAA WP-3D aircraft during the synoptic flow experiment on 8–9 September 1988. These data facilitate a better description of the initial condition for the numerical simulation of Florence. Figure 1 shows the two flight routes and the locations and release times of ODWs. The release times range from 1817 UTC 8 September 1988 to 0247 UTC 9 September 1988. Each ODW record consisted of the time and date of launch, location of launch (longitude and latitude), and the sounding data recorded at every 10 mb down from the flight level (ranged from 374 to 528 mb) to surface. The sounding data include pressure, temperature, relative humidity, geopotential height,

wind direction, wind speed, and wind uncertainty. The wind data were missing at the lowest few levels near surface in every ODW record.

The ODW data were used to enhance the NMC/RAFS 2.5° analyses in a nested-grid analysis that will be briefly discussed in section 4. The enhanced NMC/RAFS 2.5° analyses were then used as the initial data for the numerical simulation of Hurricane Florence. The enhanced NMC/RAFS 2.5° analyses were also reprocessed in an attempt to eliminate an approaching westerly UTT coming off the Rockies to study the impact of a weaker westerly UTT on the intensification of Florence.

## 3. Synoptic review of Hurricane Florence (1988)

Figure 2, from Rodgers et al. (1991), shows Florence’s position and intensity (maximum wind in  $\text{m s}^{-1}$ ) every 6 h between 0600 UTC 7 September and 1200 UTC 10 September. Hurricane Florence’s circulation started to form from a quasi-stationary frontal cloud band in the south-central Gulf of Mexico on 7 September 1988. The frontal cloud band had previously been associated with a cold front that entered the Gulf of Mexico from the northeast several days earlier. Florence was classified as a tropical depression with a maximum wind speed of 25 knots and a central pressure of 1000 mb at 0000 UTC 7 September. The circulation quickly intensified into a tropical storm with a maximum wind speed of 40 knots and a central pressure of 998 mb at 1800 UTC 7 September. It first moved eastward for 24 h and then turned northward on 8 September. It moved toward the northern Gulf Coast and became a category-1 hurricane with a maximum wind speed of 65 knots and a central pressure of 985 mb at 1800 UTC 9 September. Florence made landfall over southeastern Louisiana at 0200 UTC 10 September and quickly weakened as it

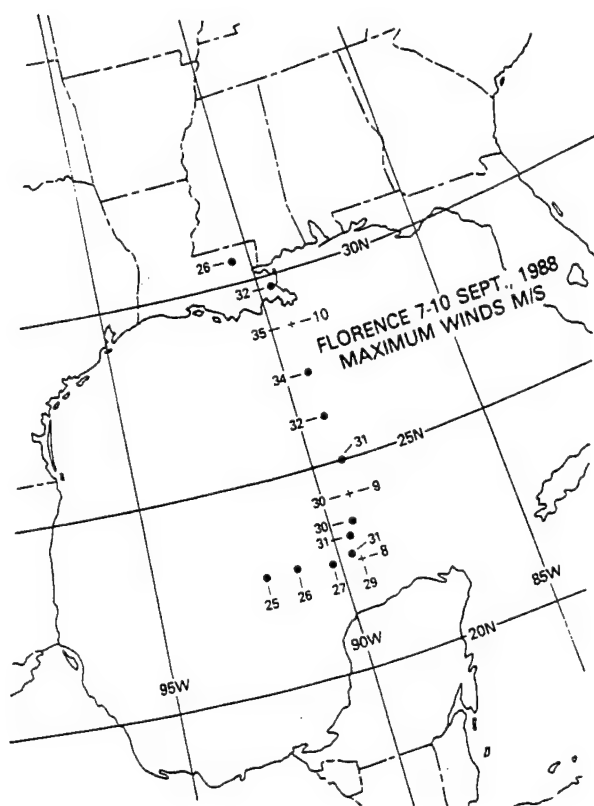


FIG. 2. Position and intensity (maximum winds in meters per second) of Hurricane Florence (7–10 September 1988) every 6 h. Crosses locate Florence's position at 0000 UTC each day. Figure adapted from Rodgers et al. (1991).

moved over the New Orleans area and dissipated on 11 September in eastern Texas (Lawrence and Gross 1989).

According to the best tracking data from the National Hurricane Center, Force was a hurricane for only 12 h (Table 1). Air Force reconnaissance flights estimated that the highest sustained surface wind was  $36 \text{ m s}^{-1}$  and the lowest surface pressure 982 mb occurring at 2300 UTC 9 September, just 3 h before landfall. Rainfall totals of up to 100 mm were observed along the path of the storm (Lawrence and Gross 1989).

#### a. Evolution of Florence's precipitation and convection

Rodgers et al. (1991) presented Geostationary Operational Environmental Satellite (GOES) infrared imagery (Fig. 3) that show the development of the second deep convective cell north of the low-level center at 1200 UTC 9 September. Figure 3 shows the GOES infrared imagery every 2 h from 0200 UTC to 1200 UTC 9 September. The second deep convective cell appeared at 0800 UTC and then expeditiously expanded and intensified. At 1200 UTC, the newly developed second deep convective cell had reached a size larger than its counterpart southeast of the low-level center. Figure 3

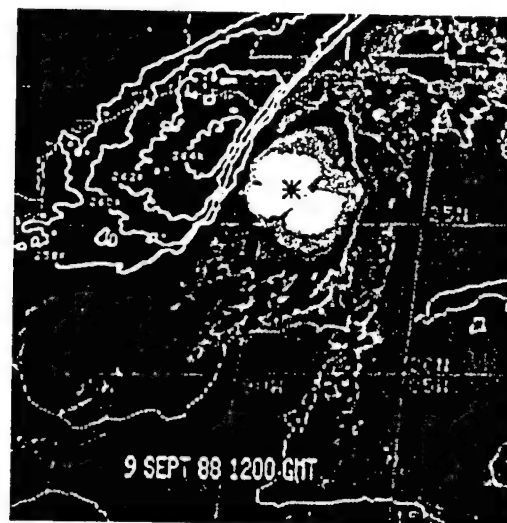
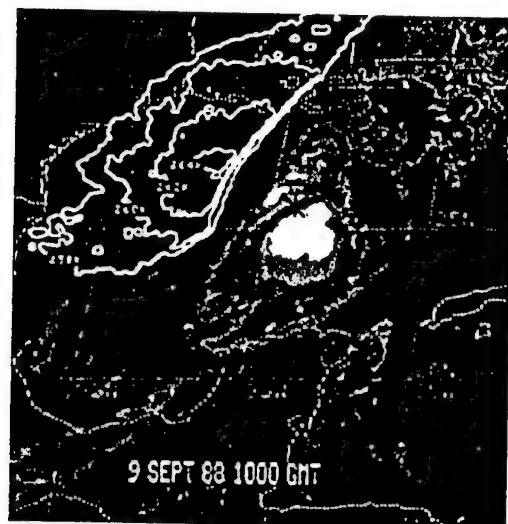
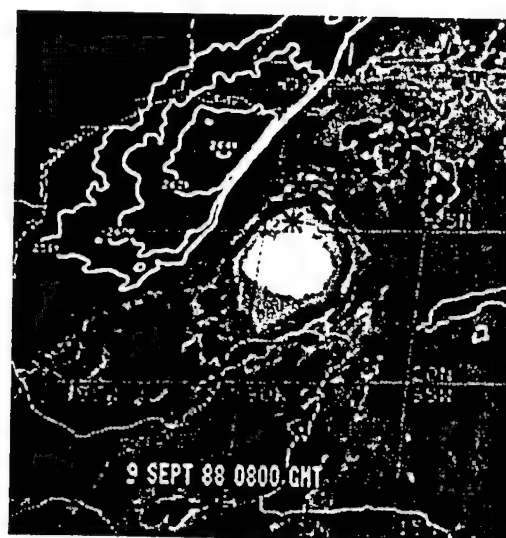
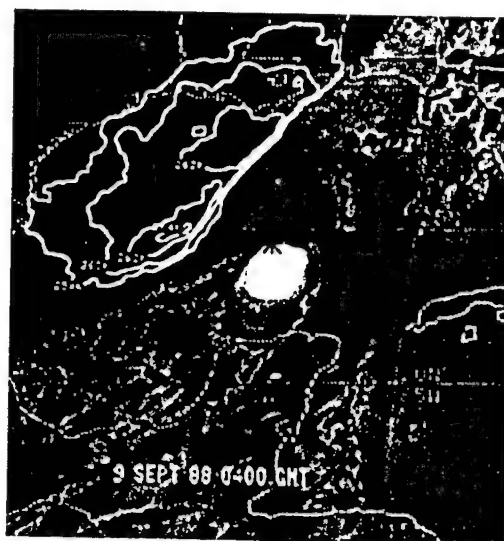
TABLE 1. Best track of Hurricane Florence, obtained from the National Hurricane Center in Miami, Florida.

Date (d/mo)	Time (UTC)	Position		Pres- sure (mb)	Wind ( $\text{m s}^{-1}$ )	Stage
		Latitude (N)	Longitude (W)			
9/07	0600	22.8	92.0	1000	12.9	Tropical depression
9/07	1200	22.8	91.2	998	15.4	Tropical depression
9/07	1800	22.7	90.2	996	20.6	Tropical storm
9/08	0000	22.6	89.6	993	23.1	Tropical storm
9/08	0600	22.7	89.8	990	23.1	Tropical storm
9/08	1200	23.1	89.7	990	23.1	Tropical storm
9/08	1800	23.4	89.5	992	23.1	Tropical storm
9/09	0000	24.2	89.2	992	25.7	Tropical storm
9/09	0600	25.0	89.2	991	25.7	Tropical storm
9/09	1200	26.1	89.2	988	28.3	Tropical storm
9/09	1800	27.4	89.2	985	33.4	Hurricane
9/10	0000	28.7	89.3	983	36.0	Hurricane
9/10	0600	29.7	89.7	988	30.9	Tropical storm
9/10	1200	30.7	90.7	998	15.4	Tropical depression
9/10	1800	31.8	91.5	1003	10.3	Tropical depression
9/11	0000	32.4	92.3	1007	7.7	Tropical depression
9/11	0600	32.7	93.3	1009	7.7	Tropical depression
9/11	1200	33.0	94.5	1010	7.7	Tropical depression
9/09	2300	28.5	89.3	982	36.0	Minimum pressure
9/10	0200	29.1	89.3	984	36.0	Landfall

also confirms the existence of a large rain band that stretched from the convective region to the area off the east coast of the Yucatan Peninsula. The Special Sensing Microwave/Imager (SSM/I) precipitation rates at the same time (Fig. 4) also reveal the development of the second deep convective cell north of the low-level center. The second convective cell eventually merged with the convection to the southeast of the low-level center and the combined convective region moved northward toward New Orleans.

#### b. Upper-tropospheric environment of Florence and its possible influences on Florence's outflow

Before Florence became a hurricane on 9 September, there was a westerly UTT approaching from the west as shown in the NMC/RAFS 2.5° analysis at 1200 UTC 8 September (Fig. 5). The trough extended from the southern part of Illinois into the eastern part of Texas. Twelve hours later, at 0000 UTC 9 September, the UTT moved eastward into the northern Gulf of Mexico, originating from Tennessee (Fig. 6). At this time, the westerly jet (Fig. 6) might have provided a channel for the forming of the outflow jet of Florence and initiated the development of the second convective cell north of Florence's center a few hours later, as described in the previous section. At 1200 UTC 9 September, the UTT (Fig. 7) moved slightly eastward and was apparently weakening as compared to the UTT in Fig. 6. During the next 12 h, the westerly jet had moved northward, judging from the shaded area representing the wind speed of  $30 \text{ m s}^{-1}$  and greater in Fig. 8. Florence had also moved under the UTT in its continuous northward



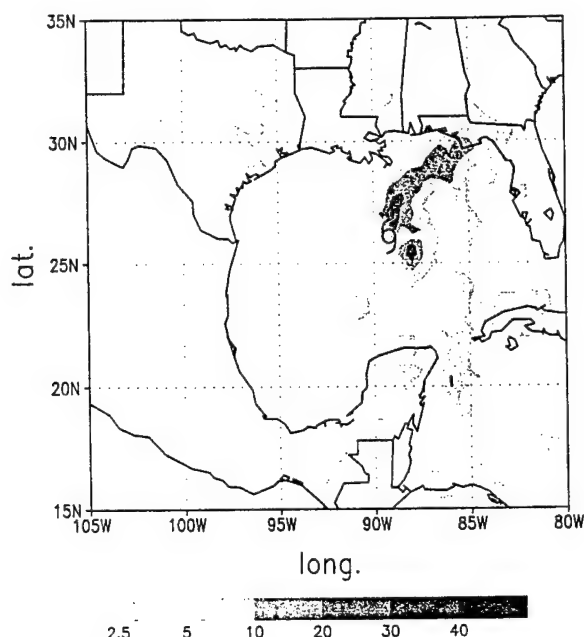


FIG. 4. SSM/I-retrieved rain rates at 1200 UTC 9 September 1988.

movement. The increasing vertical shear probably had become a negative factor of Florence's further intensification. At this time, Florence was also about to make landfall.

Rodgers et al. (1991) used satellite-derived cirrus-level winds to show the approaching of the UTT from the west. Figure 9 shows the cirrus-level streamline analyses and wind speeds at 12-h interval from 1200 UTC 8 September to 1200 UTC 9 September. At 1200 UTC 8 September (Fig. 9a), there was a UTT in the northwestern Gulf of Mexico just northwest of Florence's center. Twelve hours later (Fig. 9b), the UTT became deeper and stronger and extended further south as Florence moved northward. Figure 9c shows the development of the outflow jet located north of Florence's center at 1200 UTC 9 September, suggesting that Florence's northern outflow became channeled and enhanced as the system interacted with the UTT. Rodgers et al. (1991) speculated that the combination of the observed evolution of Florence's outflow (Fig. 9) and the convection (Figs. 3 and 4) provides some evidence that the outflow jet-induced secondary circulation might enhance the convective growth in the entrance region of the outflow jet. The mechanism was also illustrated in the numerical study of Shi et al. (1990) using an idealized tropical cyclone.

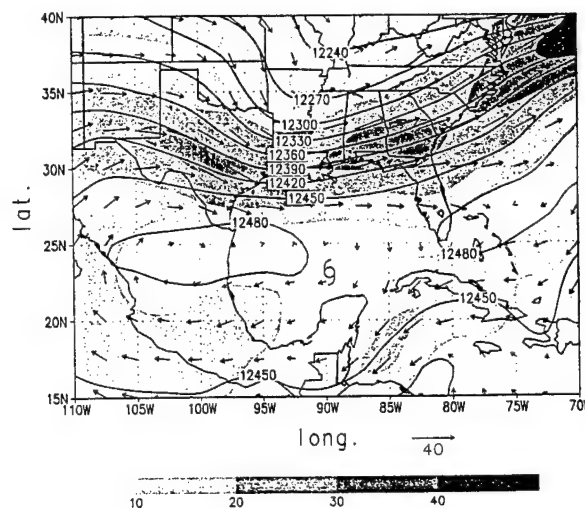


FIG. 5. 200-mb geopotential height contours (m), wind vectors, and shaded isotachs ( $\text{m s}^{-1}$ ) of the NMC/RAFS 2.5° analysis at 1200 UTC 8 September 1988. The hurricane symbol depicts the current center location of Florence from the best track record.

#### 4. Numerical model and experimental design

The Naval Research Laboratory's limited-area numerical prediction system, a research version of the Navy Operational Regional Atmospheric Prediction System, was used in this study. The system includes a data assimilation system, a vertical mode initialization (VMI), and a limited-area numerical model. The data assimilation system includes two steps. The first step is a data preparation and quality control scheme and the second step is an objective analysis scheme. The data quality control consists of a "gross" check and a "buddy" check following DiMego (1988). The objective analysis is a three-pass nested-grid Barnes scheme (Shi et al. 1991, 1996). The VMI, as described in Sashegyi and Madala (1993), produces a balanced vertical motion field and induces smaller changes to the initial mass and wind fields as compared to static initialization schemes.

The limited-area numerical model is a three-dimensional, hydrostatic, primitive equation model incorporating a split-explicit time integration scheme (Madala 1981). Details of the model are described in Madala et al. (1987), Chang et al. (1989), and Holt et al. (1990). However, in this version of the model, there are 23 layers in the vertical direction. A terrain following  $\sigma (=P/P_s)$  vertical coordinate and time-dependent lateral boundary conditions are utilized, where  $P$  is the pressure and  $P_s$  the surface pressure. Topography used in this model is derived from the U.S. Navy global 10-minute elevation

FIG. 3. GOES Visible and Infrared Spin Scan Radiometer (VISSR) infrared (11.5 mm) image of Hurricane Florence between 0200 UTC and 1200 UTC 9 September 1988 at 2-h intervals. The white contours depict the warmest VISSR infrared water vapor (6.7 mm) brightness temperature between 258° and 264 K at 2-K intervals. The star depicts Florence's center. Figure adapted from Rodgers et al. (1991).



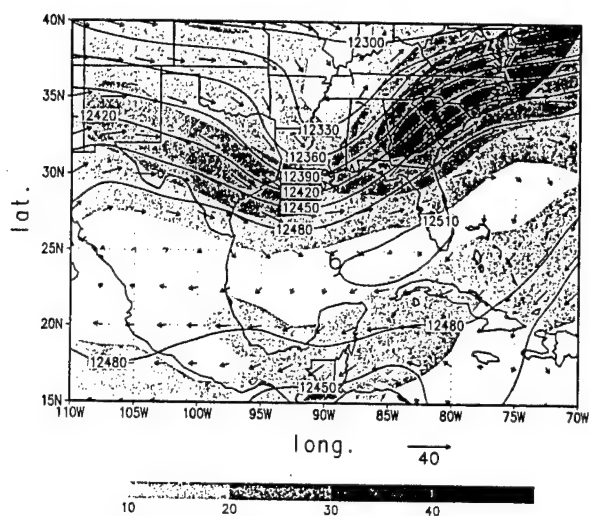


FIG. 6. Same as Fig. 5 except for 0000 UTC 9 September 1988.

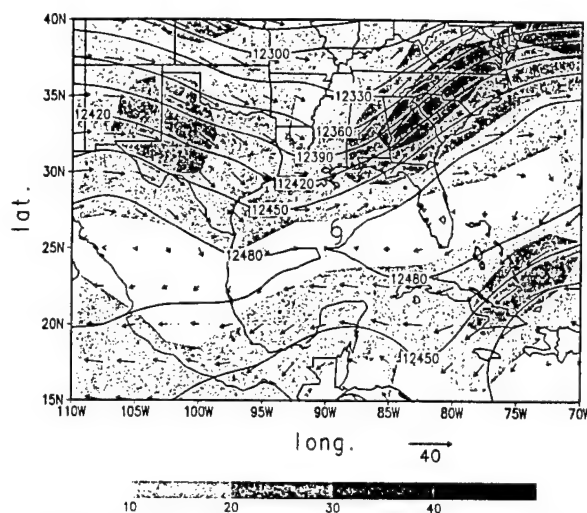


FIG. 7. Same as Fig. 5 except for 1200 UTC 9 September 1988.

data. The grid domain, from 15° to 45°N and from 110° to 65°W, covers most of the continental United States and all of the Gulf of Mexico, with horizontal resolutions of one-half and one-third degree in longitude and latitude, respectively. The main interest of this study is in the upper layer, which contains synoptic or larger scale phenomenon. Therefore, the horizontal resolution is appropriate for this study.

The planetary boundary layer parameterization of this model is based on the two-parameter formulation of Detering and Etling (1985) as described in Holt et al. (1990). Temperature at the lowest model layer ( $\sigma = 9.9975$ ) at the initial time is used as ground temperature. The sea surface temperature is obtained from the multichannel sea surface temperature (MCSST) data derived from Advanced Very High Resolution Radiometer imageries. This MCSST product is a weekly composite for the global SST at a horizontal resolution of approximately 18 km. The model uses a modified Kuo scheme for parameterizing the effect of cumulus convection (Kuo 1965; Anthes 1977). The large-scale precipitation occurs when there is a supersaturated layer in the model.

The ODW data were used to enhance the NMC/RAFS 2.5° analyses by using the three-pass nested-grid Barnes scheme. The horizontal resolution in the first two passes is one-half degree and one-sixth degree in the third pass. The selection of the different resolutions for the different passes in the objective analysis matches the ODW data resolutions (Fig. 1). As shown in Fig. 1, it is apparent that the ODW data resolution near Florence's center is about three times higher than the ODW data resolution away from Florence's center. Details of the analysis of the ODW data are described in Shi et al. (1991, 1996). The enhanced analyses were initialized by the VMI and used as the initial data of the model integration for the different numerical experiments. In this study, the limited-area model was integrated with the ODW-enhanced analyses at 0000 UTC on 9 Sep-

tember 1988 for 48 h (Expt. ODW). Details of the intensity and track simulation results were documented in Shi et al. (1996).

## 5. Simulated structure of the outflow layer of Hurricane Florence

### a. Simulated outflow structure at 200-mb level

Figure 10 shows the simulated 200-mb geopotential heights, wind vectors, and isotachs of Expt. ODW at 12 h valid at 1200 UTC 9 September. There is a westerly trough extending from western Tennessee to Louisiana and the northern Gulf of Mexico, agreeing with the NMC/RAFS 2.5° analysis at 1200 UTC 9 September (Fig. 7). There is an upper-level high pressure located near the center of the Gulf of Mexico, corresponding to the low-level center of Florence. The outflow layer is highly asymmetric, especially beyond three degrees

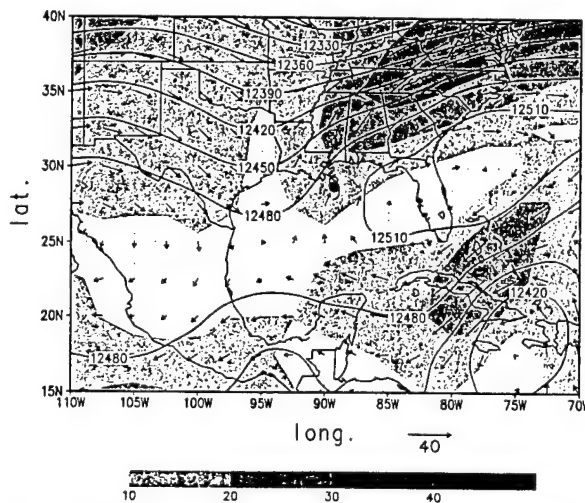


FIG. 8. Same as Fig. 5 except for 0000 UTC 10 September 1988.

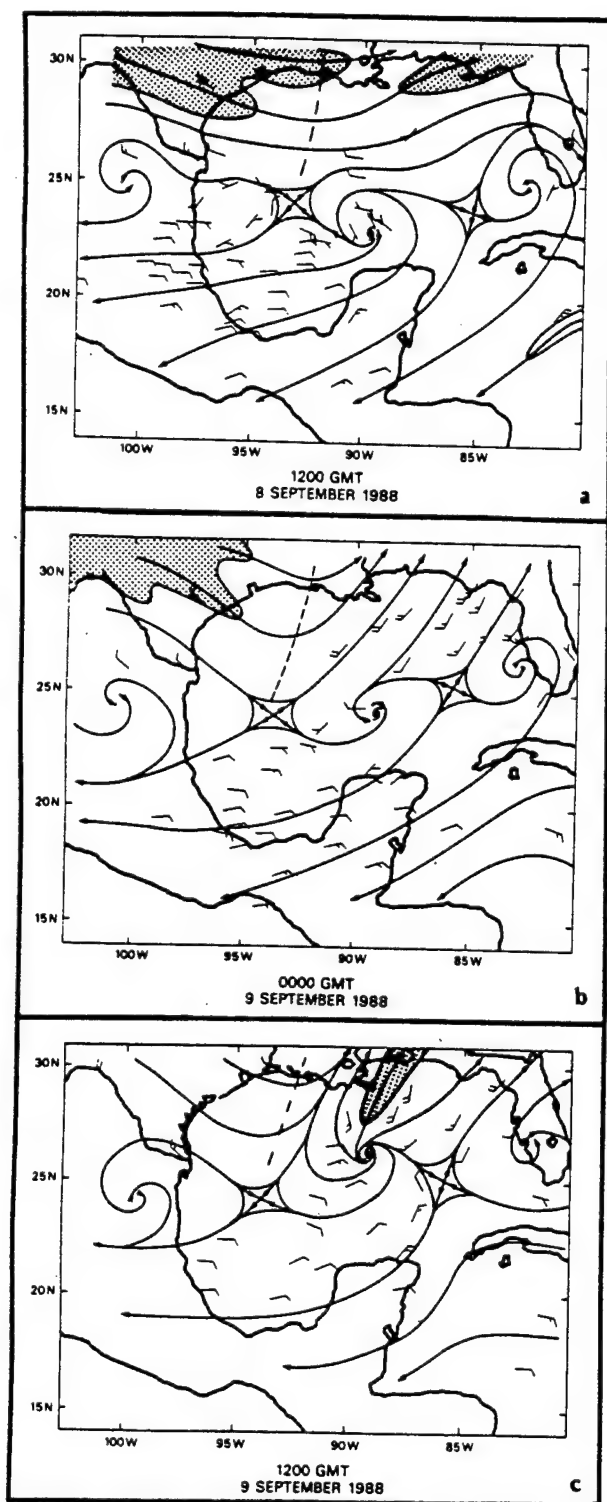


FIG. 9. Cirrus-level winds ( $\text{m s}^{-1}$ ) and streamline analysis for Hurricane Florence at (a) 1200 UTC 8 September, (b) 0000 UTC, and (c) 1200 UTC 9 September 1988. Shaded area represents wind speeds  $\geq 25 \text{ m s}^{-1}$ . Hurricane symbol depicts the center of Florence. Dashed line represents the upper-level tropospheric trough's axis. Full wind barb represents  $10 \text{ m s}^{-1}$ . Figure adapted from Rodgers et al. (1991).

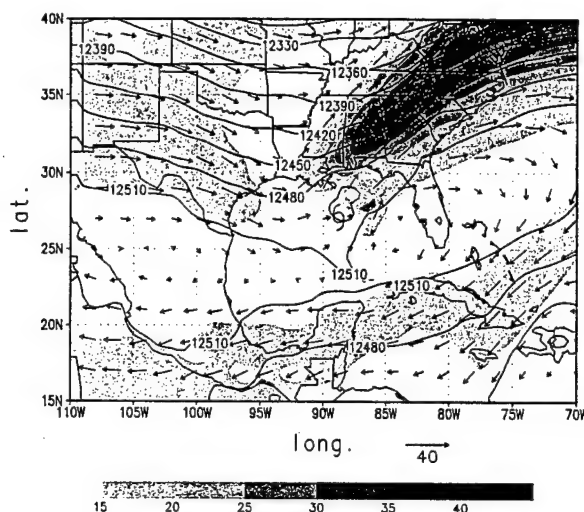


FIG. 10. 200-mb geopotential heights, wind vectors, and shaded isotachs ( $\text{m s}^{-1}$ ) of Expt. ODW at 12 h valid at 1200 UTC 9 September 1988. The hurricane symbol depicts the current center location of the simulated Florence.

radius, with an outflow channel or jet starting from about three degrees north of the center and extending northeastward into the mid-Atlantic states and Atlantic Ocean. The outflow jet is elongated with a length of roughly 2500 km and a width of 500 km as outlined by the shaded area of  $30 \text{ m s}^{-1}$  and greater (Fig. 10). The location of the outflow jet also agrees with NMC/RAFS 2.5° analysis at 1200 UTC 9 September (Fig. 7), except the simulated jet is stronger, better defined, and better connected with Florence. The simulated outflow jet has a maximum wind speed of  $42.4 \text{ m s}^{-1}$ , which is  $5.8 \text{ m s}^{-1}$  stronger than the one in the NMC/RAFS 2.5° analysis. It also shows an anticyclonic curvature. As shown in Fig. 10, at the entrance region of the jet (near the Louisiana, Mississippi, and Alabama coasts), there is a strong anticyclonic (cyclonic) shear along the southeastern (northwestern) edge of the jet core. Downstream at the exit region, the jet becomes diffused with diminishing horizontal shears at both sides of the jet. These characteristics of the outflow jet are similar to those in the idealized model by Shi et al. (1991). At 24 h valid at 0000 UTC 10 September, the 200-mb geopotential heights, wind vectors, and isotachs (Fig. 11) show that the westerly jet has moved northeastward over Virginia and becomes disassociated with Florence. Florence's center has also moved northward and into a region under the south end of the westerly trough. Increase of the mean 200–850-mb vertical wind shear in a  $5^\circ \times 5^\circ$  box centered at storm center from  $9.5 \text{ m s}^{-1}$  at 12 h to  $14.3 \text{ m s}^{-1}$  at 24 h probably prevented Florence from any further intensification. At this time, Florence is also about to make landfall, and its behavior will be dominated by the response to the landfall.

The structure of the relative humidity (RH) field at upper levels is usually determined by the three-dimen-

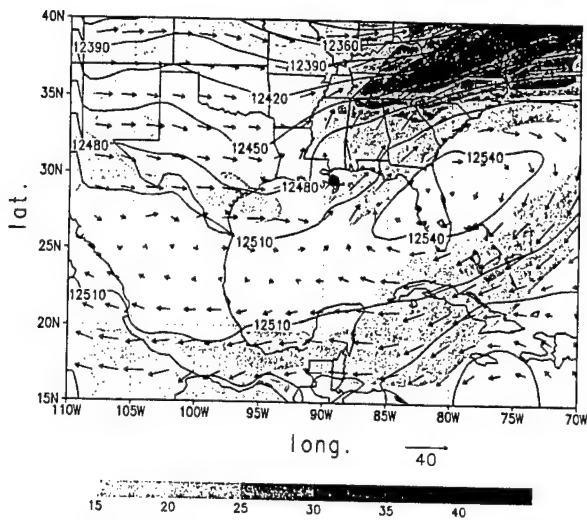


FIG. 11. Same as Fig. 10 except for 24 h valid at 0000 UTC 10 September 1988.

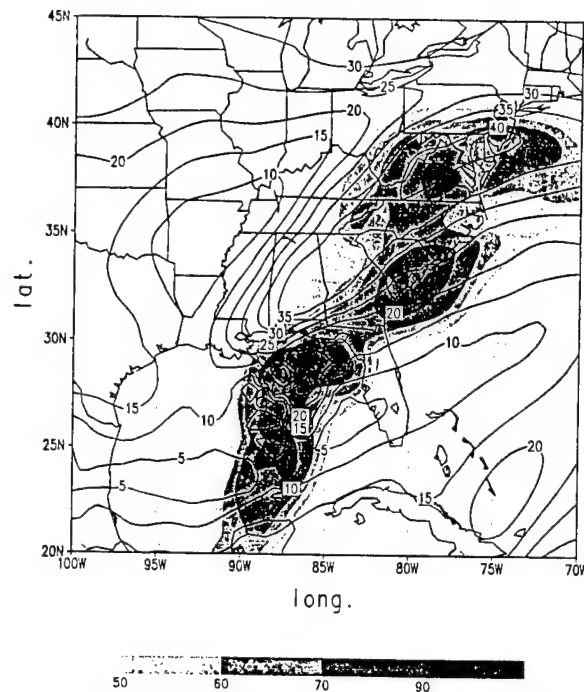


FIG. 12. 200-mb relative humidities (%) (shaded area) and isotachs (contour) of Expt. ODW at 12 h valid at 1200 UTC 9 September 1988.

sional transport process in the outflow layer, reflecting the important features of the outflow momentum field. Figure 12 shows the 200-mb RH in the outflow layer at 12 h. There is a wet canopy with  $RH > 90\%$  over the storm center, which also extends northeastward along the anticyclonic shear side of the outflow jet. The moisture field is clearly asymmetric relative to the jet core with high  $RH (> 90\%)$  on the anticyclonic shear side of the outflow jet from the Florida panhandle to the South Carolina coast and low  $RH (< 50\%)$  on the cyclonic shear side of the jet located to the northwest of the jet. This particular RH distribution suggests that there is a circum-jet secondary circulation with ascending motion on the anticyclonic shear side and descending motion on the cyclonic shear side as discussed in Shi et al. (1990). Further downwind from the jet core, a high RH region ( $> 90\%$ ) is located over Virginia, and there is a dry wedge ( $RH < 60\%$ ) located over Cape Hatteras, North Carolina. The dry wedge located downstream from the high RH cannot be the result of the horizontal transport and therefore must be caused by vertical motions at this level. The moisture field, characterized by the alternate dry and wet regions on either side of the outflow jet, is an indication of the existence of the thermally direct (indirect) secondary circulation in the entrance (exit) region of the outflow jet found in an idealized tropical cyclone (Shi et al. 1990).

#### b. Cross sections of the simulated outflow jet

To further illustrate the secondary circulations, we examine the cross-sectional structure of the wind and moisture fields. A composite cross-sectional structure of the wind and RH field is obtained by averaging the values of the cross-sections of the outflow jet. The composite cross section representing the entrance region of the outflow jet is an average of seven cross sections as

indicated in Fig. 13. In the exit region, six cross sections are computed and averaged.

Figure 14 shows the composite cross section of the wind and RH field in the entrance region at 12 h valid at 1200 UTC 9 September. The vectors are formed by the vertical velocities (in  $\text{mb h}^{-1}$ ) and horizontal wind

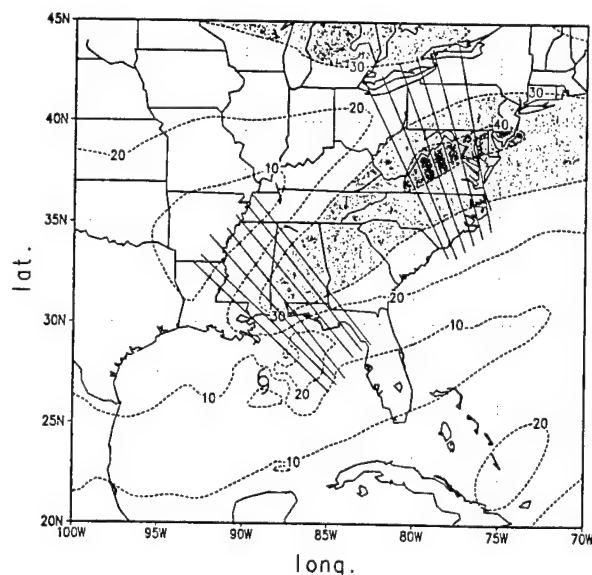


FIG. 13. Location of cross sections. Seven cross sections are in the entrance region of the outflow jet, and six cross sections are in the exit region. Contours are the 200-mb isotachs. Shaded area represents the area with wind speed greater than  $30 \text{ m s}^{-1}$ .



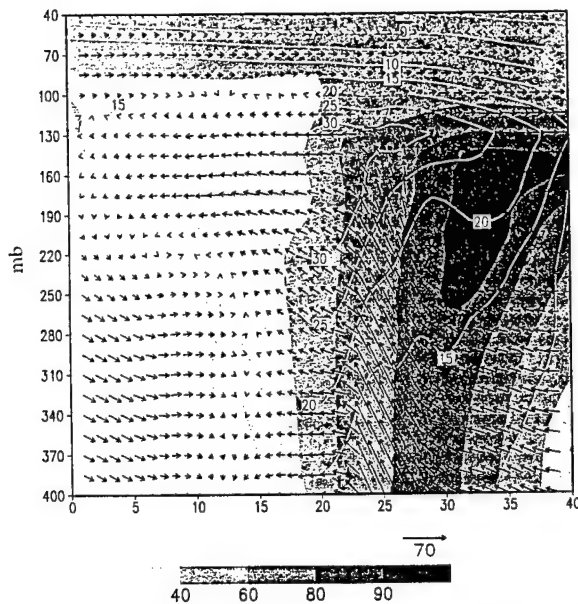


FIG. 14. Composite cross section in the entrance region of the outflow jet of Expt. ODW at 12 h. The orientation of the cross section is looking downwind along the outflow jet with approximately NW to the left and SE to the right. Contours are the wind component ( $\text{m s}^{-1}$ ) normal to the cross section (positive means blowing into the paper). Vectors are the combination of the vertical velocity ( $\text{mb h}^{-1}$ ) and the wind component ( $\text{m s}^{-1}$ ) tangential to the cross section. Shaded area are the relative humidity (%).

components (in  $\text{m s}^{-1}$ ) tangential to the cross section. The isotachs are the horizontal wind components ( $\text{m s}^{-1}$ ) normal to the cross section with positive values for the southwesterly wind (into the cross section). In the jet entrance region (Fig. 14), the high RH ( $>90\%$ ) is located on the anticyclonic shear side of the outflow jet, coinciding with a strong ascending motion, while the low RH ( $<50\%$ ) is on the cyclonic shear side coinciding with a weak descending motion. There is an abrupt, vertically aligned RH gradient at the jet core. There is also an outward (from the anticyclonic to cyclonic shear side of the outflow jet), cross-jet mean horizontal motion between 130 and 250 mb. Merrill (1984) and Shi et al. (1990) suggested that the circum-jet secondary circulation has an outward branch above the jet, an inward branch below the jet (near 400 mb), an ascending branch on the anticyclonic shear side, and a descending branch on the cyclonic shear side of the outflow jet. The result shown here also indicates the existence of the circum-jet secondary circulation in the outflow layer. The inward branch below the outflow jet in the entrance region is, however, less apparent in this study, probably due to the presence of the coastal warm front and other synoptic features. In this real case study, it is difficult to clearly separate the secondary circulations associated with the outflow jet and vertical motions that are associated with other synoptic systems.

Figure 15 shows the composite cross section in the exit region. The jet core has descended from 130–220

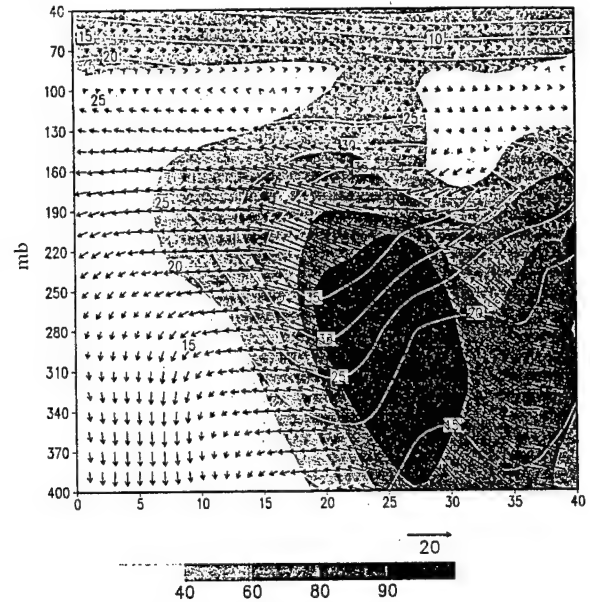


FIG. 15. Same as Fig. 14 except for the composite cross section in the exit region of the outflow jet.

mb in the entrance region to 145–280 mb in the exit region. Here, the moisture field on the cyclonic shear side has become more humid, and the anticyclonic shear side has become drier ( $<60\%$ ) between 100 and 190 mb compared to their counterpart in the entrance region (Fig. 14). Comparing Figs. 14 and 15, the high RHs in the jet have moved outward and downward downstream, consistent with the reversal of the secondary circulation. In addition, there appears to be a northwestward tilt of the high RH region, which may be related to the pre-existing coastal front along the mid-Atlantic coast. As shown in Fig. 15, there is a thermally indirect secondary circulation between 100 and 190 mb with an ascending motion on the cyclonic shear side and a descending motion on the anticyclonic shear side. The drier region on the anticyclonic shear side coincides with the descending branch of the secondary circulation. The outward branch moves through the jet core, and the inward branch is situated just above the jet.

### c. Angular momentum budget

Previous studies (Black and Anthes 1971; Holland 1983; Molinari and Vollaro 1989; DeMaria et al. 1993) showed that the inward azimuthal eddy cyclonic angular momentum flux (AMF) is important to the intensification of tropical cyclones. Challa and Pfeffer (1990) claimed that the characteristic difference between the developing and nondeveloping disturbances is the presence (in the developing disturbances) of the well-developed influx of cyclonic eddy angular momentum at outer radii in the upper troposphere. Molinari and Vollaro (1989) studied the interaction between Hurricane Elena (1985) and its upper-tropospheric environment

TABLE 2. Model and empirical angular momentum budget in the outflow layer of tropical cyclone. Units are in  $10^{22}$  g cm<sup>2</sup> s<sup>-2</sup>. The values for mean storms are adopted from Anthes (1974). The values from the current study are storm relative.

	Radius (km)	Coriolis torque	Horizontal flux		Vertical flux	
			Mean	Eddy	Mean	Eddy
Mean storm (Palmen and Riehl 1957)	0-333	-48.0	-20.0	8.0	40.0	20.0
	333-666	-143.0	76.0	23.0	—	44.0
Mean storm (Pfeffer 1958)	222-444	-54.0	46.0	20.0	5.0	—
	444-666	-78.0	-11.0	13.0	-4.0	—
Model storm (Shi et al. 1990)	0-300	-4.3	3.5	-0.7	-0.3	—
	300-1000	-47.6	13.4	35.1	1.1	-0.4
Model Florence (1988)	0-300	-8.4	5.3	-3.5	-1.8	-1.2
from Expt. ODW	300-700	-99.2	49.6	30.6	0.9	1.4
Model Florence (1988)	0-300	-8.9	5.9	-2.3	-2.8	-0.7
from Expt. ODW + WTR	300-700	-104.3	55.6	25.0	-0.6	0.3

and concluded the AMF measures the integrated effects of the interactions between the tropical cyclones and their environments, regardless of the complexity of the interactions.

The budget of the angular momentum of the outflow layer is calculated to study the importance of the eddy AMF. Following Anthes (1974) and Shi et al. (1990), the angular momentum budget equation in a cylindrical coordinate system is defined as

$$\begin{aligned}
 \frac{\partial M}{\partial t} = & -2\pi \int_{h_1}^{h_2} \int_{r_0}^{r_1} r^2 \rho(z) (\langle f \rangle \langle u \rangle + \langle f' u' \rangle) dr dz \\
 & -2\pi \int_{h_1}^{h_2} [r_1 \rho(z) (\langle m \rangle \langle u \rangle)_{r_1} - r_0 \rho(z) (\langle m \rangle \langle u \rangle)_{r_0}] dz \\
 & -2\pi \int_{h_1}^{h_2} [r_1 \rho(z) (\langle m' u' \rangle)_{r_1} - r_0 \rho(z) (\langle m' u' \rangle)_{r_0}] dz \\
 & -2\pi \int_{r_0}^{r_1} r [(\rho \langle w \rangle \langle m \rangle)_{h_2} - (\rho \langle w \rangle \langle m \rangle)_{h_1}] dr \\
 & -2\pi \int_{r_0}^{r_1} r [(\rho \langle m' w' \rangle)_{h_2} - (\rho \langle m' w' \rangle)_{h_1}] dr, \quad (1)
 \end{aligned}$$

and

$$M = \int_{h_1}^{h_2} \int_{r_0}^{r_1} \int_0^{2\pi} r m d\lambda dr dz, \quad (2)$$

where  $m = rv$  (relative angular momentum);  $u$  and  $v$  are the radial and tangential velocities in storm-relative cylindrical coordinates,  $(\lambda, r, z)$  respectively; and  $r$  is the radius from the storm center as determined by the sea level pressure (SLP). In Eq. (1), the symbol  $\langle \rangle$  represents an azimuthal mean and  $\langle \rangle'$  denotes a deviation from the mean. Vertical integrations are carried out between the geopotential heights of  $h_1 = 13\,500$  gpm and  $h_2 = 14\,500$  gpm, containing most of the outflow. The first terms on the right-hand side of Eq. (1) denotes the mean and eddy Coriolis torques and the second and third terms denote the horizontal convergence of mean and eddy angular momentum fluxes, re-

spectively. Finally, the fourth and fifth terms represent the vertical convergence of mean and eddy angular momentum fluxes, respectively. To evaluate these terms, model results are linearly interpolated to the cylindrical coordinates. Because of the size of Florence, the outer region is defined from 300 to 700 km, instead of the 300 to 1000 km used in Shi et al. (1990). The values of each term in Eq. (1) calculated from Expt. ODW's result at 12 h are listed in Table 2. For comparison, values from the idealized model tropical cyclone in Shi et al. (1990) and observed values for mean tropical storms in Palmen and Riehl (1957), as well as in Pfeffer (1958), are also listed.

Table 2 shows that the values of various terms in Eq. (1) evaluated from the modeled tropical cyclones compare reasonably with those of the observational studies and the previous model study. The vertical momentum fluxes in Palmen and Riehl (1957) contained unaccounted-for residuals. In general, the angular momentum balance in both the simulated and the observed tropical cyclones is basically maintained by the Coriolis torque and horizontal transports, especially at outer radii where the vertical transport is small. The values in Table 2 suggest that the mean horizontal AMF dominates in the inner region, while the eddy horizontal AMF is roughly equal to the contribution from the mean in the outer region. The large positive eddy horizontal AMF at large radii, meaning a large inward cyclonic eddy momentum flux, agrees with the observational study of Molinari and Vollaro (1989). All budget calculations indicate the importance of the eddy horizontal AMF for the angular momentum balance in the outer region. Results from the model storm of Shi et al. (1990) and Expt. ODW show a negative contribution of the horizontal eddy AMF in the inner region, reflecting the cyclonic circulation near the storm center in the outflow layer. The important role of the eddy momentum transport in the angular momentum budget underscores the dominance of the outflow jet in the outflow layer of the tropical cyclone, in this case, Hurricane Florence. Results from Expt. ODW+WTR will be discussed in the next section.

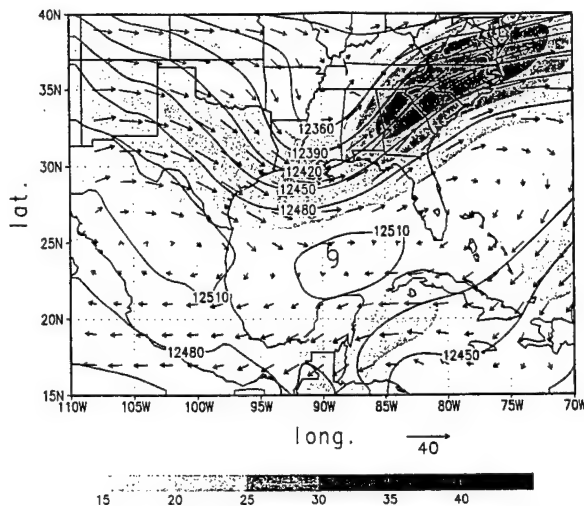


FIG. 16. 200-mb geopotential heights (m), wind vectors, and shaded isotaches ( $\text{m s}^{-1}$ ) of the ODW enhanced analyses after initialized by the VMI. The hurricane symbol depicts the current center location of Florence from the best track record.

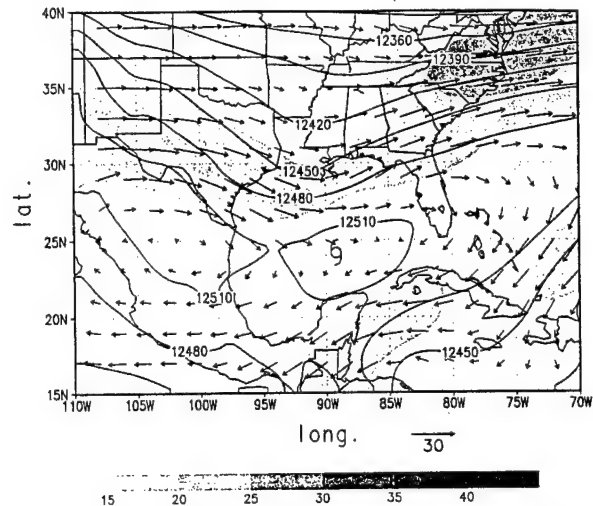


FIG. 17. Same as Fig. 16 except for the reprocessed ODW-enhanced analysis.

## 6. Upper-tropospheric environmental influences on Florence

To further isolate the cause-effect relationship between the upper-tropospheric trough and intensity and structural changes of Hurricane Florence, a numerical experiment (Expt. ODW+WTR) is conducted for this study. For this experiment, the ODW-enhanced analyses are reprocessed to reduce the cyclonic curvature of the upper-level westerly trough at 0000 UTC 9 September. This is done to determine the impact of the weakened westerly jet on the outflow layer of Florence. In the reprocessed version of the ODW enhanced analyses, the north-south component of the wind is set to zero in the layer between 100 and 500 mb and in the region between  $30^{\circ}$  and  $45^{\circ}\text{N}$ . To further weaken the temperature gradient associated with the westerly jet, the temperature at each grid point in the same region is set to the zonal mean temperature. The reprocessed data are then initialized by the VMI. Comparing Fig. 16 and 17, the amplitude of the upper-level westerly trough is apparently weakened by the reprocess, with the maximum wind speed in the upper-level westerly jet reduced by  $4.9 \text{ m s}^{-1}$  from  $34.5 \text{ m s}^{-1}$  to  $29.6 \text{ m s}^{-1}$ , a reduction of  $\sim 14\%$ . The tropical cyclone model is then integrated for 48 h with the reprocessed analyses to simulate the would-be behavior of Florence under the influence of a weakened westerly jet.

As shown in Fig. 18, the minimum SLP of Expt. ODW+WTR at 24 h is 2 mb weaker than the one of Expt. ODW, and the maximum surface wind of Expt. ODW+WTR is  $5.0 \text{ m s}^{-1}$  or 13% weaker than that of Expt. ODW. A weaker westerly trough and jet result in a weaker intensification of Florence. Figure 19 shows the simulated 200-mb geopotential heights, wind vectors, and isotaches of Expt. ODW+WTR at 12 h. It is

apparent that the maximum wind in the outflow jet of Expt. ODW+WTR is  $6.4 \text{ m s}^{-1}$  or  $\sim 15\%$  weaker than that of Expt. ODW (Fig. 10). The comparison suggests that the intensification of Florence is very much correlated to the approaching westerly jet.

Previous studies (Holland and Merrill 1984; Merrill 1984; Shi et al. 1990) suggested that the outflow jet provides a channel to remove the warm air from the core of tropical cyclones, and as a result, the convection in the core region can be enhanced. Figure 20 shows that the mean convective precipitation of Expt. ODW + WTR inside a  $2^{\circ} \times 2^{\circ}$  box centered at the storm center is reduced by about an average of 15–20% between 10 and 15 h, coinciding with the 15% reduction of the maximum wind in the outflow jet. The weaker convection in the core region between 10 and 15 h eventually results in a weaker hurricane at 24 h. These results are consistent with Holland and Merrill (1984) and Shi et al. (1990). Figure 20 also shows that the inner core convection of Expt. ODW and ODW+WTR reach their maximum at 13 h, while the intensities of both storms reach their maximum at 23 h, suggesting a 10-h lag between the maximum convection and the maximum intensity in Florence.

Figure 21 shows the 12-h 200-mb RH field of Expt. ODW+WTR. Similar to the 12-h 200-mb RH contours of Expt. ODW (Fig. 12), the moisture field features a wet region ( $\text{RH} > 90\%$ ) on the anticyclonic shear side of the jet, indicating the existence of the secondary circulation. The broader wet region is a consequence of a broader secondary circulation in this experiment. However, the secondary wet region, embedded in the cyclonic shear side of the exit region of the jet of Expt. ODW over Virginia (Fig. 12), is conspicuously absent in Expt. ODW+WTR, indicating a weaker outflow, a weaker and broader thermally direct circulation, and the

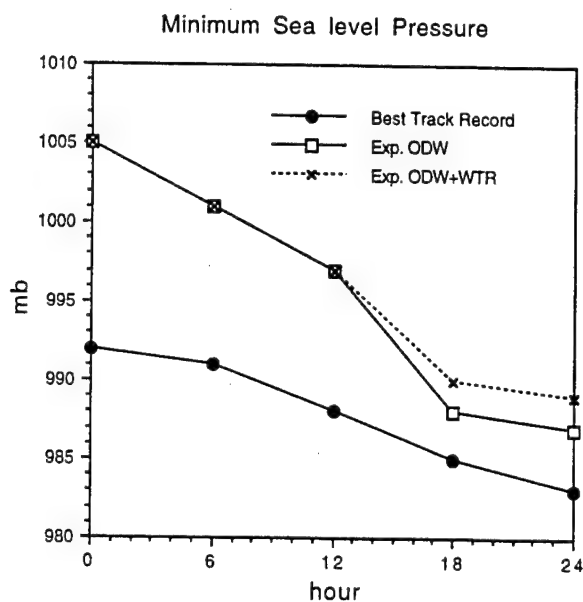


FIG. 18. Time variation of the minimum sea level pressure (mb) and maximum surface wind speed ( $\text{m s}^{-1}$ ) of Expt. ODW and ODW+WTR.

absence of the thermally indirect circulation because of a weaker approaching westerly UTT.

Table 2 also lists the storm-relative angular momentum budgets calculated from Expt. ODW+WTR's result at 12 h using Eq. (1). The result shows a larger (smaller) net horizontal import of the eddy (mean) cyclonic angular momentum corresponding to a stronger outflow jet of Expt. ODW as compared to a smaller net horizontal eddy import in Expt. ODW+WTR at large radii. This result indicates that the outflow jet and the eddy import of cyclonic angular momentum are stronger with a stronger approaching westerly UTT, consistent with Challa and Pfeffer (1990). Further evidence of the in-

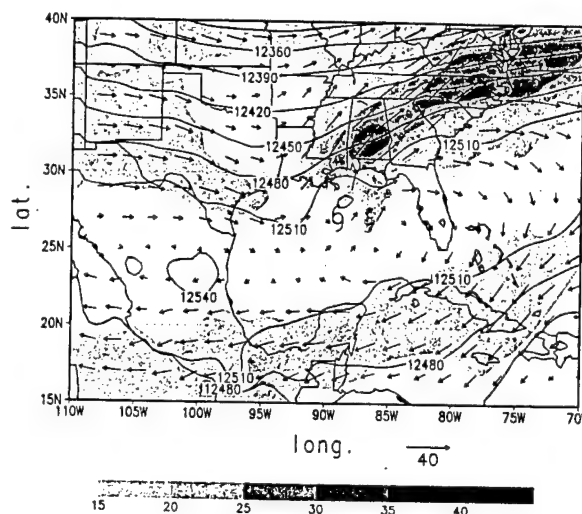


FIG. 19. Same as Fig. 10 except for Expt. ODW+WTR at 12 h.

fluence by the approaching westerly UTT can be seen in the change of storm-relative, horizontal eddy AMF (Fig. 22). In both experiments, Florence experienced an increase of horizontal import of eddy cyclonic angular momentum before 15 h. In Expt. ODW, the stronger approaching westerly UTT is correlated with a larger increase of eddy convergence flux and more intense inner core convection (Fig. 20) before 15 h. Eddy heat fluxes in the upper troposphere are also calculated. Results show that a cooling of  $4 \text{ K day}^{-1}$  by eddies exists at radius between 400 and 700 km between 15 and 18 h in Expt. ODW, up from  $2 \text{ K day}^{-1}$  at 12 h. In contrast,

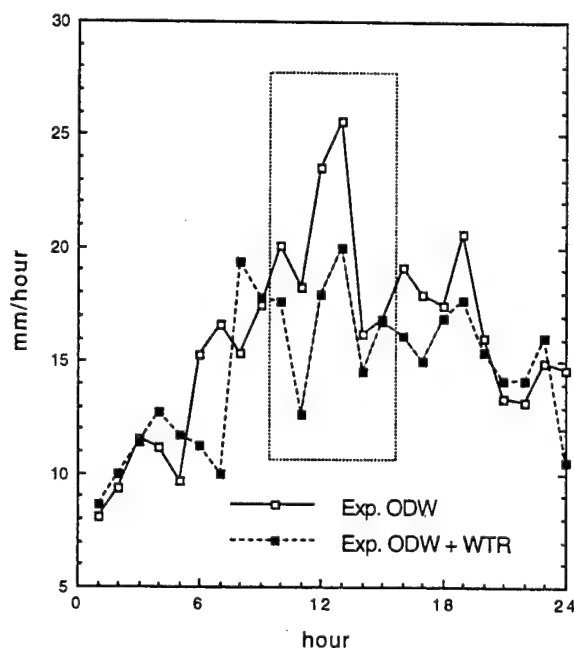


FIG. 20. Mean convective rain rates of Expt. ODW and ODW+WTR inside a  $2^\circ \times 2^\circ$  box centered at the storm center. Dashed box contains mean convective rain rates between 10 and 15 h.

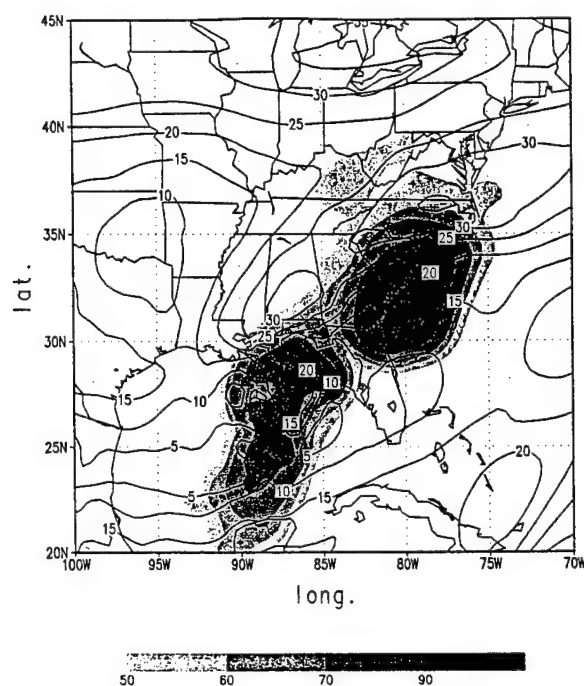
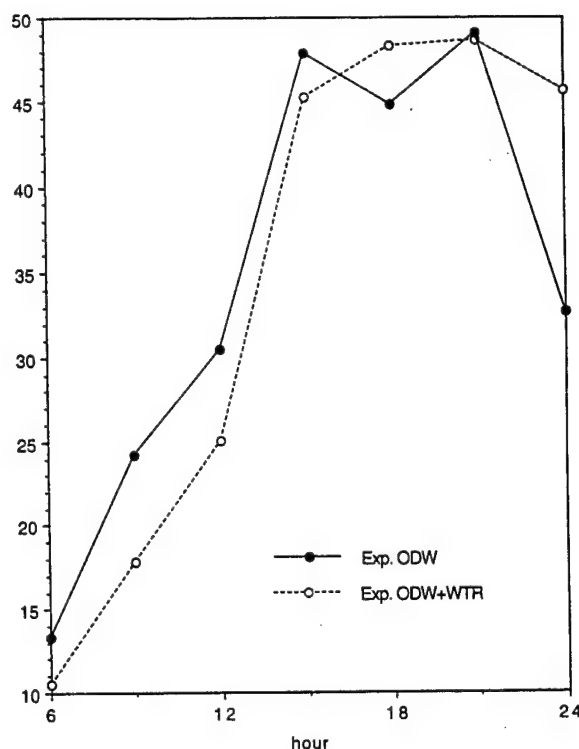


FIG. 21. Same as Fig. 12 except for Expt. ODW+WTR at 12 h.

the cooling of  $2 \text{ K day}^{-1}$  by eddies remains unchanged between 12 and 18 h in Expt. ODW+WTR. This result again indicates the influence by the approaching westerly UTT and is consistent with the estimate of Molinari and Vollaro (1990).

## 7. Conclusions and discussion

In this study, model-simulated results were analyzed to reveal the detailed structure of the outflow layer of Florence, and a numerical experiment was performed to study the interactions between the outflow layer of Florence and the upper-level westerlies. Diagnosis of the 200-mb level structure of Expt. ODW at 12 h showed that the outflow layer was highly asymmetric, especially beyond three degrees radius, with an outflow jet originating at approximately three degrees north of the storm center (Fig. 13). The outflow jet was elongated with a length of roughly 2500 km and a width of 500 km. Further diagnosis of the 12-h wind and RH in the outflow jet at the entrance and exit regions of the outflow showed that there was a thermally direct, circum-jet secondary circulation in the entrance region (Fig. 17) and a reversed thermally indirect one in the exit region (Fig. 18). The secondary circulation had an outward branch above the jet, an inward branch below the jet (near 400 mb), an ascending branch in the anticyclonic shear side, and a descending branch in the cyclonic shear side of the outflow jet. The inward branch below the outflow jet in the entrance region of the outflow jet, however, was less apparent in this study than the one shown in Shi et al. (1990).

FIG. 22. Horizontal convergence of storm-relative eddy angular momentum between 300 and 700 km radii in the outflow layer for Expts. ODW and ODW+WTR. Units are in  $10^{22} \text{ g cm}^2 \text{ s}^{-2}$ .

Because of the complexity due to the existence of other synoptic systems, including the coastal front along the U.S. east coast, it was difficult to isolate a well-defined secondary circulation. In general, the structure of the outflow layer of the simulated Florence was qualitatively similar to the idealized model study in Shi et al. (1990). In their composite study, Chen and Chou (1994) also found a similar jet streak associated with the evolution of upper-tropospheric cold vortices over the western North Pacific during the warm season. They suggested the existence of the circum-jet thermally direct (indirect) secondary circulation in the entrance (exit) region of the jet streak, based on the cloud distribution. This is also consistent with Molinari and Vollaro (1989), in which they speculated that the frontogenetical forcing in the confluence region between the cold trough and the warm hurricane outflow may have enhanced the outflow ahead of the trough via thermal wind adjustment. At 24 h, the westerly jet moved north-eastward and was located over Virginia and far away from Florence. However, Florence's center also moved northward and into a region below the south end of the westerly trough. This resulted in the increase of vertical wind shear, the reduction of outflow, and consequently the weakening of the intensity of Florence. At this moment, Florence was about to make landfall. This result is similar to the case described by Holland and Merrill



(1984) where Hurricane Kerry began to decay after the cutoff of the poleward outflow channel.

Calculation of the storm-relative angular momentum budget at 12 h (Table 2) demonstrated that the angular momentum balance was primarily maintained by the Coriolis torque and horizontal transports. It also revealed that the contribution by the horizontal import of eddy cyclonic angular momentum was the dominant feature at large radii, in agreement with the observational study by Molinari and Vollaro (1989). This result again underscored the dominance of the outflow jet in the outflow layer, and the highly asymmetric nature of the outflow layer of tropical cyclones (Black and Anthes 1971).

The most interesting numerical experiment to elucidate the interactions between Hurricane Florence (1988) and its environment is the one in which the approaching westerly UTT was very much weakened (Expt. ODW+WTR). In this numerical experiment, the weakened westerly UTT resulted in a reduction of the maximum speed of the outflow jet of Florence by  $6.4 \text{ m s}^{-1}$  (or about 15%) at 12 h. The weakened trough and outflow jet of Florence were responsible for a 2-mb minimum SLP increase and a  $5.0 \text{ m s}^{-1}$  or 13% maximum surface wind reduction. Figure 20 showed that the weakened outflow jet also resulted in weaker convections in the core region in the 10–15 h window, 8–13 h before the model storm reached its maximum intensity. Diagnosis of the 200-mb RH field of this experiment (Fig. 21) indicated a weaker outflow, a weaker and broader thermally direct circulation in the entrance region, and the absence of the thermally indirect circulation in the exit region because of an weaker approaching westerly UTT. The weakened upper-level westerly trough was also responsible for the reduction of inward cyclonic eddy AMF in this numerical experiment (Table 2 and Fig. 22). This result suggested that the large inward flux of cyclonic eddy angular momentum produced by the passage of an upper-level westerly trough was important to the intensification of Florence's inner core convection between 1000 and 1500 UTC 9 September (Fig. 20) and therefore the deepening of the minimum SLP between 1200 and 2400 UTC 9 September. This result also coincided with the cooling of up to  $4 \text{ K day}^{-1}$  by the eddy heat flux, likely induced by the passage of the upper-level westerly trough at large radii in upper troposphere, at 15 h in Expt. ODW, while the cooling was only  $2 \text{ K day}^{-1}$  in Expt. ODW+WTR, suggesting the interaction between the upper-level westerly trough and Florence. This result is consistent with the estimate shown in Molinari and Vollaro (1990).

On the other hand, the strong vertical shear associated with the upper-level westerly trough might prevent Florence from further intensifying. Merrill (1988a,b) suggested that the upper-level environmental interactions with tropical cyclones, in general, contribute negatively to intensity changes. His conclusion was based upon two observations: 1) maximum intensity of tropical cy-

clones is limited by the potential that the sea surface temperature can provide (Emanuel 1986), and tropical cyclones rarely reach to their potential maximum intensity; and 2) increasing vertical shear is usually accompanied by the approach of the upper-level westerly trough and works against the intensification of tropical cyclones. In Florence, however, because it made landfall three hours after it reached maximum intensity, it was difficult to fully determine whether or not the vertical shear associating with the approaching upper-level westerly trough had any negative effect on the intensification. Nevertheless, the result from this numerical experiment suggested that the upper-level westerly trough's contribution was important to the intensification of Florence and the timing and relative position of an approaching westerly UTT and a tropical cyclone is critical for the intensification and decay of a tropical cyclone.

Even though the model-simulated outflow structure of Hurricane Florence is very consistent dynamically and thermodynamically, it remains to be directly verified with observations. Detailed observations of the three-dimensional structure of the outflow layer of tropical cyclones are extremely scarce. The ODW observations used in this study do not provide information above 400 mb, limited by the operational altitude of NOAA WP-3D aircrafts that deployed them. Dropsonde data collected from 200 mb to surface in TCM-90 and TCM-92 experiments (Elsberry and Abbey 1991; Dunnavan et al. 1993) may be very useful in the study of the interactions between the upper-level environment and tropical cyclones. Because Florence made landfall at 0200 UTC 10 September, three hours after it reached its maximum intensity, the window of opportunity for studying interactions between Florence and the upper-level westerly trough is very short (less than a day). Therefore, it is rather difficult to study the full extent of the interactions. A real case study of the interactions between a tropical cyclone and the upper-level environment over an open ocean would be valuable for this purpose, where the timing and relative position of an UTT and a tropical cyclone can be more conveniently analyzed.

**Acknowledgments.** The authors wish to thank Dr. Keith Sashegyi of the National Research Laboratory (NRL) for his help with the NRL data analysis system and Dr. James Franklin of AOML/HRD for providing the ODW data. We acknowledge many helpful discussions with Dr. Mark DeMaria of AOML/HRD and Dr. Edward Rodgers of NASA/GSFC. This research was supported by an NRL basic research program PE601153N.

#### REFERENCES

- Anthes, R. A., 1974: The dynamics and energetics of mature tropical cyclones. *Rev. Geophys. Space Phys.*, **12**(3), 495–522.

- , 1977: A cumulus parameterization scheme utilizing a one-dimensional cloud model. *Mon. Wea. Rev.*, **105**, 270–286.
- Black, P. G., and R. A. Anthes, 1971: On the asymmetric structure of the tropical cyclone outflow layer. *J. Atmos. Sci.*, **28**, 1348–1366.
- Challa, M., and R. L. Pfeffer, 1990: The formation of Atlantic hurricanes from cloud clusters and depressions. *J. Atmos. Sci.*, **47**, 909–927.
- Chang, S. W., K. Brehme, R. V. Madala, and K. D. Sashegyi, 1989: A numerical study of the East Coast snowstorm of 10–12 February 1983. *Mon. Wea. Rev.*, **117**, 1768–1778.
- Chen, G. T.-J., and L.-F. Chou, 1994: An investigation of cold vortices in the upper troposphere over the western North Pacific during the warm season. *Mon. Wea. Rev.*, **122**, 1436–1448.
- Chen, L., and W. M. Gray, 1984: Global view of the upper level outflow patterns associated with tropical cyclone intensity changes during FGGE. Preprints, *15th Conf. on Hurricanes and Tropical Meteorology*, Miami, FL, Amer. Meteor. Soc., 224–231.
- DeMaria, M., J.-J. Baik, and J. Kaplan, 1993: Upper-level eddy angular momentum fluxes and tropical cyclone intensity change. *J. Atmos. Sci.*, **50**, 1133–1147.
- Detering, H. W., and D. Etling, 1985: Application of the E-ε turbulence model to the atmospheric boundary layer. *Bound.-Layer Meteor.*, **33**, 113–133.
- DiMego, G., 1988: The National Meteorological Center regional analysis system. *Mon. Wea. Rev.*, **116**, 977–1000.
- Dunnavan, G. M., R. L. Elsberry, P. A. Harr, E. J. McKinley, and M. A. Boothe, 1993: Overview of the tropical cyclone motion-92 (TCM-92) mini-field experiment. Preprints, *20th Conf. Hurricanes and Tropical Meteorology*, San Antonio, TX, Amer. Meteor. Soc., 1–6.
- Elsberry, R. L., and R. F. Abbey Jr., 1991: Overview of the tropical cyclone motion (TCM-90) field experiment. Preprints, *19th Conf. Hurricanes and Tropical Meteorology*, Miami, FL, Amer. Meteor. Soc., 1–6.
- Emanuel, K. A., 1986: An air–sea interaction theory for tropical cyclones. Part I: Steady-state maintenance. *J. Atmos. Sci.*, **43**, 585–604.
- Frank, W. M., 1977a: The structure and energetics of the tropical cyclone. Part I: Storm structure. *Mon. Wea. Rev.*, **105**, 1119–1135.
- , 1977b: The structure and energetics of the tropical cyclone. Part II: Dynamics and energetics. *Mon. Wea. Rev.*, **105**, 1136–1150.
- Franklin, J. L., and M. DeMaria, 1992: The impact of Omega dropwindsonde observations on barotropic hurricane track forecasts. *Mon. Wea. Rev.*, **120**, 381–391.
- , —, and C. S. Velden, 1991: The impact of Omega dropwindsonde and satellite data on hurricane track forecasts. Preprints, *19th Conf. on Hurricanes and Tropical Meteorology*, Miami, FL, Amer. Meteor. Soc., 87–92.
- Holland, G. J., 1983: Angular momentum transports in tropical cyclones. *Quart. J. Roy. Meteor. Soc.*, **109**, 187–209.
- , and R. T. Merrill, 1984: On the dynamics of tropical cyclone structural changes. *Quart. J. Roy. Meteor. Soc.*, **110**, 723–745.
- Holt, T., S. W. Chang, and S. Raman, 1990: A numerical study of the coastal cyclogenesis in GALE IOP 2: Sensitivity to PBL parameterizations. *Mon. Wea. Rev.*, **118**, 234–257.
- Kaplan, J., and J. L. Franklin, 1991: The relationship between the motion of Tropical Storm Florence (1988) and its environmental flow. Preprints, *19th Conf. on Hurricanes and Tropical Meteorology*, Miami, FL, Amer. Meteor. Soc., 93–97.
- Kuo, H. L., 1965: On formation and intensification of tropical cyclones through latent heat release by cumulus convection. *J. Atmos. Sci.*, **22**, 40–63.
- Lawrence, M. B., and J. M. Gross, 1989: Atlantic hurricane season of 1988. *Mon. Wea. Rev.*, **117**, 2248–2259.
- McBride, J., 1981: Observational analysis of tropical cyclone formation. Part III: Budget analysis. *J. Atmos. Sci.*, **38**, 1152–1166.
- Madala, R. V., 1981: Efficient time integration schemes for atmospheric and ocean models. *Finite Difference Techniques for Vectorized Fluid Dynamic Calculations*, Springer-Verlag, 56–74.
- , S. W. Chang, U. C. Mohanty, S. C. Madan, R. K. Paliwal, V. B. Sarin, T. Holt, and S. Raman, 1987: Description of the Naval Research Laboratory limited-area dynamical weather prediction model. NRL Tech. Rep. 5992, 131 pp. [NTIS A182780.]
- Merrill, R. T., 1984: Structure of the tropical cyclone outflow layer. *Proc. 15th Conf. on Hurricanes and Tropical Meteorology*, Miami, FL, Amer. Meteor. Soc., 421–426.
- , 1988a: Characteristics of the upper-tropospheric environmental flow around hurricanes. *J. Atmos. Sci.*, **45**, 1665–1677.
- , 1988b: Environmental influences on hurricane intensification. *J. Atmos. Sci.*, **45**, 1678–1687.
- Molinari, J., and D. Vollaro, 1989: External influences on hurricane intensity. Part I: Outflow layer eddy angular momentum fluxes. *J. Atmos. Sci.*, **46**, 1093–1105.
- , and —, 1990: External influences on hurricane intensity. Part II: Vertical structure and response of the hurricane vortex. *J. Atmos. Sci.*, **47**, 1902–1918.
- Ooyama, K. V., 1987: Numerical experiments of study and transient jets with a simple model of the hurricane outflow layer. Preprints, *17th Conf. on Hurricanes and Tropical Meteorology*, Miami, FL, Amer. Meteor. Soc., 318–320.
- Palmen, E., and H. Riehl, 1957: Budget of angular momentum and kinetic energy in tropical cyclones. *J. Meteor.*, **14**, 150–159.
- Pfeffer, R. L., 1958: Concerning the mechanisms of hurricanes. *J. Meteor.*, **15**, 113–119.
- , and M. Challa, 1981: A numerical study of the role of eddy fluxes of momentum in the development of Atlantic hurricanes. *J. Atmos. Sci.*, **38**, 2393–2398.
- Rodgers, E. B., J. Stout, and J. Steranka, 1986: Upper-tropospheric and lower-stratospheric dynamics associated with tropical cyclones as inferred from total ozone measurements. Preprints, *Second Conf. on Satellite Meteorology/Remote Sensing and Applications*, Williamsburg, VA, Amer. Meteor. Soc., 382–387.
- , S. W. Chang, J. Stout, J. Steranka, and J. J. Shi, 1991: Satellite observations of variations in tropical cyclone convection caused by upper-tropospheric troughs. *J. Appl. Meteor.*, **30**, 1163–1184.
- Sadler, J. C., 1976: The role of the tropical upper-tropospheric trough in early season typhoon development. *Mon. Wea. Rev.*, **104**, 1266–1278.
- , 1978: Mid-season typhoon development and intensity changes and the tropical upper-tropospheric trough. *Mon. Wea. Rev.*, **106**, 1137–1152.
- Sashegyi, K. D., and R. V. Madala, 1993: Application of vertical-mode initialization to a limited-area model in flux form. *Mon. Wea. Rev.*, **121**, 207–220.
- Shi, J. J., S. W. Chang, and S. Raman, 1990: A numerical study of the outflow layer of tropical cyclones. *Mon. Wea. Rev.*, **118**, 2042–2055.
- , —, K. D. Sashegyi, and S. Raman, 1991: Enhancement of objective analysis of Hurricane Florence (1988) with dropsonde data. Preprints, *19th Conf. on Hurricanes and Tropical Meteorology*, Miami, FL, Amer. Meteor. Soc., 335–337.
- , —, and S. Raman, 1996: Impact of assimilations of dropwindsonde data and SSM/I rain rates on numerical predictions of Hurricane Florence (1988). *Mon. Wea. Rev.*, **124**, 1435–1448.
- Steranka, J., E. B. Rodgers, and R. C. Gentry, 1986: The relationship between satellite measured convection burst and tropical cyclone intensification. *Mon. Wea. Rev.*, **114**, 1539–1546.
- Tuleya, R. E., and Y. Kurihara, 1981: A numerical study on the effects of environmental flow on tropical storm genesis. *Mon. Wea. Rev.*, **109**, 2487–2506.

**Appendix C**

**Optical Remote Sensing Calibration Facility (ORSCF)  
Calibration Log**



Date	Customer	Equipment	Calibration	page
8/19/96	ORSCF	Labsphere Unisource 4000	Radiance	1
8/23/96	Ft. Belvoir/TEC	GER SFOV 1022, GER 3700	Radiance	3
8/27/96	Tower I	PHILLS--Princeton Instruments, Inc. Model: TEA/CCD-1024EM1 Serial#: D129457 Instruments SA, Inc. Cat#: 523.01.040 3.3 g/mm Blaze: 300-1200 Serial#: 113319	Radiance Spectral Spatial	5-7
8/29/96	Ft. Belvoir/TEC	GER 3700	Radiance	9
8/29/96	Tower I	ASD	Radiance	11
9/3/96	Ft. Belvoir/TEC	Reflectance Targets 10"x10" Spectralon S/N: 0490-4736-B 18"x18" Spectralon S/N: 9377B	Reflectance	13
9/5/96	NRL	Sea Targets White Labsphere 5"x5" S/N: 001800 Gray Labsphere 10"x10" S/N: 001803	Reflectance	15
9/11/96	NRL	ASD Dual Field Spec and PS2 Remote Cosine Receptor #901 Rev A	Irradiance	17
10/1/96	NRL	ASD Dual Field Spec and PS2 Remote Cosine Receptor #901 Rev A	Irradiance	19
10/8/96		PHILLS CCD Serial #: 8840 JOBIN YVON CP140/202 NOV95/156	Radiance Spectral	21
10/16/96	Covered Lantern	PHILLS--Remote Ocean Systems ICCD Split Head Camera Serial#: 498 JOBIN YVON CP140/202 NOV 95/158	Spectral Radiance	23
10/23/96	Covered Lantern	PHILLS--Remote Ocean Systems ICCD Split Head Camera Serial#: 498 JOBIN YVON CP140/202 NOV 95/158	Radiance Spectral Spatial	25
11/22/96	ORSCF	OL750-M-S Monochromator	Line Sources	27
12/19/96 12/20/96 1/10/97 1/13/97 1/14/97	NRL	PHILLS--Princeton Instruments, Inc. Model: TEA/CCD-1024EM1 Serial#: D129457 Instruments SA, Inc. Cat#: 523.01.040 3.3 g/mm Blaze: 300-1200 Serial#: 113319	Radiance Spectral	28-29
1/16/97 1/17/97	Covered Lantern	PHILLS--Remote Ocean Systems ICCD Split Head Camera Serial#: 498 JOBIN YVON CP140/202 NOV 95/158	Radiance Spectral	30-31
1/27/97 1/28/97 1/29/97	COPE	PHILLS CCD Serial #: 8840 JOBIN YVON CP140/202 NOV95/156	Radiance Spectral Spatial	32-34
2/6/97 2/7/97	SITAC	ASD Field Spec FR	Staring Warmup Spectral 2-D FOV	35
2/11/97	TEC/HYMSMO	Reflectance Targets 10"x10" Spectralon S/N: 0490-4736-B	Reflectance	36
3/14/97	NRL	PHILLS--Princeton Instruments, Inc. Model: TEA/CCD-1024EM1 Serial#: D129457 Instruments SA, Inc. Cat#: 523.01.040 3.3 g/mm Blaze: 300-1200 Serial#: 113319	Polarization	37
4/17-25/97	HDOS	PRS3 Calibration Source	Radiance	38-45
Date	Customer	Equipment	Calibration	page
4/28/97	ORSCF	ITU-Irradiance Test Unit	Irradiance	45
4/29/97	ORSCF	Labsphere Unisource 4000	Radiance	46
5/8/97 5/29/97	ORSCF	OL 750-M-S Monochromator	Line Sources	47
5/30/97 6/2/97	ORSCF/NRL	Reflectance Targets White Labsphere 5"x5" S/N: 001800 Gray Labsphere 10"x10" S/N: 001803	Reflectance	48

6/29/97	ORSCF	Labsphere Unisource 4000	Radiance	49
7/28/97	ORSCF	ITU-Irradiance Test Unit F-399, STU-High Intensity Source	Irradiance	50
7/28/97	ORSCF	OL 750-M-S Monochromator	Line Sources	51
7/30/97	ORSCF	STU-Spectral Test Unit Detectors Measurement	Spectral Response	51
8/19/97	ORSCF	Labsphere Unisource 4000	Radiance	52
8/29/97	ORSCF	Labsphere Unisource 4000 Mapping (preliminary)	Radiance Map	53
9/18/97	ORSCF	OL 750-M-S Monochromator	Line Sources	54
9/23/97	ORSCF	OTU Adjustable Optical Slit Assembly	Fringe	55
10/16/97	ORSCF	Labsphere Unisource 4000	Radiance	56
10/30/97	ORSCF	ITU-Irradiance Test Unit F-400, F-399 STU-High Intensity Source	Irradiance	57
10/30/97	ORSCF	STU-Spectral Test Unit Detectors Measurement	Spectral Response	58
11/6/97	SEAWIFS	SIRREX 6.0		60-61
11/19/97	ORSCF	OL 750-M-S Monochromator	Line Sources	62
11/21/97		Transfer Radiometer	Radiance	63
11/26/97	ORSCF	DTU-Reflectance Targets	Reflectance	64
12/17/97	ORSCF	Labsphere Unisource 4000	Radiance	65
01/07/98	ORSCF	OL 750-M-S Monochromator	Line Sources	66
01/07/98	ORSCF	STU-Spectral Test Unit Detectors Measurement	Spectral Response	66
01/12/98	ORSCF	ITU-Irradiance Test Unit F-399 STU-High Intensity Source	Irradiance	67
02/12/98	TEC/HYMSMO	Reflectance Targets 10"x10" Spectralon S/N: 0490-4736-B	Reflectance	68
02/17/98	SITAC	ASD Field Spec FR	Radiance Spectral	69-70
02/26/98	ORSCF	Labsphere Unisource 4000	Radiance	71
03/05/98	ORSCF	OL 750-M-S Monochromator	Line Sources	72
03/11/98	ORSCF	OTU Adjustable Optical Slit Assembly	Fringe	73
03/26/98	NRL	Pixel Vision Camera Measurement	Radiance Spectral	74
03/27/98				
04/02/98	ORSCF	ITU-Irradiance Test Unit F-400, F-399 STU-High Intensity Source	Irradiance	75
04/02/98	ORSCF	STU-Spectral Test Unit Detectors Measurement	Spectral Response	76
04/07/98	ORSCF	Labsphere Unisource 4000	Radiance	77
04/08/98	NRL	Pixel Vision Camera System Calibration	Radiance Spectral	78-79
04/09/98				
05/07/98	ORSCF	OL 750-M-S Monochromator	Line Sources	80
05/08/98	ORSCF	Lumitex MV-150 Source	Radiant Power Stability	81
5/12-14/98				
05/29/98	ORSCF	DTU-Reflectance Target Standard	Reflectance	83
06/03/98	Stennis	Reflectance Targets 5"x5" Spectralon S/N: 10146-A 5"x5" Spectralon S/N: 10944-A	Reflectance	84
06/10/98	ORSCF	DTU-Reflectance Targets	Reflectance	85
06/11/98	NRL SeaLAB	Red Stick	Radiant Power	85
06/12/98	ORSCF	Labsphere Unisource 4000	Radiance	86

Date	Customer	Equipment	Calibration	page
06/12/98 06/23/98	ORSCF	Labsphere Unisource 4000 FEL xfer Calibration	Radiance	87-88
07/01/98	ORSCF	Blue Glass Filter 3440, Blue Filter Heat Absorbing Filter 2580	Transmittance	88
07/02/98	ORSCF	Labsphere Unisource 4000 FEL xfer Calibration w +w/o Blue Glass Filter	Radiance	89
07/15/98	ORSCF	OL 750-M-S Monochromator	Line Sources	90
07/16/98	ORSCF	ITU-Irradiance Test Unit F-399 STU-High Intensity Source	Irradiance	91
07/17/98	ORSCF	STU-Spectral Test Unit Detectors Measurement	Spectral Response	92
08/24/98	ORSCF	Labsphere Unisource 4000 FEL xfer Calibration	Radiance	93
09/03/98	NRL	Pixel Vision FEL/Spectralon Radiance Meas.	Radiance	94
09/17/98 09/18/98 09/24/98 09/25/98	ORSCF/NRL	Reflectance Targets Gray Labsphere 10"x10" S/N: 001803	Reflectance	94-95
09/30/98	ORSCF	Reflectance Targets Labsphere SRT-SP-100 Gray 10"x10"	Reflectance	95
09/30/98	ORSCF	OL 750-M-S Monochromator	Line Sources	96
10/06/98	ORSCF/NRL	Reflectance Targets Gray Labsphere 10"x10" S/N: 001803	Reflectance	96
11/10/98	ORSCF/NRL	Reflectance Targets Gray Labsphere 10"x10" S/N: 001803 Gray Labsphere 10"x10" 10100	Reflectance	97
11/12/98 11/13/98 11/16/98 11/24/98	SITAC	Spectral Goggles	Transmittance	97-98
12/11/98	ORSCF/NRL	Reflectance Targets Labsphere SRT-SP-100 Gray 10"x10" Gray Labsphere 10"x10" 10100 Gray Labsphere 10"x10" S/N: 001803	Reflectance	99
01/29/99	Stennis	Reflectance Targets 5"x5" Spectralon S/N: 10944-A	Reflectance	99
04/22/99	ORSCF	OL 750-M-S Monochromator	Line Sources	100
05/06/99	ORSCF	Yellow, Cyan, Magenta Subtractive filters	Transmittance	100
05/14/99	ORSCF	STU-Spectral Test Unit Detectors Measurement	Spectral Response	101
06/04/99	ORSCF	OL 750-M-S Monochromator	Line Sources	102
07/05/99	ORSCF/NRL	Reflectance Targets Gray Labsphere 10"x10" S/N: 001803	Reflectance	102
07/22/99	ORSCF	Labsphere Unisource 4000 FEL xfer Calibration w +w/o Blue Glass Filter	Radiance	103
08/04/99	ORSCF	Eclipse 1999 ND filters	Transmittance	104
08/05/99	ORSCF	STU-Spectral Test Unit Si PMT detector system response measurement	Spectral Response	104
08/11/99	ORSCF	ITU-Irradiance Test Unit F-399 system response calibration	Spectral Response	104
08/18/99	ORSCF	ITU-Irradiance Test Unit F-399 system response calibration w/OL 83A current adj.	Spectral Response	104
08/31/99 09/09/99	ORSCF	OL 750-M-S Monochromator repeatability	Hg Source	104- 105
09/17/99	ORSCF	OL 750-M-S Monochromator	Line Sources	105

## **Appendix D**

### **Calibration Schedules, Test Unit Measurement Data, and Comparison Analysis**

## Test Unit Measurement Data

Irradiance Test Unit (ITU), Radiance Test Unit (RTU), Spectral Test Unit (STU), and Diffuse-Reflectance Test Unit (DTU) measurement data recorded 4/97-9/99 follows. Data for the Labsphere Unisource 4000 also includes measurements recorded in August 1996 and preliminary mapping data from August 1997.

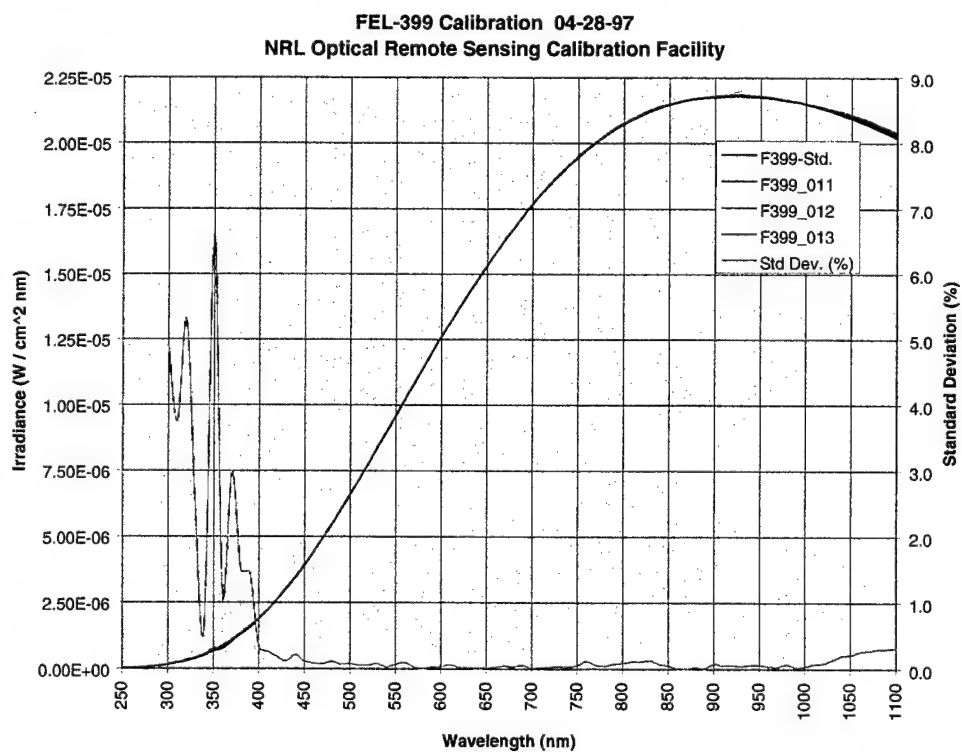
Table 1

ORSCF Test Unit Calibration Schedule (1997-98)														
Measurement		Month (X-completed)												
Test Unit	Items	A	M	J	J	A	S	O	N	D	J	F	M	A
ITU	F-399	X			X			X			X			X
	F-400	X						X						X
STU	Mono. HI Source Detector s		X		X		X		X		X		X	
		X			X			X			X			X
					X			X			X			X
RTU	Sphere Mappin g	X		X		X X		X		X		X		X
DTU	Plaques		X						X					
OTU	Slit						X						X	

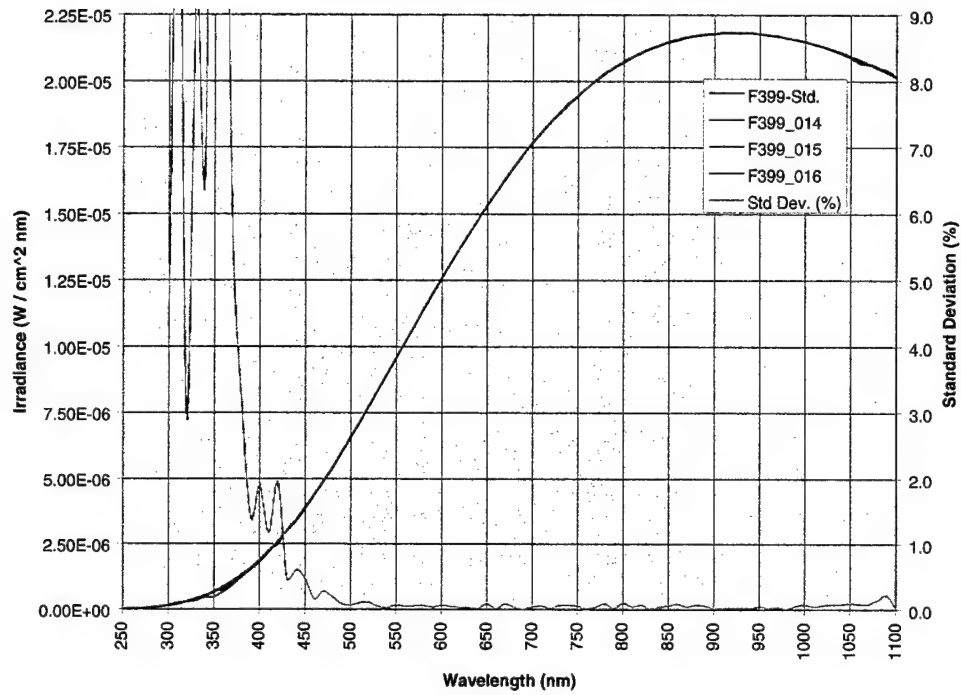
Table 2

ORSCF Test Unit Calibration Schedule (1998-99)														
Measurement		Month (X-completed),    Operational Transition												
Test Unit	Items	A	M	J	J	A	S	O	N	D	J	F	M	A
ITU	F-399	X			X			▽			▽			▽
	F-400	X						▽						▽
STU	Mono.		X		X		X		▽		▽		▽	
	HI	X			X			▽			▽			▽
	Source													
	Detector	X			X			▽			▽			▽
RTU	FEL					X								
	xfer													
	Sphere	X		X		X		▽		▽		▽		▽
	Mappin					X								
	g					X								
DTU	Plaques		▽						▽					
OTU	Slit						▽						▽	

ITU—Irradiance Test Unit



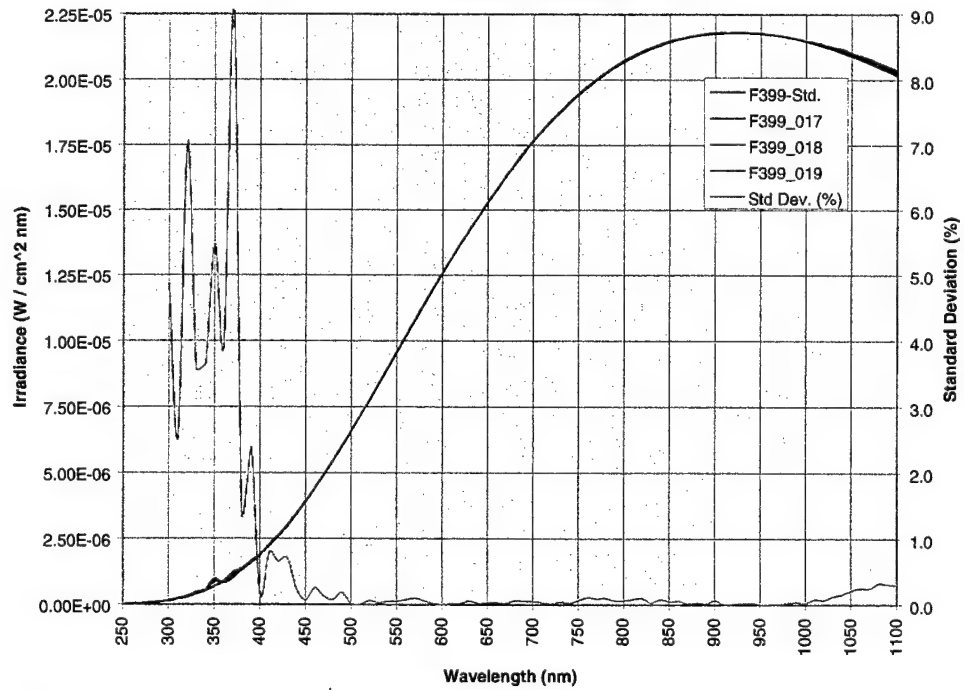
**FEL-399 Calibration 07-28-97**  
**NRL Optical Remote Sensing Calibration Facility**



f399\_072897.xls

f399\_103097.xls

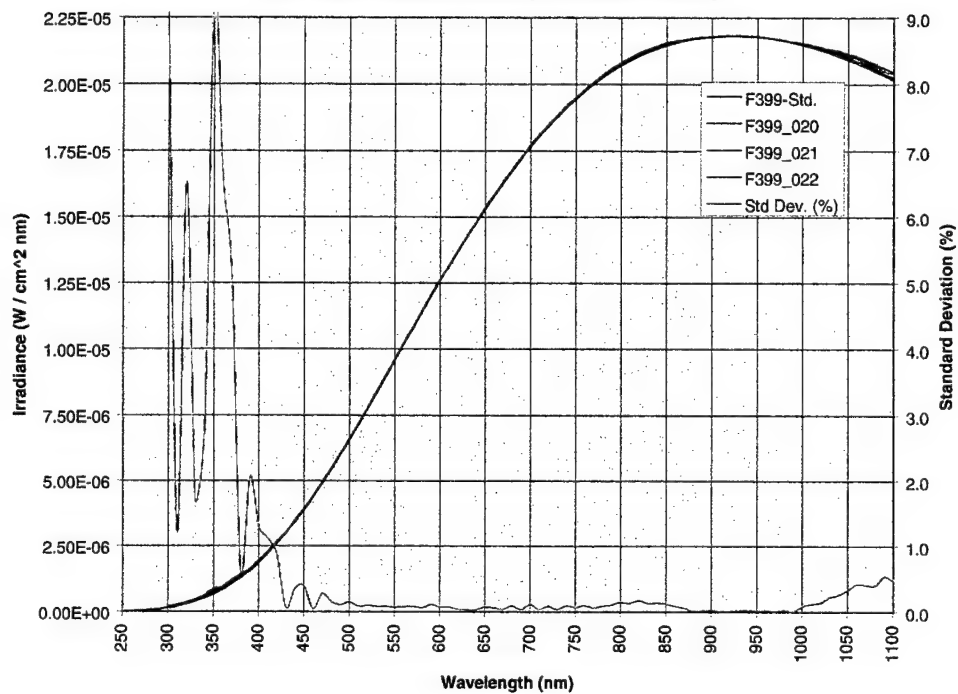
**FEL-399 Calibration 10-30-97**  
**Optical Remote Sensing Calibration Facility**



f399\_103097.xls

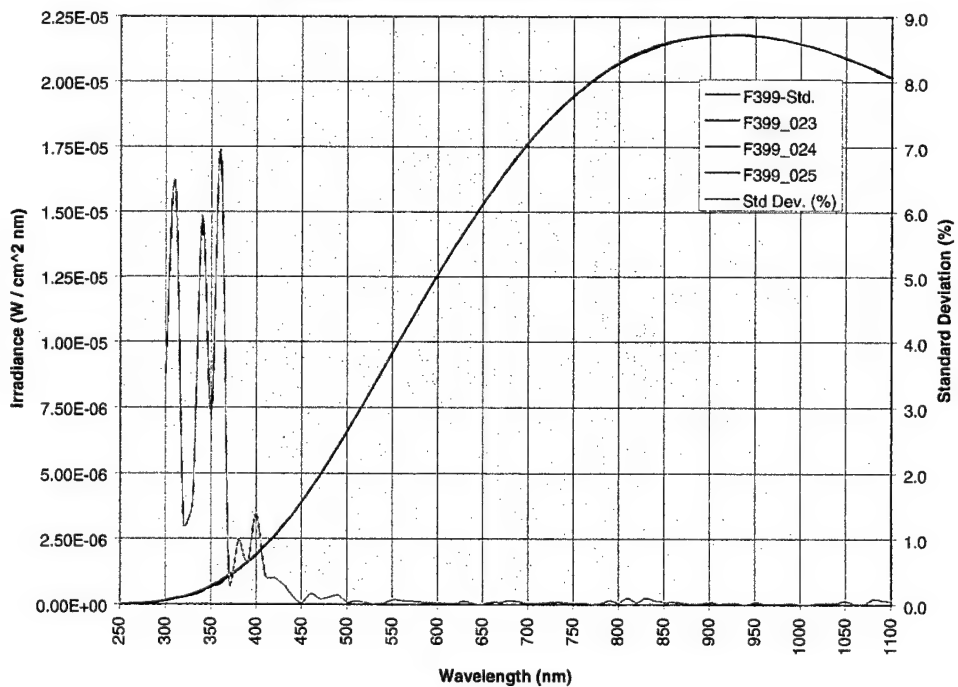
# ITU—Irradiance Test Unit

FEL-399 Calibration 01-12-98  
NRL Optical Remote Sensing Calibration Facility



f399\_011298.xls

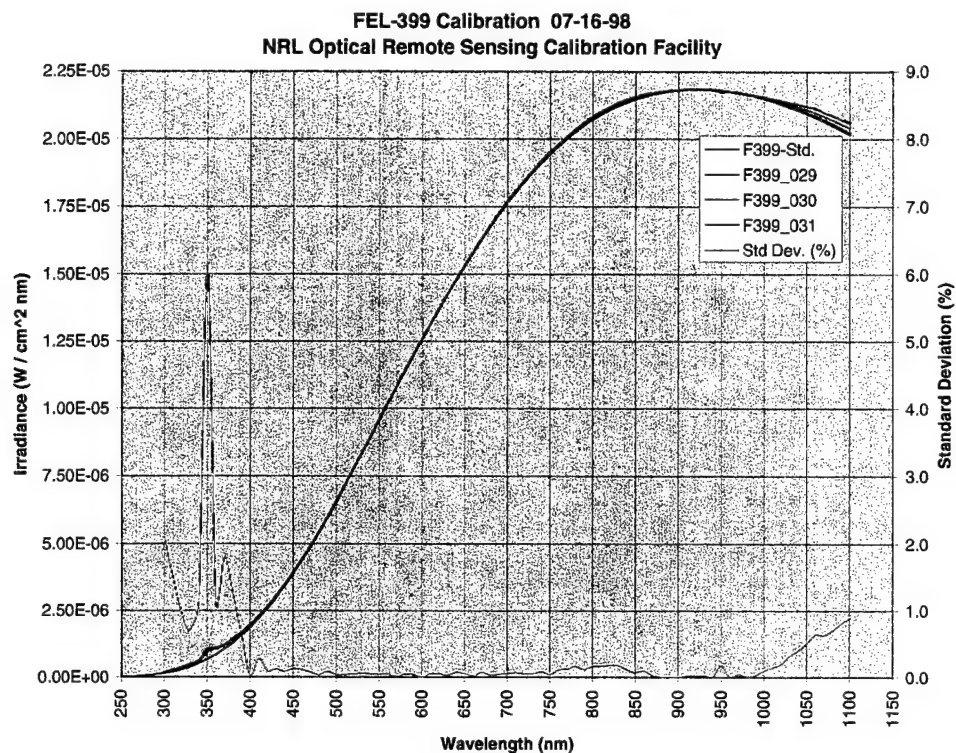
FEL-399 Calibration 04-02-98  
NRL Optical Remote Sensing Calibration Facility



f399\_040298.xls

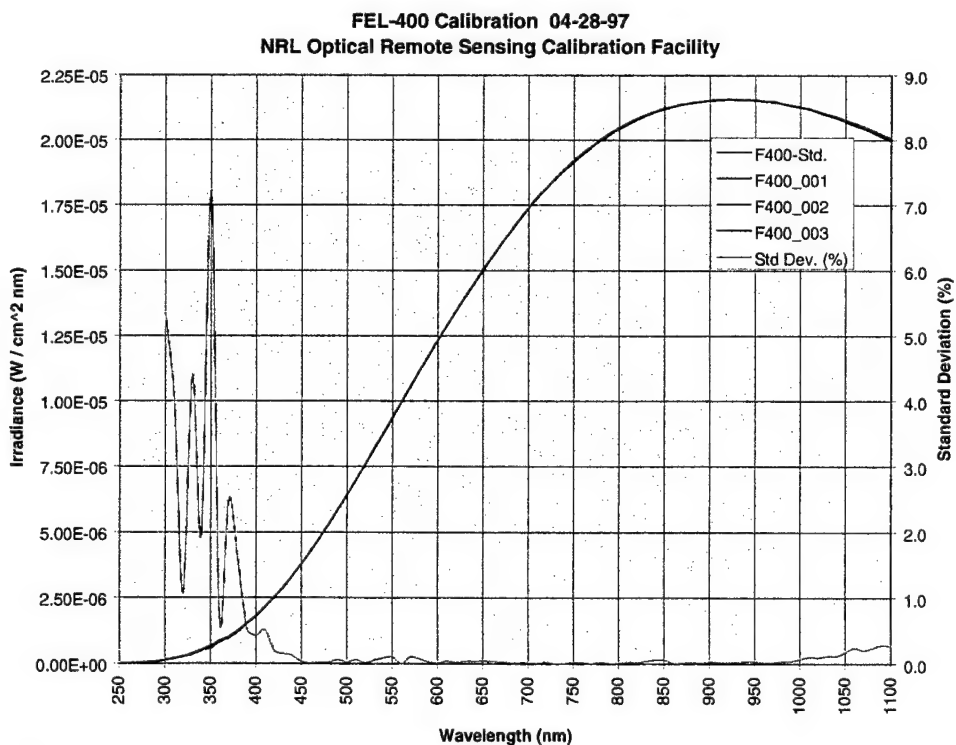


# ITU—Irradiance Test Unit



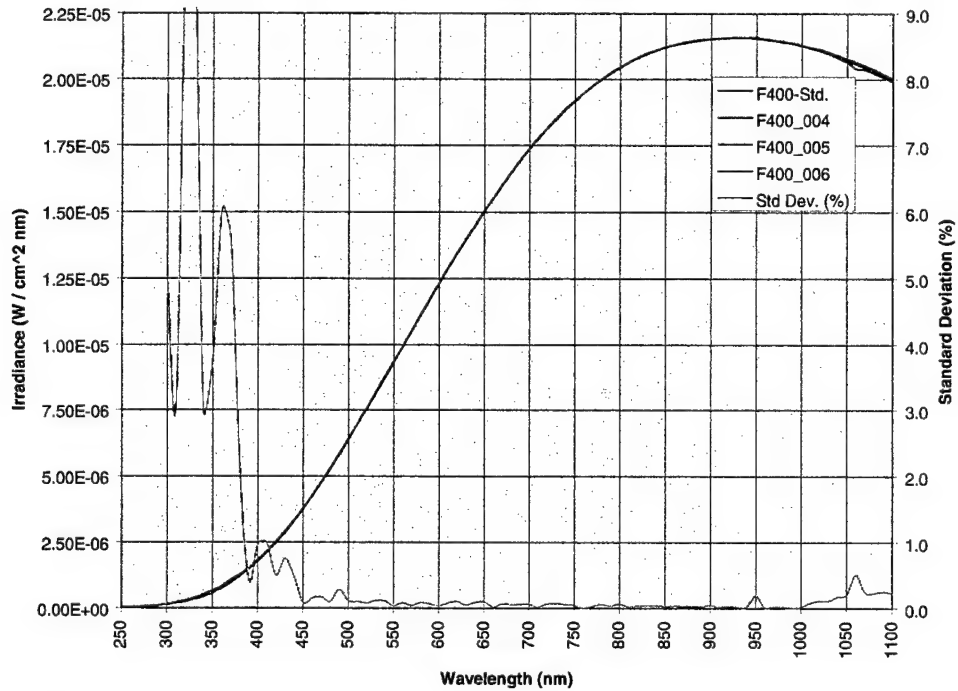
F399\_071699.xls

# ITU—Irradiance Test Unit



f400\_042897.xls

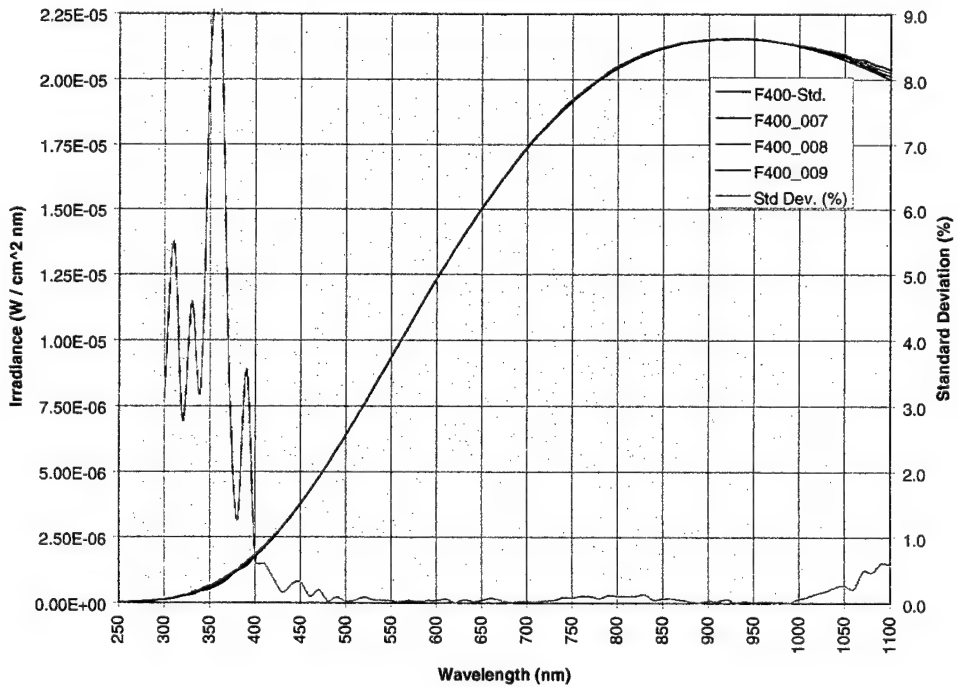
**FEL-400 Calibration 10-30-97**  
**NRL Optical Remote Sensing Calibration Facility**



f400\_103097.xls

**ITU—Irradiance Test Unit**

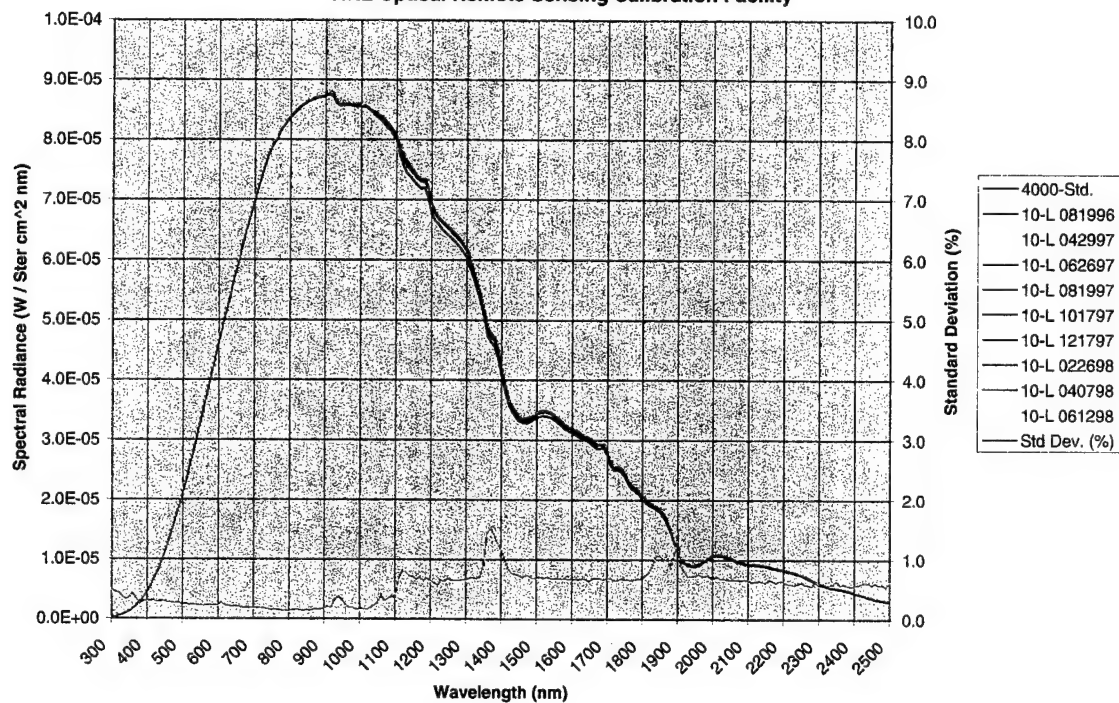
**FEL-400 Calibration 04-02-98**  
**NRL Optical Remote Sensing Calibration Facility**



f400\_040298.xls

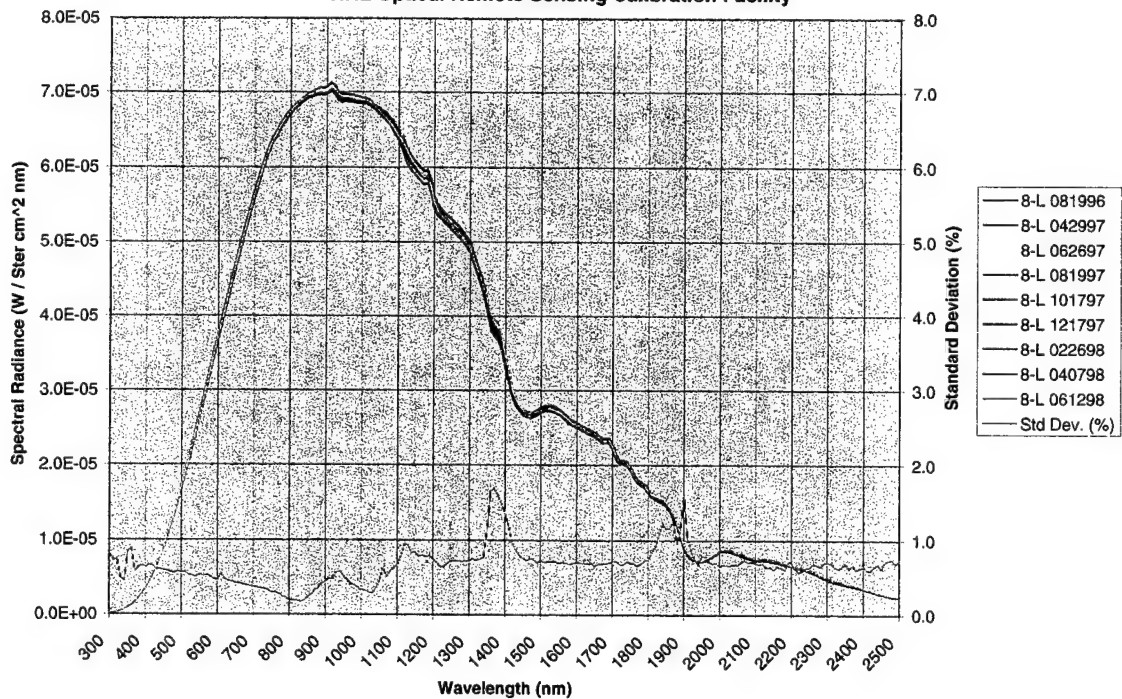
# RTU—Radiance Test Unit

Labsphere Unisource 4000 Calibration (10 Lamps) 08/96-06/98  
NRL Optical Remote Sensing Calibration Facility

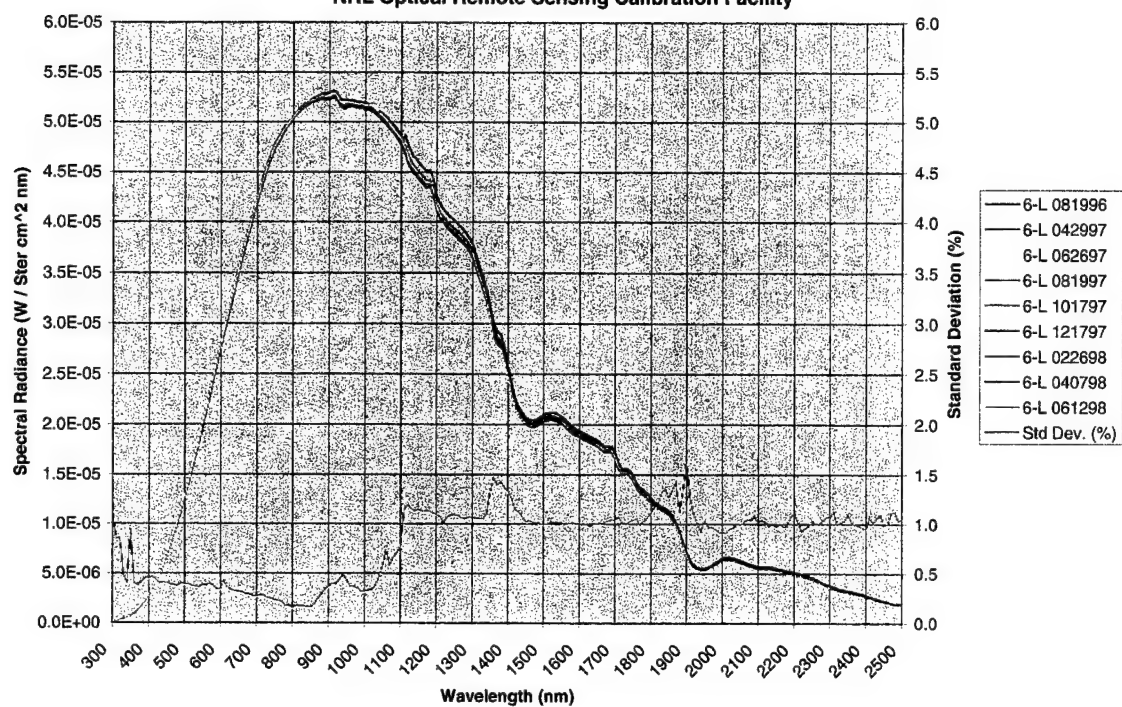


IS10\_0896-0698.xls

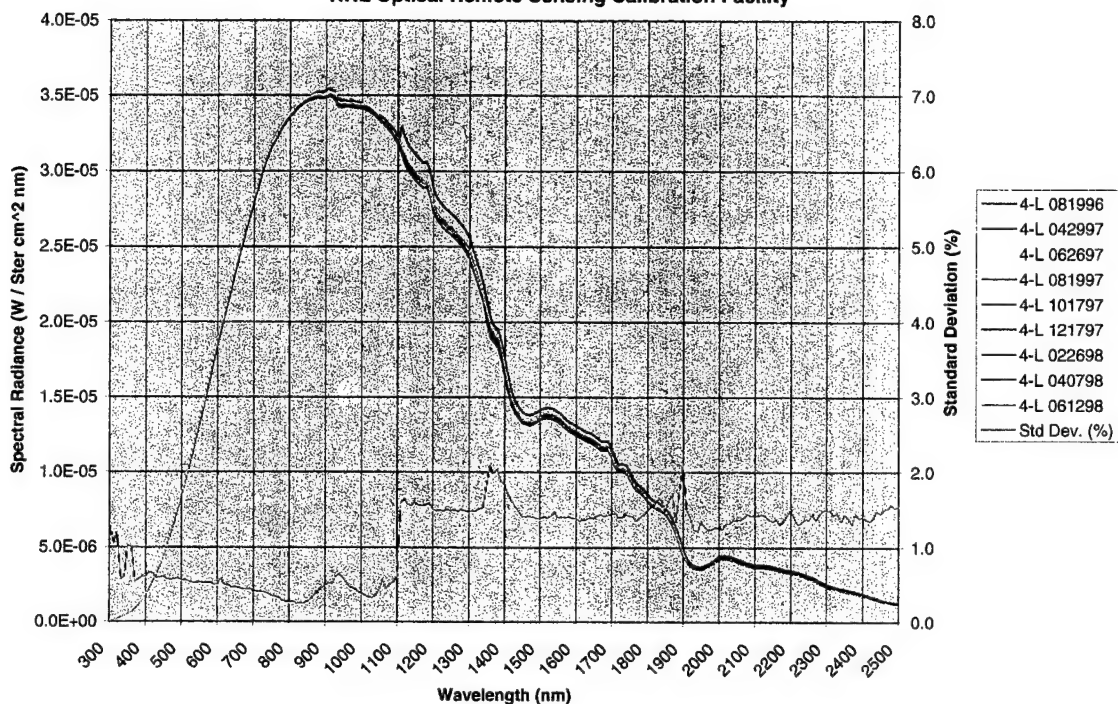
Labsphere Unisource 4000 Calibration (8 Lamps) 08/96-06/98  
NRL Optical Remote Sensing Calibration Facility



## RTU—Radiance Test Unit

Labsphere Unisource 4000 Calibration (6 Lamps) 08/96-06/98  
NRL Optical Remote Sensing Calibration Facility

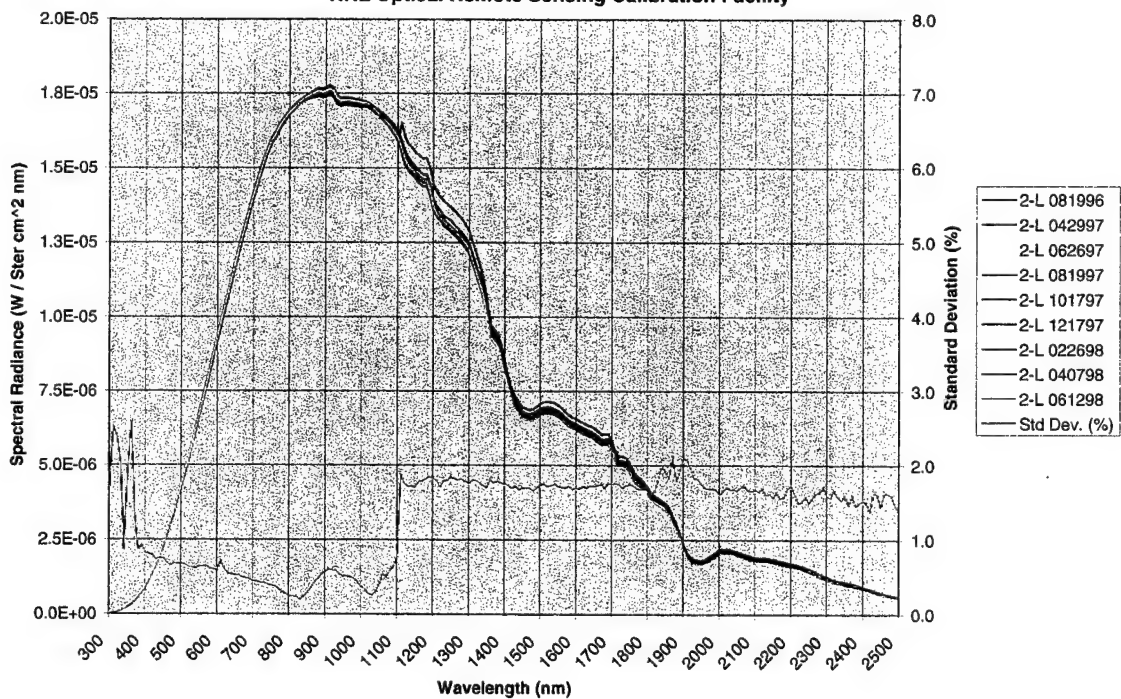
**Labsphere Unisource 4000 Calibration (4 Lamps) 08/96-06/98**  
**NRL Optical Remote Sensing Calibration Facility**



IS06\_0896-0498.xls

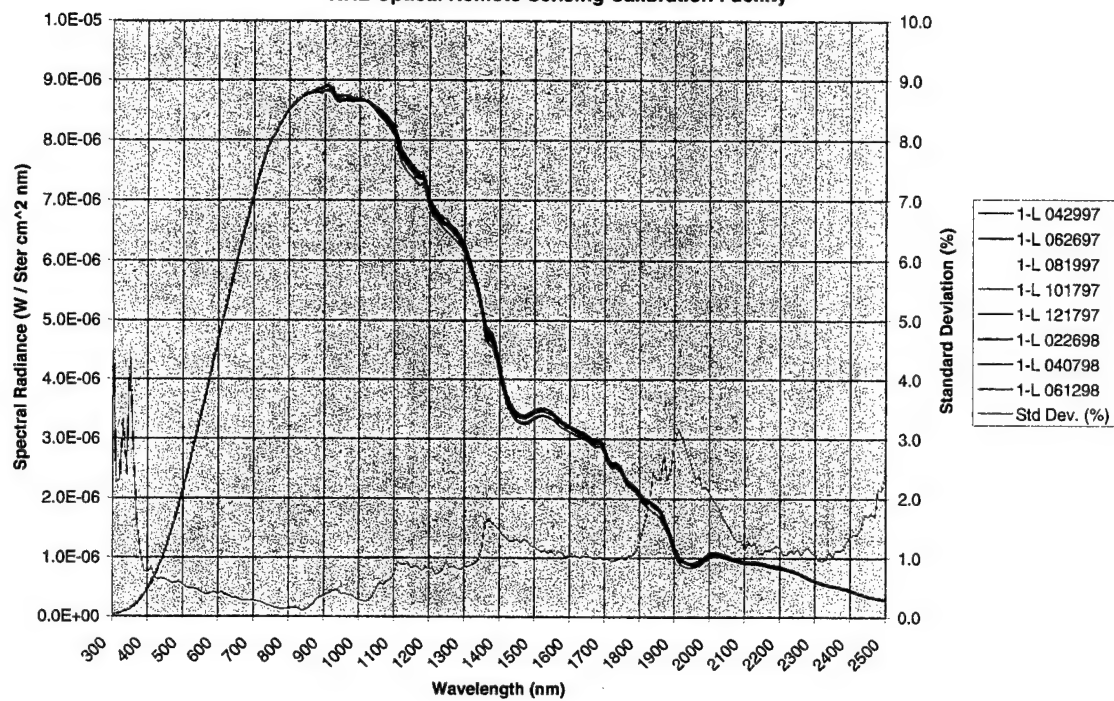
RTU—Radiance Test Unit

**Labsphere Unisource 4000 Calibration (2 Lamps) 08/96-06/98**  
**NRL Optical Remote Sensing Calibration Facility**

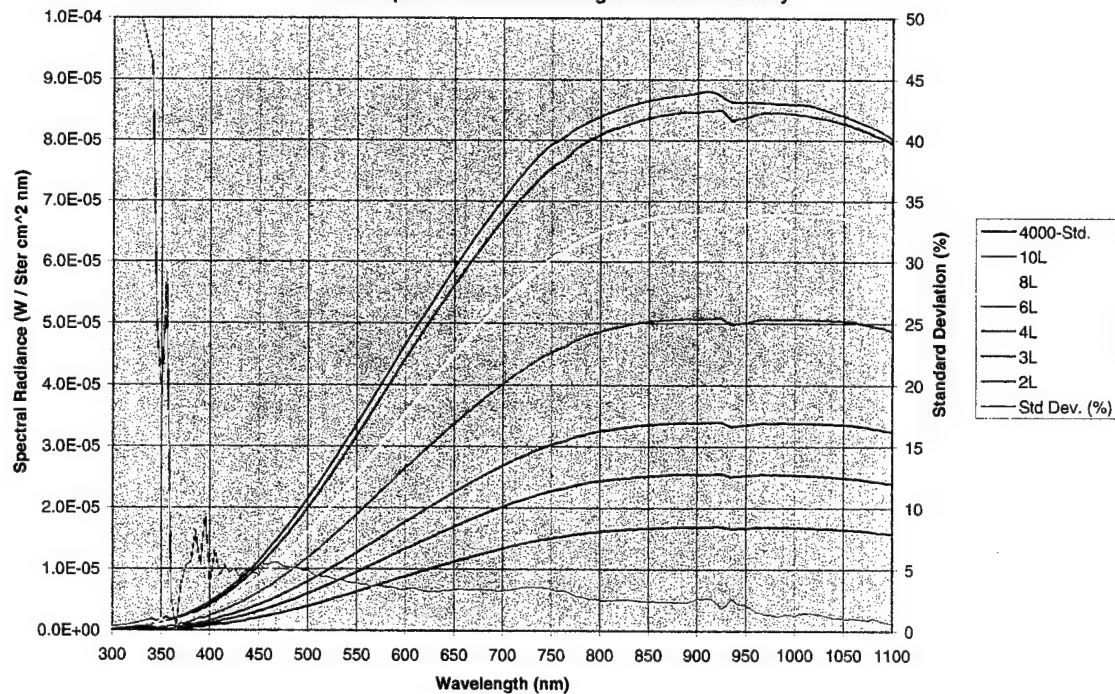




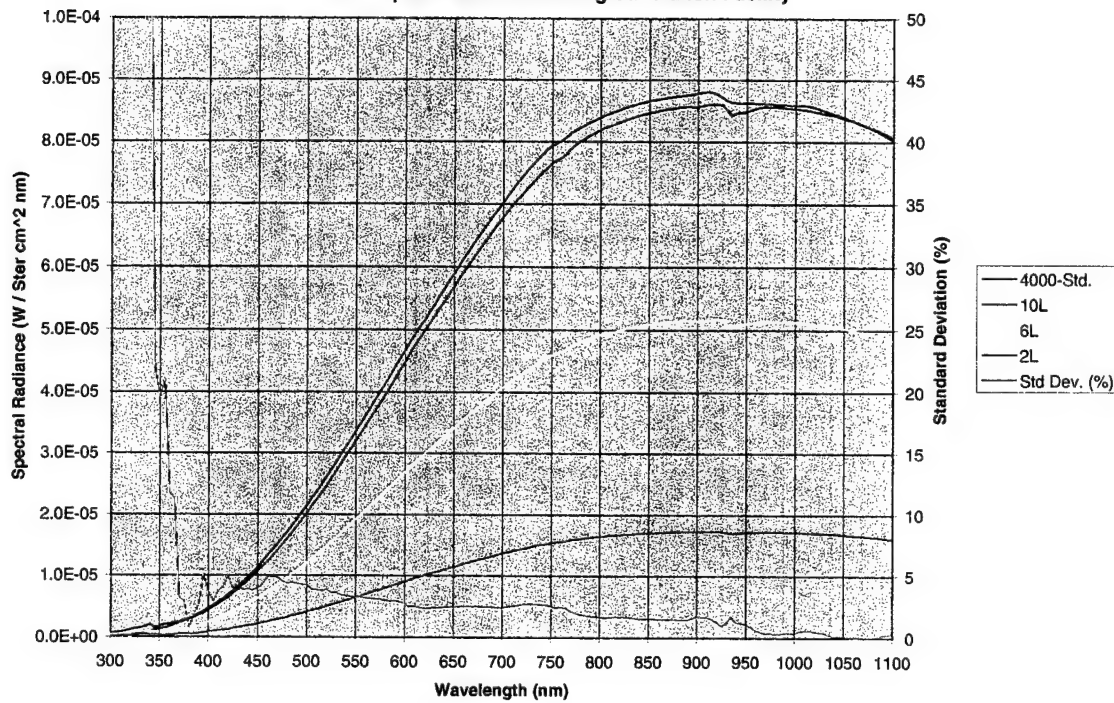
**Labsphere Unisource 4000 Calibration (1 Lamp) 08/96-06/98**  
**NRL Optical Remote Sensing Calibration Facility**



**Labsphere Unisource 4000 FEL Transfer Calibration 07-02-1998**  
**NRL Optical Remote Sensing Calibration Facility**



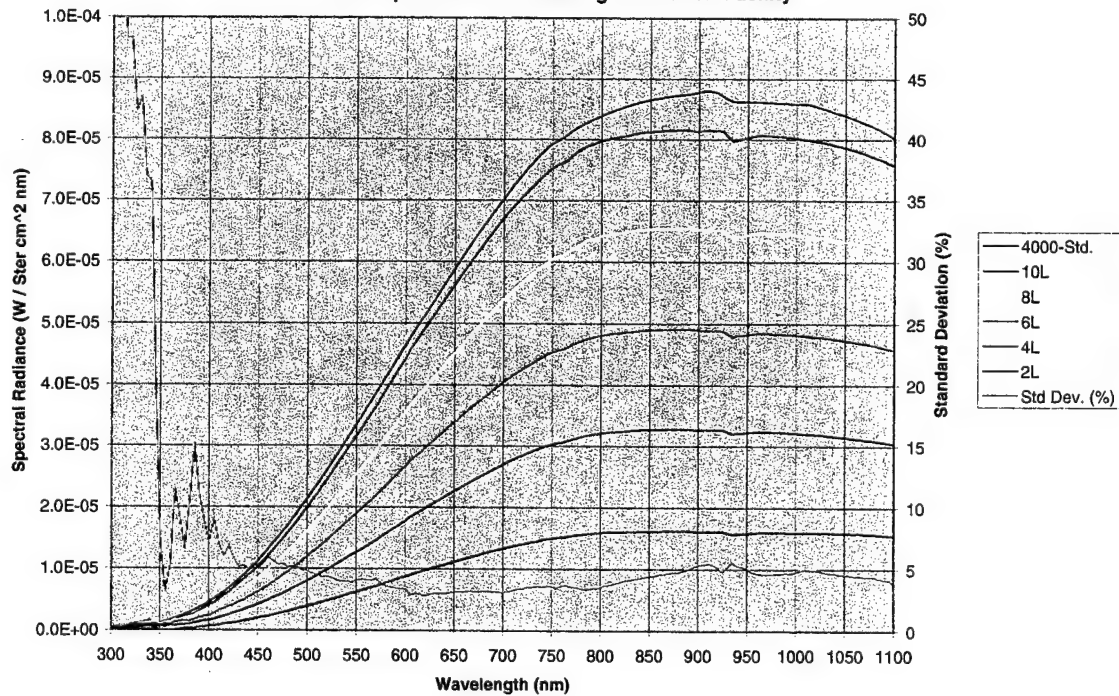
**Labsphere Unisource 4000 FEL Transfer Calibration 08-24-1998**  
**NRL Optical Remote Sensing Calibration Facility**



IS399xfer082498.xls

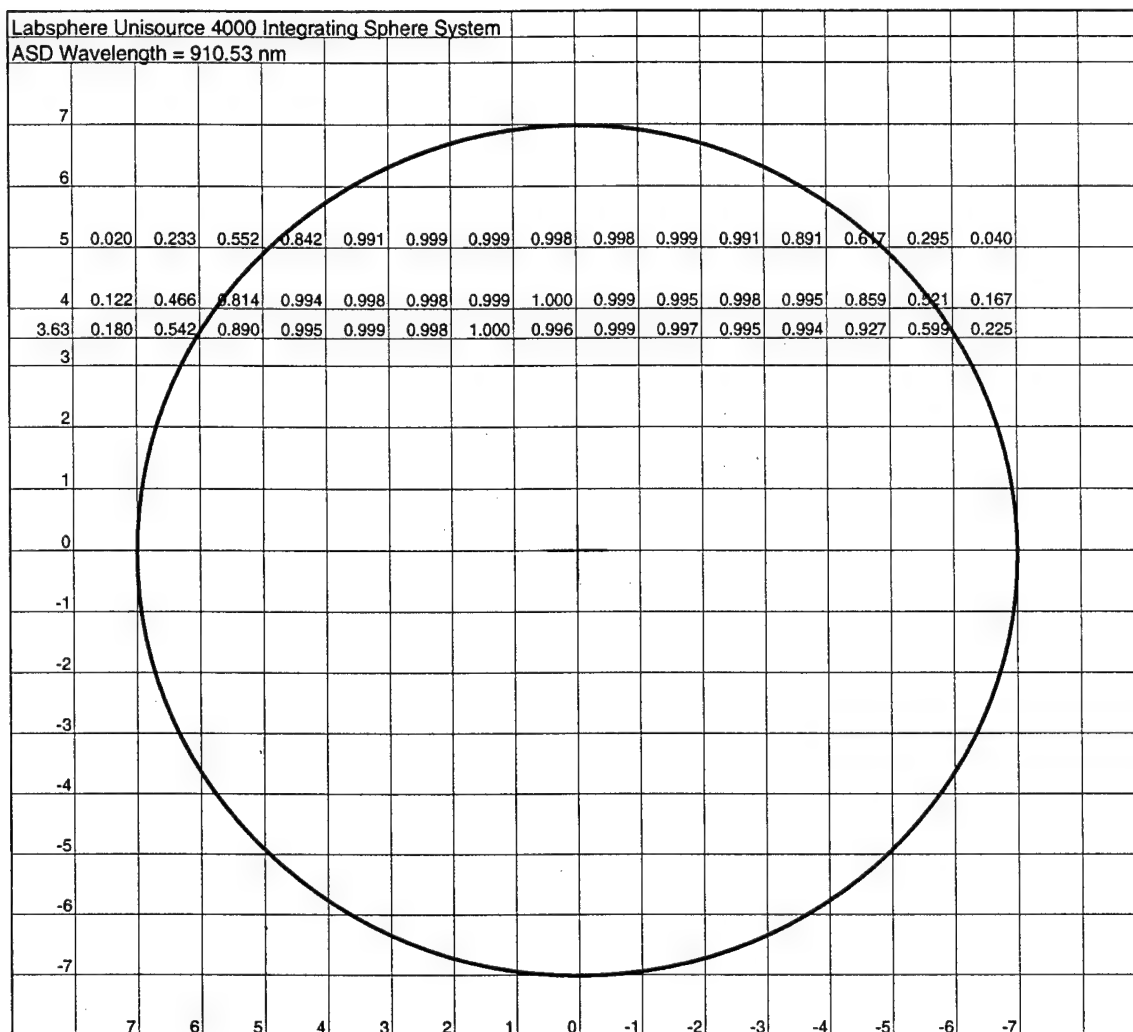
RTU—Radiance Test Unit

**Labsphere Unisource 4000 FEL Transfer Calibration 07-02-1999**  
**NRL Optical Remote Sensing Calibration Facility**



IS300xfer072299.xls

# RTU—Radiance Test Unit

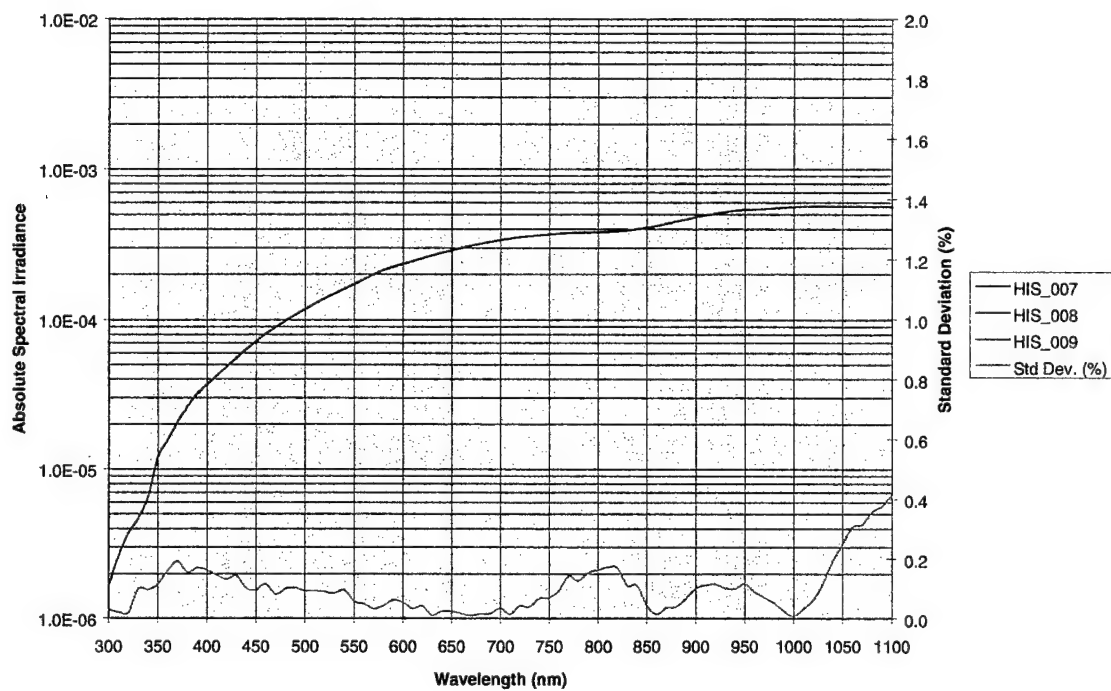


ISmap\_082997.xls



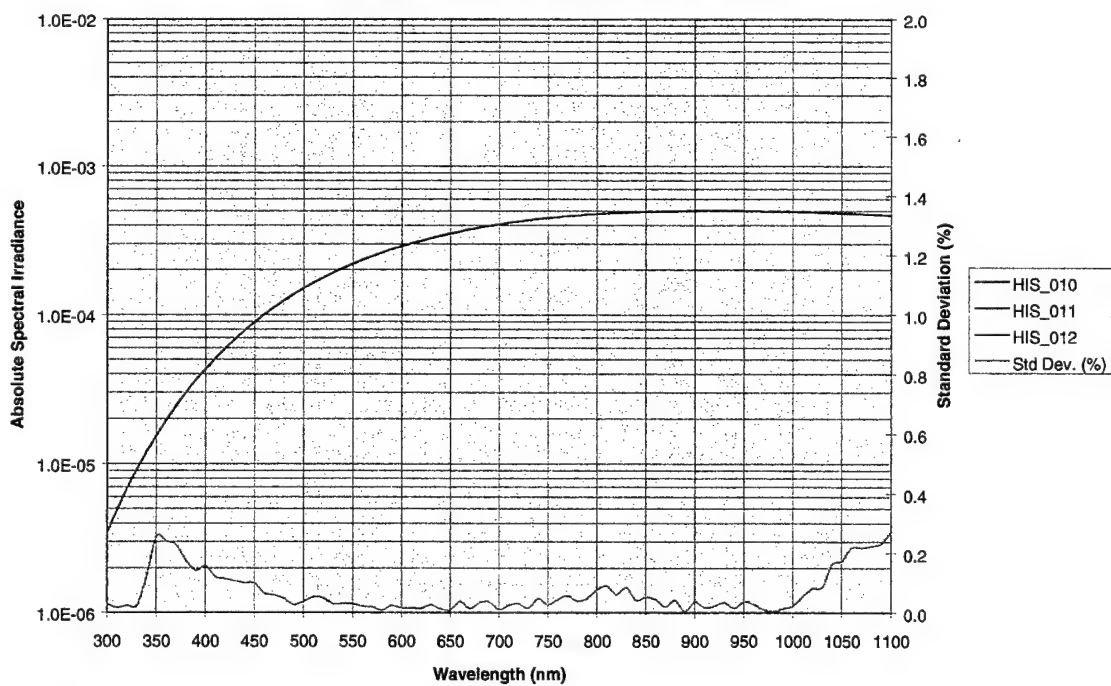
# STU—Spectral Test Unit

OL 740-20A High Intensity Source Stability Measurement 04-25-97  
NRL Optical Remote Sensing Calibration Facility



his\_042597.xls

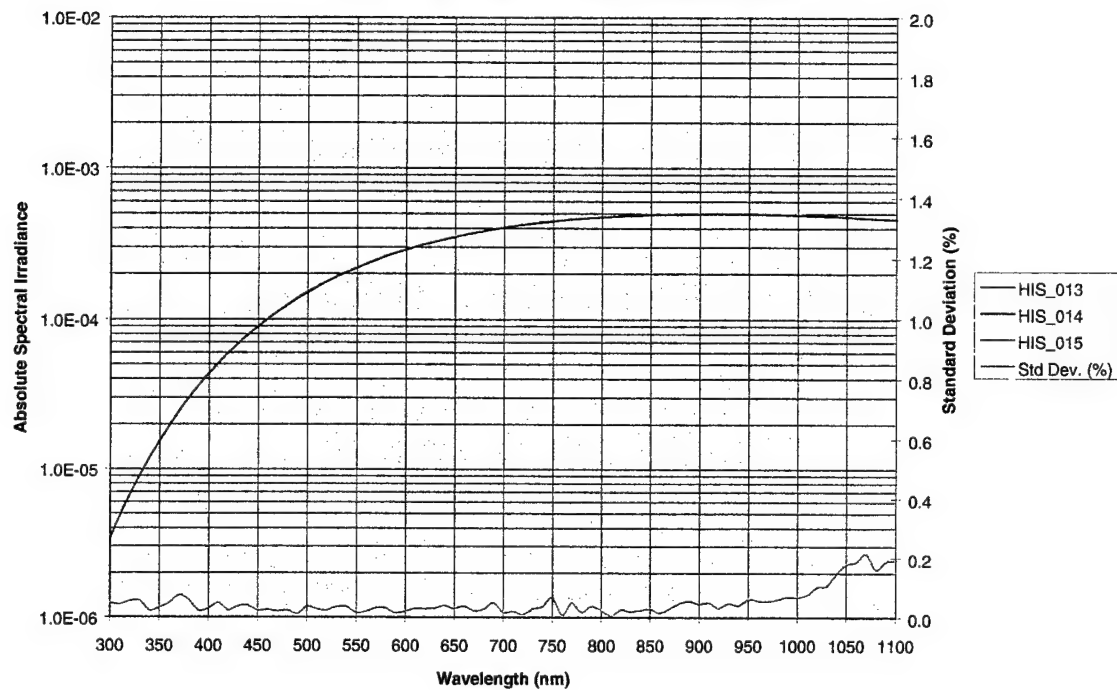
OL 740-20A High Intensity Source Stability Measurement 07-28-97  
NRL Optical Remote Sensing Calibration Facility



his\_072897.xls

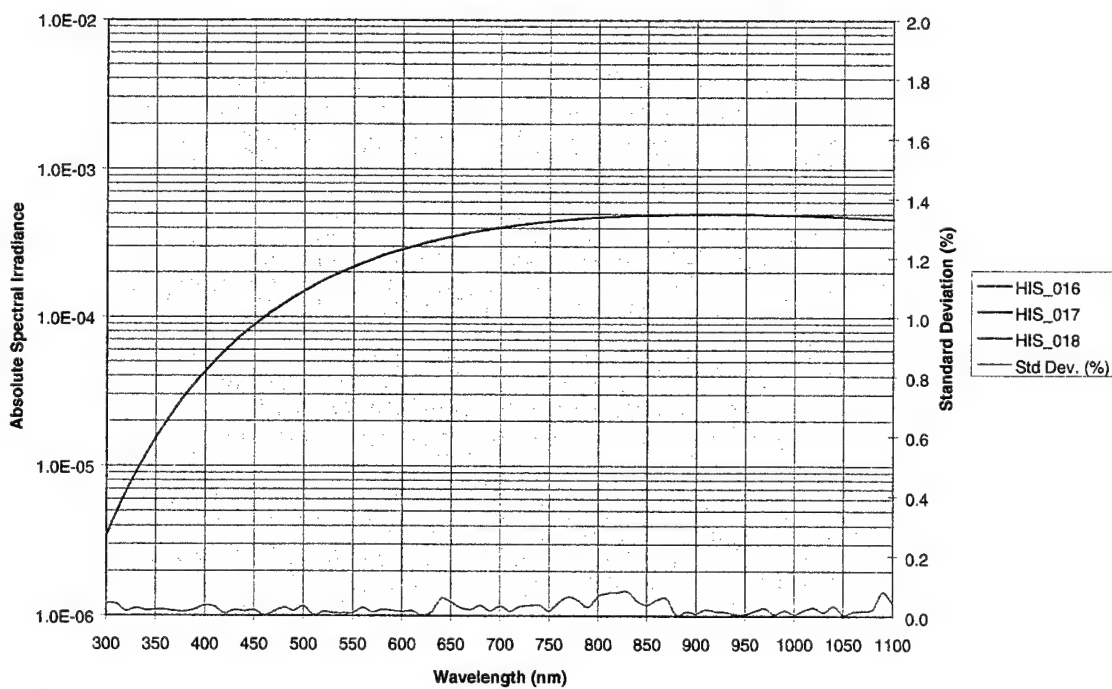
# STU—Spectral Test Unit

OL 740-20A High Intensity Source Stability Measurement 10-30-97  
NRL Optical Remote Sensing Calibration Facility



his\_103097.xls

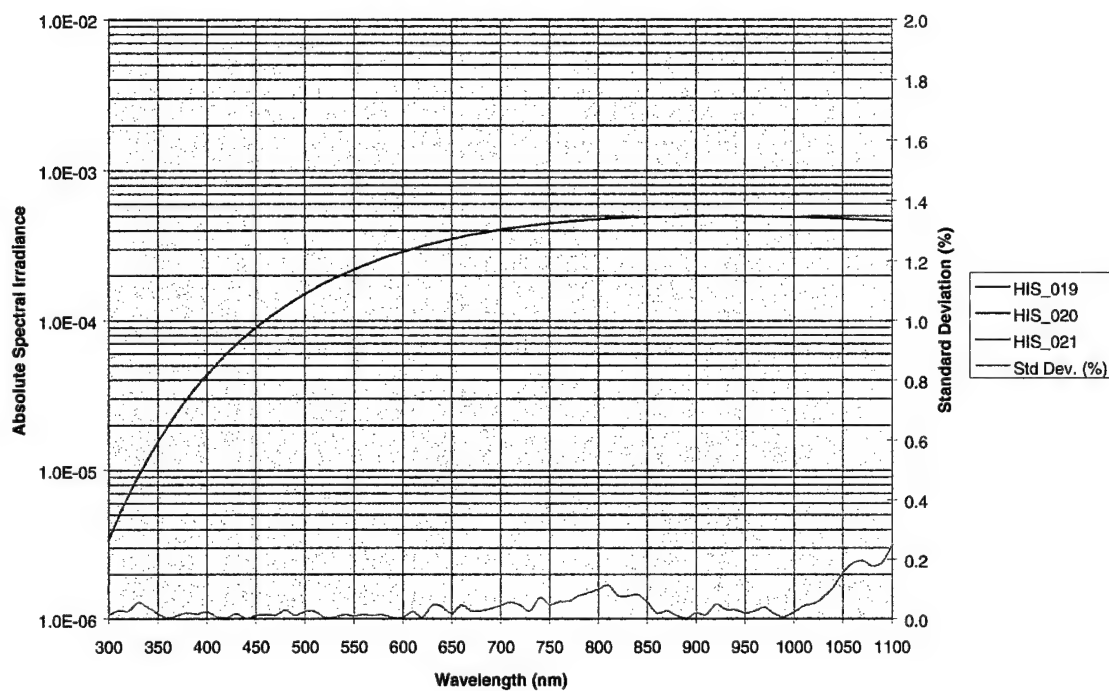
OL 740-20A High Intensity Source Stability Measurement 01-12-98  
NRL Optical Remote Sensing Calibration Facility



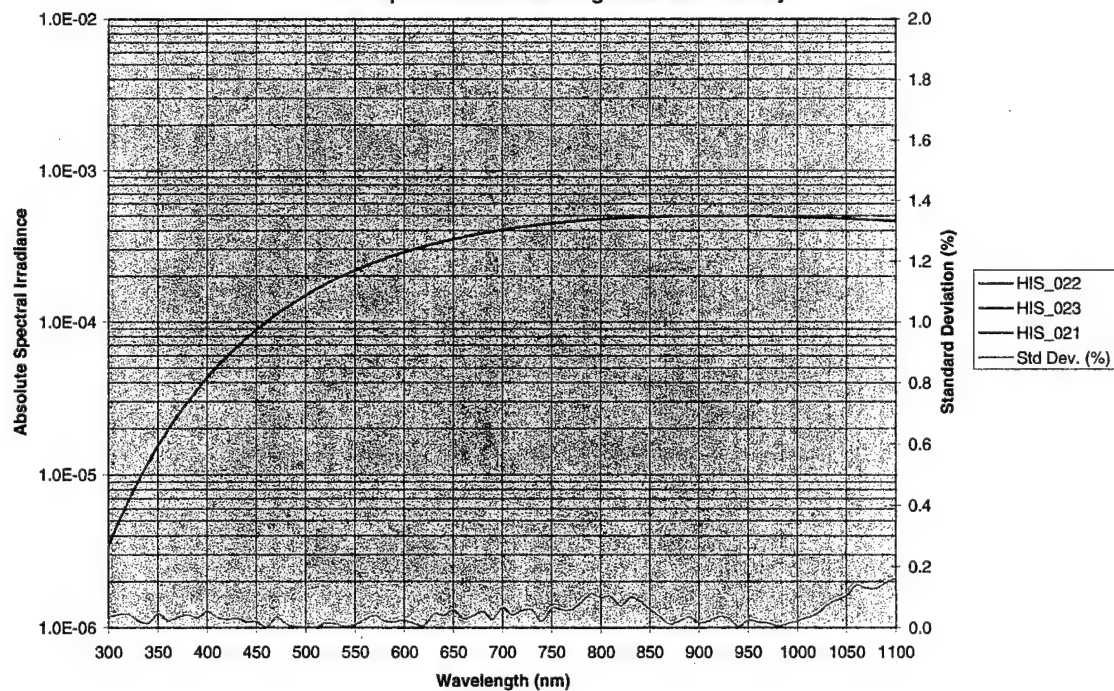
his\_011298.xls

# STU—Spectral Test Unit

OL 740-20A High Intensity Source Stability Measurement 04-02-98  
NRL Optical Remote Sensing Calibration Facility



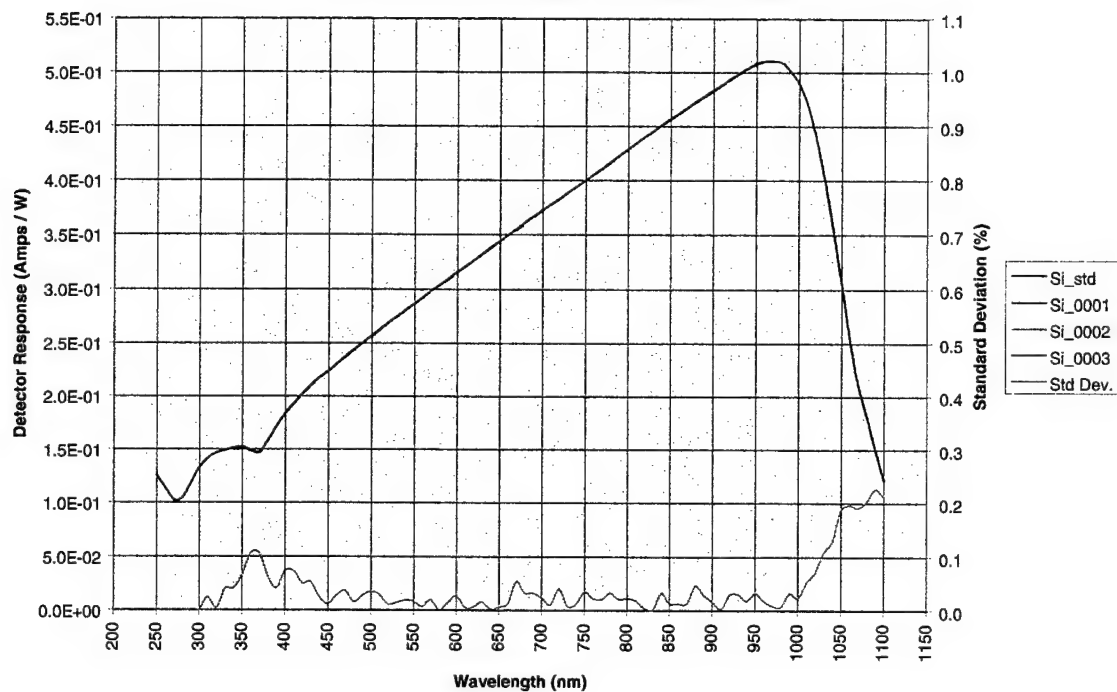
OL 740-20A High Intensity Source Stability Measurement 07-16-98  
NRL Optical Remote Sensing Calibration Facility



his\_040298.xls  
his\_071698.xls

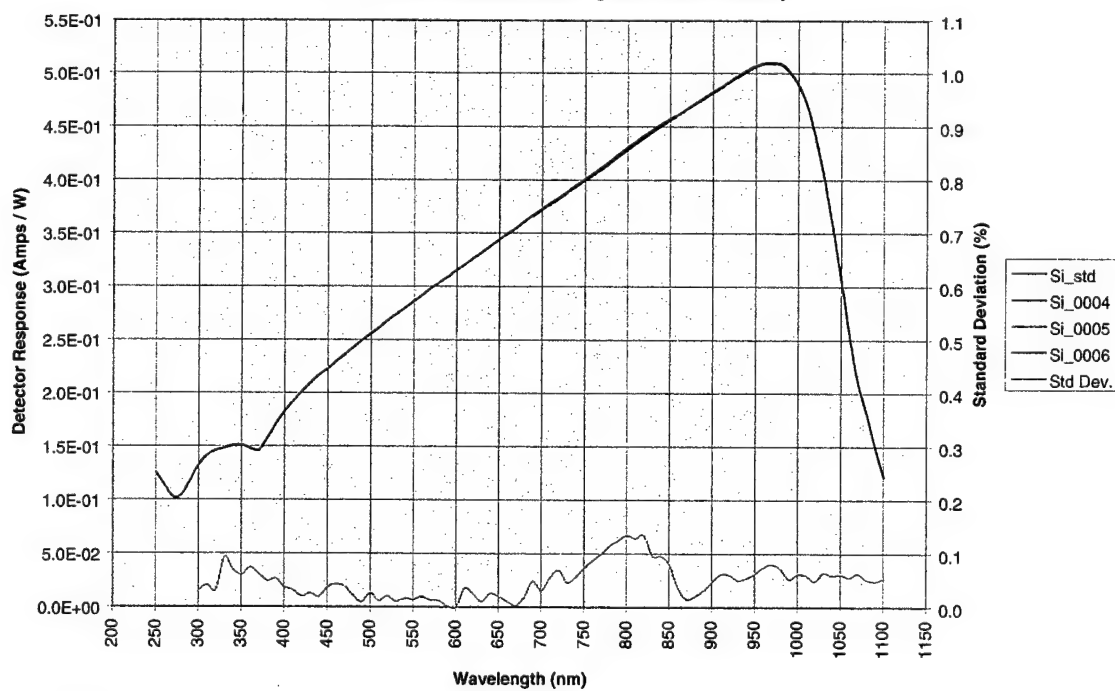
# STU—Spectral Test Unit

**DH-300C Silicon Detector (S/N: 96101054) Calibration 07-30-97**  
**NRL Optical Remote Sensing Calibration Facility**



si\_073097.xls

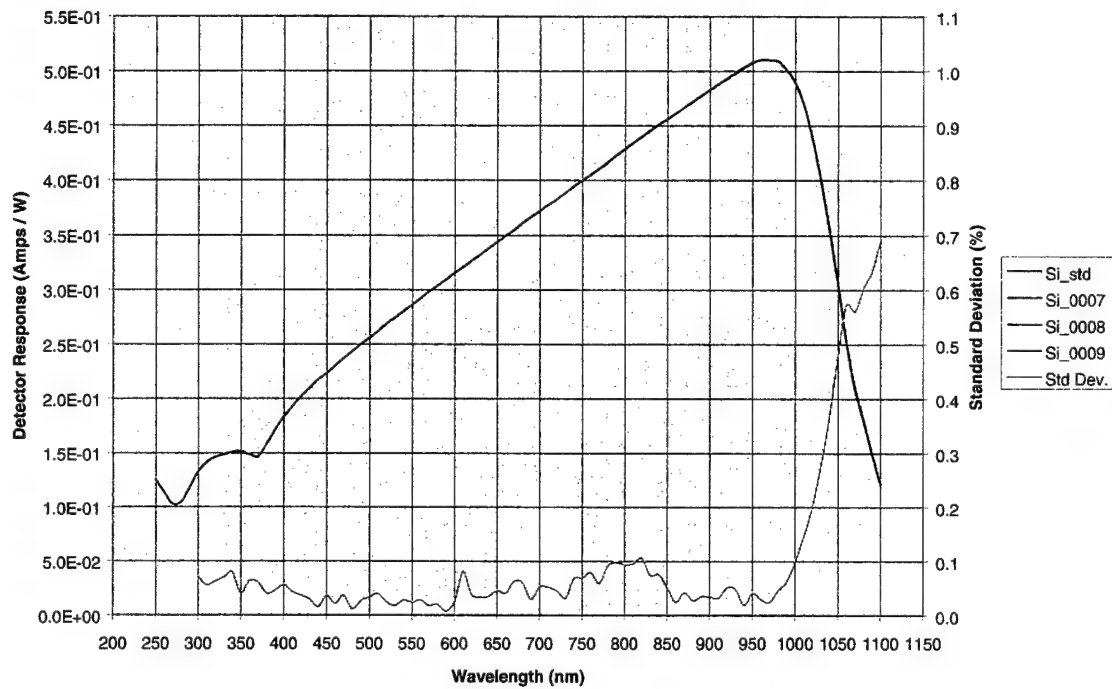
**DH-300C Silicon Detector (S/N: 96101054) Calibration 10-30-97**  
**NRL Optical Remote Sensing Calibration Facility**



si\_103097.xls

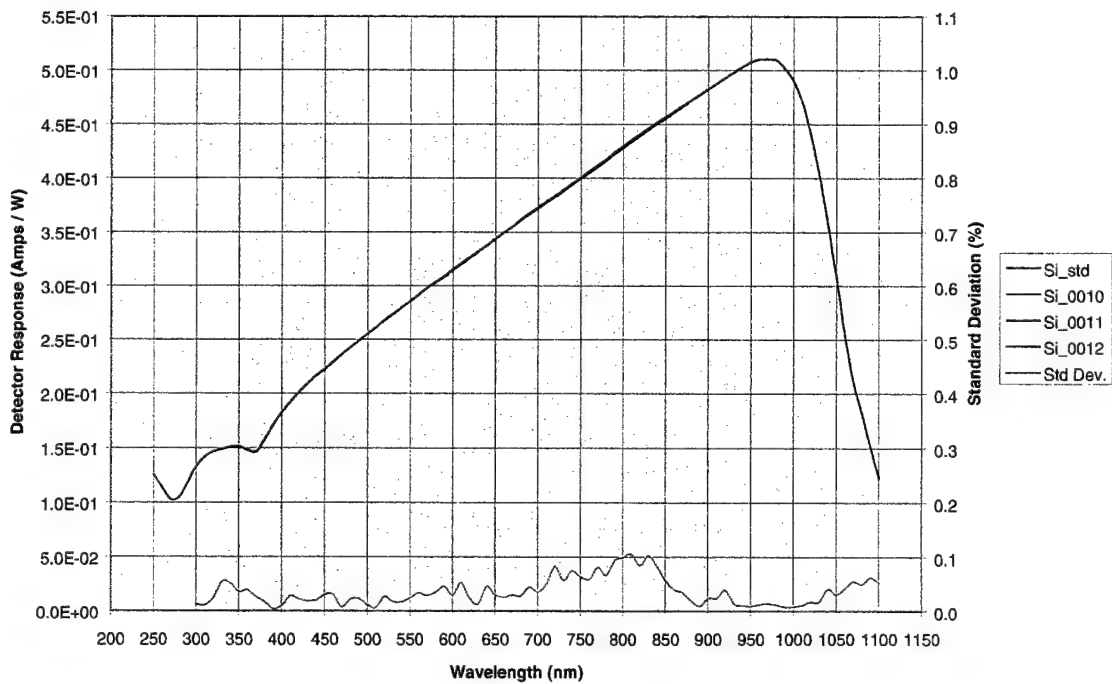
# STU—Spectral Test Unit

DH-300C Silicon Detector (S/N: 96101054) Calibration 01-07-98  
NRL Optical Remote Sensing Calibration Facility



si\_010798.xls

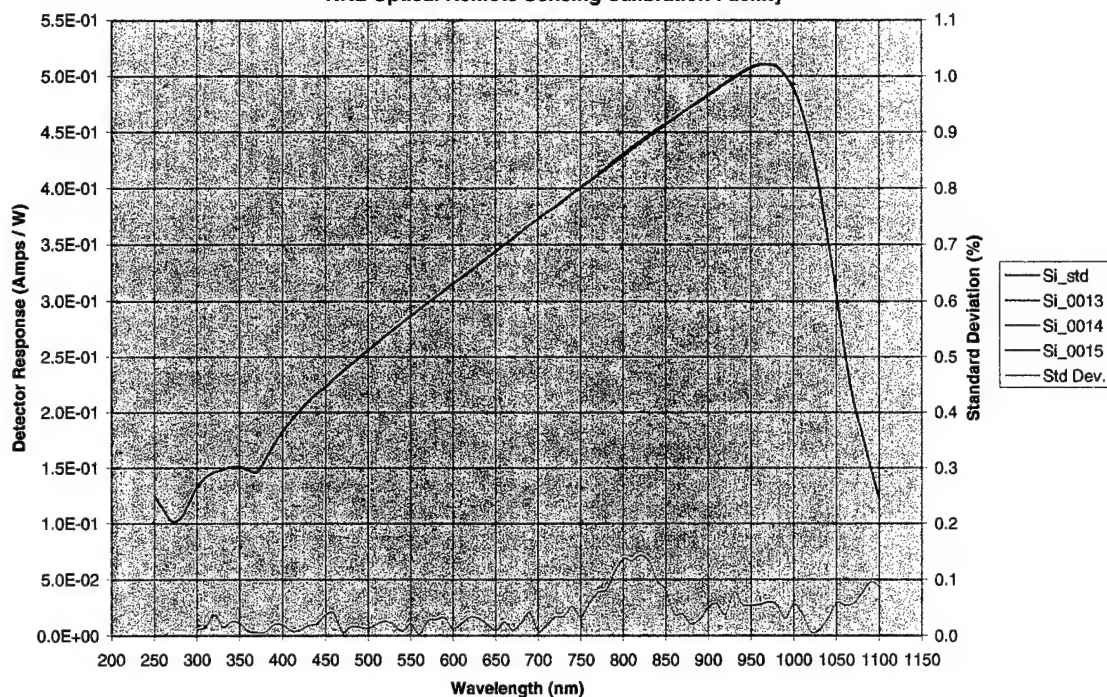
DH-300C Silicon Detector (S/N: 96101054) Calibration 04-02-98  
NRL Optical Remote Sensing Calibration Facility



si\_040298.xls

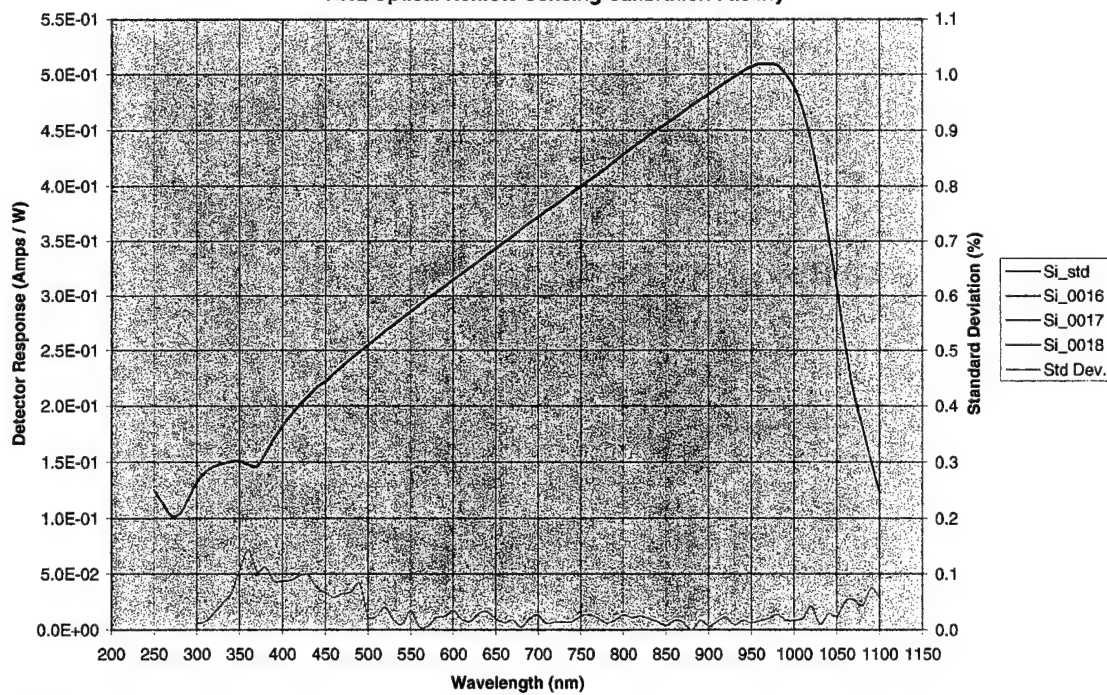
# STU—Spectral Test Unit

DH-300C Silicon Detector (S/N: 96101054) Calibration 07-17-98  
NRL Optical Remote Sensing Calibration Facility



si\_071798.xls

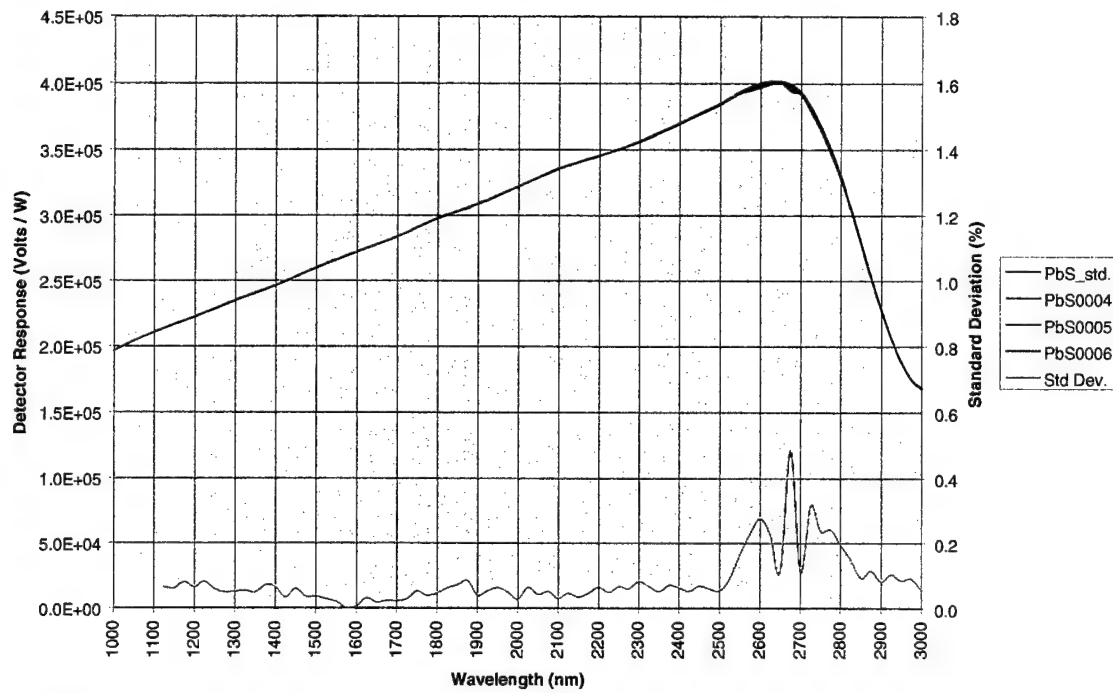
DH-300C Silicon Detector (S/N: 96101054) Calibration 05-14-99  
NRL Optical Remote Sensing Calibration Facility



si\_051499.xls

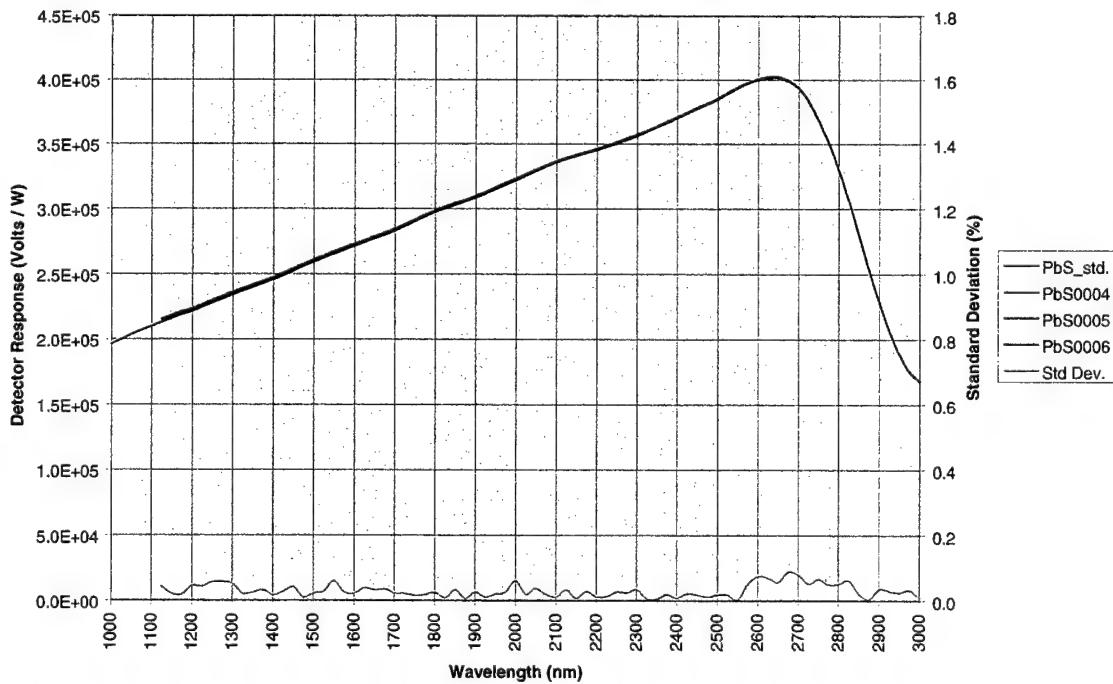
# STU—Spectral Test Unit

HSD-340C PbS Detector (S/N: 96100024) Calibration 07-30-97  
NRL Optical Remote Sensing Calibration Facility



pbs\_073097.xls

HSD-340C PbS Detector (S/N: 96100024) Calibration 10-30-97  
NRL Optical Remote Sensing Calibration Facility

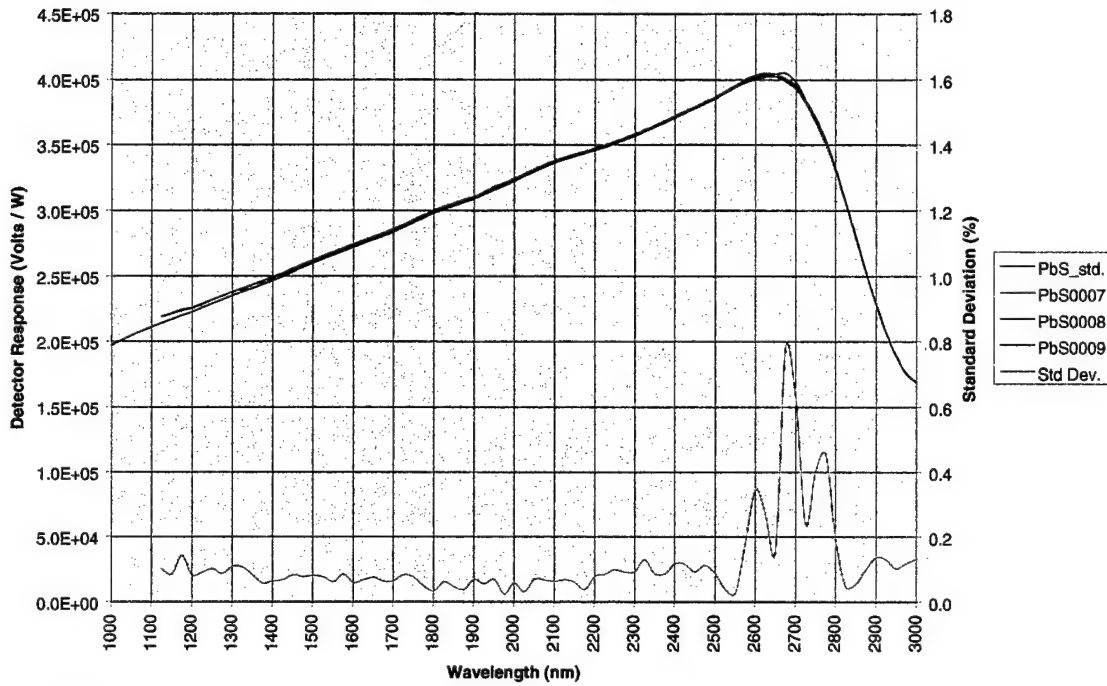


pbs\_103097.xls



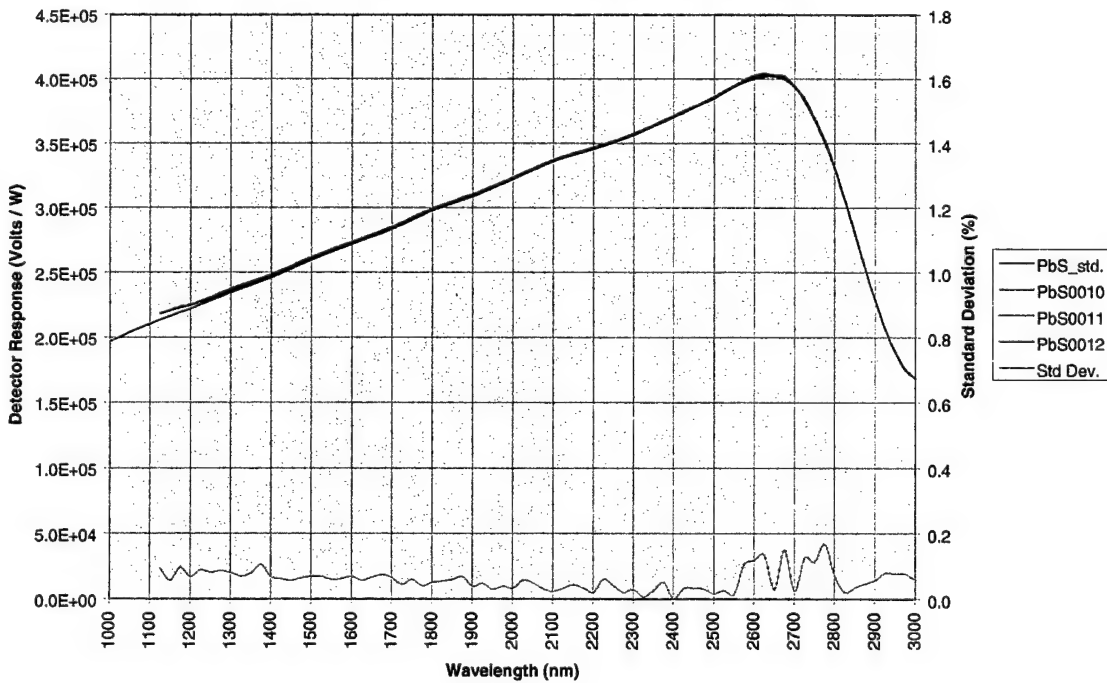
# STU—Spectral Test Unit

HSD-340C PbS Detector (S/N: 96100024) Calibration 01-07-98  
NRL Optical Remote Sensing Calibration Facility



pbs\_010798.xls

HSD-340C PbS Detector (S/N: 96100024) Calibration 04-02-98  
NRL Optical Remote Sensing Calibration Facility

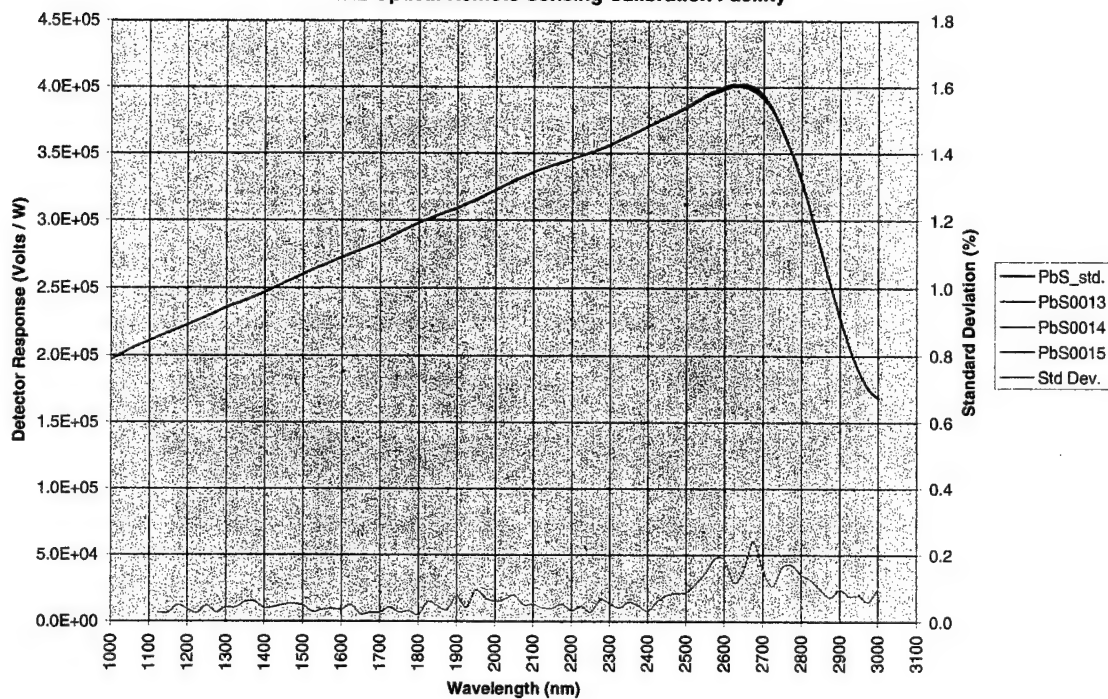


pbs\_040298.xls



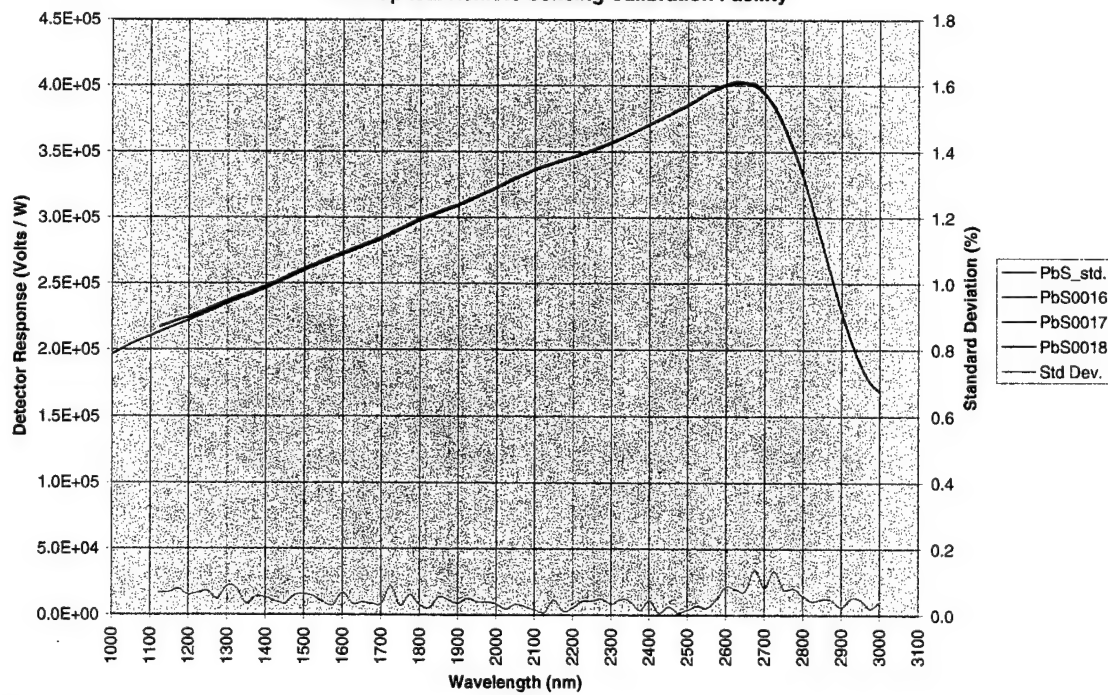
# STU—Spectral Test Unit

HSD-340C PbS Detector (S/N: 96100024) Calibration 07-17-98  
NRL Optical Remote Sensing Calibration Facility



pbs\_071798.xls

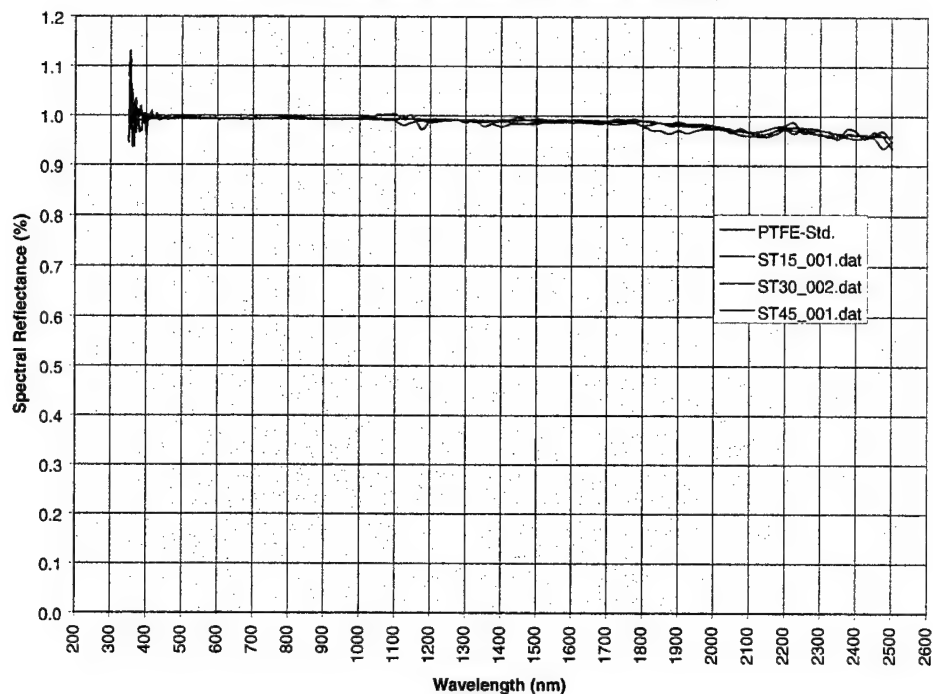
HSD-340C PbS Detector (S/N: 96100024) Calibration 05-14-99  
NRL Optical Remote Sensing Calibration Facility



pbs\_051499.xls

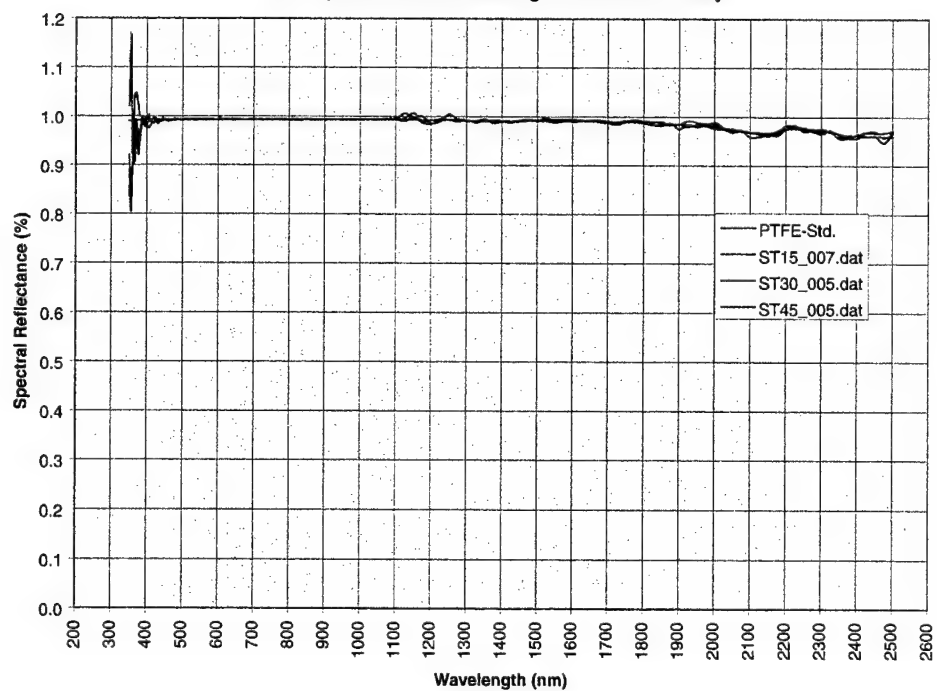
# DTU—Diffuse-Reflectance Test Unit

PTFE 55RS Reflectance Standard Measurement 05-30-97  
NRL Optical Remote Sensing Calibration Facility



st\_053097.xls

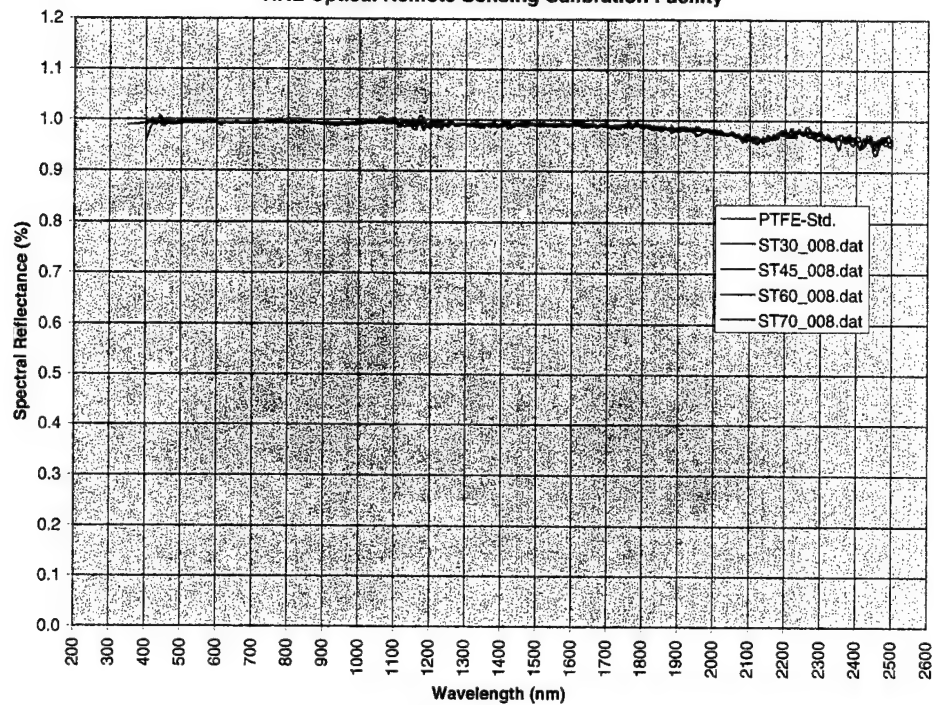
PTFE 55RS Reflectance Standard Measurement 11-26-97  
NRL Optical Remote Sensing Calibration Facility



st\_112697.xls

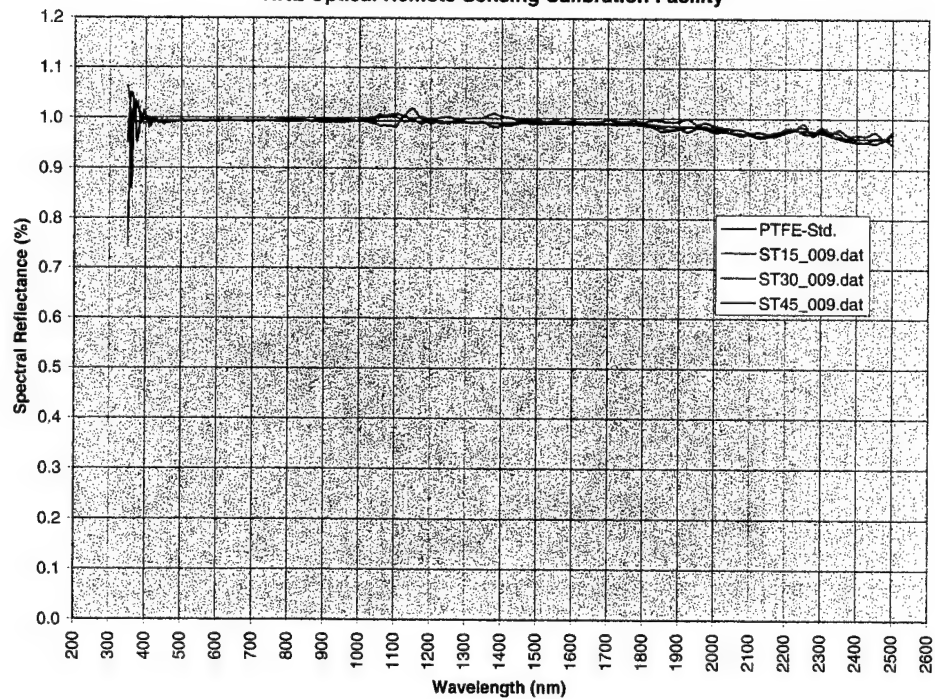
# DTU—Diffuse-Reflectance Test Unit

PTFE 55RS Reflectance Standard Measurement 02-12-98  
NRL Optical Remote Sensing Calibration Facility



st\_021298.xls

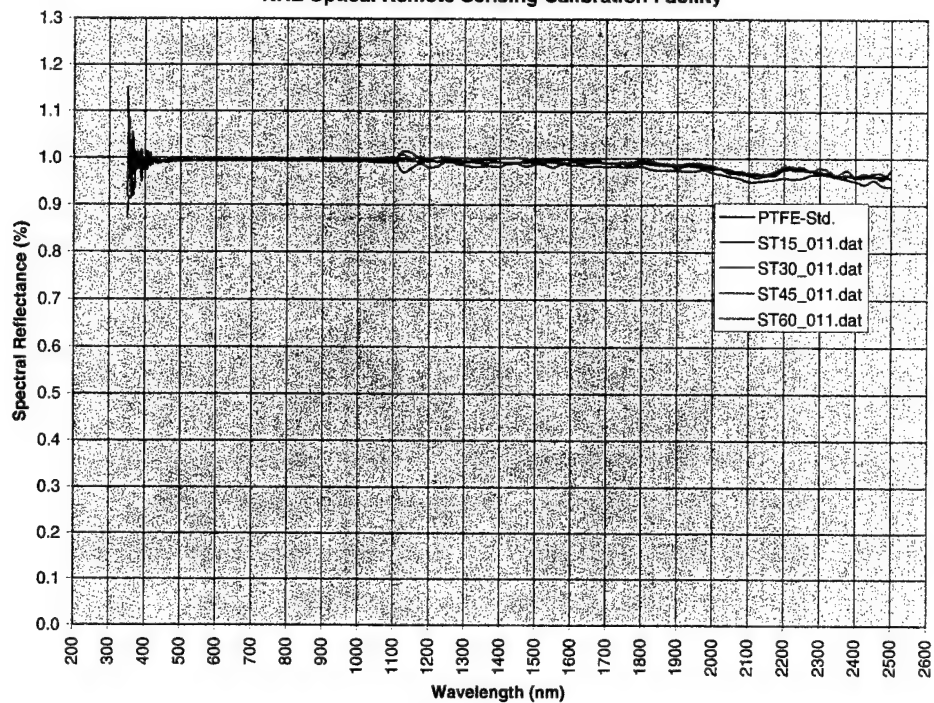
PTFE 55RS Reflectance Standard Measurement 05-29-98  
NRL Optical Remote Sensing Calibration Facility



st\_052998.xls

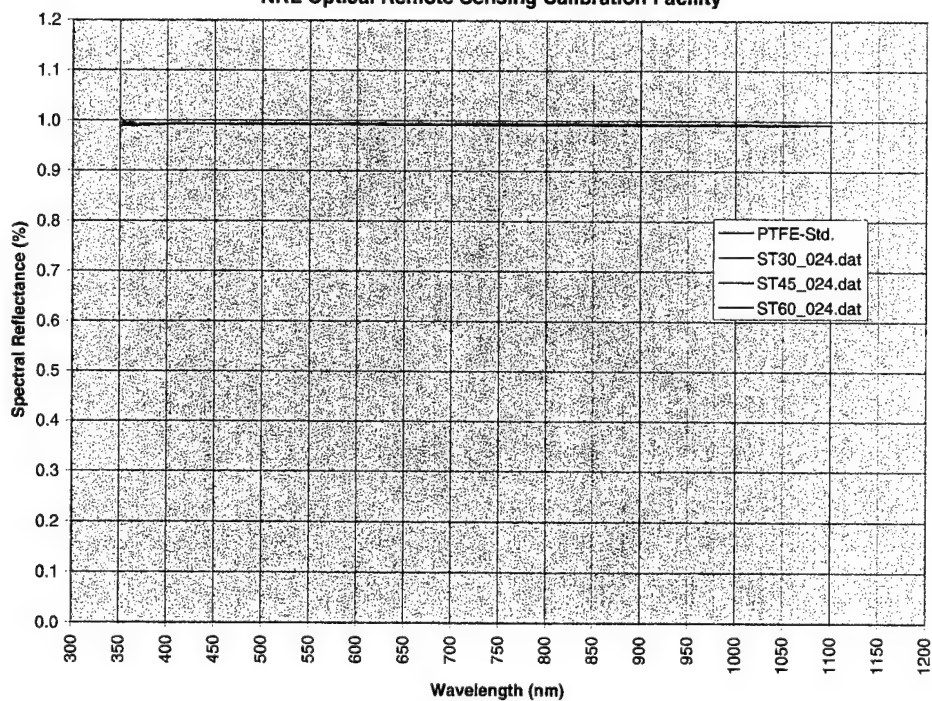
# DTU—Diffuse-Reflectance Test Unit

PTFE 55RS Reflectance Standard Measurement 06-10-98  
NRL Optical Remote Sensing Calibration Facility



st\_061098.xls

PTFE 55RS Reflectance Standard Measurement 11-10-98  
NRL Optical Remote Sensing Calibration Facility

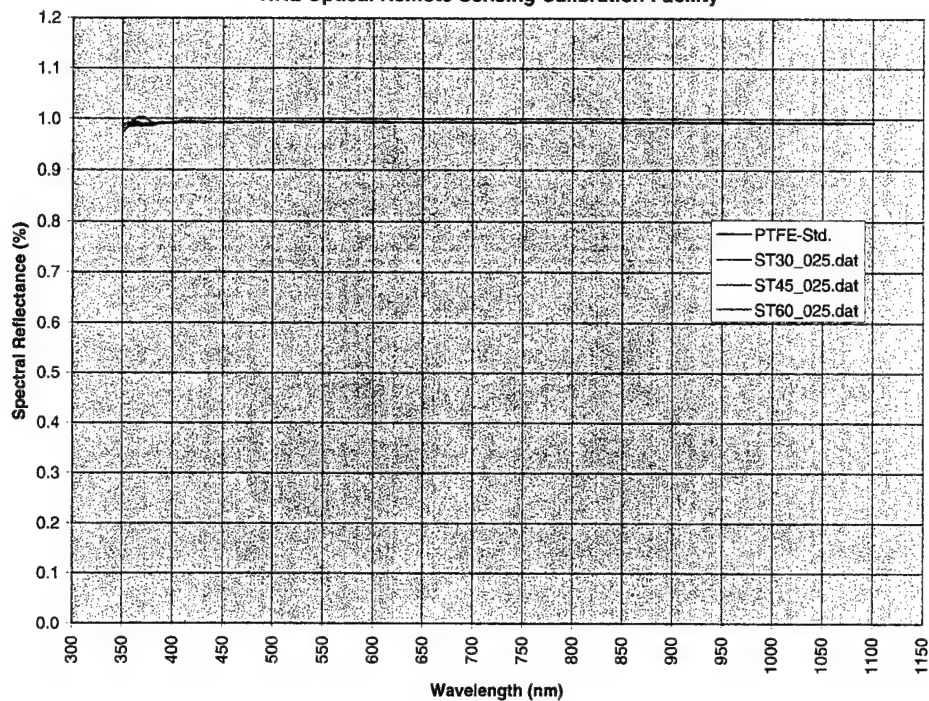


st\_111098.xls



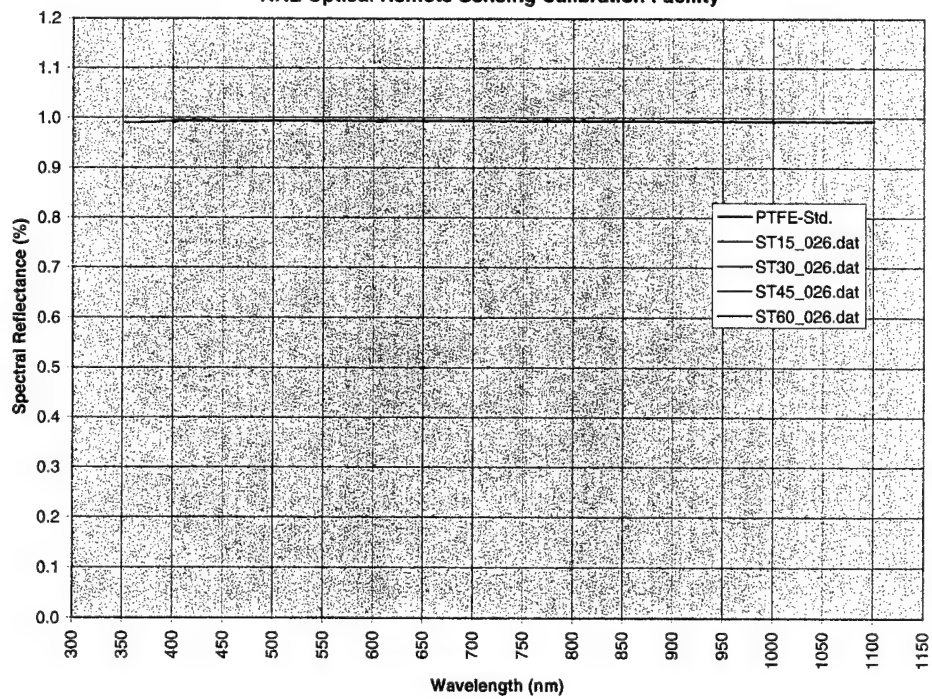
# DTU—Diffuse-Reflectance Test Unit

PTFE 55RS Reflectance Standard Measurement 12-11-98  
NRL Optical Remote Sensing Calibration Facility



st\_121198.xls

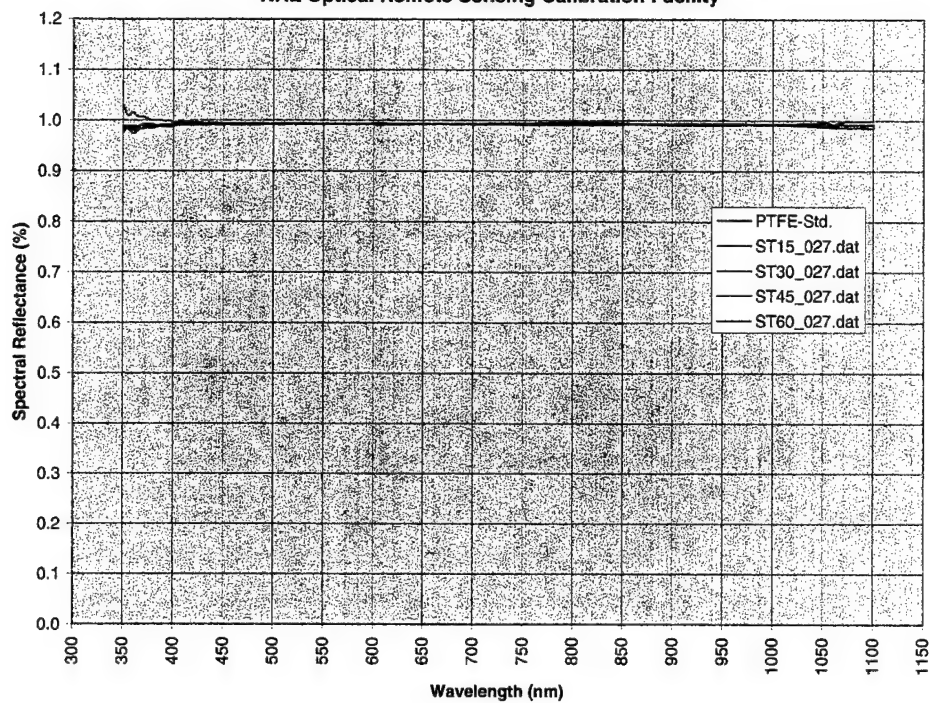
PTFE 55RS Reflectance Standard Measurement 01-29-1999  
NRL Optical Remote Sensing Calibration Facility



st\_012999.xls

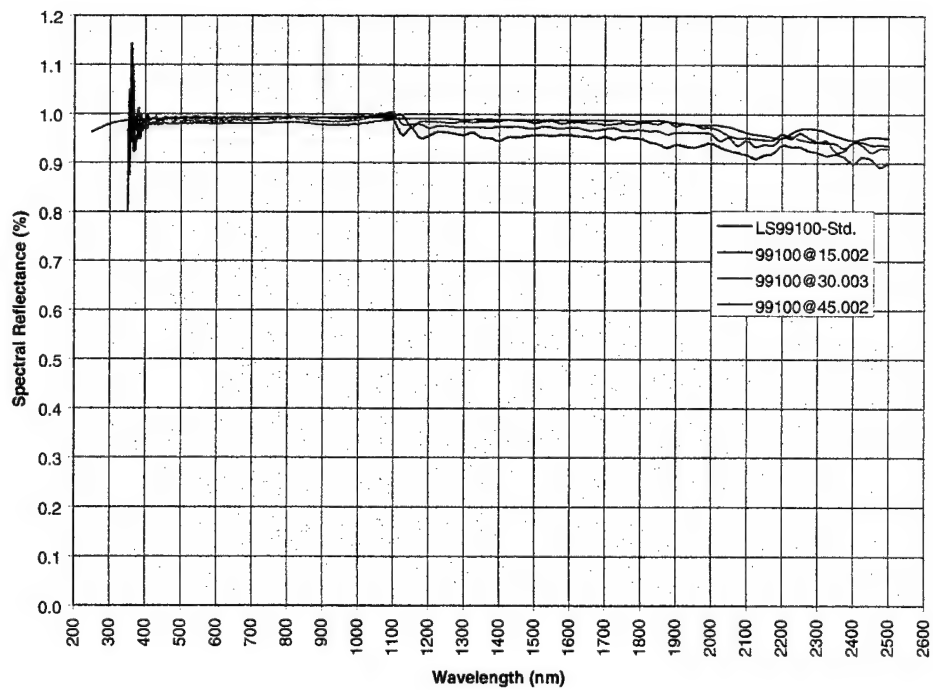
# DTU—Diffuse-Reflectance Test Unit

PTFE 55RS Reflectance Standard Measurement 07-15-1999  
NRL Optical Remote Sensing Calibration Facility



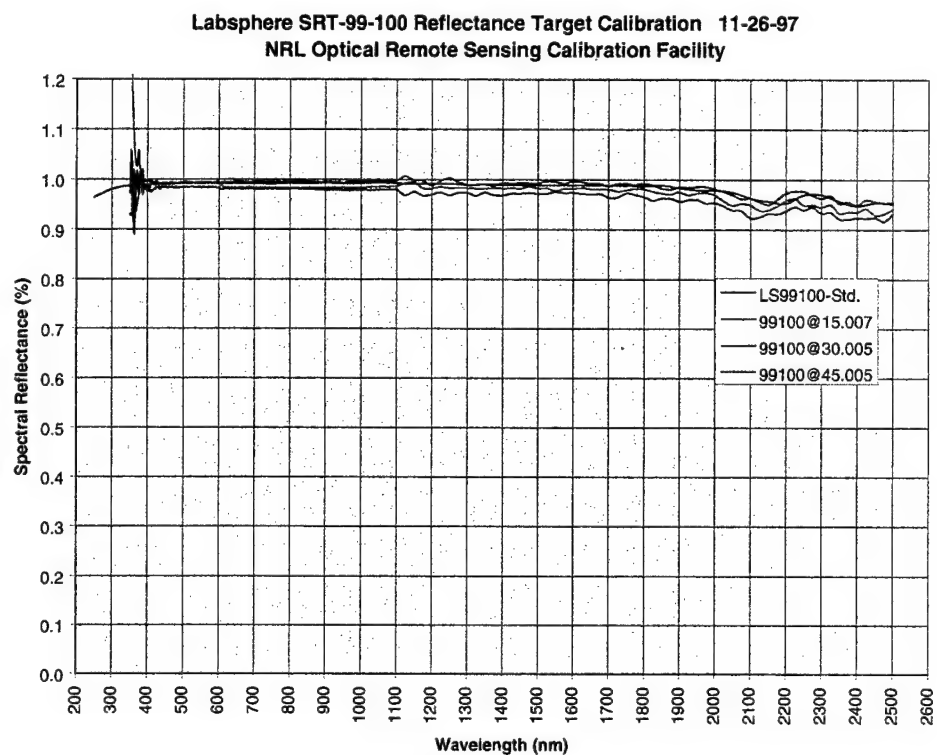
st\_071599.xls

Labsphere SRT-99-100 Reflectance Target Calibration 05-30-97  
NRL Optical Remote Sensing Calibration Facility



sp100\_053097.xls

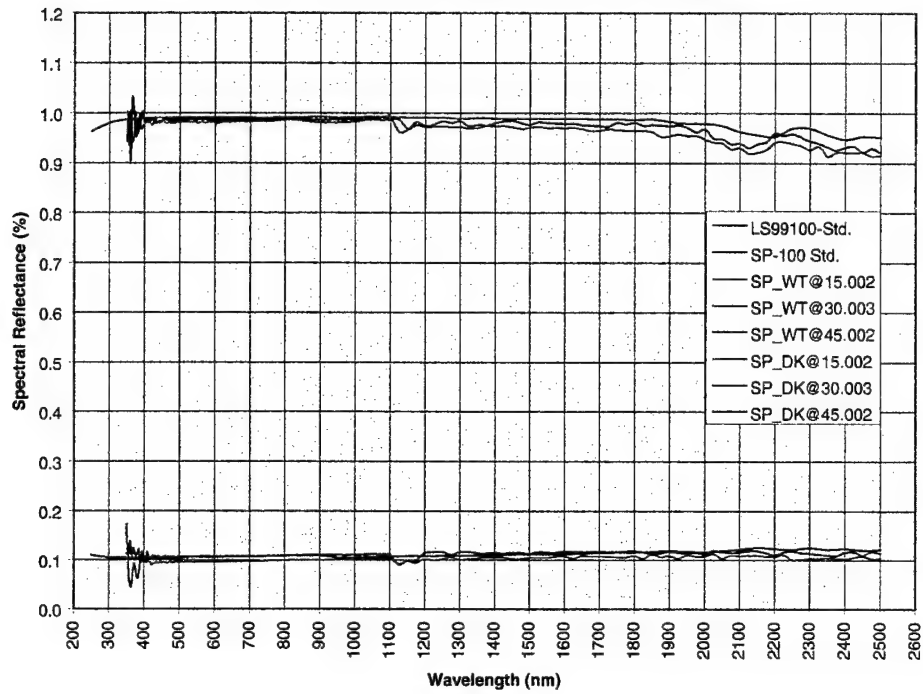
DTU—Diffuse-Reflectance Test Unit



sp100\_112697.xls

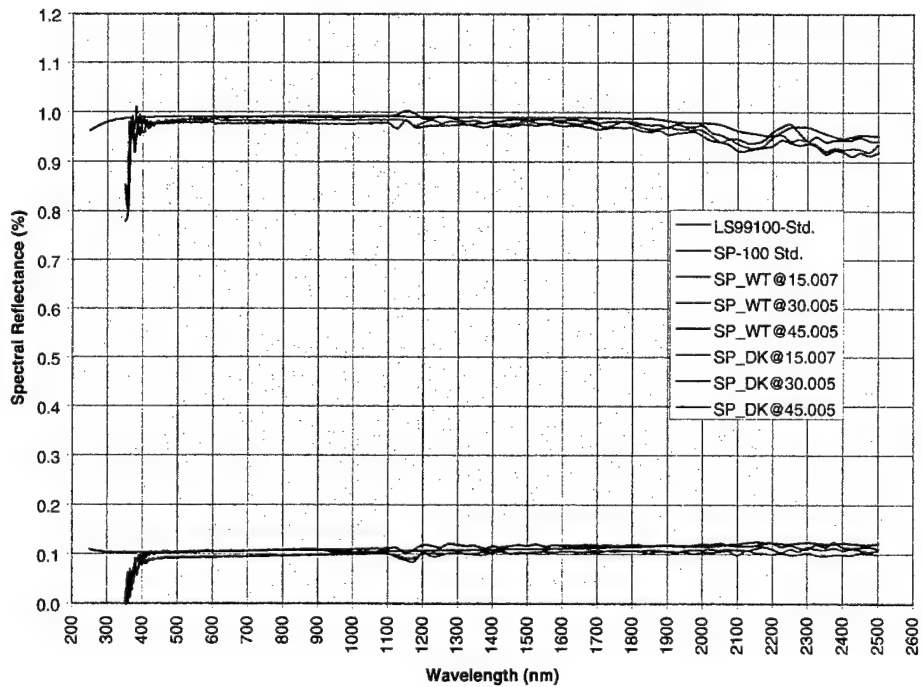
DTU—Diffuse-Reflectance Test Unit

**Labsphere SRT-SP-100 Reflectance Target Calibration 05-30-97**  
**NRL Optical Remote Sensing Calibration Facility**



99100\_053097.xls

**Labsphere SRT-SP-100 Reflectance Target Calibration 11-26-97**  
**NRL Optical Remote Sensing Calibration Facility**



99100\_112697.xls



## **Appendix E**

### **Diabatic Initialization of Stratiform Precipitation for a Mesoscale Model**

## Diabatic Initialization of Stratiform Precipitation for a Mesoscale Model

FRANK H. RUGGIERO

*Atmospheric Sciences Division, Phillips Laboratory, Hanscom Air Force Base, Massachusetts*

KEITH D. SASHEGYI AND RANGARAO V. MADALA

*Remote Sensing Division, Naval Research Laboratory, Washington, D.C.*

SETHU RAMAN

*Department of Marine, Earth, and Atmospheric Sciences, North Carolina State University at Raleigh, Raleigh, North Carolina*

(Manuscript received 8 May 1995, in final form 26 October 1995)

### ABSTRACT

A technique is described that adds diabatic forcing from stratiform precipitation to a vertical normal-mode initialization of a mesoscale model. The technique uses observed precipitation amounts and cloud-top height estimations with analyzed thermodynamic and kinematic fields to vertically distribute diabatic heating that arises from stratiform precipitation. Simulation experiments reveal the importance of incorporating this heating into the initialization. An adiabatic initialization recovered about 65%–75% of the maximum upward vertical motions, whereas a diabatic initialization, with respect to stratiform precipitation, recovered nearly all the original vertical motions. A real-data case study is presented using combined rain gauge–satellite precipitation analyses with cloud-top heights estimated from Geostationary Operational Environmental Satellite infrared brightness temperatures. The short-term precipitation forecasts from a diabatically initialized model, with respect to stratiform precipitation, demonstrate improvement over forecasts from an adiabatically initialized model.

### 1. Introduction

The impact of the spinup problem of numerical weather prediction models has been well documented (e.g., Girard and Jarraud 1982; Heckley 1985; Miyakoda et al. 1978; Donner 1988). Mohanty et al. (1986) describe the spinup problem as a lack of condensation and associated latent heat release during the early part of model integration. The problem can be traced to inadequate initial data, which principally arises from the inability of observing networks to accurately resolve humidity and divergence fields. Another complicating factor is that most model initialization routines result in adiabatically balanced initial fields. This can have a significant impact on vertical motions. Tarbell et al. (1981) have estimated that diabatic effects make up the major portion of the balance in the omega equation when considering precipitation rates  $1 \text{ cm h}^{-1}$  and higher.

Attempts have been made to overcome the spinup problem by accounting for diabatic effects before be-

ginning the model forecast. The principle ways to include the diabatic effects are through the assimilation of precipitation rates and/or satellite-inferred cloud information into the prediction models. Krishnamurti et al. (1991) describe a physical initialization technique that works by using observed precipitation rates to modify the model's moisture profile. The vertical structure of the moisture profile is determined by reversing the model's convective parameterization scheme. In addition, reversing the convective parameterization also results in a corresponding latent heat profile. The model's humidity and temperature fields are then dynamically relaxed toward the enhanced humidity and latent heating fields during a preforecast stage. By nudging the humidity and temperature fields, the idea is that the model will produce more precipitation and latent heating. This will in turn lead to continued vertical motion, as the latent heating is balanced by adiabatic ascent. This technique is particularly suited to the Tropics where there is not much synoptic data available and it sometimes takes days for a model to overcome the spinup problem. Krishnamurti et al. (1991) show that diabatic initialization in this manner can substantially reduce the amount of time needed to spin up a global model if given reasonable quality precipitation fields. Harms et al. (1993) used a technique similar to Krishnamurti et al. (1991)—they used a reverse con-

Corresponding author address: Frank H. Ruggiero, Code 7225, Naval Research Laboratory, 4555 Overlook Avenue, S.W., Washington, DC 20375-5000.  
E-mail: ruggiero@atmos.nrl.navy.mil

vective parameterization to get a vertical latent heat profile at initialization time. In their technique, the moisture fields are changed at the initialization time. The latent heat associated with the convection is added to the vertical normal-mode initialization balance, and the model-generated heating is merged with the initial latent heating during the first 3 h of model integration. Other techniques (e.g., Turpeinen et al. 1990) use the ratio of observed precipitation to that generated by the initialized fields to scale the initial vertical latent heating profiles. In areas where there is observed precipitation but none from initialized fields, a parabolic profile (Carr and Baldwin 1991) of the latent heating can be used. An alternative method is to adjust the latent heat profile to match that of nearby points with similar precipitation rates (Manobianco et al. 1994). Puri and Miller (1990) employ a diabatic normal-mode initialization similar to that of Harms et al. (1993) except that satellite outgoing longwave radiation (OLR) data are used to determine the vertical latent heat profile. For grid-scale precipitation processes, Raymond et al. (1995) use a statistical relationship based on Special Sensor Microwave/Imager (SSM/I)-derived vertically integrated liquid water and ice precipitation paths to determine the vertical latent heat distribution. Kristjánsson (1992) uses vertically integrated cloud water as determined by satellites to both initialize cloud water fields and enhance the humidity fields in the presence of clouds.

Although much of the previous work in this area has focused on the diabatic effects in the Tropics or for midlatitudinal convection, these effects are also important for short-term forecasting stratiform precipitation. Kuo and Low-Nam (1990) have shown that explicit gridpoint precipitation associated with mesoscale slantwise ascent of air over warm fronts is a significant contributor to rapid cyclone development. Currently, work is underway at the Naval Research Laboratory and Phillips Laboratory to develop a regional analysis and forecast system. It is planned that this system will, on a frequent basis, intermittently assimilate data from asynoptic sources and produce highly accurate short-term forecasts (Ruggiero et al. 1996). The frequent analysis and adiabatic initialization steps will act to continually diminish the divergence fields each time new data are assimilated. To be able to produce accurate short-term forecasts with such a system, the divergent flow must be maintained through the analysis and initialization steps. One way to accomplish this is by using a diabatic initialization. It is the purpose of this paper to describe and present test results from a technique to diabatically initialize the U.S. Navy Operational Regional Atmospheric Prediction System (NO-RAPS) model from stratiform precipitation. This technique uses as input observed precipitation, cloud-top heights, and analyzed thermodynamic and kinematic fields. The latent heating is distributed vertically in an iterative scheme. The technique to be described here

follows a framework similar to that of the diabatic initialization technique for convective precipitation described by Harms et al. (1993). Thus, the two techniques could be used in conjunction to provide a comprehensive diabatic initialization step.

## 2. Diabatic initialization methodology

The model initialization is based on that described by Sashegyi and Madala (1993). It is a vertical normal-mode initialization following the scheme of Bourke and McGregor (1983). Normal-mode initializations run adiabatically have been found to improve initial vertical velocity profiles but not eliminate the spinup problem (Lejenas 1980). The idea behind the normal-mode initialization is to minimize the amplitude and time tendencies of spurious gravity waves. This is done in limited-area models by reducing to zero the divergence and ageostrophic vorticity tendencies for the first three vertical modes of the model (Bourke and McGregor 1983). The procedure is iterative, and the tendencies of divergence and ageostrophic vorticity are computed by time stepping the model forward one step. The initialization is run for the first three vertical modes only since they will propagate at speeds faster than meteorological motions. Using additional modes would have the undesirable effect of overly constraining the meteorological features and, thus, would make the spinup problem worse. In the original version (Sashegyi and Madala 1993), the model was run adiabatically for one time step with no friction or diabatic heating. Subsequently, options were added to include diabatic heating from convective precipitation (Harms et al. 1993) and a mixed-layer PBL package (Ruggiero et al. 1996).

An alternative method of initializing mesoscale models that is finding increasing use is the digital filtering technique of Lynch and Huang (1992). It is presently being used operationally as part of the Rapid Update Cycle at the National Centers for Environmental Prediction (formerly the National Meteorological Center) (Benjamin et al. 1994). Comparisons conducted between digital filtering and vertical normal-mode initialization techniques show that both perform similarly (Huang et al. 1994). The main advantage here to the vertical normal-mode scheme used is that it is less computationally expensive than having to do the extended forward and backward model integration required in digital filtering initialization.

For the diabatic heating due to stratiform precipitation, the vertical distribution of the latent heating is determined in a manner similar to the model's large-scale precipitation routine. The procedure starts by first performing an objective analysis with all available data sources (e.g., radiosondes, surface observations, and buoys) using a short-term forecast from a previous model run as the background. Then an observed precipitation field is interpolated to the model grid. The observed precipitation is the 3-h accumulated precipi-

tation for the period just before initialization. At each horizontal grid point where precipitation is observed, a check for conditional instability is performed. If conditional instability exists at any level within the column, then the convective diabatic heating technique of Harms et al. (1993) can be used to vertically distribute the latent heating. At this time, no way has been devised to partition an input precipitation into both stratiform and convective precipitation amounts. If the column is conditionally stable, a check is made to see if there is initial upward vertical motion in the column. It is implicitly assumed that the orientations of the vertical velocities are correct, although the magnitudes may not be correct. This helps prevent the generation of diabatic heating in areas where the precipitation in the 3-h accumulated field ended before the initialization time. The proper orientation of the analyzed vertical motion is the most important factor in properly performing the diabatic initialization. If there is no initial upward vertical motion, then no diabatic heating profile is generated for the column, even if there is precipitation observed at that grid point. If there is upward vertical motion, the technique continues by estimating the cloud-top heights. The cloud-top heights are obtained in a procedure similar to that of Mailhot et al. (1989). Geostationary Operational Environmental Satellite (GOES) IR brightness temperatures of the clouds over precipitation regions are matched with the analyzed vertical temperature profiles. The height of the cloud is determined to be the model's sigma level, at which the temperature profile matches the infrared (11.24  $\mu\text{m}$ ) brightness temperature. This gives a rough approximation of the cloud-top height and is probably biased to setting the precipitating cloud tops too high. This is not a substantial problem since the model's vertical resolution is relatively coarse above 800 mb, and any precipitation generated near the top of the model is likely to be small, given the evaporation parameterization described below. An iterative scheme is then used to distribute vertically the diabatic heating from the stratiform precipitation. First, specific humidities in the two levels below the cloud top are raised to saturation specific humidity if they are not already saturated. Then the vertical moisture convergence is calculated at each level by

$$\frac{\partial q}{\partial t} = -\frac{\partial(\omega q)}{\partial p}, \quad (1)$$

where  $q$  is specific humidity,  $p$  is the pressure, and  $\omega$  is the vertical velocity  $dp/dt$ . Positive values of  $\omega$  are set to 0 so that sinking motions do not contribute to the moisture convergence. Using the updated values of specific humidity  $q'$  obtained from Eq. (1), the moisture in excess of supersaturation  $\Delta q$  at each level can be determined by

$$q' + \Delta q = q_s(T + \Delta T), \quad (2)$$

where  $q_s$  is the saturation specific humidity and is a function of the temperature  $T$  at the model level. Equation (2) can be expanded using a Taylor series on the right-hand side of the equation:

$$q' + \Delta q = q_s(T) + \left[ \frac{\partial q_s}{\partial T} \right]_p \Delta T. \quad (3)$$

Using the Clausius-Clapeyron equation to substitute for  $[\partial q_s / \partial T]_p$  and  $\Delta T$ ,  $\Delta q$  can be solved for by

$$\Delta q = (q_s - q') \left( 1 + \frac{L_c q_s}{c_p R_v T^2} \right)^{-1}, \quad (4)$$

where  $L_c$  is the latent heat release associated with condensation,  $c_p$  is the specific heat at constant pressure, and  $R_v$  is the gas constant. A fraction of the excess moisture from Eq. (4) is subtracted to simulate the precipitation partially evaporating as it falls through the lower layers. Through trial and error, the parameterization of the evaporation was found to have a large impact on the resulting latent heating profile. In the end, the relatively conservative profile in Table 1 was chosen. The total nonconvective precipitation at each model level ( $P_k$ ) is calculated by

$$P_k = -\frac{P}{g_0} \Delta q + (P_{k-1})(1 - E_{k-1}), \quad (5)$$

where  $p$  is the pressure at the  $k$ th level,  $g_0$  is the gravitational constant, and  $E_k$  the fraction of precipitation evaporated in a given layer. The estimated precipitation that falls through to the surface is compared to the interpolated observed precipitation at the particular grid point. If the estimated precipitation is less than the observed precipitation, the procedure is repeated by saturating an additional layer below the cloud top. The initial analyzed vertical velocities will tend to be

TABLE 1. The fraction of precipitation evaporated ( $E_k$ ) and height in  $\sigma$  at each model level in the diabatic initialization precipitation estimation.

$k$	$\sigma$	$E_k$
1	0.0500	1.0
2	0.1500	0.8
3	0.2500	0.6
4	0.3500	0.4
5	0.4500	0.0
6	0.5500	0.0
7	0.6500	0.0
8	0.7475	0.0
9	0.8250	0.0
10	0.8750	0.0
11	0.9100	0.0
12	0.9375	0.0
13	0.9600	0.0
14	0.9775	0.0
15	0.9900	0.0
16	0.9975	0.0

weaker than the actual vertical velocities. Therefore, there might be a tendency to spread the moistening and diabatic heating too deep in the vertical to match the observed precipitation. Again, it is assumed that within each column the proper orientation of vertical velocities will act to vertically limit the precipitation generated in the initialization and, thus, the diabatic heating. The process continues until the calculated precipitation exceeds the observed precipitation or the method has reached the bottom of the column. If the calculated precipitation exceeds the observed precipitation, then the values of specific humidity from the previous iteration are retrieved. If the procedure stops because the bottom of the column is reached, the most current enhanced specific humidity profile is used. The excess moisture calculated in Eq. (2) is used to calculate the diabatic heating at each level by

$$c_p \Delta T = -L_c \Delta q. \quad (6)$$

The vertical diabatic heating profile generated from Eq. (6) is then scaled by the ratio of the observed precipitation amount to that estimated at the bottom model level from Eq. (5). This compensates for the weak initial vertical velocities. The resulting latent heating is then incorporated into the balance that is achieved during the vertical normal-mode initialization. However, as noted by Wolcott and Warner (1981) and Turpeinen et al. (1990), the divergence from the diabatic initialization will not be sustained if there is no continuing source for latent heat release. Therefore, the humidity analysis is updated by increasing the specific humidity of the precipitation-producing layers. At grid points where there is no precipitation, the heating and moisture fields are not adjusted. Since the whole premise behind this technique is to deduce the presence of precipitation-producing clouds, there is no reason why, with some modifications, it cannot be used to help initialize cloud water fields for models that include it in their physics.

### 3. Forecast and analysis system

The forecast model used in the assimilation system is NORAPS version 6 (Liou et al. 1994). This is the latest version of the model that has been previously described by Madala et al. (1987), Hodur (1987), and Liou et al. (1990). NORAPS is currently run operationally by the U.S. Navy Fleet Numerical Meteorological and Oceanography Center for several areas of the world. NORAPS is a hydrostatic, primitive equation model written in flux form. The spatial finite-difference equations are accurate to the fourth order in the horizontal and to the second order in the vertical. Time integration is done using the efficient split-explicit scheme of Madala (1981). A Robert (1966) time filter is used to control high-frequency time oscillations. NORAPS contains a Kuo (1974) parameterization for deep convection and follows the approach of Tiedtke

et al. (1988) for shallow convection. Gridpoint stratiform precipitation is produced after the cumulus parameterization has been run by isobarically condensing regions of supersaturation, following the procedure of Manabe et al. (1965) and as detailed in Haltiner and Williams (1980). Precipitation falling into unsaturated layers is partially evaporated, depending on the relative humidities of the subcloud layers. A multilevel planetary boundary layer is solved using similarity theory in the surface layer, following Louis (1979), and vertical turbulent mixing above it. The mixing is accomplished by turbulent kinetic energy closure (Detering and Etling 1985). Surface temperatures are obtained from surface energy budget considerations using a two-layer force-restore method (Blackadar 1977). Atmospheric heating due to longwave and shortwave radiation is updated every hour, following the approach of Harshvardan et al. (1987).

The horizontal grid is a staggered Arakawa C grid (Arakawa and Lamb 1977). For the assimilation system described here, the model is run in a triple-nest configuration. The lateral boundary time tendencies for the outer grid are relaxed toward interpolated RAFS analysis time tendencies by the method of Perkey and Kreitzberg (1976). For the inner grids, the values of the variables in the boundary zones of the two grids are merged using the Davies (1976) method. The boundary updates were done for every time step. Although the nesting is only one way, it should be of minimal impact since the area of interest is within the innermost grid and the model integrations used in this study are relatively short. For the results shown here, 16 vertical terrain-following sigma ( $\sigma = p/p_s$ ) layers are used. The vertical resolution is listed in Table 1. It is the same for all three grids and increases near the surface such that seven of the layers are below  $\sigma = 0.85$ . When employing the diabatic initialization of convective precipitation, Harms et al. (1993) found it necessary to merge the forecast model's diabatic heating with that calculated in the initialization from the observed precipitation field during the first three hours of model integration. This merging was done because the model left on its own would not always sustain the latent heating that was in the diabatic initialization. The merging was done, following the procedure of Puri (1987), to ensure compatibility between the initial and model heating rates. However, no merging is done in the stratiform diabatic initialization. Enhancing the moisture fields, as described in section 2, helps perform the same function by sustaining the initial divergence field through the continued release of latent heat.

The objective analysis is accomplished by the successive correction scheme of Bratseth (1986), as adapted for upper-air data by Sashegyi et al. (1993) and surface data by Ruggiero et al. (1996). The main advantage to the Bratseth approach is that while the analysis will converge to an optimum interpolation solution, it requires less computer time and memory. The



approach avoids the limitation previous successive correction methods had of converging to the observations and giving too much weight to observations in data-dense regions. Upper-air observations were analyzed on every 50-mb surface from 100 to 1000 mb using a horizontal spatial resolution of  $1.5^\circ$  in latitude and longitude. Bogus soundings derived from operational RAFS hemispheric analyses are added to fill in data-sparse regions over the ocean. The deviations from the first guess are then vertically interpolated back to the sigma surfaces. The surface data analysis, which is constructed on the model's lowest sigma layer, is univariate and has a horizontal grid resolution of  $0.5^\circ$  in latitude and longitude. Before the surface analysis begins, corrections are made to the observations to adjust for differences in the heights between the model grid points and the observations. Sources of data for the surface data analysis include regularly reporting hourly stations, Portable Automated Mesonet System stations, and marine ship and buoy reports. The upper-air and surface data analyses are combined using a one-dimensional physical blending technique.

#### 4. Simulation experiments

A set of simulation experiments was conducted using the NORAPS model. The purpose was twofold. The first purpose was to assess the impact of including diabatic heating from stratiform precipitation in a vertical normal-mode initialization. The second was to check the sensitivity of the diabatic initialization scheme to various factors. Using simulations allowed the experiments to proceed without the uncertainty introduced by observed precipitation analyses and satellite cloud-top estimates.

##### *a. Synoptic situation*

The data selected for the experiment were from the Genesis of Atlantic Lows Experiment (GALE) intensive observation period (IOP) 2. GALE IOP 2 took place from 23 to 28 January 1986. Detailed descriptions of the synoptic and mesoscale features during the IOP can be found in Doyle and Warner (1990). GALE IOP 2 began as a cold-air damming event east of the Appalachian Mountains, as surface high pressure moved eastward over eastern Canada. A coastal front formed over the west wall of the Gulf Stream between 1200 UTC 24 and 0000 UTC 25 January 1986. The coastal front moved slowly west and eventually moved into eastern North Carolina. By 0000 UTC 26 January 1986, a small low formed along the coastal baroclinic zone just off the South Carolina coast and moved northward. This had the effect of pulling the coastal front back to the east along the North Carolina coast. In addition, it resulted in the intensification of warm frontal overrunning precipitation north of the low. At 0000 UTC 26 January 1986, precipitation was associated with the

coastal front and a developing low pressure system in the northeast Gulf of Mexico. Most of the precipitation during this period was overrunning rain and snow. There was some convection located just off the North and South Carolina coasts corresponding to the warm side of the coastal front. By 1200 UTC 27 January 1986, the surface low was located in New England. Precipitation in the GALE region was mainly convective and was associated with the low's trailing cold front, located well offshore, and wrap-around moisture in the Appalachian Mountains.

##### *b. Experiment design*

The model grids were set so that the innermost grid covered the southeast United States (Fig. 1). The horizontal resolution of the outermost grid was  $2.0^\circ$  longitude by  $1.5^\circ$  latitude. Each successive inner grid had a threefold increase in horizontal resolution over its next outer grid. The innermost grid resolution was approximately 18 km at  $35^\circ\text{N}$ . Although there might be some concern over the applicability of the Kuo (1974) scheme at this fine a resolution, NORAPS is currently being run operationally at 15 km by the Navy with no problems (Liou 1995, personal communication). The topography for the innermost grid was constructed from 10' terrain data. Sea surface temperature data were extracted from the weekly 14-km Advanced Very High Resolution Radiometer database. In addition, climatological seasonal albedo and sea ice information were used.

A list of the simulation experiments is given in Table 2. The first experiment was initialized at 1200 UTC 25 January 1986 from analyzed upper-air and surface data. The model was run for 24 h to 1200 UTC 26 January 1986. This first experiment served as the control or "truth" run. All subsequent experiments used the control run output at 0000 UTC 26 January 1986 as input to the adiabatic or diabatic vertical normal-mode initializations. Experiment 2 began by running an adiabatic initialization using the first three vertical modes on the control input fields. The fields from the adiabatic initialization were then used to generate a 12-h forecast. The same procedure in experiment 2 was used for experiment 3 except that the initialization was diabatic with respect to large-scale precipitation. The accumulated large-scale precipitation from the control run for the 3-h period prior to the diabatic initialization was used as input. For the diabatic initialization, the cloud-top heights were defined as the top sigma level over each grid point at which the large-scale condensation occurred. The diabatic initialization was performed on all three grids. Experiment 4 was the same as experiment 3 except that the specific humidities were raised to saturation specific humidity for all layers that the technique determined to be producing precipitation. For experiment 5 the specific humidities of the precipitation-producing layers were raised to 95% of the sat-

uration specific humidity, if they were not already at that level. Similarly, for experiment 6 the specific humidity was raised to 90% of saturation. Experiment 7 was similar to experiment 6 except that the total 3-h stratiform and convective precipitation from the control run was used as input to diabatic initialization. With the stability checking off all the input precipitation was assumed to be stratiform by the initialization. Experiment 8 was the same as experiment 6 except that the cloud-top levels input to the initialization were all raised one model level higher.

TABLE 2. Configuration of the set of simulation experiments.

Experiment number	Initialization at 0000 UTC 26 January 1986	Diabatic heating	Humidity enhancement	Input precipitation
1	no	no	no	no
2	yes	no	no	no
3	yes	yes	no	stratiform
4	yes	yes	100%	stratiform
5	yes	yes	95%	stratiform
6	yes	yes	90%	stratiform
7	yes	yes	90%	total
8	yes	yes	90%	stratiform

### c. Results

#### 1) IMPACT OF DIABATIC HEATING ON INITIALIZATION

Figure 2 contains the 3-h accumulated large-scale and convective precipitation from the control run valid at 0000 UTC 26 January 1986. There are three main regions of moderate large-scale precipitation. The areas of precipitation in southern Alabama and northeast Georgia are associated with a developing low pressure center that was just off the Gulf Coast at this time. The other area of large-scale precipitation over Chesapeake Bay is associated with the northern edge of the Carolina coastal front. Figure 3 contains the 700-mb vertical velocity fields valid at 0000 UTC 26 January 1986 for experiments 1–3. Corresponding to the large-scale precipitation areas in Fig. 2a are well-defined negative vertical velocity maxima in the control case. For the diabatic initialization in experiment 2, the three negative vertical velocity maxima associated with the areas of large-scale precipitation are about one-quarter to one-third less in magnitude than in the control run. In experiment 3, which uses the large-scale precipitation in Fig. 2a as input to the diabatic initialization, the vertical motion associated with the large-scale precipitation is

almost completely retained. Thus, the inclusion of the latent heating due to stratiform precipitation is necessary to retain the control run's initial divergence fields.

The importance of including the latent heat in the initialization can be seen by comparing the forecasts of the experiment 2 and experiment 3 initialized runs to the control case. Figure 4 contains the 700-mb vertical velocity valid at 0300 UTC 26 January 1986 for the control run and the 3-h forecasts from experiments 2 and 3. It can be seen that while the negative vertical motion maximum located on the northern edge of Chesapeake Bay is close for the two cases to the control run, the negative vertical motion maximum in southern Alabama is  $2 \mu\text{b s}^{-1}$  weaker for the diabatic initialized forecast than in the control run. The forecast from the diabatic initialization also underforecasts the negative maximum in Alabama, but only by  $1 \mu\text{b s}^{-1}$ . Figure 5 contains the 3-h accumulated precipitation for the three experiments valid at 0300 UTC 26 January 1986. Again, the experiment 2 and experiment 3 forecasts do fairly well with the maximum located on the northern edge of Chesapeake Bay. Both forecasts underdo the

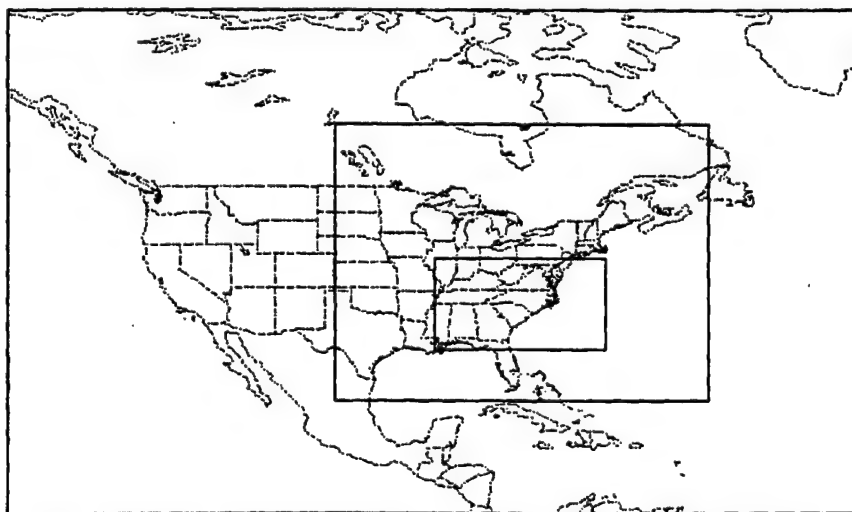


FIG. 1. The domain of the three NORAPS model horizontal nests, as used in this study.



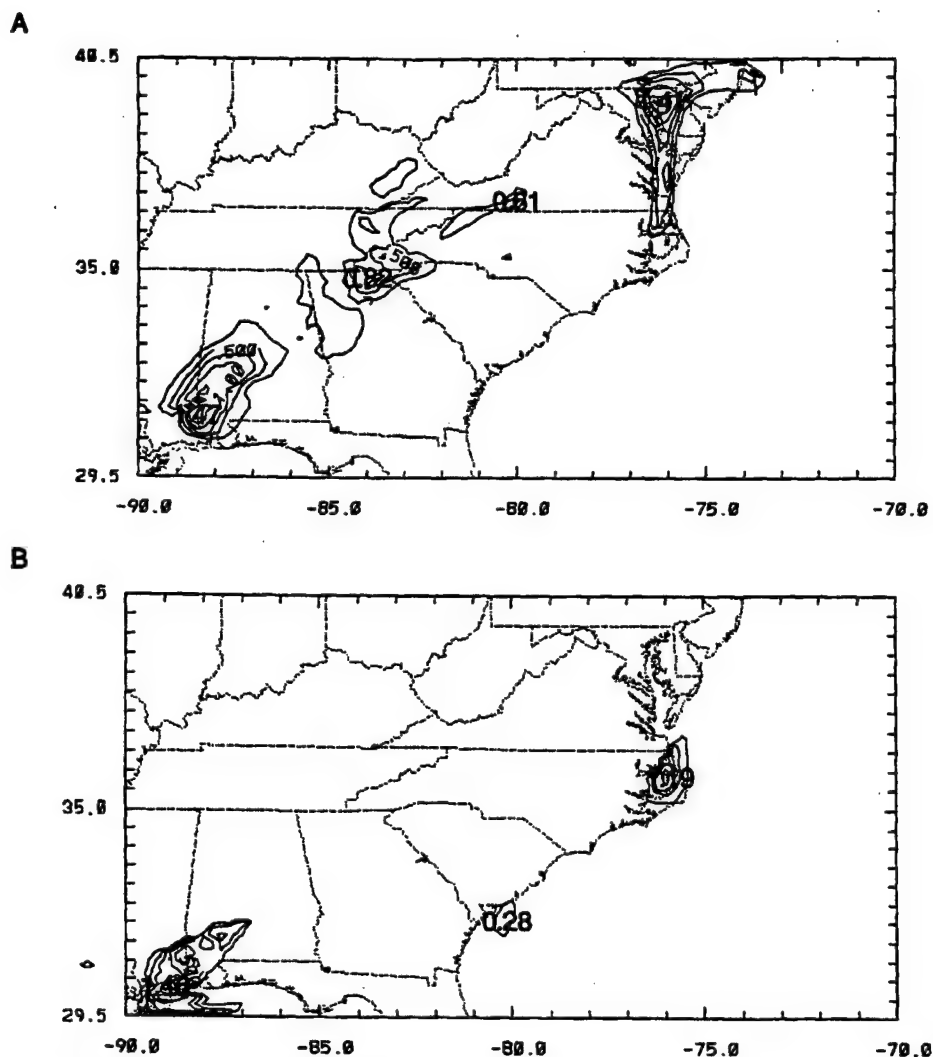


FIG. 2. Experiment 1 control run 3-h accumulated precipitation valid at 0000 UTC 26 January 1986 for (a) large-scale and (b) convective precipitation. Contours are for every 0.25 cm.

amount of precipitation in Alabama, although the diabatic initialization forecast is significantly closer.

## 2) SENSITIVITY OF FORECASTS TO MOISTURE ENHANCEMENT

As mentioned above, previous researchers attempting to include diabatic effects in a model initialization have found it necessary to incorporate some sort of mechanism to ensure that the diabatic part of the initialization is retained by the model. Generally this is done by enhancing or nudging the model's diabatic heating for a few hours or enhancing the moisture fields at initialization time. In the diabatic initialization implemented here, the moisture fields may be modified so that sufficient precipitation can be produced by the model in the early part of integration to sustain the initial vertical motion. The use of the moisture en-

hancement is a powerful tool for creating and sustaining vertical motion. One has to be careful not to add too much moisture to the analysis lest the moisture fields be artificially distorted. Experiments 4–6 were run to judge the sensitivity of the forecasts produced by the diabatic initialization to the amount of moisture enhancement and to select the amount of moisture enhancement to use for the real data cases. Comparing the plots of forecast 3-h accumulated large-scale precipitation (not shown) to the control run, it would seem that the experiment that saturates the precipitation-producing layers (experiment 4) produces the best forecasts. However, these precipitation plots can be misleading. The model coupled with the vertical normal-mode initialization has a tendency to dump out a relatively large amount of precipitation during the first minute of model integration regardless of whether an adiabatic or diabatic initialization is used. Enhancing

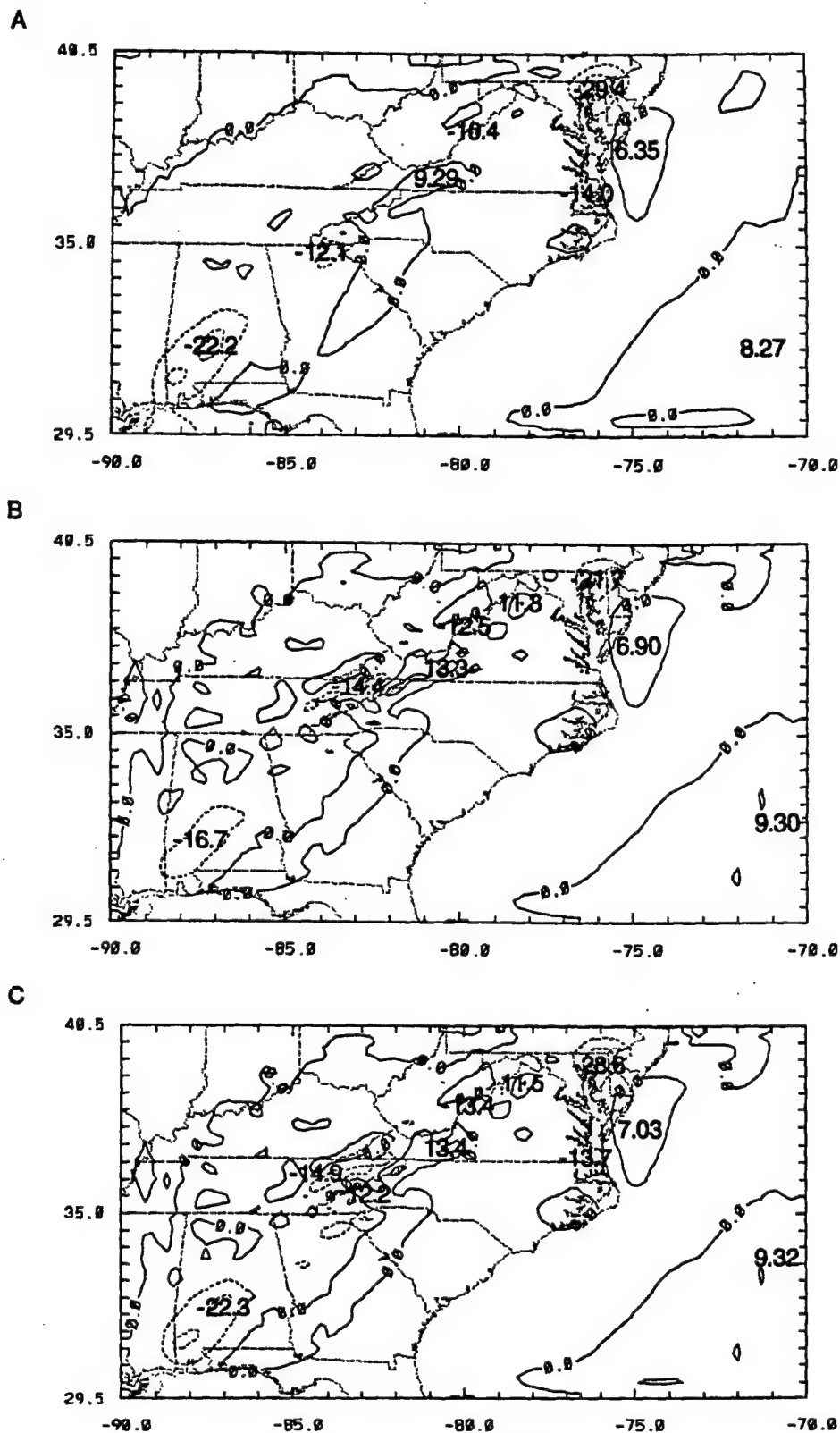


FIG. 3. Vertical velocity ( $\mu\text{b s}^{-1}$ ; contoured every  $10 \mu\text{b s}^{-1}$ ; negative contours are dashed) at 700 mb valid at 0000 UTC 26 January 1986 for (a) experiment 1 control case, (b) experiment 2 adiabatic initialization, and (c) experiment 3 diabatic initialization.

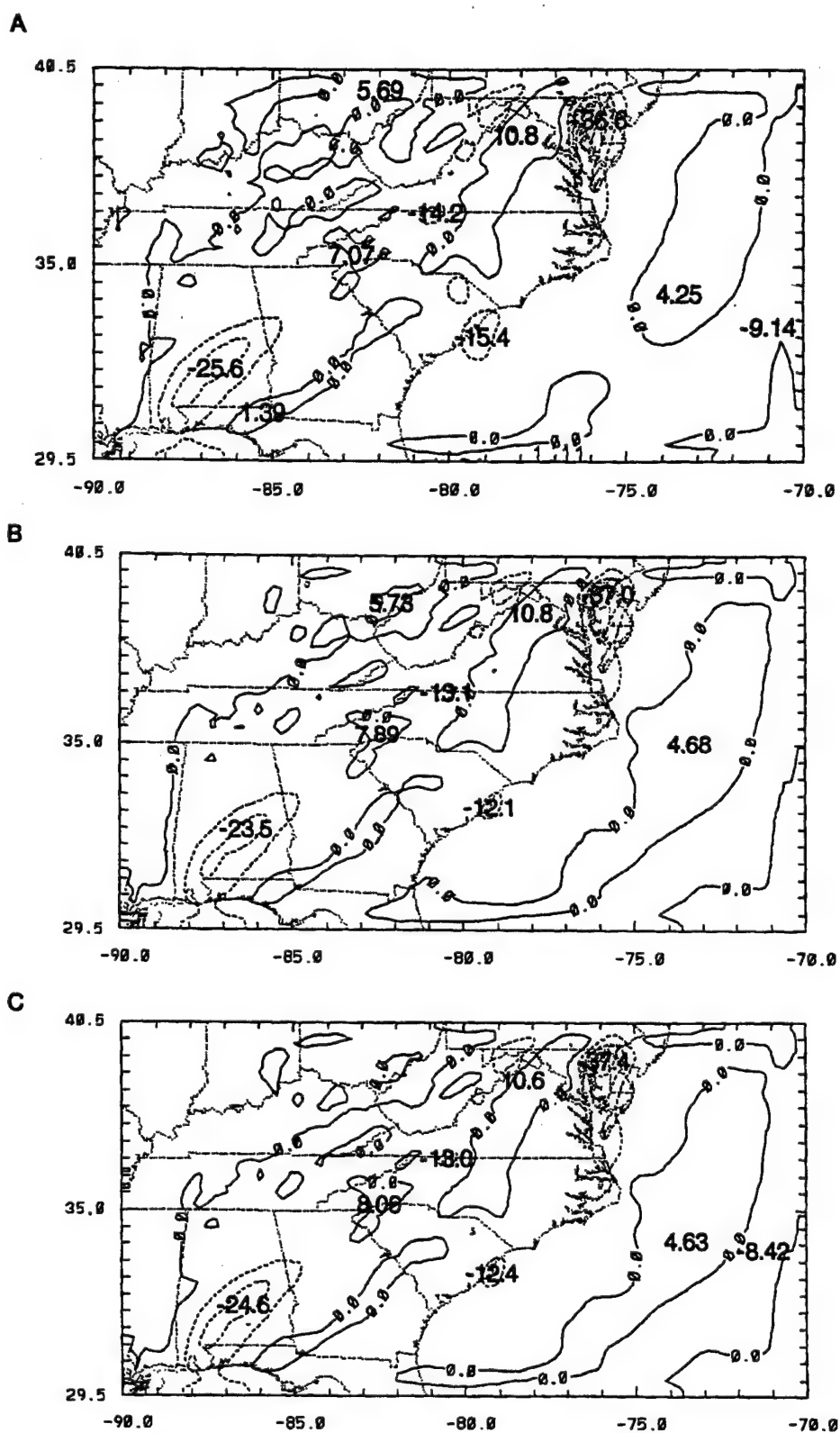


FIG. 4. Same as Fig. 3 valid at 0300 UTC 26 January 1986 for (a) experiment 1 control case, (b) experiment 2 3-h forecast from adiabatic initialization, and (c) experiment 3 3-h forecast from diabatic initialization.



the moisture fields will result in more precipitation being generated in this very early stage. Thus, even though the experiment 4 precipitation forecast looks good, it is producing too much precipitation too early, and thus the contours are probably misplaced by a grid point or two. Looking at the comparative threat scores (Anthes 1983) for the forecasts gives a better indication of forecast skill. Table 3 contains the threat scores for the 0.25- and 1.00-cm levels for experiments 2–6. By this comparison, the full saturation run of experiment 4 produces the worse forecast, almost as poor as the adiabatic run. On the basis of this method of comparison, the experiment 6 run, which moistens up to 90% of the saturation specific humidity, results in the best precipitation forecast. It was slightly better than the experiment 3 and experiment 5 forecasts.

The effect of the washout of moisture during the first minute of integration can be seen if we compute the threat scores neglecting the accumulated precipitation during the first minute of integration in experiment 4. In that case, the threat score for experiment 4 at 0.25 cm increases to 0.8413. It is believed that the high initial precipitation rates occur because the three grids are initialized independently, and some short-lived gravity waves may be generated as the model meshes the grids together. In addition, the resolution of the innermost grid may be at the edge of the applicability of vertical normal-mode initialization.

When increasing the amount of moisture in humidity analyses, one also has to be careful that the excess moisture does not wind up producing too much convective precipitation. Figure 6 shows the 3-h accumulated convective precipitation valid at 0300 UTC 26 January 1986 for the control run and 3-h forecasts from the adiabatic initialization and the experiment 6 diabatic initialization. With the exception of the area in south-central Alabama, the amounts of convective precipitation produced by the adiabatic and diabatic initialized forecasts are close. For the area in south-central Alabama, the moisture from the stratiform diabatic initialization actually winds up bringing the forecast convective precipitation closer to that of the control run.

### 3) SENSITIVITY OF DIABATIC INITIALIZATION FOR STRATIFORM PRECIPITATION TO INPUT FIELDS

The technique that vertically distributes latent heat and moisture is very dependent on the orientation of the vertical motion fields. If the analysis fields show a large area of positive vertical motion associated with an area of stable precipitation, then it will be impossible to generate any heating profile. Experiments 7 and 8 were run to test the sensitivity of the technique to other input parameters, namely precipitation and incorrect cloud-top height estimations.

In experiment 7 the initialization procedure was run exactly as in experiment 6 except that the 3-h total precipitation was used as input. This consisted of the sum

TABLE 3. Precipitation threat scores at 0.25-cm and 1.00-cm levels for forecasts valid at 0300 UTC 26 January 1986 for experiments 2–6.

Experiment number	0.25	1.00
2	0.8110	0.1304
3	0.8434	0.1447
4	0.8124	0.1483
5	0.8419	0.1483
6	0.8456	0.1483

of the large-scale and convective precipitation shown in Fig. 2. The check for conditional stability was turned off so that all the input precipitation is treated as stratiform. The initialized 700-mb vertical velocity fields from experiment 7 are shown in Fig. 7. Comparing this to the field from experiment 3 in Fig. 3c, one can see that there are only small differences. This is due to the fact the areas of precipitation that are mainly convective do not have large areas of initial negative vertical motion associated with them, and thus no heating can be produced.

The estimation of cloud-top heights from satellites is also a likely source of error. As mentioned above, the estimates are most likely to be too high. To see what kind of impact this would have on the latent heat distribution technique, experiment 8 was run. Experiment 8 was the same as experiment 6 except that all the cloud-top estimations were made one vertical level higher (lower sigma) in the atmosphere. Figure 8 is the initialized 700-mb vertical velocity field from experiment 8. When this is compared to the initial vertical velocity fields in Fig. 3, it is seen that the error introduced to the cloud-top estimations has minimal effect. This is due to two factors. The first is that the input vertical velocities may not support negative velocities above the real cloud tops, and the second is the effect of the evaporation profile, which forces more of the precipitation to be produced at the midlevels.

## 5. Real data experiments

To see the performance of diabatically initializing a mesoscale model with respect to stratiform precipitation under more realistic conditions, a series of initializations and forecasts using observed data were run.

### a. Experiment design

The real data test cases used observations from GALE IOP 2, and the NORAPS model was configured exactly as described in section 4. The observed precipitation fields were obtained from 3-h rain gauge analyses over land in the model's innermost nest. The precipitation analyses came from the GALE Data Center and had a resolution of 80 km. These analyses were supplemented by rain rates generated by the University of Wisconsin (Martin et al. 1988) from the OLR sensor

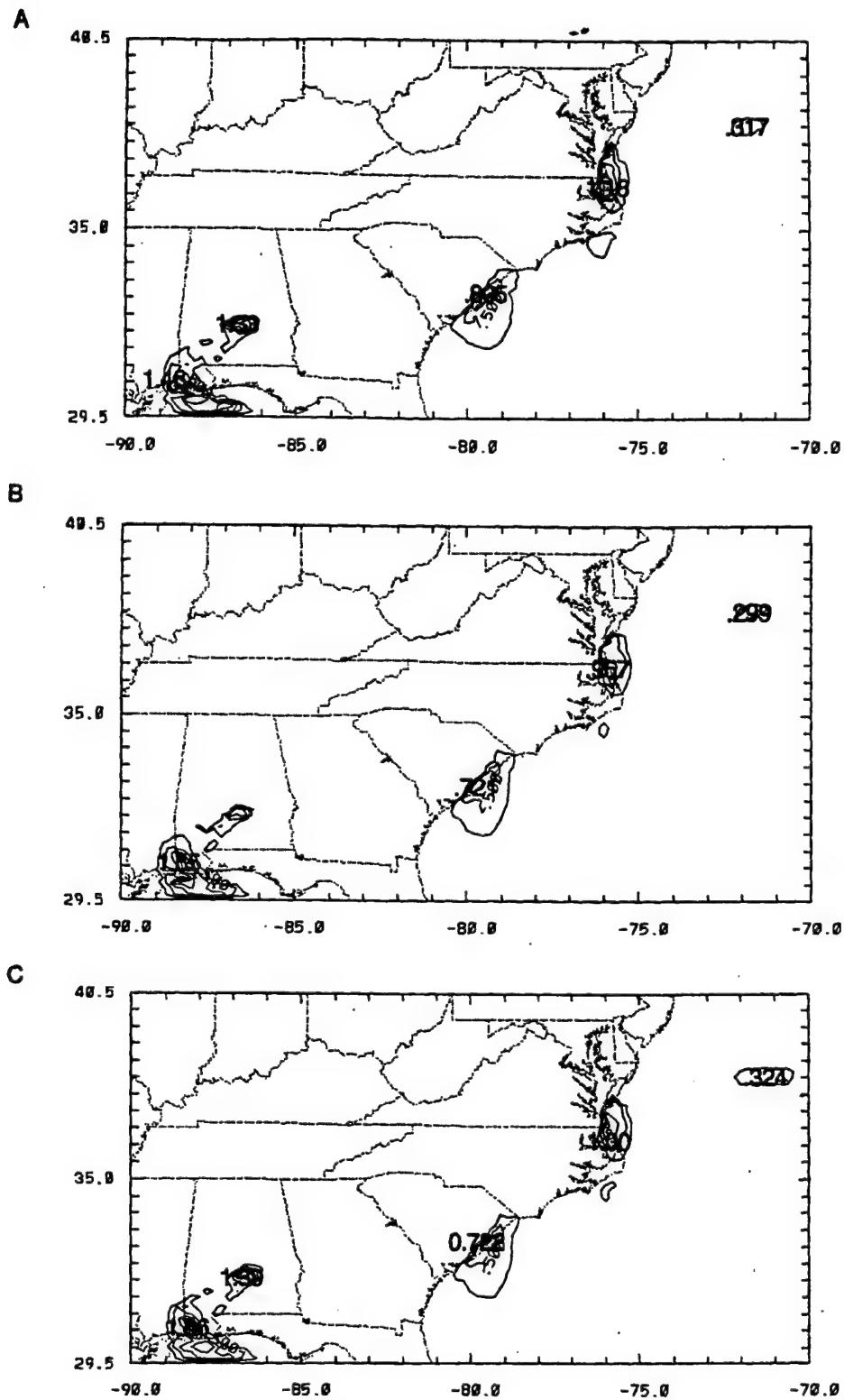


FIG. 6. Three-hour accumulated convective precipitation (cm; contoured every 0.25 cm) valid at 0300 UTC 26 January 1986 for (a) experiment 1 control case, (b) experiment 2 3-h forecast from adiabatic initialization, and (c) experiment 6 3-h forecast from diabatic initialization.

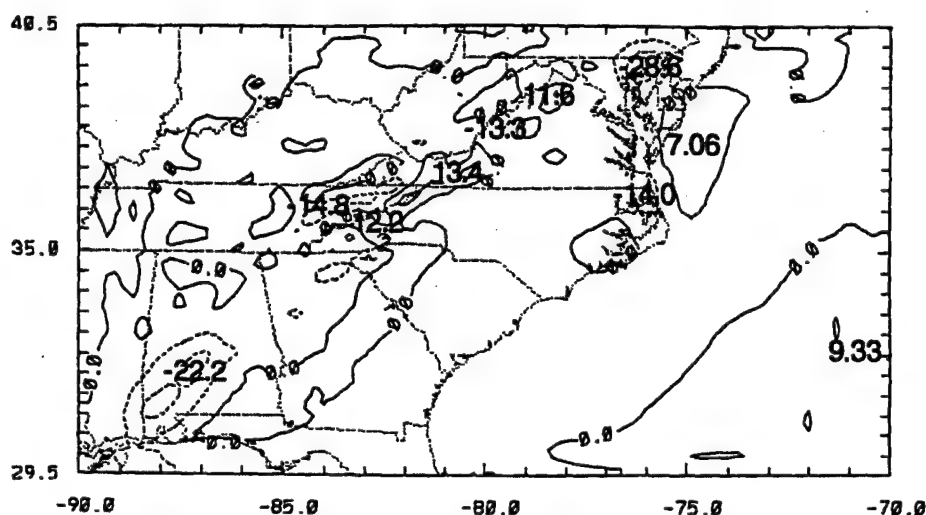


FIG. 7. Same as Fig. 3 except that initialization is valid at 0300 UTC for experiment 7.

onboard GOES. The OLR data had  $1^\circ$  resolution and was used over the open ocean. The satellite-derived precipitation estimations were given as 6-h accumulations and, therefore, had to be temporally interpolated to 3-h accumulations. Cloud-top heights were obtained from the GOES IR brightness temperatures by the method outlined in section 2. At 0000 and 1200 UTC 26 January 1986 and 0000 UTC 27 January 1986, upper-air and surface data analyses were performed using the procedures of Sashegyi et al. (1993) and Ruggiero et al. (1996). For each analysis time an adiabatic vertical normal-mode initialization for the first three vertical modes was run using three iterations. This resulted in the initial fields used in the adiabatically initialized model runs. For the diabatic initializations, the vertical

normal-mode initialization was first run adiabatically as above to produce a set of vertical velocities. Then the initialization was run diabatically using the first three vertical modes, with respect to stratiform precipitation, for three additional iterations. The input precipitation fields for each run are given in Fig. 9. A second set of diabatic initializations and forecasts was run as above except that the convective diabatic initialization was used along with that for stratiform precipitation. For all cases the model was subsequently integrated for 12 h.

#### b. Results

Figure 10 contains plots of the threat scores at the 0.25-cm level for the forecasts from the three types of

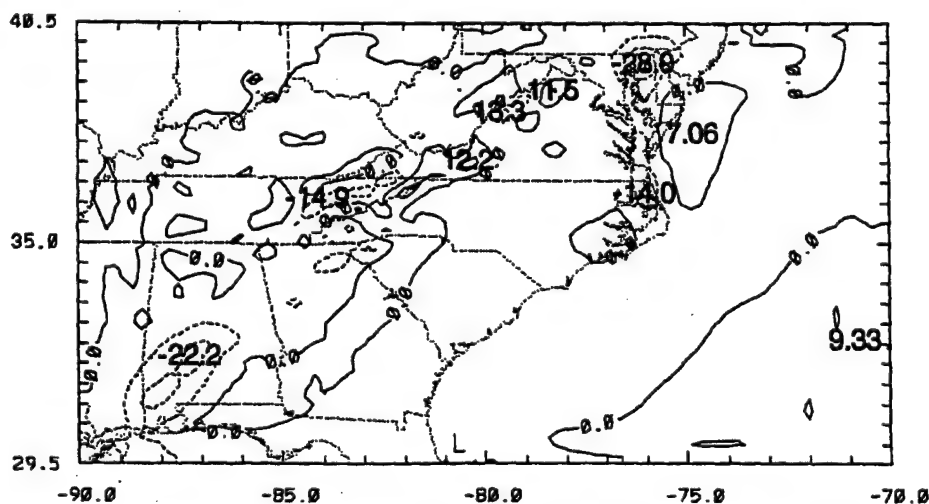


FIG. 8. Same as Fig. 3 except that initialization is valid at 0300 UTC 26 January 1986 for experiment 8.



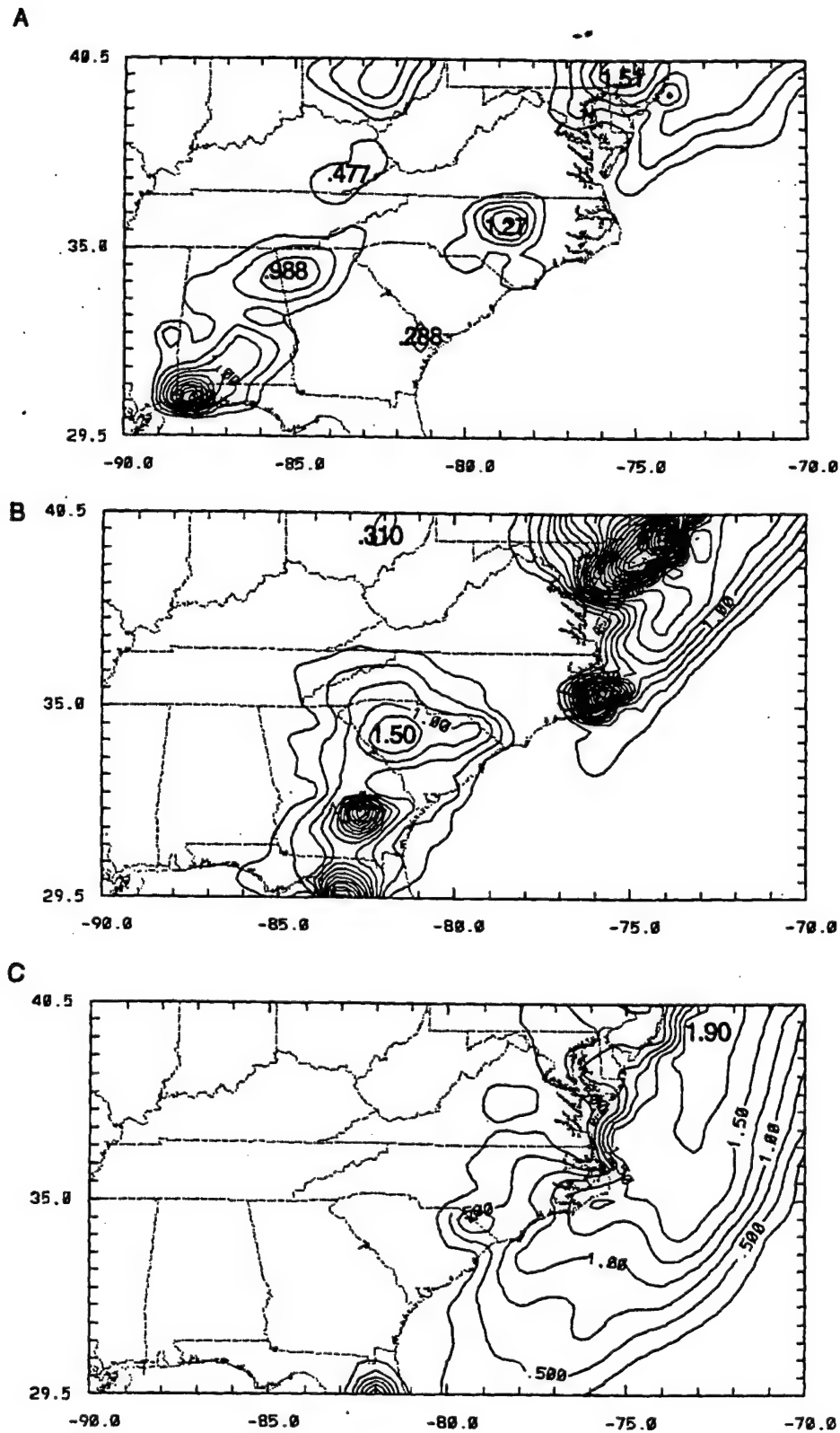


FIG. 9. Observed 3-h accumulated precipitation (cm, contoured every 0.25 cm) valid at (a) 0000 UTC 26 January 1986, (b) 1200 UTC 26 January 1986, and (c) 0000 UTC 27 January 1986.

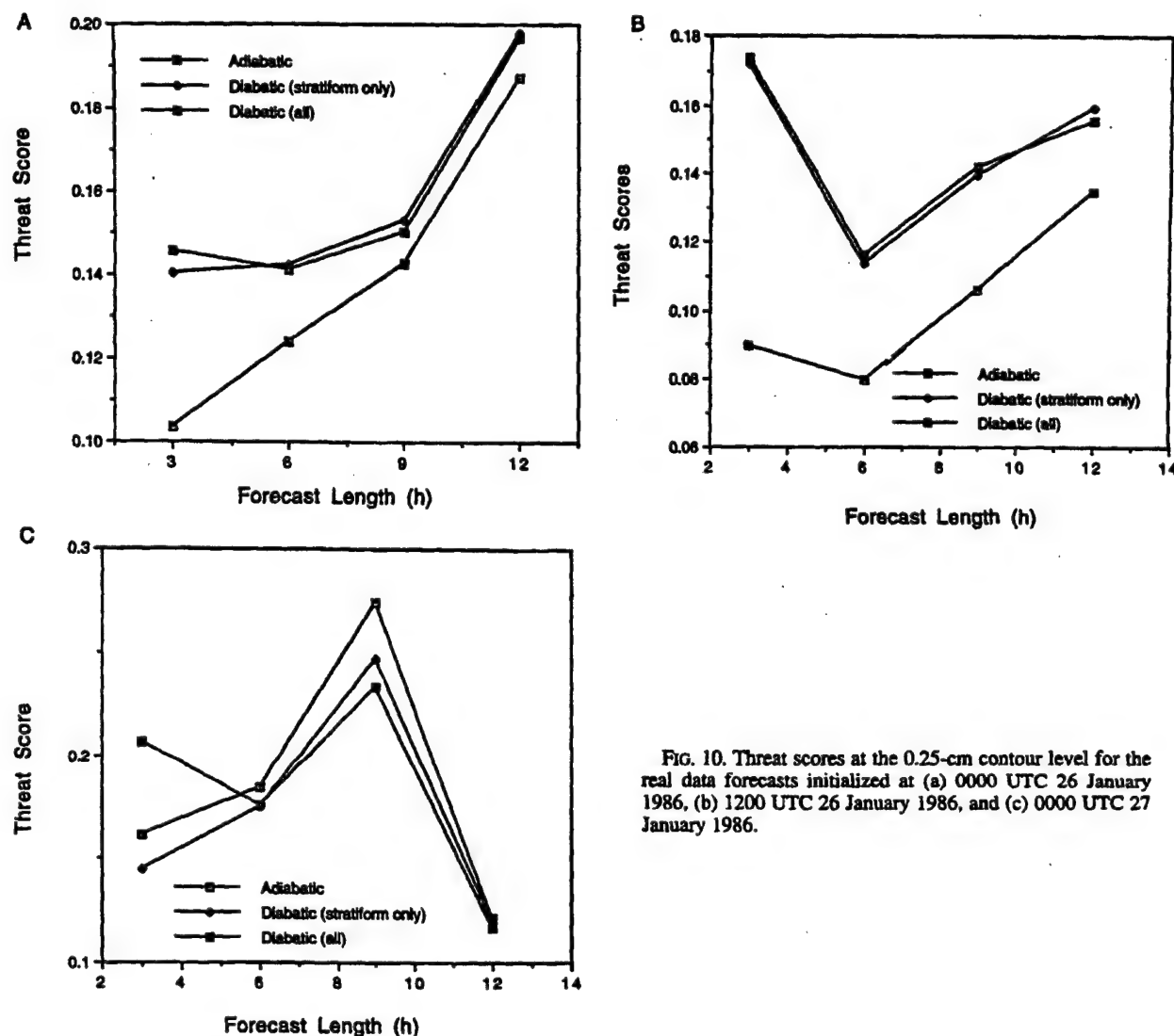


FIG. 10. Threat scores at the 0.25-cm contour level for the real data forecasts initialized at (a) 0000 UTC 26 January 1986, (b) 1200 UTC 26 January 1986, and (c) 0000 UTC 27 January 1986.

initialization for each of the three different forecast periods. In general, the forecast scores are fairly low. Although this is partly due to the problems of forecasting precipitation with a numerical weather prediction model, it also is due to the smoothness of the coarse resolution observed precipitation fields and the certainty of the OLR estimations. For the first two forecast periods the diabatic initialization produces precipitation forecasts superior to those from the adiabatic initialization. In each of these first two periods, the trends are the same in that the forecasts from the diabatic initialization show the most improvement over the forecast from the adiabatic initialization during the first 6 h of the forecast period. In the second 6-h period, the accuracy of the forecasts comes closer together, as the adiabatic initialized forecast becomes spun up. For the third forecast period, the forecast from the adiabatic initialization produces higher threat scores than all but the 3-h forecast using the full diabatic initialization.

This is because the precipitation is winding down as the surface low moves out of the inner-grid domain. The technique essentially applies a constant diabatic component for the first 90 min or so of model integration. If precipitation is steady or increasing, then integrating from a diabatically initialized field in this manner will produce a better result than using an adiabatic initialization. However, the opposite is true if the precipitation rate is decreasing.

Figure 11 contains the total 3-h accumulated precipitation values for the analysis and the adiabatic and diabatic initialized forecasts valid at 1500 UTC 26 January 1986. In general, the forecasts from the adiabatic and diabatic initialized forecast underplay the amount and coverage of the observed precipitation. As explained above, the smoothness of the analysis might help explain part of the undercoverage. Regardless, the forecast from the diabatic initialization is superior to that from the adiabatic initialization in several respects.

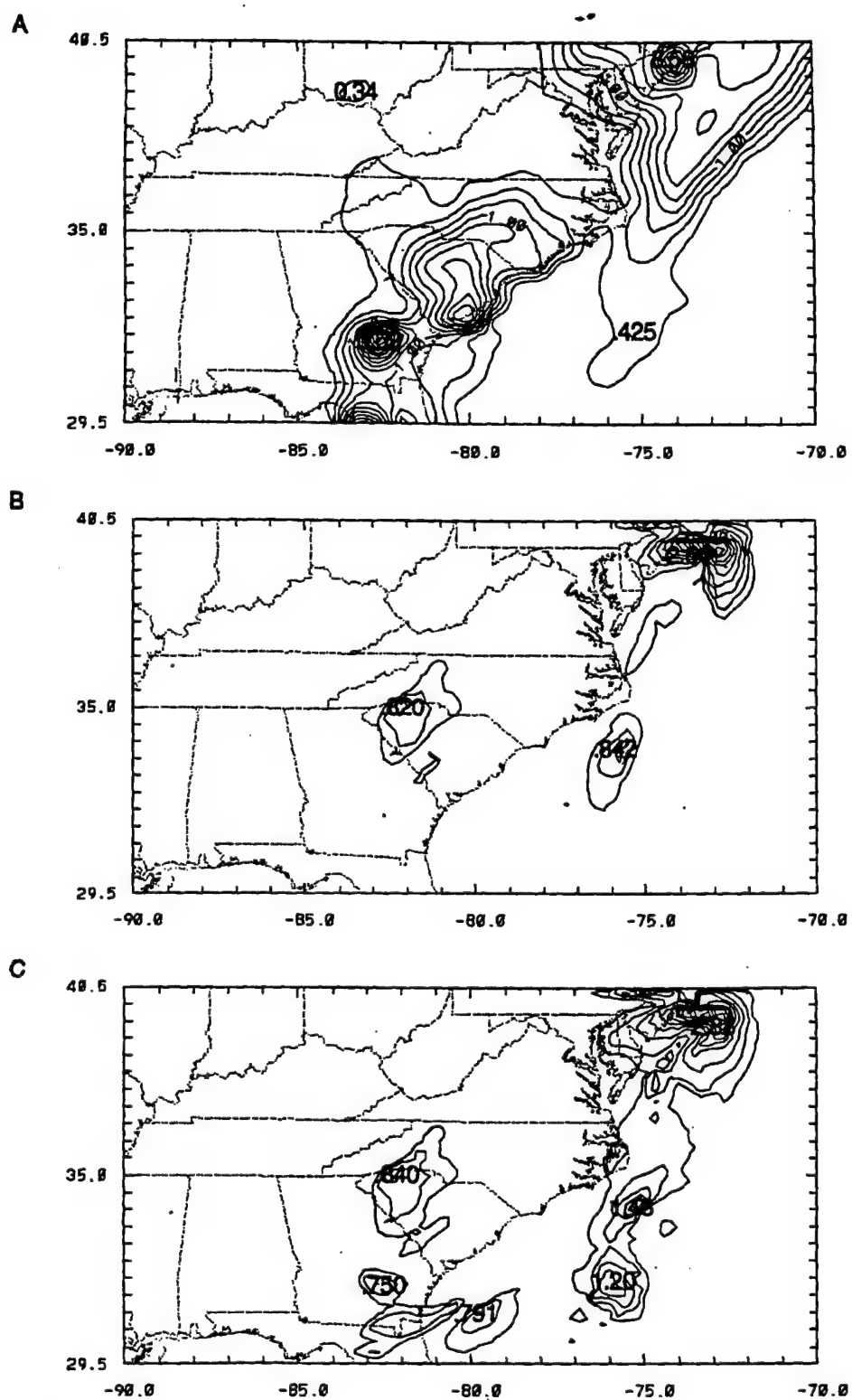


FIG. 11. Same as Fig. 5 except from real data experiments valid at 0300 UTC 26 January 1986 for (a) observed, (b) 3-h forecast from adiabatic initialization, and (c) 3-h forecast from diabatic initialization.

## **Appendix F**

### **The Use of Surface Observations in Four-Dimensional Data Assimilation Using a Mesoscale Model**

Both forecasts capture the precipitation maximum located off the New Jersey coast, but the diabatic forecast is a little closer in amount. The forecast from the diabatic initialization also does a better job depicting the large area of precipitation stretching to the south from the New Jersey coast. Last of all, the diabatic initialized forecast picks up on the precipitation located in the southeast quadrant of Georgia that the adiabatic initialized forecast misses.

## 6. Conclusions

A method has been described to include diabatic heating from stratiform precipitation as input to a vertical normal-mode initialization. This is done to alleviate the spinup problem in short-term midlatitude forecasts. The method uses precipitation amounts and cloud-top heights in an iterative scheme to vertically distribute the diabatic heating. In addition, moisture fields are enhanced by increasing specific humidities in precipitation-producing layers. This new method is meant to complement the existing scheme of Harms et al. (1993) for the diabatic initialization of convective rainfall. A set of simulation experiments revealed the importance of the diabatic heating from stratiform precipitation. Compared to the control case, the addition of diabatic heating from stratiform precipitation to the initialization balance resulted in almost no degradation of the divergence fields. However, in the adiabatic initialization, the maximum upward vertical motions were about 25%–35% less than in the control case. Model integration from a diabatic initialization, with respect to stratiform precipitation, combined with the moisture enhancement, produced a superior short-term precipitation forecast compared to an adiabatically initialized model run. The moisture enhancement helped to sustain the vertical motions that were generated in the diabatic initialization and allowed a smooth transition to the model-driven vertical motions. The technique also worked well when applied to real data cases using combined rain gauge–satellite-derived rain rates and cloud-top heights estimated by GOES IR brightness temperatures. The real data forecasts generated from diabatic initialization were better than those from the adiabatic initializations except in the cases where the precipitation rates were decreasing.

Among the main limitations in the operational application of this technique are the errors that can occur as a result of incorrect cloud-top height estimations and low resolution precipitation analyses. Improved precipitation analyses can be achieved by using radar-derived rainfall, perhaps combined with rain gauges. A better way to denote the height at which precipitation begins is to use volume-scan data from a network of radars. If a way can be found to account for the radar reflectivity bright band that is caused by precipitation phase change, then detailed three-dimensional radar reflectivities might be used to vertically distribute the latent

heating to be used in the diabatic initialization. Another improvement to the technique would be to include a temporal component to the diabatic forcing in the initialization. In addition, the limited sophistication of the physics in the latent heat distribution scheme needs to be addressed. Among the more important items that need to be considered are the horizontal advection of moisture and a more dynamic method of parameterizing evaporation.

**Acknowledgments.** Computer support for this research was provided by the Naval Research Laboratory for time on their Cray Y-MP-EL and the Strategic Environmental Research and Development Program for time on the University of Nevada at Las Vegas Cray Y-MP. The authors thank Gary Wade of the National Oceanic and Atmospheric Administration National Environmental Satellite, Data, and Information System for providing GOES IR satellite imagery on the Man-Computer Interactive Direct Access System (MCIDAS), Kevin J. Schrab of CIRA-CSU for his software to convert the MCIDAS imagery to brightness temperatures, and Randall J. Alliss of North Carolina State University at Raleigh for his help processing the GOES data on the MCIDAS terminal. The authors also thank George D. Modica and Donald C. Norquist for their review of this manuscript.

## REFERENCES

- Anthes, R. A., 1983: Regional models of the atmosphere in middle latitudes. *Mon. Wea. Rev.*, **111**, 1306–1335.
- Arakawa, A., and V. R. Lamb, 1977: Computational design of the basic dynamical processes of the UCLA general circulation model. *Methods in Computational Physics*, Vol. 17, *General Circulation Models of the Atmosphere*, J. Chang, Ed., Academic Press, 173–265.
- Benjamin, S. G., K. J. Brundage, P. A. Miller, T. L. Smith, G. A. Grell, D. Kim, J. M. Brown, and T. W. Schlatter, 1994: The rapid update cycle at NMC. Preprints, *10th Conf. on Numerical Weather Prediction*, Portland, OR, Amer. Meteor. Soc., 566–568.
- Blackadar, A. K., 1977: High resolution models of the planetary boundary layer. *Advances in Environmental Science and Engineering*, Vol. 1, Gordon and Breach, 50–85.
- Bourke, W., and J. L. McGregor, 1983: A nonlinear vertical mode initialization scheme for a limited area prediction model. *Mon. Wea. Rev.*, **111**, 2285–2297.
- Bratseth, A. M., 1986: Statistical interpolation by means of successive corrections. *Tellus*, **38A**, 439–447.
- Carr, F. H., and M. Baldwin, 1991: Incorporation of observed precipitation estimates during the initialization of synoptic and mesoscale storms. Preprints, *First Int. Symp. on Winter Storms*, New Orleans, LA, Amer. Meteor. Soc., 71–75.
- Davies, H. C., 1976: A lateral boundary formulation for multilevel prediction models. *Quart. J. Roy. Meteor. Soc.*, **102**, 408–418.
- Detering, H. W., and D. Etling, 1985: Application of the E-eps turbulence model to the atmospheric boundary layer. *Bound.-Layer Meteor.*, **33**, 113–133.
- Donner, L. J., 1988: An initialization for cumulus convection in numerical weather prediction models. *Mon. Wea. Rev.*, **116**, 377–385.
- Doyle, J. D., and T. T. Warner, 1990: Mesoscale coastal processes during GALE IOP 2. *Mon. Wea. Rev.*, **118**, 283–308.
- Girard, C., and M. Jarraud, 1982: Short and medium range forecast differences between a spectral and grid point model: An extension.

- sive quasi-operational comparison. Tech. Rep. 32, 176 pp. [Available from the European Centre for Medium-Range Forecasts, Shinfield Park, Reading RG2 9AX, United Kingdom.]
- Haltiner, G. J., and R. T. Williams, 1980: *Numerical Prediction and Dynamic Meteorology*, John Wiley and Sons, 477 pp.
- Harms, D. E., R. V. Madala, S. Raman, and K. D. Sashegyi, 1993: Diabatic initialization tests using the Naval Research Laboratory limited-area numerical weather prediction model. *Mon. Wea. Rev.*, **121**, 3184–3190.
- Harshvardan, R. Davies, D. Randall, and T. Corsetti, 1987: A fast radiation parameterization for atmospheric circulation models. *J. Geophys. Res.*, **92**, 1009–1015.
- Heckley, W. A., 1985: Systematic errors of the ECMWF operational forecasting model in tropical regions. *Quart. J. Roy. Meteor. Soc.*, **111**, 709–738.
- Hodur, R. M., 1987: Evaluation of a regional model with an update cycle. *Mon. Wea. Rev.*, **115**, 2707–2718.
- Huang, X.-Y., A. Cederskow, and E. Kallen, 1994: A comparison between digital filtering initialization and nonlinear normal-mode initialization in a data assimilation system. *Mon. Wea. Rev.*, **122**, 1001–1015.
- Krishnamurti, T. N., J. Xue, H. S. Bedi, K. Ingles, and D. Oosterhof, 1991: Physical initialization for numerical weather prediction over the tropics. *Tellus*, **43A**, 53–81.
- Kristjánsson, J. E., 1992: Initialization of cloud water in a numerical weather prediction model. *Meteor. Atmos. Phys.*, **50**, 21–30.
- Kuo, H. L., 1974: Further studies of the influence of cumulus convection on large scale flow. *J. Atmos. Sci.*, **31**, 1232–1240.
- Kuo, Y.-H., and S. Low-Nam, 1990: Prediction of nine explosive cyclones over the western Atlantic Ocean with a regional model. *Mon. Wea. Rev.*, **118**, 3–25.
- Lejenas, H., 1980: On the influence of the technique of nonlinear normal mode initialization on the nonconvective precipitation rate. *Mon. Wea. Rev.*, **108**, 1465–1468.
- Liou, C.-S., C. H. Walsh, S. M. Heikinen, and R. L. Elsberry, 1990: Numerical studies of cyclogenesis events during the second intensive observation period (IOP-2) of GALE. *Mon. Wea. Rev.*, **118**, 218–233.
- , R. M. Hodur, and R. H. Langland, 1994: Navy Operational Atmospheric Prediction System (NORAPS): A triple nested mesoscale model. Preprints, *10th Conf. on Numerical Weather Prediction*, Portland, OR, Amer. Meteor. Soc., 423–425.
- Louis, J. F., 1979: A parametric model of vertical eddy fluxes in the atmosphere. *Bound.-Layer Meteor.*, **17**, 187–202.
- Lynch, P., and X.-Y. Huang, 1992: Initialization of the HIRLAM model using a digital filter. *Mon. Wea. Rev.*, **120**, 1019–1034.
- Madala, R. V., 1981: Efficient time integration schemes for atmosphere and ocean models. *Finite Difference Techniques for Vectorized Fluid Dynamic Calculations*, Springer Verlag, 56–74.
- , S. W. Chang, U. C. Mohanty, S. C. Madan, R. K. Paliwal, V. B. Sarin, T. Holt, and S. Raman, 1987: Description of the Naval Research Laboratory limited area dynamical weather prediction model. NRL Memo. Rep. 5992, Naval Research Laboratory, Washington, DC, 132 pp. [NTIS A182780.]
- Mailhot, J., C. Chouinard, R. Benoit, M. Roch, G. Verner, J. Cote, and J. Pudykiewicz, 1989: Numerical forecasting of winter coastal storms during CASP: Evaluation of the Regional Finite-Element model. *Atmos.–Ocean*, **27**, 24–58.
- Manabe, S., J. Smagorinsky, and R. F. Strickler, 1965: Simulated climatology of a general circulation model with a hydrologic cycle. *Mon. Wea. Rev.*, **93**, 769–798.
- Manobianco, J., S. Koch, V. M. Karyampudi, and A. J. Negri, 1994: The impact of assimilating satellite-derived precipitation rates on numerical simulations of the ERICA IOP 4 cyclone. *Mon. Wea. Rev.*, **122**, 341–365.
- Martin, D. W., B. Auvine, and B. Hinton, 1988: Atlantic Ocean rain maps for GALE. Rep. on Contract NAG5-742. Space Science and Engineering Center, University of Wisconsin—Madison, Madison, WI, 98 pp. [Available from University of Wisconsin—Madison, Madison, WI, 53706.]
- Miyakoda, K., R. F. Stricker, and J. Chludinsky, 1978: Initialization with the data assimilation method. *Tellus*, **30**, 32–54.
- Mohanty, U. C., A. Kasahara, and R. Errico, 1986: The impact of diabatic heating on the initialization of a global forecast model. *J. Meteor. Soc. Japan*, **64**, 805–817.
- Perkey, D. J., and C. W. Kreitzberg, 1976: A time-dependent lateral boundary scheme for limited-area primitive equation models. *Mon. Wea. Rev.*, **104**, 1513–1526.
- Puri, K., 1987: Some experiments on the use of tropical diabatic heating information for initial state specification. *Mon. Wea. Rev.*, **115**, 1394–1406.
- , and M. J. Miller, 1990: The use of satellite data in the specification of convective heating for diabatic initialization and moisture adjustment in numerical weather prediction models. *Mon. Wea. Rev.*, **118**, 67–93.
- Raymond, W. H., W. S. Olson, and G. Callen, 1995: Diabatic forcing and initialization with assimilation of cloud water and rain water in a forecast model. *Mon. Wea. Rev.*, **123**, 366–382.
- Robert, A. J., 1966: The investigation of a low order spectral form of the primitive meteorological equations. *J. Meteor. Soc. Japan*, **44**, 237–245.
- Ruggiero, F. H., K. D. Sashegyi, R. V. Madala, and S. Raman, 1996: The use of surface observations in four-dimensional data assimilation using a mesoscale model. *Mon. Wea. Rev.*, **124**, 1018–1033.
- Sashegyi, K. D., and R. V. Madala, 1993: Application of vertical-mode initialization to a limited-area model in flux form. *Mon. Wea. Rev.*, **121**, 207–220.
- , D. E. Harms, R. V. Madala, and S. Raman, 1993: Application of the Bratseth scheme for the analysis of GALE data using a mesoscale model. *Mon. Wea. Rev.*, **121**, 2331–2350.
- Tarbell, T. C., T. T. Warner, and R. A. Anthes, 1981: An example of the initialization of the divergent wind component in a mesoscale model. *Mon. Wea. Rev.*, **109**, 77–95.
- Tiedtke, M., W. A. Heckley, and J. Slingo, 1988: Tropical forecasting at ECMWF: The influence of physical parameterization on the mean structure of forecasts and analysis. *Quart. J. Roy. Meteor. Soc.*, **114**, 639–664.
- Turpeinen, O. M., L. Garand, R. Benoit, and M. Roch, 1990: Diabatic initialization of the Canadian Regional Finite-Element (RFE) model using satellite data. Part I: Methodology and application to a winter storm. *Mon. Wea. Rev.*, **118**, 1381–1395.
- Wolcott, S. W., and T. T. Warner, 1981: A humidity initialization utilizing surface and satellite data. *Mon. Wea. Rev.*, **109**, 1989–1998.

## The Use of Surface Observations in Four-Dimensional Data Assimilation Using a Mesoscale Model

FRANK H. RUGGIERO

*Atmospheric Sciences Division, Phillips Laboratory, Hanscom AFB, Massachusetts*

KEITH D. SASHEGYI AND RANGARAO V. MADALA

*Remote Sensing Division, Naval Research Laboratory, Washington, D.C.*

SETHU RAMAN

*Department of Marine, Earth, and Atmospheric Sciences, North Carolina State University, Raleigh, North Carolina*

(Manuscript received 23 January 1995, in final form 12 October 1995)

### ABSTRACT

A system for the frequent intermittent assimilation of surface observations into a mesoscale model is described. The assimilation begins by transforming the surface observations to model coordinates. Next, the lowest-level model fields of potential temperature, relative humidity,  $u$  and  $v$  component winds, and surface pressure are updated by an objective analysis using the successive correction approach. The deviations of the analysis from the first guess at the lowest model layer are then used to adjust the other model layers within the planetary boundary layer. The PBL adjustment is carried out by using the model's values of eddy diffusivity, which are nudged to reflect the updated conditions, to determine the influence of the lowest-layer deviations on the other model layers. Results from a case study indicate that the frequent intermittent assimilation of surface data can provide superior mesoscale analyses and forecasts compared to assimilation of synoptic data only. The inclusion of the PBL adjustment procedure is an important part of generating the better forecasts. Extrapolation of the results here suggests that two-dimensional data can be successfully assimilated into a model provided there is a mechanism to smoothly blend the data into the third dimension.

### 1. Introduction

Recently, increased focus has been put on the operational applicability of mesoscale analysis and forecast systems. Advances in computer technology make it possible that in the next few years mesoscale models ( $\Delta x \approx 15\text{--}30$  km) will be routinely run at local forecast offices (Warner and Seaman 1990; Cotton et al. 1994). These models will be used to generate spatially and temporally detailed forecasts in the 3–36-h range. The models can be expected to have their own data assimilation system using centrally prepared forecasts and analyses only for the outermost horizontal boundary conditions. This local forecast office configuration of the near future raises two important questions. First, will the forecasters want to rely on a model that is only initialized at the synoptic times of 0000 and 1200 UTC (when radiosonde data is available). If forecasters are expected to produce highly accurate 3–6-h forecasts,

it will be necessary to assimilate data into the model more often than twice a day. The second question is whether the current network of radiosonde observations is the best source of data for the increasingly high-resolution mesoscale models. As technology advances, there are a host of new data sources to be tapped. These data sources include automated surface observation systems, Doppler radars and wind profilers, automated aircraft reports, and increasingly sophisticated spaceborne sensors, which can provide high spatial and/or temporal resolution in limited regions.

Since its introduction by Charney et al. (1969), four-dimensional data assimilation (FDDA) has become the standard method of producing analyses for the initialization of global and regional models (Daley 1991; Harms et al. 1992a). FDDA involves using the temporal evolution of fields of meteorological variables in combination with a numerical weather prediction model to provide enhanced meteorological analysis. This enhanced analysis is then used for model initialization or a detailed diagnostic dataset. A typical procedure for an operational assimilation system is that used by the National Meteorological Center's (NMC) Global Data Assimilation System, which assimilates new data every 6 h at the usual synoptic hours of 0000

Corresponding author address: Frank H. Ruggiero, Naval Research Laboratory, Code 7225, 4555 Overlook Avenue SW, Washington, DC 20375-5000.  
E-mail: ruggiero@atmos.nrl.navy.mil



and 1200 UTC and at the asynoptic hours of 0600 and 1800 UTC (Kanamitsu 1989).

In preparation for new high-frequency observation systems, research has been carried out to simulate the impact of the more frequent assimilation of asynoptic data on limited-area models. Harms et al. (1992b) used intermittent assimilation of the frequent upper-air data that were available during the Genesis of Atlantic Lows Experiment (GALE). During GALE, upper-air radiosonde soundings were available every 3 h during intensive observation periods (IOP). In addition, the spatial coverage was increased over the eastern Carolinas and the adjacent Atlantic Ocean. The results showed that the analyses created during the assimilation were superior to those available from the Regional Analysis and Forecast System (RAFS) analysis, particularly with respect to accurately defining mesoscale features. Stauffer and Seaman (1990) used temporally interpolated NMC analyses to simulate frequent asynoptic wind and thermodynamic observations. These data were assimilated by Newtonian nudging and resulted in analyses that accurately produced meteorological features on a scale smaller than the spatial resolution of the assimilated data. Although these first studies of asynoptic data assimilation were successful, they did have the advantage of either using or simulating three-dimensional data that contained both mass and wind fields. In reality most of the new data sources are not as ideal. Manobianco et al. (1991), for example, used a nudging method to assimilate the special 3-h soundings and surface data from GALE IOP 10 with limited success in improving forecasts produced with a limited-area model.

Research has been ongoing at the National Oceanic and Atmospheric Administration's Forecast Systems Laboratory to develop assimilation systems for the meso- (Benjamin et al. 1991) and local scales (McGinley et al. 1991; Snook et al. 1994). These systems rely heavily on asynoptic data sources and use short assimilation cycles. This work has led to the operational installation at NMC of the Rapid Update Cycle (Benjamin et al. 1994), which assimilates in real time 3-h asynoptic data. In addition, NMC also uses 3-h asynoptic data in the off-line assimilation that is run in the 12 h before the Nested Grid Model's initialization (DiMego et al. 1992).

Currently, hourly surface observations are one of the most abundant sources of asynoptic data. Miller and Benjamin (1992) describe a system for the assimilation of surface data that uses a 1-h persistence forecast as the background to produce a detailed mesoscale analysis. The current average spatial resolution of hourly surface reporting stations in the United States is approximately 80 km as opposed to about 350 km for radiosonde stations. This will soon be augmented by the deployment of the Automated Surface Observing Systems to airports where observations are currently not available (Friday 1994). In addition, several areas

of the country are also served by automated surface mesonets. Assimilating hourly surface data into a model should yield a better planetary boundary layer (PBL) forecast due to the more-frequent boundary forcing by the surface data. Better PBL representation is important because a large number of forecast requirements are within the boundary layer. Although surface data do not produce direct observations of the upper air, Yee and Jackson (1988) have outlined a scheme where differences between surface observations and the bottom layer model forecast can be used to adjust the other model layers.

This paper will describe a system for the asynoptic assimilation of hourly surface observations into the limited-area model from the Navy's Operational Regional Atmospheric Prediction System (NORAPS). This is part of a larger research effort to produce a prediction and analysis system for local forecast office use that is efficient enough to work on a high-performance workstation and yet sophisticated enough to produce useful and accurate short-term forecasts. In this study, the impact of the surface observations on the objective analysis and model forecasts will be examined. In addition to using the surface data to modify the lowest level of the model fields, a physically based technique will be described that adjusts model layers within the PBL on the basis of the deviations of the surface analysis from the forecast model's lowest layer. Because surface observations are but one important asynoptic data source, what is learned here might also be useful in assimilating other asynoptic data sources.

## 2. Assimilation system description

### a. Assimilation method

The limited-area modeling system developed here follows the form of intermittent assimilation. A flowchart detailing how the intermittent assimilation works is given in Fig. 1. Intermittent assimilation combines in an objective analysis a set of observa-

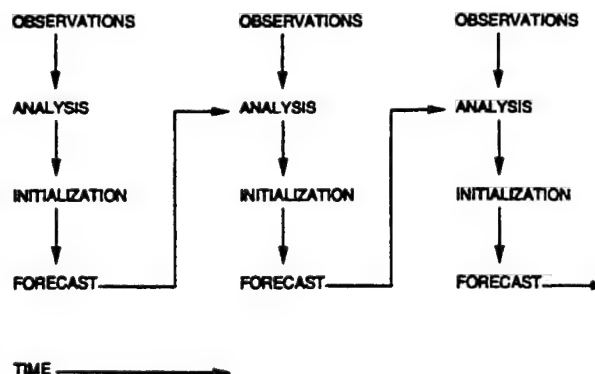


FIG. 1. Flowchart of intermittent assimilation analysis-forecast stream.

tions with a short-term forecast valid at the same time. The new analysis is run through a model initialization step before being used to generate the next set of forecasts. Admittedly, intermittent assimilation does not represent the most advanced FDDA method, but it does satisfy the constraint that the limited-area assimilation system must work quickly on a high-performance workstation. Advanced FDDA techniques such as the adjoint and Kalman-Bucy filter are very computer intensive and will probably remain in the realm of major forecast centers and large main-frame computers for the near future. The advantages of intermittent assimilation are that it is efficient and relatively easy to implement. Another important attribute of analyses and forecasts produced by intermittent assimilation is that the meteorological inconsequential fast-mode gravity waves in the initial conditions can be significantly reduced when the mass and wind fields are balanced by the application of a normal mode initialization scheme for the limited-area model (Bourke and McGregor 1983). This lessens the chance that the model will be shocked by unbalanced new data, an important consideration, particularly in the first 6 or 12 h of integration using a limited-area forecast model. Walko et al. (1989) illustrated what can happen when nudging the prognostic equations toward wind observations. After a period of assimilation, the assimilated wind field was rejected by the model because of the generated imbalance between mass and wind fields. For longer forecasts (>12 h), the gravity wave noise can be removed by the imposed damping that occurs in the lateral boundary regions of the limited-area models. There may be some disadvantages, however, of having to perform an initialization every time new data are assimilated. The main one is that the divergent portion of the wind generated by the model may be removed if the analysis corrections are large or there are substantial differences in diabatic heating generated by the model and that used by the initialization scheme. Thus, how frequently the assimilation cycle should be applied is open to subjective judgment. Another potential problem with intermittent assimilation of synoptic surface data (or any other single-level data) is that the initialization can reject some of the features added to the analysis by the observations. This could occur if the assimilated surface data deviated substantially from the first guess provided by the model forecast. The initialization would see discontinuities between the model's lower levels and could perceive them as gravity waves and damp the surface deviations out. Barwell and Lorenc (1985) showed this to be a cause of the limited retention of assimilated single-level aircraft wind data in subsequent forecasts. For this reason, an attempt is made in the analysis to adjust layers above the model's lowest layer.

#### *b. Forecast model*

The model used in this assimilation system is NORAPS version 6 (Liou et al. 1994). This is the latest version of the model that has been previously described by Madala et al. (1987), Hodur (1987), and Liou et al. (1990). NORAPS is currently run operationally by the U.S. Navy Fleet Numerical Meteorological and Oceanography Center for several areas of the world on a CRAY C90 supercomputer. Work is underway to port the model to a high-performance workstation. Initial tests on a RISC-type workstation with a floating point performance of 30 Mflops using a simplified configuration of the model have produced a 12-h model forecast in approximately 30 min (Sashegyi et al. 1994). NORAPS is a hydrostatic, primitive equation model written in flux form. The spatial finite difference equations are fourth-order accurate in the horizontal and second-order accurate in the vertical. Time integration is done using the efficient split-explicit scheme of Madala (1981). A Robert (1966) time filter is used to control high-frequency time oscillations. NORAPS contains a Kuo (1974) parameterization for deep convection and follows the approach of Tiedtke et al. (1988) for shallow convection. Large-scale precipitation is produced after the cumulus parameterization has been run by isobarically condensing of regions of supersaturation following the procedure of Manabe et al. (1965). Precipitation falling into unsaturated layers is evaporated. A multilevel planetary boundary layer is solved using similarity theory in the surface layer following Louis (1979) and vertical turbulent mixing above it. The mixing is accomplished by turbulent kinetic energy closure (Detering and Etling 1985). Surface temperatures are obtained from surface energy budget considerations using a two-layer force-restore method (Blackadar 1979). Atmospheric heating due to longwave and shortwave radiation is updated every hour following the approach of Harshvardhan et al. (1987).

The horizontal grid is a staggered Arakawa C grid (Arakawa and Lamb 1977). The model is triple nested with the lateral boundary time tendencies for the outer grid relaxed toward interpolated global analysis and forecast time tendencies by the method of Perkey and Kreitzberg (1976). For the inner grids, the values of the variables on the two grids are merged using the Davies (1976) method.

#### *c. Upper-air analysis*

The objective analysis of the upper-air data is accomplished by the successive correction scheme of Bratseth (1986) as adapted by Sashegyi et al. (1993). One advantage of this scheme is that although the analysis will converge to the optimum interpolation solution, it requires less computer time and memory. Thus, it is well suited for implementation on a high-perfor-

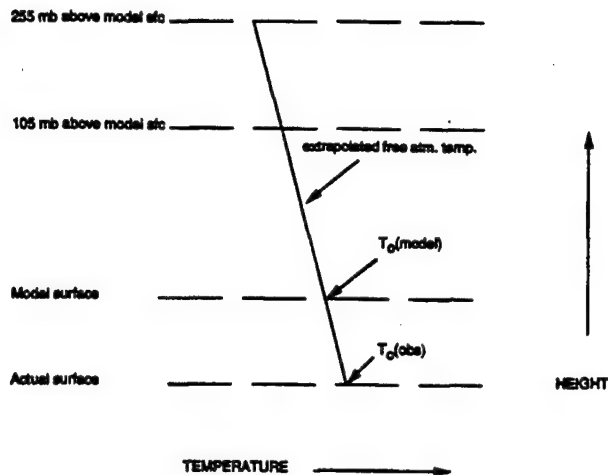


FIG. 2. Schematic of  $T_0$  calculation for sea level pressure reduction.

mance workstation. The Bratseth analysis scheme also avoids the limitation previous successive correction methods had of converging to observations and giving too much weight to observations in data-dense regions. Upper-air observations are analyzed on every 50-mb surface from 100 to 1000 mb using a horizontal spatial resolution of  $1.5^\circ$  in latitude and longitude. At the synoptic hours, bogus soundings derived from operational analyses for a larger domain regional or global model are added to fill in data-sparse regions over the ocean. The deviations from the first guess are then vertically interpolated back to the sigma surfaces. Extrapolation is used for sigma surfaces below 1000 mb. For the regions of the model grid that lie outside the analysis domain, the analysis corrections are computed by interpolation from the operational larger domain analysis at the synoptic hours, whereas the analysis reverts to the background field at the asynoptic hours.

#### d. Surface data analysis

At synoptic and asynoptic hours the bottom model level variables of pressure, temperature, moisture, and winds are updated by a modified version of the Sashegyi et al. (1993) analysis using surface observations only.

##### 1) TRANSFORMATION OF SURFACE DATA TO MODEL COORDINATES

The lowest sigma layer is  $\sigma = 0.9975$  and is approximately 20 m above the model's surface. The surface variables are typically measured at heights between 1.5 and 10 m above ground level. Differences of altitude above mean sea level between the observations and the lowest model sigma layer can also arise. This occurs because of the finite horizontal resolution of the model's topography. Therefore, it is important to take out any altitude bias from the differences of the obser-

vations to the model background. For surface pressure, this is accomplished by reducing the model and observed surface pressures to sea level. The analysis is done using the sea level pressures and then converted back to surface pressure on the model topography. The conversion to and from sea level pressure is done using the following standard equation:

$$p_{sl} = p_{sfc} \left( \frac{T_0 + \gamma z}{T_0} \right)^{g/\gamma R}, \quad (1)$$

where  $p_{sl}$  and  $p_{sfc}$  are the sea level and surface pressures, respectively,  $\gamma$  is the standard lapse rate,  $R$  is the dry gas constant,  $g$  is the gravitational constant, and  $T_0$  is the effective virtual temperature at the top of a fictitious column of air that lies between the surface and sea level. Following a variation of the procedure of Benjamin and Miller (1990), the upper-air data provided by the model background field is used to determine a  $T_0$  that is free of any boundary layer influences. A schematic showing how  $T_0$  is derived is given in Fig. 2. This is done by determining an atmospheric lapse rate using virtual temperatures at 105 and 255 mb above the model's surface from the background data. The levels of 105 and 255 mb above the surface were chosen to ensure that the lapse rate was calculated above the PBL. The lapse rate is then used to extrapolate the temperature at 105 mb above the surface down to the surface of either the model or observation. The observation and background may have slightly different  $T_0$  values. This is due to the differences in elevation of the observations and the model's surface.

For the surface temperature, the analysis is carried out using the deviation of observed surface potential temperature from the potential temperature extrapolated from a mean profile. A schematic of how the potential temperature deviations are arrived at is shown in Fig. 3. The mean potential temperature profile is de-

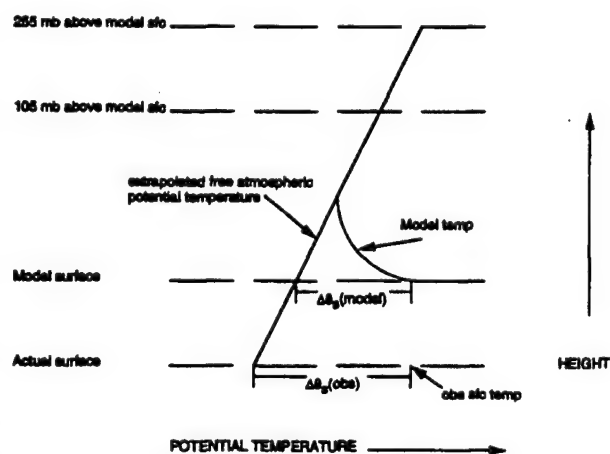


FIG. 3. Schematic of surface potential temperature deviation estimation.

terminated by using the free atmospheric potential temperature lapse rate in the same manner as described above. The profile extends from the model potential temperature at 105 mb above the model's surface down to both the model's lowest sigma layer and the observation height. The deviations of the model surface potential temperature from that of the extrapolated mean profile,  $\Delta\theta_s(\text{model})$ , form the background field of the analysis. The differences between the observed potential temperature and the corresponding extrapolated potential temperature from the mean profile,  $\Delta\theta_s(\text{obs})$ , are the analyzed variables. In the diagram in Fig. 3, although the observed and model potential temperatures are the same, the deviation of the observed surface potential temperature is larger than the deviation computed from the model's lowest layer. The observation indicates more surface heating than the model when taking into account the altitude difference between the model and observation surfaces. By analyzing the deviations from the mean potential temperature profile, differences due to altitude are minimized. When the analysis is complete, the analyzed differences are then added back to the potential temperature from the mean profile corresponding to the lowest model level.

Because moisture varies with altitude mainly because of temperature and pressure, the moisture analysis is conducted using relative humidity as opposed to mixing ratio. Winds generally do not behave as a function of absolute elevation, but as a function of height above the surface. However, the difference above ground level between model height and observation height is generally only about 10 m. A height transformation for the horizontal wind suitable for all stability categories does not exist. Therefore, no altitude adjustments for winds have been attempted.

## 2) OBJECTIVE ANALYSIS

The objective analysis for the surface data is similar to that used for the upper-air data. The analysis procedure of Sashegyi et al. (1993) was adapted to take advantage of the increased resolution of the surface data. The analysis was performed on a domain the same as the upper-air analysis but with the resolution set at  $0.5^\circ$  latitude and longitude to account for the increased data density of surface observations. Observations within  $0.33^\circ$  latitude and  $0.41^\circ$  longitude of each other are averaged to form superobs. Univariate analyses are conducted for sea level pressure and potential temperature deviations, relative humidity, and  $u$  and  $v$  wind components on the lowest model sigma layer. The successive correction method works in an iterative fashion updating the background fields using the difference between the observed values and observational estimates derived from the analysis. At a grid point  $x$ , the updated analysis value for the  $u$  component wind is given by

$$u_x(k+1) = u_x(k) + \sum_{j=1}^n \alpha_{xj}[u_j^o - u_j(k)], \quad (2)$$

where  $u_x(k)$  is the analysis value at a grid point at the  $k$ th iteration,  $u_j^o$  is the observation at the  $j$ th station,  $u_j(k)$  is the observational estimate at the  $j$ th station and  $k$ th iteration,  $n$  is the total number of observations that influence a particular grid point, and  $\alpha_{xj}$  is the weighting function between the  $j$ th observation and the grid point  $x$ . The weights contain functions that spatially correlate observation and analysis locations with themselves and each other (Bratseth 1986). The correlation functions used for sea level pressure, potential temperature, relative humidity, and horizontal winds were the same as those used by Miller and Benjamin (1992) in their optimal interpolation analysis. The functions follow a basic Gaussian form with additional terms included to account for differences in terrain elevation for potential temperature and potential temperature gradients for winds and humidity. Instead of using a polynomial interpolation of the updated analysis to calculate a new value of the observational estimate, the same interpolating formula as Eq. (2) is used in the Bratseth scheme,

$$u_i(k+1) = u_i(k) + \sum_{j=1}^n \alpha_{ij}[u_j^o - u_j(k)], \quad (3)$$

where  $u_j(k)$  is the observational estimate at the  $i$ th observation location for the  $k$ th iteration. The main difference between Eqs. (2) and (3) lies in the definition of the weights. The weights used to compute the observation estimates contain an additional term that accounts for observational error. This has the practical effect of allowing the observational estimate to converge more quickly to the observation values than the analysis. The error function included in the observation estimate weighting function is defined as the ratio of the observation error variance to the first-guess error variance. The first-guess error standard deviation is estimated by summing the standard deviation of the observational error and forecast error growth (Sashegyi et al. 1993). The observation error standard deviations and forecast error growth rates used for in this study are given in Table 1. Selection of the error values is important in the analysis to determine the closeness of fit of the analysis to the observations. Ideally, the values chosen should be based on a large sample of the model and observations. In a research mode this is usually impossible. The values used here are generally based

TABLE 1. Standard deviation of the observational errors and the forecast error growth rates for a 6-h forecast period.

Field	Observation error	6-h forecast error growth rate
Sea level pressure (mb)	1.5	1.0
Potential temperature (K)	2.5	2.5
Relative humidity (%)	13	2
$u, v$ wind ( $\text{m s}^{-1}$ )	2.5	1.1



on values used at NMC for the RAFS analysis (Di-Mego 1988). Trial and error testing of the analysis were carried out to check if the values chosen were suitable. This led to an increase in both the observation error and forecast error growth for the surface potential temperature analysis. In addition, the ratio of observed-to-forecast error for potential temperature was increased. After the set of experiments described in section 3 were completed, the standard deviations of the observations from the model forecast were compared to ensure that they generally fit within the specifications in Table 1. For the surface data analyses at synoptic times the model forecast valid at that time serves as the background field for the analysis and  $u_s(1)$  and  $u_i(1)$  are set to zero. At 0000 and 1200 UTC the analysis of the upper-air data is done first, and that result serves as the first iteration in the surface data analysis and observational estimates. The analysis proceeds using the model forecast as the background field and continues for four to five iterations as was used in the upper-air analysis (Sashegyi et al. 1993).

### 3) PBL ADJUSTMENT

Unique to this assimilation system is a procedure that modifies model fields above the lowest layer on the basis of deviations between the surface observations and the background field. The reason for putting in the adjustment procedure is to have a smooth transition from the lowest model layer analysis to the rest of the model. This provides the subsequent initialization procedure with a more vertically consistent set of fields so that it retains more of the deviations from the analysis. Benjamin (1989) was able to vertically distribute the influence of surface observations by performing the analysis on isentropic surfaces. The procedure described here is carried out on pressure surfaces and is an outgrowth of the work by Yee and Jackson (1988), who described how one might blend surface data with radiosonde data. They postulated that the deviations of the observations from the background at the surface could be used to influence the background levels above the surface. For their testing, Yee and Jackson (1988) used a simple linear weighting function as the influence function. However, they saw the need for a more physically based function. For this effort an adjustment procedure based on parameterized values from the heat and momentum fluxes from the background fields was developed. The derivation of the adjustment procedure is illustrated by looking at the adjustment procedure for temperature. Starting with the equation for the conservation of heat in turbulent flow (e.g., Stull 1988),

$$\frac{\partial \bar{\theta}}{\partial t} + \bar{u} \frac{\partial \bar{\theta}}{\partial x} + \bar{v} \frac{\partial \bar{\theta}}{\partial y} + \bar{w} \frac{\partial \bar{\theta}}{\partial z} = -\frac{1}{\bar{p} C_p} \times \left( L_v E + \frac{\partial \bar{Q}_*}{\partial x} + \frac{\partial \bar{Q}_*}{\partial y} + \frac{\partial \bar{Q}_*}{\partial z} \right) - \frac{\partial (\overline{w'\theta'})}{\partial z}. \quad (4)$$

Here  $\theta$  is potential temperature,  $u$ ,  $v$ , and  $w$  are the component winds,  $\rho$  is the density,  $C_p$  is the specific heat constant,  $L_v$  is the latent heat of the vaporization of water,  $E$  is the phase rate of change,  $Q_*$  is the component of net radiation, and  $\overline{w'\theta'}$  is the turbulent heat flux. The heat flux can be parameterized by  $-K_h[\partial(\bar{\theta})/\partial z]$  where  $K_h$  is the thermal vertical diffusion coefficient, which allows Eq. (4) to consist entirely of the mean quantities of variables and the overbar notation to be dropped. The next step is to separate these mean variables into background and analysis deviation components. In so doing, all the terms that consist solely of background terms can be deleted assuming the background is in balance. Thus, Eq. (4) becomes

$$\begin{aligned} \frac{\partial \theta_d}{\partial t} = & -u_{bg} \frac{\partial \theta_d}{\partial x} - u_d \frac{\partial \theta_{bg}}{\partial x} - u_d \frac{\partial \theta_d}{\partial x} - v_{bg} \frac{\partial \theta_d}{\partial y} - v_d \frac{\partial \theta_{bg}}{\partial y} \\ & - v_d \frac{\partial \theta_d}{\partial y} - w_{bg} \frac{\partial \theta_d}{\partial z} - w_d \frac{\partial \theta_{bg}}{\partial z} \\ & - w_d \frac{\partial \theta_d}{\partial z} + \frac{\partial}{\partial z} K_h \frac{\partial \theta_d}{\partial z}. \end{aligned} \quad (5)$$

The subscript  $bg$  denotes background terms and  $d$  the deviation terms. A scale analysis on the terms in Eq. (5) reveals that the tendency of  $\theta_d$  and vertical diffusion terms are approximately two orders of magnitude larger than the other terms and Eq. (5) is simplified to

$$\frac{\partial \theta_d}{\partial t} = \frac{\partial}{\partial z} K_h \frac{\partial \theta_d}{\partial z}. \quad (6)$$

Likewise for the wind and moisture fields, the following can be derived:

$$\frac{\partial u_d}{\partial t} = \frac{\partial}{\partial z} K_m \frac{\partial u_d}{\partial z}, \quad (7)$$

$$\frac{\partial v_d}{\partial t} = \frac{\partial}{\partial z} K_m \frac{\partial v_d}{\partial z}, \quad (8)$$

$$\frac{\partial q_d}{\partial t} = \frac{\partial}{\partial z} K_h \frac{\partial q_d}{\partial z}. \quad (9)$$

Using these relationships, the adjustment procedure is used to solve for deviations from the background field above the lowest model layer by stepping forward in time. When solving the vertical system of equations, the deviation values at the lowest and highest model layers are held constant. At the top, the deviations are 0 and at the bottom the deviations are set by the surface data analysis. Equations (6)–(9) attempt to represent physically the vertical distribution of deviations caused by the surface-layer forcing. Implicit here is that the vertical propagation of the deviations will be restricted to the boundary layer. This is acceptable based on the scale analysis. Equations (6)–(9) are evaluated starting with the model's diffusion coefficients. After each iteration a new set of coefficients is calculated using

TABLE 2. Configuration of assimilation experiments.

Number	Upper-air updates (h)	Surface data updates (h)	PBL adjustment
1	12	—	No
2	12	12	No
3	12	12	Yes
4	12	6	Yes
5	12	3	Yes

the mixed layer approach (Blackadar 1979). The original diffusion coefficients are then nudged toward the new values following the approach of Stauffer and Seaman (1990). The coefficients are nudged instead of replaced because recalculating the coefficients completely in the beginning would lead to erroneous coefficient values. The new coefficients would be affected because of the discontinuity between the lowest sigma layer and those above. An example would be when the updated bottom sigma layer temperature is significantly cooler than the forecast. This could result in an extremely shallow stable layer and a new coefficient calculated for this layer would be near zero. This would shut down any cooling of the layers above. The idea in nudging the coefficients is that at the end of the PBL adjustment an equilibrium of the vertical momentum, thermodynamic, and eddy diffusivity values can be achieved. Because the model values of diffusion coefficients are based on turbulent kinetic energy and can contain some high-frequency noise, a light horizontal filter is passed over the deviations at each iteration of Eqs. (6)–(9). Because the lowest layer analysis deviation grows over the forecast period, the length of the forecast would then be the upper bound on how long to run the PBL adjustment. In application, however, care must be taken in how much one would want to infer changes above the surface in the absence of direct observations. If the adjustment is carried out too long, the result could be a strong vertical discontinuity at the top of the boundary layer instead of the lowest model layer. A time period of 30 min for performing the PBL adjustment was selected after experimentation.

#### e. Initialization

The assimilation system uses the nonlinear normal vertical mode initialization as described by Sashegyi and Madala (1993). The initialization procedure minimizes the time tendencies of the first three vertical (nonmeteorological) modes to reduce spurious oscillations caused by gravity waves. As described by Sashegyi and Madala (1993), the initialization is carried out without any boundary layer forcing or diabatic heating. For this adiabatic assimilation procedure a first-order closure mixing length PBL package was added to the physical forcing.

### 3. Experiment design

Data from GALE IOP 2 is used for the purpose of testing the assimilation system. GALE IOP 2 took place from 23 to 28 January 1986. Detailed accounts of the case can be found in Riordan (1990) and Doyle and Warner (1990). GALE IOP 2 began as a cold air damping event east of the Appalachian Mountains as surface high pressure moved eastward over eastern Canada. A coastal front formed over the west wall of the Gulf Stream between 1200 UTC 24 January and 0000 UTC 25 January. The coastal front moved slowly west and eventually came onshore into eastern North Carolina. By 0000 UTC 26 January a small low formed along the coastal baroclinic zone just off the South Carolina coast and moved northward. This had the effect of pulling the coastal front back to the east along the North Carolina coast.

Five experiments were run to assess the impact of surface data assimilation. The key features of each experiment are listed in Table 2 and a schematic delineating the assimilation and forecast periods is shown in Fig. 4. All the experiments start off with a 12-h run of the NORAPS model initialized at 1200 UTC 24 January 1986 using 2.5° RAFS hemispheric analysis fields. Experiment 1 assimilated upper-air data only at 0000 and 1200 UTC 25 January. Where radiosonde soundings were not available at 0000 and 1200 UTC, the RAFS hemispheric analysis fields are used to provide bogus soundings over the Atlantic and analysis corrections outside the analysis domain (see section 2c). Experiment 2 is the same as experiment 1 except that a surface data analysis was conducted after the upper-air analysis. The surface observations used included regularly reporting hourly stations, Portable Automated Mesonet System (PAMS) stations that were located in the eastern part of North and South Carolina during GALE, and marine ship and buoy reports. Experiment 3 is the same as experiment 2 except that after each

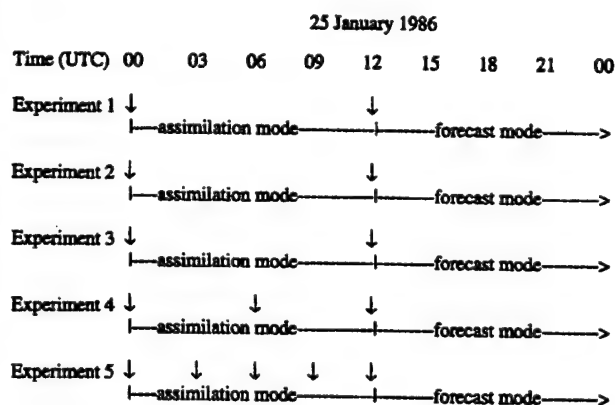


FIG. 4. Depiction of assimilation and forecast periods for the experiments in Table 2. The downward pointing arrows indicate times at which updates were performed.

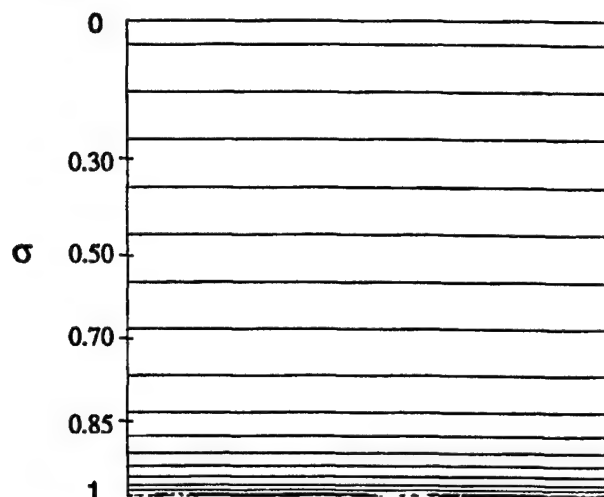


FIG. 5. Vertical distribution of the 16 $\sigma$  levels for NORAPS model configuration used in this study.

surface data analysis, the PBL adjustment procedure was used to merge the surface data analysis with the upper-air analysis at model levels above the surface. Experiment 4 was similar to experiment 3 except that a 6- instead of 12-h assimilation cycle was used. At nonsynoptic hours only the surface data analysis and PBL adjustment procedure modifying the model first guess were run. Experiment 5 was the same as experiment 4 except a 3-h assimilation cycle was used. For all the experiments the model was run to 12 h without further assimilation from 1200 UTC 25 January. The purpose of this was to be able to gauge for how long the surface data assimilation can improve a forecast. For the experiments, the NORAPS model was run with 16 vertical terrain following sigma ( $\sigma = p/p_s$ ) layers. The vertical resolution is depicted in Fig. 5. It is the same for all three grids and increases near the surface such that seven of the layers are below  $\sigma = 0.85$ . The domains of the three model grids used in this study are shown in Fig. 6. The horizontal resolution of the out-

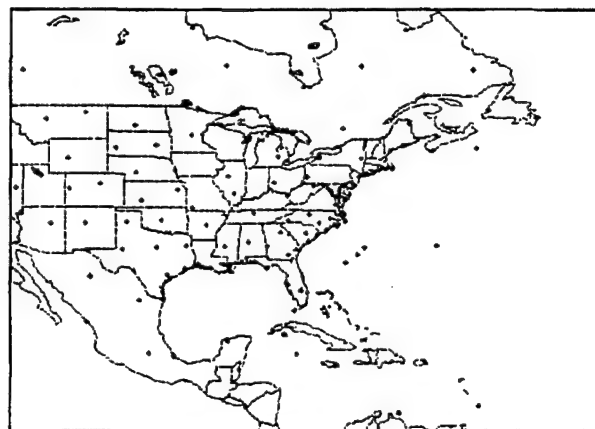


FIG. 7. Location of upper-air stations within the objective analysis domain reporting at 0000 UTC 25 January 1986.

ermost grid was  $2.0^\circ$  longitude by  $1.5^\circ$  latitude, with each successive inner grid having a threefold increase of resolution over its outer grid. The innermost resolution was approximately 18 km. Interpolated RAFS analysis values were used for the horizontal boundary conditions of the outermost grid. The topography for the innermost grid was constructed from 10' terrain data. Sea surface temperature data from the weekly 14-km AVHRR database were used as well as climatological seasonal albedo and sea ice information. The analysis domain for both upper-air and surface data is  $10.0^\circ$ – $60.5^\circ$ N,  $115.5^\circ$ – $44.5^\circ$ W. The domain is shown in Figs. 7 and 8 along with examples of the number and density of upper-air and surface reporting stations.

For the purposes of objective evaluation, the analyses and forecasts generated by the surface data assimilation are compared to the independent analyses presented by Doyle and Warner (1990). Doyle and Warner (1990, hereafter referred to as DW) constructed a

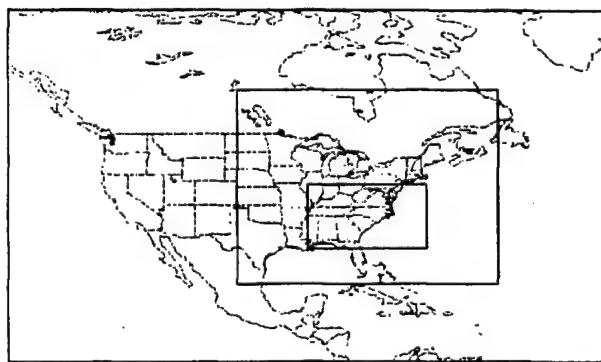


FIG. 6. The domain of the three NORAPS model horizontal nests as used in this study.

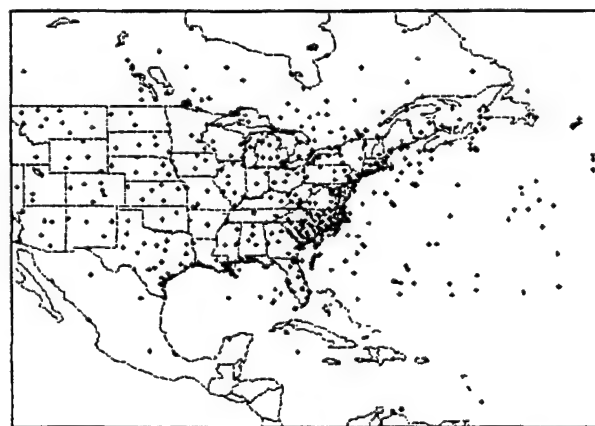


FIG. 8. Location of surface data stations within the objective analysis domain reporting at 0000 UTC 25 January 1986.



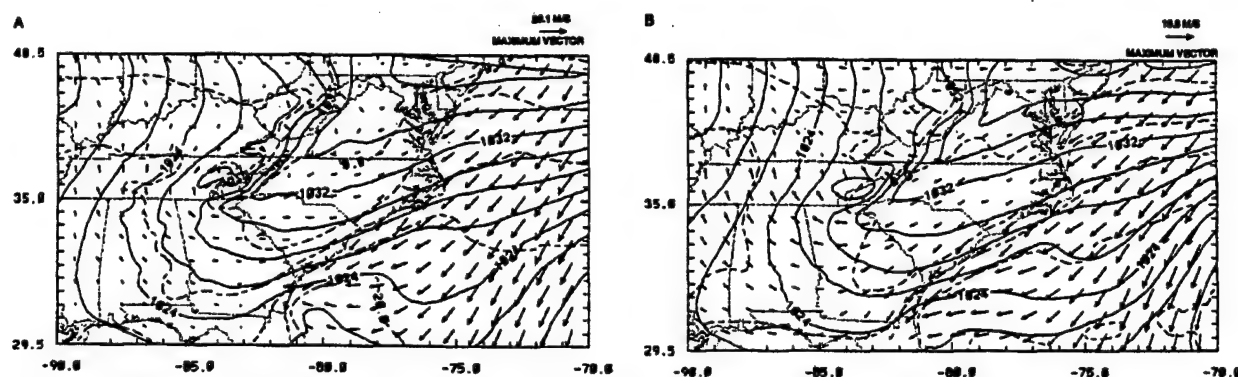


FIG. 9. Analyses of sea level pressure (solid contours), lowest sigma layer temperature (dashed contours), and wind vectors valid at 0000 UTC 25 January 1986 for (a) experiment 1 and (b) experiment 2. Temperature is contoured every 5°C, sea level pressure every 2 mb, and wind vectors are meters per second.

series of analyses for the IOP. High-resolution surface analyses were generated on a 20-km resolution grid. Lower-resolution surface and upper-air analyses were constructed over a 44-km resolution grid. DW used data from all the available sources during GALE and pursued rigorous quality control methods to rid the data of errors and systematic biases. In comparing the analyses and forecasts generated by the surface data assimilation with those of DW, emphasis is put on the positioning and strength of the coastal front. Because the coastal front is generated in part by differential surface diabatic heating (Bosart et al. 1972), it is an ideal feature to evaluate the impact of surface data assimilation in an analysis and forecast system. Coastal fronts are also an important feature to be able to forecast because they can have a large impact on the mesoscale location, amount, and phase of precipitation (Bosart et al. 1972; Marks and Austin 1979) and can, in some cases, have a sizable impact on the synoptic scale (Uccellini et al. 1987). Operational numerical weather prediction models have, in the past, had trouble forecasting the existence and strength of cold-air damming (Bell and Bosart 1988) as well as coastal frontogenesis. This has been due in part to the model's inability to reproduce some of the important physical mechanisms used to generate cold-air damming and coastal frontogenesis due to the limited horizontal and vertical model resolution used. However, high-resolution mesoscale models have been successfully used to simulate these phenomena (Ballentine 1980; Doyle and Warner 1993a,b).

#### 4. Results

During this case study the NORAPS model had a general tendency to underforecast the strength of the cold-air damming in the short range 0–12-h forecasts considered here. This led to the model not retaining the proper location or gradient of the coastal front. The principal mechanisms for establishing and maintaining

the cold-air damming are cold-air advection generated by a northerly low-level jet east of the Appalachian Mountains and evaporative cooling from precipitation aloft (Bell and Bosart 1988). Cold-air damming and coastal fronts are very shallow features (<1000 m) and it is possible that the configuration of the NORAPS model used here with 7 layers below 850 mb does not contain enough low-level vertical resolution for them compared to the 15 layers used below 850 mb by Doyle and Warner (1993a). A further reason for the forecast error is due to the boundary conditions generated by the intermediate grid for the inner grid. On the intermediate grid the horizontal resolution (about 50 km) is also probably not sufficient to generate the strong cold-air damming and northerly flow at the northern edge of the finest grid's domain. With this weaker damming on the intermediate grid, there is insufficient cold-air advection into the finest grid. Although the resolution problems can be corrected with increased vertical resolution and a larger domain for the finest inner grid, that is not the purpose here. Instead, given this model bias, the corrective influence of the surface data assimilation is readily assessed in this paper.

##### a. Impact of assimilation of surface observations at synoptic times

Figure 9 contains analyses of the lowest model level winds, temperature, and sea level pressure valid at 0000 UTC 25 January 1986 for experiments 1 (upper-air data only) and 2 (upper-air and surface data). The addition of the surface data enhances the low-level analysis in several ways. The thermal gradient from the developing coastal front off the North Carolina coast is better depicted with the inclusion of surface data. At this time the coastal front was still offshore (see DW Fig. 5a) in agreement with the surface data analysis, where the thermal gradient is closer to the coast and stronger than the upper-air data analysis. The surface data analysis also enhances the inverted high pressure

ridge in northern Virginia. The winds for the surface data analysis, particularly in South Carolina, contain more of a northerly component. All together the surface data analysis better depicts the detailed mesoscale features of the cold-air damming and coastal frontogenesis situation compared to the upper-air data analysis alone. Twelve hours later, at 1200 UTC 25 January, the convergence along the coastal front became more developed (see DW Fig. 5c). The surface data analysis for this time (not shown) improves the upper-air data analysis by correctly positioning the convergence zone and associated sea level pressure trough along the coast.

*b. Impact of the PBL adjustment procedure on analyses and model forecasts*

Figure 10 contains three profiles each of potential temperature in the lower troposphere for Beaufort, North Carolina (34.71°N, 76.67°W), and Petersburg, Virginia (37.18°N, 77.52°W). The profiles are 1) the 6-h model forecast that serves as the background, 2) observed soundings that were taken as part of the supplemental soundings during GALE, and 3) the profiles that result from the surface data analysis and PBL adjustment procedure. In Fig. 10a, the background sounding for Beaufort is more than 9 K warmer than the observation at the bottom level because of the incorrect placement of the coastal front that is located in the region. The surface data analysis is able to reduce the difference to slightly less than 4 K (the thermal gradient in the area was too tight for the analysis to fully resolve). If no further changes were made to the new

three-dimensional analysis field, the result would have been a strong but extremely shallow stable layer. However, the PBL adjustment procedure allows for a much smoother vertical transition. The background and analysis profiles converge near the top of the boundary layer. The figure shows that not only does the analysis and adjustment procedure bring the mean potential temperature for the lower level closer to the observed, but in this case it also replicates the general stability of the lowest 50 mb. The profiles for Petersburg, which was well into the cold-air damming and away from the strong thermal gradient, are shown in Fig. 10b. Again, as in Fig. 10a, the low level of the observed sounding is cooler than the background profile. In this case, the surface data analysis matches almost exactly to the surface observation. The mean value of the lower-level profile is again brought closer to the observed sounding. However, for Petersburg, the general stability profile is not as well replicated as for Beaufort. Even with the adjustment procedure, the strongest stable layer remains near the surface.

The utility of the surface data analysis and PBL adjustment procedure can be seen in a broader context by looking at a comparison of vertical cross sections. Figure 11 contains cross sections of potential temperature and wind speed from Asheville, North Carolina (35.35°N, 82.47°W), to Cape Hatteras, North Carolina (35.27°N, 75.55°W), resulting from a 6-h model forecast valid at 0600 UTC 25 January 1986 and a surface data analysis and PBL adjustment for the same time. For comparison, Fig. 10b of DW is a cross section for the same horizontal domain based on five supplemental

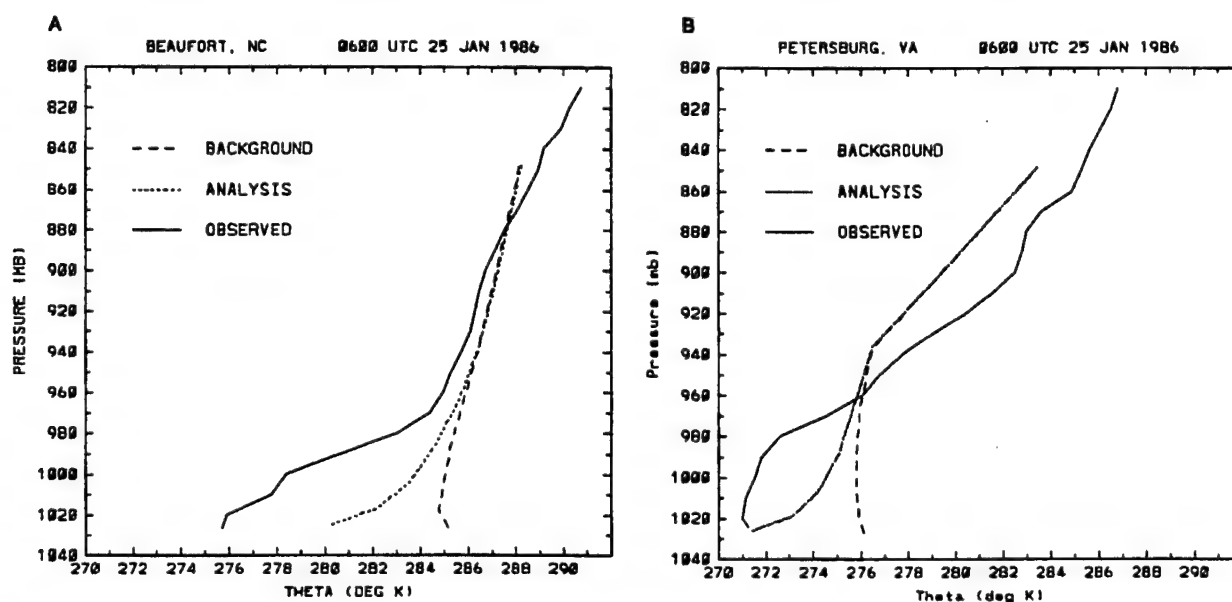


FIG. 10. Potential temperature (K) profiles in the lower troposphere valid at 0600 UTC 25 January 1986 for (a) Beaufort, North Carolina, and (b) Petersburg, Virginia. The observed profile (solid line) is from a radiosonde observation, the background profile (large dash line) from a 6-h forecast initialized at 0000 UTC and the analysis profile (small dash line) that results from the surface data analysis and the PBL adjustment procedure.

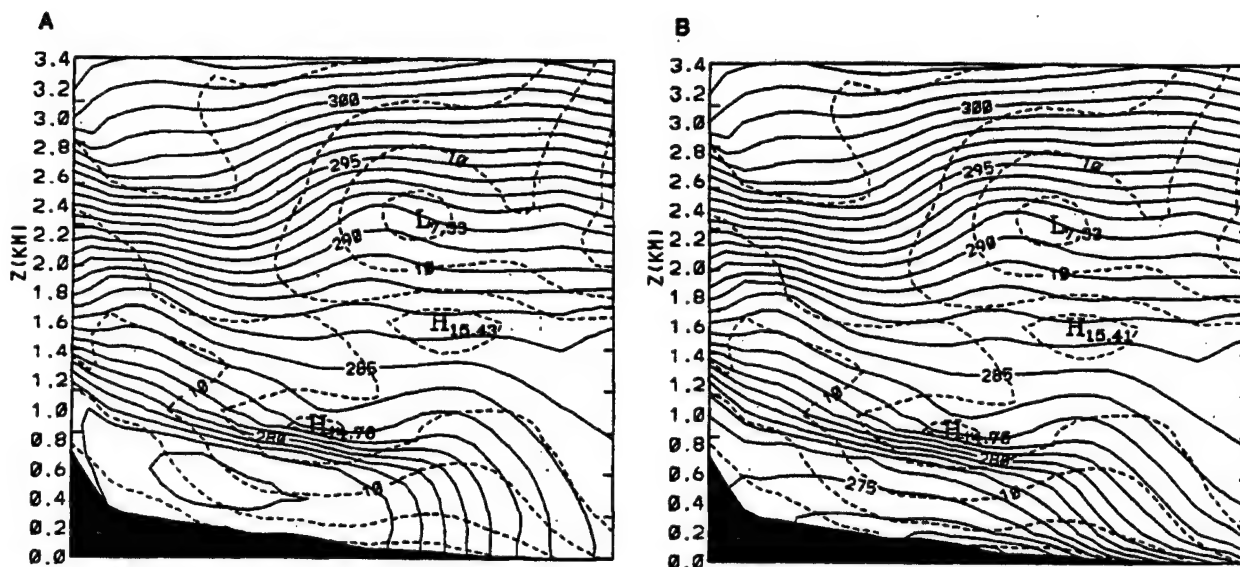


FIG. 11. Vertical cross sections of potential temperature (K; contours every 1 K) and vector wind speed ( $\text{m s}^{-1}$ ; contours every  $5 \text{ m s}^{-1}$ ) valid at 0600 UTC 25 January 1986 from a 6-h forecast initialized at 0000 UTC (a) and from the surface data analysis and PBL adjustment performed at 0600 UTC (b).

soundings available during GALE. The forecast cross section does show some cold-air damming although not as strong as indicated in DW. In the analysis cross section the magnitude of the cold-air dome is increased and the thermal gradient is pushed further toward the coast. Both of these changes bring the analysis closer to the observed cross section of DW. One problem with the analysis is that the slope of the isentropes over the surface front near Cape Hatteras should be steeper. This arises partly because the surface is cooler than the background's higher layers and the nudging toward the updated eddy diffusivities act to brake the vertical mixing of the deviations.

A reason for the implementation of the PBL adjustment procedure was to help merge the bottom model layer's surface data analysis with the rest of the first-guess fields. Preliminary testing revealed that many of

the changes produced by the surface data analysis alone were lost though the initialization process. Because it would infer the presence of gravity waves, the initialization procedure would damp out the features the surface data analysis put in. To demonstrate that the PBL adjustment could alleviate this situation, the analysis in Fig. 9b was initialized without the adjustment procedure for experiment 2 (Fig. 12a) and with the adjustment procedure for experiment 3 (Fig. 12b). The initialization with the adjustment procedure retains more details of the surface data analysis thermal fields. It also has the least modification to the analysis wind fields, particularly to the west of the Appalachian mountains. Both initialization runs weaken the inverted ridging occurring east of the Appalachians. The utility of the PBL adjustment scheme can also be seen in the model forecasts. Figure 13 contains 12-h forecasts valid at 0000

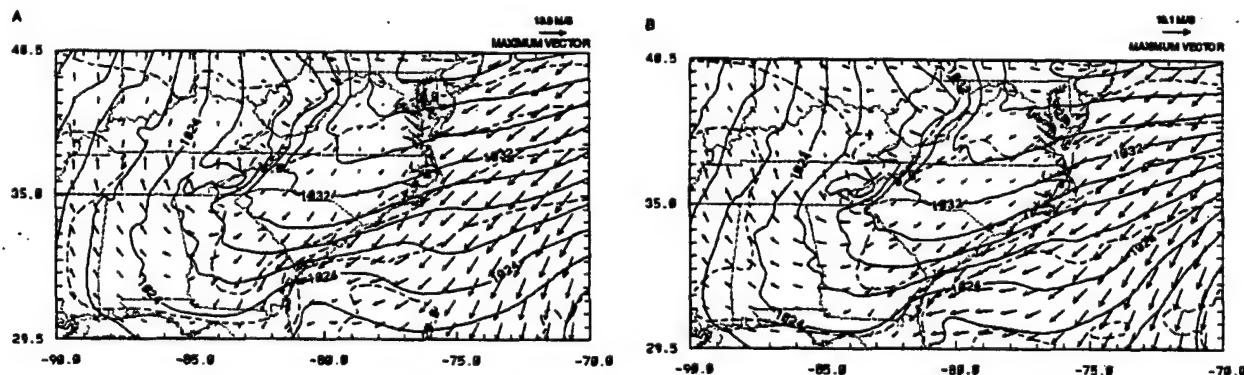


FIG. 12. Same as Fig. 9 except initialized fields (a) without and (b) with the PBL adjustment procedure.

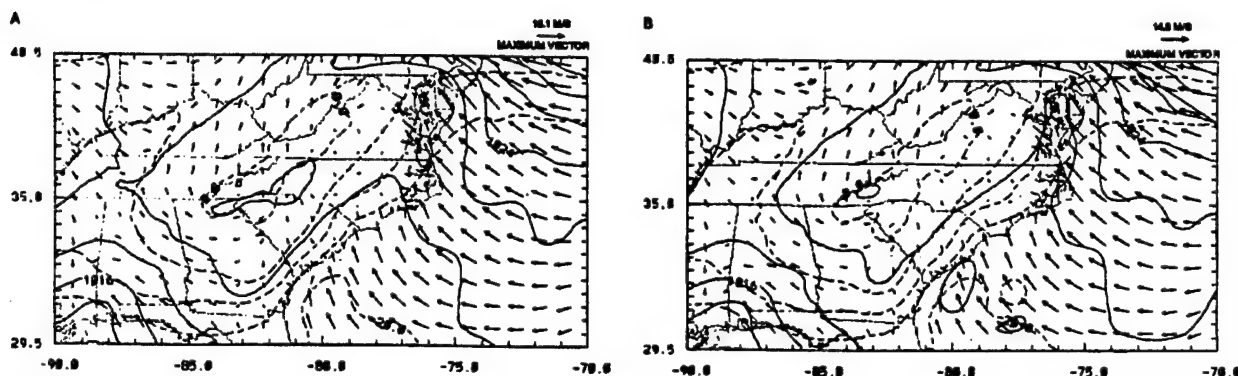


FIG. 13. Same as Fig. 9 except 12-h model forecasts valid at 0000 UTC 26 January 1986 from (a) experiment 2 and (b) experiment 3.

UTC 26 January 1986 for experiments 2 and 3. Although the forecast temperature and wind fields are similar for the two forecasts, the forecast with the PBL adjustment does a better job depicting the sea level pressure field. The experiment 3 forecast correctly shows the details of the inverted trough associated with the coastal front and the developing low off the Georgia and South Carolina coasts. Because sea level pressure is a vertically integrated quantity, it is reasonable that it would benefit from the PBL adjustment procedure.

*c. Impact of frequent assimilation of surface observations on analyses and model forecasts*

Surface forecasts that are valid at 1200 UTC 25 January 1986 are compared for the different assimilation cycles in Fig. 14. Figure 14a is the lowest-layer temperature and wind fields along with sea level pressure for a 12-h forecast from the 12-h assimilation cycle of experiment 3. Figure 14b contains the same fields for the latest 3-h forecast from the 12-h upper-air and 3-h surface data assimilation cycle in experiment 5. The experiment 5 forecast shows the benefit of the more frequent surface data assimilation in that it retains a tighter gradient near the coastal front and keeps the

lower-level temperatures east of the Appalachian mountains colder. In addition, the experiment 5 forecast still retains the strong convergence along the South Carolina and Georgia coasts even though it has undergone three additional analysis and initialization steps. Both sea level pressure forecasts show the presence of a trough associated with the coastal front. However, the 3-h surface data assimilation forecast has a sharper trough and positions it closer to its observed position along the mid-Atlantic coast (see DW Fig. 5c). Overall, these results indicate that in a continuing data assimilation system, for a short-term forecast, it is beneficial to include the latest surface observations into a model even if there is no corresponding upper-air data.

It is interesting to see the impact that these differing forecasts have on the resultant lower-level analyses. Figure 15 is the result of the upper-air and surface data analysis at 1200 UTC 25 January using the 12-h forecast from Fig. 14a as the background. Figure 15b uses the forecast fields from the 3-h surface data assimilation cycle in Fig. 14b as the first guess in the analysis. Because the objective of an assimilation system is to blend the high-resolution features generated by the model with observed data, it should come as no surprise that the analysis that used the 3-h assimilation cycle forecast

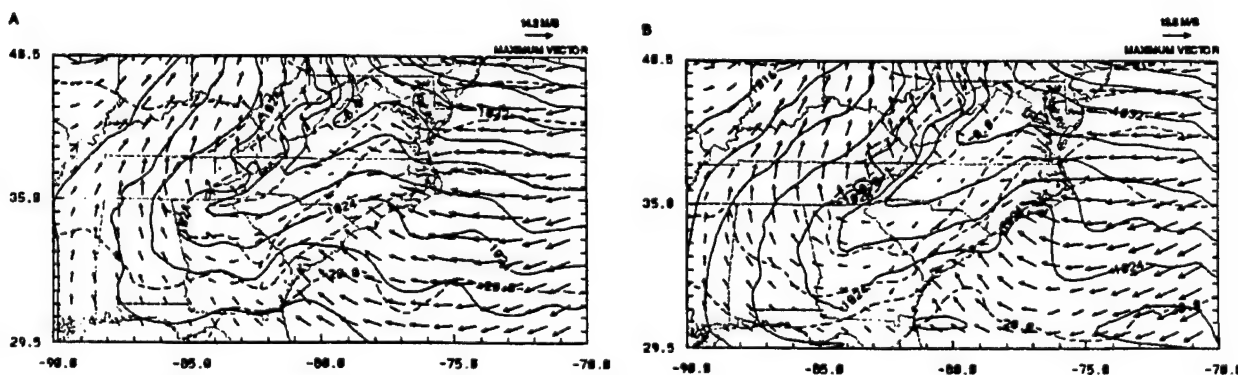


FIG. 14. Same as Fig. 9 except 12-h forecast from (a) experiment 3 and (b) 3-h forecast from experiment 5. Both forecasts are valid at 1200 UTC 25 January 1986.



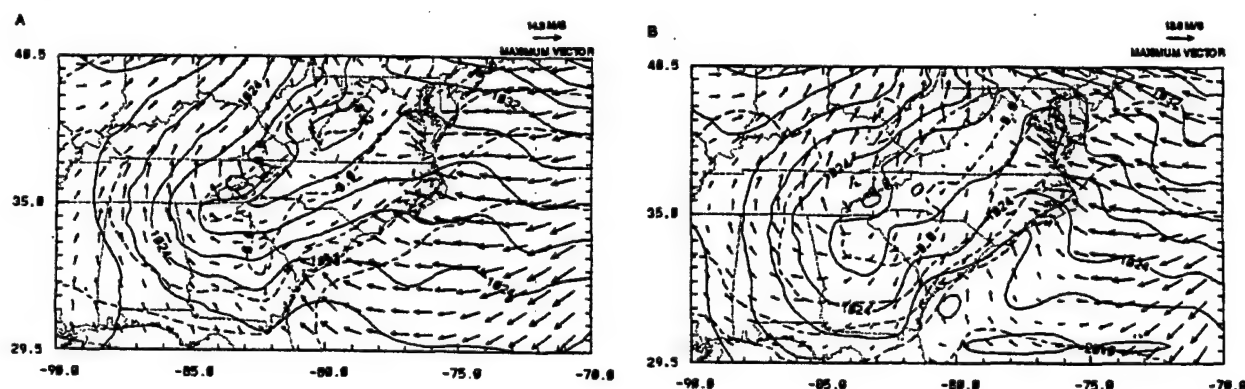


FIG. 15. Same as Fig. 9 except analyses valid at 1200 UTC 25 January 1986 for (a) experiment 3 and (b) experiment 5.

as background, with its tighter gradients and sharper features, is superior. The analysis from the 3-h assimilation cycle has a tighter thermal gradient along the coast, which the analysis moved slightly to the east from the first guess. It also retains the sharp inverted trough associated with the coastal front and positions it favorably compared to DW's analysis for the same time. The 12-h assimilation analysis has only a broad shallow trough that is placed too far east, off the North Carolina coast. One of the reasons that the 3-h assimilation results in a more detailed analysis than the 12-h assimilation is the effect of the error weighting described in section 3b. Because the 3-h assimilation

analysis uses a 3-h forecast compared to a 12-h forecast, there is less forecast error growth, and thus the background field takes on more importance than in the 12-h assimilation.

Figure 16 contains forecasts ranging from 3 to 12 h, all initialized using the analysis from experiment 2 at 1200 UTC 25 January 1986. Figure 17 contains forecasts of the same lengths and valid times as Figure 16 but uses the analysis from experiment 5. For all the runs the forecasts initialized with the more frequent assimilated surface data show tighter thermal gradients for the front along the coast of the Carolinas. The differences in the gradients diminish over the length of the

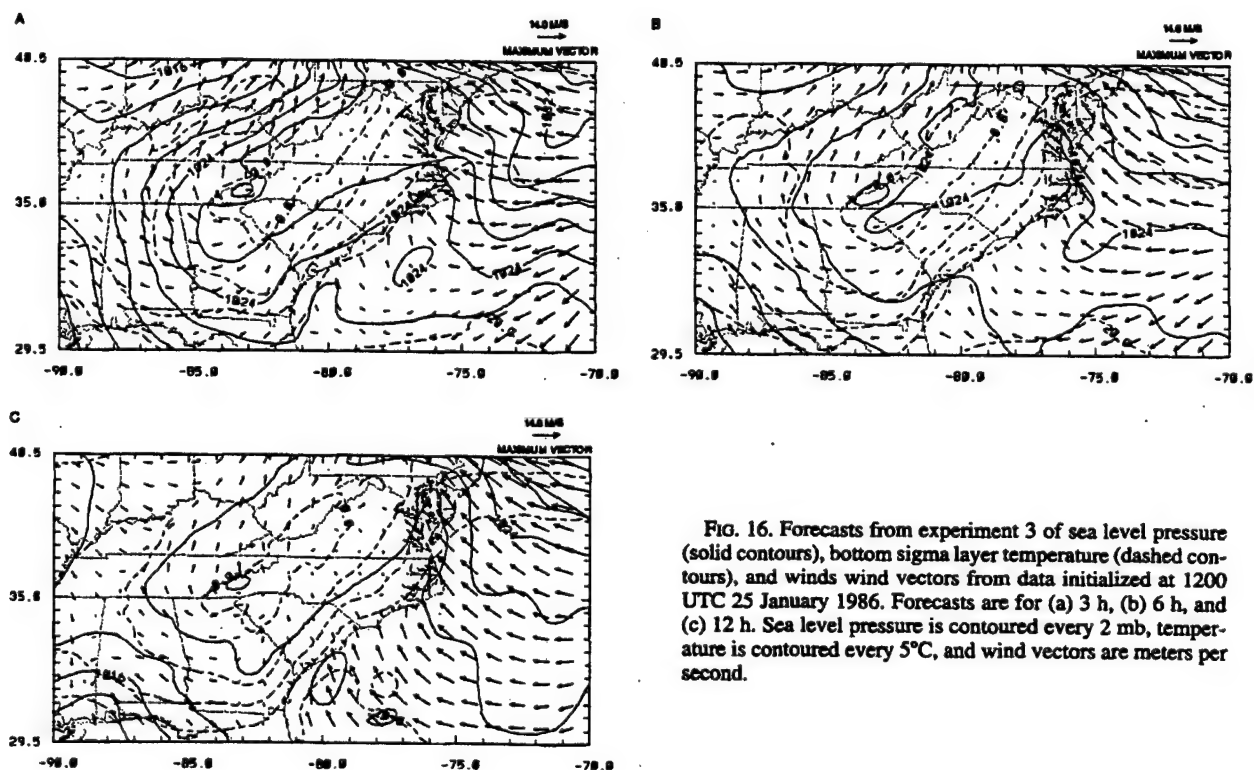


FIG. 16. Forecasts from experiment 3 of sea level pressure (solid contours), bottom sigma layer temperature (dashed contours), and winds wind vectors from data initialized at 1200 UTC 25 January 1986. Forecasts are for (a) 3 h, (b) 6 h, and (c) 12 h. Sea level pressure is contoured every 2 mb, temperature is contoured every 5°C, and wind vectors are meters per second.

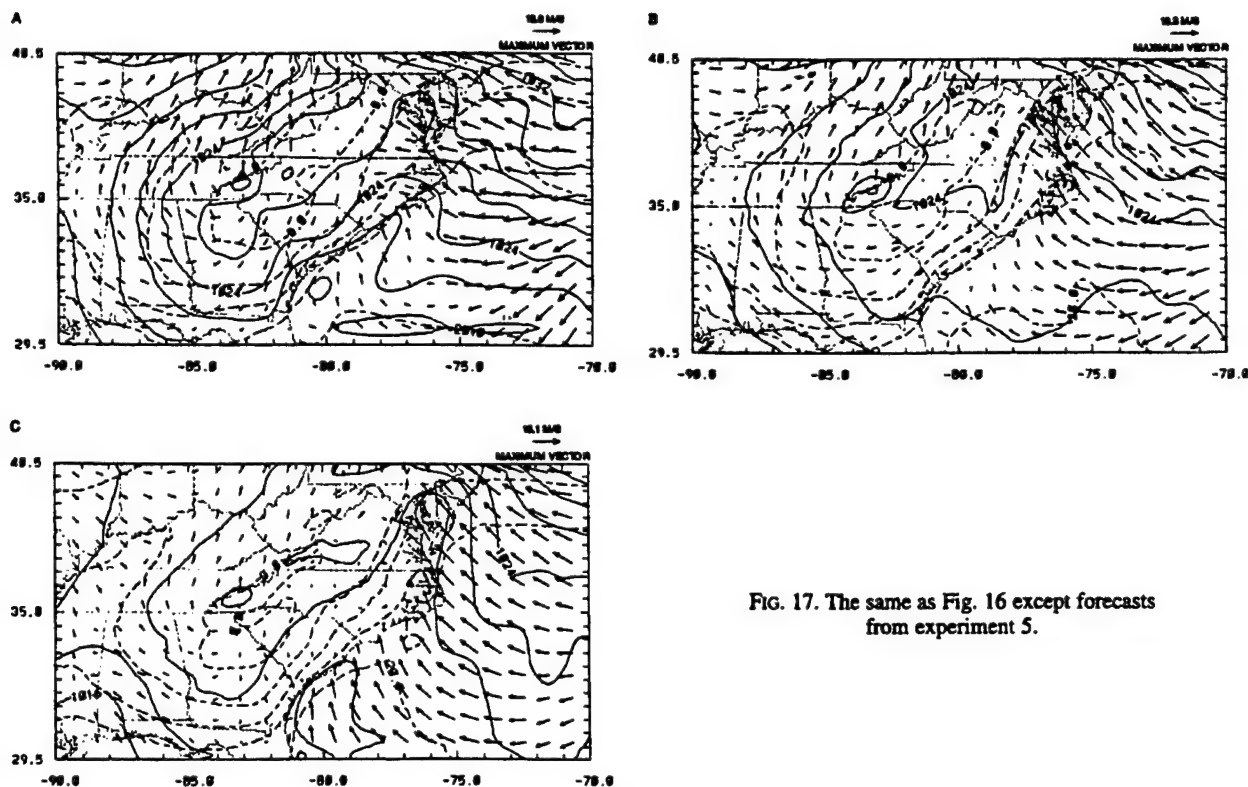


FIG. 17. The same as Fig. 16 except forecasts from experiment 5.

forecast. The inverted surface trough associated with the coastal front is more sharply defined by the experiment 5 forecast at 3 h (Fig. 17a). At 6 h (1800 UTC) the definition of the coastal trough is close for both forecasts but the experiment 5 forecast (Fig. 17b) positions the trough slightly further inland, which compares favorably to DW analysis (see DW Fig. 5d). Although not perfectly accurate in the position, the temperature pattern in Fig. 17b for the experiment 5 forecast indicates the existence of a wave along the front in North Carolina. By 12 h, the advantage of having assimilated the surface data every 3 h is less noticeable.

Comparison of surface data analysis with and without PAMS data (not shown) revealed that the high spatial density PAMS data had little effect. This occurred because the PAMS data density (50 km) is approximately the same as the surface data analysis grid. As detailed by Koch et al. (1983), an ideal ratio between analysis grid and observational spacing is 0.3–0.5. Although the analysis resolution could have been increased for the PAMS data, it would have required that the model's inner grid resolution be also increased to provide sufficient resolution for the background field. This would have caused problems regarding the hydrostatic assumption and some of the model's physical parameterizations. The effect of the frequent data assimilation on the model's coarser ( $\Delta x \approx 50$  km) intermediate grid can be seen in Fig. 18, which contains 6-h

forecasts valid at 1800 UTC 25 January from experiments 3 and 5. Over North America, the forecasts are practically identical, with differences of contour line positions of only a grid point or so. The surface data analysis is most likely identifying features that are too small to be resolved by the intermediate grid. This probably is exacerbated by the presence of a horizontal diffuser in the model.

## 5. Conclusions

A system for intermittent assimilation of synoptic surface observations using a mesoscale model has been presented. After making adjustments to the observations to account for model and observation height differences, an objective analysis step on the model's lowest sigma layer is carried out. Once the bottom model layer is updated, the deviations from the model background field at that level are blended vertically within the boundary layer. The vertical distribution of the deviations is accomplished by a physically based PBL adjustment scheme that uses the model's values of eddy diffusivity that are nudged to reflect the updated values. In the case study presented here, the PBL adjustment scheme was shown to have a beneficial impact when combining upper-air and surface data in a 12-h assimilation update cycle. A 3-h surface data analysis and PBL adjustment assimilation cycle, coupled with upper-air data assimilated every 12 h, yielded better anal-

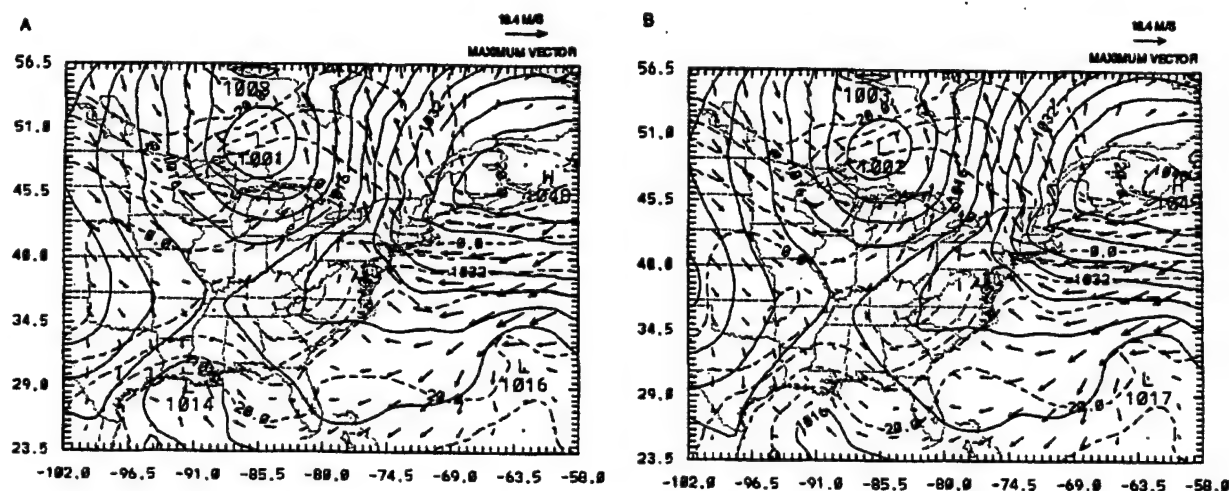


FIG. 18. Six-hour forecasts of sea level pressure (mb; contoured every 4 mb), lowest model layer temperature ( $^{\circ}\text{C}$ ; contoured every  $5^{\circ}\text{C}$ ) and wind vectors ( $\text{m s}^{-1}$ ) on  $1.5^{\circ}$  resolution intermediate model grid valid at 1800 UTC 25 January 1986 for (a) experiment 3 and (b) experiment 5.

yses and forecasts in the 3–12-h range compared to analyses and forecasts that used only 12-h assimilated upper-air and surface data. The impact of the frequent surface data assimilation dissipates for larger model grid spacing. The improvement in analyses and forecasts come about from better resolution of mesoscale features. Improved short-term forecasts can be achieved by continuing to assimilate surface data beyond the traditional synoptic cutoff times. The results suggest that as model resolution increases, the beneficial impact of including high-resolution data sources will increase. It is possible, given the results here that in an operational setting at a local forecast office, limitations imposed on the physics and resolution of a mesoscale model can be overcome through the use of the FDDA of asynoptic surface observations. Extrapolation of the results presented here would indicate that other two-dimensional data sources can be useful in FDDA as long as there is reasonable method for blending the data into the third dimension. Future improvements to the technique will involve increasing the sophistication of the PBL adjustment procedure by using the temporal evolution of the PBL during background forecast period and updating.

**Acknowledgments.** Computer time for this work was provided by the Naval Research Laboratory Central Computer Facility. The authors thank Donald A. Chisholm, Samuel Y. K. Yee, and George D. Modica for their helpful suggestions on improving this manuscript.

#### REFERENCES

- Arakawa, A., and V. R. Lamb, 1977: Computational design of the basic dynamical processes of the UCLA general circulation model. *General Circulation Models of the Atmosphere*, J. Chang, Ed., *Methods in Computational Physics*, Vol. 17, Academic Press, 173–265.
- Ballentine, R. J., 1980: A numerical investigation of New England coastal frontogenesis. *Mon. Wea. Rev.*, **108**, 1479–1497.
- Barwell, B. R., and A. C. Lorenc, 1985: A study of the impact of aircraft wind observations on a large-scale analysis and numerical weather prediction system. *Quart. J. Roy. Meteor. Soc.*, **111**, 103–129.
- Bell, G. D., and L. F. Bosart, 1988: Appalachian cold-air damming. *Mon. Wea. Rev.*, **116**, 137–161.
- Benjamin, S. G., 1989: An isentropic meso- $\alpha$ -scale analysis system and its sensitivity to aircraft and surface observations. *Mon. Wea. Rev.*, **117**, 1586–1603.
- , and P. A. Miller, 1990: An alternative sea level pressure reduction and a statistical comparison of geostrophic wind estimates with observed surface winds. *Mon. Wea. Rev.*, **118**, 2099–2116.
- , K. A. Brewster, R. L. Brümmer, B. R. Jewett, T. W. Schlatter, T. L. Smith, and P. A. Stamus, 1991: An isentropic three-hourly assimilation system using ACARS aircraft observations. *Mon. Wea. Rev.*, **119**, 888–906.
- , K. J. Brundage, P. A. Miller, T. L. Smith, G. A. Grell, D. Kim, J. A. Brown, and T. A. Schlatter, 1994: The rapid update cycle at NMC. Preprints, *10th Conf. on Numerical Weather Prediction*, Portland, OR, Amer. Meteor. Soc., 566–568.
- Blackadar, A. K., 1979: High resolution models of the planetary boundary layer. *Advances in Environmental Science and Engineering*, Vol. 1, J. R. Pfallin and E. N. Ziegler, Eds. Gordon and Breach, 50–85.
- Bosart, L. F., C. J. Vaude, and J. H. Helsdon Jr., 1972: Coastal frontogenesis. *J. Appl. Meteor.*, **11**, 1236–1258.
- Bourke, W., and J. L. McGregor, 1983: A nonlinear vertical mode initialization scheme for a limited area prediction model. *Mon. Wea. Rev.*, **111**, 2285–2297.
- Bratseth, A. M., 1986: Statistical interpolation by means of successive corrections. *Tellus*, **38A**, 439–447.
- Charney, J., M. Halem, and R. Jastrow, 1969: Use of incomplete historical data to infer the present state of the atmosphere. *J. Atmos. Sci.*, **26**, 1160–1163.
- Cotton, W. R., G. Thompson, and P. W. Mielke Jr., 1994: Real-time mesoscale predictions on workstations. *Bull. Amer. Meteor. Soc.*, **75**, 349–362.
- Daley, R., 1991: *Atmospheric Data Analysis*. Cambridge University Press, 457 pp.
- Davies, H. C., 1976: A lateral boundary formulation for multi-level prediction models. *Quart. J. Roy. Meteor. Soc.*, **102**, 408–418.



- Detering, H. W., and D. Etling, 1985: Application of the E- $\epsilon$  turbulence model to the atmospheric boundary layer. *Bound.-Layer Meteor.*, **33**, 113–133.
- DiMego, G. J., 1988: The National Meteorological Center regional analysis system. *Mon. Wea. Rev.*, **116**, 977–1000.
- , K. E. Mitchell, R. A. Petersen, J. E. Hoke, and J. P. Gerrity, 1992: Changes to NMC's Regional Analysis and Forecast System. *Wea. Forecasting*, **7**, 185–197.
- Doyle, J. D., and Warner, T. T., 1990: Mesoscale coastal processes during GALE IOP 2. *Mon. Wea. Rev.*, **118**, 283–308.
- , and —, 1993a: A numerical investigation of coastal frontogenesis and mesoscale cyclogenesis during GALE IOP 2. *Mon. Wea. Rev.*, **121**, 1048–1077.
- , and —, 1993b: Nonhydrostatic simulations of coastal mesoscale vortices and frontogenesis. *Mon. Wea. Rev.*, **121**, 3371–3392.
- Friday, E. W., Jr., 1994: The modernization and associated restructuring of the National Weather Service: An overview. *Bull. Amer. Meteor. Soc.*, **75**, 43–52.
- Harms, D. E., S. Raman, and R. V. Madala, 1992a: An examination of four-dimensional data-assimilation techniques for numerical weather prediction. *Bull. Amer. Meteor. Soc.*, **73**, 425–440.
- , K. D. Sashegyi, R. V. Madala, and S. Raman, 1992b: Four dimensional data assimilation of GALE data using a multivariate analysis scheme and mesoscale model with diabatic initialization. NRL Memo. Rep. 7147, Naval Research Laboratory, Washington D.C., 219 pp. [NTIS A256063.]
- Harshvardhan, R. Davies, D. Randall, and T. Corsetti, 1987: A fast radiation parameterization for atmospheric circulation models. *J. Geophys. Res.*, **92**, 1009–1015.
- Hodur, R. M., 1987: Evaluation of a regional model with an update cycle. *Mon. Wea. Rev.*, **115**, 2707–2718.
- Kanamitsu, M., 1989: Description of the NMC Global Data Assimilation and Forecast System. *Wea. Forecasting*, **4**, 335–342.
- Koch, S. E., M. Desjardins, and P. J. Kocin, 1983: An interactive Barnes objective map analysis scheme for use with satellite and conventional data. *J. Climate Appl. Meteor.*, **22**, 1487–1503.
- Kuo, H.-L., 1974: Further studies of the influence of cumulus convection on large scale flow. *J. Atmos. Sci.*, **31**, 1232–1240.
- Liou, C.-S., C. H. Walsh, S. M. Heikkinen, and R. L. Elsberry, 1990: Numerical studies of cyclogenesis events during the second intensive observation period (IOP-2) of GALE. *Mon. Wea. Rev.*, **118**, 218–233.
- , R. M. Hodur, and R. H. Langland, 1994: Navy Operational Atmospheric Prediction System (NORAPS): A triple nested mesoscale model. Preprints, *10th Conf. on Numerical Weather Prediction*, Portland, OR, Amer. Meteor. Soc., 423–425.
- Louis, J. F., 1979: A parametric model of vertical eddy fluxes in the atmosphere. *Bound.-Layer Meteor.*, **17**, 187–202.
- Madala, R. V., 1981: Efficient time integration schemes for atmosphere and ocean models. *Finite Difference Techniques for Vectorized Fluid Dynamic Calculations*, D. L. Book, Ed., Springer Verlag, 56–74.
- , S. W. Chang, U. C. Mohanty, S. C. Madan, R. K. Paliwal, V. B. Sarin, T. Holt, and S. Raman, 1987: Description of the Naval Research Laboratory limited area dynamical weather prediction model. NRL Memo. Rep. 5992, Naval Research Laboratory, Washington, D.C., 132 pp. [NTIS A182780.]
- Manabe, S., J. Smagorinsky, and R. F. Strickler, 1965: Simulated climatology of a general circulation model with a hydrologic cycle. *Mon. Wea. Rev.*, **93**, 769–798.
- Manobianco, J., L. W. Uccellini, K. F. Brill, and P. J. Kocin, 1991: Contrasting the impact of dynamic data assimilation on the numerical simulations of cyclogenesis during GALE IOP 10 and IOP 1. *Meteor. Atmos. Phys.*, **45**, 41–63.
- Marks, F. D., Jr., and P. M. Austin, 1979: Effects of the New England coastal front on the distribution of precipitation. *Mon. Wea. Rev.*, **107**, 53–67.
- McGinley, J. A., S. C. Albers, and P. A. Stamius, 1991: Validation of a composite convective index defined by a real-time local analysis system. *Wea. Forecasting*, **6**, 337–356.
- Miller, P. A., and S. G. Benjamin, 1992: A system for the hourly assimilation of surface observations in mountainous and flat terrain. *Mon. Wea. Rev.*, **120**, 2342–2359.
- Perkey, D. J., and C. W. Kreitzberg, 1976: A time-dependent lateral boundary scheme for limited-area primitive equation models. *Mon. Wea. Rev.*, **104**, 1513–1526.
- Riordan, A. J., 1990: Examination of the mesoscale features of the GALE coastal front of 24–25 January 1986. *Mon. Wea. Rev.*, **118**, 258–282.
- Robert, A. J., 1966: The investigation of a low order spectral form of the primitive meteorological equations. *J. Meteor. Soc. Japan*, Ser. 2, **44**, 237–245.
- Sashegyi, K. D., and R. V. Madala, 1993: Application of vertical-mode initialization to a limited-area model in flux form. *Mon. Wea. Rev.*, **121**, 207–220.
- , D. E. Harms, R. V. Madala, and S. Raman, 1993: Application of the Bratseth scheme for the analysis of GALE data using a mesoscale model. *Mon. Wea. Rev.*, **121**, 2331–2350.
- , R. V. Madala, D. E. Harms, and S. Raman, 1994: A numerical weather prediction system for regional and mesoscale forecasting on a high performance workstation. Preprints, *10th Conf. on Numerical Weather Prediction*, Portland, OR, Amer. Meteor. Soc., 363–365.
- Snook, J. S., J. M. Gram, and J. M. Schmidt, 1994: The "P" in LAPS: A local scale operational forecast system. Preprints, *10th Conf. on Numerical Weather Prediction*, Portland, OR, Amer. Meteor. Soc., 454–456.
- Stauffer, D. R., and N. L. Seaman, 1990: Use of four-dimensional data assimilation in a limited-area mesoscale model. Part I: Experiments with synoptic-scale data. *Mon. Wea. Rev.*, **118**, 1250–1277.
- Stull, R. B., 1988: *An Introduction to Boundary Layer Meteorology*. Kluwer Academic Publishers, 666 pp.
- Tiedtke, M., W. A. Heckley, and J. Slingo, 1988: Tropical forecasting at ECMWF: The influence of physical parameterization on the mean structure of forecasts and analysis. *Quart. J. Roy. Meteor. Soc.*, **114**, 639–664.
- Uccellini, L. W., R. A. Peterson, K. F. Brill, P. J. Kocin, and J. J. Tuccillo, 1987: Synergistic interactions between an upper-level jet streak and diabatic processes that influence the development of a low level jet and a secondary coastal cyclone. *Mon. Wea. Rev.*, **115**, 2227–2261.
- Walko, R. L., C. J. Tremback, and W. R. Cotton, 1989: Assimilation of Doppler radar wind data into a numerical prediction model: A demonstration of certain hazards. Preprints, *24th Conf. on Radar Meteor.*, Tallahassee, FL, Amer. Meteor. Soc., 248–250.
- Warner, T. T., and N. L. Seaman, 1990: A real-time mesoscale numerical weather-prediction system for research, teaching, and public service at Pennsylvania State University. *Bull. Amer. Meteor. Soc.*, **71**, 792–805.
- Yee, S. Y. K., and A. J. Jackson, 1988: Blending of surface and rawinsonde data in mesoscale objective analysis. AFGL Tech. Rep. 88-0144, Air Force Geophysics Laboratory, Hanscom AFB, Massachusetts, 31 pp. [NTIS ADA203984.]

## **Appendix G**

### **Monsoon Rainfall Simulations with the Kuo and Betts-Miller Schemes**

<sup>1</sup> Department of Marine, Earth and Atmospheric Sciences, North Carolina State University, North Carolina, U.S.A.

<sup>2</sup> Naval Research Laboratory, Washington, U.S.A.

<sup>3</sup> Centre for Atmospheric Sciences, Indian Institute of Technology, New Delhi, India

## Monsoon Rainfall Simulations with the Kuo and Betts–Miller Schemes

K. Alapathy<sup>1</sup>, S. Raman<sup>1</sup>, R. V. Madala<sup>2</sup>, and U. C. Mohanty<sup>3</sup>

With 14 Figures

Received March 23, 1993

Revised June 23, 1993

### Summary

Two numerical experiments are performed using a nested grid regional model to study the performance of the Kuo and the Betts–Miller cumulus parameterization schemes in simulating the rainfall during an active monsoon period. Results indicate that the monsoon circulation features, such as the Somali jet and monsoon depression are better simulated with the Kuo scheme. With the Kuo scheme, predicted intensity and associated rainfall of the monsoon depression are in good agreement with the observations. Uncertainty in the adjustment parameters in the Betts–Miller scheme appears to have led to the poor prediction of rainfall. Also, the Betts–Miller scheme showed considerable sensitivity to the convergence in the lower troposphere in the initial conditions over the Arabian Sea, leading to a prediction of a spurious intense tropical cyclone. This cyclone replaced the normal heat-low over the desert region. Rainfall distribution and its maximum along the west coast of India were predicted better with the Kuo scheme. Area-averaged convective heating rates indicated that the cumulus convection is deeper and more intense with the Kuo scheme. Also, area averaged evaporation rates far exceeded the rainfall rates with the Betts–Miller scheme while with the Kuo scheme these rates are in balance after the spinup period. Forecast errors in the zonally averaged specific humidities indicate that the model atmosphere is more humid with the Betts–Miller scheme.

### 1. Introduction

During the southwest monsoon season (June to September), Indian subcontinent and surrounding regions receive heavy rainfall. Monsoon depressions form over the Bay of Bengal as low

pressure centers, develop into storms and some times into severe cyclonic storms giving rise to heavy rainfall over India. Also, west coast of India is one of the areas where heavy rainfall rates are observed very frequently. Lower level westerlies approach the Western Ghats almost at right angles after traveling thousands of kilometers over the warm Indian Ocean and the Arabian Sea giving rise to large rainfall rates. These mountains are located about 50 km inland, parallel to the west coast of India. Orographic lifting of the humid monsoon westerlies causes heavy rainfall over this region.

Several two dimensional analytical and numerical studies (e.g., Smith and Lin, 1983; Grossman and Durran, 1984; Ogura and Yoshizaki, 1988) indicate that the sensible and latent heat fluxes from the surrounding oceans, vertical wind shear, and Western Ghats play important roles on the rainfall rates along the west coast of India. Even though these studies gave some insight into the physical processes involved, they cannot simulate the observed spatial and temporal variation of rainfall. In order to simulate the observed rainfall rates more realistically, one needs a nonlinear three dimensional model. Such a model should have proper representation of dynamics, thermodynamics, topography and relevant physics. Physical processes associated with the monsoon

circulations should be realistically represented to simulate the observed spatial and temporal distribution of the rainfall. In addition, the model domain must be sufficiently large to simulate the synoptic-scale circulations.

Largescale and mesoscale weather prediction models use parameterization schemes to represent sub-grid scale cumulus convection processes. Detailed physical processes that occur during life cycle of convective clouds are side-stepped and hence only bulk effects are considered in cumulus parameterizations such as the Kuo scheme (Kuo 1965, 1974), Betts–Miller scheme (Betts, 1986), and other schemes. Perhaps, the most widely used cumulus convection scheme in several research and operational models is the Kuo scheme, because of its simplicity and dependency on the largescale dynamics. Also, over the past two decades choices of different values for moistening parameter ( $b$ ) were widely studied (e.g., Anthes, 1977; Geleyn, 1985; Molinari, 1983; Das et al., 1988). In the context of long-range weather prediction, it was noticed that the choice of small (almost equal to zero) moistening parameter can cause unrealistic drying of the atmosphere.

Based on observations, a new convective adjustment scheme was proposed by Betts (1986). The deep convection in this scheme is similar to the other moist convective adjustment schemes except that it uses observed quasi-equilibrium thermodynamic profile as a reference state rather than a moist adiabat. Baik et al. (1990a, 1990b) showed that the Betts–Miller scheme can simulate different stages of an idealized tropical cyclone starting from a weak initial vortex. Their results indicated that the simulated idealized tropical cyclone is sensitive to the saturation pressure departure parameter. Junker and Hoke (1990) compared performances of the 1965 Kuo scheme and the Betts–Miller scheme in predicting rainfall during winter season over the southern United States with the National Meteorological Center (NMC) nested grid model. Though the Betts–Miller scheme gave favorable precipitation scores, it showed a tendency for the mid-latitude cyclones to over-deepen. Puri and Miller (1990) studied the sensitivity of the cumulus parameterization schemes to the structure of four tropical cyclones observed during the Australian Monsoon Experiment (AMEX). Their results showed better vertical consistency of atmospheric structures with the

Betts–Miller scheme than with the Kuo scheme. Both the analyses and forecasts showed considerable sensitivity to the Betts–Miller scheme by generating more intense cyclonic systems as compared to the Kuo scheme.

The Betts–Miller scheme has been used in the past either to simulate observed tropical or mid-latitude cyclones with a coarse horizontal resolutions ( $> 80$  km). The performance of the Betts–Miller scheme has not been studied for the monsoon region. This paper compares the performance of the Kuo and the Betts–Miller schemes in simulating monsoon rainfall and associated circulations using a three dimensional limited area nested grid model.

## 2. The Model

The Naval Research Laboratory and North Carolina State University (NRL/NCSU) nested grid model is used in the present study. It is a primitive equation model written in  $\sigma$ -coordinate system having a one-way interacting nested grid network. The  $\sigma$ -coordinate is defined by  $\sigma = p/p_s$ , where  $p$  is the level pressure and  $p_s$  the surface pressure. For further model details, readers are referred to Madala et al. (1987). Various physical processes that are included in the model are discussed below.

### 2.1 Physical Processes

The model physics includes latent heat, sensible heat, and momentum exchange between the atmospheric boundary layer and the underlying surface using the surface layer similarity theory (Businger et al., 1971), grid-scale precipitation, dry convection, and diffusion processes. Moist convective parameterization schemes used in the model are described in the next subsection. The short and long wave radiative processes are not included in the present model. A second-order diffusion for momentum on  $\sigma$ -surfaces and for heat and water vapor on  $p$ -surfaces is used to account for the cascading of energy into unresolved subgrid-scale waves. If super-saturation exists at any level, the excess moisture is assumed to condense and fall out to the next lower layer and evaporate or continue to fall depending upon the degree of the saturation at that level. The model has a dry convective adjustment procedure to remove dry

convective instability that can occur during model integration.

## 2.2 Cumulus Parameterization Schemes

Two cumulus convection parameterization schemes are used in the model simulations. In the first simulation, the Kuo scheme is used. The moistening parameter  $b$  is calculated according to the method suggested by Anthes (1977) and is given by

$$b = [1 - \langle RH_g \rangle]^n, \quad (1)$$

where  $\langle RH_g \rangle$  is the mean environmental relative humidity. We have used  $n = 3$  for the moisture partitioning in the Eq. 1 consistent with the study on the convective heating rates over the monsoon region (Das et al., 1988). The Betts-Miller convective adjustment scheme assumes that in the presence of cumulus convection the local thermodynamic structures are constrained by the convection and adjusted towards observed quasi-equilibrium thermodynamic state. The Betts-Miller scheme contains shallow convection as well as deep convection. However, since the Kuo scheme deals with the deep convection, only the deep convection part of the Betts-Miller scheme is used for the comparative purpose. Adjustment parameters used in the Betts-Miller scheme are same as those used by Puri and Miller (1990) and Baik et al. (1990a). For further details, reader is referred to Betts (1986) and Baik et al. (1990a).

## 2.3 Numerical Method and Nesting Technique

The time integration scheme utilized in the present model is a split-explicit method which allows a larger time step by effectively separating various terms in the prognostic equations into parts governing slow-moving Rossby modes and fast-moving gravity modes. For the first and second fast-moving gravity modes smaller time step is used and for all other modes a larger time step is used. The implementation of these varying time steps is the basis for the split-explicit method. The time steps for the slow moving modes in the coarse-grid and the fine-grid domains are 300s and 100s, respectively, and appropriate smaller time steps satisfying CFL criterion are used for the fast-moving modes. For the horizontal differencing, a staggered grid network (Arakawa C-grid) is used with  $p_s$ ,  $q$ ,  $T$ ,  $\phi$ ,  $\sigma$  specified at the same horizontal points, and  $u$  and  $v$  interlaced between them where

$p_s$  is the surface pressure,  $q$  the specific humidity,  $T$  the temperature,  $\phi$  the geopotential,  $\sigma$  the vertical velocity,  $u$  the zonal wind velocity, and  $v$  is the meridional wind velocity. The finite difference technique used in the model is second-order accurate. It conserves total energy, mass, and momentum in the absence of the heat and momentum sources. In the model, the fine-grid mesh (FGM) overlaps one-third of the coarse-grid mesh (CGM) and the FGM is nested into the CGM such that every third grid point in the FGM is collocated with that in the CGM. The nested grid is positioned so that its boundary rows and columns overlap the CGM interior rows and columns. This nesting configuration enables the Fine-Grid Mesh domain boundary values to be specified by the Coarse-Grid Mesh interior grid points.

## 2.4 Data and Simulation Domain

Initial conditions are obtained from the European Center for Medium Range Weather Forecasts (ECMWF) analysis. Analyzed data are at  $1.875^\circ \times 1.875^\circ$  resolution at 14 vertical levels. Horizontal grid resolutions in the CGM and the FGM domains are  $1.5^\circ$  and  $0.5^\circ$ , respectively, and the vertical grid resolution in  $\sigma$ -coordinate is 0.1. Simulation domain is shown in the Fig. 1 and the CGM domain covers from  $37.5^\circ$  E to  $112.5^\circ$  E and

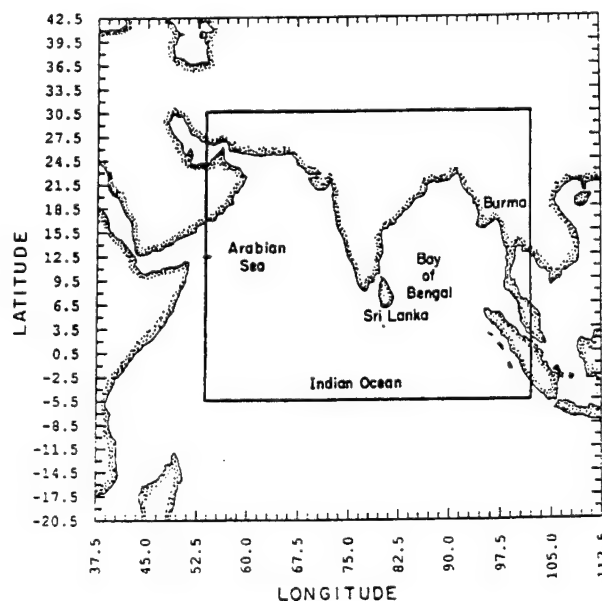


Fig. 1. The model domain of numerical simulation in the Coarse-Grid Mesh (CGM) and the Fine-Grid Mesh (FGM)

20.5°S to 42.5°N and the FGM domain from 54°E to 102°E and 5.5°S to 30.5°N. Model topography was obtained from the navy 10' global topography data for 1.5° and 0.5° horizontal resolutions. Model sea surface temperatures (SST) were obtained from the 1° resolution global climatological values based on a 10 year average for the month of July. Davies scheme (1976, 1983) is employed to provide lateral boundary conditions using ECMWF analysis in the present version of the model. At the model top and bottom, the boundary for  $\sigma$  is zero.

### 2.5 Numerical Experiments

Two numerical simulations are performed for 48 hours starting at 12 UTC 16 July 1988. In the first experiment model simulations are performed with the Kuo scheme and in the second experiment with the Betts-Miller scheme. Coastline in both the CGM and the FGM domains are determined by the model topography data. Dark solid contours with bold zeros in all plots represent the model coastline.

### 2.6 Synoptic Conditions

Monsoon trough is one of the low-level features associated with the monsoon circulations. The orientation and its geographical location changes with the advancement of the monsoon. During the active monsoon period the monsoon trough

has a northwest to southwest orientation with the western end located over northwest Rajasthan and the eastern end over the head Bay of Bengal. During such active monsoon periods, low pressure centers often develop over the bay of Bengal. These low pressure centers develop into monsoon depressions and some of these intensify into tropical cyclones giving rise to heavy rainfall over many parts of India. Due to the orographic lifting and associated convection, heavy rain occurs along the west coast of India. Also, the presence of a monsoon depression over Bay of Bengal can strengthen wind flow along the west coast of India leading to larger rainfall rates over this region.

Monsoon was active during the simulation period (12 UTC 16 July to 12 UTC 18 July) and large rainfall rates were observed. A monsoon depression was present over the Bay of Bengal close to the east coast of India. Analyzed streamline distribution and horizontal winds for the 850 hPa at 12 UTC 16 July 1988 (initial conditions) are shown in Fig. 2. Cyclonic circulation over the Bay of Bengal close to the east coast of India indicate the location of the monsoon depression. This depression moved northwest and made landfall during the next 24 h and later it moved further inland and was located over northeast India at 12 UTC 18 July. Large rainfall rates were reported over northeast India resulting from this monsoon depression. Along the west coast of India and offshore large rainfall rates are also observed. The low-level Somali Jet, also referred as to east

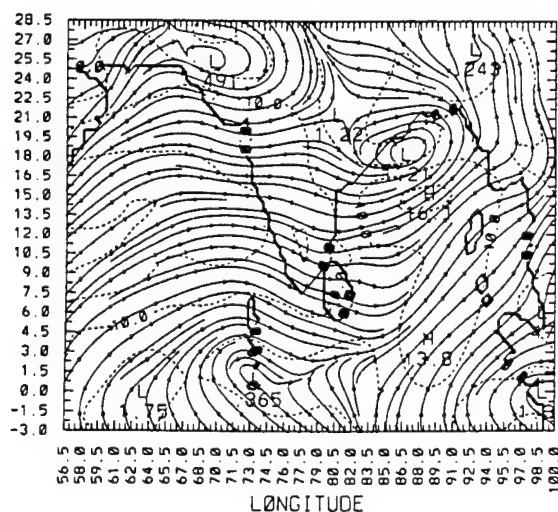


Fig. 2. Analyzed horizontal streamline and wind distribution at  $\sigma = 0.85$  at 12 UTC 16 July 1988 (initial conditions). Contour interval is  $5 \text{ m s}^{-1}$

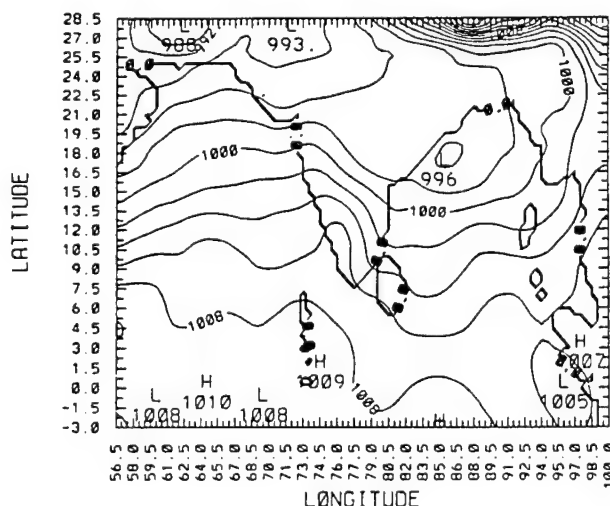


Fig. 3. Analyzed mean sea level pressure at 12 UTC 16 July 1988 (initial conditions). Contour interval is 2 hPa



African Jet, off the east coast of Africa is situated at a height of about 1.5 km from the surface. Strong winds (broken lines are isotachs) over the east coast of Africa are associated with the Somali jet over this region. The interaction of Somali jet with the monsoon circulation and its impact on the monsoon dynamics is still not well understood. analyzed mean sea level pressure at 12 UTC 16 July 1988 is shown in Fig. 3. The low pressure center off the east coast is the monsoon depression. Low pressure center over northwest India is due to the strong heating over the desert regions and is called the heat-low.

### 3. Discussion of Results

Model predictions using the Kuo and the Betts-Miller scheme are referred to as the KUO and the BMS, respectively. In this section, results from the KUO and the BMS are compared with the observations. Results from the coarse-grid model and fine-grid model are referred to as the CGM and the FGM, respectively.

#### 3.1 Monsoon Circulation Features

At 12 UTC 16 July 1988 observed monsoon depression was located over the Bay of Bengal close to the east coast of India. During the next 24 h, monsoon depression made landfall and moved further inland in a northwesterly direction and at 12 UTC 18 July 1988 it was located over central India. Analyzed mean sea level pressure distribution for the FGM at 12 UTC 18 July 1988 is shown in Fig. 4a. Low pressure center over the central India indicates the location of the monsoon depression. Mean sea level (MSL) pressure distribution for the FGM at 48 h of simulation (12 UTC 18 July 1988) in the KUO and the BMS is shown in Fig. 4b and 4c, respectively. In the KUO, predicted location of the monsoon depression is about 3° south of the observed location and the orientation of the monsoon trough is similar to that of the observations (Fig. 4a). In the BMS, predicted monsoon depression is about 2° north-east of the observed location. Predicted trough is also northwest of the observed location. Comparing the MSL pressure at the center of the analyzed monsoon depression with that in the model predictions, it can be seen that the KUO predicted same value (993 hPa) as observed while the BMS pre-

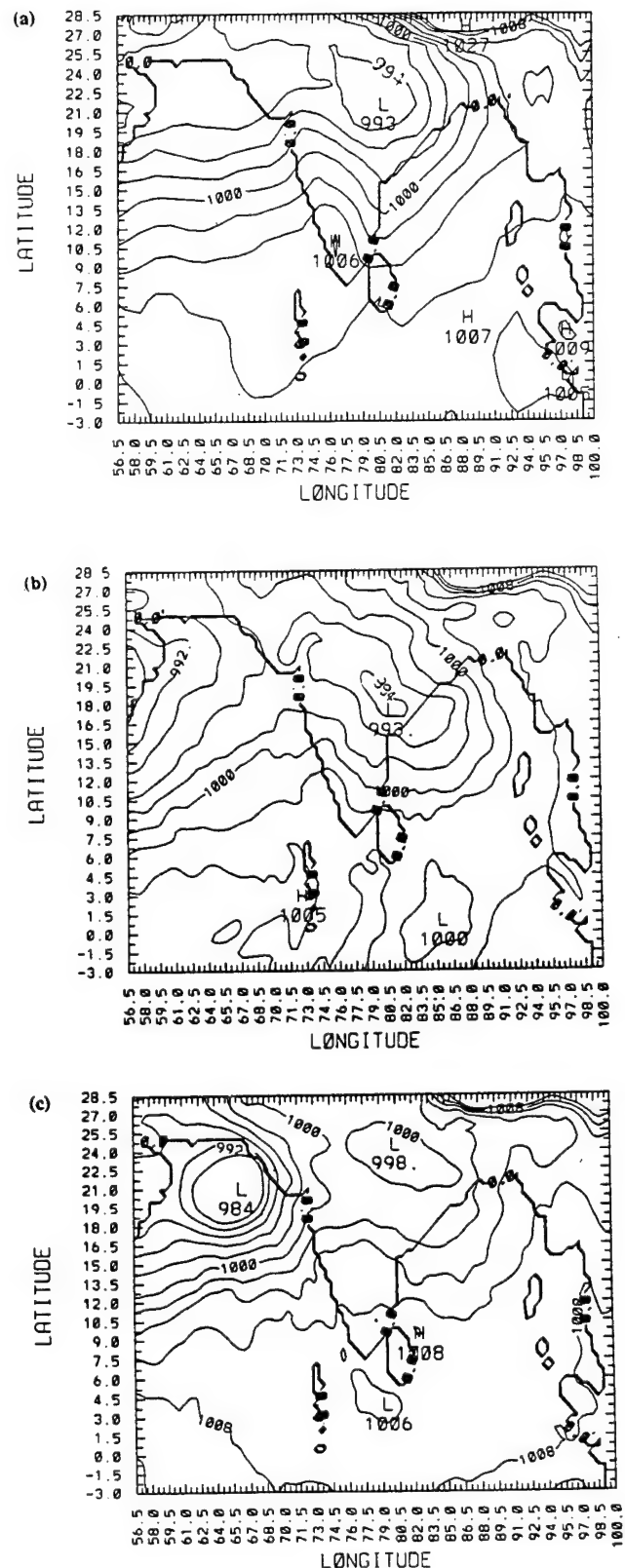


Fig. 4. Mean sea level pressure distribution for the FGM at 12 UTC 18 July 1988, from (a) analysis and from model predictions (b) in the KUO and (c) in the BMS. Contour interval is 2 hPa



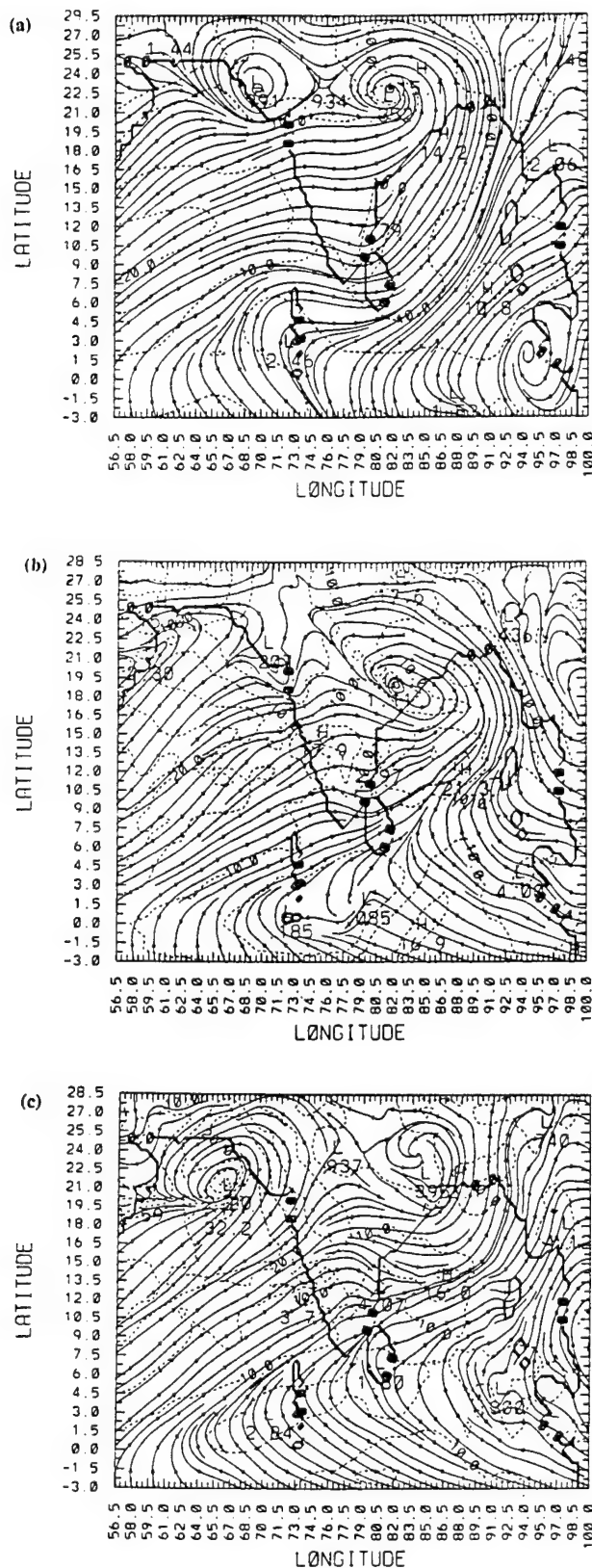


Fig. 5. Horizontal streamline and wind distribution at  $\sigma = 0.85$  for the FGM at 12 UTC 18 July from (a) the analysis and from model predictions (b) in the KUO and (c) in the BMS. Contour interval is  $5 \text{ m s}^{-1}$

dicted about 998 hPa. Thus, in the BMS, predicted monsoon depression is relatively weaker.

Mean sea level pressure distribution from the analysis (Fig. 4a) indicates that the heat-low is located over northwest India and the 994 hPa isoline indicates location of the heat-low ( $73^\circ \text{E}$ ,  $24^\circ \text{N}$ ). Consistently, analyzed flow patterns in the lower levels indicates convergence (Fig. 5a) with cyclonic circulations over this region. In the KUO, mean sea level pressure distribution over the Arabian Sea is somewhat similar to that in the observations. Predicted pressure over the heat-low region is about 996 hPa, close to the observed value. On the other hand, mean sea level pressure distribution in BMS show different pattern. A superious low pressure system with cyclonic circulations is predicted over northern Arabian Sea. As indicated by the central pressure (984 hPa), this system is much stronger than the monsoon depression. This spurious system is a direct result of migration of the predicted heat-low to the Arabian sea in the BMS. Initially, (at 12 UTC 16 July 1988), observed heat-low was located northwest of India and during the next 48 h it had moved south to a location close to the west coast of India ( $73^\circ \text{E}$ ,  $24^\circ \text{N}$ ). Convergence associated with this heat-low resulted in large evaporation and convective rainfall over this region (shown in a later section) leading to the intensification of the dislocated heat-low. As mentioned, predicted heat-low has become a spurious tropical cyclone, as indicated by its central pressure, winds and associated rainfall. This is further discussed in conjunction with the predicted rainfall in a later section.

Analyzed horizontal streamline distribution at about 850 hPa for the FGM at 12 UTC 18 July is shown in Fig. 5a. Broken lines represent isotachs. As discussed above, cyclonic circulations over the central and the northwest India are due to the presence of a monsoon depression and the heat-low, respectively. Corresponding predicted horizontal stream line patterns in the KUO and the BMS are shown in Fig. 5b and 5c, respectively. Streamline patterns in analyzed data and model predictions are consistent with the respective mean sea level pressure distributions over the regions of monsoon depressions and the heat-low. In the KUO, the heat-low as indicated by cyclonic circulations is located just south of the observed location but still over land, consistent with the

analyzed data. In the BMS, heat-low is absent over the land.

As mentioned earlier, analyzed wind data (isotachs) show the presence of Somali jet, indicated by strong winds off the east coast of Africa (Fig. 5a). Predicted wind distributions in the KUO (Fig. 5b) and in the BMS (Fig. 5c) also show the presence of Somali jet over this region. In the BMS, prediction of spurious low pressure system over the Arabian Sea resulted in stronger winds, particularly over the southwest sector of the system. This is due to the fact that the flow direction south of this spurious low pressure system is in the same direction as the mean flow of the Somali jet. Spatial distribution of wind in the KUO and the BMS are somewhat comparable to that in the analyzed data in other regions. Results from the CGM predictions (not shown) are qualitatively similar to that in the FGM predictions except that the winds are relatively weaker. This is obviously due to the coarser horizontal resolution of the CGM.

In order to compare the predicted wind field of the entire monsoon region with the observations, the CGM model predictions are considered since it covers a larger domain. Latitude-height section of the observed zonally averaged zonal winds for the CGM at 12 UTC 18 July is shown in Fig. 6a. Low level wind maximum between  $6.5^\circ$  and  $18.5^\circ$  N indicates the observed location of the Somali jet. Usually this jet is located at about 1.5 km from

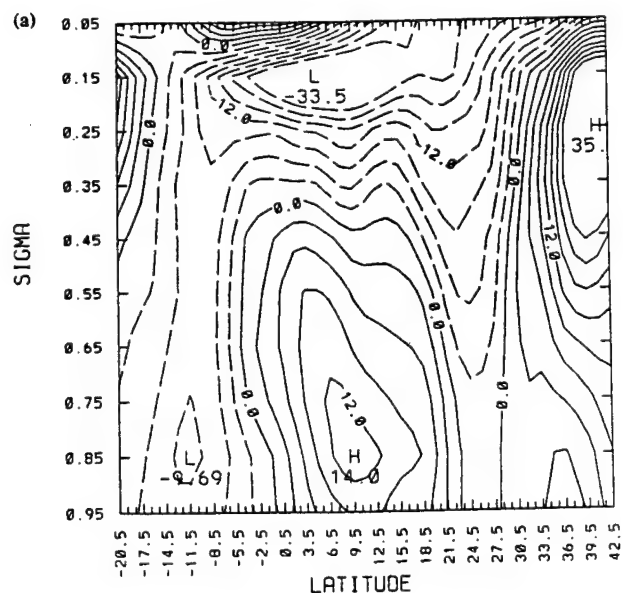


Fig. 6. (Continued)

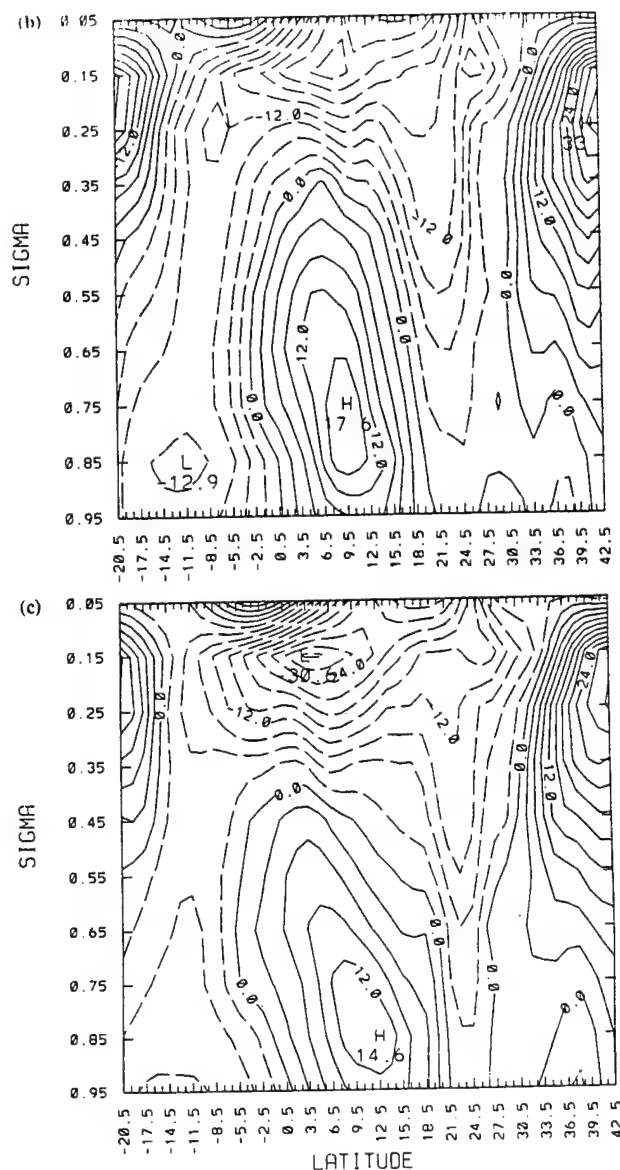


Fig. 6. Latitude-height section of zonally averaged zonal winds for the CGM at 12 UTC 18 July from (a) the analysis, and from the model predictions (b) in the KUO and (c) in the BMS. Contour interval is  $3 \text{ m s}^{-1}$ .

the surface over the Arabian Sea, as can be seen in Fig. 6a. Wind maximum at upper levels (at  $\sigma = 0.15$ ) is due to the presence of the Tropical Easterly Jet (TEJ). A strong vertical wind shear exists from the lower troposphere to the upper troposphere over this region. Wind maxima on the left and right side boundaries of Fig. 6a are due to the presence of subtropical westerly jets in the southern and the northern hemispheres, respectively. Corresponding latitudinally averaged zonal winds for the KUO and the BMS are shown

in Fig. 6b and 6c, respectively. In the KUO, predicted Somali jet is stronger than that in the BMS while the easterly jet is weaker in the KUO. Subtropical westerly jets over both the hemispheres are better simulated in the KUO while these jets are weaker in the BMS. In general, zonal winds are qualitatively similar in both the simulations.

Zonal average of analyzed meridional winds at 12 UTC 18 July for the CGM are shown in Fig. 7a. Meridional circulation north of equator indicates a reverse Hadley circulation with inflow at low levels and outflow at higher levels. During the summer monsoon season this kind of flow pattern is common over this region. Corresponding model predictions in the KUO and the BMS are shown in Fig. 7b and 7c, respectively. In both the forecasts, model predicts same intensity of the low level inflow up to a level of about 850 hPa. The upper level return flow (northerly component) is better simulated in the KUO although it is more intense than the observations. This indicates strong divergent flow at upper levels. The strong northerly flow in the upper levels is in conjunction with a strong southerly flow at lower levels. This in turn makes the westerly flow at lower levels somewhat weaker resulting in a weaker easterly jet.

### 3.2 Water Vapor Budget

Observations indicated that the monsoon was active during July 1988 with large rainfall rates

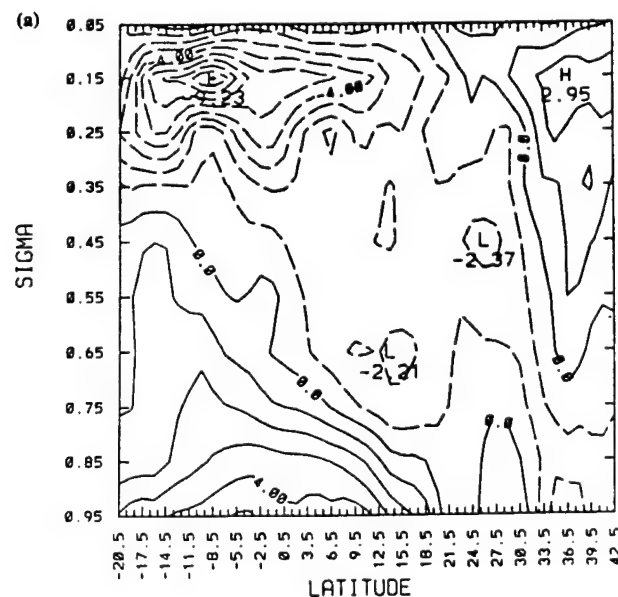


Fig. 7. (Continued)

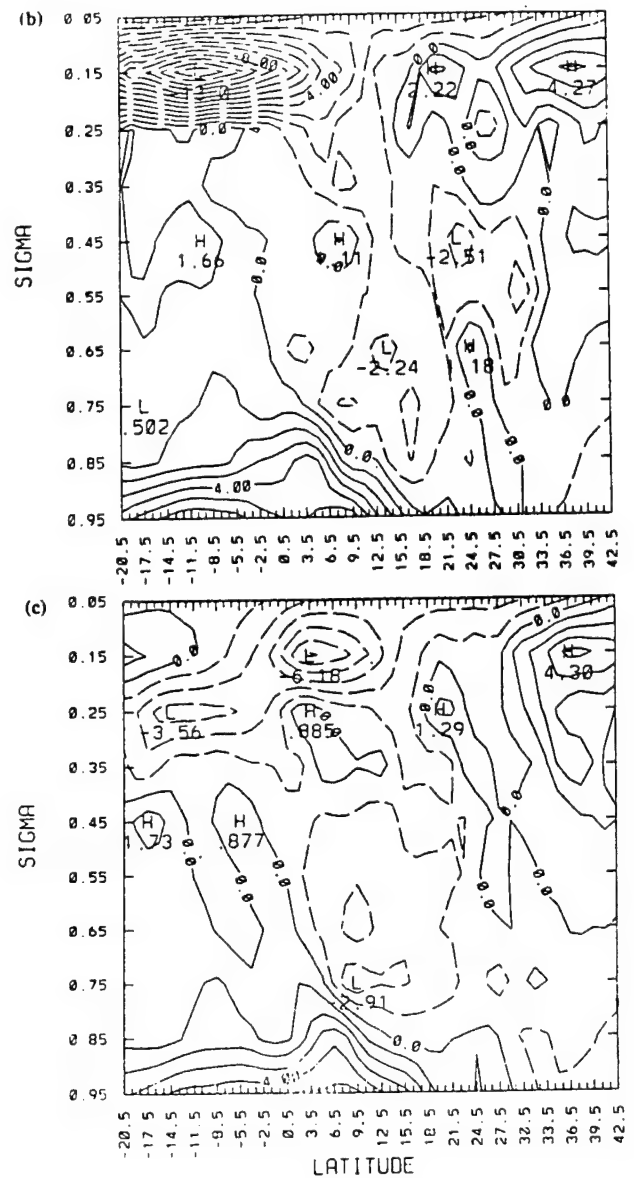


Fig. 7. Latitude-height section of zonally averaged meridional winds for the CGM at 12 UTC 18 July from (a) the analysis, and from the model predictions (b) in the KUO and (c) in the BMS. Contour interval is  $1 \text{ m s}^{-1}$

(about  $100$  to  $200 \text{ mm day}^{-1}$ ). Along the west coast of India observed rainfall is mainly due to the orographic-convective processes while over the central India it was due to the monsoon depression. During the period, 16 to 17 July 1988, the monsoon depression made landfall causing large rainfall rates of about  $100$  to  $160 \text{ mm day}^{-1}$  over central India (Fig. 8a). During the next 24 h, monsoon depression moved further northwest causing rainfall over this region (Fig. 8b). For these two days, observations (Fig. 8a and 8b) also

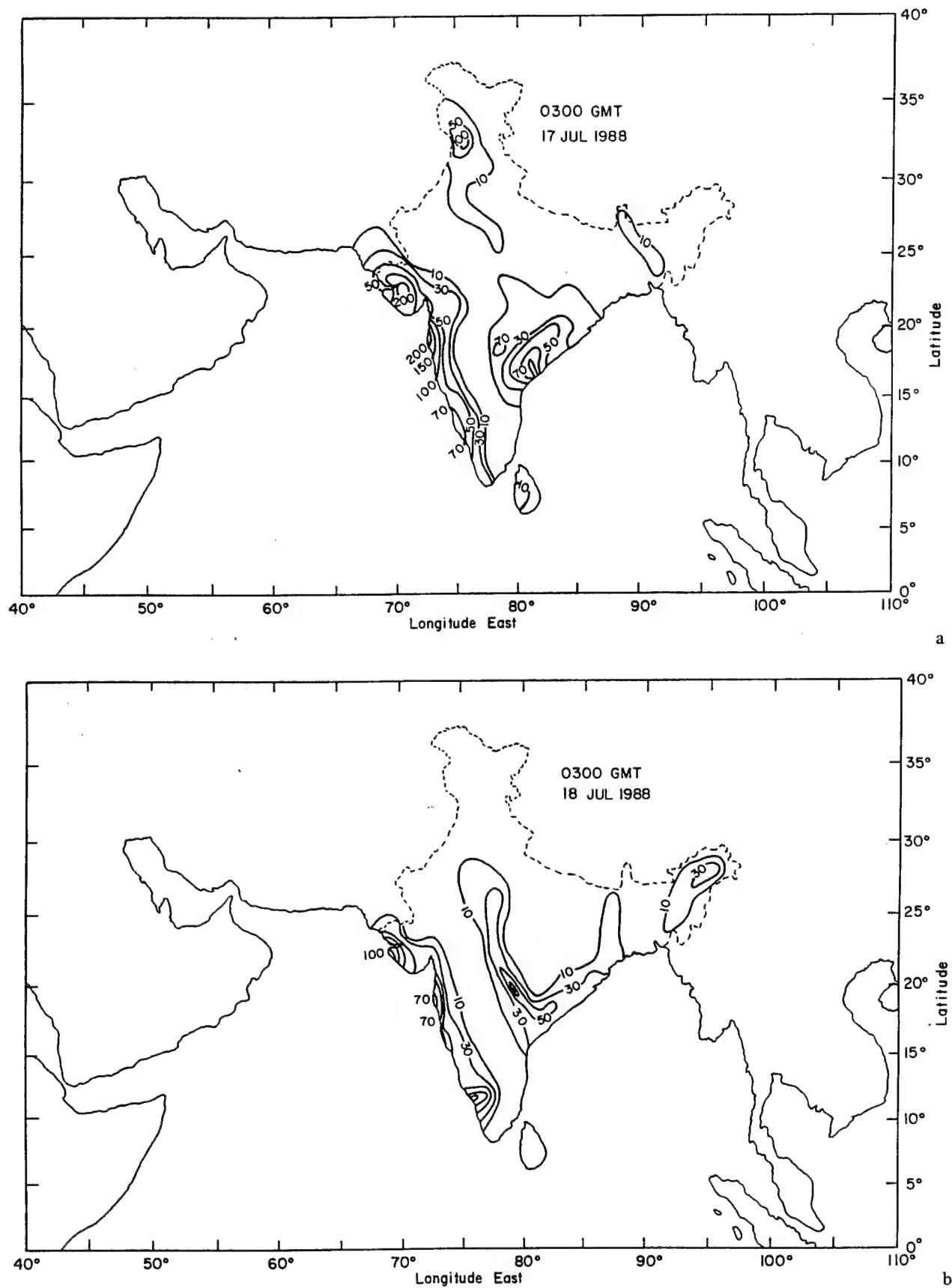


Fig. 8. Observed rainfall rates for a period of 24 hours (a) ending at 03 UTC 17 July 1988 and (b) 03 UTC 18 July 1988

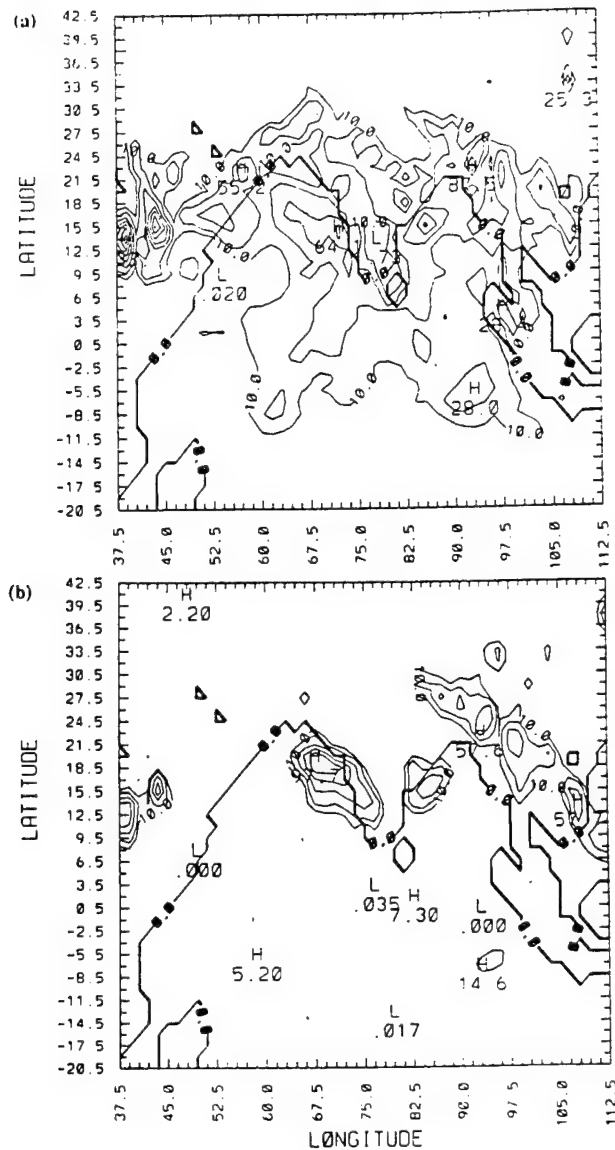


Fig. 9a, b. Predicted rainfall for the CGM domain for a period of 24 hours ending at 12 UTC 17 July 1988 in (a) the Kuo and the (b) BMS, respectively. Contour intervals are 10, 20, 50, 80, 100, 125  $\text{mm d}^{-1}$

indicated rainfall rates of about 100–200  $\text{mm day}^{-1}$  among the west coast of India. In general, there is an offshore extension of the rainfall over the Arabian sea (Ramakrishnan and Gopinatha Rao, 1958; Ramachandran, 1972). Krishnamurti et al. (1983) indicated that the location of the rainfall maximum during 1979 monsoon was just offshore. However, no observations are available offshore for this case study.

Predicted rainfall for the CGM ending at 12 UTC 17 July in the Kuo and the BMS are shown in Figs. 9a and 9b, respectively. In both the forecasts

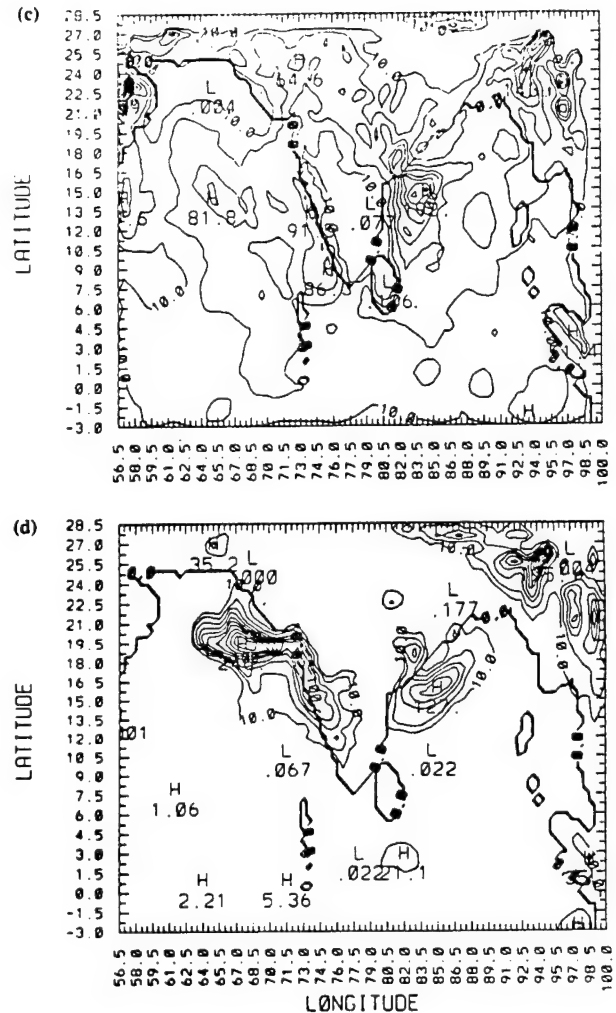


Fig. 9c, d. Predicted rainfall for the FGM domain for a period of 24 hours ending at 12 UTC 17 July 1988 in (c) the Kuo and the (d) BMS, respectively. Contour intervals are 10, 25, 50, 75, 100, 125  $\text{mm d}^{-1}$

model predicts more rainfall over the southwest sector of the monsoon depression. This is due to an increase in the low-level wind speed as the wind accelerated over the water and increased convergence caused by the movement of the depression relative to this low-level winds. Increase in low-level winds in the southwest sector of an offshore monsoon depression has been observed before (Rao, 1976). Spatial distribution of the rainfall over central India in the Kuo is also consistent with the observed rainfall over that region. In the BMS, rainfall is limited to a small coastal region with none over the central India. Rainfall associated with the orography along the west coast of India is predicted by both the Kuo and the BMS. In the Kuo, rainfall maximum is located just

offshore of the west coast of India consistent with the generally observed pattern while in the BMS it is located over northern Arabian Sea, in conjunction with the spurious low. About 10 to 40 mm day<sup>-1</sup> rainfall predicted over the Indian Ocean in the KUO. However, the BMS does not predict much rainfall over the Indian Ocean.

Predicted rainfall for the FGM ending at 12 UTC 17 July in the KUO and the BMS are shown in Figs. 9c and 9d, respectively. As expected, increased horizontal resolution in the FGM contributed to higher rainfall rates. Spatial distribution

of rainfall associated with the model predicted monsoon depression for the FGM in the KUO is similar to that of the CGM but with higher rates ( $\sim 192 \text{ mm day}^{-1}$ ). Predicted rainfall along the monsoon trough in the KUO is closer to the observations. In the BMS, rainfall maximum associated with the monsoon depression is only about  $127 \text{ mm day}^{-1}$ , less than that in the KUO. Also, in the BMS, predicted rainfall is confined to the east coast of India. Along the westcoast, about  $91 \text{ mm day}^{-1}$  rainfall was predicted in the KUO with maximum located just offshore. In the BMS, on the other hand, rainfall is predicted on the lee side of the Western Ghats as well as along the coast. However, largest rainfall rates ( $246 \text{ mm day}^{-1}$ ) are predicted over the northern Arabian

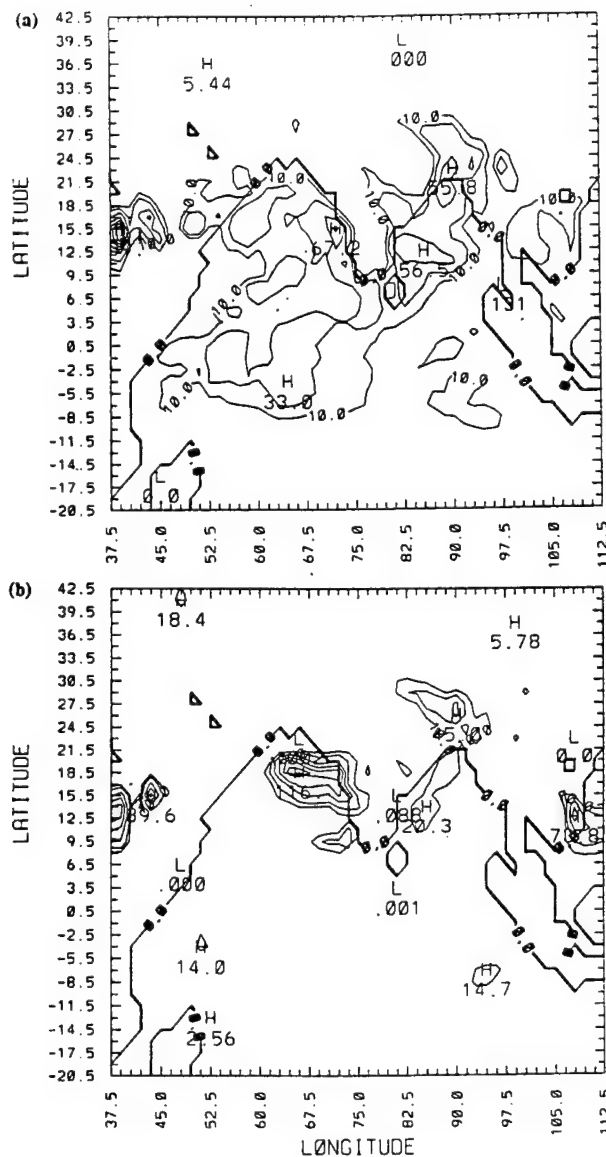


Fig. 10a,b. Predicted rainfall for the CGM domain for a period of 24 hours ending at 12 UTC 18 July 1988 in (a) the KUO and the (b) BMS, respectively. Contour intervals are 10, 20, 50, 80, 100, 125 mm d<sup>-1</sup>

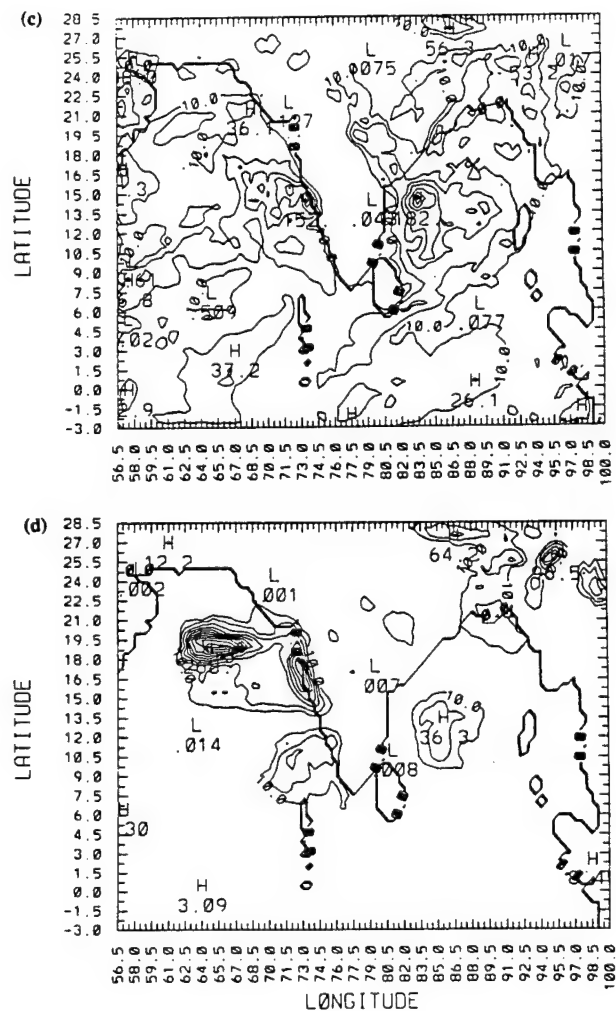


Fig. 10c,d. Predicted rainfall for the FGM domain for a period of 24 hours ending at 12 UTC 18 July 1988 in (c) the KUO and the (d) BMS, respectively. Contour intervals are 10, 25, 50, 75, 100, 125 mm d<sup>-1</sup>



Sea in conjunction with the spurious low pressure system. Meager rainfall rates are predicted in the BMS over the Indian Ocean, indicating the some of the adjustment parameters such as saturation pressure departure, relaxation time scale and stability weights on the moist adiabat, used in the Betts–Miller scheme may not be suitable for the monsoon region.

Model predicted rainfall for the CGM during the second day of simulation ending at 12 UTC 18 July in the KUO and the BMS are shown in Figs. 10a and 10b, respectively. In the KUO,

predicted rainfall along the monsoon trough region is smaller compared to the previous day. Along the west coast of India spatial distribution of rainfall is somewhat similar to that during the previous day. In the BMS, rainfall associated with the monsoon depression is very small as compared to that in the KUO. As mentioned earlier, predicted monsoon depression in the BMS has weakened during the second day as indicated by the rainfall predictions. On the other hand, spurious rainfall over the Arabian Sea in the BMS is larger as compared to that during the first day

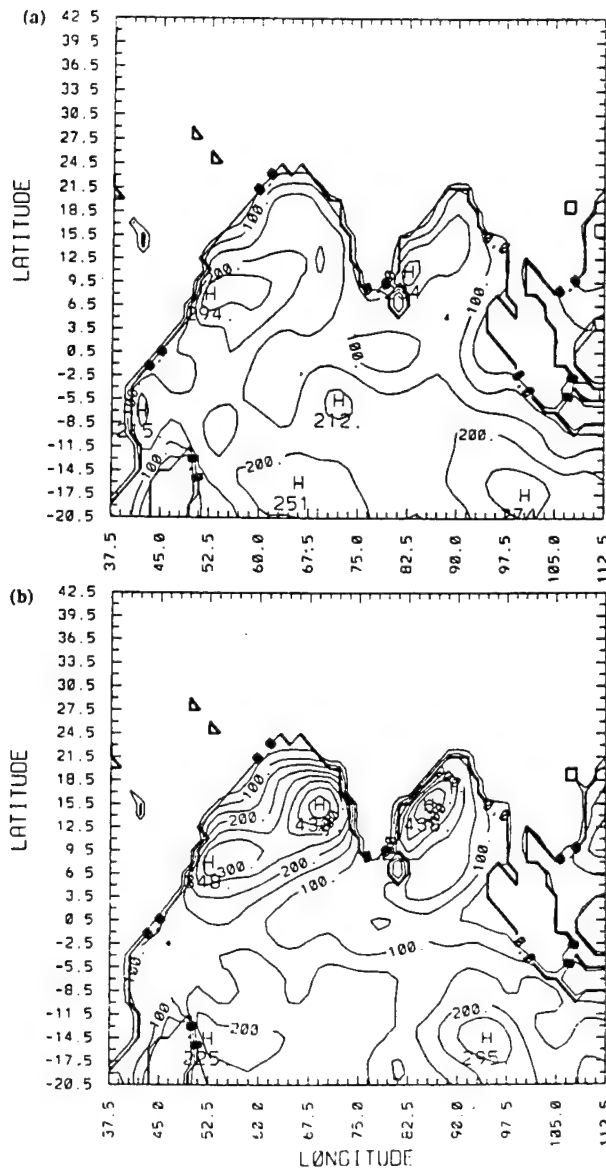


Fig. 11a, b. Mean latent heat fluxes from the surrounding oceans for 24 h ending at 12 UTC 17 July for the CGM (a) in the KUO and (b) the BMS. Contour interval is  $50 \text{ W m}^{-2}$

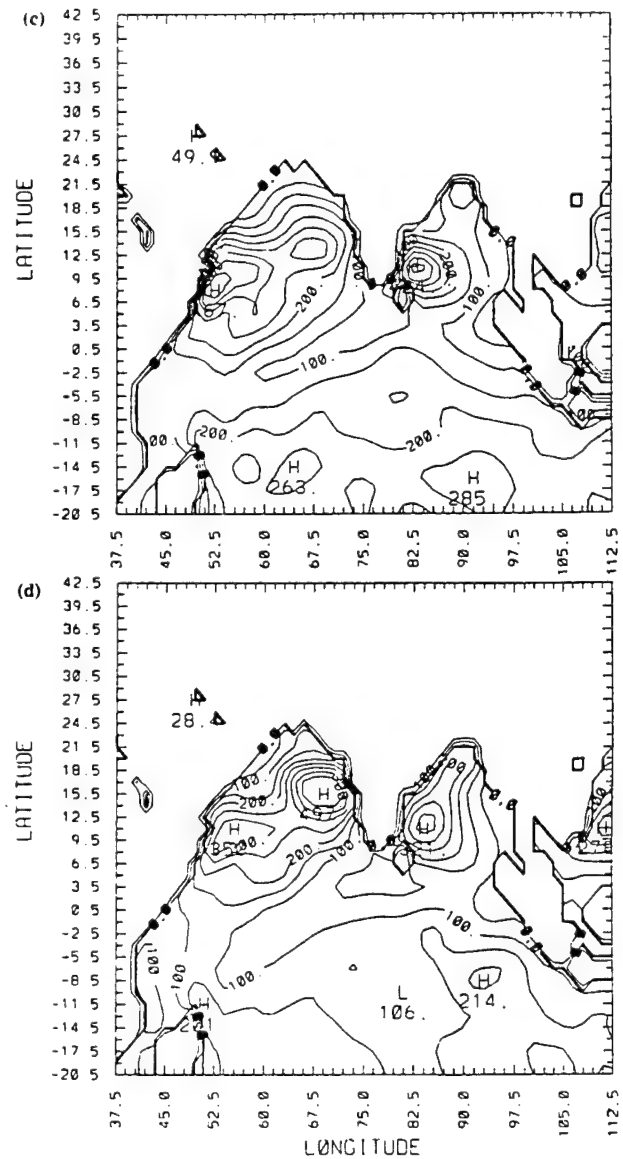


Fig. 11c, d. Mean latent heat fluxes from the surrounding oceans for 24 h ending at 12 UTC 18 July for the CGM (c) in the KUO and (d) the BMS. Contour interval is  $50 \text{ W m}^{-2}$



of simulation. However, in the KUO, rainfall maximum just offshore of the west coast of India is again consistent with the observations.

Predicted rainfall for the FGM during the second day of simulation ending at 12 UTC 18 July in the KUO and the BMS are shown in Figs. 10c and 10d, respectively. As can be seen from the observations (Fig. 8b), a rainfall band along the monsoon trough region over central India is again well predicted in the KUO. In the BMS, rainfall over this region is again almost negligible ( $10 \text{ mm day}^{-1}$ ). Again, over the surrounding oceans the BMS predicts lower rainfall rates as compared to that in the KUO. Along the west coast of India rainfall maximum predicted in the KUO is just offshore while in the BMS the spurious low pressure system has further intensified resulting in larger rainfall (about  $268 \text{ mm day}^{-1}$ ).

The predicted rainfall should conform to the evaporation from the surrounding oceans. Daily average latent heat fluxes from the surrounding oceans for the first day of simulation for the coarse-grid mesh in the KUO and the BMS are shown in Figs. 11a and 11b, respectively. Since evaporation from the surface over land is not considered in the model, no latent heat fluxes exist over the land. Distribution of the latent heat fluxes in the KUO and the BMS are in good agreement with the climatological observations (Basu, 1990) off the Somali coast. Large latent heat fluxes in this region are caused by the presence of Somali Jet. But larger latent heat fluxes over the northern Arabian sea in the BMS are caused by the

spurious storm and are not observed (Holt and Raman, 1985).

Daily average latent heat fluxes for second day of simulation for the CGM in the KUO and the BMS are shown in Figs. 11c and 11d, respectively. Off the Somali coast latent heat fluxes are larger in the KUO than that in the BMS. This is due to the intensification of the Somali jet in the KUO and stronger low level winds over this region. In general, latent heat fluxes of about  $200$  to  $400 \text{ W m}^{-2}$  can be seen in both the KUO and the BMS forecasts. Again, the BMS predicts larger latent heat fluxes over northern Arabian sea. Over the Bay of Bengal (near the east coast of India), the spatial distribution of latent heat fluxes are similar.

### 3.3 Spinup and Forecast Errors

To determine the spinup time of the model, area average of rainfall for the entire CGM simulation domain is considered. Temporal variations of the area averaged rainfall and evaporation in the KUO and the BMS are shown in Fig. 12a. Solid line represents the hourly accumulated rainfall and dashed line represents the hourly accumulated evaporation in the KUO. In the BMS these fields are represented by respective lines with closed circles. Spinup signature can be seen in the KUO during the first day of simulation. After about 30 h of simulation the KUO shows good agreement between rainfall and the evaporation and there exists a balance between these two fields. In the

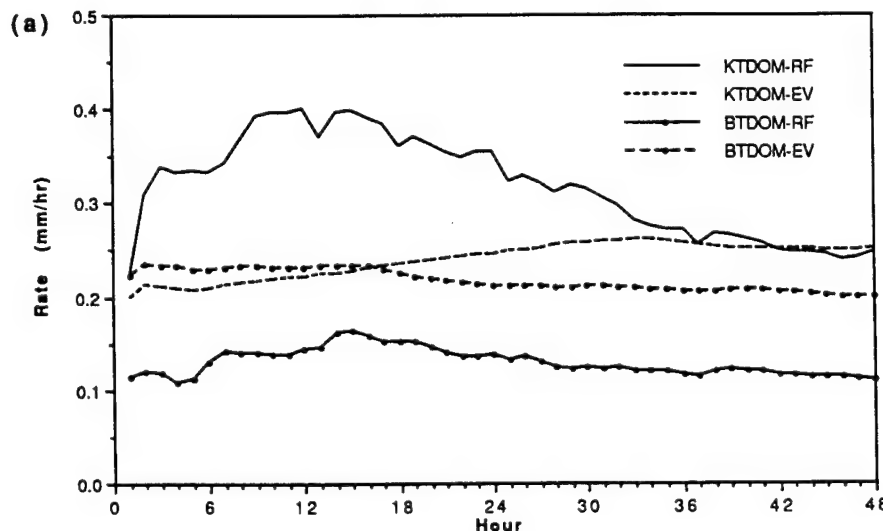


Fig. 12a. Temporal variation of hourly accumulated and area averaged (total domain) rainfall and evaporation in the KUO and the BMS

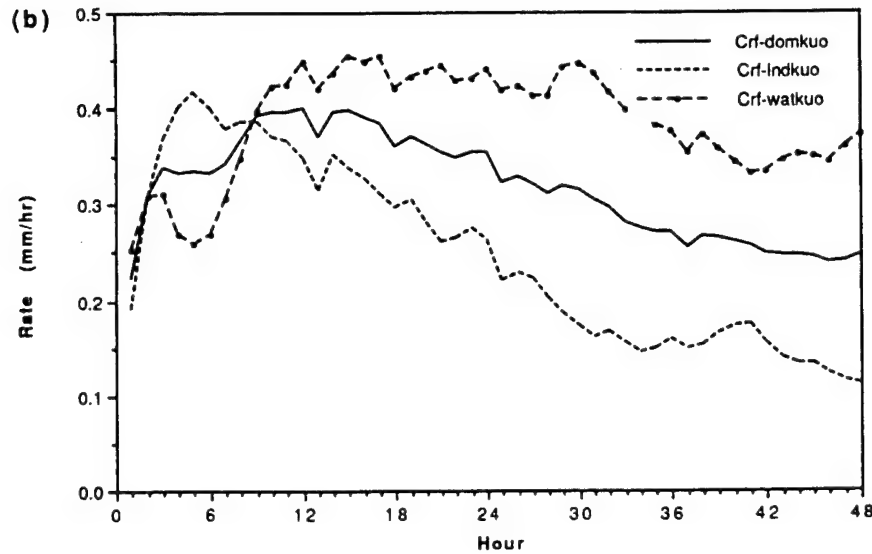


Fig. 12b. Temporal variation of hourly accumulated and area averaged rainfall (b) in the KUO for the entire domain (solid line), for the land-covered grid cells (dashed line) and for the water-covered grid cells (dashed line with closed circles)

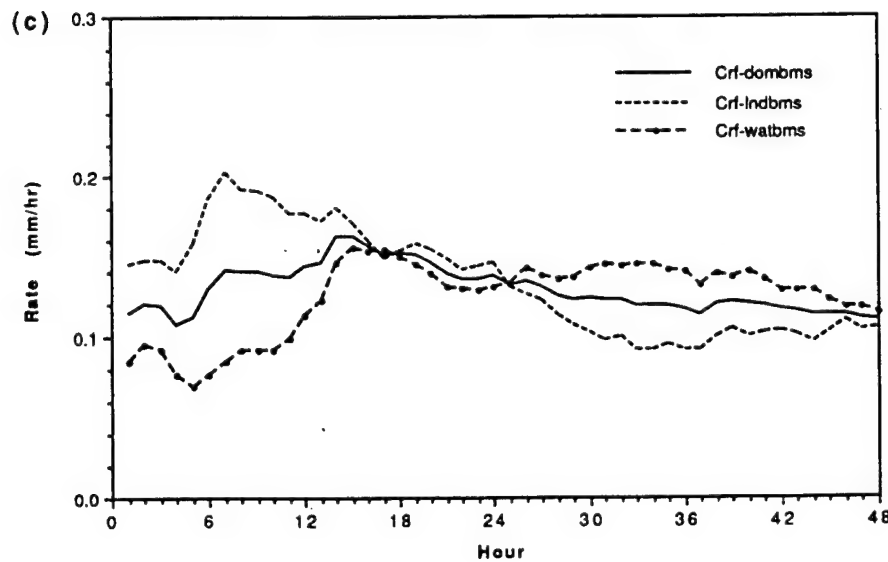


Fig. 12c. Temporal variation of hourly accumulated and area averaged rainfall (c) in the BMS for the entire domain (solid line), for the land-covered grid cells (dashed line) and for the water-covered grid cells (dashed line with closed circles)

BMS, accumulated rainfall is found to be under-predicted and shows a spinup time of about 18 h from the initial time. Up to 18 h of integration, model predicted similar rates of domain averaged evaporation for both the parameterization schemes. For the rest of the simulation model predicted higher evaporation rates with the BMS. This is due to the presence of spurious cyclone over the northern Arabian Sea. Winds are much more accelerated over the southern Arabian Sea, resulting in stronger southwesterlies over this region with the BMS. As a result, higher evaporation rates are predicted with the BMS. Evaporation in the BMS is found to be much higher than the rainfall though it showed a small decrease from first day to the second day. However, evaporation is found to be higher than the rainfall by about

$0.1 \text{ mm h}^{-1}$ . On the average, the KUO shows about  $0.25 \text{ mm h}^{-1}$  of rainfall and evaporation rates whereas the BMS shows an average of about  $0.1 \text{ mm h}^{-1}$ . Thus, for the monsoon region after the spinup phase it is found that the rainfall predicted in the KUO is in better balance with evaporation as compared to that in the BMS.

In order to investigate the spinup problem, rainfall rates for the CGM over the land and over the ocean were separated. Temporal variations of hourly area averaged rainfall in the KUO for the entire domain (solid line), for the land-covered grid cells (dashed line) and for the water-covered grid cells (dashed line with closed circles) are shown in Fig. 12b. It is found that there is a spinup process for the model over both the land and the oceans for the first 12 h. Then the rainfall rate over

the oceans stabilized for the next 24 h. However, over land after 12 h, there is a continuous decrease in rainfall. Evaporation over land is not considered in the present version of the model and also the boundary layer processes are represented through bulk technique. These two factors might have contributed to the sharp decrease in the rainfall rates over the land.

Temporal variations of hourly area averaged rainfall in the BMS for the entire domain (solid line), for the land-covered grid cells (dashed line) and for the water-covered cells (dashed line with closed circles) are shown in Fig. 12c. Rainfall variation in this case indicates a spinup time of

16 h after which these rainfall rates are stabilized. During the first say of simulation rainfall rates over land are found to be higher than those over the oceans.

In order to investigate the nature of the cumulus convection, area averaged (total domain) convective heating rates in the KUO and the BMS are considered. Time-height section of the area averaged convective heating rates for the FGM in the KUO and the BMS are shown in Figs. 13a and 13b, respectively. In the KUO, convective heating is found to be higher than in the BMS by about  $0.2$  to  $0.4^\circ \text{K h}^{-1}$  and maximum is located at about 400 hPa ( $0.4\sigma$ ). In the BMS, convective heating rates are smaller with an average heating of the atmosphere by about  $0.15^\circ \text{K h}^{-1}$ . In both the KUO and the BMS forecasts, convective heating maximum is present during early hours of integration as is reflected in the rainfall rates. Maximum convective heating in the KUO is located at about 400 hPa through out the simulation period. In the BMS, convection is rather shallow during the first day of simulation as compared to that in the KUO. Cumulus convection gradually deepened during the second day in the BMS, as indicated by the location of the maximum heating. Thus, more intense and deeper cumulus convection is found in the KUO as compared to that in the BMS.

To find out in the differences between the model predictions and the observations, latitudinal averages of atmospheric temperatures were considered. In the middle and upper troposphere the KUO indicated warming of the atmosphere while in the BMS warming was confined to only lower and middle troposphere. Also, warming of the atmosphere in the KUO was larger than that in the BMS. These features are consistent with the convective heating rates.

Forecast errors in the zonally averaged specific humidities for the CGM in the KUO and the BMS at 48 h are shown in Figs. 14a and 14b, respectively. Over the oceanic regions low level moistening in both the KUO and BMS is due to the evaporation from the surface. In the KUO, atmosphere above the boundary layer and the middle troposphere is drier. On the other hand, in the BMS atmosphere is more moist except for a thin layer between 850 and 750 hPa. This may be due to the fact that the cumulus convection is not deep and rainfall rates are smaller in the BMS. Dry atmosphere in the KUO is mainly due to the

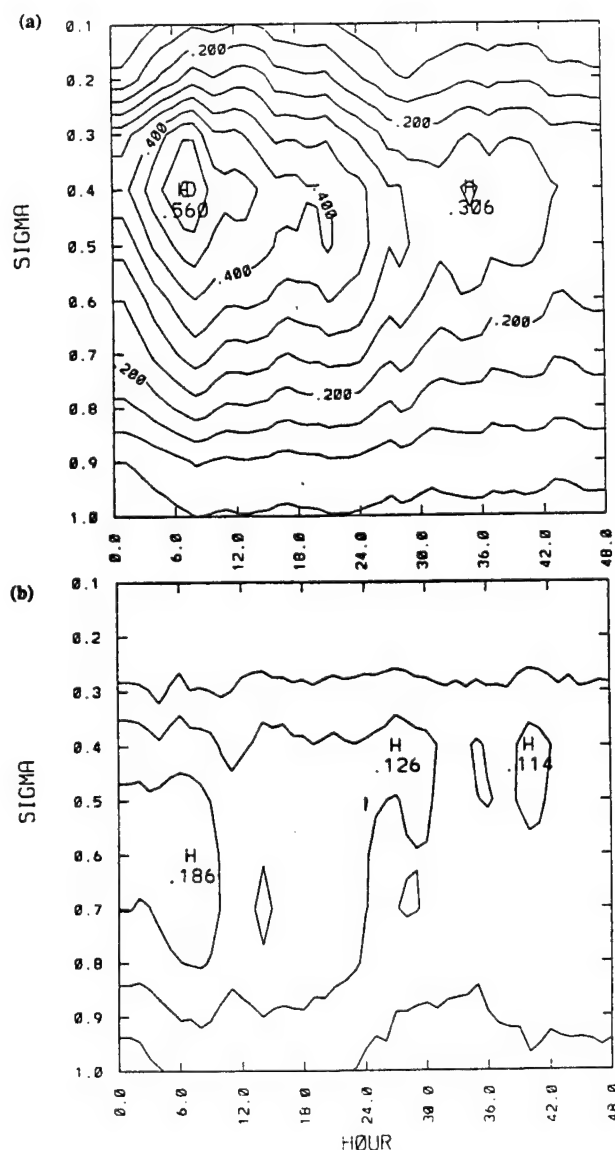


Fig. 13. Time-height section of the area averaged (total domain) convective heating for the FGM (a) in the KUO and (b) in the BMS. Contour interval is  $0.05^\circ \text{K h}^{-1}$

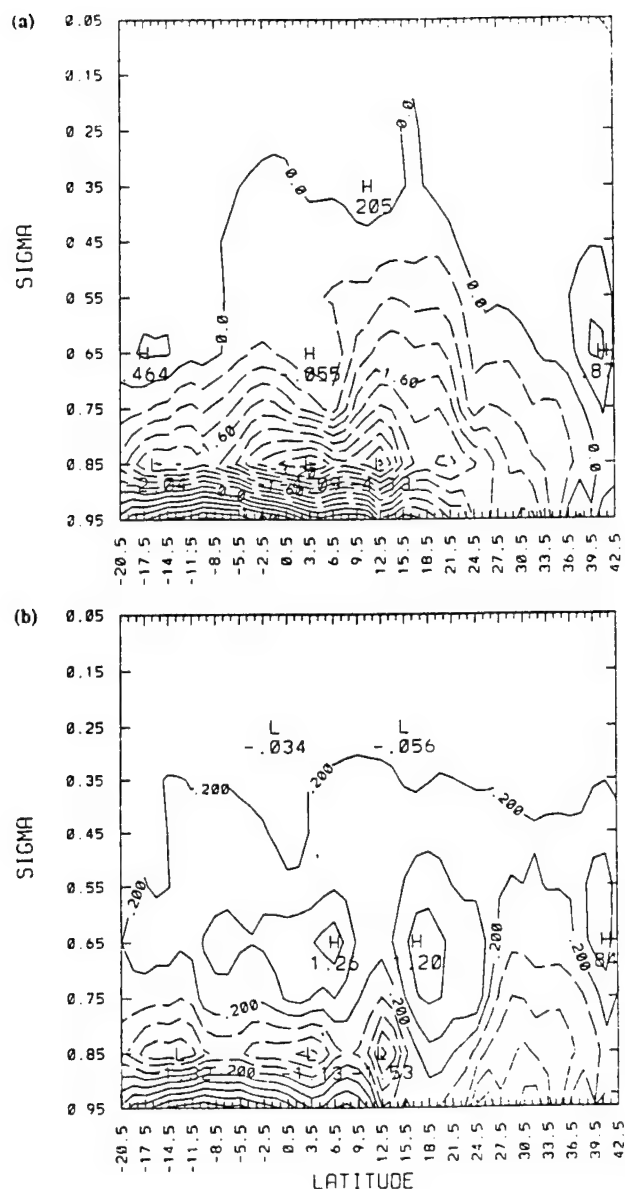


Fig. 14. Latitude-height section of zonal average of specific humidity differences between model predictions and the analyzed data (a) in the Kuo and (b) in the BMS for the CGM at 12 UTC 18 July 1988. Contour interval is  $0.4 \text{ gm Kg}^{-1}$

intense and deep convection resulting in large rainfall rates as compared to those in the BMS. Thus, both the temperature and the moisture fields are consistent with the convective processes in both the forecasts.

#### 4. Conclusions

A ten-layer regional nested grid model is used to study the performance of two different cumulus parameterization schemes. Two numerical simulations are performed for 48 h starting at 12 UTC 16

July 1988 using the Kuo and the Betts-Miller schemes. Main features associated with the monsoon circulations such as the Somali jet, reverse Hadley cell, heat-low and monsoon depression are better predicted in the model simulations when the Kuo scheme is used. Predicted rainfall associated with the monsoon depression is in better agreement with the observations when the Kuo scheme is used. Surface pressure at the center of the monsoon depression and the location of the heat-low predicted with the Kuo scheme agree better with observations. Results indicate that the thermodynamic adjustment parameters used in the Betts-Miller scheme are very sensitive to the low-level cyclonic circulations over the Arabian sea. As a consequence, predicted heat-low moved south over the Arabian Sea and developed into an intense tropical cyclone when the Betts-Miller scheme is used.

Along the west coast of India, predicted rainfall rates due to the orographic lifting are lower compared to the observations with the Betts-Miller scheme. Comparison of area averaged rainfall indicated that the Kuo scheme yields more rainfall than the Betts-Miller scheme and evaporation predicted with the Betts-Miller scheme far exceed the predicted rainfall. Rainfall associated with the spurious storm over the Arabian Sea is also included in the area averaged rainfall rates and even with these large amounts domain averaged rainfall is lower compared to that with the Kuo scheme. In contrast, results from Australian Monsoon Experiment (Puri and Miller, 1990) indicate that the vertical structure and intensity of four tropical cyclones are better simulated with the Betts-Miller scheme. In spite of the fact that the thermodynamic adjustment parameters used for the Betts-Miller scheme in this present study are very similar to those used by the Puri and Miller (1990), the conclusions in the present study on the overall performance of the Kuo and the Betts-Miller schemes differ significantly. However, results from this single case study indicate that the Betts-Miller scheme need systematic sensitivity studies regarding the suitability of the adjustment parameters for the monsoon region.

Comparison of the zonally averaged predicted specific humidities with the observations, indicated that the model atmosphere is more moist when Betts-Miller scheme is used, consistent with the

predicted rainfall amounts. Inclusion of evaporation from the land surface and longwave cooling of the atmosphere may improve the model predictions with the Kuo scheme. In general, model predictions with the Kuo scheme compared better with the observations. Our future research is to include more case studies and study the sensitivity of model predictions to different values of thermodynamics adjustment parameters such as saturation pressure departure, relaxation time scale and stability weights on the moist adiabat used in the Betts-Miller scheme.

#### Acknowledgements

This work was supported in part by the Naval Research Laboratory, Washington, D.C. and by the Division of International Program, National Science Foundation under grant INT-9008926. Computer resources were provided by the North Carolina Supercomputing Center, Research Triangle Park, NC.

#### References

- Anthes, R. A., 1977: A cumulus parameterization scheme utilizing a one-dimensional cloud model. *Mon. Wea. Rev.*, **105**, 207-286.
- Baik, J.-J., DeMaria, M., Raman, S., 1990a: Tropical cyclone simulations with the Betts convective adjustment scheme. Part I: Model description and control simulation. *Mon. Wea. Rev.*, **118**, 513-528.
- Baik, J.-J., DeMaria, M., Raman, S., 1990b: Tropical cyclone simulations with the Betts convective adjustment scheme. Part II: Sensitivity experiments. *Mon. Wea. Rev.*, **118**, 529-541.
- Basu, B. K., 1990: A study on air-sea fluxes over Indian sea. In: Sikka, D. R., Singh, S. S. (eds.) *Physical Processes in Atmospheric Models*. New York: Wiley Eastern Edition, 179-192.
- Betts, A. K., 1986: A new convective adjustment scheme. Part I: Observational and theoretical basis. *Quart. J. Roy. Meteor. Soc.*, **112**, 677-691.
- Businger, J. A., Wyngaard, J. C., Izumi, Y., Bradley, E. F., 1971: Flux-profile relationship in the atmospheric surface layer. *J. Atmos. Sci.*, **28**, 181-189.
- Das, S., Mohanty, U. C., Sharma, O. P., 1988: Study of Kuo-type cumulus parameterizations during different epochs of the Asian summer monsoon. *Mon. Wea. Rev.*, **116**, 715-729.
- Davies, H. C., 1976: A lateral boundary formulation for multi-level prediction models. *Quart. J. Roy. Meteor. Soc.*, **102**, 405-418.
- Davies, H. C., 1983: Limitations of some common lateral boundary schemes used in regional NWP models. *Mon. Wea. Rev.*, **111**, 1002-1012.
- Geleyn, J.-F., 1985: On a simple, parameter-free partition between moistening and precipitation in the Kuo scheme. *Mon. Wea. Rev.*, **113**, 405-407.
- Grossman, R. L., Durran, D. R., 1984: Interaction of low-level flow with the western Ghat Mountains and offshore convection in the summer monsoon. *Mon. Wea. Rev.*, **112**, 652-672.
- Holt, T., Raman, S., 1987: A study of mean boundary-layer structures over the Arabian sea and the Bay of Bengal during active and break monsoon periods. *Bound.-Layer Meteor.*, **38**, 73-94.
- Junker, N. W., Hoke, J. E., 1990: An examination of nested grid model precipitation forecasts in the presence of moderate-to-strong low-level southerly inflow. *Wea. Forecasting*, **5**, 333-344.
- Krishnamurti, T. N., Cocke, S., Pasch, R., Low-Nam, S., 1983: Precipitation estimates from rainguage and satellite observations: Summer MONEX. Department of Meteorology, Florida State University, 377 pp.
- Kuo, H. L., 1965: On the intensification of tropical cyclones through latent heat release by cumulus convection. *J. Atmos. Sci.*, **22**, 40-63.
- Kuo, H. L., 1974: Further studies of the parameterization of the influence of cumulus convection on large-scale flow. *J. Atmos. Sci.*, **31**, 1232-1240.
- Madala, R. V., Chang, S. W., Mohanty, U. C., Madan, S. C., Paliwal, R. K., Sarin, V. B., Holt, T., Raman, S., 1987: Description of the Naval Research Laboratory limited area dynamical weather prediction model. NRL Memo. Rep., No. 5992, Naval Research Laboratory, Washington, D.C., 131 pp.
- Molinari, J., 1983: A method for calculating the effects of deep cumulus convection in numerical models. *Mon. Wea. Rev.*, **110**, 1527-1534.
- Ogura, Y., Yoshizaki, M., 1988: Numerical study of orographic-convective precipitation over the eastern Arabian Sea and the Ghat mountains during the summer monsoon. *J. Atmos. Sci.*, **45**, 2097-2122.
- Puri, K., Miller, M. J., 1990: Sensitivity of ECMWF analyses-forecasts of tropical cyclones to cumulus parameterization. *Mon. Wea. Rev.*, **118**, 1709-1741.
- Ramachandran, G., 1972: The role of orography on wind and rainfall distribution in and around a mountain gap: Observational study. *Indian J. Meteor. Geophys.*, **23**, 41-44.
- Ramakrishnan, K. P., Gopinatha Rao, 1958: Some aspects of the nondepressional rain in peninsular India during the southwest monsoon. *Proc. Symp. on the Monsoon World*, Indian Meteorological Department.
- Rao, Y. P., 1976: Southwest Monsoon. Meteorological Monograph, Synoptic Meteorology No. 1/1976, India Meteorological Department, India, 367 pp.
- Smith, R. B., Lin, Y.-L., 1983: Orographic rain on the western Ghat. In: Reiter, E. R., Baozhen, Z., Youngfu, Q. (eds.) *Proc. First Sino-American Workshop on Mountain Meteorology*, pp 71-94.

Authors' addresses: K. Alapathy, S. Raman, Department of Marine, Earth and Atmospheric Sciences, North Carolina State University, N.C. 27695-8208, U.S.A.; R.V. Madala, Naval Research Laboratory, Washington, D.C., 20375, U.S.A.; U. C. Mohanty, Centre for Atmospheric Sciences, Indian Institute of Technology, New Delhi, 110016, India.

## **Appendix H**

### **Simulation of Monsoon Boundary Layer Processes Using a Regional Scale Nested Grid Model**

# SIMULATION OF MONSOON BOUNDARY-LAYER PROCESSES USING A REGIONAL SCALE NESTED GRID MODEL

KIRAN ALAPATY, SETHU RAMAN and R. V. MADALA\*

*Department of Marine, Earth and Atmospheric Sciences, North Carolina State University,  
N.C. 27695-8208, U.S.A*

(Received in final form 21 June, 1993)

**Abstract.** A nested grid regional model with a high vertical resolution in the atmospheric boundary layer is used to simulate various atmospheric processes during an active monsoon period. A turbulence kinetic energy closure scheme is used to predict the boundary-layer structure. Model predictions indicate different structures of the boundary layer over land and oceans, as observed. Significant diurnal variation in boundary-layer structure and associated processes is predicted over land and negligible variations over oceans. The Somali jet over the Arabian Sea is well predicted. Location of the predicted monsoon depression and the associated rainfall are in good agreement with the observations. Also, predicted rainfall and its spatial distribution along the west coast of India are in good agreement with the observations.

## 1. Introduction

It is well known that atmospheric boundary-layer (ABL) processes play an important role on the dynamics and the thermodynamics of the atmosphere. Mesoscale models using higher order closure techniques for boundary-layer physics showed better performance in predicting mean ABL structure (e.g., Deardorff, 1980; Yamada and Mellor 1975; Sun and Hsu, 1988; Huang Raman, 1989; Holt and Raman, 1990). Numerical studies (Holt and Raman, 1988) indicate that the turbulent kinetic energy-dissipation (TKE- $\epsilon$ ) closure is preferable to first-order closure in predicting turbulence structure of the ABL. A sensitivity study of a numerical model to various boundary-layer parameterizations (Holt *et al.*, 1990) indicates that the mesoscale structure of the winds, temperature and moisture are more accurately predicted with the higher order turbulence closure. Holt *et al.* (1990) also found that increased vertical resolution in the ABL without better boundary-layer physics showed no improvement in model predictions.

Monsoon weather is characterized by the presence of strong low-level westerly flow. Boundary-layer processes over this region are complex due to the presence of the low-level Somali jet over the Arabian Sea and convective processes associated with orographic lifting of moist air along the west coast of India. Observational studies of the mean structure of the marine boundary layer over the Arabian sea (Holt and Raman, 1985, 1987) during MONEX 79 indicate that the

\* Naval Research Laboratory, Washington, D.C., 20375, U.S.A.



monsoon boundary layer is affected by the large-scale flow. Over regions of cumulus activity, Holt and Raman (1985, 1987) found that the prevailing Somali jet structure is depressed in height. It was also found that (Holt and Raman, 1987) latent heat fluxes over the Arabian Sea during the active monsoon conditions are about two to three times larger than those during the "break" conditions and that sensible heat fluxes increased considerably during the monsoon onset as compared to premonsoon conditions.

The objective of this paper is to simulate the monsoon circulations and associated processes using a sophisticated boundary-layer parameterization scheme with high vertical resolution in the ABL. We also examine boundary-layer structure over land and over the adjacent oceans during an active monsoon period and compare the results with observations.

## 2. Model Description

The present study utilizes a nested grid model developed at the Naval Research Laboratory and North Carolina State University based on the limited area dynamical weather prediction model developed earlier by Madala *et al.* (1987). It is a primitive equation model written in a pressure-based  $\sigma$ -coordinate system having a one-way interacting nested grid network. The  $\sigma$ -coordinate is defined by  $\sigma = p/p_s$ , where  $p$  is the pressure and  $p_s$  the surface pressure. Various physical processes are included either explicitly or in parameterized form. The model physics includes latent heat, sensible heat, and momentum exchange between the ABL and the underlying surface, grid-scale precipitation, dry convection, and diffusion processes. (Boundary-layer parameterization used in the model is described in the following section.) The cumulus parameterization scheme suggested by Kuo (1974) and Anthes (1977) is used in the model. Short- and long-wave radiative processes are not included in the present model. Second-order diffusion for momentum on  $\sigma$ -surfaces and for heat and water vapor on  $p$ -surfaces is used to account for the cascading of energy into unresolved subgrid-scale waves. If super-saturation exists at any level, the excess moisture is assumed to condense and fall out to the next lower layer and evaporate or continue to fall depending upon the degree of saturation at that level. The model has a dry convective adjustment procedure to remove dry convective instability that can occur during model integration.

The time integration scheme utilized in the present model is a split-explicit method which allows a larger time step by effectively separating various terms in the prognostic equations into parts governing slow-moving Rossby modes and fast-moving gravity modes. For the first and second fast-moving gravity modes, a smaller time step is used than for all other modes. The implementation of these varying time steps is the basis for the split-explicit method. The time steps for the slow moving modes in the CGM (Coarse-Grid Mesh) and the FGM (Fine-Grid Mesh) are 300 and 100 s, respectively, and appropriate smaller time steps are used for the fast-moving modes. For further details, the reader is referred to Madala

*et al.* (1987). For the horizontal differencing, a staggered grid network (Arakawa C-grid) is used with  $p_s$ ,  $q$ ,  $T$ ,  $\phi$ ,  $\sigma$  specified at the same horizontal points, and  $u$  and  $v$  interlaced between them where  $p_s$  is the surface pressure,  $q$  the specific humidity,  $T$  the temperature,  $\phi$  the geopotential,  $\sigma$  the vertical velocity of  $\sigma$ ,  $u$  the zonal wind velocity, and  $v$  the meridional wind velocity. The finite difference technique used is second-order accurate. It conserves total energy, mass, and momentum in the absence of heat and momentum sources.

Model topography was obtained from the navy 10' global topography data for 1.5° and 0.5° horizontal resolutions. Model sea surface temperatures (SST) were obtained from the 1° resolution global climatological values based on a 10 year average for the month of July. The Davies scheme (1976, 1983) is employed to provide lateral boundary conditions in the present version of the model. For any independent variable  $a$ , it can be written as,  $a = (1 - \alpha)a_m + \alpha a_b$ , where the subscript  $m$  represents model-computed values and the subscript  $b$  represents the boundary values obtained either from observations or from a coarser version of the model. The merging is done over six points at the boundaries of both domains. The  $\alpha$  is defined as a quadratic function of the minimum distance from the lateral boundary in units of the grid spacing (Gronas *et al.*, 1987). At each time step, the boundary values  $a_b$  for the coarse grid are obtained through a linear interpolation in time from the ECMWF data. For the FGM domain, lateral boundary conditions  $a_b$  are obtained through a linear interpolation in time and space from the CGM domain. At the model top and bottom, the boundary condition for  $\sigma$  is zero.

## 2.1. BOUNDARY-LAYER PARAMETERIZATION

The atmosphere up to about 850 hPa is divided into seven nonuniform layers as shown in Table I. The surface boundary layer is parameterized based on similarity theory (Monin and Yaglom, 1971) and the nondimensional functions can be written as,

$$\begin{aligned}\frac{kz}{u_*} \frac{\partial u}{\partial z} &= \phi_m(z/L), \\ \frac{kz}{\theta_*} \frac{\partial \Theta}{\partial z} &= \phi_h(z/L), \\ \frac{kz}{q_*} \frac{\partial q}{\partial z} &= \phi_q(z/L),\end{aligned}\tag{1}$$

where the nondimensional stability parameters  $\phi_m$ ,  $\phi_h$  and  $\phi_q$  for momentum, heat and moisture are functions of the Monin-Obukhov length,  $L$  (Businger *et al.*, 1971). In the mixed layer, the coefficient of vertical eddy diffusion is determined by the prognostic calculation of turbulence kinetic energy and its dissipation rates using the  $E-\epsilon$  closure technique (Holt and Raman, 1988) with the constants

TABLE I

Model  $\sigma$  levels and corresponding pressures for a surface at 1000 hPa

Model level <i>K</i>	Sigma and pressure levels	
	$\sigma$	$p$ (hPa) (Approx)
1	0.05	50
2	0.15	150
3	0.25	250
4	0.35	350
5	0.45	450
6	0.55	550
7	0.65	650
8	0.75	750
9	0.82	820
10	0.86	860
11	0.90	900
12	0.935	935
13	0.96	960
14	0.9775	977
15	0.99	990
16	0.9975	997

suggested by Detering and Etling (1985). Prognostic equations for turbulence kinetic energy ( $E$ ) and its dissipation ( $\epsilon$ ) can be written as:

$$\begin{aligned} \frac{\partial E}{\partial t} = & -\overline{u'w'} \frac{\partial u}{\partial z} - \overline{v'w'} \frac{\partial v}{\partial z} + \frac{g}{\Theta} \overline{w'\theta'} - \\ & - \frac{\partial}{\partial z} \left( \overline{w'E} + \frac{\overline{p'w'}}{\rho} \right) - \epsilon, \end{aligned} \quad (2)$$

$$\begin{aligned} \frac{\partial \epsilon}{\partial t} = & \frac{c_1 \epsilon}{E} \left( -\overline{u'w'} \frac{\partial u}{\partial z} - \overline{v'w'} \frac{\partial v}{\partial z} + \frac{g}{\Theta} \overline{w'\theta'} \right) - \\ & - \frac{c_2 \epsilon^2}{E} + c_3 \frac{\partial}{\partial z} \left( K_m \frac{\partial \epsilon}{\partial z} \right), \end{aligned} \quad (3)$$

where  $\overline{u'w'}$  and  $\overline{v'w'}$  are turbulence fluxes of momentum,  $\rho$  the density,  $p'$  the fluctuating pressure, and  $K_m$  the eddy exchange coefficient. The first two terms on the right hand side (rhs) of (2) represent shear production, the third, buoyancy production, fourth, turbulence transport and the fifth, the dissipation. The three terms on the rhs of (3) represent the production, destruction, and the vertical transport of turbulent kinetic energy dissipation, respectively.

## 2.2. GROUND TEMPERATURE

The ground temperature  $T_g$  is predicted by a soil slab model (Blackadar, 1976), which predicts ground temperature, based on the surface energy equation (Chang, 1979):

$$\frac{\partial T_g}{\partial t} = \frac{I}{C_g} + \omega(T_m - T_g) + \frac{\rho c_p}{C_g} (\overline{w'\theta'})_0, \quad (4)$$

where  $I$  is the net radiation,  $C_g$  the heat capacity per unit area of soil slab,  $\omega$  the inverse of the time scale for heat conduction in the soil ( $2\pi/1$  day),  $T_m$  the deep soil temperature,  $c_p$  the specific heat of air, and  $(\overline{w'\theta'})_0$  is the kinematic heat flux defined as:

$$(\overline{w'\theta'})_0 = -u_* T_*. \quad (5)$$

The terms on the rhs of (4) represent net radiation, soil heat flux and surface turbulent heat flux, respectively. Net radiation  $I$  is the sum of incoming solar radiation absorbed at the surface  $I_S$ , atmospheric longwave back-scattering radiation  $I_L$  and outgoing longwave surface radiation  $O_L$ . Incoming solar radiation is estimated as:

$$I_S = S \cos Z (1 - A) b^{\sec Z}, \quad (6)$$

where  $S$  is the solar constant,  $Z$  the solar zenith angle,  $b$  the atmospheric turbidity, which is a function of precipitation rate, and  $A$  the surface albedo which is assumed as 0.28 over land and 0.08 over water. Water vapor is not considered in the relationship for net longwave radiation computed using Brunt's equation (Seller, 1965):

$$I_L - O_L = -\epsilon_m (1 - 0.61) \beta T_g^4, \quad (7)$$

where  $\epsilon_m$  is soil emissivity (0.7) and  $\beta$  is the Stefan-Boltzmann constant. Heat capacity of the soil slab  $C_g$  is approximated as an 80 m deep air layer (Chang, 1979).

## 2.3. SIMULATION DOMAIN, INITIAL CONDITIONS AND NUMERICAL EXPERIMENTS

The domain of simulation in the Coarse-Grid Mesh (CGM) and the Fine-Grid Mesh (FGM), the latter being located over India and the surrounding oceans is shown in Figure 1. The horizontal resolutions of the CGM and the FGM are  $1.5^\circ$  and  $0.5^\circ$ , respectively. Envelope topography was obtained from the navy  $10'$  global topography data. Initial conditions were obtained from the European Centre for Medium Range Weather Forecast (ECMWF) analysis, available at 14 nonuniform vertical levels with  $1.875^\circ \times 1.875^\circ$  horizontal resolution. These data were interpolated to model grid points in the coarse-grid and fine-grid model. To achieve the objective of this study, numerical simulations were performed for 48 h starting at 12 UTC 16 July 1988.

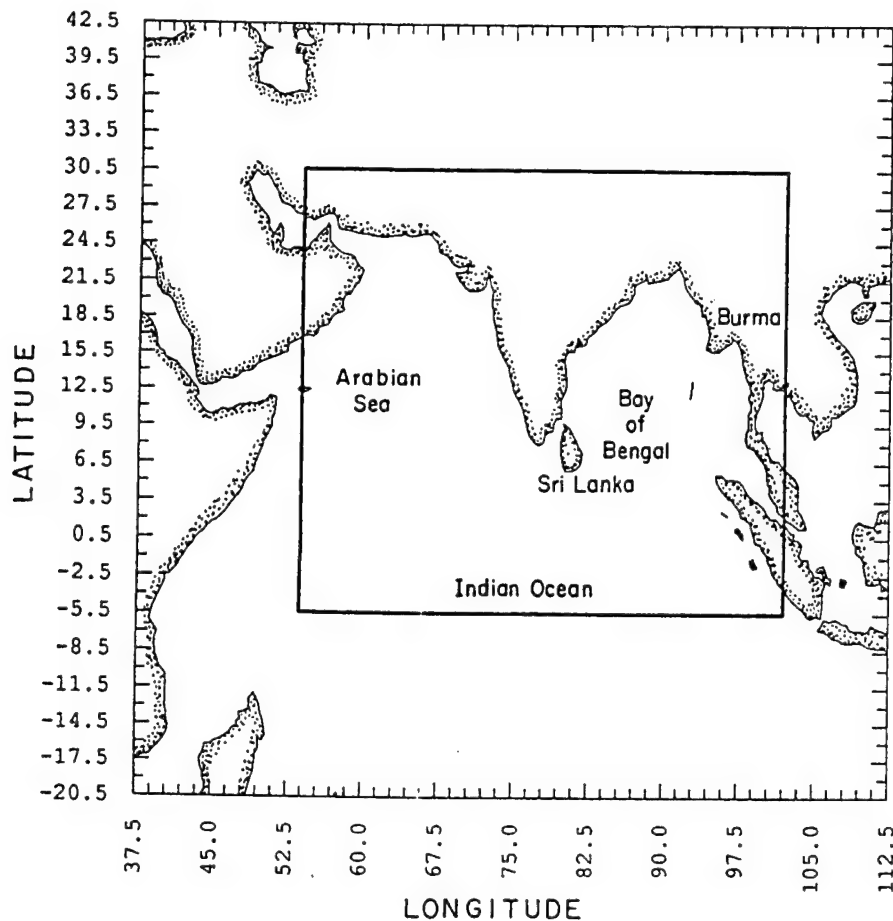


Fig. 1. The model domain of numerical simulation in the Coarse-Grid Mesh (CGM) and the Fine-Grid Mesh (FGM).

### 3. Synoptic Conditions

A monsoon depression was present over the Bay of Bengal close to the east coast of India during the simulation period (12 UTC 16 July to 12 UTC 18 July) and large rainfall rates were observed. Analyzed streamline distribution and horizontal winds for the 850 hPa at 12 UTC 16 July 1988 (initial conditions) are shown in Figure 2. Cyclonic circulations over the Bay of Bengal close to the east coast of India indicate the location of the monsoon depression. This depression moved northwest and made landfall during the next 24 h, moving farther inland to be centred over northeast India at 12 UTC 18 July. Large rainfall rates were reported over northeast India resulting from the monsoon depression. Along the west coast of India and offshore, large rainfall rates were also observed. The Somali jet, also

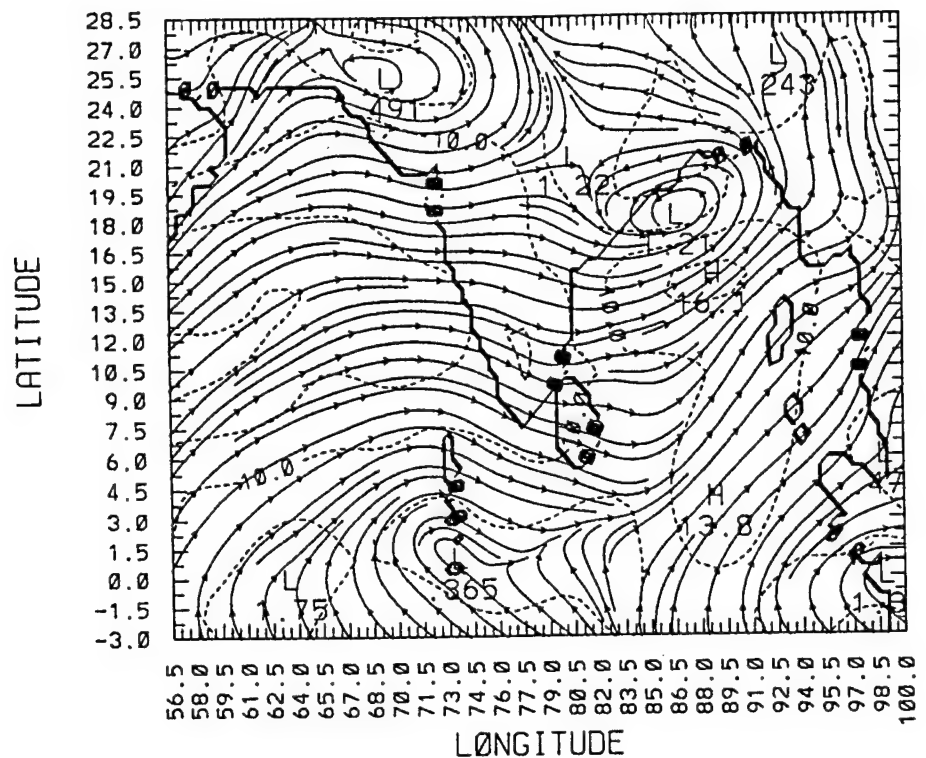


Fig. 2. Analyzed horizontal streamline and wind distribution at  $\sigma = 0.85$  at 12 UTC 16 July 1988 (initial conditions). Contour interval is  $5 \text{ m s}^{-1}$ .

referred to as the east African Jet, is another feature present during the summer monsoon season. It is a low level jet situated at a height of about 1.5 km from the surface. Strong winds (broken lines in Figure 2 are isotachs) over the east coast of Africa are due to the presence of the Somali jet over this region. The interaction of the Somali jet with the monsoon circulation and its impact on the monsoon dynamics are still not well understood. Analyzed mean sea level pressure at 12 UTC 16 July 1988 indicated a low pressure center off the east coast of India consistent with the location of the cyclonic circulations seen in Figure 2. The low pressure center over west India is due to strong heating over the desert regions and is called the heat-low.

#### 4. Discussion of Results

##### 4.1. STRUCTURE OF THE MONSOON BOUNDARY LAYER

A time-height section of the area-averaged winds for the region,  $8^\circ$  to  $14^\circ \text{ N}$  and  $60^\circ$  to  $67.5^\circ \text{ E}$  over the Arabian Sea is shown in Figure 3. The presence of the

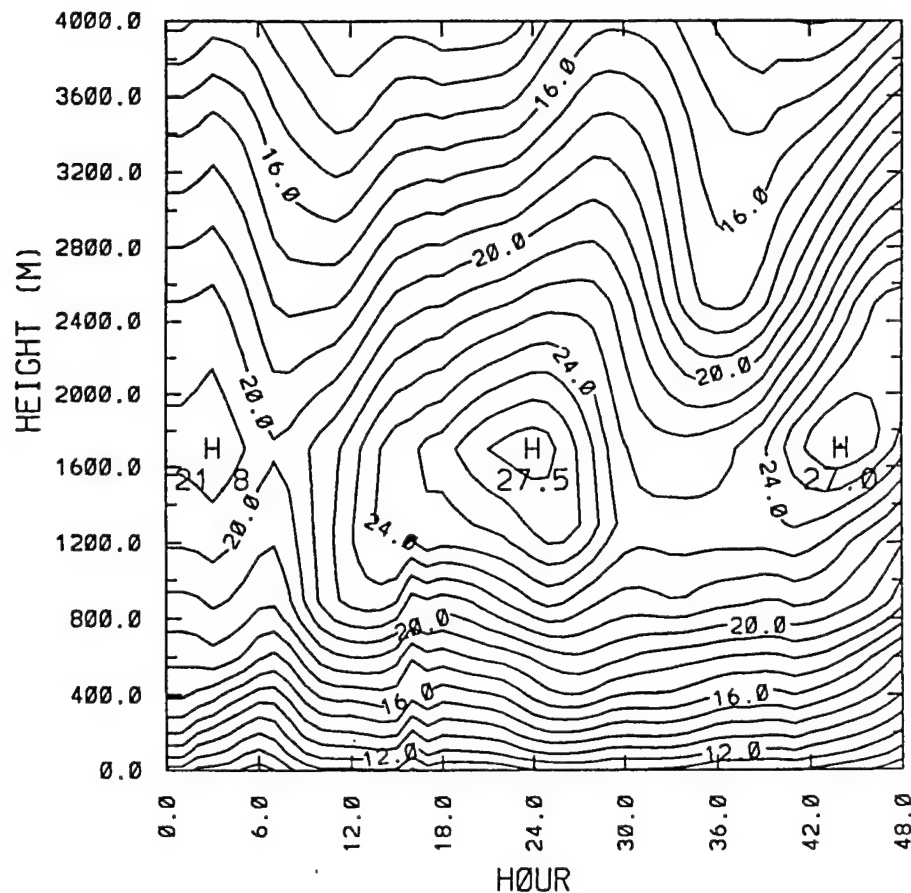


Fig. 3. Time-height section of area-averaged wind speed over the Arabian Sea for 48 h of simulation. Contour interval is  $1 \text{ m s}^{-1}$ .

Somali jet is indicated by the wind maximum at about 1600 m. During the period of simulation, the Somali jet showed a small diurnal variation. Wind speeds reached maximum values at the end of 23 h and 45 h of simulation which correspond to 1600 and 1400 LST. An observational study of the diurnal variation of the Somali jet over a land station Garissa, Kenya ( $0.5^\circ \text{S}$ ,  $39.5^\circ \text{E}$ ) by Findlater (1966, 1969a, 1971a, 1974) revealed that the Somali jet attains its maximum speed by early morning, at 0500 GMT. Minimum speeds were observed during the afternoons, at about 1100 GMT, when surface heating is a maximum. Observations (Findlater, 1977) also indicate winds ranging from 25 to  $50 \text{ m s}^{-1}$  along the core of the Somali jet over the Arabian sea. Limited observational studies over the Arabian sea region indicate that there is a spatial variation of the height of the Somali jet and its intensity (Findlater, 1977; Holt and Raman, 1987), as found in the model predictions. But the diurnal variation can not be verified due to lack



of sufficient observations over the Arabian Sea. This diurnal variation in wind speed may be attributed to the response of the monsoon flow to the diurnal variations of the temperature contrasts between the Arabian sea and the Indian subcontinent. Predicted wind shear (Figure 3) is larger in the lower layers (below 1000 m) than aloft and the predicted height and magnitude of the wind speed maximum ( $27 \text{ m s}^{-1}$ ) in the Somali jet over the Arabian Sea are consistent with the observations (Holt and Raman, 1986). A latitude-height section of the predicted wind speeds along  $68.5^\circ \text{E}$  also indicated a jet-like structure at an altitude of 1600 m between latitudes  $9^\circ \text{N}$  and  $15^\circ \text{N}$ . Elsewhere, over the ocean, predicted wind shear is weak.

Climatic sea surface temperatures (SSTs) for the month of July are used during the period of simulation. Over land, ground temperatures are prognostically determined using the surface energy budget. A time-height section of the area-averaged ( $8^\circ$  to  $14^\circ \text{N}$ ,  $60^\circ$  to  $67.5^\circ \text{E}$ ) predicted virtual potential temperature over the western Arabian Sea is shown in Figure 4. A near-constant  $\theta_v$  is predicted in the marine boundary layer indicating a mixed layer. In general, the area-averaged  $\theta_v$  profile over the Arabian Sea indicates a boundary-layer height of about 800 m with a capping inversion in close agreement with the observations (Holt and Raman, 1987). The time-height section of the virtual potential temperature of the atmosphere predicted by the model over land indicated a strong diurnal variation in the boundary layer with a well-mixed layer during day time. The mixed-layer height ranged from 1000 m to 1800 m over land. Mixed-layer heights can also be inferred from the diurnal variation of TKE discussed in the following section.

#### 4.2. STRUCTURE OF THE TURBULENCE IN THE PBL

In order to determine the turbulence structure of the boundary layer, a time history of the turbulence kinetic energy (TKE) and its budget over a land station Bangalore ( $12.5^\circ \text{N}$ ,  $78^\circ \text{E}$ ; hereafter referred to as BNG) are considered along with the area-averaged TKE budgets over the Western Arabian Sea ( $8^\circ$  to  $14^\circ \text{N}$ ,  $60^\circ$  to  $67.5^\circ \text{E}$ ). Predicted TKE profiles for BNG at 1400 LST on the first and second days of simulations indicated a PBL height of between 1700 and 2100 m. There is some uncertainty ( $\sim 400 \text{ m}$ ) about the exact height because of the coarse vertical resolution of the model at these altitudes.

The time-height section of the TKE predicted by the model for BNG is shown in Figure 5. During the two days of simulation, maximum TKE is predicted at 1500 LST (22 and 46 h) with a magnitude of about  $0.92 \text{ m}^2 \text{ s}^{-2}$  for the first day and  $1.12 \text{ m}^2 \text{ s}^{-2}$  for the second day. Since there is a strong diurnal variation over the land, there is a significant change in the TKE from early morning (0200 UTC) to the afternoon (0800 UTC). During night time, the stable boundary-layer height is only about 100–250 m compared to a daytime convective boundary-layer height of  $\sim 1800 \text{ m}$ . Also, during the night time there is little variation with time in boundary-layer height, which is consistent with the generally observed pattern over land (Stull, 1989). At 1500 LST, for the second day of simulation, turbulence

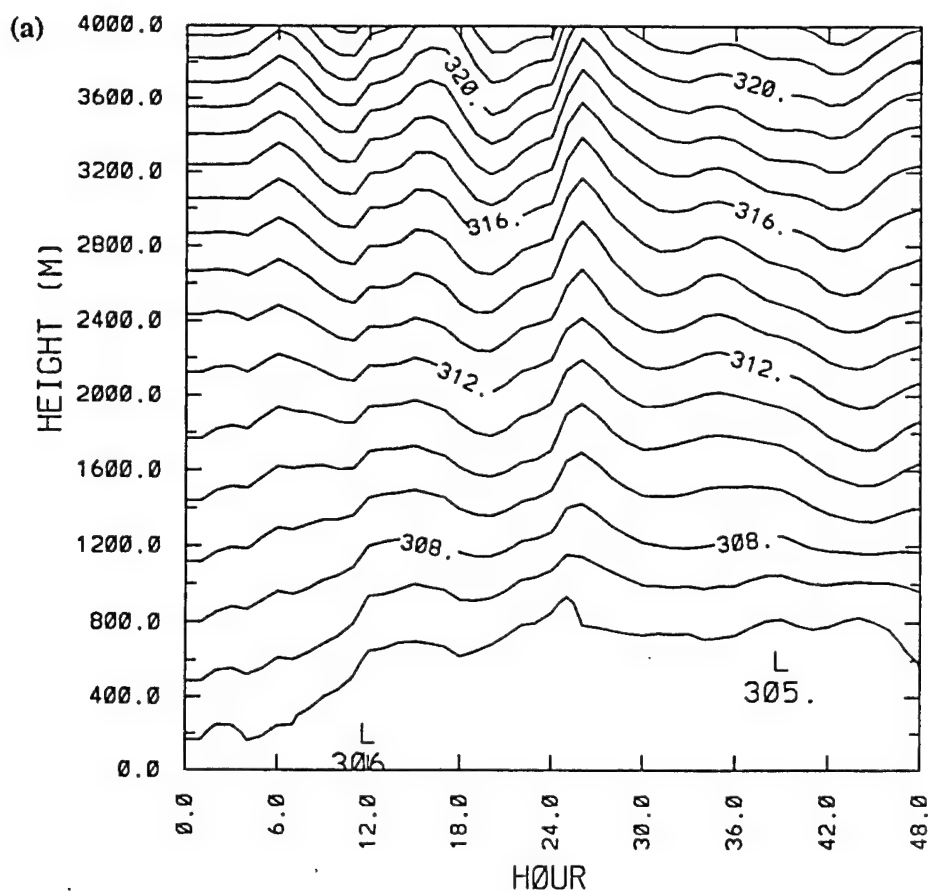


Fig. 4. Time-height section of area-averaged virtual potential temperature over the Arabian Sea. Contour interval is 1 K.

kinetic energy in the lowest layers has increased as compared to the previous day, accompanied by a small increase in PBL height. Observations of the height of the boundary layer for the present period of simulation are not available but a height of about 1000 m was observed during the 1987 monsoon over this region (Raman *et al.*, 1990). We believe that the relatively larger boundary-layer heights predicted by the model may be due to the neglect of soil moisture and evaporation over land. In the present model, surface hydrology is not considered and a dry soil with an albedo of 0.28 is assumed. Observational studies of boundary-layer heights during active and break monsoon periods (Kusuma *et al.*, 1991) also indicate that soil moisture depletion is one of the factors contributing to the increase in boundary-layer heights. A day-to-day variation in the height of the nocturnal boundary layer was also found.

Predicted vertical profiles of the TKE budget for BNG at 1400 LST and 0200

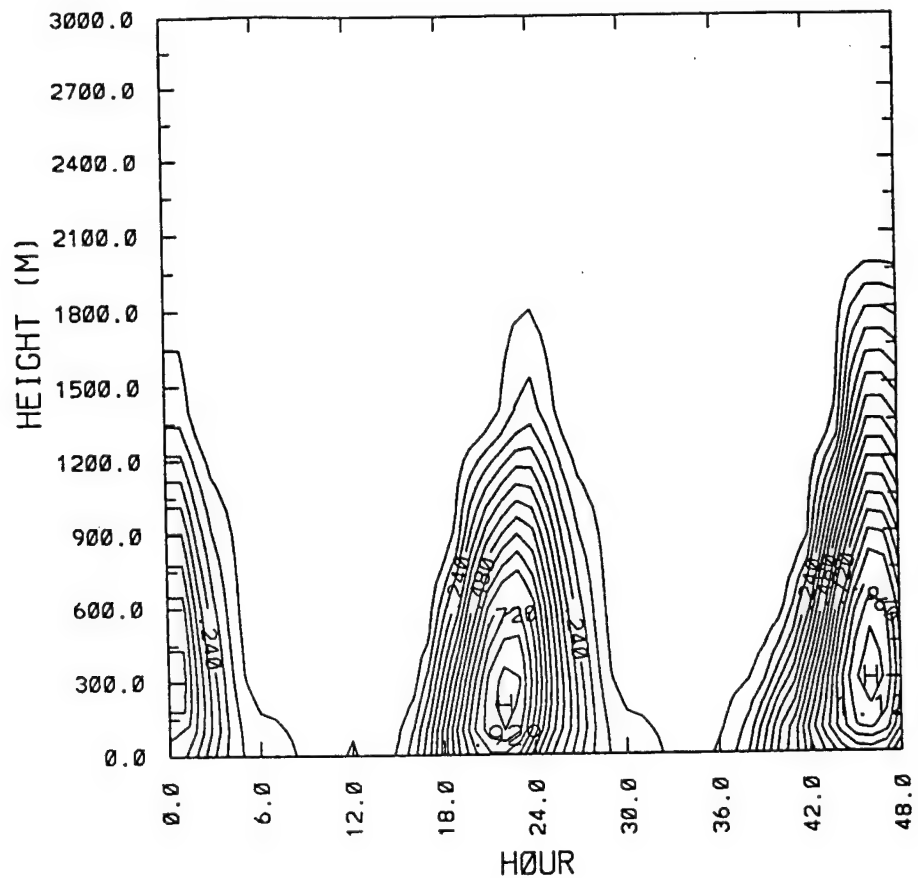


Fig. 5. Time-height section of turbulent kinetic energy over a land station (Bangalore) for 48 h of simulation. Contour interval is  $0.06 \text{ m}^2 \text{ s}^{-2}$ .

LST for the first day of simulation are shown in Figure 6a and 6b, respectively. Except near the surface, the buoyancy production term (denoted by B) is the major source term and the shear production term (denoted by A) is the secondary source term for generation of turbulence; the primary sink is the dissipation term (denoted by D). The turbulence transport term (denoted by C) is a secondary sink in the lower layers of the boundary layer. At altitudes of 500 m and above, the shear production term becomes negligible. Above 1200 m, the buoyancy production term becomes negative because of entrainment of air from the free atmosphere. The turbulence transport term becomes a source term above 900 m. Also, the dissipation term becomes small in these layers. The small imbalance term (denoted by E) is believed to be primarily due to the neglect of pressure transport and advection of turbulence. During the night time (Figure 6b), the major source for turbulence is the shear production term (denoted by A) while the buoyancy

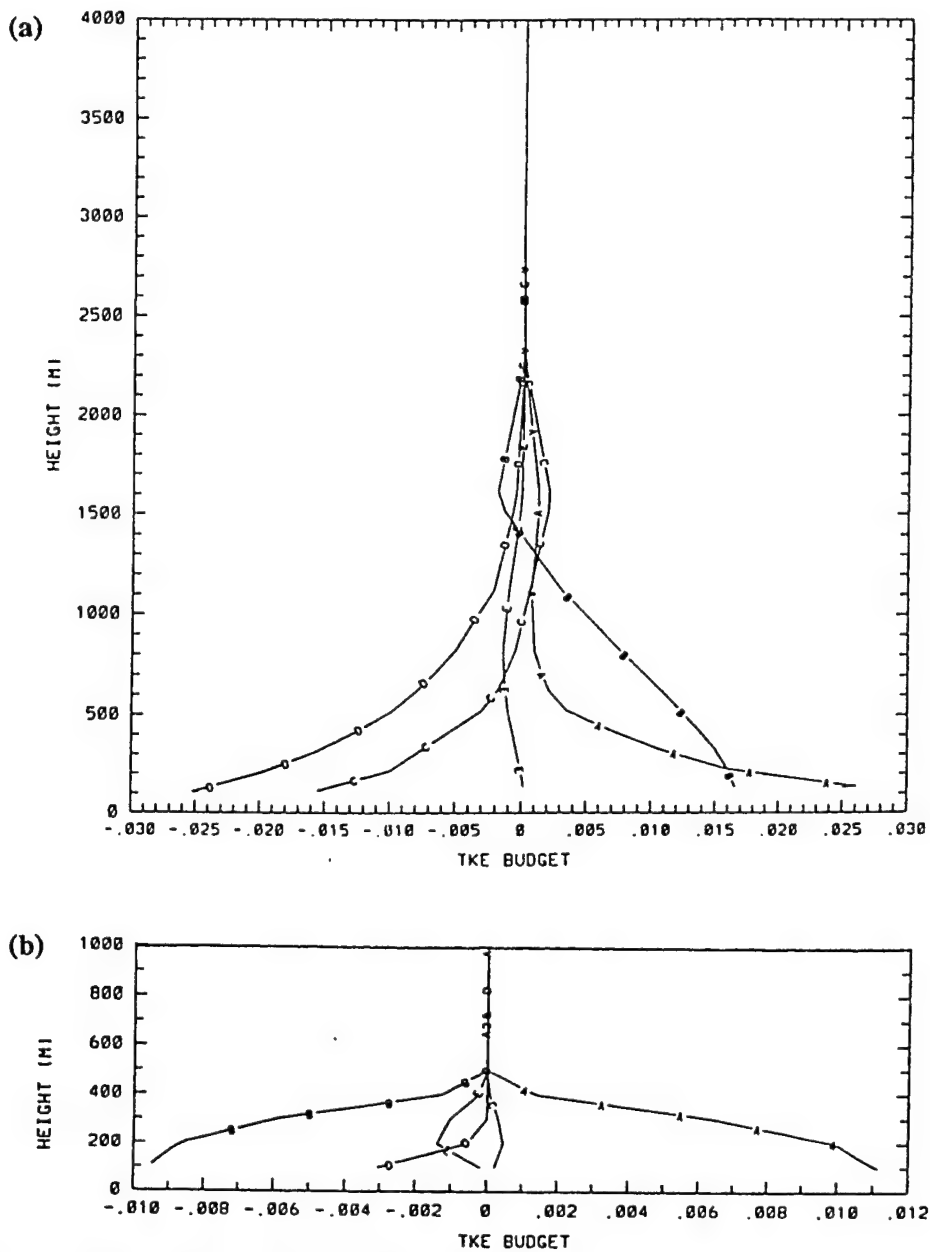


Fig. 6. Vertical profiles of turbulence kinetic energy budget terms over a land station (Bangalore) at (a) 14 LST, and (b) 02 LST for day 1. Shear production A, Buoyancy production B, Transport C, Dissipation D and the Imbalance E.

term is the major sink term (denoted by B). Contrary to the daytime TKE budget, dissipation (denoted by D) is a smaller sink term.

The time-height section of the area-averaged TKE over the Arabian Sea ( $8^{\circ}$  to  $14^{\circ}$  N,  $60^{\circ}$  to  $67.5^{\circ}$  E) is shown in Figure 7a. Major differences from the land site

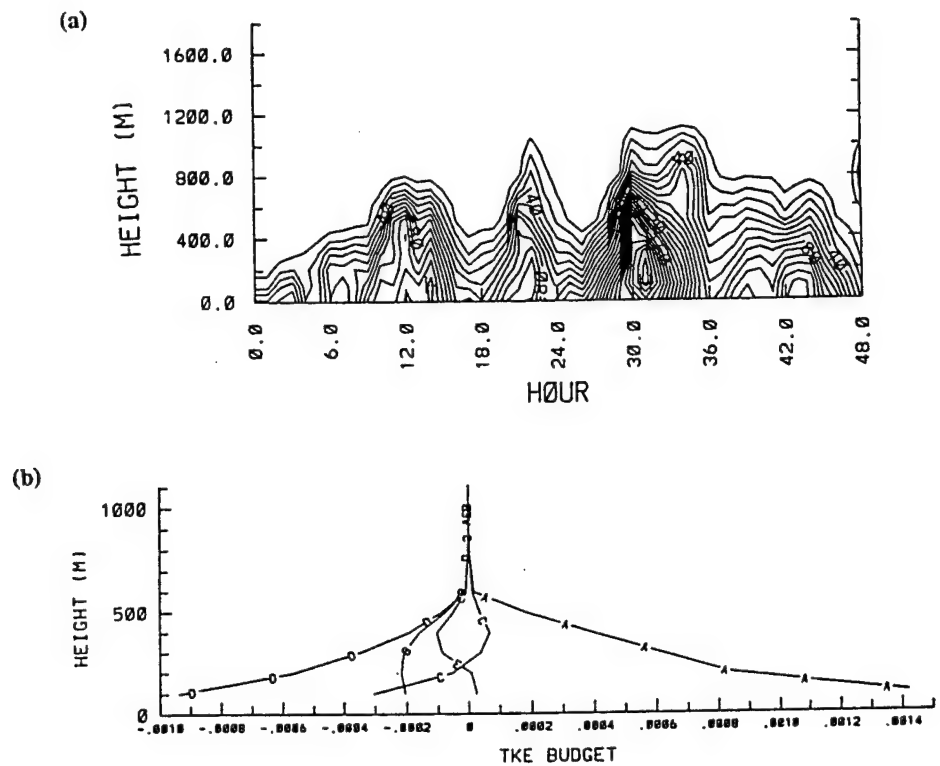


Fig. 7. (a) Time-height section of area-averaged turbulence kinetic energy over the Arabian Sea ( $8^{\circ}$  to  $14^{\circ}$  N,  $60^{\circ}$  to  $67.5^{\circ}$  E) for 48 h of simulation. Contour interval is  $1.0 \times 10^{-3} \text{ m}^2 \text{ s}^{-2}$ . (b) Vertical profiles of area-averaged turbulent kinetic energy budget terms over the Arabian Sea ( $8^{\circ}$  to  $14^{\circ}$  N,  $60^{\circ}$  to  $67.5^{\circ}$  E) at 14 LST for day 1. Shear production A, Buoyancy production B, Transport C, Dissipation D and the Imbalance E.

are the lack of a strong diurnal variation and somewhat lower values of TKE. The maximum value of the TKE predicted by the model over this region is  $\sim 0.015 \text{ m}^2 \text{ s}^{-2}$  compared to  $0.88 \text{ m}^2 \text{ s}^{-2}$  over land. Area-averaged TKE budget profiles over this region at 1400 LST of the first day of simulation are shown in Figure 7b. Near-neutral to slightly stable conditions are predicted over this region. Buoyancy production is a minor sink term for TKE in the lower layers. Shear production is the major source of TKE which gradually decreases with height. The dissipation and buoyancy terms are major sinks in the lower layers over this region, in the upper layers, the transport term is a secondary source term for TKE. The imbalance term (denoted by E) is small. Temporal variation of area-averaged TKE over the Bay of Bengal region (not shown) is somewhat similar to that over the Arabian Sea except that the magnitudes are slightly (about 5 to 10%) smaller. This may be partly due to the presence of a monsoon depression over the Bay of Bengal causing strong winds over this region. The maximum height of the area-averaged marine boundary layer over the Bay of Bengal is

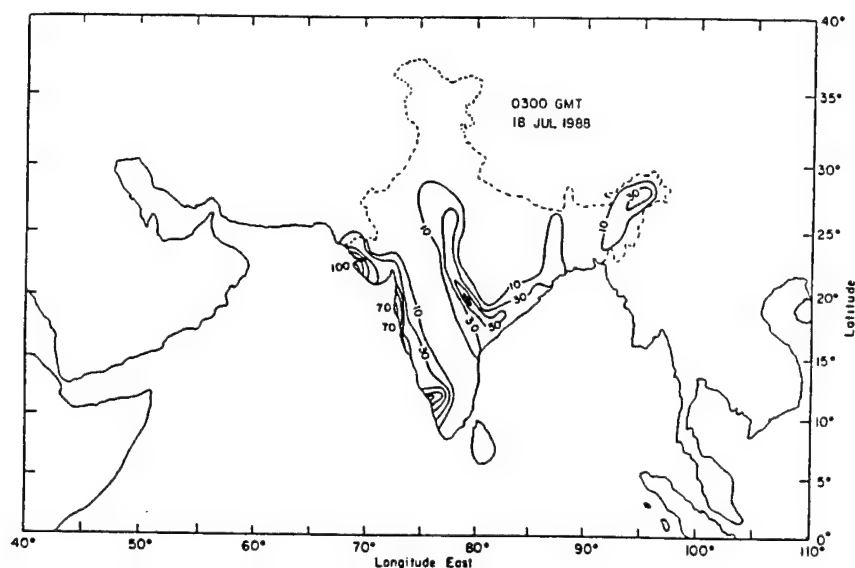


Fig. 8. Observed rainfall rates for a period of 24 h ending at 03 UTC 18 July 1988.

about 1000 m. The vertical profiles of area-averaged TKE budgets for this region are also somewhat similar to that over the Arabian Sea. The mean  $\theta_v$  profile over this region indicates that the boundary layer is stable.

#### 4.3. DYNAMICS OF THE MONSOON

Observations indicated that the monsoon was active during July 1988 with large rainfall rates (about 100 to 200 mm d<sup>-1</sup>). Along the west coast of India, observed rainfall was due to the orographic-convective processes while over central India it was due to a monsoon depression. At 12 UTC 16 July 1988, a monsoon depression was located offshore of the east coast of India. During the next 24 h, the monsoon depression made landfall, leading to large rainfall rates of about 100 to 160 mm d<sup>-1</sup> over the central and east coast of India. During the next 24 h, the monsoon depression moved northwest and produced rainfall over this region (Figure 8). For these two days, observations also indicated rainfall rates of about 100–200 mm d<sup>-1</sup> along the west coast of India. Observations indicate that a preferred location of the rainfall maximum is offshore (Ramakrishnan and Gopinatha Rao, 1958; Ramachandran, 1972). There was a considerable spatial and temporal variation of rainfall during the 1979 monsoon season with a maximum rate of ~200 mm d<sup>-1</sup> over the Arabian Sea off the west coast of India (Krishnamurti *et al.*, 1983).

As expected, increased horizontal resolution in the FGM resulted in the prediction of higher rainfall rates than that in the CGM. Also, the spatial distribution of rainfall associated with the monsoon depression is predicted better by the FGM.

For the first day of simulation, the rainfall maximum (not shown) over the Bay of Bengal over the east coast of India was about  $100 \text{ mm d}^{-1}$ , about two times higher than that in the CGM and comparing well with observations. Along the west coast of India, the predicted rainfall was about  $117 \text{ mm d}^{-1}$  with the maximum located just offshore.

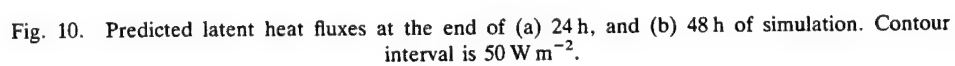
Predicted rainfall for the CGM during the second day of simulation ending at 12 UTC 18 July is shown in Figure 9a. At this time, the monsoon depression is located over northeast India, producing heavy rainfall. Rainfall over this region for the second day is larger compared to that during the first day of simulation. Along the west coast of India, the spatial distribution of rainfall is somewhat similar to that during the previous day for the CGM. However, the rainfall maximum offshore of the west coast of India is again consistent with the observations. Predicted rainfall for the FGM during the second day of simulation ending at 12 UTC 18 July is shown in Figure 9b. As can be seen from the observations (Fig. 8), a rainfall band along the monsoon trough over central India is again well predicted. Along the west coast of India, the predicted rainfall maximum is just offshore with a rate of about  $202 \text{ mm d}^{-1}$ . In general, predicted rainfall and its spatial distribution for the FGM are in better agreement with the observations than those for the CGM. For both days, the model-predicted grid-scale (large-scale) rainfall is much less than the subgrid-scale (convective) rainfall except over the high elevation mountains. Near the Western Ghats region, grid-scale rainfall is negligible, indicating that most of the rainfall over this region is from deep convection.

Latent heat fluxes from the surrounding oceans for the first and the second simulation day are shown in Figures 10a and 10b, respectively. The spatial distribution of latent heat fluxes reflects the low level flow pattern. Latent heat fluxes indicate maximum values offshore of the east coast of Africa and over the central Arabian Sea due to the presence of stronger winds. Latent heat fluxes for the second day of simulation (Figure 10b) indicate similar features as found during the first day but with greater magnitudes. Latent heat fluxes over the southern Indian Ocean are larger than those during the first day. The maximum value of latent heat fluxes over the Arabian Sea was about  $187 \text{ W m}^{-2}$ , comparable to the observed value of  $200 \text{ W m}^{-2}$  for the 1979 monsoon (Holt and Raman, 1985). Predicted latent heat fluxes over the Indian Ocean (closer to the southern boundary) were about  $50$  to  $150 \text{ W m}^{-2}$  and estimated latent heat fluxes (Simon and Desai, 1991) over this region during the MONEX79 indicate similar values ( $50$  to  $200 \text{ W m}^{-2}$ ).

In order to compare predicted wind fields for most of the monsoon region to those in the analyzed data, model predictions for the CGM are considered. Latitude-height section of zonally averaged zonal winds obtained from analysis for the CGM at 12 UTC 18 July is shown in Figure 11a. One of the distinct features in the flow pattern is the presence of a low level wind maximum between  $6.5^\circ$  and  $18.5^\circ \text{ N}$ , indicating the observed location of the Somali jet at  $1.5 \text{ km}$ . The wind







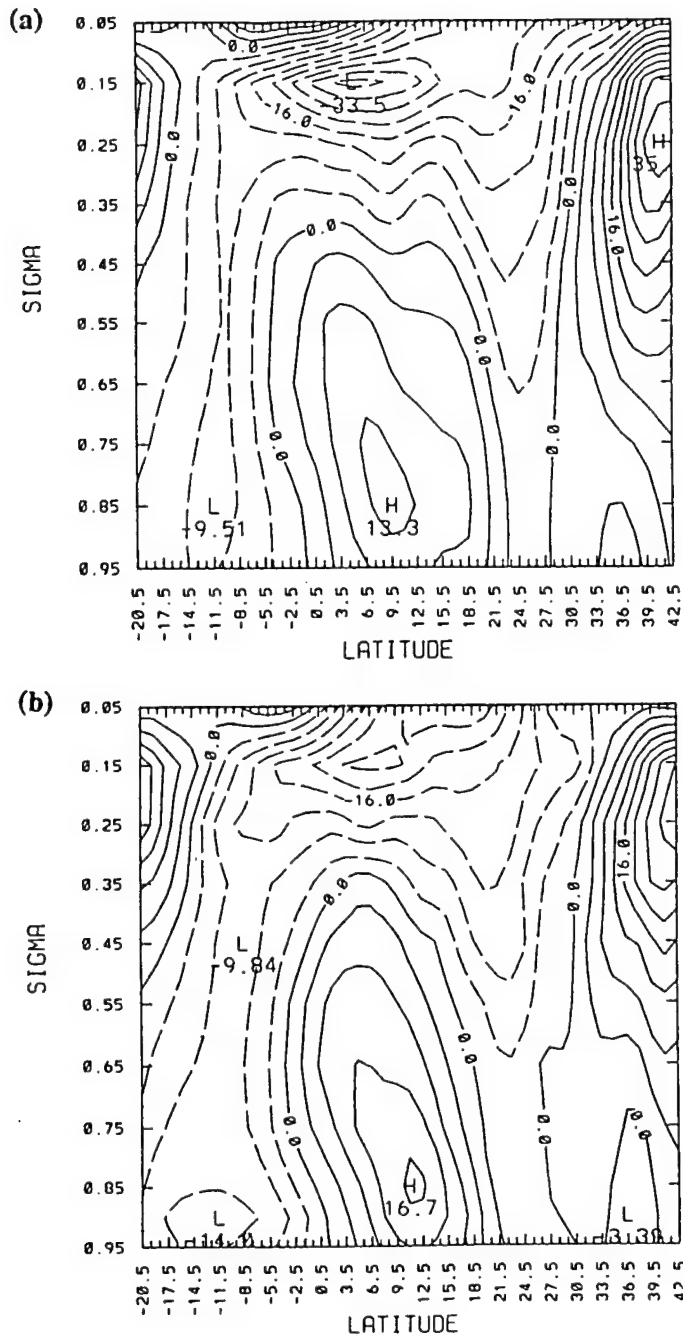


Fig. 11. Latitude-height section of zonally averaged zonal winds for the CGM at 12 UTC 18 July from (a) the analysis, and (b) from the model predictions. Contour interval is 4 m s<sup>-1</sup>.

maximum at upper levels (at  $0.15\sigma$ ) is due to the presence of a tropical easterly jet. It can be seen that there exists a strong vertical wind shear from the lower to the upper troposphere over this region. Wind maxima on the left and right side boundaries of Figure 11a are due to the presence of subtropical westerly jets in the southern and northern hemispheres, respectively. Corresponding latitudinally averaged zonal winds from the model predictions are shown in Figure 11b. The predicted Somali jet is stronger than that in the analysis while the easterly jet is weaker. Subtropical westerly jets over both hemispheres are simulated well.

### 5. Conclusions

A nested grid mesoscale model with a TKE turbulence closure scheme is used to simulate the atmospheric processes during an active monsoon period. As expected, the diurnal variation of boundary-layer height over land is significant whereas over the oceans, the height of the boundary layer does not vary very much. The monsoon depression is reasonably well simulated and the predicted spatial distributions of winds, rainfall, and latent heat fluxes are close to observed ones. The main features associated with the monsoon circulations such as the Somali jet and monsoon depression are well predicted and are in good agreement with the observations. The spatial distribution of the predicted rainfall and the location of a maximum off the west coast of India are in agreement with the observed ones. Prediction of relatively deeper boundary layers over the land compared to observations may be due to the neglect of surface hydrological processes. Inclusion of evaporation from the land surface may improve model predictions. Our future research will involve inclusion of diabatic initialization and the physics related to surface hydrological processes, and atmospheric radiation in the model.

### Acknowledgements

The authors would like to acknowledge assistance provided by Dr. Teddy Holt during the model development. This work was supported in part by the Naval Research Laboratory and by the Division of International Programs, National Science Foundation by Grant INT-9008926. Computer resources were provided by the North Carolina Supercomputing Center, Research Triangle Park, NC.

### References

- Anthes, R. A.: 1977, 'A Cumulus Parameterization Scheme Utilizing a One-Dimensional Cloud Model', *Mon. Wea. Rev.* **105**, 207-286.
- Blackadar, A. K.: 1976, 'Modeling the Nocturnal Boundary Layer', Preprints, *Third Symposium on Atmospheric Turbulence, Diffusion and Air Quality*, Raleigh, Amer. Meteor. Soc., pp. 46-49.
- Businger, J. A.: Wyngaard, J. C., Izumi, Y., and Bradley, E. F., 1971, 'Flux-Profile-Relationship in the Atmospheric Surface Layer', *J. Atmos. Sci.* **28**, 181-189.

- Chang, S. W.: 1979, 'An Efficient Parameterization of Convective and Non-Convective Planetary Boundary Layers for Use in Numerical Models', *J. Appl. Meteorol.* **18**, 1205-1215.
- Chang, S. W.: 1981, 'Test of a Planetary Boundary Layer Parameterization Based on a Generalized Similarity Theory in Tropical Cyclone Models', *Mon. Wea. Rev.* **109**, 843-853.
- Davies, H. C.: 1976, 'A Lateral Boundary Formulation for Multi-Level Prediction Models', *Quart. J. Roy. Meteorol. Soc.* **102**, 405-418.
- Davies, H. C.: 1983, 'Limitations of Some Common Lateral Boundary Schemes Used in Regional NWP Models', *Mon. Wea. Rev.* **111**, 1002-1012.
- Deardorff, J. W.: 1980, 'Stratocumulus-Capped Mixed Layers Derived from a Three-Dimensional Model', *Boundary-Layer Meteorol.* **18**, 495-527.
- Deterling, H. W. and Etling, D.: 1985, 'Application of E-e Turbulence Model to the Atmospheric Boundary Layer', *Boundary-Layer Meteorol.* **33**, 113-133.
- Gerber, H., Chang, S. and Holt, T.: 1989, 'Evolution of a Marine Boundary Layer Jet', *J. Atmos. Sci.* **46**, 1312-1326.
- Gronas, S., Foss, A. and Lystad, M.: 1987, 'Numerical Simulations of Polar Lows in the Norwegian Sea', *Tellus* **39A**, 334-353.
- Grossman, R. L., and Durran, D. R.: 1984, 'Interaction of Low-Level Flow with the Western Ghat Mountains and Offshore Convection in the Summer Monsoon', *Mon. Wea. Rev.* **112**, 652-672.
- Holt, T., and Raman, S.: 1985, 'Aircraft and Ship Observations of the Mean Structure of the Marine Boundary Layer over the Arabian Sea during MONEX 79', *Boundary-Layer Meteorol.* **33**, 259-282.
- Holt, T. and Raman, S.: 1987, 'A Study of Mean Boundary-Layer Structures over the Arabian Sea and the Bay of Bengal During Active and Break Monsoon Periods', *Boundary-Layer Meteorol.* **38**, 73-94.
- Holt, T. and Raman, S.: 1988, 'A Review and Comparative Evaluation of Multilevel Boundary Layer Parameterizations for First-Order and Turbulent Kinetic Energy Closure Schemes', *Reviews Geophys.* **26**, 761-780.
- Holt, T., Chang, S., and Raman, S.: 1990, 'A Numerical Study of the Coastal Cyclogenesis in GALE IOP 2: Sensitivity to PBL Parameterizations', *Mon. Wea. Rev.* **118**, 234-257.
- Huang, C. Y. and Raman, S.: 1989, 'Numerical Simulations of Cold Air Advection over the Appalachian Mountain and the Gulf Stream', *Mon. Wea. Rev.* **118**, 343-362.
- Krishnamurti, T. N., Cocke, S., Pasch, R., and Low-Nam, S.: 1983, 'Precipitation Estimates from Rain gauge and Satellite Observations: Summer MONEX', Dept. of Meteorology, Florida State University, 377 pp.
- Kuo, H. L.: 1974, 'Further Studies of the Parameterization of the Influence of Cumulus Convection on Large-Scale Flow', *J. Atmos. Sci.* **31**, 1232-1240.
- Kusuma, G. R., Raman, R., and Prabhu, A.: 1991, 'Boundary-Layer Heights over the Monsoon Through Region During Active and Break Phases', *Boundary-Layer Meteorol.* **57**, 129-138.
- Madala, R. V., Chang, S. W., Mohanty, U. C., Madan, S. C., Paliwal, R. K., Sarin, V. B., Holt, T., and Raman, S.: 1987, 'Description of the Naval Research Laboratory Limited Area Dynamical Weather Prediction Model', NRL Memo. Rep., No. 5992, Naval Research Laboratory, Washington, D.C., 131 pp.
- Monin, A. S. and Yaglom, A. M.: 1971, *Statistical Fluid Mechanics. Vol. I*, MIT Press, 468-504.
- Raman, S., Templeman, B., Templeman, S., Holt, T., Murthy, A. B., Singh, M. P., Agarwal, P., Nigam, S., Prabhu, A., and Ameenullah, S.: 1990, 'Structure of the Indian Southwesterly Pre-monsoon and Monsoon Boundary Layers: Observations and Numerical Simulation', *Atmos. Env.* **24A**, 723-734.
- Seller, W. D.: 1965, *Physical Climatology*, University of Chicago Press, 53-54.
- Simon, B., and Desai, P. S.: 1991, 'Estimation of Heat Fluxes over Indian Ocean using Satellite Data', *Indo-US Seminar on Parameterization of Sub-grid Scale Processes in Dynamical Models of Medium Range Prediction and Global Climate*, IITM, Pune, India, 193-99.
- Stull, R. B.: 1989, *An Introduction to Boundary Layer Meteorology*, Kluwer Academic Publishers, 666 pp.
- Sun, W. Y. and Hsu, W. R.: 1988, 'Numerical Study of a Cold Air Outbreak over the Ocean', *J. Atmos. Sci.* **45**, 1205-1227.
- Yamada, T. and Mellor, G.: 1975, 'A Simulation of Wangara Atmospheric Boundary Layer Data', *J. Atmos. Sci.* **12**, 2309-2329.

## **Appendix I**

### **Numerical Simulation of Orographic-Convective Rainfall with Kuo and Betts-Miller Cumulus Parameterization Schemes**

**Numerical Simulation of Orographic-Convective  
Rainfall with Kuo and Betts-Miller Cumulus  
Parameterization Schemes**

**By Kiran Alapaty, Rangarao V. Madala and Sethu Raman**  
Department of Marine, Earth and Atmospheric Sciences,  
North Carolina State University, Raleigh, N.C. 27695-8208, U.S.A

*(Manuscript received 22 March 1993, in revised form 13 December 1993)*

Journal of the Meteorological Society of Japan  
Vol. 72, No. 1  
Meteorological Society of Japan



## Numerical Simulation of Orographic-Convective Rainfall with Kuo and Betts-Miller Cumulus Parameterization Schemes

By Kiran Alapaty, Rangarao V. Madala<sup>1</sup> and Sethu Raman

*Department of Marine, Earth and Atmospheric Sciences, North Carolina State University,  
Raleigh, N.C. 27695-8208, U.S.A.*

*(Manuscript received 22 March 1993, in revised form 13 December 1993)*

### Abstract

Two different cumulus parameterization schemes, one developed by Kuo and the other by Betts-Miller, are used to simulate the orographic-convective rainfall associated with the Western Ghats for two days during which monsoon rainfall was moderate to heavy. A ten-layer primitive equation limited area nested grid model is used to perform numerical simulations. It is found that predicted rainfall near the Western Ghats with the Kuo scheme agrees well with the observations. With the Betts-Miller scheme, model failed to predict rainfall over this region.

To find out uncertainties in the adjustment parameters used in the Betts-Miller scheme, five sensitivity experiments are performed. Different values are assigned to the two adjustment parameters, namely the relaxation time scale and the saturation pressure departure, in each of the sensitivity experiments. Results from these sensitivity studies indicate that specification of relaxation time scale depends on the model horizontal resolution. Relaxation time scale needs to be smaller as the model horizontal resolution increases. Also, rainfall predictions are less sensitive to different values of relaxation time scales than those for the saturation pressure departure. Variations in the prescribed thermodynamic reference profiles caused by small prescribed changes in the values of saturation pressure departure led to improvements in the rainfall predictions. It was also found that there exists a lower limit on the values of relaxation time scales and saturation pressure departures for the monsoon region beyond which predicted rainfall rates do not show further improvement.

### 1. Introduction

Cumulus convection is an important physical process that influences the dynamic and thermodynamic state of the tropical atmosphere. It is included in numerical models either explicitly or in a parameterized form depending on the model horizontal grid resolution. Since convective elements have a horizontal length scale of the order of 0.1 to 10 km, fine horizontal resolution is required in numerical models for an explicit treatment of the convective processes. On the other hand, parameterization schemes allow us to use coarser grid resolution in numerical simulations. Except the hybrid-closure schemes, cumulus parameterization schemes can be categorized into three groups: the moisture convergence scheme (Kuo, 1965, 1974), the mass-flux type scheme (Arakawa and Schubert, 1974), and the moist convective adjustment scheme (Manabe *et al.*, 1965).

Because of its simplicity and ease of implemen-

tation in numerical models compared to mass-flux type schemes, the Kuo scheme is widely used in several research and operational models. The original Kuo (1965) scheme had a tendency for too much moistening of the atmosphere. A moistening parameter (b) was introduced to correct this tendency (Kuo, 1974). Since a proper choice of b is crucial for estimating convective heating and moistening rates, several studies (*e.g.*, Anthes, 1977; Geleyn, 1985) have been made to estimate this parameter. A semiprognostic study using several versions of the Kuo scheme for the Indian summer monsoon period was done by Das *et al.* (1988). Their results showed that the 1974 Kuo scheme provides considerable improvement in simulating the heating, moistening, and rainfall rates when combined with the moistening parameter proposed by Anthes (1977). They also noticed that the choice of small (almost equal to zero) moistening parameter can cause unrealistic drying of the atmosphere.

Based on observational studies Betts (1982, 1986) proposed a new convective adjustment scheme which includes both deep and shallow convection. The

<sup>1</sup>Present affiliation: Naval Research Laboratory Washington, D.C. 20375, U.S.A.

deep convection scheme is similar to the other moist convective adjustment schemes except that it uses observed quasi-equilibrium thermodynamic profile as a reference state rather than a moist adiabat. Baik *et al.* (1990a and b) incorporated the Betts-Miller scheme in an axisymmetric tropical cyclone model and showed that the scheme can simulate developing, rapidly intensifying, and mature stages of a tropical cyclone starting from a weak initial vortex. Their results indicated that simulated idealized tropical cyclone is sensitive to the saturation pressure departure, an adjustment parameter in the Betts-Miller scheme. In the present study, we will use a version of the Betts-Miller scheme similar to that used by Baik *et al.* (1990a).

Junker and Hoke (1990) compared performances of the 1965 Kuo scheme and the Betts-Miller scheme in predicting rainfall during winter season over the southern United States with the NMC (National Meteorological Center) nested grid model. The Betts-Miller scheme gave favorable precipitation scores, but it showed the tendency for the mid-latitude cyclones to overdeepen. Puri and Miller (1990) studied the sensitivity of the cumulus parameterization schemes to the structure of four tropical cyclones observed during the AMEX (Australian Monsoon Experiment). Their results showed better vertical consistency when the Betts-Miller scheme is used in comparison to the Kuo scheme. Both the analyses and forecasts showed considerable sensitivity to the Betts-Miller scheme by generating more intense cyclonic systems as compared to the Kuo scheme. Their result is somewhat consistent with that of Junker and Hoke (1990). The Betts-Miller scheme has been used in the past either to simulate observed tropical or mid-latitude cyclones with a coarse horizontal resolution ( $>80$  km). It will be of interest to study the performance of the Betts-Miller scheme in simulating the orographic-convective precipitation in a model with a finer resolution. Simulation of the orographic-convective precipitation associated with the Western Ghats, a mountain range of about 1 km high along the west coast of the Indian peninsula, will be the subject of this paper.

During the southwest monsoon season (June to September), west coast of India is one of the areas where heavy rainfall rates are observed very frequently. This region is of particular interest because (i) lower level westerlies approach the Western Ghats almost at right angles after traveling thousands of kilometers over the warm Indian Ocean and the Arabian Sea, and (ii) convective instability, which can trigger deep convection giving rise to convective rainfall, exists. These mountains running parallel to the west coast are located about 50 km inland. Figure 1 shows the domain of simulation in the Coarse-Grid Mesh (CGM) and the Fine-Grid Mesh (FGM), the latter being located over India and

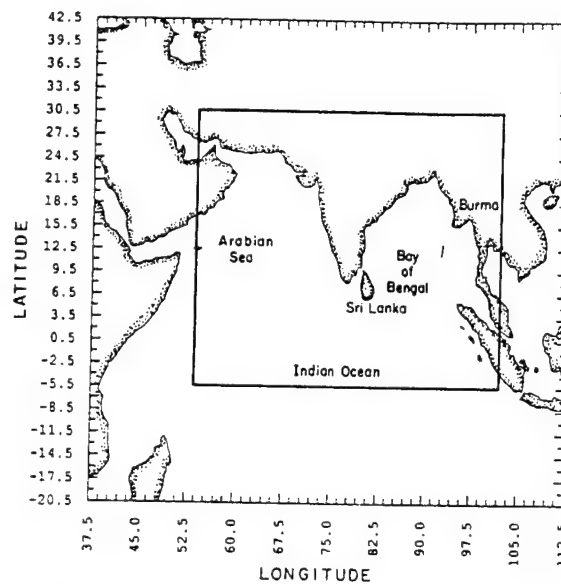


Fig. 1. The model domain of numerical simulation in the Coarse-Grid Mesh (CGM) and the Fine-Grid Mesh (FGM).

the surrounding oceans.

An analytical study of Smith and Lin (1983) using a steady-state linear model concluded that in the absence of convective instability the dynamic forcing by the Western Ghats is insufficient to produce the observed rainfall rates. Utilizing the aircraft observations over the Arabian Sea and using a nonlinear mountain-flow interaction model, Grossman and Durran (1984) concluded that the Western Ghats are responsible for offshore convection. The lifting predicted by a model was applied to mean dropwindsonde soundings for the days with and without offshore convection and it was found that spells in the rainfall can be attributed to the cooler surface layer and the dry layer above the boundary layer which might have originated from the Arabian desert. In a numerical study using the PSU/NCAR mesoscale model Vukicevic and Errico (1990) found that topography has an important role in the predictability of the mesoscale and synoptic-scale circulations. So, it is important to represent mountains realistically in three dimensional numerical simulation studies to capture their important role. Using a cloud model, Ogura and Yoshizaki (1988) showed that the fluxes of sensible heat and moisture from the ocean and vertical wind shear are two important factors that decide the intensity and location of the rainfall near the Western Ghats. An observational study of cloud diameter and height ratios by LeMone (1989) also shows that vertical shear of the horizontal wind may enhance convective precipitation. This is in agreement with a numerical study of Ogura and Yoshizaki (1988) indicating the importance of wind shear in

the vertical near the Western Ghats.

The above studies of orographic-convective rainfall are two dimensional and have some limitations. Smith and Lin (1983) specified the heating over the ocean and Grossman and Durran (1984) omitted air-sea interactions, latent heating and wind shear. Even though these studies gave some insight into the physical processes involved, they cannot simulate the observed spatial and temporal variation of rainfall. In order to simulate the observed rainfall rates more realistically, one needs a nonlinear three dimensional model. Such a model should have proper representation of dynamics, thermodynamics, topography and relevant physics.

Significant features of the problem of orographic-convective rainfall near the Western Ghats can be summarized as follows:

- (i) The Western Ghats cause the orographic lifting of the air parcels.
- (ii) Convective instability over this region can lead to deep convection.
- (iii) Moisture flux from the Arabian Sea can contribute to the rainfall.
- (iv) Vertical wind shear can alter the location and the amount of the rainfall.

These processes should be realistically represented to simulate the observed spatial and temporal structure of the orographic-convective rainfall. In addition, the model domain must be sufficiently large to simulate the synoptic-scale circulations.

The paper compares the simulated orographic-convective rainfall near the Western Ghats region using a three dimensional limited area nested grid model with the Kuo and the Betts-Miller cumulus parameterization schemes.

## 2. The model

### 2.1 Governing equations

The present study utilizes a nested grid model developed at the Naval Research Laboratory and North Carolina State University based on the limited area dynamical weather prediction model developed earlier by Madala *et al.* (1987). It is primitive equation model written in pressure-based  $\sigma$ -coordinate system having a one-way interacting nested grid network. The  $\sigma$ -coordinate is defined by  $\sigma = p/p_s$ , where  $p$  is the pressure and  $p_s$  the surface pressure. Various physical processes are included in the model either explicitly or in parameterized form and are discussed below.

### 2.2 Physical processes

The model physics includes latent heat, sensible heat, and momentum exchange between the boundary layer and the underlying surface using the surface layer similarity theory (Businger *et al.*, 1971),

grid-scale precipitation, dry convection, and diffusion processes. Moist convective parameterization schemes used in the model are described in the next subsection. The short and long wave radiative processes are not included in the present model. A second-order diffusion for momentum on  $\sigma$ -surfaces and for heat and water vapor on  $p$ -surfaces is used to account for the cascading of energy into unresolved subgrid-scale waves. If super-saturation exists at any level, the excess moisture is assumed to condense and fall out to the next lower layer and evaporate or continue to fall depending upon the degree of the saturation at that level. The model has a dry convective adjustment procedure to remove dry convective instability that can occur during model integration.

#### 2.2.1 Kuo cumulus parameterization scheme

Kuo's (1965) parameterization scheme accounts for the effects of cumulus convection and resulting changes in the large-scale humidity and temperature fields. The heating ( $Q_T$ ) and moistening ( $Q_q$ ) imparted to the environment by the cumulus clouds is assumed to be proportional to the temperature and specific humidity differences between the environment and the cloud and can be written as (Kuo, 1974)

$$Q_T = \frac{gL(1-b)M_t(T_c - T_g)}{c_p(p_a - p_t)\langle T_c - T_g \rangle}, \quad (1)$$

$$Q_q = \frac{gbM_t(q_c - q_g)}{(p_a - p_t)\langle q_c - q_g \rangle}, \quad (2)$$

respectively, where  $g$  is the gravitational acceleration,  $L$  the latent heat of evaporation,  $M_t$  the total moisture accession rate per unit horizontal area, and  $p_a$  and  $p_t$  the pressures at the lowest model level and at cloud top, respectively. The quantities in the angular bracket represent the values averaged from  $p = p_t$  to  $p_a$ . The subscripts  $g$  and  $c$  stand for model grid-point value and cloud, respectively.  $T_c$  and  $q_c$  are the temperature and specific humidity on the moist adiabat passing through the lifting condensation level of an air parcel at the lowest model level. The moistening parameter  $b$  is calculated according to the method suggested by Anthes (1977) and is given by

$$b = [1 - \langle RH_g \rangle]^n, \quad (3)$$

where  $\langle RH_g \rangle$  is the mean environmental relative humidity averaged from  $p = p_t$  to  $p = p_a$ . We have used  $n = 3$  for the moisture partitioning in the Eq. (3) consistent with the study on the convective heating rates over the monsoon region (Das *et al.*, 1988).

### 2.2.2 Betts-Miller deep cumulus parameterization scheme

The Betts-Miller convective adjustment scheme assumes that in the presence of cumulus convection, the local thermodynamic structures are constrained by the convection and adjusted towards observed quasi-equilibrium thermodynamic state. The convective heating ( $Q_T$ ) and moistening ( $Q_q$ ) terms are represented by

$$Q_T = \frac{T_r - T_g}{\tau}, \quad (4)$$

$$Q_q = \frac{q_r - q_g}{\tau}, \quad (5)$$

where the subscript  $r$  denotes the reference state and  $g$  the grid-point value before convection and the factor  $\tau$  is the adjustment (or relaxation) time scale. The adjustment time scale represents the lag between the large-scale forcing and the convective response. The Betts-Miller scheme contains shallow convection as well as deep convection. However, since the Kuo scheme deals with the deep convection, only the deep convection part of the Betts-Miller scheme is used for the comparative purpose. The stability weight on the moist adiabat is a measure of instability and determines the slope of the reference profile with respect to the moist adiabat. The saturation pressure departure is a measure of subsaturation, *i.e.*, how far an air parcel must be vertically displaced to become saturated and hence is a measure of relative humidity. The stability weight on the moist adiabat, relaxation time scale and the saturation pressure departure at the lowest model level are specified as 0.8, 7200 sec and -30 hPa, respectively.

### 2.3 Numerical method and nesting technique

The time integration scheme utilized in the present model is a split-explicit method which allows a larger time step by effectively separating various terms in the prognostic equations into parts governing slow-moving Rossby modes and fast-moving gravity modes. For the first and second fast-moving gravity modes smaller time step is used and for all other modes a larger time step is used. The implementation of these varying time steps is the basis for the split-explicit method. The time steps for the slow moving modes in the CGM and the FGM are 300 s and 100 s, respectively, and appropriate smaller time steps satisfying CFL criterion are used for the fast-moving modes. For further details, reader is referred to Madala *et al.* (1987). For the horizontal differencing, a staggered grid network (Arakawa C-grid) is used with  $p_s$ ,  $q$ ,  $T$ ,  $\phi$ ,  $\dot{\sigma}$ , specified at the same horizontal points, and  $u$  and  $v$  interlaced between them where  $p_s$  is the surface pressure,  $q$  the specific humidity,  $T$  the temperature,  $\phi$  the geopotential,  $\dot{\sigma}$  the vertical velocity of  $\sigma$ ,  $u$  the

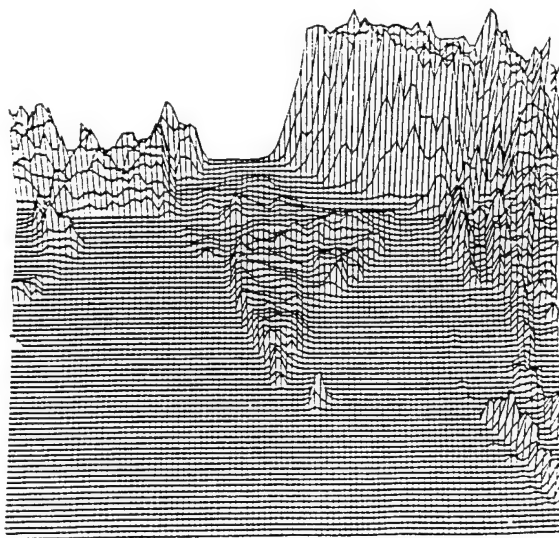


Fig. 2. The topography in the Fine-Grid Mesh (FGM). Large surface elevations over the northern region are the Himalayan mountains and the Western Ghats are located along the west coast of India.

zonal wind velocity, and  $v$  the meridional wind velocity, respectively. The finite difference technique used in the model is second-order accurate. It conserves total energy, mass, and momentum in the absence of the heat and momentum sources.

In the present version of the model, the FGM overlaps one-third of the CGM and the FGM is nested into the CGM such that every third grid point in the FGM is collocated with that in the CGM. The nested grid is positioned so that its boundary rows and columns overlap the CGM interior rows and columns. This nesting configuration enables the Fine-Grid Mesh domain boundary values to be specified by the Coarse-Grid Mesh interior grid points.

### 2.4 Model domain, topography and sea surface temperature

Analyzed data from the European Centre for Medium-Range Weather Forecast (ECMWF) are utilized to specify the initial conditions. Analyzed data are of 1.875° resolution at 14 vertical levels. Bicubic polynomial interpolation technique is used for the horizontal interpolation to model grid points. Horizontal grid resolutions in the CGM and the FGM domains are 1.5° and 0.5°, respectively, and the vertical grid resolution in  $\sigma$ -coordinate is 0.1. The CGM domain covers from 37.5°E to 112.5°E and 20.5°S to 42.5°N and the FGM domain from 54°E to 102°E and 5.5°S to 30.5°N (Fig. 1).

Model topography was obtained from the navy 10' global topography data for 1.5° and 0.5° horizontal resolutions. Figure 2 shows the fine grid topog-

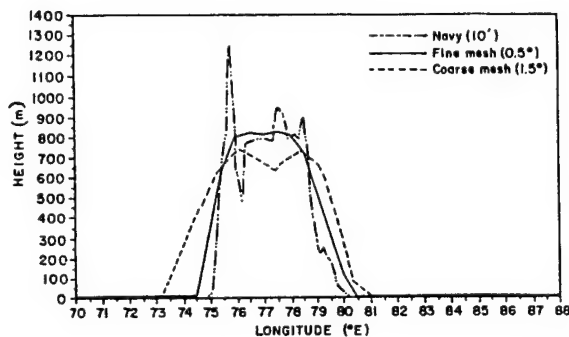


Fig. 3. The cross section of the Western Ghats at 13°N in the CGM and the FGM along with the navy 10' data.

raphy. Large surface elevations over the northern region are the Himalayan mountains. The Western Ghats are located along the west coast of India. The Western Ghats extend about 1600 km in a north-south direction with average heights of 800–900 m although individual peaks have heights exceeding 1200 m. Orographic lifting of the humid monsoon westerlies causes heavy rainfall over this region. The cross sections of the topography at 13°N in the CGM and the FGM along with the actual 10' data are shown in Fig. 3. Comparison of surface elevation data in the CGM and in the FGM domains shows that the mountains are higher and steeper in the FGM domain than in the CGM domain. Peak of the Western Ghats is ~725 m in the CGM domain and ~850 m in the FGM. Peaks are at different locations for different model grid resolutions. The ten minute topography data (Fig. 3) indicates that the Western Ghats peaks are about 100 km away from the west coast. In the coarse-grid domain peaks are located one grid point (~150 km) from the coast and in the fine-grid domain these are located two grid points (~100 km) away from the coast. Model sea surface temperatures (SST) were obtained from the 1° resolution global climatological values based on a 10 year average for the month of July.

#### 2.5 Boundary conditions

Davies scheme (1976, 1983) is employed to provide lateral boundary conditions in the present version of the model. For any independent variable  $a$ , it can be written as

$$a = (1 - \alpha)a_m + \alpha a_b, \quad (6)$$

where the subscript  $m$  represents model-computed values and the subscript  $b$  represents the boundary values obtained either from observations or from coarser version of the model. The merging is done over six grid points at the boundaries of both domains. The  $\alpha$  is defined as a quadratic function of the minimum distance from the lateral boundary in

units of the grid spacing (Gronas *et al.*, 1987). At each time step, the boundary values  $a_b$  for the coarse grid are obtained through a linear interpolation in time from the ECMWF analysis at 24 hour intervals. For the FGM domain, lateral boundary conditions  $a_b$  are obtained through a linear interpolation in time and space from the CGM domain. Also, for consistency, topographic heights at the lateral boundaries of the FGM are specified same as those in the CGM domain. At the model top and bottom, the boundary condition for  $\sigma$  is zero.

#### 2.6 Numerical experiments

Numerical simulations are performed for 48 hours starting at 12 UTC 12 July 1988 using either the Kuo or the Betts-Miller cumulus parameterization scheme. Coastline in both the CGM and the FGM domains are determined by the model topography data. Darker lines in all horizontal space plots, *e.g.*, Figs. 5, 6, etc..., represent the model coastline.

#### 3. Synoptic conditions

During the simulation period, from 12 UTC 12 July to 12 UTC 14 July 1988, monsoon was moderately active over the Indian subcontinent. Figure 4a and 4b show the cumulative rainfall ending at 03 UTC 13 and 14 July 1988, respectively. Due to the orographic lifting and associated convection, heavy rain occurs along the west coast of India. Seaward increase of rainfall indicates that the maximum rainfall associated with the Western Ghats during this period seems to be located offshore. Maximum rainfall just offshore of the west coast of India is about 100 and 140 mm d<sup>-1</sup>, respectively for the two days. Rainfall was also observed over the central regions of India with a maximum of about 100 to 140 mm d<sup>-1</sup> during the period of simulation.

#### 4. Discussion of results

Results from the numerical simulations are compared with the observations in this section. In the following, model results with the Kuo and the Betts-Miller schemes are referred to as the KUO and the BMS, respectively.

Predicted rainfall (mm d<sup>-1</sup>) for the first day of simulation for the CGM domain in the KUO and the BMS are shown in Fig. 5a and 5b, respectively. Rainfall predictions are quite different with the KUO and the BMS. Predicted rainfall along the west coast of India with the KUO is about 20 mm d<sup>-1</sup> while the BMS predicts no rainfall. Observations indicate rainfall about 100 mm d<sup>-1</sup> along the west coast. Both the schemes predict a rainfall of about 20 mm d<sup>-1</sup> over central regions of India, but again much lower than the observations. Model-predicted rainfall for the first day of simulation for the FGM domain in the KUO and the BMS are shown in Fig. 5c and 5d, respectively. Finer horizontal resolution

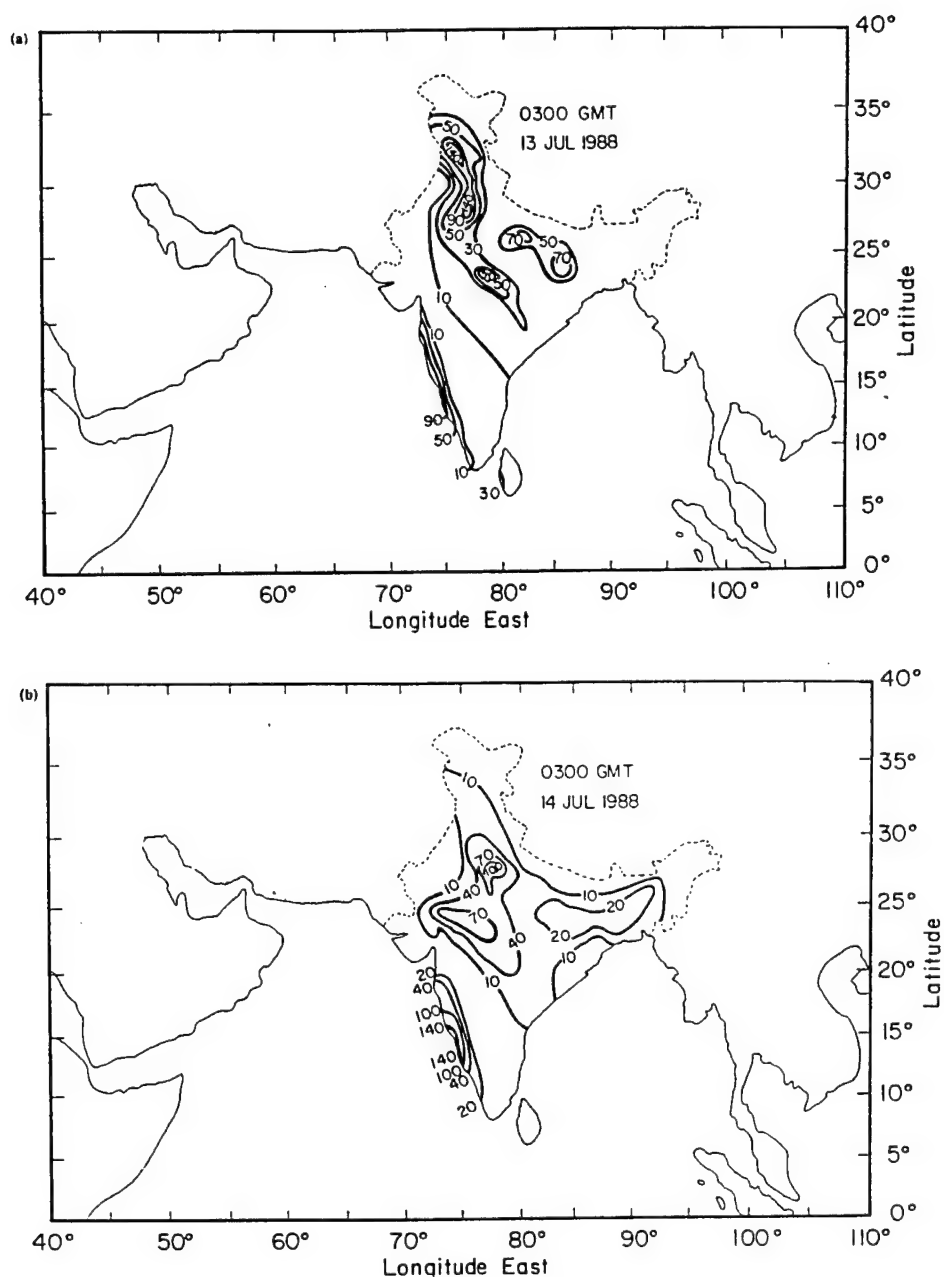


Fig. 4. Accumulated rainfall distribution ending at (a) 03 UTC 13 and (b) 03 UTC 14 July 1988.

in the FGM resulted in higher rainfall rates in both the schemes. In the KUO, predicted rainfall along the west coast of India is closer to the observations with a maximum of about  $73 \text{ mm d}^{-1}$  located offshore. With the Betts-Miller scheme model again fails to predict rainfall along the west coast except about  $10 \text{ mm d}^{-1}$  over a small region offshore (over the Arabian Sea). Over land, rainfall rates predicted by the KUO and the BMS are lower than those in the observations. However, with the Kuo scheme predicted rainfall values are somewhat closer

to the observations than those with the Betts-Miller scheme.

Predicted rainfall for the CGM domain for the second day of simulation in the KUO and the BMS are shown in Fig. 6a and 6b, respectively. About  $140 \text{ mm d}^{-1}$  of rainfall was observed offshore of the west coast of India (Fig. 4b). The spatial distribution of observed rainfall is somewhat similar to the previous day (July 13) but with relatively higher rates along the west coast of India. In the KUO, the model predicts a rainfall maximum of about 48



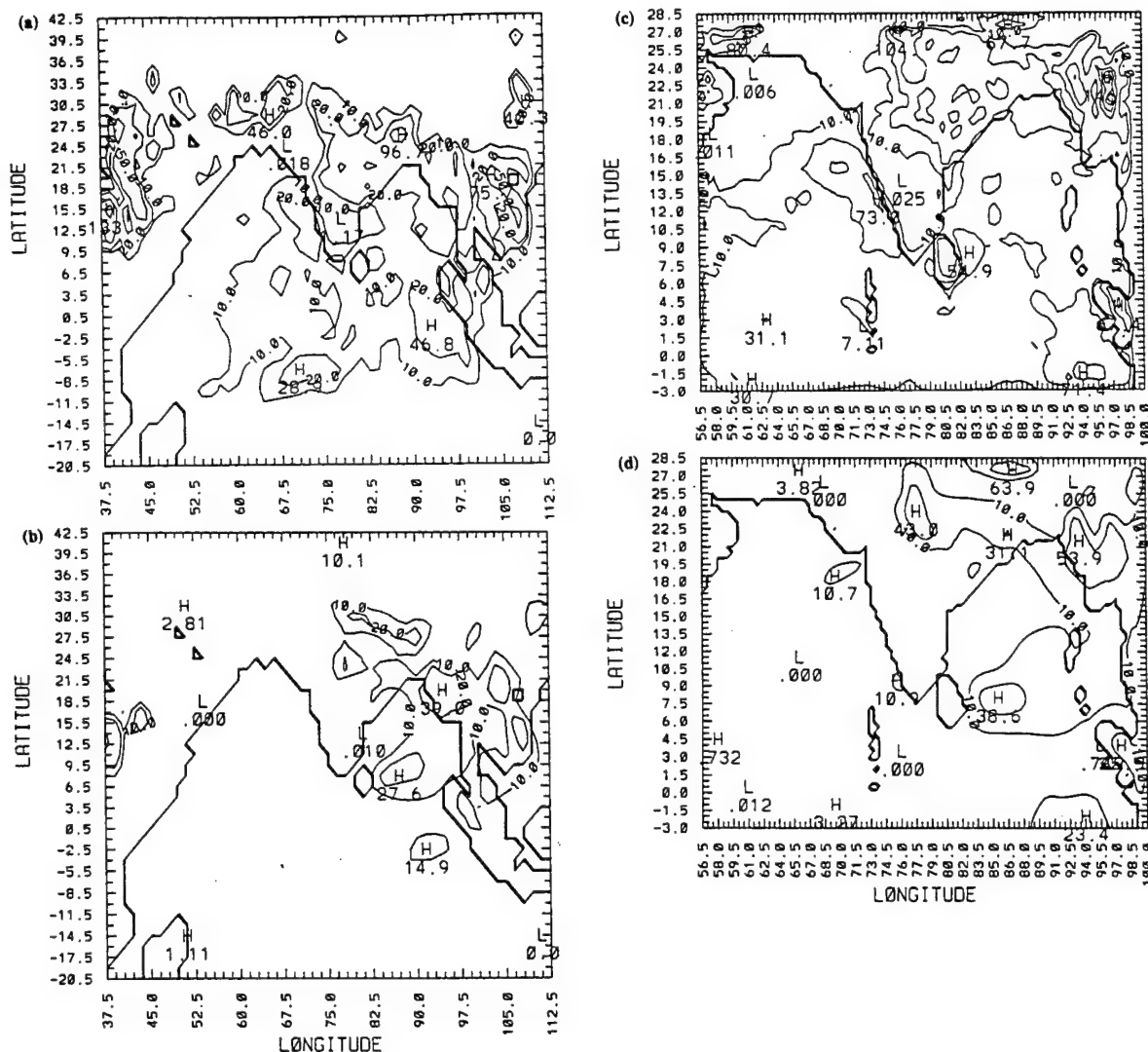


Fig. 5. Predicted rainfall for the CGM domain for a period of 24 hours ending at 12 UTC 13 July 1988 in the (a) KUO and the (b) BMS, respectively. Contour intervals are 10, 20, 50, 80 mm d<sup>-1</sup>. Predicted rainfall for the FGM domain for a period of 24 hours ending at 12 UTC 13 July 1988 in the (c) KUO and the (d) BMS, respectively. Contour intervals are 10, 25, 50, 75, 100 mm d<sup>-1</sup>.

mm d<sup>-1</sup> offshore of the west coast of India, about one-third of the observed value. In the BMS, model predicts a rainfall maximum of about 13 mm d<sup>-1</sup> over the same region, but for a smaller area. In general, over land, predicted rainfall rates with the Kuo scheme are closer to the observations than with the Betts-Miller scheme. Figure 6c and 6d show predicted rainfall for the FGM domain for the second day of simulation in the KUO and the BMS, respectively. In the KUO, predicted rainfall maximum is just offshore of the west coast of India with a maximum of about 144 mm d<sup>-1</sup>, very similar to the observed value. In the BMS, model predicts rainfall maximum just offshore of the west coast of India

with a maximum of about 23 mm d<sup>-1</sup>. In the BMS, model predicts very little rainfall over the Arabian Sea (less than 0.1 mm d<sup>-1</sup>) while the KUO predicts larger rainfall rates. It is difficult to compare the relative performances of the Kuo and the Betts-Miller schemes in data sparse regions such as the oceans. However, over the central regions of India, the KUO predicts rainfall somewhat closer to the observations while the BMS predicts lower rates.

In summary, predicted spatial distributions of rainfall offshore of the west coast of India with the Kuo scheme are in good agreement with the observations for the two days of simulation for the FGM. As expected, predicted rainfall rates are larger for the fine-grid domain as compared to the coarse-grid



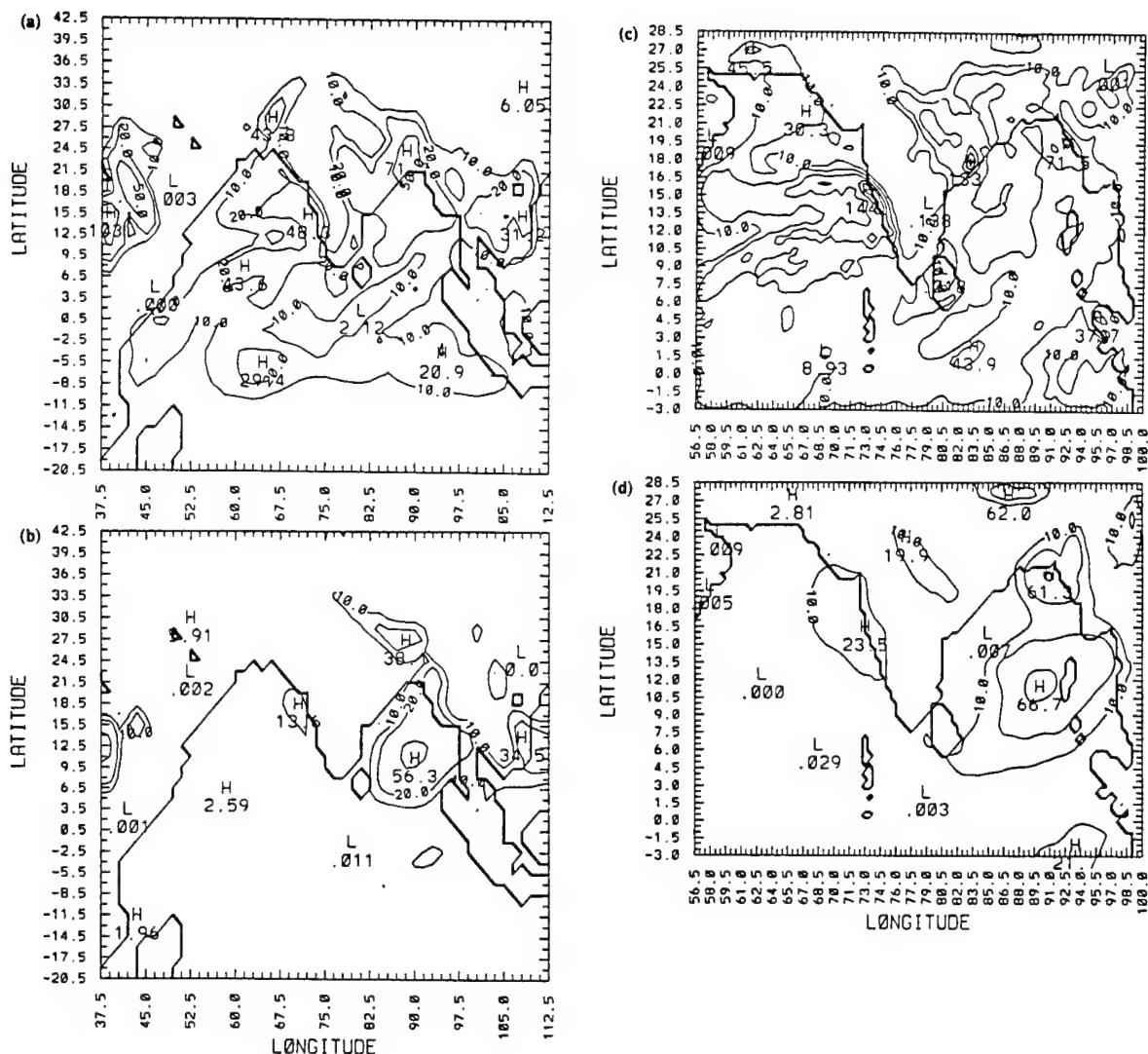


Fig. 6. Predicted rainfall for the CGM domain for a period of 24 hours ending at 12 UTC 14 July 1988 in the (a) KUO and the (b) BMS, respectively. Contour intervals are 10, 20, 50, 80  $\text{mm d}^{-1}$ . Predicted rainfall for the FGM domain for a period of 24 hours ending at 12 UTC 14 July 1988 in the (c) KUO and the (d) BMS, respectively. Contour intervals are 10, 25, 50, 75, 100, 125, 150  $\text{mm d}^{-1}$ .

domain for the cumulus parameterizations. Model fails to predict the observed spatial and temporal distribution of rainfall when the Betts-Miller scheme is used. Convective adjustment parameters in the Betts-Miller scheme used in this study are good only for tropical cyclone simulations (Betts, 1986; Baik *et al.*, 1990; Puri and Miller, 1990). For the monsoon region, particularly for the orographically induced rainfall, validity of these parameters need to be studied. Flow patterns and associated thermodynamic structure of the atmosphere for a tropical cyclone are different from those present in the monsoon circulations. Also, unlike in a tropical cyclone monsoon westerlies are humid only up to about 400 hPa. Analyzed data indicate presence of strong vertical shear from surface to tropopause near the Western Ghats

region and cumulus convection can be influenced by this shear present in the environment. For these reasons, several sensitivity studies are performed with the Betts-Millers scheme.

Sensitivity studies on the simulation of an idealized axisymmetric tropical cyclone (Baik *et al.*, 1990) with the Betts-Miller scheme indicated that their model predictions are very sensitive to two convective adjustment parameters, namely, relaxation time scale and saturation pressure departure. Other convective adjustment parameters in the Betts-Miller scheme such as stability weight on moist adiabat, etc..., were found to have lesser significance on their model predictions. In view of the model failure to predict observed rates of rainfall with the Betts-Miller scheme in the present study,

Table 1. List of sensitivity experiments with the Betts-Miller Scheme

CASE	$\tau$ (s)	$S$ (hPa)	Grid
CASE-1	7200	-30	CGM & FGM
CASE-2	3600	-30	CGM & FGM
CASE-3	3600	-30	CGM
	1200		FGM
CASE-4	1800	-30	CGM
	600		FGM
CASE-5	1800	-40	CGM
	600		FGM
CASE-6	1800	-50	CGM
	600		FGM

sensitivities of rainfall predictions to the two convective adjustment parameters (relaxation time scale and saturation pressure departure) with the Betts-Miller scheme are studied in the following section.

#### 4.2 Sensitivity of rainfall predictions to convective adjustment parameters

Five sensitivity experiments are performed by assigning different values for relaxation time scale ( $\tau$ ) and saturation pressure departure ( $S$ ) parameters. Table 1 shows the values assigned for the  $\tau$  and the  $S$  in each of the sensitivity experiment. As mentioned earlier, the coarse-grid domain is referred to as the CGM and the fine-grid to as the FGM. Simulation results with the Betts-Miller scheme described above are considered as those for the control experiment and is referred to as CASE-1 in the Table 1. In the simulations from CASE-1 to CASE-4 saturation pressure departure is kept the same while the relaxation time scale is decreased from 7200 to 600 s. Note that relaxation time scales are different for the CGM and the FGM from CASE-3 through CASE-6. Betts (1986) found that for a given  $S$  value there was a limit for  $\tau$  in the model used at ECMWF and it also strongly depended on the model horizontal resolution. For this reason we also selected different relaxation time scales for the CGM and the FGM.

The adjustment or relaxation time scale parameter ( $\tau$ ) determines the lag of the convective response to large-scale forcing. As the  $\tau$  values becomes smaller, adjustment of the model atmosphere towards specified thermodynamic reference profile will become more rapid. On the other hand, usage of larger  $\tau$  values will result in increased grid scale rainfall. For Indian monsoon region, observations indicate that most of the rainfall is from the deep cumulus convection while large scale rainfall is smaller. So, for the monsoon region relaxation time scale should be smaller and should be on the order of two hours or less. The saturation pressure departure ( $S$ ) is related to the subsaturation and hence to the equilibrium relative humidity. Though it does not significantly influence the equivalent po-

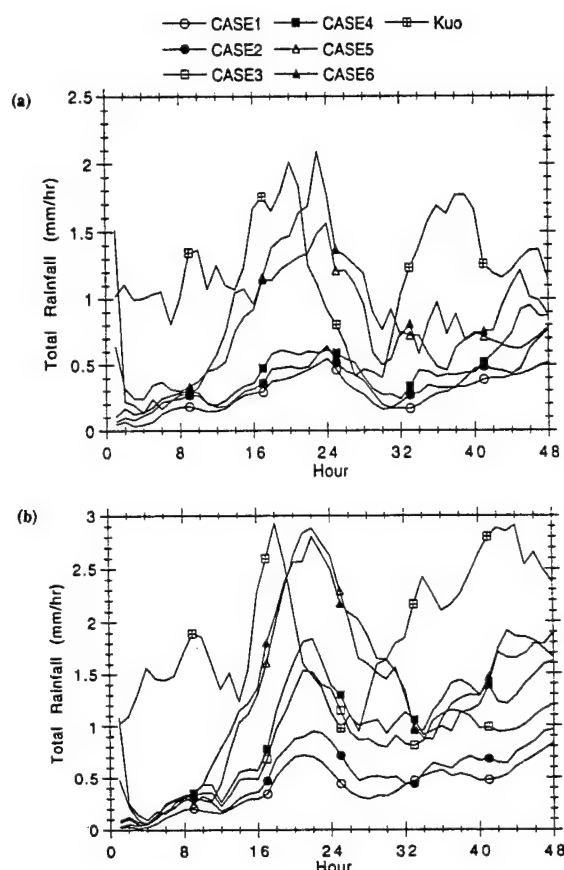


Fig. 7. Temporal variation of the averaged total rainfall for the area 8° to 20°N and 70.5° to 76.5°E for the (a) coarse-grid domain and (b) fine-grid domain in all numerical experiments.

tential temperature but a decrease in  $S$  value will lead to warming and drying of the vertical column in the model. In other words, decrease in  $S$  should lead to an increase in sub-grid scale rainfall.

In order to compare the effects of different values of relaxation time scale and saturation pressure departure on the model predictions, area-average of predicted rainfall over an area, 8° to 20°N and 70.5° to 76.5°E covering most of the region surrounding the Western Ghats is considered. Figure 7a and 7b show temporal variation of area-averaged total rainfall for the above region for the CGM and the FGM domains, respectively. Decrease of the relaxation time scale,  $\tau$ , from 7200 to 1800 s, i.e., from the CASE-1 through CASE-4 had little effect on the predicted total rainfall. In general, there is a slight increase in rainfall rates from the starting time to end of the simulation period (Fig. 7a) for the CGM domain. When the saturation pressure departure,  $S$ , is decreased from -30 to -50 hPa there exists major differences in the predicted rainfall rates, particularly after ninth hour of simulation. Also, during

the first two hours of simulation a decrease in the  $S$  resulted in large rainfall rates and is indicated by a spike in the CASE-5 and CASE-6. This is due to the fact that decrease in the  $S$  value caused reference profiles for temperature and specific humidity to deviate largely from the model soundings over these convectively active regions resulting in large rainfall rates. This indicates some uncertainty in the initial conditions. After the adjustment period of two hours, predicted rainfall rates are similar to those in the other cases. For the monsoon region, variations in the  $S$  have larger impact on the model predictions than variations in the  $\tau$ . Also, rainfall rates in the CASE-6 are almost higher than those in the rest of the simulations.

On the other hand, rainfall predictions for the FGM domain (Fig. 7b) show some differences as compared to those in the CGM domain. Decrease of  $\tau$  from CASE-1 through CASE-4 indicate continuous increase in the predicted rainfall rates. Decrease in the  $S$  values resulted in further increased rainfall rates. Also, differences in the predicted rainfall rates between the CASE-5 and the CASE-6 on average are very small (less than  $0.1 \text{ mm hr}^{-1}$ ) as compared to those in the CGM domain. This result indicates that further decrease in the  $S$  and the  $\tau$  values for the FGM domain may not result in significant increase in the predicted rainfall rates. But, for the CGM domain, further decrease in these adjustment parameters may give slightly increased rainfall rates. Rainfall rates predicted in the CASE-6 for the CGM and the FGM domains on average are higher than those in the rest of the cases. It can be seen that for both the CGM and the FGM domains, rainfall predictions are more sensitive to the values of  $S$  than to the values of  $\tau$ . Predicted rainfall rates with the Kuo scheme show earlier occurrence of rainfall maxima during the first day of simulation while the rainfall maximum with the Betts-Miller scheme lags behind by about four hours. After 30 hours of simulation, rainfall rates predicted with the Kuo scheme are much higher than those with any of the simulations using the Betts-Miller scheme.

Temporal variations of area-averaged evaporation for the region between  $8^\circ$  to  $20^\circ\text{N}$  and  $70.5^\circ$  to  $76.5^\circ\text{E}$  for the CGM and the FGM domains are shown in Fig. 8a and 8b, respectively. Temporal average of the predicted evaporation rate with the Kuo scheme is about  $0.16 \text{ mm hr}^{-1}$  for the CGM while with the Betts-Miller scheme (in all cases) it is relatively higher. This is due to the fact that the Kuo scheme dried upper layers of the atmosphere more than those near cloud base. This resulted in humid layers near to the surface limiting the evaporation rates. On the other hand, results obtained using the Betts-Miller scheme indicated weaker vertical gradients in the convective heating profiles with relatively drier layers near to the surface as compared to those

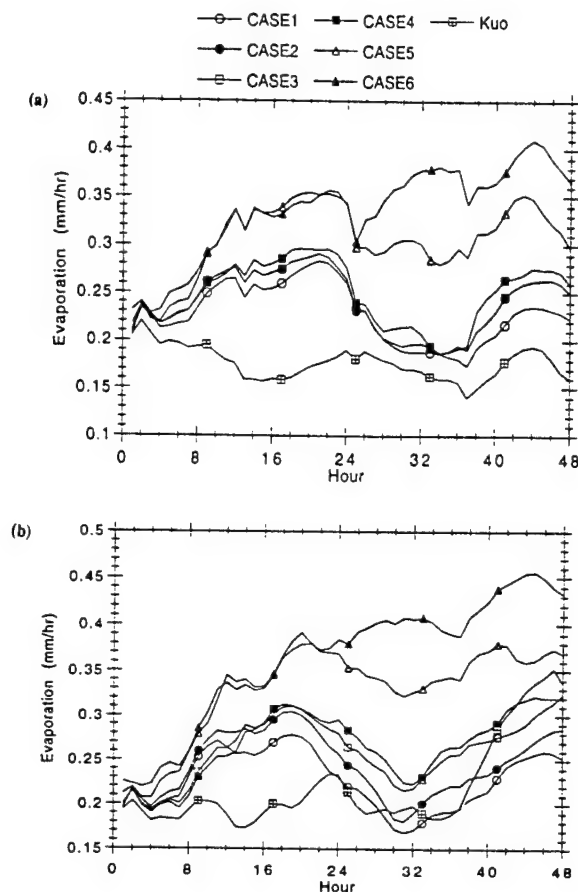


Fig. 8. Temporal variation of the averaged evaporation for the area  $8^\circ$  to  $20^\circ$  and  $70.5^\circ$  to  $76.5^\circ\text{E}$  for the (a) coarse-grid domain and (b) fine-grid domain in all numerical experiments.

present in the KUO. This factor along with the differences in the wind speeds led to larger evaporation rates in the BMS. For the FGM (Fig. 8b) evaporation rates are somewhat similar to those in the CGM but are slightly higher. Also, after 24 h of simulation average evaporation rates in the KUO as well as in the CASE-1 through CASE-4 are somewhat similar for the FGM. Circulation patterns associated with the deep cumulus convection are only marginally different for CASE-1 through CASE-4. Interestingly, decrease in saturation pressure departure values in CASE-5 and CASE-6 caused increased evaporation rates in the CGM and FGM. This is due to the fact that decrease in the  $S$  values triggered intense cumulus convection. Increased convective heating caused stronger circulation patterns over this region leading to stronger surface-level winds, which resulted in increased evaporation.

In order to analyze the effects of different values of the  $S$  and  $\tau$  on the grid scale and sub-grid scale rainfall, area-averages for the region between  $8^\circ$  to

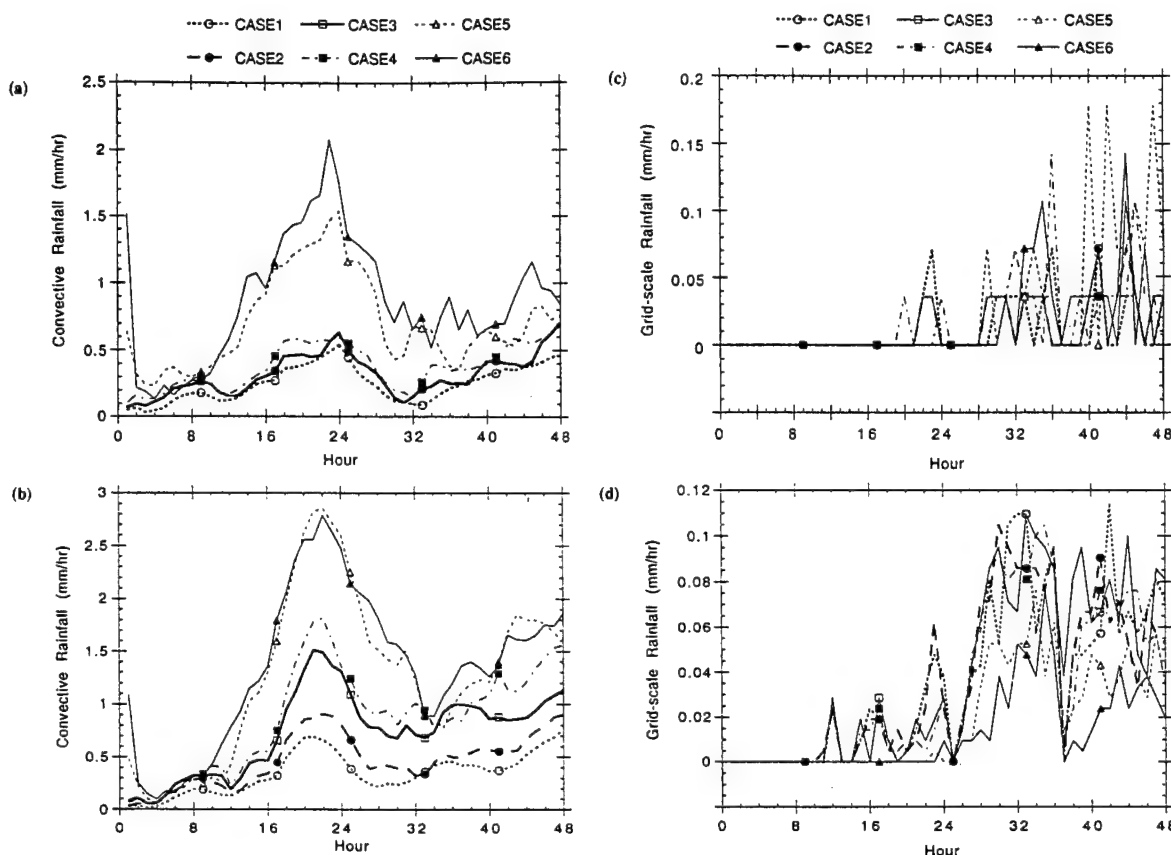


Fig. 9. Temporal variation of the averaged sub-grid scale rainfall for the area  $8^{\circ}$  to  $20^{\circ}\text{N}$  and  $70.5^{\circ}$  to  $76.5^{\circ}\text{E}$  for the (a) coarse-grid domain and (b) fine-grid domain in all numerical experiments. Temporal variation of the averaged grid-scale rainfall for the area  $8^{\circ}$  to  $20^{\circ}\text{N}$  and  $70.5^{\circ}$  to  $76.5^{\circ}\text{E}$  for the (c) coarse-grid domain and (d) fine-grid domain in all numerical experiments.

$20^{\circ}\text{N}$  and  $70.5^{\circ}$  to  $76.5^{\circ}\text{E}$  is considered. Figure 9a and 9b show temporal variation of area-averaged sub-grid scale (parameterized) rainfall for the CGM and the FGM, respectively for all the cases (CASE-1 through CASE-6) using the Betts-Miller scheme. Note that sub-grid scale rainfall rates are very similar to the total rainfall rates (shown in Fig. 7a and 7b). This is expected because most of the rainfall over the monsoon region is from the deep cumulus convection. Temporal variation of area-averaged grid scale rainfall for the CGM and the FGM are shown in Fig. 9c and 9d, respectively. It can be seen that grid scale rainfall rates are about an order of magnitude smaller than the sub-grid scale rainfall rates for the CGM and the FGM domains. Consistently, increased horizontal resolution in the FGM domain resulted in reduced grid scale rainfall rates as compared to those rates in the CGM domain. For the CGM and the FGM domains there is a continuous decrease in grid scale rainfall from CASE-1 to CASE-4. In the CASE-5 the  $S$  value is lower than that in the CASE-1, CASE-2, CASE-3 and CASE-4. Decreased  $S$  value in CASE-5 leads to increased

grid scale rainfall, as a result of stronger vertical circulations, as explained earlier. But further decrease in the  $S$  value in CASE-6 also results in further decrease in the grid scale rainfall.

The construction of reference profiles and the specification of the relaxation time scales are the two major components of the Betts-Miller cumulus parameterization scheme. It can be seen from the above discussed results that model predictions of rainfall depend more strongly on the saturation pressure departure parameter rather than on the relaxation time scale. Also, constructed reference profiles for moisture are based on the saturation pressure departure parameter and hence rainfall predictions are more sensitive to the  $S$  values. These results are consistent with the sensitivity experiments with an axisymmetric tropical cyclone model (Baik *et al.*, 1990b). Their results indicated that the convective adjustment parameters in the Betts-Miller scheme affect the grid-scale precipitation as well as the convective precipitation. Also, precipitation was found to be more sensitive to changes in the saturation pressure departure than in the adjustment time

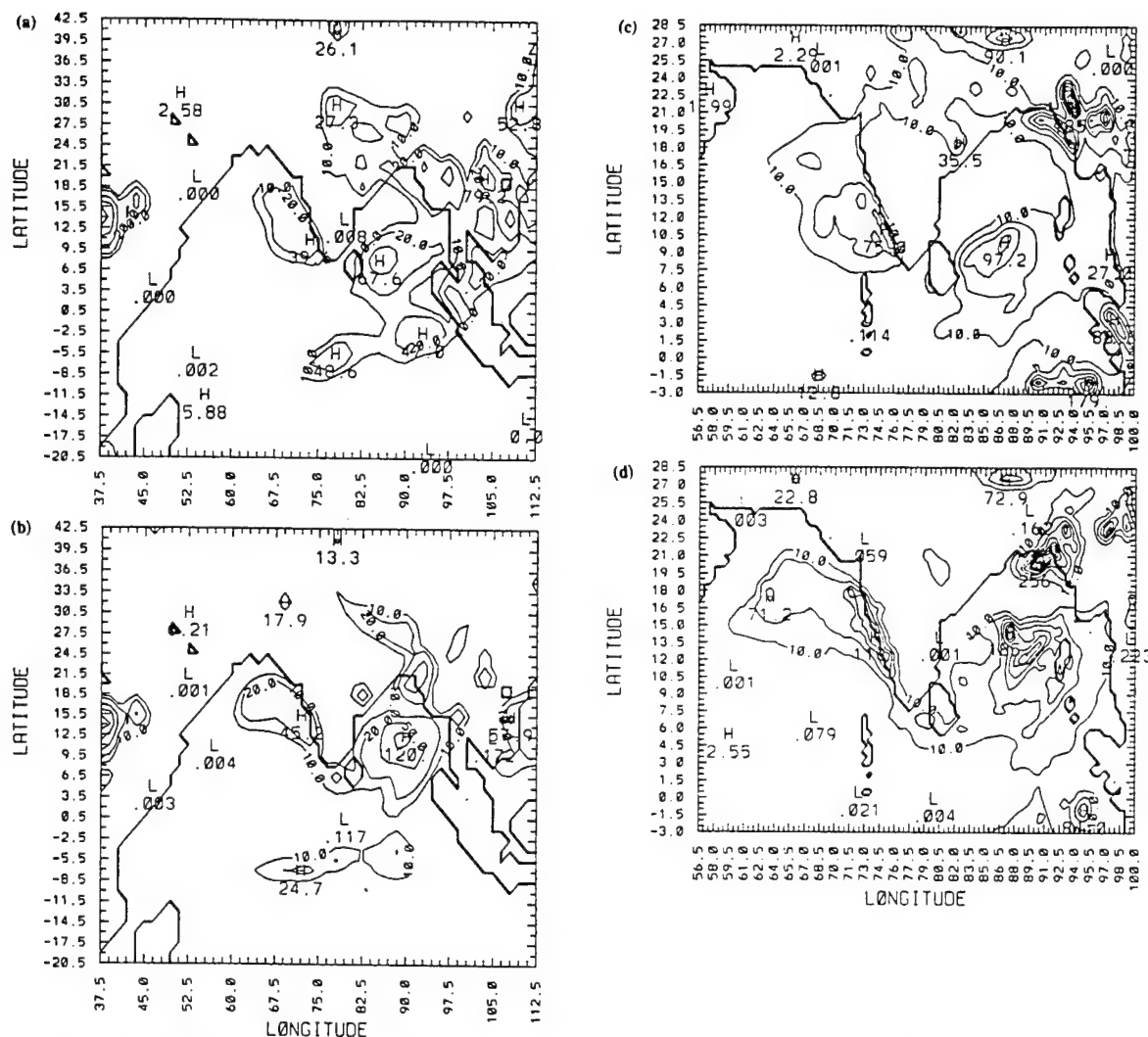


Fig. 10. Predicted rainfall for the CGM domain for a period of 24 hours ending at 12 UTC (a) 13 July and (b) 14 July, 1988 in the BMS for the CASE-6. Contour intervals are 10, 20, 50, 80  $\text{mm d}^{-1}$ . Predicted rainfall for the FGM domain for a period of 24 hours ending at 12 UTC (a) 13 July and (b) 14 July, 1988 in the BMS for the CASE-6. Contour intervals are 10, 25, 50, 75, 100, 150  $\text{mm d}^{-1}$ .

scale.

To evaluate the model prediction of rainfall with the Betts-Miller scheme, results from CASE-6 are compared with the observations and with the Kuo scheme. Figure 10a and 10b show the total rainfall predicted in the CGM for the first day and second day, respectively. For the first day and the second day of simulation predicted rainfall is about 39 and 45  $\text{mm d}^{-1}$  near the Western Ghats with maxima occurring just offshore of the west coast of India. In the control experiment (CASE-1) model did not predict rainfall along the west coast for the entire period of simulation. Also, predicted rainfall over land is higher than that in the control experiment. Predicted rainfall in the CASE-6 with the Betts-Miller scheme is comparable to that with the Kuo scheme (Figs. 5a and 6a) for both the days of simulation.

There exist some differences in the predicted rainfall rates over oceanic regions in the KUO and the BMS. Due to the lack of observational data, rainfall predictions over surrounding oceans could not be verified. Figure 10c and 10d show the total rainfall predicted in the FGM for the first day and second day, respectively for CASE-6. As expected, predicted rainfall rates are higher than those in the CGM and much higher than those in CASE-1. Comparing with the rainfall rates predicted using the Kuo scheme (Figs. 5c and 6c), it can be noticed that in CASE-6 predicted rainfall over land (northwest regions of India) is far lower than those obtained with the Kuo scheme. Though predicted rainfall rates along the west coast of India with the Kuo and the Betts-Miller scheme are comparable with the observations, the Betts-Miller scheme still fails to predict rainfall

Table 2. Comparison of observed and predicted rainfall maxima associated with the Western Ghats.

Description	24 Hours ending 12 UTC 13 July		24 Hours ending 12 UTC 14 July	
	Rate (mm/day)		Rate (mm/day)	
	CGM	FGM	CGM	FGM
Observations	110	110	140	140
Kuo	20	73	48	144
Betts-Miller	0	10	13	23
CASE-1				
CASE-2	0	20	16	33
CASE-3	0	49	16	86
CASE-4	16	69	21	95
CASE-5	35	72	35	111
CASE-6	39	75	45	118

over land regions reasonably. Also, over northern and central Bay of Bengal, large rainfall rates (185 and 256 mm d<sup>-1</sup>) are predicted in the CASE-6 with the Betts-Miller scheme while with the Kuo scheme these rates are negligible (10 to 30 mm d<sup>-1</sup>).

It can be seen that with the Kuo scheme predicted rainfall rates are higher than those with the Betts-Miller scheme while the evaporation rates are higher with the Betts-Miller scheme. Temporal variation of forecast errors (not shown) for the zonally averaged specific humidity indicated that model atmosphere is relatively humid with the Betts-Miller scheme. Also, forecast errors in the circulation patterns near the Western Ghats region are marginally different with both the schemes.

It can be seen that the upper limit for the  $\tau$  can be as high as about 2 hours while the lower limit depends on the model horizontal resolution. To determine the lower limit of  $\tau$  for the fine-grid mesh domain, another experiment with  $\tau$  as 500 s was performed while keeping the  $\tau$  value for the CGM same as that in the CASE-6. It was found that model predictions are very similar to that in the CASE-6 for the FGM except that during 6th and 10th hour of simulation computed sub-grid scale rainfall was negative and is about -0.1 to -0.3 mm hr<sup>-1</sup>. Since negative rainfall was not allowed in the model simulations, it has no effect on the subsequent integration of the model. This negative precipitation is a direct result of the rapid adjustment of the model toward the prescribed thermodynamic profiles and also due to insufficient time given to the large-scale forcing to moisten the model atmosphere. For these reasons, the lower limit on  $\tau$  for the present study of monsoon rainfall simulations can be considered as 600 s for the FGM domain.

Table 2 gives a summary of the model predicted rainfall maxima near the Western Ghats for all of the cases in the Coarse-Grid Mesh and the Fine-Grid

Mesh domains during the two days of simulation using the Kuo and the Betts-Miller cumulus parameterization schemes along with the observed rainfall rates. It can be seen that with the Kuo scheme, predicted rainfall rates for the FGM domain are closer to the observations. With the Betts-Miller scheme, there is a gradual improvement of rainfall predictions from the CASE-1 to the CASE-6. Also, spatial distribution of rainfall showed increased aerial coverage from CASE-1 to the CASE-6. Thus, results from the CASE-6 are the best in terms of comparison to those from the Kuo scheme and the observations.

## 5. Summary and conclusions

A ten-layer primitive equation limited area nested grid model was used to study the performance of the Kuo and the Betts-Miller cumulus parameterization schemes and the role of the horizontal grid resolution in simulating the orographic-convective rainfall associated with the mountains along the west coast of India. Two numerical experiments were performed for 48 hours using the Kuo and the Betts-Miller cumulus parameterization schemes. The initial conditions for the model integrations were obtained from the ECMWF analysis.

As expected, fine-grid resolution (FGM) model results compare better with the observations than those of the coarse-grid resolution (CGM). With the Kuo scheme, predicted rainfall rates along the west coast of India and over other land regions are comparable to those in the observations. With the Betts-Miller scheme, model underpredicted rainfall rates by about an order of magnitude. Previous studies (Betts, 1986; Baik *et al.*, 1990b; Puri and Miller, 1990) indicate that the convective adjustment parameters used in the Betts-Miller scheme are good for simulating a tropical cyclone. To find out the relevancy of values used for these adjustment parameters for the monsoon region, five sensitivity experiments are performed by systematically changing the values.

Relaxation time scale ( $\tau$ ) and saturation pressure departure ( $S$ ) are two key adjustment parameters in the Betts-Miller scheme. The values of  $\tau$  and  $S$  are changed systematically to determine the model sensitivity to these adjustment parameters. Results indicate that a significant decrease in the  $\tau$  values leads to only a minor improvement in rainfall predictions. It was also found that for a give horizontal resolution of the model there exists a lower limit on the  $\tau$  value. Decrease of  $\tau$  for the CGM from 7200 to 1800 s showed negligible improvement in the rainfall predictions. So, further decrease in  $\tau$  for the CGM may not result in improvement in the rainfall predictions. Also, it may not be critically important to find out the lower limit of  $\tau$  for the CGM as the CGM is mainly used to capture the synoptic scale monsoon circulations and to provide lateral bound-



ary conditions to the FGM. The lower limit for  $\tau$  the finer-grid model is found to be about 600 s. Further decrease in the  $\tau$  value in the FGM leads to a reduction in the predicted rainfall rates. This is due to the fact that as the relaxation time scale becomes smaller, adjustment of the model atmosphere towards the prescribed thermodynamic reference profiles becomes more rapid. This rapid adjustment does not allow large scale forcing to moisten the atmosphere sufficiently.

However, predicted rainfall rates are found to be more sensitive to the changes in the saturation pressure departure parameter. A decrease of 20 hPa in the value of saturation pressure departure at the lowest level of the model (level closer to the ground) resulted in a significant improvement in the model predictions of rainfall. It is found that major improvement occurs when  $S$  is decreased from  $-30$  to  $-40$  hPa. Further decrease in the  $S$  value to  $-50$  hPa leads to only slight changes in the rainfall rates. Also, spatial distribution of rainfall with  $S = -50$  hPa is similar to those obtained with  $S = -40$  hPa but with a slight increase (by about  $7 \text{ mm d}^{-1}$ ) in the maximum near the Western Ghats. This result suggests that further decrease of  $S$  value may not result in the improvement of rainfall predictions. Also, further decrease in the  $S$  value may result in unrealistic rainfall predictions during early hours of simulation. Thus, for the monsoon conditions present during the simulation period,  $S = -50$  hPa appears to give better rainfall rates comparable to observations near the Western Ghats region.

Though predicted rainfall rates with the Kuo scheme are closer to the observations near the Western Ghats region, some differences do exist between model prediction and observed rainfall rates over northwest regions of India. With the Betts-Miller scheme these differences are very large over land regions with the exception to the Western Ghats. Also, predicted rainfall rates over surrounding oceanic regions (Bay of Bengal, Indian Ocean and Arabian Sea) differ significantly with the Kuo and the Betts-Miller schemes. Performance comparison of these two schemes over the oceans could not be made due to lack of observations.

Though this is a single case study, it highlights the role of key adjustment parameters in the Betts-Miller scheme and suggests suitable values for the monsoon region. Increased model vertical resolution with better boundary layer physics, inclusion of shallow convection in both the Kuo and the Betts-Miller schemes and a diabatic initialization scheme to initialize the data among other improvements will be necessary to improve the model predictions over land regions.

#### Acknowledgments

The authors would like to acknowledge Dr.

U.C. Mohanty, National Center for Medium Range Weather Forecast, for his help in providing data and rainfall charts. This work was supported by the Naval Research Laboratory, Washington, D.C. Computer resources were provided by the North Carolina Supercomputing Program, Research Triangle Park, NC.

#### References

- Anthes, R.A., 1977: A cumulus parameterization scheme utilizing a one-dimensional cloud model. *Mon. Wea. Rev.*, **105**, 207-286.
- Arakawa, A. and W.H. Schubert, 1974: Interaction of a cumulus cloud ensemble with the large-scale environment, Part I. *J. Atmos. Sci.*, **31**, 674-701.
- Baik, J.-J., M. DeMaria and S. Raman, 1990a: Tropical cyclone simulations with the Betts convective adjustment scheme. Part I: Model description and control simulation. *Mon. Wea. Rev.*, **118**, 513-528.
- Baik, J.-J., M. DeMaria and S. Raman, 1990b: Tropical cyclone simulations with the Betts convective adjustment scheme. Part II: Sensitivity experiments. *Mon. Wea. Rev.*, **118**, 529-541.
- Betts, A.K., 1982: Saturation point analysis of moist convective overturning. *J. Atmos. Sci.*, **39**, 1484-1505.
- Betts, A.K., 1986: A new convective adjustment scheme. Part I: Observational and theoretical basis. *Quart. J. Roy. Meteor. Soc.*, **112**, 677-691.
- Businger, J.A., J.C. Wyngaard, Y. Izumi and E.F. Bradley, 1971: Flux-profile relationship in the atmospheric surface layer. *J. Atmos. Sci.*, **28**, 181-189.
- Das, S., U.C. Mohanty and O.P. Sharma, 1988: Study of Kuo-type cumulus parameterizations during different epochs of the Asian summer monsoon. *Mon. Wea. Rev.*, **116**, 715-729.
- Davies, H.C., 1976: A lateral boundary formulation for multi-level prediction models. *Quart. J. Roy. Meteor. Soc.*, **102**, 405-418.
- Devies, H.C., 1983: Limitations of some common lateral boundary schemes used in regional NWP models. *Mon. Wea. Rev.*, **111**, 1002-1012.
- Geleyn, J.-F., 1985: On a simple, parameter-free partition between moistening and precipitation in the Kuo scheme. *Mon. Wea. Rev.*, **113**, 405-407.
- Gronas, S., A. Foss and M. Lystad, 1987: Numerical simulations of polar lows in the Norwegian Sea. *Tellus*, **39A**, 334-353.
- Grossman, R.L. and D.R. Durran, 1984: Interaction of low-level flow with the western Ghat Mountains and offshore convection in the summer monsoon. *Mon. Wea. Rev.*, **112**, 652-672.
- Junker, N.W. and J.E. Hoke, 1990: An examination of nested grid model precipitation forecasts in the presence of moderate-to-strong low-level southerly inflow. *Wea. Forecasting*, **5**, 333-344.
- Kuo, H.L., 1965: On the intensification of tropical cyclones through latent heat release by cumulus convection. *J. Atmos. Sci.*, **22**, 40-63.



- Kuo, H.L., 1974: Further studies of the parameterization of the influence of cumulus convection of large-scale flow. *J. Atmos. Sci.*, **31**, 1232-1240.
- LeMone, M.A., 1989: The influence of vertical wind shear on the diameter of cumulus clouds in CCOPE. *Mon. Wea. Rev.*, **117**, 1480-1491.
- Madala, R.V., S.W. Chang, U.C. Mohanty, S.C. Madan, R.K. Raliwal, V.B. Sarin, T. Holt and S. Raman, 1987: Description of the Naval Research Laboratory limited area dynamical weather prediction model. NRL Memo. Rep., No. 5992, Naval Research Laboratory, Washington, D.C., 131 pp.
- Manabe, S., J. Smagorinski and R.F. Stierckler, 1965: Simulated climatology of general circulation model with a hydrological cycle. *Mon. Wea. Rev.*, **93**, 769-798.
- Ogura, Y. and M. Yoshizaki, 1988: Numerical study of orographic-convective precipitation over the eastern Arabian Sea and the Ghat mountains during the summer monsoon. *J. Atmos. Sci.*, **45**, 2097-2122.
- Puri, K. and M.J. Miller, 1990: Sensitivity of ECMWF analyses-forecasts of tropical cyclones to cumulus parameterization. *Mon. Wea. Rev.*, **118**, 1709-1741.
- Smith, R.B. and Y.-L. Lin, 1983: Orographic rain on the western Ghat. *Proc. First Sino-American Workshop on Mountain Meteorology*, E.R. Reiter, Z. Baozhen and Q. Younghu, Eds., 71-94.
- Vukicevic, T. and R.M. Errico, 1990: The influence of artificial and physical factors upon predictability estimates using a complex limited-area model. *Mon. Wea. Rev.*, **118**, 1460-1482.

## Kuo と Betts-Miller の積雲対流パラメタリゼーション・スキームを用いた 地形性の対流性降雨の数値シミュレーション

Kiran Alapaty · Rangarao V. Madala<sup>1</sup> · Sethu Raman

(米国ノースカロライナ州立大学海洋地球大気科学部)

2つの異なる積雲対流パラメタリゼーションである Kuo と Betts-Miller のスキームを用いて、西ゴーツ山脈に関連した地形性の対流性降雨を、モンスーンの雨が並もしくは多かった2日間についてシミュレートする。数値シミュレーションには、プリミティブ方程式による10層狭領域ネステッド格子モデルを用いる。Kuo スキームで予想された西ゴーツ山脈付近の降雨は観測とよく一致しているが、Betts-Miller スキームではこの領域の雨は予想されなかった。

Betts-Miller スキームで用いられた調節パラメータの不確定性を明らかにするために、5つの感度実験を行った。それぞれの実験では、緩和時間と飽和気圧差という2つの調節パラメータに異なる値を与える。感度実験の結果は、緩和時間の与え方がモデルの水平解像度に依存することを示しており、水平解像度が増加するにつれて小さくする必要がある。また雨の予想は、緩和時間の値より飽和気圧差の値に敏感である。飽和気圧差を少し変えることによって基準となる熱力学的なプロファイルが変わり、雨の予想が改善される。モンスーン地域における緩和時間と飽和気圧差の値には、それより小さくしても降水量の予想が改善されないような下限が存在することもわかった。

<sup>1</sup>現在所属：米国海軍研究所

## **Appendix J**

### **Sensitivity of Monsoon Rainfall Predictions to Initialization Procedures**

## Sensitivity of monsoon rainfall predictions to initialization procedures

K. Alapaty<sup>a</sup>, R.V. Madala<sup>b</sup> and S. Raman<sup>a</sup>

<sup>a</sup>*Department of Marine, Earth and Atmospheric Sciences, North Carolina State University, Raleigh, NC 27695, USA*

<sup>b</sup>*Naval Research Laboratory, Washington, D.C. 20375, USA*

(Received November 2, 1992; revised and accepted March 18, 1993)

### ABSTRACT

Prediction of orographic-convective rainfall during an active monsoon period is studied with an adiabatic and a diabatic vertical mode initialization schemes. A nested grid mesoscale model is used to perform two numerical simulations. In the diabatic initialization scheme, vertical distribution of latent heat released in convective clouds is obtained using the Kuo scheme from analyzed rainfall rates. Results indicate that the model predicted significantly higher rainfall rates when the initial conditions are obtained using a diabatic initialization scheme. Also, predicted rainfall rates are persistently higher almost throughout the period of simulation with a considerable increase during the first nine hours of integration when initial conditions are obtained from a diabatic initialization scheme. Use of diabatic initialization scheme lead to the prediction of stronger winds, stronger circulation patterns associated with the cumulus convection and higher latent heat fluxes from surrounding oceans, leading to higher rainfall rates.

### RÉSUMÉ

On étudie la prévision de précipitation orographique convective pendant une période active de mousson à l'aide de schémas avec initialisation en mode vertical adiabatique et diabatique. On utilise un modèle de mésoéchelle à grilles emboîtées afin de réaliser deux simulations numériques. Dans le schéma à initialisation diabatique, la distribution verticale de la chaleur latente libérée dans les nuages convectifs est obtenue à l'aide du schéma de Kuo à partir de l'analyse des taux de précipitation. Les résultats montrent que le modèle prédit des taux de précipitation nettement plus élevés lorsque les conditions initiales sont obtenues par un schéma d'initialisation diabatique. De plus, dans ce cas, les taux prévus de précipitation sont plus élevés pendant pratiquement toute la période de simulation, avec une augmentation considérable dans les neuf premières heures d'intégration. L'utilisation d'un tel schéma conduit à la prévision de vents plus rapides, d'une circulation plus forte associée à la convection nuageuse et d'un flux de chaleur latente plus élevé à partir des océans, le tout conduisant à des taux de précipitation plus forts.

### INTRODUCTION

Short range prediction of rainfall in the regional and global scale models is mainly affected by the inaccuracies in the input data namely, the divergence,

moisture and the mass fields. A numerical study of the effect of initial moisture analysis on the rainfall predictions (Wolcott and Warner, 1981) indicates that the most realistic amounts of rainfall are produced when a saturation constraint was imposed by the use of satellite and surface-based observations. Also, it was found (Wolcott and Warner, 1981) that the cumulus convection in the model sustains only in the presence of proper convergence field in the initialized initial conditions. Using a general circulation model, Mohanty et al. (1986) studied the impact of diabatic heating on the initialization of divergent circulations in the tropics. They also found that the initial large-scale divergent circulations were not retained during the forecast period unless the model was forced to generate a diabatic heating sufficiently similar to the observed heating. Puri (1987) studied the use of tropical diabatic heating information for initial state specification and found that the persistence of dynamical balance during model integrations is strongly dependent on the compatibility between the specified heating during initialization and the heating during the model integration. One of the shortcomings in these studies is the a priori assumption of the magnitude and the vertical distribution of heating rates used in the diabatic initialization schemes. To alleviate this problem, satellite-based data such as infrared and visible imagery data (Turpeinen et al., 1990) or outgoing longwave radiation data (Puri and Miller, 1990) are used to estimate the initial convective heating rates for use in the initialization schemes.

During the monsoon season, the westcoast of India is one of the regions where large rainfall rates are observed. Analyzed rainfall data for the monsoon region (Krishnamurti et al., 1983) indicate maximum rates of about  $200 \text{ mm d}^{-1}$  along the westcoast of India. Though there exists some uncertainty in the analyzed rainfall rates, (pers. commun. with T.N. Krishnamurti), these provide an unique opportunity to study the effects of initialization procedures on a model forecast. The objective of this paper is to study the effects of diabatic and adiabatic initialization procedures on the monsoon rainfall prediction using a nested grid mesoscale model.

#### THE MODEL

A nested grid model developed at the Naval Research Laboratory and North Carolina State University is used for numerical simulations. It is a primitive equation model written in pressure-based terrain-following  $\sigma$ -coordinate system having a one-way interacting nested grid network. Physics included in the model are for convective and nonconvective precipitation, and atmospheric boundary layer processes. Atmospheric radiation is not considered because of the relatively short model integration time (48 h). Convective precipitation is parameterized using modified Kuo scheme (Kuo, 1974; Anthes, 1977). Nonconvective precipitation occurs in the model when super satura-

tion is reached on the resolvable scale. Excess moisture precipitates into lower model layers and evaporates or falls to the surface. A dry convective adjustment scheme, which conserves total static energy, is included in the model above the atmospheric boundary layer to remove superadiabatic lapse rates. There are ten uniform vertical levels in the model and the lowest layer represent the boundary layer. For the horizontal differencing, a staggered grid network (Arakawa C-grid) is used with  $p_s$ ,  $q$ ,  $T$ ,  $\phi$ , and  $\sigma$  specified at the same horizontal points, and  $u$  and  $v$  are interlaced between them, where  $p_s$  is the surface pressure,  $q$  the specific humidity,  $T$  the temperature,  $\phi$  the geopotential,  $\sigma$  the vertical velocity,  $u$  the zonal wind and  $v$  the meridional wind. Horizontal grid resolutions in the coarse-grid mesh (CGM) and the fine-grid mesh (FGM) domains are  $1.5^\circ$  and  $0.5^\circ$ , respectively. Figure 1 shows the simulation domain for the CGM and the FGM. The CGM domain covers from  $37.5^\circ$  E to  $112.5^\circ$  E and  $20.5^\circ$  S to  $42.5^\circ$  N and the FGM domain from  $56.5^\circ$  E to  $100.0^\circ$  E and  $3.0^\circ$  S to  $28.5^\circ$  N. Envelop topography was obtained from the navy  $10'$  global topography data for  $1.5^\circ$  and  $0.5^\circ$  horizontal resolutions. Model sea surface temperatures (SST) were obtained from the  $1^\circ$  resolution global climatological values based on a 10 year average for the month of July. Davies scheme (1976, 1983) is employed to provide lateral boundary conditions. At the model top and bottom, the boundary condition for  $\sigma$  is assumed zero. A split-explicit method is used for the model integrations with

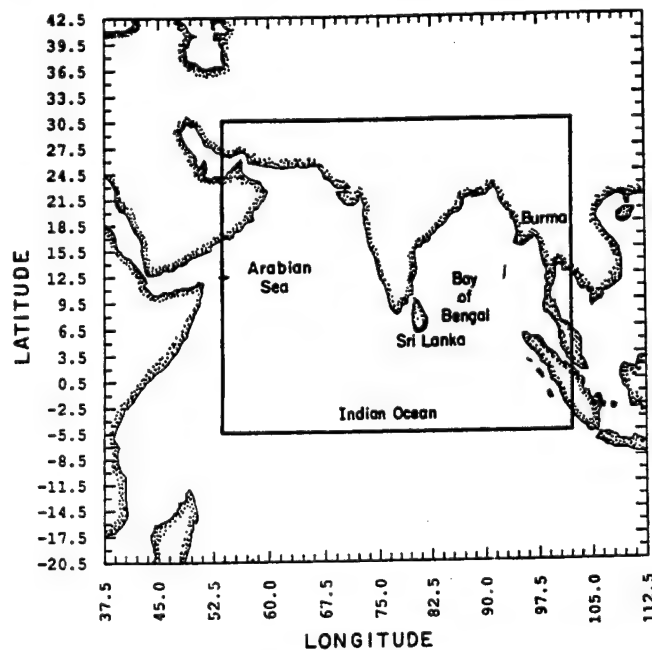


Fig. 1. Model domain of simulation in the coarse grid mesh and the fine grid mesh.

time steps of 300 s and 100 s, in the coarse-grid mesh and the fine-grid mesh domains, respectively. The First GARP Global Experiment (FGGE) level III A data is used to specify the initial conditions.

#### INITIALIZATION PROCEDURE

An adiabatic vertical mode initialization (AVMI) scheme developed at the Naval Research Laboratory was used to develop a diabatic version (DVMI) of the scheme. To incorporate the latent heat forcing into the AVMI scheme,

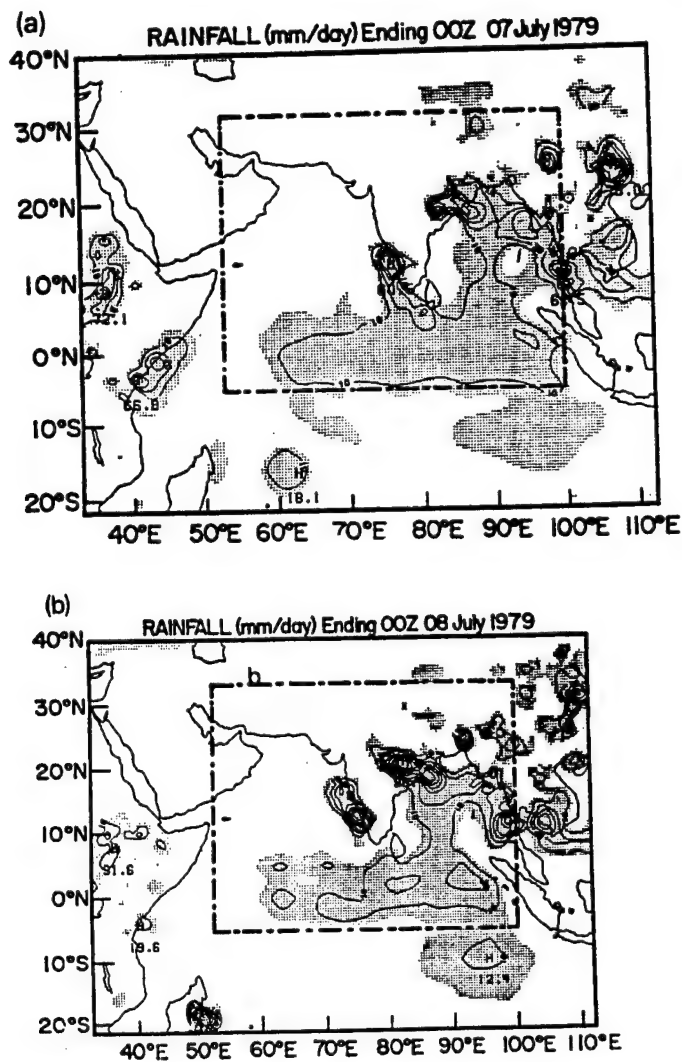


Fig. 2. Analyzed accumulated rainfall distribution by Krishnamurti et al. (1983) for the days (a) 7 and (b) 8 July 1979. Rainfall maximum is located offshore of west coast of India.

a reverse Kuo scheme was used. Figure 2a and b shows the analyzed accumulated rainfall distribution (Krishnamurti et al., 1983) ending at 00 UTC 7 and 8 July 1979, respectively, for the simulation domain. Dashed box indicates the nested domain. Rainfall rates over the land were obtained from more than 3000 rain gages using a successive correction objective analysis procedure. Rainfall rates over the oceanic region were estimated from the satellite brightness. Though the analyzed rainfall rates over the oceanic region are subject to uncertainties, seaward increase of rainfall indicates that the maximum rainfall associated with the Western Ghats during this period was located just offshore. Rainfall over the Bay of Bengal and eastern India was due to the monsoon depression. Since the rainfall received over the simulation domain was almost due to the cumulus convection, large scale rainfall is thus negligible. Since hourly rainfall rates are not readily available, it is assumed that the previous day of the starting time of simulation has a constant rate of rainfall throughout that day. This constant rainfall rate is converted into convective heating using the reverse Kuo scheme for use in the diabatic initialization scheme. Further, model produced convective heating rates and rainfall for the first three hours of simulation are merged with the corresponding rates from the diabatic initialization scheme. A nonlinear weighting factor ( $\alpha$ ) is employed where  $\alpha = 1$  at  $t = 0$  and  $\alpha = 0$  at  $t = 3$  h. The relation is given by:

$$R_m = \alpha R_i + (1 - \alpha) R_c \quad (1)$$

where  $R_i$  is the convective rainfall rate used in the DVMI,  $R_c$  the model-produced convective rainfall rate,  $R_m$  the merged rain rate, and  $\alpha$  is given by:

$$\alpha = 1 - [1 + \sin(\pi t/3) - (\pi/2)]/2 \quad (2)$$

The above relations allow the influence of the initialized heating and rain rates to approach to zero in a smooth manner. This procedure is done only for the diabatic initialization case.

#### SYNOPTIC CONDITIONS AND NUMERICAL EXPERIMENTS

During the simulation period (00 UTC 6 to 00 UTC 8 July 1979), monsoon was active and the winds were steady along the westcoast of India. Western Ghats, the mountain range is located about 100 km inland from the westcoast of India. Low level winds approached the westcoast of India almost perpendicular to the Western Ghats. Orographically lifted air generally triggers convective instability over this region, leading to large rainfall rates. A monsoon depression was located over the Burma Coast at 00 UTC 6 July 1979 and moved westward during the next 48 h.

Two numerical simulations are performed for 48 h starting at 00 UTC 6 July 1979. In the first experiment, initial conditions are balanced using the



adiabatic vertical mode initialization scheme while in the second experiment the diabatic vertical mode initialization scheme is used. The coastline in the simulation domain is determined by the model topography data. Thick and bold contours with bold zeros in all plots represent the coastline. Since the coarse-grid model is primarily used to capture the large scale circulations associated with the monsoon flow and also to provide the boundary conditions for the fine-grid model, we present only the results obtained from the fine-grid model simulations. Since the horizontal resolution of the FGGE data is too coarse ( $2.5^\circ$ ), the monsoon depression can not be represented adequately. The analyzed wind speeds, vorticity and divergence associated with the monsoon depression are very weak in the initial conditions.

## RESULTS AND DISCUSSION

Model-predicted rainfall using adiabatic and diabatic VMI schemes are compared with the observations. We refer the results obtained using the adiabatic VMI scheme to as AB case and those obtained using the diabatic VMI to as DB case. As mentioned before, because of some uncertainty in the analyzed rainfall maxima, only spatial distribution of the predicted rainfall is compared with the observations.

### *Comparison of rainfall rates*

Figure 3a and b shows the predicted accumulated rainfall at the end of the first day of simulation (ending at 00 UTC 7 July) for the AB case and the DB case, respectively. It can be noticed that predicted rainfall in both the cases are somewhat similar. For the DB case, areal coverage of predicted rainfall is larger with higher rainfall maximum than that for the AB case. Predicted maximum in both cases exists offshore of the west coast of India with a rate of 74 and 107 mm  $d^{-1}$ , for the AB case and DB case, respectively. Comparing with the observations (Fig. 2a), the predicted offshore rainfall maximum seems to be higher for both cases and spatial distribution is somewhat similar. As mentioned earlier, estimated rainfall rates over the oceans are subject to errors, only spatial distribution of observed rainfall is compared with the model predictions rather than the reported maximum rates. Predicted rainfall distribution due to the model's monsoon depression (off the Burma coast) and over the Bay of Bengal in the DB case compares better with the observations (Fig. 2a) than with that for the AB case. In both the AB and DB cases, model does not predict rainfall northeast of India (closer to the eastcoast) while observations indicate a rainfall rate of 50 mm  $d^{-1}$ . Predicted circulation patterns associated with the predicted monsoon depression indicated horizontal convergence but cumulus convection did not sustain because of the advection of relatively drier air from the north. Also, vertical cross sec-

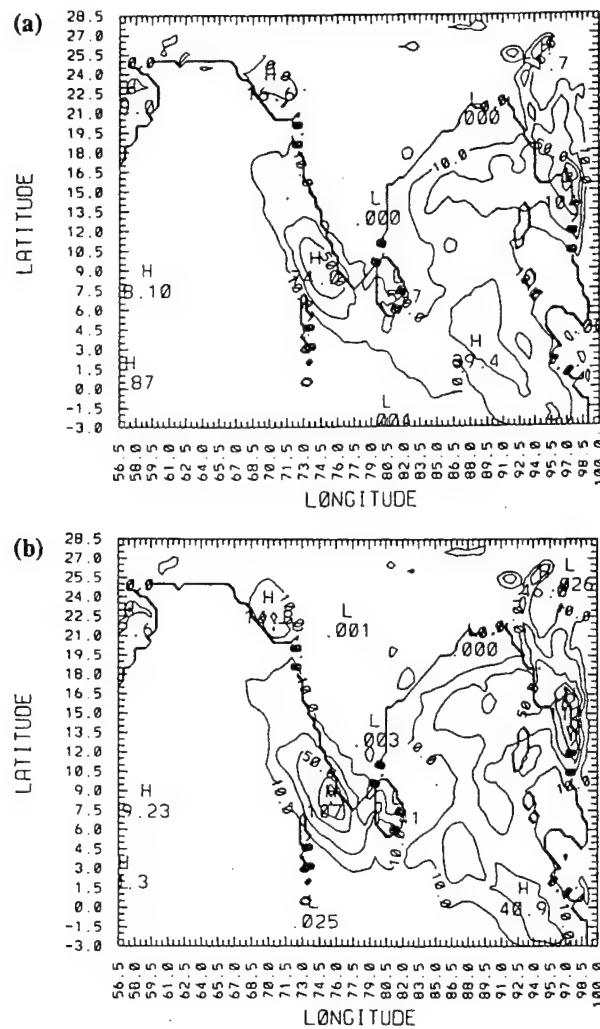


Fig. 3. Predicted rainfall for a period of 24 h ending 00 UTC 7 July (a) in the AB case and (b) in the DB case, respectively. Contour intervals are 10, 25, 50, 75, 100, 125 mm d<sup>-1</sup>.

tions of the relative humidity at different times during the model integration (not shown) indicated low values, particularly over the northern Indian subcontinent. Uncertainties in the moisture filed in the analyzed FGGE data lead to the poor prediction of rainfall associated with the monsoon depression.

Predicted rainfall rates for the second day of simulation for the AB case and the DB case are shown in Fig. 4a and b, respectively. Predicted rainfall over the oceanic regions is higher in the DB case than in the AB case. Again, predicted rainfall offshore of westcoast of India is higher in the DB case (187

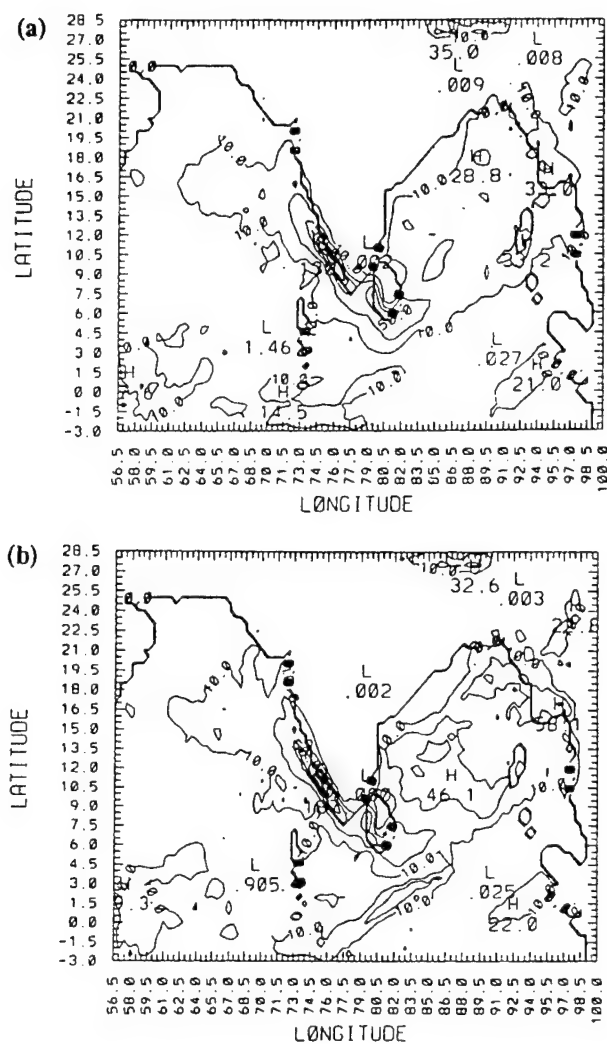


Fig. 4. Predicted rainfall for a period of 24 h ending 00 UTC 8 July (a) in the AB case and (b) in the DB case, respectively. Contour intervals are 10, 25, 50, 75, 100, 125, 150, 175, 200 mm  $d^{-1}$ .

mm  $d^{-1}$ ) than that predicted in the AB case (130 mm  $d^{-1}$ ) while spatial distribution is similar. Also, comparing with the observed rainfall (Fig. 2b) both the AB and DB cases predict higher rainfall rates and spatial distribution of rainfall in both cases is somewhat comparable to that in the observations. Again, similar to the previous day, in both cases the model did not predict rainfall over the land (over foot hills of Western Ghats closer to the west coast, northeast India closer to the east coast) and is due to the presence of drier

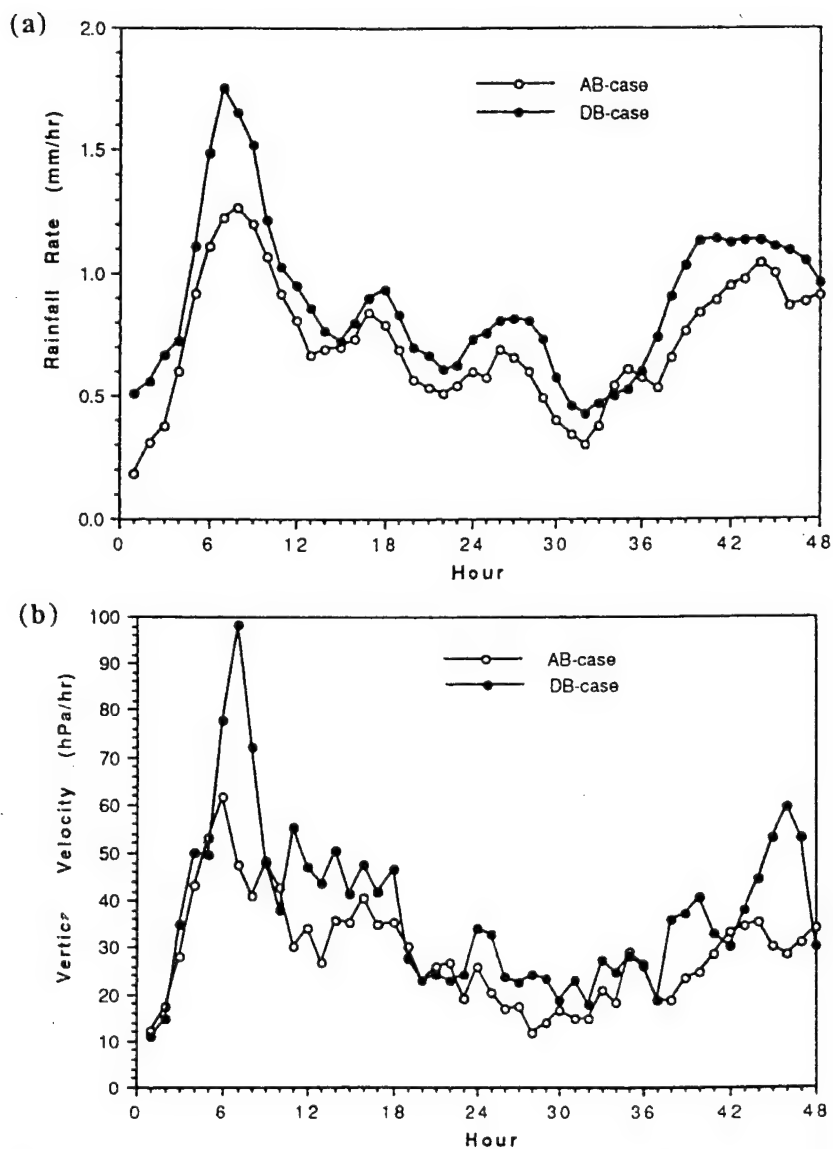


Fig. 5. Temporal variation of (a) area averaged convective rainfall for the area between  $6^{\circ}$  to  $20^{\circ}$  N and  $70.5^{\circ}$  to  $76.5^{\circ}$  E in the AB case and the DB case, respectively, and (b) domain maximum vertical velocity ( $\omega$ ) for the region  $6^{\circ}$  to  $20^{\circ}$  N and  $70.5^{\circ}$  to  $76.5^{\circ}$  E at the end of each hour of simulation.

layers. Essentially, predicted rainfall rates are higher for the DB case for both days of simulation, indicating the influence of the diabatic initialization procedure.

To further investigate the effects of the diabatic initialization on the model forecast, area average of accumulated convective rainfall for an area between  $6^{\circ}$  to  $20^{\circ}$  N and  $70.5^{\circ}$  to  $76.5^{\circ}$  E covering most of the rainfall region near the Western Ghats is considered. Figure 5a shows the temporal variation of area averaged accumulated convective rainfall for the AB case (circles) and for the DB case (dots). During the first nine hours of simulation, predicted area averaged rainfall rates are much higher for the DB case than those in the AB case. This result is due to the enhanced convergence in the lower layers in the DB case where initial conditions are obtained using the diabatic VMI scheme. Also, in the DB case area averaged rainfall is almost persistently higher compared to that in the AB case. This indicates the improvement of model predictions in the DB case where diabatic initialization is used. Signature of the model spinup can be clearly seen in the Fig. 5a where predicted convective rainfall peaks to a maximum at about seven hours starting from the initial time. Also, spinup time required by the model is almost the same for both the simulations. These results are consistent with the results found in other studies mentioned earlier. Also, Turpeinen et al. (1990) found that the diabatic initialization had little impact on the reduction of the spinup time unless the humidity field in the initial conditions was enhanced. Puri and Miller (1990) used the Betts–Miller scheme and rainfall rates derived from the OLR data to initialize the initial moisture field and their results also indicated that reduction in the spinup time occurred only when diabatic initialization and moisture adjustments are performed together.

Figure 5b shows the temporal variation of domain maximum vertical velocity (minimum  $\omega$  velocity) with in the region considered above for the AB and DB cases. Some noise is present since only instantaneous values of vertical velocities are considered. The vertical velocity field also shows similar behavior to that in the rainfall shown in the Fig. 5a, indicating the presence of model spinup during the early hours of numerical integration. This result also supports the argument (Puri and Miller, 1990; Turpeinen et al., 1990) that diabatic initialization may help in increasing the predicted rainfall rates with no reduction of the spinup time associated with the model.

#### *Comparison of surface moisture fluxes and winds*

As mentioned before, the predicted area averaged rainfall and domain maximum vertical velocities for the DB case are almost persistently higher than those in the AB case. Particularly, during the first twelve hours of simulation these are considerably higher. These results indicate that the amount of moisture available for precipitation in the DB case seems to be higher than that in the AB case. To confirm this, accumulated evaporation from the oceans for each day of simulation are considered. Figure 6a and b shows the spatial distribution of latent heat fluxes (averaged for 24 h) for the AB case and the

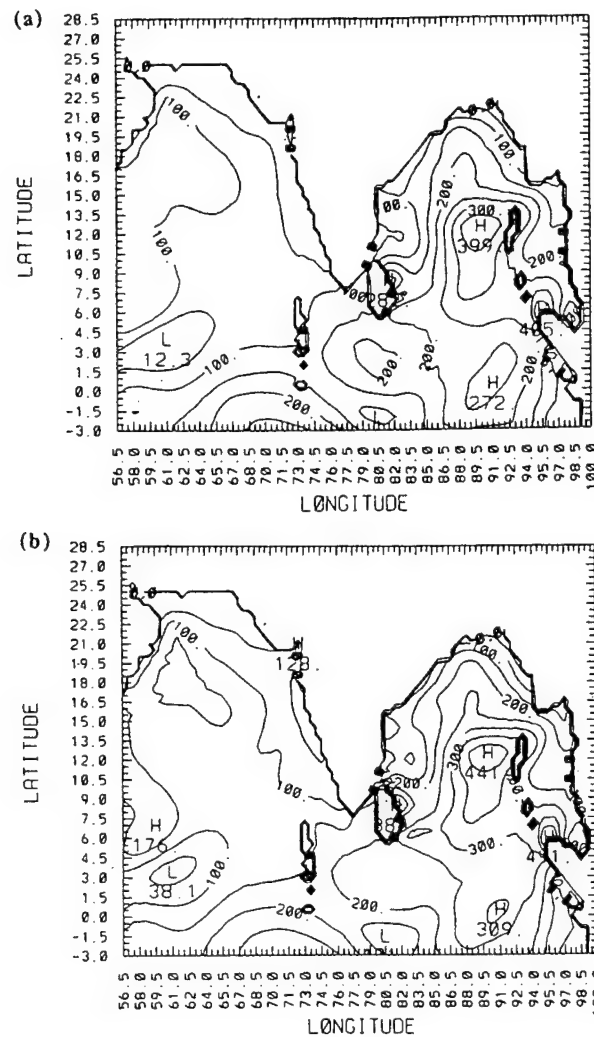


Fig. 6. Spatial distribution of predicted latent heat fluxes at the end of 24 h of simulation (a) in the AB case and (b) in the DB case, respectively. Contour interval is  $50 \text{ W m}^{-2}$ .

DB case, respectively for the first day of simulation. Increase in the latent heat fluxes over the central Arabian sea, Indian Ocean and the central Bay of Bengal can be noticed. In general, there is an increase in latent heat fluxes of about  $40 \text{ W m}^{-2}$  can be seen over these regions.

In the diabatic initialization scheme, analyzed rainfall rates are used in estimating the convective heating rates and its vertical distributions. To that effect an additional term is added in the system of equations where calculation of the divergence is of primary interest. As one would expect, the spatial

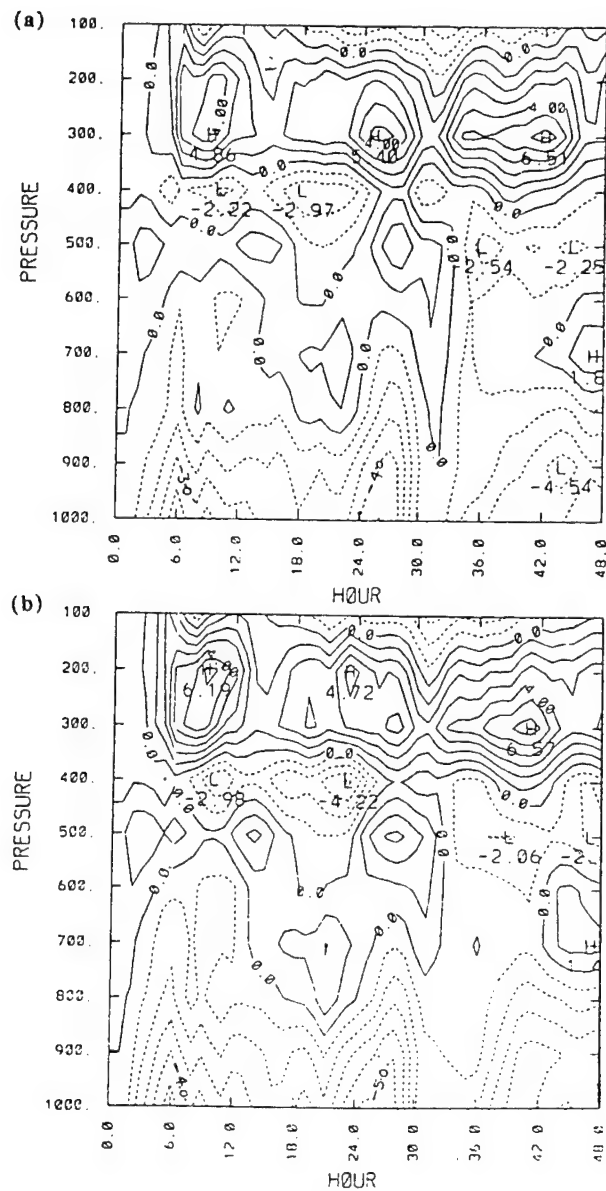


Fig. 7. The height-time section of area averaged divergence for the area between  $6^{\circ}$  to  $20^{\circ}$  N and  $70.5^{\circ}$  to  $76.5^{\circ}$  E (a) in the AB case and (b) in the DB case, respectively. Contour interval is  $1.0 \times 10^{-4} \text{ h}^{-1}$ .

distribution of the wind field in the initial conditions for the DB case is different than that for the AB case. Increased convergence in the lower layers (and corresponding increase in the divergence in the upper layers) over the regions of observed rainfall caused local accelerations of the wind for the DB case. The presence of persistently stronger winds over these regions in the DB case lead to the increase in the evaporation from the oceans. Spatial distri-



bution of winds over the Bay of Bengal and Arabian sea for the convectively active regions in the DB case are slightly stronger (about  $1.5 \text{ m s}^{-1}$ ) than those in the AB case during the period of simulation. The differences in the wind fields lead to the differences in the latent heat fluxes. Vertical velocities in the DB case are higher than in the AB case and also larger areal coverage of vertical velocities in the DB case is consistent with the areal increase in the predicted rainfall shown in Fig. 3b. Comparison of these fields for the second day of simulation also indicate somewhat similar results, in agreement with differences in the predicted rainfall in the AB and the DB cases.

Further, to compare differences in the circulation patterns time-height sections of the area averaged (between  $6^\circ$  to  $20^\circ \text{ N}$  and  $70.5^\circ$  to  $76.5^\circ \text{ E}$ ) divergence field for the AB case and the DB case, respectively are considered and are shown in the Fig. 7a and b. During the first twelve hours of simulation, the area averaged convergence in the lower layers is relatively higher in the DB case than that in the AB case. Consistently, area averaged divergence in the upper layers during this period is also higher in the DB case, indicating stronger vertical circulations. During the rest of the simulation period also convergence in the lower layers is slightly stronger in the DB case than in the AB case.

Model prediction of monsoon depression is similar in both AB and the DB cases and location of the predicted depression (not shown) is in agreement with the observations. Since the analyzed rainfall over the location of monsoon depression at the starting time of integration is very small ( $\sim 10 \text{ mm d}^{-1}$ ), differences of the computed vorticity and divergence associated with the monsoon depression between the AB and the DB cases in the initial conditions are negligible. Also, computed vorticity and divergence maximum associated with the model's monsoon depression in both AB and DB cases are very weak compared to those in the observations. Monsoon depression is not adequately resolved in the initial conditions and this is due to the coarse resolution of the FGGE data. These problems lead to the poor prediction of rainfall associated with the monsoon depression in both the AB and DB cases.

#### CONCLUSIONS

To study the effects of the initialization procedure on the numerical simulation of monsoon rainfall, two different initial states are specified using adiabatic and diabatic vertical mode initialization schemes. A nested grid model is used to perform simulations for the period 00 UTC 6 July to 8 July. Analyzed rainfall rates for the previous day of starting time are utilized to compute the initial convective heating rates using the Kuo scheme. Results indicate that (a) diabatic initialization helps in predicting higher rainfall rates almost throughout the simulation period, (b) differences in the initialization procedures lead to the prediction of relatively stronger winds and circulation patterns associated with the cumulus convection which in turn increased the evaporation from the surrounding oceanic regions and (c) spinup time re-

mains the same whether initial conditions are prepared using adiabatic or diabatic initialization schemes.

These results also suggest that a proper moisture initialization scheme in conjunction with diabatic initialization scheme may help in improving the model rainfall prediction particularly over the land areas. Also, to improve the model forecast of rainfall associated with the monsoon depression, augmentation of data in the initial conditions is required. Our future work is to incorporate a moisture initialization scheme similar to the one used by Puri and Miller (1990) in to the diabatic initialization scheme and to study its impact on the model forecast and the spinup time.

#### ACKNOWLEDGEMENTS

This work was supported in part by the Naval Research Laboratory, Washington, D.C. and in part by the Division of International Programs, National Science Foundation under the grant INT-9008926. Computer resources were provided by the North Carolina Supercomputing Center, Research Triangle Park, NC.

#### REFERENCES

- Anthes, R.A., 1977. A cumulus parameterization scheme utilizing a one-dimensional cloud model. *Mon. Weather Rev.*, 105: 207–286.
- Davies, H.C., 1976. A lateral boundary formulation for multi-level prediction models. *Q. J. R. Meteorol. Soc.*, 102: 405–418.
- Davies, H.C., 1983. Limitations of some common lateral boundary schemes used in regional NWP models. *Mon. Weather Rev.*, 111: 1002–1012.
- Krishnamurti, T.N., Cocke, S., Pasch, R. and Low-Nam, S., 1983. Precipitation estimates from rainguage and satellite observations: Summer MONEX. *Dep. Meteorol., Florida State Univ.*, 377 pp.
- Kuo, H.L., 1974. Further studies of the parameterization of the influence of cumulus convection on large-scale flow. *J. Atmos. Sci.*, 31: 1232–1240.
- Mohanty, U.C., Kasahara, A. and Errico, R., 1986. The impact of diabatic heating on the initialization of divergent circulations in a global forecast model. *J. Meteorol. Soc. Jpn.*, 64(6): 805–817.
- Puri, K. and Miller, M.J., 1990. The use of satellite data in the specification of convective heating for diabatic initialization and moisture adjustment in numerical weather prediction models. *Mon. Weather Rev.*, 118: 67–93.
- Puri, K., 1987. Some experiments on the use of tropical diabatic heating information for initial state specification. *Mon. Weather Rev.*, 115: 1394–1406.
- Turpeinen, O.M., Garand, L., Benoit, R. and Roch, M., 1990. Diabatic initialization of the Canadian regional finite-element (RFE) model using satellite data. Part I: Methodology and application to a winter storm. *Mon. Weather Rev.*, 118: 1381–1395.
- Turpeinen, O.M., 1990. Diabatic initialization of the Canadian regional finite-element (RFE) model using satellite data. Part II: Sensitivity to humidity enhancement, Latent-heating profile and rain rates. *Mon. Weather Rev.*, 118: 1396–1407.
- Wolcott, S.W. and Warner, T.T., 1981. A moisture analysis procedure utilizing surface and satellite data. *Mon. Weather Rev.*, 113: 1989–1998.

## **Appendix K**

### **Application of the Bratseth Scheme for the Analysis of GALE Data Using a Mesoscale Model**

## Application of the Bratseth Scheme for the Analysis of GALE Data Using a Mesoscale Model

KEITH D. SASHEGYI\*

*Science Applications International Corporation, McLean, Virginia*

DEWEY E. HARMS

*Department of Marine, Earth and Atmospheric Sciences, North Carolina State University, Raleigh, North Carolina*

RANGARAO V. MADALA

*Naval Research Laboratory, Washington, D.C.*

SETHU RAMAN

*Department of Marine, Earth and Atmospheric Sciences, North Carolina State University, Raleigh, North Carolina*

(Manuscript received 14 April 1992, in final form 15 February 1993)

### ABSTRACT

The successive correction scheme of Bratseth, which converges to optimum interpolation, is applied for the numerical analysis of data collected during the Genesis of Atlantic Lows Experiment. A first guess for the analysis is provided by a 12-h forecast produced by integrating a limited-area model from a prior coarse operational analysis. Initially, univariate analyses of the mass and wind fields are produced. To achieve the coupling of the mass and wind fields, additional iterations on the geopotential are performed by extrapolating the geopotential to grid points, using improving estimates of the geostrophic wind. This improved geostrophic wind is then used to update the geostrophic component of the initial univariate wind analysis. Use of a background forecast produces much improved mesoscale structures in the analysis. Enhanced gradients of the geopotential and larger wind shears are the result of the coupling of the mass and wind fields, particularly in regions of lower data density. Application of the vertical mode initialization scheme of Bourke and McGregor is used to diagnose the divergent component of the mesoscale circulations produced with the analysis scheme.

### 1. Introduction

During the 1960s and 1970s, the most widely used objective analysis technique in operational data assimilation and forecast systems was the method of successive corrections. This type of analysis was first introduced by Berghörsson and Döös (1955), and a number of versions have been developed by Cressman (1959), Barnes (1973), and others. It is still widely used for the analysis of mesoscale systems in the research community (e.g., Koch et al. 1983; Benjamin and Seaman 1985). However, these successive correction schemes possessed a couple of undesirable attributes. First the analysis always converges to the data,

which should not be the case when errors exist in the data and the background. Second, observations in regions of high data density are given excessive weight relative to observations in areas of low data density.

In the 1980s, emphasis shifted in the operational community toward the more mathematically complex and computationally expensive method of statistical interpolation, better known as optimal interpolation. With optimal interpolation, analysis errors are minimized with respect to the spatial structure of observational and forecast errors. A concise review of objective analysis can be found in Schlatter (1988). Recently, the method of optimum interpolation has been applied with success to operational limited-area modeling systems (DiMego 1988; Benjamin 1989; Mills and Seaman 1990). In these limited-area forecast systems using optimal interpolation the length scales of the correlation functions are usually reduced from those used with global models to provide more detail at the smaller scales (DiMego 1988).

A paper by Bratseth (1986) has caused a recent resurgence of the successive correction method. He in-

---

\* Current affiliation: Naval Research Laboratory, Washington, D.C.

---

Corresponding author address: Dr. Keith Sashegyi, Remote Sensing Physics Branch, Code 7220, Naval Research Laboratory, Washington, D.C. 20375-5351.

introduced a successive correction scheme, in which the solution converges toward the solution obtained by optimal interpolation. His technique alleviates the aforementioned shortcomings of previous successive correction methods by using the correlation function for the forecast errors to derive weights that are reduced in regions of higher data density. Additionally, the Bratseth method requires much less computational expense than do optimal interpolation methods. Therefore, it is very attractive for use for a limited-area forecast system when only limited resources are available. This approach to successive correction methodology is currently being used operationally in a multivariate analysis for the limited-area forecast system at the Norwegian Meteorological Institute (Grønås and Midtbø 1987). After a number of iterations of the scheme, the length scale of the correlation functions is further reduced for subsequent iterations to speed the convergence of the scheme at the smaller scales (Grønås and Midtbø 1987; Seaman 1988). A further advantage of reducing the length scale of the correlation function with increasing iteration is that the geostrophic coupling of the geopotential and the wind can be relaxed for the smaller scales (Bratseth 1986). An algorithm similar to the Bratseth scheme has been applied at the U.K. Meteorological Office to directly insert data into both the global and regional models (Lorenc et al. 1991). With each iteration of the U.K. Meteorological Office scheme, the mass and wind variables are updated in a sequential fashion. To maintain balance in their models, changes to the geostrophic component of the wind are derived from any mass changes; the wind changes are nondivergent, and the divergence during integration is damped.

A simplified multivariate, successive correction objective analysis scheme using the Bratseth method has been developed at the U.S. Naval Research Laboratory (NRL) to analyze high-resolution datasets obtained from such field experiments as the Genesis of Atlantic Lows Experiment (GALE), which occurred from 15 January through 15 March 1986. Our scheme also sequentially couples the analyses of mass and wind but in a manner very different from the U.K. Meteorological Office scheme. During the intensive observing periods (IOPs) of GALE, more frequent upper-air soundings were taken at selected National Weather Service sites over the eastern United States, supplemented by additional sites along the coast, dropsondes deployed from aircraft offshore, and a denser set of surface observations (Dirks et al. 1988; Raman and Riordan 1988).

To better use this data, a prior forecast generated by the NRL limited-area weather prediction model is used, as in the operational limited-area models, to provide a first guess for the analysis scheme. The model consists of a fine grid covering the eastern United States and Atlantic offshore, with a resolution of about 55 km, nested inside a coarse grid covering the continental

United States and western North Atlantic with a resolution of about 170 km. A prior operational analysis is used to provide the initial conditions for integrating the NRL limited-area model. The analysis covers a similar region as the fine grid but at a lower resolution of  $1.5^\circ$  in latitude and longitude. The analysis grid spacing is consistent with the average upper-air station spacing of about 350 km over the eastern United States. By using such a high-resolution model to generate realistic mesoscale features for the first guess, the resulting analysis should be of a higher resolution than would be possible if a first guess were not used. To remove bad data or data inconsistent with the scales resolved by the numerical model, an efficient quality control procedure was implemented in a manner similar to DiMego (1988).

In this paper, we give a general description of our objective analysis method and provide a qualitative evaluation of the scheme using data from the second IOP of GALE. Results with our new analysis scheme are compared to a Barnes (1973) scheme that was used in the past to enhance large-scale operational analyses (Chang et al. 1989; Shi et al. 1991). The vertical-mode initialization scheme of Bourke and McGregor (1983) is used to diagnose the divergent circulations associated with the analyzed mesoscale features and upper-level jet streaks. The interaction of these secondary circulations in the jet streaks can be important for cyclone development (e.g., Uccellini et al. 1984; Uccellini and Kocin 1987). The impact the new scheme has on these derived mesoscale circulations is tested and compared with the earlier Barnes scheme.

## 2. The NRL objective analysis scheme

We use a simplified application of the Bratseth scheme compared to the full multivariate implementation used at the Norwegian Meteorological Institute by Grønås and Midtbø (1987). In our scheme, we first perform univariate analyses of the mass and wind fields using the successive correction approach of Bratseth (1986). We analyze for the deviations from a first-guess field, which is derived from a prior 12-h forecast generated by our limited-area model. To provide the coupling between the wind and mass fields, we use the analyzed wind as an initial estimate of the geostrophic wind for a further iteration on the geopotential. The geostrophic wind is used to extrapolate the geopotential to the gridpoint locations, in a fashion similar to Cressman (1959). In each subsequent iteration, an improved geostrophic wind estimate is then defined by the new geopotential gradient, and not by the original wind as was widely used with the Cressman scheme. This change in the geostrophic wind estimate is then used to update the geostrophic component of the initial univariate wind analysis, as in Kistler and McPherson (1975). Further iterations of the wind analysis are performed to enhance the ageostrophic component of the

wind. The initial univariate temperature analysis can then be corrected for the new geopotential thicknesses.

To test the scheme, a set of surface data and upper-air soundings were obtained for the second IOP of GALE from the GALE Data Center (GDC) at Drexel University (Mercer 1987). The data were provided at 10-mb levels from the surface up to 100 mb, and covered a domain over the eastern United States and western North Atlantic from 115° to 45°W and from 10° to 60°N. A higher density of upper-air soundings and surface data is found in the inner GALE region covering the Carolinas and southern Virginia from the Gulf Stream to the Appalachians. The analysis grid covered the data domain with a resolution of 1.5° in latitude and longitude, extending from 116° to 44°W and from 9° to 61.5°N. The initial conditions for the 12 h forecast of our limited-area model are derived from operational analyses obtained at 12-h intervals on a 2.5° hemispheric grid from the National Meteorological Center (NMC). A quality control of the data prior to the analysis is used to remove any data that are inconsistent with this forecast first guess, are not supported by neighboring observations, or are of a scale too small to be resolved by the analysis scheme. In areas without data, such as over the ocean and around the lateral boundaries of the analysis grid, bogus data are derived from the NMC analysis at that analysis time. The analyses are performed on pressure surfaces every 50 mb from 1000 to 100 mb. In a zone along the lateral boundaries of the analysis grid, the analyzed corrections are further merged with corrections to the first guess derived from the NMC analysis. The resulting corrections are bicubically interpolated to the model horizontal fine grid and added to the first guess for display on pressure surfaces. The components of our analysis scheme are

- (i) limited-area model forecast,
- (ii) data preparation and quality control,
- (iii) univariate analysis of the mass and wind field,
- (iv) enhancement of the geopotential gradient,
- (v) enhancements of the wind field and temperature gradient, and
- (vi) boundary values and interpolation to model grid.

We now briefly describe each of these components in turn. More details can be found in the report by Harms et al. (1992).

#### *a. Limited-area model forecast*

The limited-area model was developed at the Naval Research Laboratory and is detailed in several NRL technical memorandum reports by Madala et al. (1987), Sashegyi and Madala (1990), and Harms et al. (1992). This is a primitive equation model in terrain-following sigma coordinates having a doubly nested grid network. A coarse grid covers a domain including

the continental United States from 40° to 140°W and 10° to 70°N, with a horizontal resolution of 2° longitude (170 km at 40°N)  $\times$  1.5° latitude (166.5 km). The coarse grid provides the lateral boundary conditions for an inner fine grid, which covers a smaller domain including the eastern half of the United States and extending out over the Gulf Stream from 58° to 102°W and 23.5° to 56.5°N with a finer horizontal resolution of 0.67° longitude (56.7 km at 40°N)  $\times$  0.5° latitude (55.5 km). In the vertical, both grids use ten equally spaced sigma levels. Model topography for both grid domains is obtained from the U.S. Navy's 10-min global topographical data. For each model grid point, the average is computed over the grid square with one standard deviation added, and the result smoothed. Climatological mean sea surface temperatures for the month of January of 1° resolution, taken from Reynolds (1982), are interpolated to the model grids. A sea-ice boundary is derived from the U.S. Navy climatological sea-ice boundaries for the months of January and February.

To provide the first guess for the data quality control and analysis we integrate our limited-area forecast model for 12 h starting from a prior NMC analysis. The NMC 2.5° hemispheric analyses are interpolated to the horizontal model grids using Lagrangian cubic polynomial interpolation. The interpolated analyses are then initialized separately on both coarse and fine grids for the first three vertical modes of the numerical model using the vertical mode scheme of Bourke and McGregor (1983), as applied to the NRL model (Sashegyi and Madala 1993). This scheme generates a balanced divergent part of the wind field, while producing only small changes in the geopotential and vorticity. For the coarse grid, lateral boundary values for the model integrations are derived from these initialized NMC analyses by linear interpolating in time.

#### *b. Data preparation and quality control*

An efficient quality control procedure has been developed for use with the analysis scheme, similar to those at operational weather centers. After checking the upper-air soundings for hydrostatic consistency, we smooth the soundings in the vertical and recompute consistent geopotentials. The temperatures and the  $u$  and  $v$  wind components are averaged over 20-mb intervals, weighted by the log of pressure for the temperatures and by the mass for the  $u$  and  $v$  wind components. The humidities, which are more noisy (C. Kreitzberg 1987, personal communication), are smoothed by averaging over 50-mb intervals using the mixing ratios weighted by the mass. Data are retained at 50-mb levels to be more representative of our ten-layer model vertical resolution. For efficiency, the soundings are sorted into 5° latitude-longitude boxes for each pressure level from sea level to 100 mb.

As in the regional analysis at NMC (DiMego 1988),



we perform a "gross" check and a "buddy" check, in which observations with large deviations from the first guess or from neighboring observations are removed. In the gross check, those upper-air observations that differ in magnitude by more than four standard deviations from the first guess are rejected. For sea level pressure a limit of two and a half times the standard deviation is used. Estimates of the standard deviation of the observations from the first-guess forecast are obtained by adding a forecast error growth to the observational error. The values used were slight modifications to those used at operational centers (Dimego 1988; Shaw et al. 1987) and are listed in Table 1. For sea level pressure, an observational error of 1.5 mb is used with forecast error growth of 1.0 mb in 6 h. For the remaining quality control procedures and the analysis, only the deviations of the data from the first guess are retained. As shown by Bratseth (1986), close observations slow the convergence of the iterative scheme. To speed the convergence of the scheme, close observations are replaced by an average "super" observation (superob). To further prevent isolated data from adversely affecting the analysis by aliasing to the larger analysis scales, any remaining isolated observations are also eliminated. In data-sparse regions over the ocean, we use additional bogus soundings, derived from the difference between the first-guess forecast and the NMC 2.5° hemispheric analysis, for the analysis time of interest. To match the resolution of the NMC analysis, we use two bogus soundings spaced  $5/3^\circ$  apart in latitude and longitude in each empty  $5^\circ$  data box in the interior.

### c. Univariate analysis of the mass and wind field

In the first univariate analysis step, sea level pressure, geopotential, temperature, and humidity corrections to the first guess are successively adjusted at each iteration using the Bratseth (1986) scheme. In this scheme estimates of both the interpolated correction and an observation correction are computed using the iterative formulas. For the geopotential corrections, the interpolated value  $\phi_x$  at the grid point  $x$  is given by

$$\phi_x(k+1) = \phi_x(k) + \sum_{j=1}^n \alpha_{xj} [\phi_j^o - \phi_j(k)], \quad (1)$$

while the new estimate of the value of the observation correction is given by

$$\phi_i(k+1) = \phi_i(k) + \sum_{j=1}^n \alpha_{ij} [\phi_j^o - \phi_j(k)], \quad (2)$$

where  $\phi_j^o$  is the value of the observation,  $\phi_x(k)$  and  $\phi_j(k)$  are the interpolated values at the grid point and the estimate of the observation value, respectively, for the  $k$ th iteration. The sum is over all the  $n$  observations. The starting corrections  $\phi_x(1)$  and  $\phi_j(1)$  are zero. The weights, which are dependent on the covariance of the corrections to the first guess, are in each case given by

TABLE 1. Standard deviation of the observational errors and forecast error growth (in parentheses) for a 6-h forecast period.

Pressure (mb)	Height (m)	Temperature ( $^\circ\text{C}$ )	Relative humidity (%)	u, v wind ( $\text{m s}^{-1}$ )
1000	5 (8)	1.8 (0.6)	13 (2)	2.5 (1.1)
950	5 (8)	1.8 (0.6)	13 (2)	2.5 (1.1)
900	5 (8)	1.8 (0.5)	13 (2)	2.5 (1.1)
850	6 (8)	1.5 (0.5)	13 (2)	2.5 (1.1)
800	6 (8)	1.5 (0.4)	13 (2)	2.5 (1.1)
750	6 (8)	1.4 (0.3)	12 (2)	2.5 (1.2)
700	6 (8)	1.3 (0.3)	12 (2)	2.5 (1.2)
650	6 (8)	1.2 (0.3)	12 (3)	3.0 (1.3)
600	7 (9)	1.0 (0.3)	12 (3)	3.0 (1.4)
550	8 (10)	1.0 (0.3)	13 (3)	3.0 (1.5)
500	9 (12)	1.0 (0.3)	13 (4)	3.0 (1.6)
450	10 (14)	1.0 (0.4)	13 (4)	3.5 (1.6)
400	12 (16)	1.0 (0.5)	13 (4)	3.5 (1.7)
350	14 (17)	1.0 (0.5)	15 (4)	4.0 (1.7)
300	14 (18)	1.0 (0.6)	17 (4)	4.0 (1.6)
250	14 (18)	1.5 (0.6)	—	4.0 (1.6)
200	15 (18)	1.8 (0.5)	—	4.0 (1.5)
150	18 (18)	1.8 (0.6)	—	4.0 (1.4)
100	20 (17)	2.0 (0.7)	—	3.5 (1.3)

$$\alpha_{xj} = \frac{\phi_x^i \phi_j^o}{m_j \sigma^2} = \frac{\rho_{xj}}{m_j} \quad (3)$$

$$\alpha_{ij} = \frac{\phi_i^i \phi_j^o}{m_j \sigma^2} = \frac{(\rho_{ij} + \epsilon^2 \delta_{ij})}{m_j}, \quad (4)$$

where the covariances are defined in terms of a correlation function  $\rho$  for the true values  $\phi^i$ ,  $\epsilon^2$  is the ratio of the observation error variance  $\sigma_i^2$  to the first-guess (forecast) error variance  $\sigma^2$ , and  $m_j$  is a "local data density" at the observation location. Here  $\delta_{ij}$  represents the Kronecker delta function, which is defined to be unity for  $i = j$ , and zero otherwise. For the forecast error variance, we use the same variance used in the quality control for the variance of the observations from the first-guess forecast (see Table 1). Further, the data density  $m_i$  at an observation location is defined by

$$m_i = \frac{1}{\sigma^2} \sum_{j=1}^n \phi_i^o \phi_j^o = \sum_{j=1}^n \rho_{ij} + \epsilon^2. \quad (5)$$

With observation errors included, the estimate of observation is not equal to the analyzed value interpolated to the observation location, but it converges rapidly to the value of the observation itself (Bratseth 1986). However, if there is no observation error, the analyzed value and the observation estimate are both the same value.

We model the correlation function  $\rho(r)$  for the geopotential corrections as a Gaussian,

$$\rho(r) = e^{-r^2/d^2}, \quad (6)$$

which is a function of the distance  $r$ . The length scale  $d$  for the correlation function is defined by 600 km, similar to that used at NMC in the regional model



(DiMego 1988). After the first three or four iterations the length scale is reduced to 330 km for one additional iteration, to speed convergence of the scheme (see also Grønås and Midtbø 1987). After the first pass of our analysis scheme, the data are again checked for inconsistency with the first-pass analysis. Any inconsistent data, which differ by more than 2.5 times (1.5 times for sea level pressure) the standard deviation from the first pass, are removed and the first pass is repeated. The same correlation function is used for the univariate analysis of sea level pressure, temperature, and relative humidity.

For the univariate analysis of wind corrections to the first-guess wind field, different correlation functions are used. The functional form of the correlation functions  $\rho_u$  and  $\rho_v$  used for the components of the wind field are given by

$$\rho_u = \left[ 1 - \frac{(y - y_j)^2}{d_u^2} \right] \rho(r) \quad (7)$$

$$\rho_v = \left[ 1 - \frac{(x - x_j)^2}{d_u^2} \right] \rho(r), \quad (8)$$

where  $\rho(r)$  is the correlation function for the geopotential,  $(x, y)$  and  $(x_j, y_j)$  are the Cartesian positions of an arbitrary point and an observation, respectively,

$$\phi_x(k+1) = \phi_x(k)$$

$$+ \sum_{j=1}^n \alpha_{xj} \{ \phi_j^o - \phi_j(k) - c_j(y - y_j)f_j[u_{g,j}(k) - u_{g,j}(k-1)] + c_j(x - x_j)f_j[v_{g,j}(k) - v_{g,j}(k-1)] \}, \quad (9)$$

and the observation estimate  $\phi_i(k+1)$  is

$$\phi_i(k+1) = \phi_i(k)$$

$$+ \sum_{j=1}^n \alpha_{ij} \{ \phi_j^o - \phi_j(k) - c_j(y_i - y_j)f_j[u_{g,j}(k) - u_{g,j}(k-1)] + c_j(x_i - x_j)f_j[v_{g,j}(k) - v_{g,j}(k-1)] \}, \quad (10)$$

where  $\phi_j^o$  is the value of the observation,  $\phi_j(k)$  is the observation estimate, and  $u_{g,j}(k)$  and  $v_{g,j}(k)$  are estimates of the geostrophic wind correction at the observation point for the  $k$ th iteration. Here  $u_{g,j}(k-1)$  and  $v_{g,j}(k-1)$  are the prior estimates of the value of the geostrophic wind at the observation point. In the above,  $f$  is the Coriolis parameter and  $c$  is a geostrophy factor that reduces to zero near the equator. For the next iteration, an improved estimate of the geostrophic wind correction is computed at the grid points from the new interpolated values of the geopotential given by Eq. (9). Values  $u_{g,j}(k+1)$  and  $v_{g,j}(k+1)$  of the geostrophic wind at the observation point are then computed by linear interpolation. For the four iterations a single correlation scale  $d$  of 600 km is used. In this way, we correct the larger scales only, without changing the smaller scales that are not as geostrophic.

In computing the new estimates of the geostrophic

and  $d_u$  is a further length scale. The correlation functions for the wind components can be derived from the correlation function  $\rho(r)$  for the geopotential, in which case the length scale  $d_u$  is given by the length scale  $d$  used for  $\rho(r)$  (Grønås and Midtbø 1987). Here we have chosen to use the modified length scale  $d_u$  of 700 km, which fits the length scale found by Hollingsworth and Lönnberg (1986) where the transverse correlations in the wind reach zero. These correlation functions effectively give smaller weights across the direction of the wind than along it, without having to compute wind direction, as in Benjamin and Seaman (1985). After three to four iterations, the length scales  $d$  and  $d_u$  are reduced to 330 and 380 km, respectively, for one more iteration to, again, speed convergence.

#### d. Enhancement of the geopotential gradient

A further four iterations are used for the geopotential correction, using improving estimates of the geostrophic wind at each iteration to extrapolate the geopotential correction to the grid points. An initial estimate of geostrophic wind is obtained from the previous univariate  $u, v$  wind corrections by linear interpolation. The interpolated value  $\phi_x(k+1)$  at the grid point is now given after the  $k$ th iteration by

wind components  $u_{g,x}, v_{g,x}$  from the new geopotential  $\phi_x$  at the grid points, the same geostrophy factor  $c$  and a modified Coriolis parameter  $f^*$  are used, where

$$u_{g,x} = -\frac{c}{f^*} \frac{\partial \phi_x}{\partial y} \quad (11)$$

$$v_{g,x} = \frac{c}{f^*} \frac{\partial \phi_x}{\partial x}. \quad (12)$$

The geostrophy factor  $c$  depends on the latitude  $\theta$  in degrees as

$$c = \begin{cases} 1, & \text{for } |\theta| > 30^\circ \\ 0.5(1 + \cos 12\theta), & \text{for } 15^\circ \leq |\theta| \leq 30^\circ \\ 0, & \text{for } |\theta| < 15^\circ, \end{cases} \quad (13)$$

and  $f^*$  only differs from  $f$  in a  $15^\circ$  latitude band around the equator where its magnitude is given by that at  $15^\circ\text{N}$ , and it has the same sign as  $f$ .

*e. Enhancements to the wind and temperature gradients*

Following Kistler and McPherson (1975), we adjust the geostrophic part of the corrections to the wind field to match the new corrections for the geopotential. That is, the univariate wind corrections are modified by adding the difference in the geostrophic wind between the enhanced and univariate analysis of the geopotential. In this way the enhanced horizontal shear of the geostrophic wind is preserved in the wind analysis. A further four univariate passes of the wind analysis are then performed to improve the corrections for the ageostrophic component of the wind. After the corrections have been computed at all pressure levels of the analysis, the univariate temperature corrections are adjusted to match the computed thickness corrections.

*f. Boundary values and interpolation to model grid*

In a nine-point zone along the lateral boundaries of our analysis grid, we merge the analyzed corrections with values interpolated from the NMC analysis. The analyzed corrections in the first six points closest to the boundary are replaced by the NMC values, while a linear weighting of (0.25, 0.75), (0.5, 0.5), (0.75, 0.25) is used to merge the next three interior analyzed values with the NMC values. The final corrections are then bicubically interpolated to the horizontal fine grid of the model and added to the first guess for display of the final analysis on pressure surfaces.

For use on the forecast model grid, the analysis corrections are also interpolated to the sigma levels of the

model. An initial estimate of new surface pressure is first computed from the analyzed full fields on the pressure levels. The surface pressure of the background forecast is similarly computed from the temperature and height on the pressure levels. The difference in surface pressure between the two is then added to the original surface pressure of the background forecast to obtain the corrected surface pressure. The analysis deviations are then linearly interpolated in the vertical to the model sigma levels and added to the first-guess model forecast. The thermodynamic variables (temperature and humidity) are interpolated to the model sigma levels, assuming they are linear in log of pressure, while wind components are interpolated assuming they are linear in pressure. A balanced divergent part of the wind can then be obtained by applying the initialization procedure described in Sashegyi and Madala (1993).

### 3. Testing the analysis scheme

Analyses were made with the new scheme using the surface and atmospheric sounding data collected during IOP 2 of GALE for the period 0000 UTC 23 January to 1200 UTC 28 January 1986. During this period, cold-air damming occurred east of the Appalachians and a coastal front developed along the east coast of the United States, followed by cyclone development off Cape Hatteras. This range of mesoscale and synoptic-scale features occurred in the region of data coverage and provided an ideal test of the new scheme. The mesoscale features produced with the new scheme could also be compared to the mesoscale analyses of this period by Bosart (1988) and Doyle and Warner (1990). The NMC hemispheric analyses will provide a comparison for the synoptic-scale features produced with our new scheme. The impact of the different components of our new scheme are demonstrated using the analysis for 1200 UTC January 25. The effect of

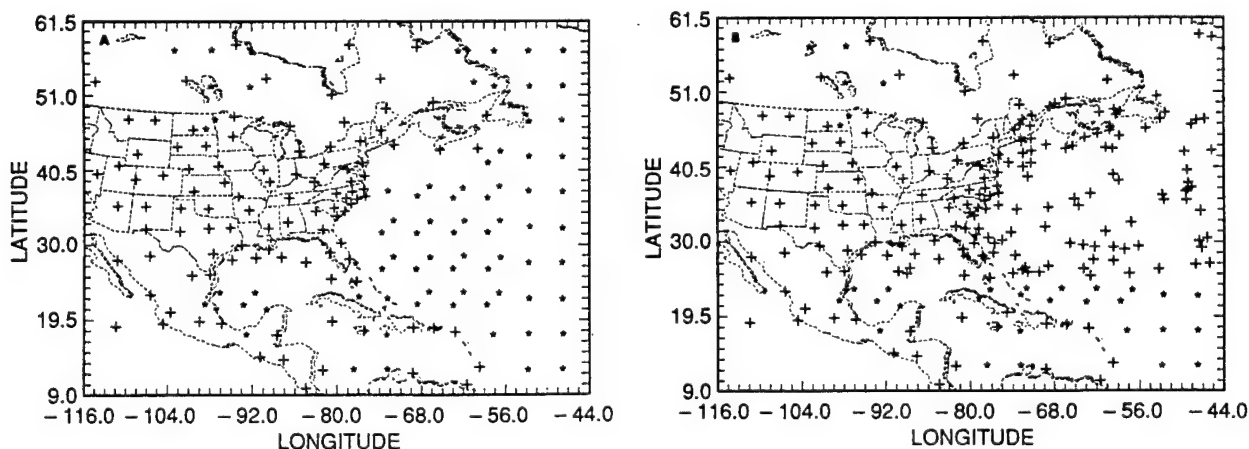


FIG. 1. The location of the data after quality control at 1200 UTC 25 January for (a) the geopotential height at 500 mb and (b) the sea level pressure. The observations are indicated by the plus sign, while bogus values are indicated by the asterisk. The analysis grid is indicated by the tick marks along the domain boundary.

reducing the width of the correlation function and of using superobs is also tested.

For 1200 UTC January 25, the locations of the data that remain after the quality control are shown in Fig. 1 on the domain of the analysis grid. The locations of the observations are shown by the crosses, while the stars show the NMC bogus data, which have been added in data-sparse regions. The analysis grid is indicated by the small tick marks every  $1.5^\circ$  along the latitude and longitude axes. With the 500-mb geopotential height data, few superobs were required but many NMC bogus soundings were added over the ocean. With the sea level pressure data, many more observations were available, many of which have been averaged and replaced by superobs.

To provide a fair comparison on the synoptic scales at the same resolution as our new analysis scheme, the NMC  $2.5^\circ$  hemispheric analyses are themselves enhanced by applying the Barnes (1973) scheme we have used in Chang et al. (1989) to this GALE data. In this application of the Barnes (1973) scheme, a two-step correction of the deviations of the GALE data from the NMC hemispheric analyses are performed using Gaussian weighting defined according to the criterion of Koch et al. (1983). Using an average spacing for the upper-air data over the eastern United States of 350 km, the criterion gives a length scale [ $d$  in Eq. (6)] of about 500 km for the Gaussian weighting function for the first pass and 275 km for the second pass. As in Shi et al. (1991), the same quality control described in section 2b is also applied here to the data using the standard deviation of the observational errors listed in Table 1. The first pass for this enhancement of the NMC fields is performed here on the same grid as the new analysis. However due to the decreasing data density outside the region of the eastern United States, the second pass of the Barnes scheme must be limited to a smaller domain, if aliasing is not to occur. The region for the second pass is bounded by longitudes  $108^\circ$ ,  $68^\circ$ W and latitudes  $25.5^\circ$ ,  $49.5^\circ$ N for the upper-air data, and  $22.5^\circ$ ,  $49.5^\circ$ N for the sea level pressure data. A linear weighting is then used to merge the first and second passes over four more analysis grid points inside the second-pass domain. In contrast, this restriction is not necessary with the Bratseth scheme, which adjusts the weights for the changing data density over the whole analysis domain. The synoptic situation during GALE IOP 2 is now described using these enhanced NMC analyses.

#### *a. Description of the synoptic situation*

Riordan (1990) and Doyle and Warner (1990) describe in detail the development of the coastal front during GALE IOP 2. With the movement of a cold front off the east coast of the United States at 1200 UTC 23 January, a wedge of cold air is formed behind the front between the Appalachian Mountains and the

coast in the next 24 h. The temperature gradient across the coastline is enhanced by the strong sensible heating of the air over the Gulf Stream (Warner et al. 1990). In the subsequent onshore easterly flow behind the cold front, a coastal front develops offshore along the Carolina coast, and by 1200 UTC on 25 January, a 1000-km-long coastal front paralleled the coastline. The easterly flow regime can be seen in the enhanced NMC analysis for 1000 mb shown in Fig. 2a on the model's horizontal fine grid. The enhanced NMC analysis is, however, unable to resolve the strong thermal gradient along the coast. In the upper levels of the atmosphere, a broad, long-wave trough was present over the central United States at this time (Fig. 2b). During the next 24 h, the trough moved eastward and deepened rapidly due to a second short-wave digging southward in the long-wave trough. By 0000 UTC 26 January, the coastal front extended from Georgia to southern New England and a weak low moved up the coast along the front, reaching the Chesapeake Bay by 1200 UTC 26 January (Fig. 2c). In the next 12 h the coastal low merges with a weak trough, seen in Fig. 2c, moving eastward from the Great Lakes.

The disturbance that ultimately became the first of the major cyclones of GALE was present (Fig. 2a) as a minor frontal wave in extreme southeast Texas at 1200 UTC 25 January. Aloft a major short wave was digging southeastward in the long-wave trough. The surface disturbance remained weak as it advanced along the Gulf coast, and on 26 January the surface wave weakened further as it moved across Georgia. In response to the strong upper-level short wave reaching the East Coast, a new center formed off Cape Hatteras, which deepened rapidly as it moved north, as it combined with the preexisting waves associated with the northward-moving coastal low and eastward-moving trough. By 1200 UTC 27 January, the well-developed low pressure center can be seen (Fig. 2d) crossing the New England coast.

#### *b. Impact of the new scheme*

We demonstrate the impact of each of the components of our new analysis scheme with the analysis for 1200 UTC 25 January. The first-guess for the analysis is generated by a 12-h forecast with our limited-area model, where the initial conditions are derived from the NMC  $2.5^\circ$  hemispheric analysis for 0000 UTC 25 January 1986. The resulting first guess is illustrated in Fig. 3, which shows the sea level pressure, 1000-mb winds and temperature, and the 500-mb prediction of height, wind, and temperature on the model's horizontal fine grid. The model has produced a strong wedge of cold air and strong ridging east of the Appalachians (Fig. 3a). The strong temperature gradient along the Carolina coast in the region of strong onshore flow shows conditions favorable for the development of a coastal front. The 1200 UTC 25 January analysis

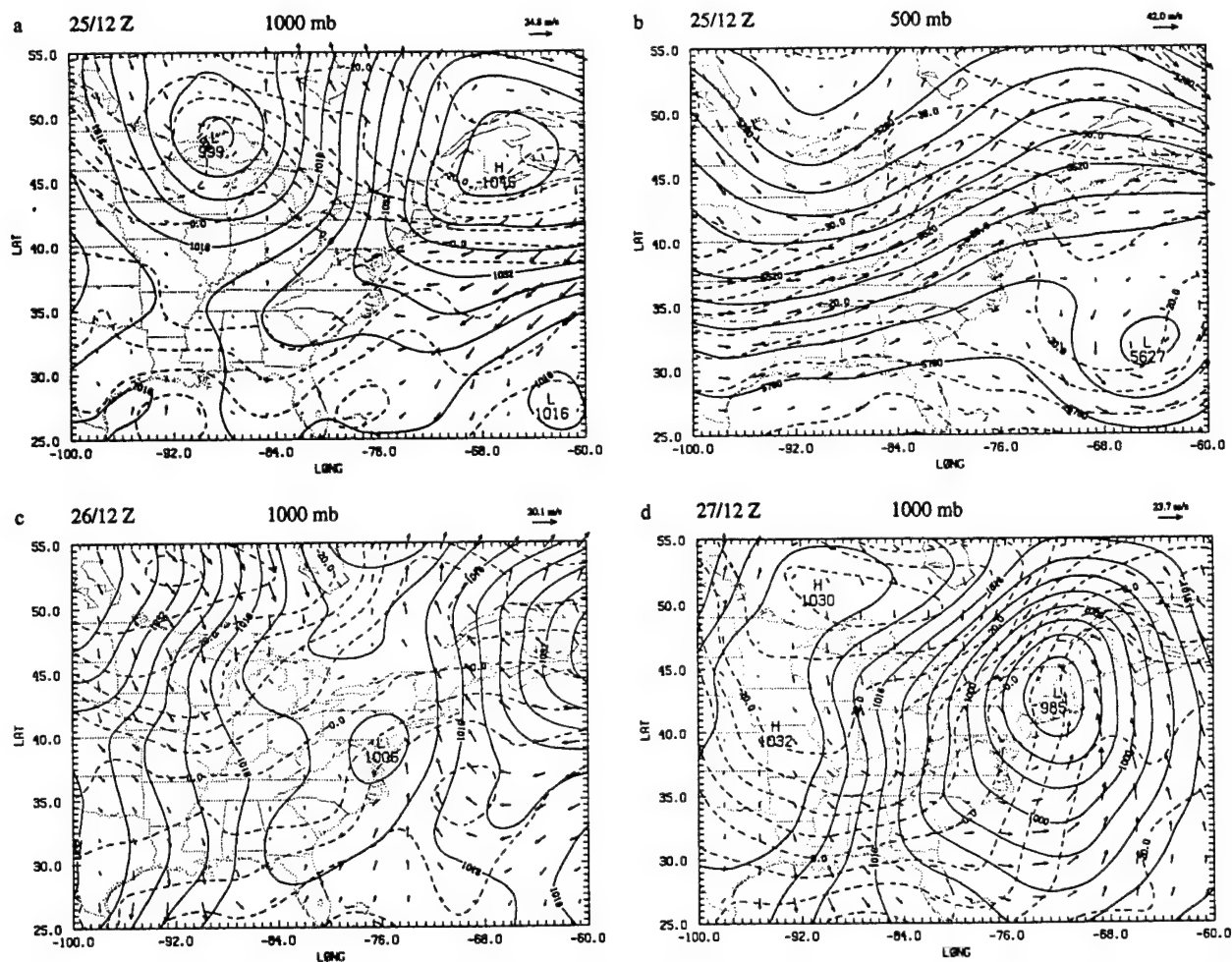


FIG. 2. (a) Sea level pressure (mb), temperature ( $^{\circ}\text{C}$ ), and winds at 1000 mb, and (b) geopotential height (gpm), temperature ( $^{\circ}\text{C}$ ), and winds at 500 mb for the enhanced NMC analysis for 1200 UTC 25 January. Here (c) and (d) are as in (a) except for 1200 UTC 26 and 27 January, respectively. Contours of sea level pressure are 4 mb and  $5^{\circ}\text{C}$  for temperature at 1000 mb. At 500 mb, contours are 60 gpm for geopotential and  $2.5^{\circ}\text{C}$  for temperature. Maximum wind vectors indicated by labeled arrow in meters per second. Model horizontal grid indicated by small tick marks along axes.

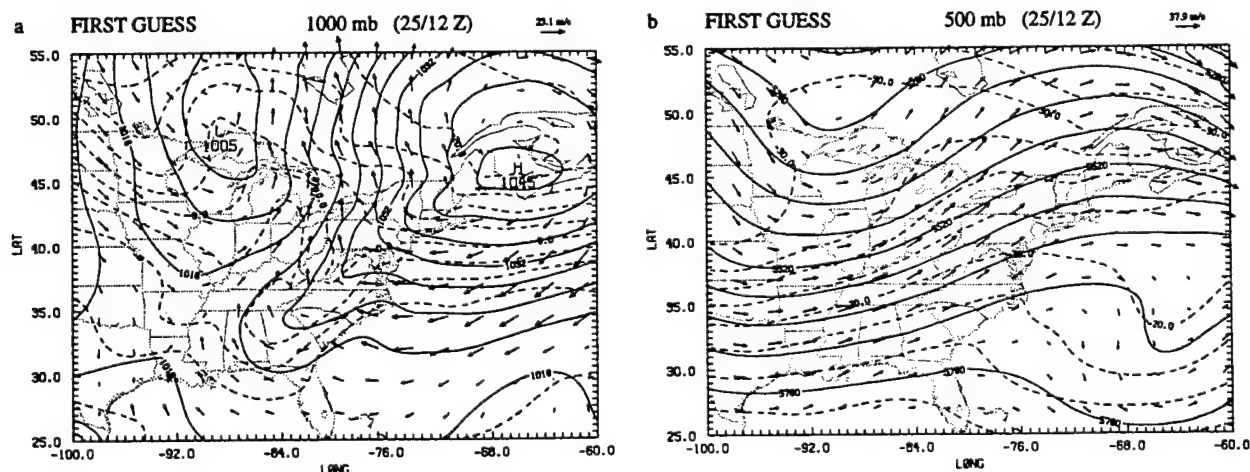


FIG. 3. The first guess at 1200 UTC 25 January for (a) sea level pressure (mb), 1000-mb temperature ( $^{\circ}\text{C}$ ), and winds; and for (b) geopotential height (gpm), temperature ( $^{\circ}\text{C}$ ), and winds at 500 mb. Contours as in Fig. 2.

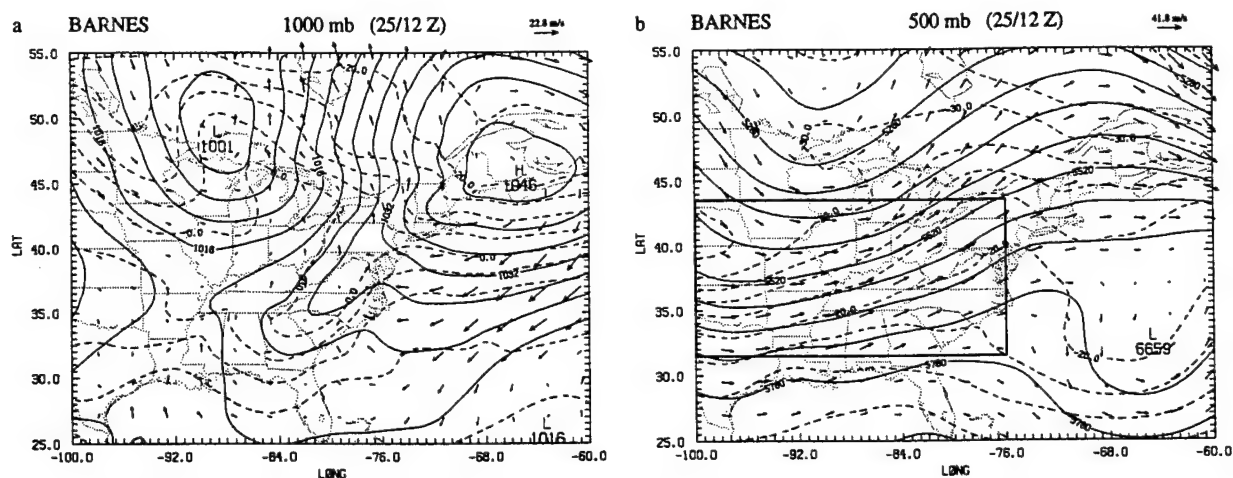


FIG. 4. The Barnes analysis at 1200 UTC 25 January for (a) sea level pressure (mb), 1000-mb temperature ( $^{\circ}\text{C}$ ), and winds; and for (b) geopotential height (gpm), temperature ( $^{\circ}\text{C}$ ), and winds at 500 mb. Contours as in Fig. 2.

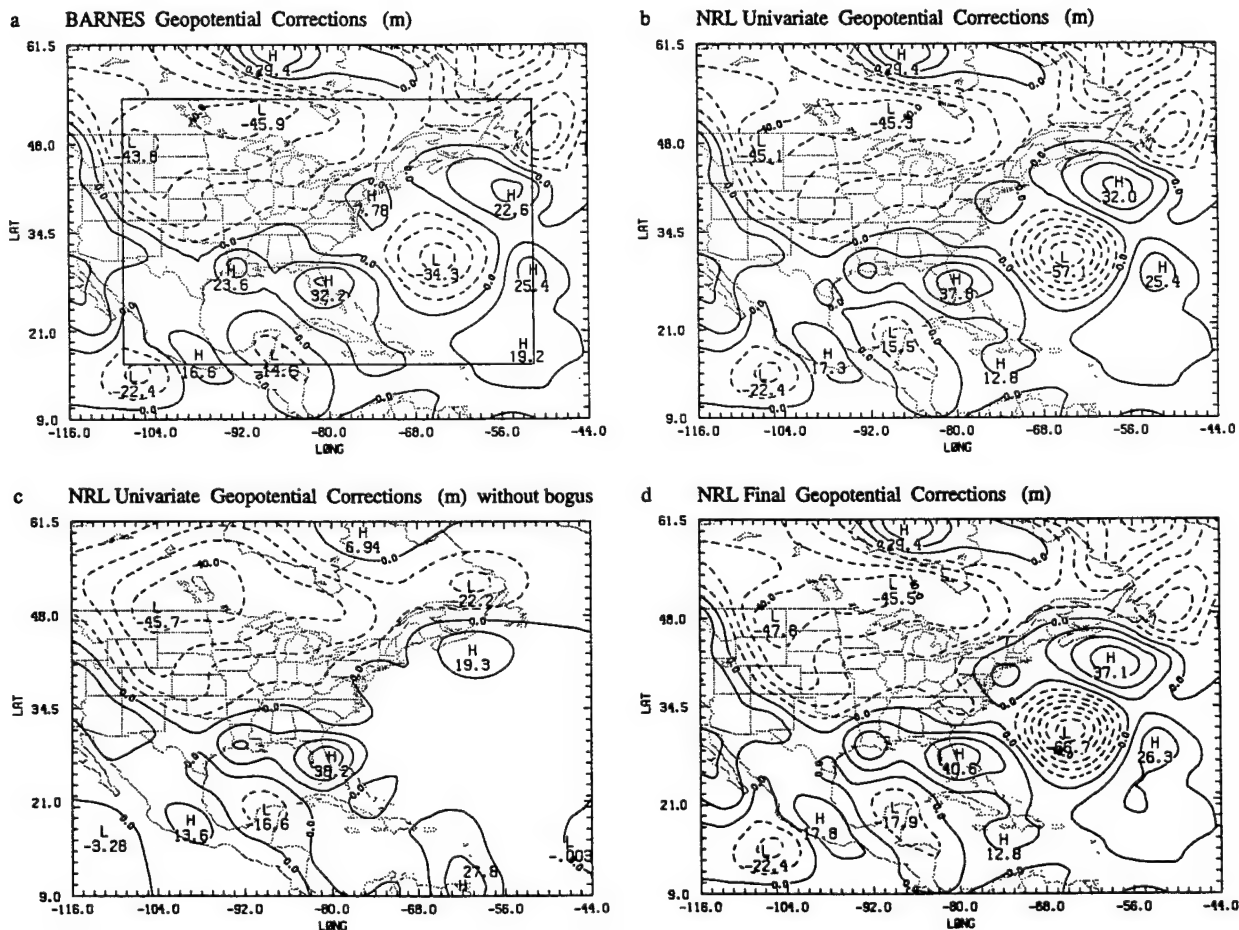


FIG. 5. The geopotential height corrections (gpm) at 500 mb for 1200 UTC 25 January with (a) the Barnes scheme, (b) the NRL univariate analysis, (c) the NRL univariate analysis without bogus data, and (d) the NRL multivariate analysis. Contours of geopotential corrections are every 10 gpm. Analysis grid points indicated by the tick marks along the axes.



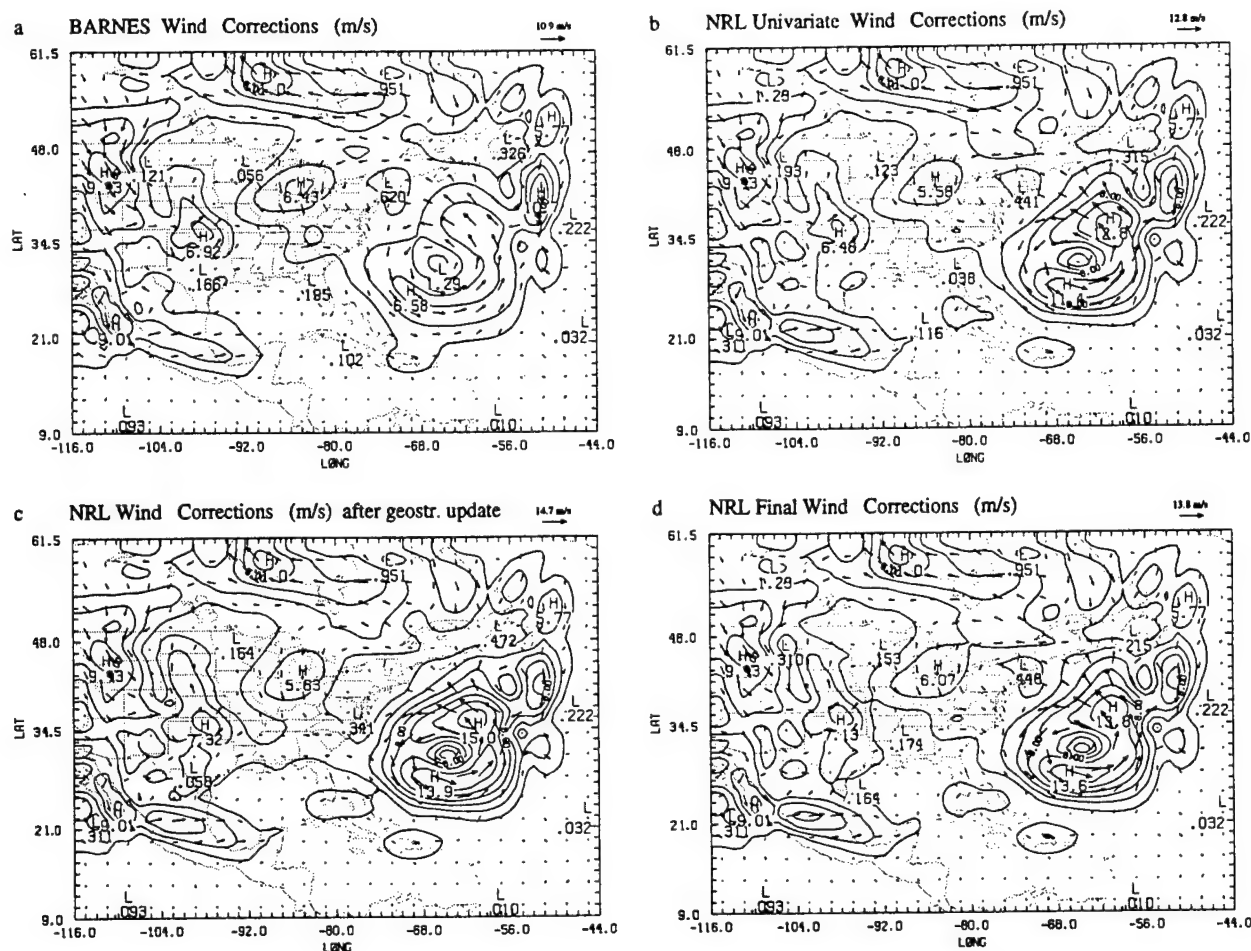


FIG. 6. The wind corrections ( $\text{m s}^{-1}$ ) at 500 mb for 1200 UTC 25 January with (a) the Barnes scheme, (b) the NRL univariate analysis, (c) the NRL analysis after updating the geostrophic wind, and (d) the NRL multivariate analysis. Contours of wind speed corrections are every  $2 \text{ m s}^{-1}$ .

of Doyle and Warner (1990) verifies that the cold-air damming and coastal front with the strong onshore flow were indeed present (see Fig. 2b of Doyle and Warner). This tight thermal gradient along the coast could not be resolved in our enhanced NMC analysis shown in Fig. 2a. However, the low of 1005 mb over Lake Superior is too weak in the first guess (Fig. 3a) when compared to the enhanced NMC analysis (Fig. 2a). Aloft at 500 mb, the long-wave trough over the eastern United States in Fig. 3b is also too weak, and model forecast has failed to produce the cutoff low over the western Atlantic, which can be seen in the enhanced NMC analysis in Fig. 2b. The cutoff low in the enhanced NMC analysis is about 70 m deeper than the weak trough present in the first guess.

The improvement achieved alone by using a model-generated background field is first illustrated by repeating the Barnes analysis (which was used earlier for the enhancement of the NMC hemispheric analysis) using the aforementioned 12-h model forecast as the

background field. The resulting Barnes analysis for 1000 and 500 mb is shown in Fig. 4. The surface low over Lake Superior is corrected to within a millibar in Fig. 4a, and the cold-air damming and strong temperature gradient from the first guess are retained. Aloft at 500 mb, both the long-wave trough and the low off the coast have been correctly deepened in Fig. 4b. We can also see that the  $-30^{\circ}\text{C}$  temperature contour has been shifted eastward in closer agreement with the enhanced NMC analysis in Fig. 2b. Therefore, in the region over the eastern United States, where there is a large amount of data, the Barnes scheme using the limited-area model forecast as a first guess, is able to produce a good synoptic-scale analysis and retain the mesoscale cold wedge and tight temperature gradient along the coast from the first guess. But the cutoff low over the western Atlantic in the Barnes analysis is still too weak by some 32 m when compared to the enhanced NMC analysis. However, the cutoff low does lie outside of the region influenced by the second pass of the

Barnes scheme (see beginning of section 3). The region fully updated by the second pass is shown by the solid rectangle inside Fig. 4b.

In Figs. 5 and 6, we compare the analysis corrections for the 500-mb geopotential height and winds after each of the remaining components of the new analysis scheme with that produced by the Barnes scheme. The figures show the entire region of the analysis grid, with the analysis grid points indicated by the small tick marks along the axes. The geopotential and wind corrections to the first guess obtained with the Barnes scheme are shown in Figs. 5a and 6a. The six-point region around the boundary, where analyzed values are replaced with values interpolated from the NMC 2.5° hemispheric analysis, is indicated by the solid rectangle in Fig. 5a (see section 2f). The deepening of the long-wave trough and a strong cutoff low are readily apparent in the geopotential height corrections in Fig. 5a. The winds around the cutoff low are strengthened in Fig. 6a, and an ageostrophic flow south of the Great Lakes is produced. In Figs. 5b and 6b we compare the result after the initial univariate analysis of the geopotential height and wind is carried out with the new analysis scheme as described in section 2c. The only change is that the Bratseth scheme is used for the analysis instead of the Barnes scheme. In the data-rich area over the eastern United States, only small differences are found in the 500-mb geopotential height and wind corrections. The maximum in the ageostrophic flow south of the Great Lakes is somewhat weaker with the Bratseth scheme. Over the western Atlantic, the cutoff low is much deeper when using the Bratseth scheme, which is able to adjust the weights for the changing data density and can be applied without restriction over the whole analysis domain. The influence of the bogus data used in the analysis can be seen in Fig. 5c, which shows the 500-mb geopotential corrections produced when no bogus data are used with the Bratseth scheme. The bogus data clearly define the cutoff low over the western Atlantic in Fig. 5b, providing a good check of our scheme.

The impact of using the wind information to extrapolate the geopotential heights in the second stage of the new scheme (section 2d) is demonstrated in Fig. 5d. The cutoff low is seen to be further deepened. The long-wave trough over the central United States is also deepened somewhat and heights are lowered over the Carolinas. After updating the geostrophic component of the wind field for the new geopotential height corrections (section 2e), we see the winds around the cutoff low in Fig. 6c are also strengthened with a stronger wind shear to the south of the low center. With the enhancement of the ageostrophic flow in the final stage of the scheme (section 2e), the intensity of the wind maxima around the south and western sides of the cutoff low have been reduced in Fig. 6d, but the wind shear is maintained. The reduction in the peak winds is not surprising, since the geostrophic wind is an over-

estimate of the actual wind in a low. The ageostrophic flow from the Great Lakes to the coast has also been strengthened somewhat.

### c. Convergence of the new scheme

We illustrate in Fig. 7 the rate of convergence of the Bratseth (1986) scheme for our case with a fixed correlation length scale of 600 km for the univariate analysis of the 500-mb geopotential height at 1200 UTC 25 January. The curves in the figure show the root-mean-square (rms) errors for both the analyzed values and the observation estimates (computed here as differences from the observation values), as a function of the iteration number. With increasing iteration, the observation estimate rapidly approaches the value of the observation, while the analyzed value rapidly converges to a value different from the observation but the same as that which would be produced by optimum interpolation (Bratseth 1986). As described in section 2c, the length scale of the correlation function is reduced to 330 km after just four iterations in our case to speed the convergence of the scheme. A large decrease results in the magnitude of the rms errors for both the analyzed value and observation estimate of the 500-mb geopotential, as shown by the crosses in Fig. 7. The rms error for the analyzed values is then within 5% of the optimum value that is produced after 100 iterations with a fixed length scale. The differences between the analyzed fields produced in either case are small.

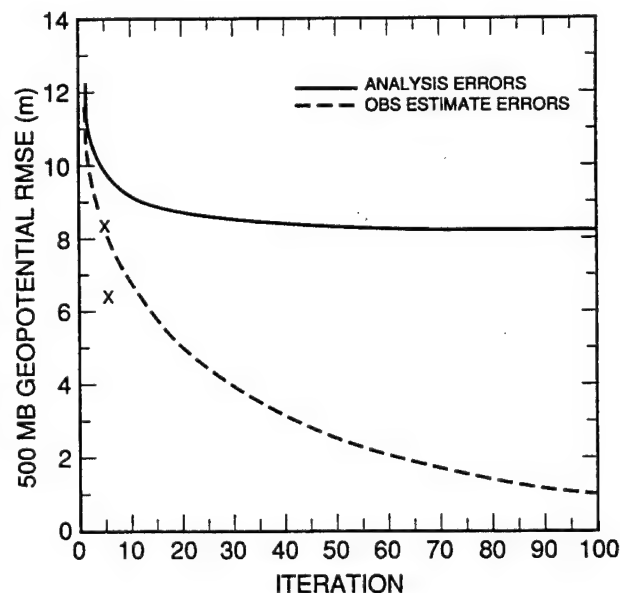


FIG. 7. The rms errors for the analyzed values [derived from Eq. (1)] at the observation locations (solid curve) and for the observation estimates obtained using Eq. (2) (dashed curve) for the geopotential at 500 mb, as a function of the iteration number. The rms errors obtained after just four iterations followed by a further iteration with a reduced length scale are indicated by the "X".



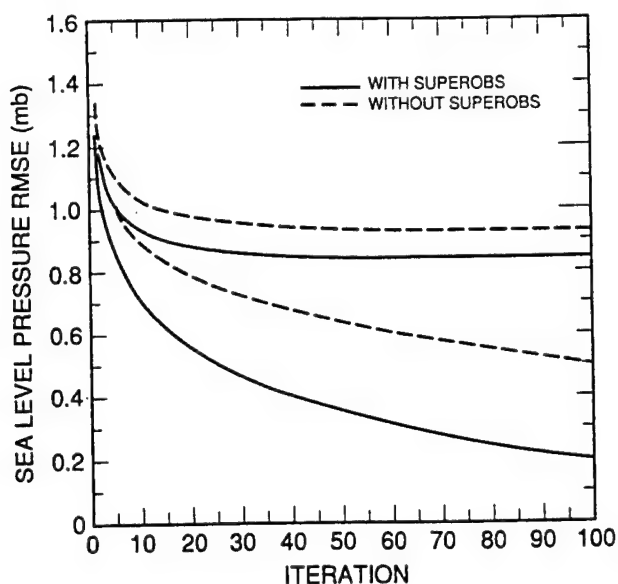


FIG. 8. As in Fig. 7 but for the rms errors of sea level pressure for the case with superobs (solid curve) and without superobs (dashed curve).

In Fig. 8, we illustrate the influence that using superobs has on the rate of convergence of the scheme for the sea level pressure data. The figure compares the rms errors for the analyzed values and the observation estimates of the sea level pressure at the data locations, for cases when superobs are used (solid curve) and when they are not used (dashed curve). Without the superobs, the rate of convergence of the observation estimate is much slower due to the many closely spaced observations (see Bratseth 1986). Even with the superobs, however, the resulting optimum analyses of the sea level pressure (produced after 100 iterations) differ from each other by only 10% in the rms error.

#### 4. Results

The analyses with the new scheme of the cold-air damming, coastal front, subsequent capture of a weak coastal low by a jet streak and the cyclogenesis offshore are described. The results are compared with the enhanced NMC analyses produced with our old Barnes scheme in section 3a. Mesoscale features produced in the new scheme are compared with those described by Bosart's (1988) detailed hand analyses and by Doyle and Warner (1990). Application of the vertical-mode initialization scheme on both the enhanced NMC analyses and our new analyses is used to compare the mesoscale vertical motions and ageostrophic wind derived for each case.

##### a. Cold-air damming and coastal front

The final 1000-mb analysis produced with the new scheme of the cold-air damming and coastal frontogenesis at 1200 UTC 25 January is shown in Fig. 9a. The analysis has retained the cold-air damming and the temperature contrast along the East Coast, which was produced by the model forecast. In fact, the differences between this 1000-mb analysis in Fig. 9a and that using the Barnes scheme shown in Fig. 4a are small. However, the temperature gradient across the cold front south of the low center over Lake Superior is somewhat stronger with the new analysis. In the new 500-mb analysis shown in Fig. 9b, both the long-wave trough and the cutoff low of 5625 m are in close agreement with the enhanced NMC analysis shown in Fig. 2b. However, as shown in the preceding section, the cutoff low produced with the Barnes scheme in Fig. 4b was much weaker. The  $-30^{\circ}\text{C}$  isotherm in the new analysis is east of Lake Superior in agreement with the enhanced NMC analysis in Fig. 2b, whereas the Barnes analysis in Fig. 4b has it lagging to the west around Lake Superior. A jet streak can be seen at 250 mb in

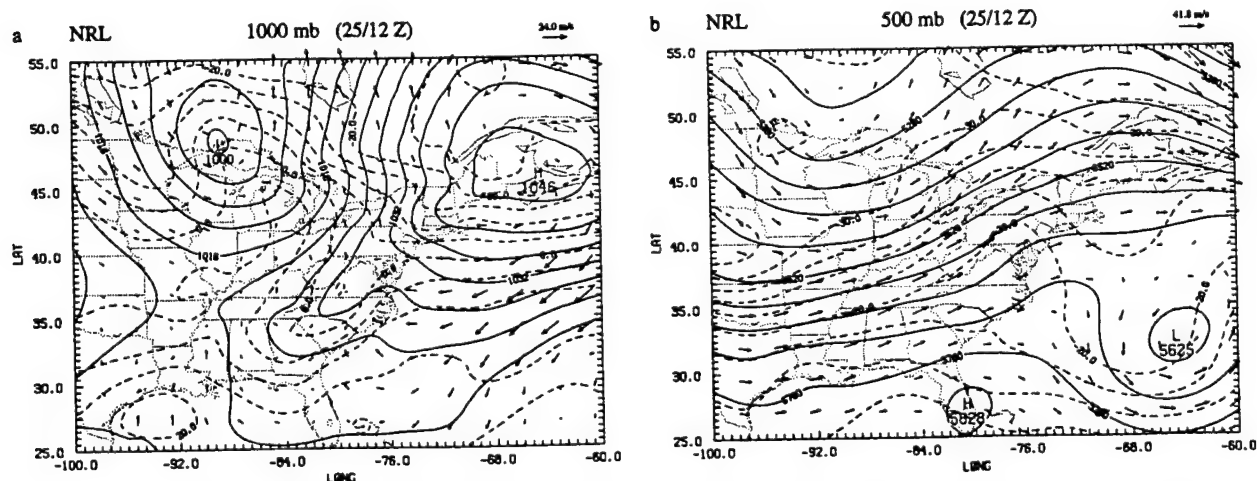


FIG. 9. The NRL analysis for 1200 UTC 25 January of (a) sea level pressure (mb), 1000-mb temperature ( $^{\circ}\text{C}$ ), and winds, and of (b) the geopotential height (gpm), temperature ( $^{\circ}\text{C}$ ), and winds at 500 mb. Contours as in Fig. 2.

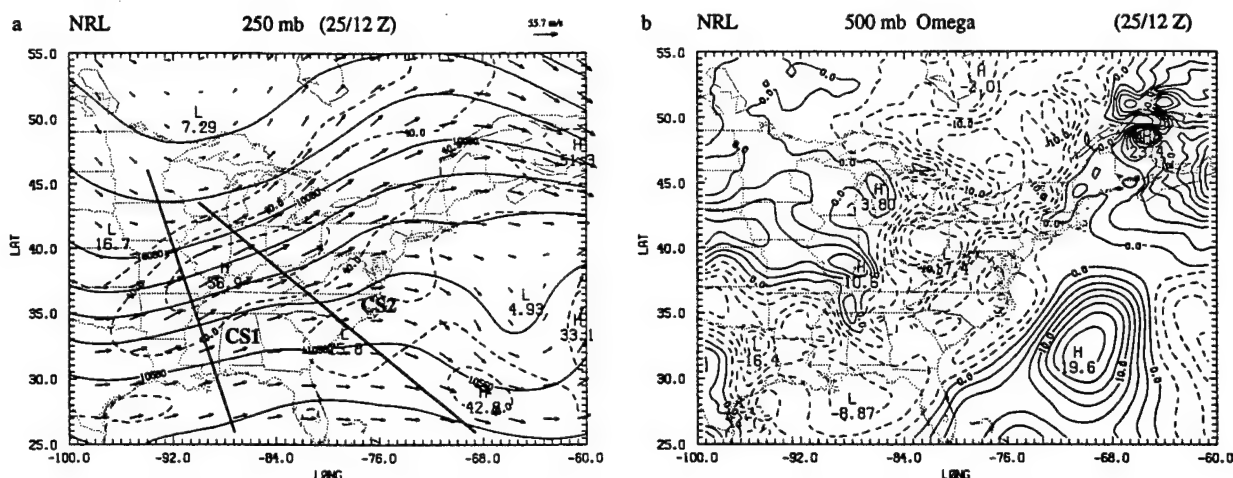


FIG. 10. The NRL analysis for 1200 UTC 25 January of (a) the geopotential height (gpm), temperature ( $^{\circ}\text{C}$ ), and winds at 250 mb, and of (b) the vertical velocity ( $\text{mb h}^{-1}$ ) at 500 mb. Contours of geopotential are every 120 gpm, and isotachs above  $30 \text{ m s}^{-1}$  are shown every  $10 \text{ m s}^{-1}$ . Vertical motion of magnitudes  $20 \text{ mb h}^{-1}$  or less are contoured every  $2.5 \text{ mb h}^{-1}$ .

Fig. 10a on the east side of the long-wave trough in the polar jet stream. The subtropical jet stream lies farther to the south across Florida and south of the cutoff low.

The field of vertical motion at 500 mb, which has been derived from the NRL analysis by application of the vertical-mode initialization procedure, is shown in Fig. 10b. Strong ascent from Ohio northeastward on the east side of the long-wave trough and strong subsidence west of the cutoff low are found in close agreement with that that can be derived from the enhanced NMC analysis (not shown). However, the major difference is that the rising motion associated with the developing coastal front along the Carolina coast in

the first-guess field is also retained in the NRL analysis. Also two separate centers of rising motion, associated with the surface cyclone located on the southeast Texas coast and the secondary circulation of the upper-level jet's entrance region, are evident over eastern Texas and northern Mississippi. In contrast, only a broad region of ascent can be derived from the enhanced NMC analysis.

To further show the secondary circulations associated with the entrance region of the upper-level jet and the coastal front, cross sections were produced using the initialized fields derived from the new NRL analysis at 1200 UTC 25 January. The locations of the

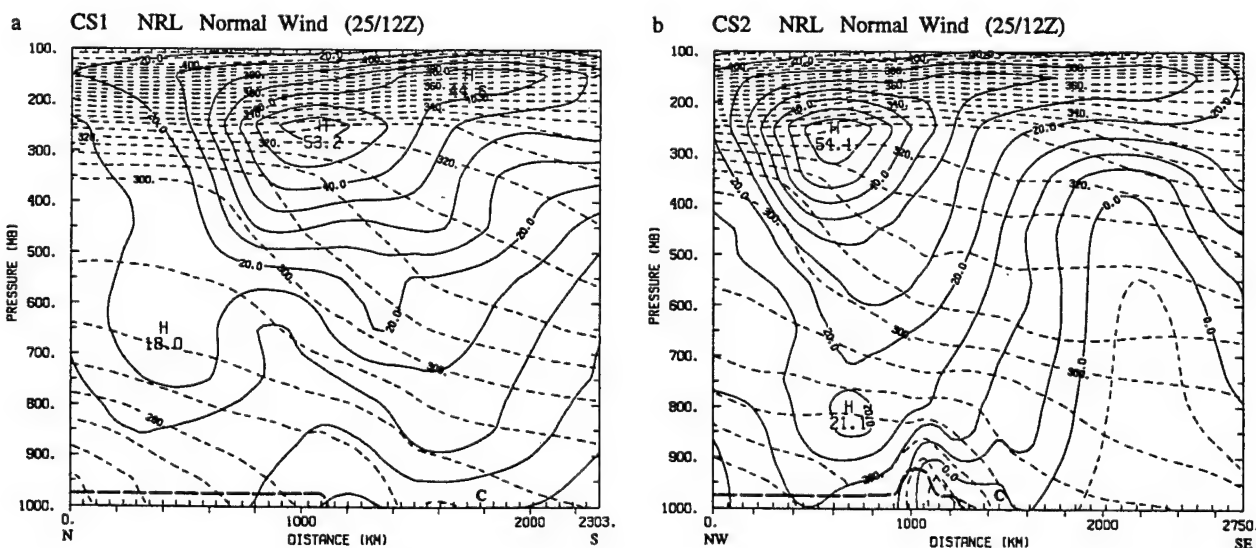


FIG. 11. The wind normal to the plane of the cross sections (a) CS1 from  $46^{\circ}\text{N}$ ,  $94^{\circ}\text{W}$  to  $26^{\circ}\text{N}$ ,  $87.3^{\circ}\text{W}$  and (b) CS2 from  $43.5^{\circ}\text{N}$ ,  $90^{\circ}\text{W}$  to  $26^{\circ}\text{N}$ ,  $68.7^{\circ}\text{W}$  for the NRL analysis at 1200 UTC 25 January. Contours every  $5 \text{ m s}^{-1}$ . The potential temperature (K) is also shown by the dashed contours every 5 K in the troposphere. The position of the model grid points every  $0.5^{\circ}$  in latitude are shown by the inner tick marks, and coastline by the "C."

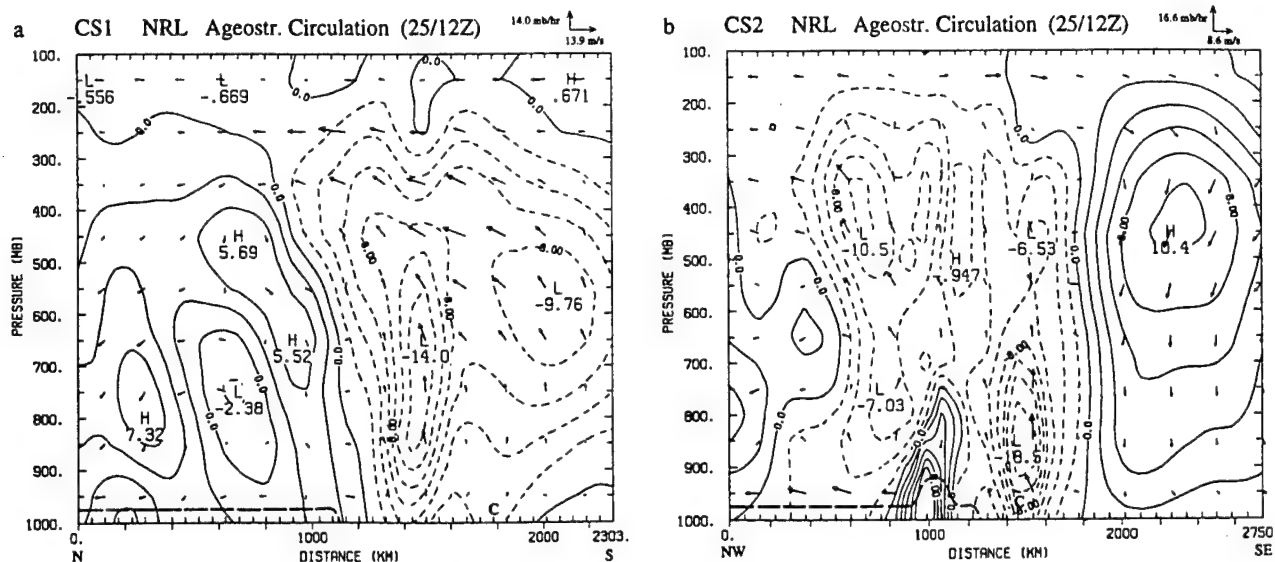


FIG. 12. As in Fig. 11 but for the vertical motion and ageostrophic wind in the plane of the cross sections (a) CS1 and (b) CS2. Contours of the vertical motion are every 2 mb h<sup>-1</sup>. Scale of vectors indicated by labeled arrows.

two cross sections are displayed in Fig. 10a. Cross section CS1, which extends from Minnesota to the central Gulf of Mexico, cuts across the entrance region of the upper-level polar jet. In Fig. 11a, the wind speed normal to cross section CS1 shows the core of the polar jet at 250 mb and the subtropical jet lying farther to the south at 150 mb. A narrow region of ascending motion with a maximum ascent of 14 mb h<sup>-1</sup> can be seen in Fig. 12a over northern Mississippi in the right rear flank of this polar jet. Aloft, a strong southerly ageostrophic flow across the jet is followed by weaker subsidence to the north. Such a thermally direct circulation in the rear of the jet streak is well known (e.g., Uccellini and

Johnson 1979; Keyser and Shapiro 1986). Weaker ascent associated with the subtropical jet stream to the south is also evident in the figure. In comparison, the secondary circulation produced by the enhanced NMC analysis has a broader region of ascending motion in the rear of the polar jet streak (Fig. 13a). The second cross section CS2, which is perpendicular to the Carolina coast, cuts across the region of the coastal front and through the polar jet aloft. The cold air trapped between the coast and the Appalachians can be seen in Fig. 11b, with the jet core aloft to the northwest. The low-level jet west of the Appalachians in the figure provides the inflow to the low pressure system over

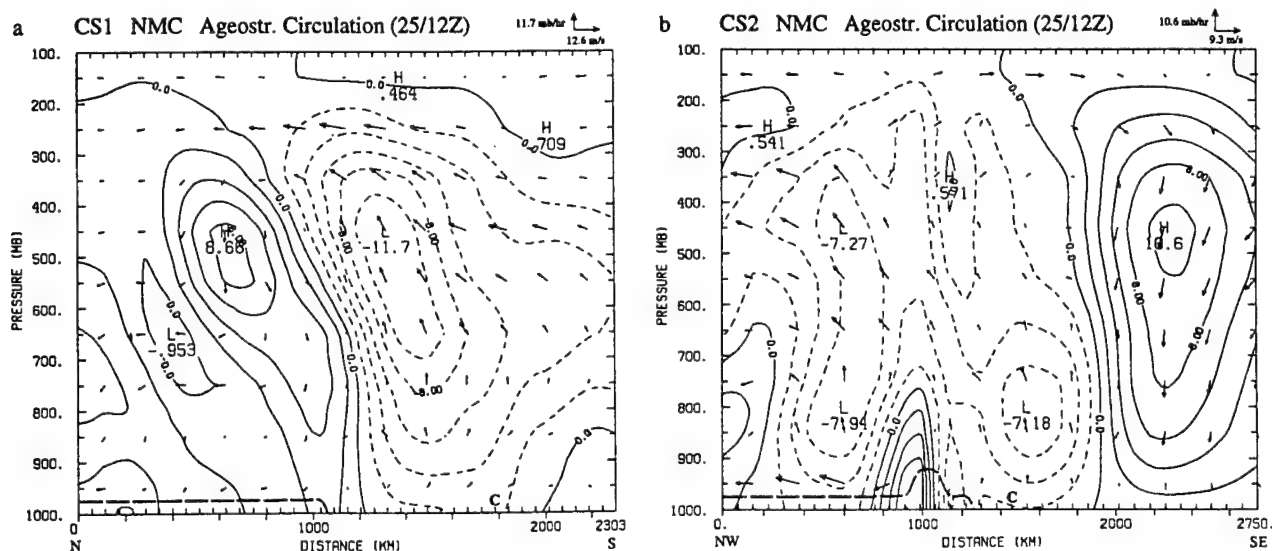


FIG. 13. The vertical motion and ageostrophic wind in the plane of the cross sections (a) CS1 and (b) CS2 for the enhanced NMC analysis. Contours as in Fig. 12.

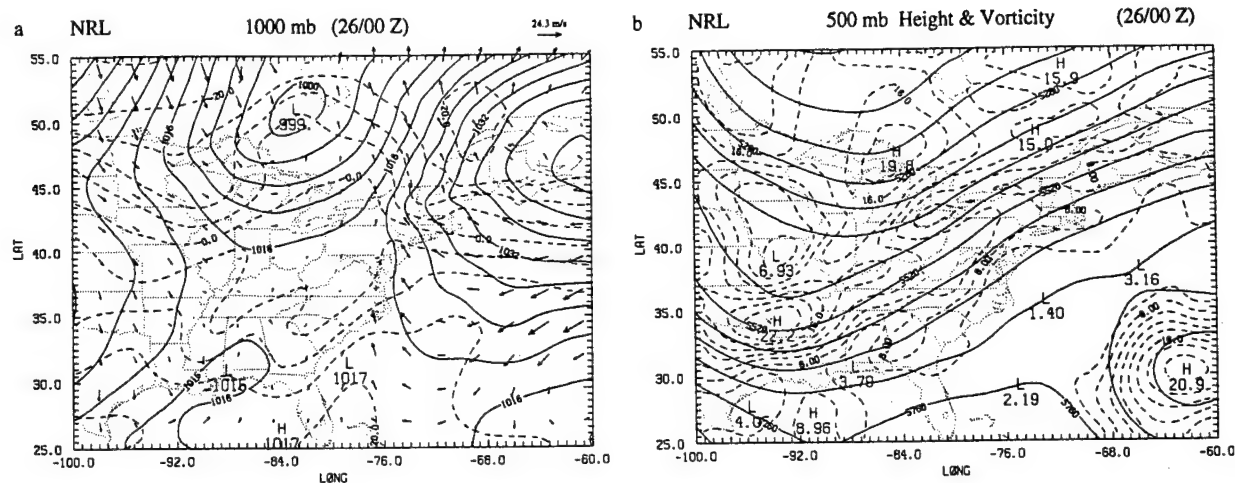


FIG. 14. The NRL analysis for 0000 UTC 26 January of (a) sea level pressure (mb), 1000-mb temperature ( $^{\circ}\text{C}$ ), and winds; and of (b) the geopotential height (gpm), absolute vorticity ( $\times 10^{-5} \text{ s}^{-1}$ ) at 500 mb. Contours of vorticity are every  $2 \times 10^{-5} \text{ s}^{-1}$  for values above  $6 \times 10^{-5} \text{ s}^{-1}$ .

Lake Superior (Fig. 9a). In Fig. 12b, shallow ascent with maximum of  $18.5 \text{ mb h}^{-1}$ , which is associated with the coastal front generated in the first-guess forecast, can be seen in a narrow band at the coastline. This ascent is in good agreement with that shown by Doyle and Warner (1990) in their cross section normal to the coastal front (see their Fig. 15). The subsidence west of the cutoff low in the subtropical jet stream and ascent east of the approaching upper-level trough can also be seen in Fig. 12b. The coastal front circulation is much stronger and more well defined with the new analysis than the circulation shown in Fig. 13b, which is derived from the enhanced NMC analysis.

#### b. Interaction of jet streak with coastal front

By 0000 UTC January 26, the coastal front had developed from Georgia to southern New England in an onshore easterly flow regime and led to the erosion of the cold dome east of the Appalachians (Doyle and Warner 1990). The strong thermal gradient associated with the coastal front is seen along the coast of the Carolinas in the NRL 1000-mb analysis illustrated in Fig. 14a. In this case, the NRL analysis was able to significantly sharpen the temperature contrast between the Carolina coast and the Appalachians compared to that which was produced by the first-guess forecast (see

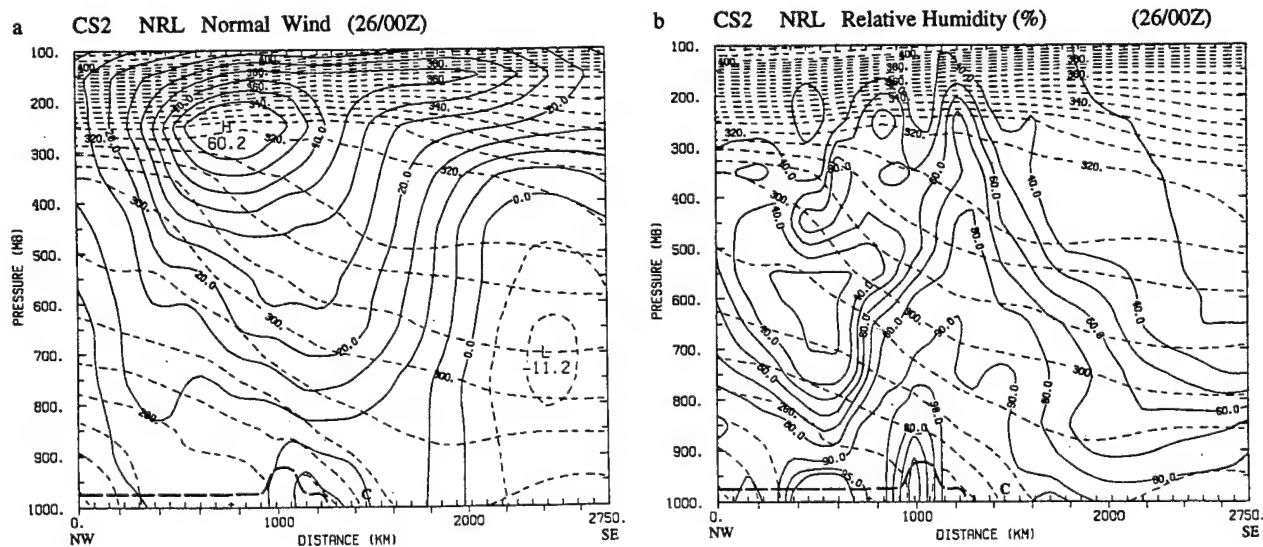


FIG. 15. (a) The wind normal to the plane of cross section CS2 and (b) the relative humidity (%) in the plane of the same cross section for the NRL analysis at 0000 UTC 26 January. Contours as in Fig. 11.

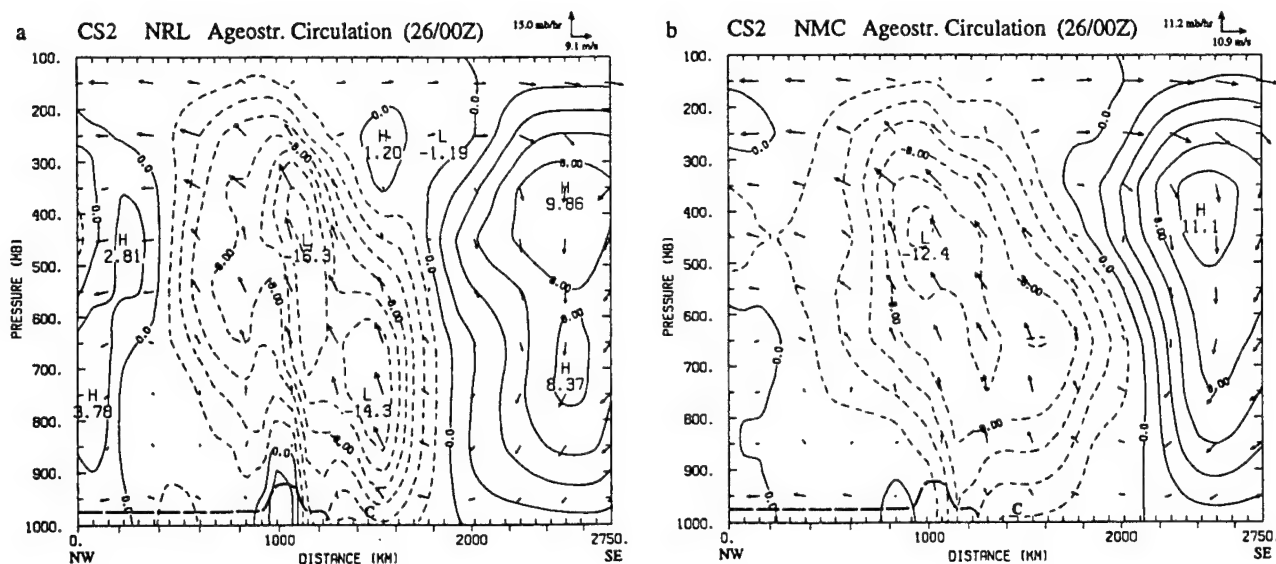


FIG. 16. The vertical motion and ageostrophic wind in the plane of cross section CS2 at 0000 UTC 26 January for (a) the NRL analysis and for (b) the enhanced NMC analysis. Contours as in Fig. 12.

Harms et al. 1992). The weak coastal low, which developed at the southern end of the coastal front (Bosart 1988; Doyle and Warner 1990), is also indicated in our analysis. The surface low associated with the a major short wave can be seen along the Alabama coast. This short wave can be seen as a strong vorticity maximum at the base of the long-wave trough at 500 mb in Fig. 14b. The polar jet across the eastern United States is strengthening as the short wave over the Great Lakes is moving eastward, producing a confluent flow into the jet. A weaker vorticity maximum can be seen over Georgia in the region of the interaction of the secondary circulation in the entrance region of the strengthening jet with the weak low on the coastal front.

This interaction of the secondary circulation in the entrance region of the jet with the weak coastal low at the southern end of the coastal front can be seen in the cross section CS2 across the coast shown in Figs. 15 and 16. Figure 15a shows the strengthening winds in the jet at 250 mb, while the ageostrophic flow and vertical motion are shown in Fig. 16a. A deep circulation can be seen linking the coastal low with the easterly ageostrophic flow across the upper-level jet. A further component of the circulation is linked to the subsidence west of the cutoff low in the subtropical jet stream to the southeast. Much weaker ascent is found in the lower troposphere when using the enhanced NMC analysis to derive the circulation (Fig. 16b). High

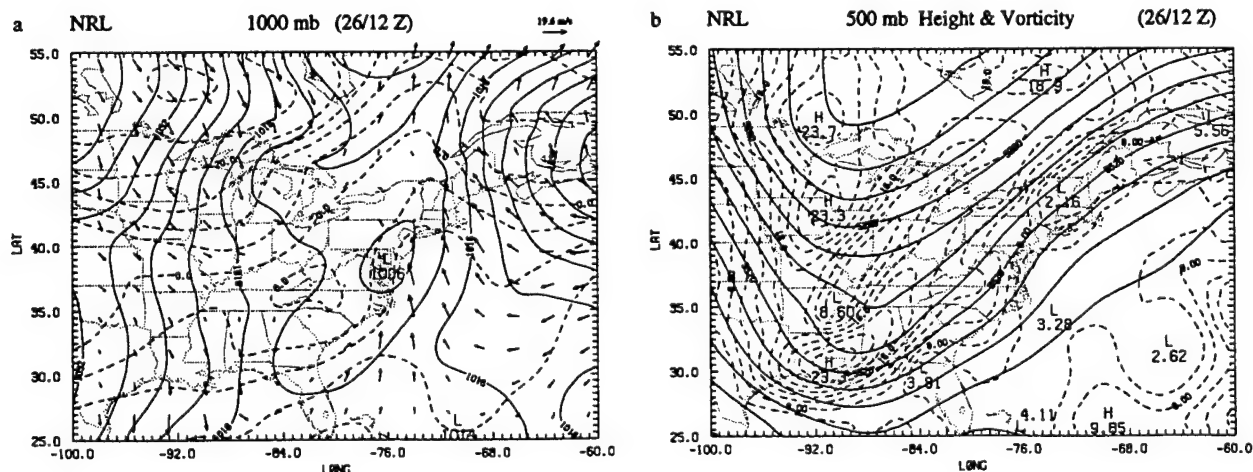


FIG. 17. The NRL analysis for 1200 UTC 26 January of (a) sea level pressure (mb), 1000-mb temperature ( $^{\circ}\text{C}$ ), and winds, and (b) the geopotential height (gpm), absolute vorticity ( $\times 10^{-5} \text{ s}^{-1}$ ) at 500 mb. Contours as in Fig. 14.



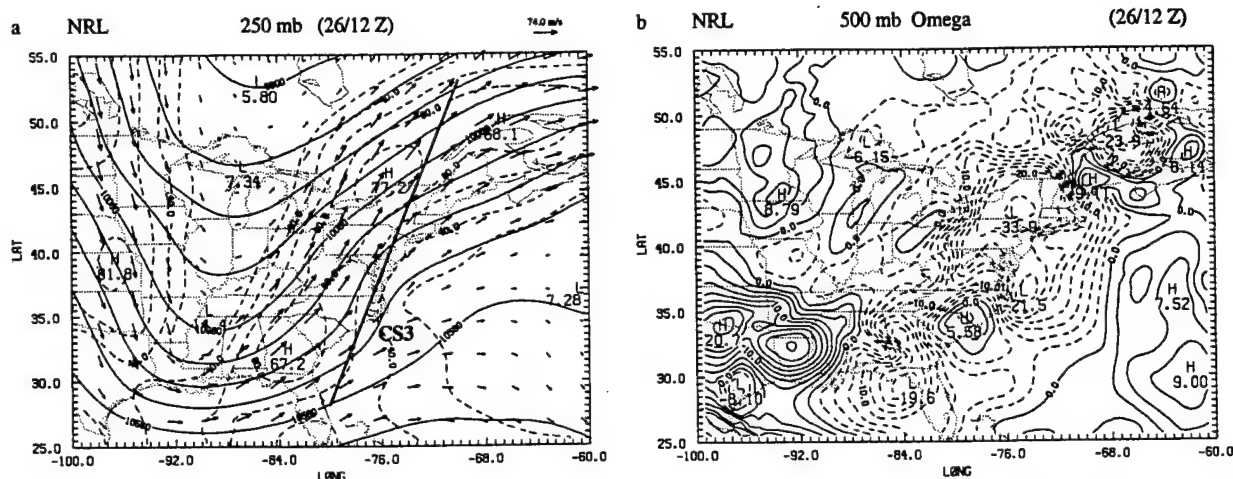


FIG. 18. (a) The geopotential height (gpm), temperature ( $^{\circ}\text{C}$ ), and winds at 250 mb; and (b) the vertical velocity ( $\text{mb h}^{-1}$ ) at 500 mb for the NRL analysis at 1200 UTC 26 January. Contours as in Fig. 10.

humidities of greater than 90% are analyzed in Fig. 15b over the coastal front, consistent with developing precipitation observed in the region (Doyle and Warner 1990).

### c. Cyclogenesis offshore

The 1000-mb analysis for 1200 UTC 26 January in Fig. 17a shows the coastal low has moved north to the Chesapeake Bay and is merging with a large region of weak low pressure over the northeast. Over the Great Lakes, a secondary wave is developing along a strong front. The surface pressure is falling over the southeast as the strong southern short wave aloft can be seen

reaching the base of the long-wave trough in Fig. 17b. The short wave from the Great Lakes has merged with the northern jet as it moved northeastward, contributing to stronger vorticity gradients over the St. Lawrence River in the right rear flank of the jet. The weak vorticity maximum from Georgia (Fig. 14b) has moved northeastward to southwest Virginia in Fig. 17b, with the coastal low moving ahead of it. Figure 18a shows the northern jet approaching the top of the ridge and the southern jet at the base of the long-wave trough at 250 mb. At 500 mb, two strong centers of ascent can be seen to have developed in Fig. 18b over New York State below the right rear flank of the northern jet, as it strengthened, and off Cape Hatteras to the southeast

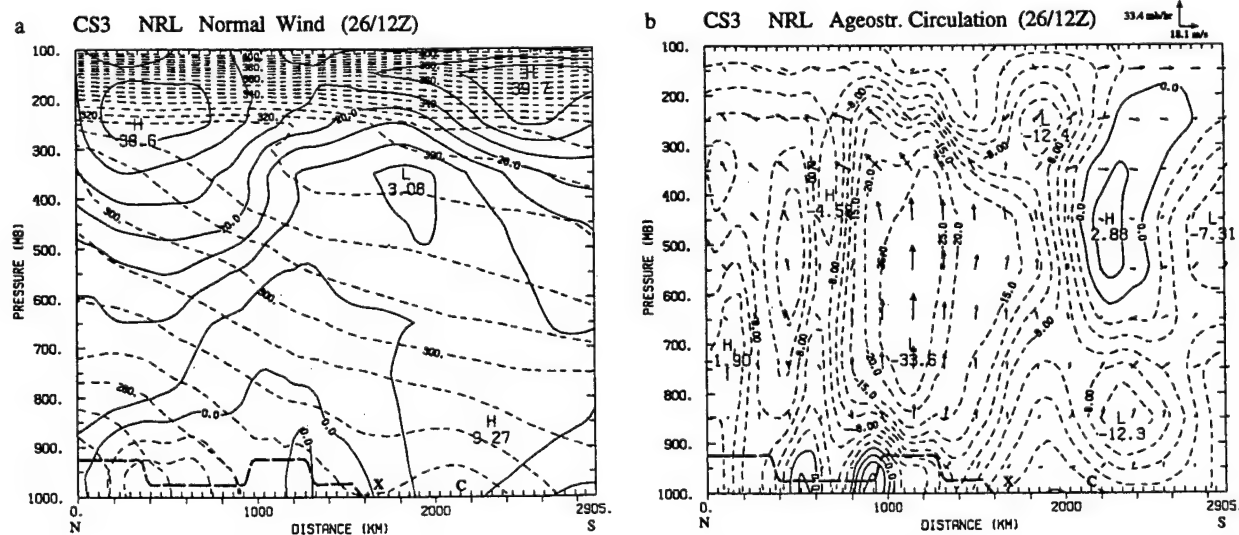


FIG. 19. (a) The wind normal to the cross section CS3 from  $53^{\circ}\text{N}$ ,  $70^{\circ}\text{W}$  to  $28^{\circ}\text{N}$ ,  $80^{\circ}\text{W}$  and (b) the vertical motion ( $\text{mb h}^{-1}$ ) and ageostrophic wind ( $\text{m s}^{-1}$ ) in the plane of cross section for 1200 UTC 26 January. Contours as in Figs. 11 and 12 except that contours of vertical motion less than  $-12$  and  $-40 \text{ mb h}^{-1}$  are every 5 and 15  $\text{mb h}^{-1}$ , respectively.

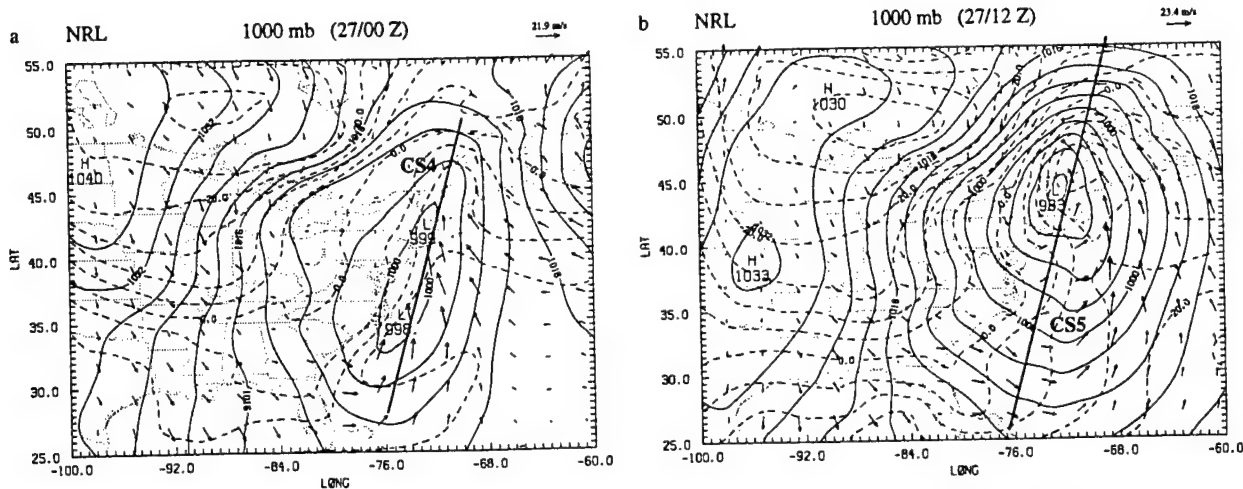


FIG. 20. The sea level pressure (mb), 1000-mb temperature ( $^{\circ}\text{C}$ ), and winds for the NRL analysis at (a) 0000 UTC and (b) 1200 UTC on 27 January. Contours as in Fig. 2.

of the center of the coastal low as it moved with the jet. The region of ascent over Florida is in response to the exit region of the southern jet at the base of the long-wave trough.

The merging of the circulations associated with the entrance region of the northern jet and the coastal low are illustrated in a cross section CS3 along the coastline cutting through the northern jet and coastal low (see Fig. 18a). The northern jet at 250 mb and the subtropical jet stream to the south at 150 mb can be seen in the wind normal to the cross section in Fig. 19a. The corresponding ageostrophic circulation in the plane of the cross section is shown in Fig. 19b. A strengthened direct secondary circulation in the entrance region of the northern jet can be seen with maximum ascent of  $33.6 \text{ mb h}^{-1}$  and southerly ageostrophic flow aloft to the north. The northerly ageostrophic flow to the south in the upper troposphere is associated with the subtropical jet stream. The position of the coastal low is shown by the "X" to the rear of the region of strongest ascent in the northern jet's secondary circulation. Ascent at the southern end of the cross section is associated with the exit region of the approaching jet at the base of the long-wave trough.

The 1000-mb analyses for 0000 and 1200 UTC 27 January are shown in Figs. 20a and 20b. They show the development of a new low off Cape Hatteras, which moves northward and deepens rapidly to overshadow the earlier coastal low. Cross sections CS4 and CS5 are taken along the coast to show the evolution of the secondary circulations associated with the two jets during this period. The positions of the jets for each cross section can be seen in Figs. 21a and 21c, and the corresponding ageostrophic circulations in Figs. 21b and 21d. The positions of the lows are indicated by the "X" in the figures. As the southern jet rounds the long-wave trough and crosses the coast at 0000 UTC, the new

low can be seen developing beneath strong ascent and northerly ageostrophic flow aloft in the exit region of this jet (Fig. 21b). The circulation associated with the northern jet and surface low is a separate circulation to the north at this stage. The rapid development of the new low in the next 12 h can be seen in Figs. 21c and 21d to be associated with the movement of the southern jet and its secondary circulation northward. By 1200 UTC, this secondary circulation in the southern jet has caught up with the circulation in the entrance region of the northern jet, so that they cooperate in strengthening the ascent in the rapidly developing low. Such cooperation has been found in other cases analyzed by Uccellini and Kocin (1987).

## 5. Summary and conclusions

During the last decade optimal interpolation replaced successive correction methods as the dominant objective analysis technique in operational weather forecasting systems. However, with the advent of Bratseth's (1986) analysis scheme, which converges to the optimal interpolation solution, the less expensive approach of successive correction has become a powerful and attractive alternative analysis method. The objective analysis scheme developed for use with the NRL limited-area weather prediction model uses the Bratseth scheme, in which the data weights are dependent on the covariance between observations, are reduced in regions of higher data density, and include observational errors. We have devised a computationally inexpensive method for linking the mass and momentum fields that is different from earlier methods reported in the literature (e.g., Cressman 1959; Lorenc et al. 1991). The key element is obtaining the gradient of the geopotential change from the change in an estimated geostrophic wind at each iteration to enhance the initial



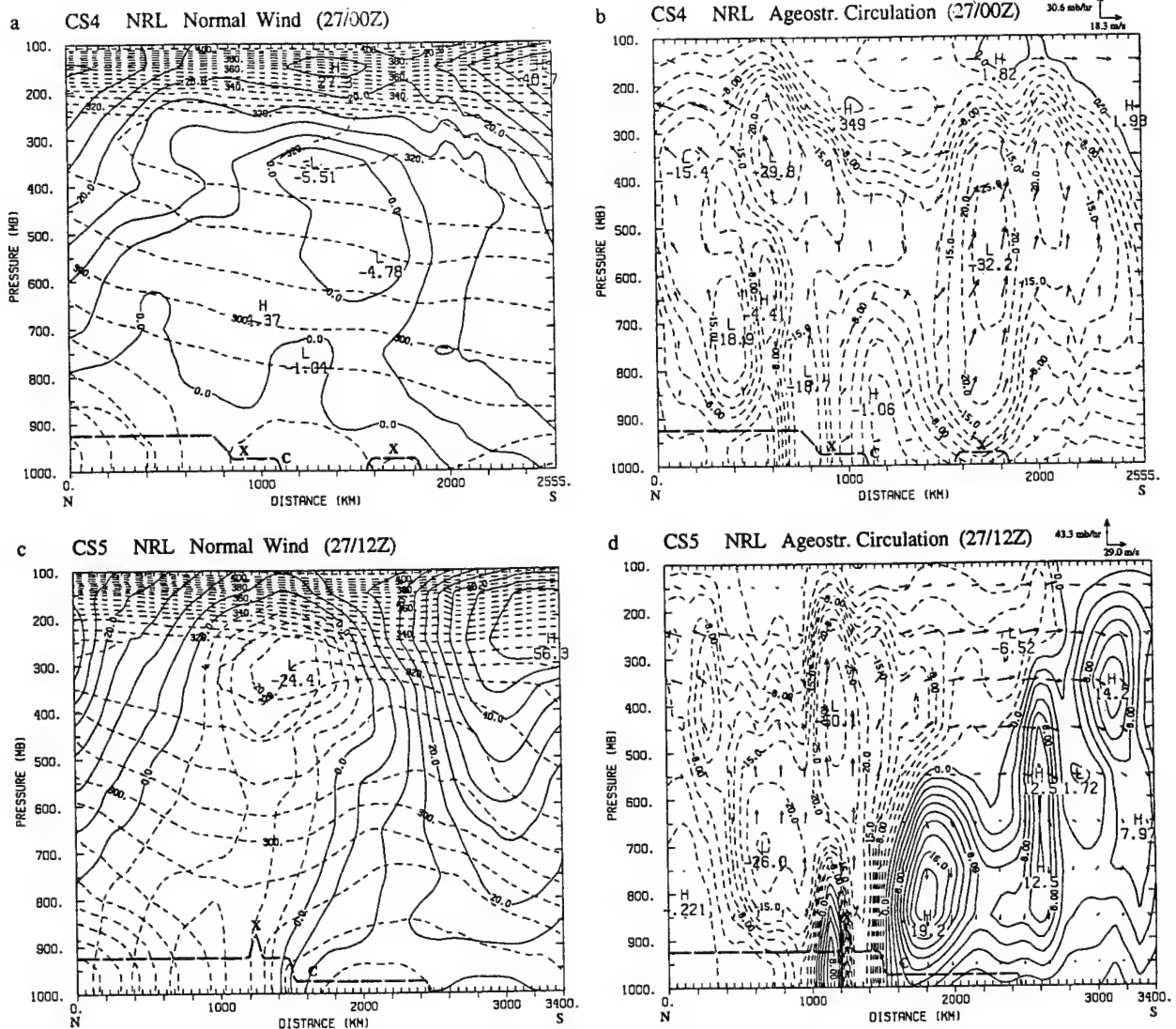


FIG. 21. (a) The wind normal to a cross section CS4 from 50.5°N, 70°W to 28°N, 76°W and (b) the vertical motion ( $\text{mb h}^{-1}$ ) and ageostrophic wind ( $\text{m s}^{-1}$ ) in the plane of cross section CS4 for the NRL analysis at 0000 UTC 27 January. Here (c) and (d) are the same as (a) and (b) but for cross section CS5 from 55.5°N, 68.7°W to 25.5°N, 76.7°W at 1200 UTC 27 January. Contours as in Fig. 19.

univariate analysis of the geopotential. We use the initial univariate wind analysis to provide only the starting estimate of the geostrophic wind for the first iteration. For subsequent iterations, the geostrophic wind is estimated from the updated geopotential gradient. After this enhancement of the geopotential, the univariate wind analysis is updated for the change in the geostrophic wind.

An evaluation of the NRL objective analysis scheme has been accomplished using a GALE IOP 2 dataset. The use of a prior model forecast as a first guess for the analysis was crucial in obtaining mesoscale features in the analysis. Such features were not produced by our earlier scheme, which used a Barnes (1973) scheme to enhance NMC hemispheric analyses (Chang et al. 1989; Shi et al. 1991). Over the region of the eastern

United States, where there is a large amount of data, the Barnes scheme produced as good an analysis as the Bratseth (1986) scheme, when the same first-guess forecast is used. The Bratseth scheme was more superior in the other regions where it could adjust for the changing data density. Our simple geostrophic method for linking the mass and wind-field analyses provided tighter gradients in these fields, particularly in the regions of lower data density outside of the eastern United States.

For the second IOP of GALE, the vertical circulations were derived from the analyses by application of the vertical-mode initialization scheme of Bourke and McGregor (1983). Superior mesoscale vertical circulations were produced in the coastal low and upper-tropospheric jet streaks with the new NRL analysis

scheme when compared to that derived from the earlier Barnes enhancement of the NMC hemispheric analyses. These circulations clearly demonstrated the interaction of the coastal low with the entrance region of a jet streak in the upper troposphere. The cooperation of the secondary circulations in two jets during offshore cyclogenesis is also shown. Being able to produce such mesoscale circulations using these analysis and initialization schemes is important for providing accurate initial conditions for generating forecasts with the limited-area model. Future work will use these improved analyses with the initialization scheme to test assimilating the GALE data in a limited-area analysis-forecast system.

**Acknowledgments.** This research was sponsored by NRL's basic research program and by SPAWAR of the U.S. Navy. The first author was supported at Science Applications International Corporation under Contract N00014-89-R-HB08 with NRL, and the second author was supported as a graduate student at North Carolina State University by the U.S. Air Force. Part of the computer time was provided by the North Carolina Super Computing Center, Research Triangle Park.

#### REFERENCES

- Barnes, S. L., 1973: Mesoscale objective map analysis using weighted time-series observations. NOAA Tech. Memo., ERL NSSL-62, Norman, OK, 60 pp.
- Benjamin, S. G., 1989: An isentropic meso-scale analysis system and its sensitivity to aircraft and surface observations. *Mon. Wea. Rev.*, **117**, 1586-1603.
- , and N. L. Seaman, 1985: A simple scheme for objective analysis in curved flow. *Mon. Wea. Rev.*, **113**, 1184-1198.
- Bergthörsson, P., and B. R. Döös, 1955: Numerical weather map analysis. *Tellus*, **7**, 329-340.
- Bosart, L. F., 1988: Coastal frontogenesis and cyclogenesis during GALE IOP #2. Preliminary Reports, GALE/CASP Workshop, Virginia Beach, VA, NCAR 75-93. [Available from GALE Project Office, P.O. Box 3000, Boulder CO 80807.]
- Bourke, W., and J. L. McGregor, 1983: A nonlinear vertical mode initialization scheme for a limited area prediction model. *Mon. Wea. Rev.*, **111**, 2285-2297.
- Bratseth, A. M., 1986: Statistical interpolation by means of successive corrections. *Tellus*, **38A**, 439-447.
- Chang, S., K. Brehme, R. Madala, and K. Sashegyi, 1989: A numerical study of the East Coast snow storm of 10-12 February 1983. *Mon. Wea. Rev.*, **117**, 1768-1778.
- Cressman, G., 1959: An operational objective analysis system. *Mon. Wea. Rev.*, **87**, 367-374.
- DiMego, G. J., 1988: The National Meteorological Center regional analysis system. *Mon. Wea. Rev.*, **116**, 977-1000.
- Dirks, R. A., J. P. Kuettner, and J. A. Moore, 1988: Genesis of Atlantic Lows Experiment (GALE): An overview. *Bull. Amer. Meteor. Soc.*, **69**, 148-160.
- Doyle, J. D., and T. T. Warner, 1990: Mesoscale coastal processes during GALE IOP 2. *Mon. Wea. Rev.*, **118**, 283-308.
- Grønås, S., and K. H. Midtbø, 1987: Operational multivariate analyses by successive corrections. Collection of papers presented at WMO/IUGG numerical weather prediction symposium, Tokyo, 4-8 August 1986. *J. Meteor. Soc. Japan*, 61-74.
- Harms, D. E., K. D. Sashegyi, R. V. Madala, and S. Raman, 1992: Four-dimensional data assimilation of GALE data using a multivariate analysis scheme and a mesoscale model with diabatic initialization. NRL Tech. Memo. Rep., No. 7147, Naval Research Laboratory, Washington D.C., 236 pp. [NTIS A256063.]
- Hollingsworth, A., and P. Lönnberg, 1986: The statistical structure of short-range forecast errors as determined from radiosonde data. Part I: The wind field. *Tellus*, **38A**, 111-136.
- Keyser, D., and M. A. Shapiro, 1986: A review of the structure and dynamics of upper-level frontal zones. *Mon. Wea. Rev.*, **114**, 452-499.
- Kistler, R. E., and R. D. McPherson, 1975: On the use of a local wind correction technique in four-dimensional data assimilation. *Mon. Wea. Rev.*, **103**, 445-449.
- Koch, S. E., M. DesJardins, and P. J. Kocin, 1983: An interactive Barnes objective map analysis scheme for use with satellite and conventional data. *J. Climate Appl. Meteor.*, **22**, 1487-1503.
- Lorenc, A. C., R. S. Bell, and B. MacPherson, 1991: The Meteorological Office analysis correction data assimilation scheme. *Quart. J. Roy. Meteor. Soc.*, **117**, 59-89.
- Madala, R. V., S. W. Chang, U. C. Mohanty, S. C. Madan, R. K. Paliwal, V. B. Sarin, T. Holt, and S. Raman, 1987: Description of the Naval Research Laboratory Limited Area Dynamical Weather Prediction Model. NRL Tech. Memo. Rep., No. 5992, Naval Research Laboratory, Washington, D.C., 131 pp. [NTIS A182780.]
- Mills, G. A., and R. S. Seaman, 1990: The BMRC regional data assimilation system. *Mon. Wea. Rev.*, **118**, 1217-1237.
- Mercer, T. J., 1987: *Genesis of Atlantic Lows Experiment (GALE): Data Users Guide*. GALE Data Center, Department of Physics and Atmospheric Science, Drexel University, 106 pp.
- Raman, S., and A. J. Riordan, 1988: Genesis of Atlantic Lows Experiment: The planetary-boundary-layer subprogram of GALE. *Bull. Amer. Meteor. Soc.*, **69**, 161-172.
- Reynolds, R. W., 1982: A monthly averaged climatology of sea surface temperatures. NOAA Tech. Rep., NWS-31, Climate Analysis Center, National Weather Service, Washington, D.C., 35 pp.
- Riordan, A. J., 1990: Examination of the mesoscale features of the GALE coastal front of 24-25 January 1986. *Mon. Wea. Rev.*, **118**, 258-282.
- Sashegyi, K. D., and R. V. Madala, 1990: Tests of initialization procedures with the NRL limited area numerical weather prediction model. NRL Tech. Memo. Rep., No. 6648, Naval Research Laboratory, Washington D.C., 88 pp. [NTIS A223549.]
- , and —, 1993: Application of vertical mode initialization to a limited area model in flux form. *Mon. Wea. Rev.*, **121**, 207-220.
- Schlatter, T. W., 1988: Past and present trends in the objective analysis of meteorological data for nowcasting and numerical forecasting. Preprints, *Eighth Conf. on Numerical Weather Prediction*, Baltimore, MD, Amer. Meteor. Soc., J9-J25.
- Seaman, R. S., 1988: Some real data tests of the interpolation accuracy of Bratseth's successive correction method. *Tellus*, **40A**, 173-176.
- Shaw, D. B., P. Lönnberg, A. Hollingsworth, and P. Undén, 1987: Data assimilation: The 1984/85 revisions of the ECMWF mass and wind analysis. *Quart. J. Roy. Meteor. Soc.*, **113**, 533-566.
- Shi, J. J., S. Chang, K. Sashegyi, and S. Raman, 1991: Enhancement of objective analysis of Hurricane Florence (1988) with dropsonde data. Preprints, *19th Conf. on Hurricanes and Tropical Meteorology*, Miami, Amer. Meteor. Soc., 335-337.
- Uccellini, L. W., and D. R. Johnson, 1979: The coupling of lower tropospheric jet streak and implications for the development of severe convective storms. *Mon. Wea. Rev.*, **107**, 682-703.
- , and P. J. Kocin, 1987: The interaction of jet streak circulations during heavy snow events along the east coast of the United States. *Wea. Forecasting*, **2**, 289-308.
- , R. A. Petersen, C. H. Wash, and K. F. Brill, 1984: The Presidents' Day cyclone of 18-19 February 1979: Synoptic overview and analysis of the subtropical jet streak influencing the pre-cyclogenetic period. *Mon. Wea. Rev.*, **112**, 31-55.
- Warner, T. T., M. N. Lakhtakia, J. D. Doyle, and R. A. Pearson, 1990: Marine atmospheric boundary layer circulations forced by Gulf Stream sea surface temperature gradients. *Mon. Wea. Rev.*, **118**, 309-323.

## **Appendix L**

### **Diabatic Initialization Tests Using the Naval Research Laboratory Limited-Area Numerical Weather Prediction Model**

Reprinted from MONTHLY WEATHER REVIEW, Vol. 121, No. 11, November 1993  
American Meteorological Society

**Diabatic Initialization Tests Using the Naval Research Laboratory Limited-Area  
Numerical Weather Prediction Model**

DEWEY E. HARMS

RANGARAO V. MADALA

SETHU RAMAN

KEITH D. SASHEGYI

## NOTES AND CORRESPONDENCE

## Diabatic Initialization Tests Using the Naval Research Laboratory Limited-Area Numerical Weather Prediction Model

DEWEY E. HARMS

*Department of Marine, Earth and Atmospheric Sciences, North Carolina State University, Raleigh, North Carolina*

RANGARAO V. MADALA

*Naval Research Laboratory, Washington, D.C.*

SETHU RAMAN

*Department of Marine, Earth and Atmospheric Sciences, North Carolina State University, Raleigh, North Carolina*

KEITH D. SASHEGYI

*Naval Research Laboratory, Washington, D.C.*

22 June 1992 and 9 April 1993

## ABSTRACT

Diabatic forcing has been incorporated into a nonlinear normal-mode initialization scheme to provide more realistic initial conditions and to alleviate the problem of the spinup time of the Naval Research Laboratory Limited-Area Numerical Weather Prediction Model. Latent heating profiles are computed from the observed rainfall and from the model-generated convective rainfall at locations where there were no observations. The latent heating is distributed in the vertical according to the cumulus convective parameterization scheme (Kuo scheme) of the model. The results of a case study from the Genesis of Atlantic Lows Experiment indicated that model spinup of forecast rainfall can be reduced when diabatic initialization with merging of heat and/or rain is used.

## 1. Introduction

The dominant forcing in the troposphere within areas of large precipitation is diabatic heating (convective and radiative heating, and large-scale condensation). The present study deals strictly with diabatic heating from cumulus convection. A convective heating term is incorporated in the balance condition for the high-frequency normal modes (Bengtsson 1981; Errico and Rasch 1988; Kitade 1983; Wergen 1983). With the inclusion of heating corresponding to observed rainfall data in the diabatic forcing term, the initialization can force the model state toward the real atmospheric state. As a result, the diabatic initialization can improve the model's forecast fields. Possibly, the primary benefit of initialization with diabatic forcing and moisture initialization is that the spinup problem can be reduced. That is, diabatic nonlinear normal-

mode initialization (DNNMI) produces an initial model state that already includes realistic heating.

Model spinup appears in all numerical forecast systems both in midlatitudes and tropics (Kasahara et al. 1988). It is one of the most serious problems in numerical weather prediction (NWP), and has been documented in research and operational models. Girard and Jarraud (1982) and Heckley (1985) documented spinup in the operational models used by the European Centre for Medium-Range Weather Forecasts, whereas Miyakoda et al. (1978) and Donner (1988) illustrated different aspects of the spinup phenomena in research models at the Geophysical Fluid Dynamics Laboratory and National Center for Atmospheric Research, respectively.

Inadequate physical parameterizations and incorrect initial specifications of divergence, moisture, and thermal fields are the primary causes of spinup (Mohanty et al. 1986). Most normal-mode initialization methods have been adiabatic in nature; that is, the existing latent heating at the initial model time was excluded, leaving out a significant heat source that affected the adjustment between the mass and momentum fields. Lejenas

---

*Corresponding author address:* Prof. Sethu Raman, Department of Marine, Earth and Atmospheric Sciences, College of Physical and Mathematical Sciences, North Carolina State University, Box 8208, Raleigh, NC 27695-8208.

(1980) found that adiabatic normal-mode initialization, while providing improved vertical velocity profiles, does not alleviate the spinup problem. Data assimilation techniques that incorporate a more realistic background field in the analysis of observed data have been developed (Lejenas 1980). At the start of each update cycle of the assimilation, the background forecast field is corrected using the observations of mass, momentum, and humidity. During this process, the divergent part of the wind is not represented properly, because the divergence has the same order of magnitude as the errors in the wind field. A consistent diabatic circulation can be generated if the analysis at each cycle of the assimilation is initialized with a diabatic initialization procedure. Turpeinen et al. (1990) concluded that the inclusion of observed low-level latent heat sources with a consistent and higher-resolution moisture analysis are critical components in reducing the underestimation of initial divergence and, hence, precipitation rates.

Throughout the 1980s, NWP models incorporating initial latent heating based on rain rates have been developed. Turpeinen et al. (1990) summarized the main features of some of these models. Mohanty et al. (1986) investigated the inclusion of diabatic heating in the normal-mode initialization (NMI) and found that the divergent circulation was rapidly destroyed by the integrated model heating if it differed too much from the observed heating. In the present study, we have merged the model-produced heating, during the first few hours of integration, with the heating used in the initialization.

The major thrust of this paper is to incorporate the latent heat forcing released due to convective precipitation estimated from the conventional and satellite observations into the normal-mode initialization of the Naval Research Laboratory (NRL) Limited-Area Numerical Weather Prediction Model in an effort to shorten the spinup time. Our goal is also to demonstrate that NMI with diabatic forcing provides improved initialized fields over adiabatic NMI. We have included a diabatic heating term, derived from "spinup" model convective rainfall and observed rainfall, in our nonlinear normal-mode initialization (NNMI) to better define the initial conditions for model integration.

Several model runs (test cases) are made to test the effectiveness of DNNMI as compared to initialization excluding the heating term, or adiabatic NNMI (ANNMI). The NRL mesoscale model is briefly described in the next section. The procedure for computing the diabatic heating for the initialization is then described, followed by the experimental design and results.

## 2. Model description

The model used in the present study was developed at the Naval Research Laboratory, and is detailed in Holt et al. (1990) and in NRL memorandum reports

by Madala et al. (1987) and Sashegyi and Madala (1992). This is a primitive equation model in terrain-following coordinates having a one-way interacting nested grid network. The coarse grid covers a domain including the continental United States from  $10^{\circ}$  to  $70^{\circ}\text{N}$  and  $40^{\circ}$  to  $140^{\circ}\text{W}$ , with a horizontal resolution of  $2^{\circ}$  longitude ( $170\text{ km}$  at  $40^{\circ}\text{N}$ )  $\times$   $1.5^{\circ}$  latitude ( $166.5\text{ km}$ ). The Genesis of Atlantic Lows Experiment (GALE) (inner or fine) grid covers a smaller domain including the eastern half of the United States and extending out over the Gulf Stream from  $23.5^{\circ}$  to  $56.5^{\circ}\text{N}$  and  $58^{\circ}$  to  $102^{\circ}\text{W}$  with a finer horizontal resolution of  $0.67^{\circ}$  longitude ( $56.7\text{ km}$  at  $40^{\circ}\text{N}$ )  $\times$   $0.5^{\circ}$  latitude ( $55.5\text{ km}$ ). In the vertical, both grids use 10 equally spaced sigma levels. Model topography for both grid domains is obtained from navy 10-min global topographical data. Even though this paper addresses latent heat release due to convective precipitation, there are two reasons for selecting this extratropical case. One is the availability of a comprehensive GALE dataset. The other is the existence of mesoscale convection over the ocean and the coastal areas due to strong boundary-layer baroclinicity.

The continuous governing equations are written in flux form, and the model's time integration scheme is the split-explicit method that allows larger time steps by effectively separating various terms in the prognostic equations into parts governing the slow-moving Rossby modes and fast-moving gravity modes. A staggered grid network (Arakawa's C grid) is used for horizontal differencing. Lateral boundary conditions suggested by Davies (1976, 1983) are employed in the present version of the model. Monin-Obukhov similarity theory (Yamada 1979) is used to determine the surface transfer of momentum, sensible heat, and latent heat. The cumulus convective parameterization scheme used in this model is the one suggested by Kuo (1974) and modified by Anthes (1977). The parameterization of large-scale or nonconvective precipitation follows Hal-tiner and Williams (1980); that is, the excess moisture in a supersaturated layer is condensed out isobarically.

## 3. Diabatic heating in model initialization

Until recently, the NRL model was initialized exclusively using an adiabatic nonlinear normal-mode initialization. The procedure is detailed by Sashegyi and Madala (1990, 1993). In their NNMI, only the first three modes—the external mode and first two internal modes of the model—are initialized. Sashegyi and Madala (1990) showed that the first two modes require only two iterations of the scheme to converge. The third mode converged after five iterations.

Adiabatic NNMI has proven to be extremely effective in controlling spurious large-amplitude gravity-wave oscillations due to initial imbalances between the mass and wind fields in primitive equation models (Puri and Miller 1990; Sashegyi and Madala 1990).



However, the use of adiabatic NNMI (ANNMI) leads to a drastic depletion of the divergent circulation.

Wergen (1983, 1987) introduced a procedure to overcome this problem, in which average diabatic heating is obtained by integrating the model for a few time steps prior to the initialization. The average heating is then included in the nonlinear forcing of the iterative initialization process. The fixed diabatic heating is determined as the time-mean heating generated by model physics (cumulus parameterization and large-scale heating) during the short integration. Unfortunately, most forecast models do not produce realistic heating rates during the first few hours. Therefore, in our experiments we chose to integrate the model for 9 h before accumulating the model latent heating and convective rainfall from which our time-mean heating and rainfall rates were derived. The diabatic NNMI (DNNMI) used in this study is similar to Wergen's, but it is original in that spunup model heating is applied in the initialization rather than the heating from the first few hours of integration, as is usually done. The procedure involves the following steps.

1) The model is integrated for 12 h from adiabatically initialized fields. Convective rainfall, from which the diabatic heating is derived, is accumulated from 9 to 12 h of this initial integration (control run), allowing ample time for model spinup.

2) Time average convective rainfall rates over the 3-h period are derived for all grid points using conventional and satellite-derived observations. Model rainfall was used for locations over the coastal ocean, since satellite rainfall data were unreliable.

3) The model is tested for convective instability at the observed rainfall locations. The average rain rates are converted into vertical profiles of heating using a reverse Kuo cumulus parameterization only at the locations where the atmosphere is convectively unstable. Inversion of the Kuo scheme is essentially straightforward and is done only when the atmosphere is convectively unstable at a location (Harms et al. 1992). This vertical distribution of the latent heating is based on the cumulus convective scheme of the model. Thus, no simplifying hypotheses are needed. The advantage of the present approach is an improved consistency obtained with the physical parameterization scheme of the model.

4) This three-dimensional diabatic heating field is then added as a forcing term in the NNMI thermodynamic energy balance equation as the DNNMI is performed. As a result, diabatic effects are explicitly included in the specification of the heating field.

The aforementioned diabatic initialization is primarily for heating associated with convective precipitation. The heating is nearly zero in the lower troposphere and varies significantly from case to case in the upper troposphere. The first three modes of the model account for 40%–50% of the convective heating in the upper troposphere. Therefore, we assume that the

method described here accounts for a significant part of the divergence field. The iterative scheme used in the DNNMI does not converge to a solution with the inclusion of the fourth mode, although it may contribute significantly to convection.

The conversion of rainfall rates into vertical profiles of convective heating depends on the stability of the environment as determined by the cumulus parameterization. If convective instability occurs, a heating function is computed using the reverse Kuo scheme. This heating function is then used to distribute the diabatic heating, derived from the average rainfall rates, in the vertical direction. If the environment is convectively stable, the diabatic heating associated with the two-dimensional rainfall distribution will be taken as zero. Therefore, nonconvective precipitation does not contribute to the diabatic heating in the present initialization scheme.

The persistence of balance achieved by DNNMI during the early stages of the model integration depends heavily on the compatibility between the specified heating during initialization and the model-produced heating during integration (Puri and Miller 1990). Puri (1987) suggested that one possible way of retaining this compatibility in the heating rates would be to adjust the moisture field until the model-produced heating rates determined by the convective parameterization in the model are similar to those used during DNNMI. Here, two procedures are used to retain this desired compatibility in heating rates. First, the model rainfall and heating rates produced during the first 3 h of integration are merged with the corresponding rates from the initialization. A nonlinear weighting factor  $\alpha$  is employed where  $\alpha = 1$  at  $t = 0$  h and  $\alpha = 0$  at  $t = 3$  h. The relation is given by

$$R_m = \alpha R_i + (1 - \alpha) R_c, \quad (1)$$

where  $R_i$  is the convective rainfall rate (from the control) used in DNNMI,  $R_c$  is the model-produced convective rainfall rate,  $R_m$  is the merged rain rate, and  $\alpha$  is given by

$$\alpha = 1 - \frac{[1 + \sin(\pi t/3 - \pi/2)]}{2}. \quad (2)$$

The foregoing relations allow the influence of the initialized heating and rain rates to approach zero in a smoother manner than a simple linear relationship would allow. Merging is applicable only for DNNMI cases, since ANNMI, by definition, does not include a diabatic heating term in its balance equation.

The second method involves adjusting the humidity fields prior to initialization. The importance of moisture adjustment in diabatic initialization was emphasized by Wolcott and Warner (1981). They argued that if the environment is not humid enough, the upward motion associated with the initialized divergence field will not be sustained by latent heat release. In the pres-



ent study, specific humidity is enhanced only at grid points where convective rainfall is occurring and the relative humidity is less than 95%. At those points, the specific humidity is increased to 95% of the saturation specific humidity at the three lowest model levels. However, we found that the changes in the humidity fields were small and, as a result, the adjustment had minimal effect on the convective rainfall. Since the modeled large-scale condensation occurs only upon supersaturation, not at 95% relative humidity, this moisture adjustment would have little effect on non-convective precipitation.

#### 4. Experimental design

Before the experiments are described, the synoptic situation for our study is given.

##### *a. Synoptic setting*

During the period 0000 UTC 25 January–0000 UTC 27 January 1986, coastal frontogenesis and cyclogenesis took place along the eastern seaboard. At 0000 UTC 26 January, the coastal front extended from Georgia to southern New England. Cold-air damming and warming of the air over the Gulf Stream led to the strong thermal gradient along the coast. By 1200 UTC 26 January 1986, a weak surface disturbance was located across the Carolinas and Georgia. This disturbance would strengthen over the next 12 h due to cold-air advection aloft approaching from the northwest in association with a cold front in the Ohio River valley. The surface cyclone center became evident off the Carolina coast around 0000 UTC 27 January 1986.

By 1200 UTC 27 January 1986, a developing low pressure system was found off the New Jersey coast, replacing the coastal front wave that had moved northward into New England and disappeared. Behind the developing cyclone, cold air associated with a midtropospheric vortex continued southeastward. This influx of cold air over the warm waters of the Gulf Stream fueled coastal frontogenesis south of the developing cyclone.

##### *b. Description of the model experiments*

Initially, three test cases (model runs) were performed to determine improvements (if any) in the model initial state and subsequent forecasts using DNNMI versus ANNMI. The first is a control run in which the model is initialized at 1200 UTC 26 January 1986 using the NMC analyzed data. These fields of 2.5° resolution are first interpolated to the model grid and then initialized with the ANNMI for the first three vertical normal modes of the model. The model is then integrated for 24 h. The 12-h forecast from the control run serves as the initial fields for experiments 2 and 3. In case 2, the model is initialized using DNNMI on the forecast fields from case 1 valid at 0000 UTC 27

January 1986. The analyzed rainfall that includes the observations and the model rainfall in data-void areas (2100 UTC 26 January–0000 UTC 27 January 1986 of the control) is used to compute heating rates at each vertical level of the model for the DNNMI. The model is then integrated for 12 h, with heat and/or rain merging. The initialization for the next case (run 3) is simply an ANNMI on the control run's 12-h forecast.

For this study, the control run is compared against the other two cases; from 1200 UTC 26 January to 0000 UTC 27 January 1986 of the control run, the model should have developed the divergent part of the wind reasonably well. By using model-generated rainfall rates in the DNNMI (case 2), one would expect a negligible spinup during the subsequent forecast. Also, one might expect little change due to the initialization using model rain since the model heating function is consistent with other model parameters. By comparing the initialized and subsequent forecast fields from case 2 with the corresponding fields from the control, one can determine if the model-generated rainfall, which is a 2D distribution, can re-create the 3D distribution of vertical heating rates accurately.

#### 5. Results

The results obtained by making qualitative comparisons of meteorological fields from the different model initializations and forecasts of the three test cases indicate that the differences between cases 2 and 3 of their respective initialized fields of 1000-, 500-, and 250-mb geopotential height, temperature, and winds are extremely small. As expected, the first-order analysis fields (12-h forecast of run 1) changed little with each initialization in these test cases, and as a result, the forecasts (valid at 1200 UTC 27 January 1986) of these variables from these two runs are almost identical and agree well with the control run forecast.

##### *a. Comparison of initialized vertical velocity*

Since vertical velocity or  $\omega$  ( $dp/dt$ ) is directly related to diabatic heating, we can expect noticeable differences between the initial states of omega from cases 2 and 3. Furthermore, the effectiveness of diabatic heating in inducing divergent circulations can be seen by comparing omega fields from DNNMI and those resulting from ANNMI. As expected, in geographic areas absent of precipitation, vertical velocity patterns in cases 2 (DNNMI) and 3 (ANNMI) are approximately the same and very close to the "control simulation" (Fig. 1). Off the East Coast, an area of strong ascent stretches along the eastern seaboard, and is associated with the old frontal boundary and the developing cyclone off the North Carolina coast. In this region, where the control run ("truth") predicts heavy rain at initialization time (0000 UTC 27 January 1986), the initialized state for run 2 is very close to the control simulation. The pattern and positions of maxima and minima in

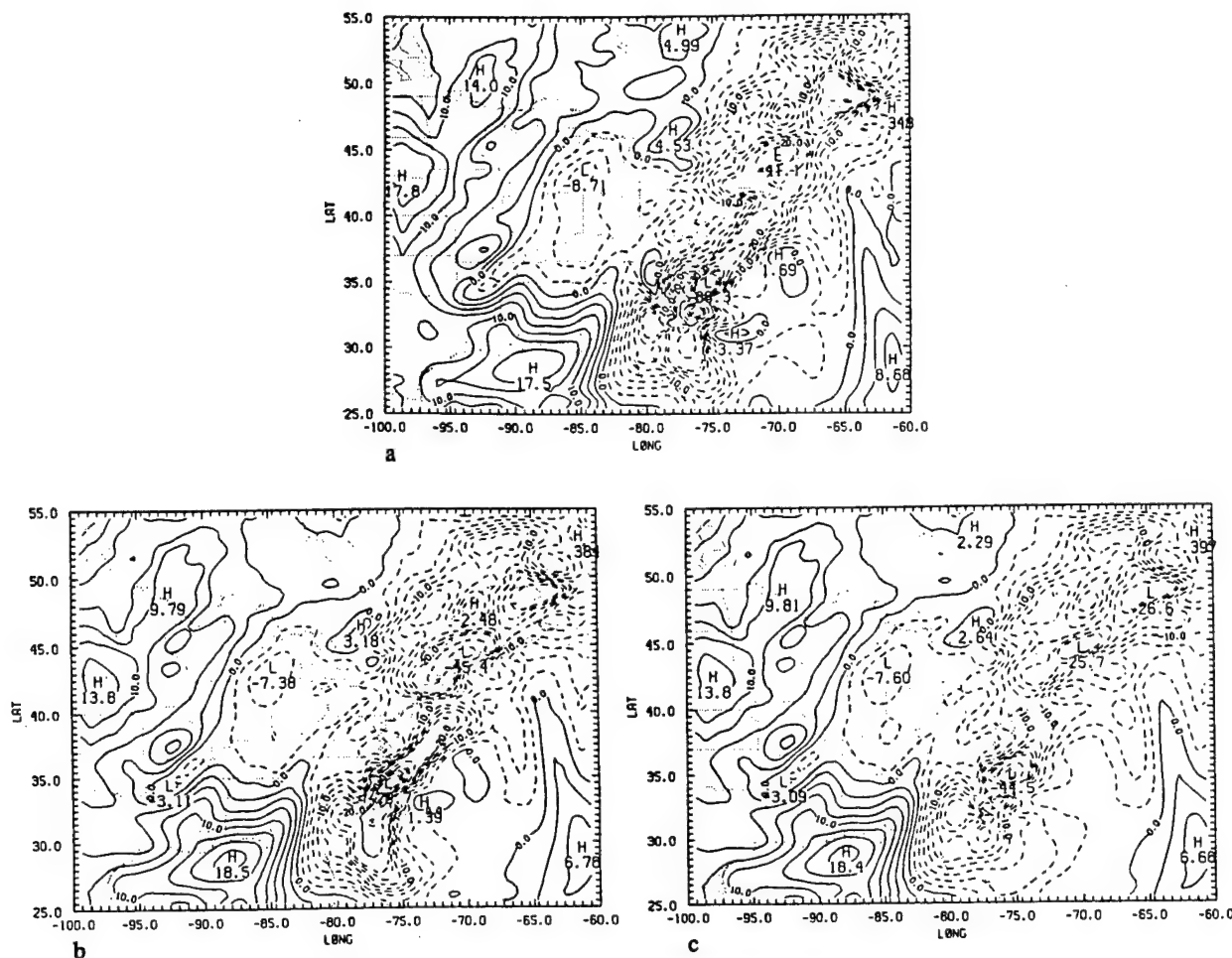


FIG. 1. Vertical-motion fields ( $\text{mb h}^{-1}$ ) for 500 mb valid at 0000 UTC 27 January 1986: (a) from 12-h forecast of the control run, (b) after DNNMI (case 2), and (c) after ANNMI (case 3).

the omega field show little change from the control run, suggesting the 3D structure of model convective heating can be re-created from a 2D rain distribution. A further comparison between case 2 and case 3 reveals the deficiency of ANNMI. In the vicinity of the developing cyclone, the magnitude of  $\omega$  has changed substantially using ANNMI; the maximum upward velocity is only about 60% of that resulting from DNNMI. Since a significant amount of the divergence (and hence vertical motions) associated with heavy precipitation events may be forced by latent heat release, and since the nonlinear step in the ANNMI does not include this diabatic forcing, the divergence due to this forcing will be removed as if it were associated with unwanted gravity waves. As a result, the vertical velocities are underestimated.

#### b. Forecast precipitation comparisons

The patterns of 12-h (0000–1200 UTC 27 January 1986) rainfall in runs 2 and 3 are very similar to each other and to the control (run 1) in areal coverage and

accumulation. The 12-h rainfall forecast from the adiabatically initialized fields is just as good as the forecast originating from the diabatically initialized fields. Since the physics and dynamics of the nonlinear normal-mode procedure are internally consistent with the numerical model (which provided the analysis fields), the initialization procedure, whether with or without diabatic heating, changes the model forecast fields only a small amount. As a result, the subsequent forecasts are essentially the same. Therefore, additional model experiments were performed in which GALE 3-h surface and upper-air data at 0000 UTC 27 January 1986 were analyzed using a multivariate, successive correction objective analysis scheme (Sashegyi et al. 1993). Model forecast fields served as the first guess for the analyses. Adiabatic (ANNMI) and diabatic (DNNMI) initializations were performed on the analysis fields. In the latter case, rain data from conventional rain gauges over land and from satellite-based observations over water were combined with the model-produced rainfall for computation of the 3D heating function in the model initialization procedure.

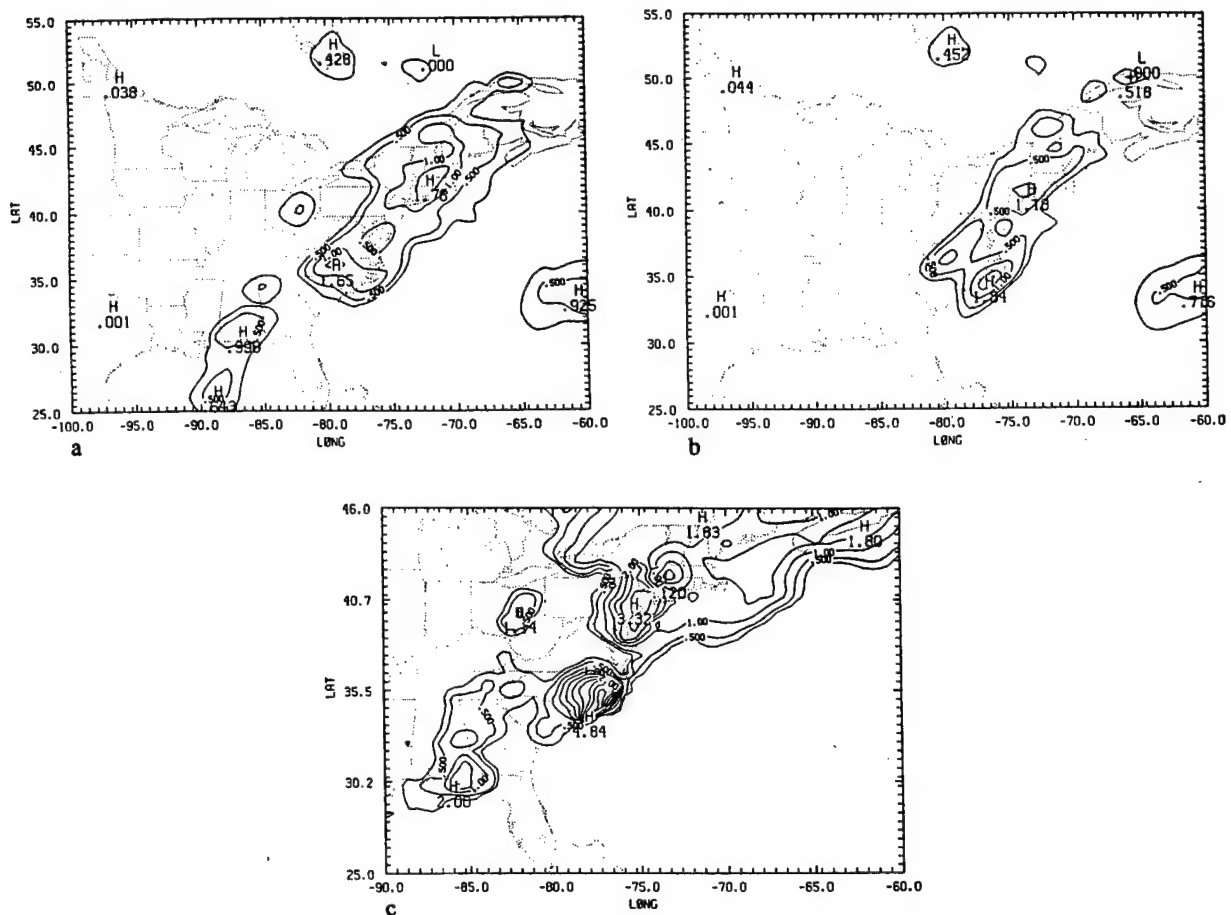


FIG. 2. Forecasts of accumulated total precipitation (cm) (0000–0600 UTC 26 January 1986) originating from (a) DNNMI and (b) ANNMI. (c) Observed precipitation (cm) for the same period.

Figure 2 shows 6-h observed rainfall and accumulated forecast rainfall valid 0000–0600 UTC 26 January 1986. The observations over the GALE area were obtained using raingages and were averaged over 6 h. Over the open ocean away from coastal regions and over the land west of 90°W and north of 45°N, where conventional rainfall data were not available, data were obtained from the University of Wisconsin and consisted of rainfall rates derived from the outgoing long-wave radiation (OLR) sensor aboard *GOES-6* with 1° resolution. Near the coastal ocean where OLR data is not reliable, model-produced rainfall rates are used. These three datasets are blended in a way to ensure smooth transition. Forecast and observed rainfalls in this figure include both convective and nonconvective precipitation. Since this version of the model is the same as the NORAPS (Navy Operational Regional Analysis Prediction System) used by Liou et al. (1990), the breakdown of the convective versus stratiform precipitation is essentially similar to their results. The forecast in Fig. 2a was initialized with DNNMI at 0000 UTC 26 January. The rainfall pattern is similar to the observed; in particular, over Alabama and along the central Gulf coast region, the model was able to predict

the precipitation during this short-range forecast. However, the forecast originating from ANNMI (Fig. 2b) fails to capture any rainfall over the Gulf coast associated with the developing short wave. The absence of diabatic heating from the NNMI has caused a spinup problem in this case. Root-mean-square differences between these forecasts and observed rainfall were computed. The differences were computed only at grid points in which at least 0.01 cm of either forecast or observed rainfall accumulated during the 6-h period. When initializing with ANNMI and DNNMI, the rms differences were 0.9 and 0.7 cm, respectively. The larger rms difference in the ANNMI case is due to model spinup. The disparity between these two cases would be even greater, if only the accumulated rainfall from the first 3 h of model integration was compared.

## 6. Summary and conclusions

In this study, we took the viewpoint that the “best” initialized states were those that were least altered by initialization. From comparisons of vertical velocity fields, we found that DNNMI with the analyzed rain produced an initial state very similar to the control

simulation and, thus, successfully re-created the 3D distribution of convective heating from the 2D model rain distribution. The ANNMI (case 3) changed the analysis significantly by reducing the maximum vertical velocities to about 60% of that resulting from DNNMI. With the diabatic heating term that forces (to a large degree) convective precipitation, the DNNMI (unlike the ANNMI) retains the divergence (or vertical motion) associated with the convection.

When DNNMI is performed on the analysis fields, model spinup time is reduced. The preforecast integration of the model ensures that the analyses are spun up and that the circulations in these analyses are consistent with the model resolution and external parameters such as topography. The initializations and forecasts were performed in this study for the midlatitudes, which dictates a relatively short spinup. In the data-sparse tropics, spinup can be expected to be much greater. In the tropical case, DNNMI with merging will be critical in reducing spinup time.

In the present study, we considered only diabatic heating associated with convective precipitation. We plan to investigate the latent heating resulting from large-scale, nonconvective rainfall in the near future. The spunup model heating approach will again be incorporated and tested.

**Acknowledgments.** This research was supported by NRL's basic research program, by SPAWAR, and by the U.S. Air Force. Part of the computer time was provided by the North Carolina Super Computing Center, Research Triangle Park.

#### REFERENCES

- Anthes, R. A., 1977: A cumulus parameterization scheme utilizing a one-dimensional cloud model. *Mon. Wea. Rev.*, **105**, 270–286.
- Bengtsson, L., 1981: Current problems in four-dimensional data assimilation. *Data Assimilation Methods. ECMWF Seminar 1980*, ECMWF, 195–217. [Available from the European Centre for Medium-Range Weather Forecasts, Shinfield Park, Reading RG29AX, England.]
- Davies, H. C., 1976: A lateral boundary formulation for multi-level prediction models. *Quart. J. Roy. Meteor. Soc.*, **102**, 405–418.
- , 1983: Limitations of some common lateral boundary schemes used in regional NWP models. *Mon. Wea. Mon.*, **111**, 1002–1012.
- Donner, L. J., 1988: An initialization for cumulus convection in numerical weather prediction models. *Mon. Wea. Rev.*, **116**, 377–385.
- Errico, R. M., and P. J. Rasch, 1988: A comparison of various normal-mode initialization schemes and the inclusion of diabatic processes. *Tellus*, **40A**, 1–25.
- Girard, C., and M. Jarraud, 1982: Short and medium range forecast differences between a spectral and grid point model: An extensive quasi-operational comparison. Tech. Rep. No. 32, European Centre for Medium-Range Weather Forecasts, 176 pp. [Available from ECMWF, Shinfield Park, Reading, England.]
- Haltiner, G. J., and R. T. Williams, 1980: *Numerical Prediction and Dynamic Meteorology*. 2d ed. John Wiley and Sons, 477 pp.
- Harms, D. E., K. D. Sashegyi, R. V. Madala, and S. Raman, 1992: Four dimensional data assimilation of GALE data using a multivariate analysis scheme and a mesoscale model with diabatic initialization, Tech. Rep. NRL/MR/4223-92-7147, 219 pp. [Available from Naval Research Laboratory, Washington, DC 20375-5320.]
- Heckley, W. A., 1985: Systematic errors of the ECMWF operational forecasting model in tropical regions. *Quart. J. Roy. Meteor. Soc.*, **111**, 709–738.
- Holt, T., S. Chang, and S. Raman, 1990: A numerical study of the coastal cyclogenesis in GALE IOP 2: Sensitivity to PBL parameterizations. *Mon. Wea. Rev.*, **118**, 234–257.
- Kasahara, A., R. C. Balgovind, and B. B. Katz, 1988: Use of satellite radiometric imagery data for improvement in the analysis of divergent wind in the tropics. *Mon. Wea. Rev.*, **116**, 866–883.
- Kitade, T., 1983: Nonlinear normal mode initialization with physics. *Mon. Wea. Rev.*, **111**, 2194–2213.
- Kuo, H.-L., 1974: Further studies of the influence of cumulus convection on large-scale flow. *J. Atmos. Sci.*, **31**, 1232–1240.
- Lejenas, H., 1980: On the influence of the technique of nonlinear normal mode initialization on the nonconvective precipitation rate. *Mon. Wea. Rev.*, **108**, 1465–1468.
- Madala, R. V., S. W. Chang, U. C. Mohanty, S. C. Madan, R. K. Paliwal, V. B. Sarin, T. Holt, and S. Raman, 1987: Description of the Naval Research Laboratory Limited Area Dynamical Weather Prediction Model. NRL Memo. 5992, Naval Research Laboratory, Washington, D.C., 131 pp.
- Miyakoda, K., R. F. Stricker, and J. Chludinsky, 1978: Initialization with the data assimilation method. *Tellus*, **30**, 32–54.
- Mohanty, U. C., A. Kasahara, and R. Errico, 1986: The impact of diabatic heating on the initialization of a global forecast model. *J. Meteor. Soc. Japan*, **64**, 805–817.
- Puri, K., 1987: Some experiments on the use of tropical diabatic heating information for initial state specification. *Mon. Wea. Rev.*, **115**, 1394–1406.
- , and M. J. Miller, 1990: The use of satellite data in the specification of convective heating for diabatic initialization and moisture adjustment in numerical weather prediction models. *Mon. Wea. Rev.*, **118**, 67–93.
- Sashegyi, K. D., and R. V. Madala, 1990: Tests of initialization procedures with the NRL limited area numerical weather prediction model. NRL Memo. 6648, Washington, D.C., 88 pp.
- , and —, 1992: Test of a nested mesoscale model for the case of the development of an extratropical cyclone during GALE. Tech. Memo., Naval Research Laboratory, Washington, D.C.
- , and —, 1993: Application of vertical mode initialization to a limited area model in flux form. *Mon. Wea. Rev.*, **121**, 207–220.
- , D. E. Harms, R. V. Madala, and S. Raman, 1993: Application of the Bratseth scheme for the analysis of GALE data using a mesoscale model. *Mon. Wea. Rev.*, **121**, 2331–2350.
- Turpeinen, O. M., L. Garand, R. Benoit, and M. Roch, 1990: Diabatic initialization of the Canadian regional finite-element (RFE) model using satellite data. Part I: Methodology and application to a winter storm. *Mon. Wea. Rev.*, **118**, 1381–1395.
- Wergen, W., 1983: Initialization. Interpretation of Numerical Weather Prediction Products, *ECMWF Seminar/Workshop 1982*, ECMWF, 31–57. [Available from the European Centre for Medium-Range Weather Forecasts, Shinfield Park, England RG29AX, England.]
- , 1987: Diabatic nonlinear normal mode initialization for a spectral model with a hybrid vertical coordinate. ECMWF Tech. Rep. No. 59, ECMWF, 83 pp.
- Wolcott, S. W., and T. T. Warner, 1981: A humidity initialization utilizing surface and satellite data. *Mon. Wea. Rev.*, **109**, 1989–1998.
- Yamada, T., 1979: PBL similarity profiles determined from a level-2 turbulence-closure model. *Bound.-Layer Meteor.*, **17**, 333–351.

## **Appendix M**

### **A Study of the Effect of the Gulf Stream and the Appalachian Mountains on Carolina Coastal Frontogenesis Using a Nonlinear Numerical Model**

# A study of the effect of the Gulf Stream and the Appalachian Mountains on Carolina coastal frontogenesis using a nonlinear numerical model<sup>1</sup>

L. Xu, R.V. Madala and S. Raman

UCAR Visiting Scientist Program, Naval Res. Lab., Monterey, CA 93943, USA

Naval Res. Lab., Washington, D C 20375, USA

North Carolina State Univ., Dept of Marine Earth & Atmos. Sci., Raleigh, NC 27695-8208, USA

(Received March 1996)

**Abstract.** *The role of the Gulf Stream and the Appalachian Mountains on the formation of the coastal frontogenesis along the mid-Atlantic coast during winter months was studied using a nonlinear, 3-dimensional mesoscale numerical model. This model consists of 10 layers in the vertical with an one-way interactive triple nested domain in the horizontal. The model physics includes dry convective adjustment, explicit large scale precipitation, parameterized convective scale circulations and parameterized boundary layer physics using a similarity theory formulation. Initial conditions for the numerical model were obtained from the Second Intensive Observation Period (IOP-2) of the Genesis of Atlantic Lows Experiment (GALE). Three numerical experiments were conducted using this model.*

*Results of the numerical experiments show that the Gulf Stream plays a significant role in developing coastal frontogenesis through transfer of large amounts of sensible and latent heats to the cold, dry atmospheric air of Arctic origin. The Gulf Stream is also found to be crucial in producing convective precipitation along the Carolina coast. On the other hand, the Appalachian mountains, which are responsible for cold air damming, are found to play only a minor role in the coastal frontogenesis.*

## 1 INTRODUCTION

The Carolina coastal front, which is often observed during winter, is a shallow mesoscale phenomenon that separates warm moist oceanic air mass from the cold dry continental air mass, and is marked by a large thermal contrast and cyclonic shear. Based on east coast cyclone climatology, Colucci [15] and Whittaker and Horn [33] have shown that the coastal front plays a key role in the genesis of the

<sup>1</sup>This work was supported by the Naval Res. Lab. Computational resources were provided by the North Carolina Supercomputing Ctr., Res. Triangle Park; National Supercomputing Ctr. for Energy & the Environment; U S Army CEWES High Performance Computing Ctr.  
©1997 Journals Oxford Ltd.



offshore cyclones. Hoskins et al. [20] hypothesized that the cyclogenesis is essentially the result of interaction between the low-level positive Isentropic Potential Vorticity (IPV) anomaly and an upper-level one. The coastal front can provide the needed low-level positive IPV anomaly to trigger the cyclogenesis. The coastal frontogenesis has a great impact on the local weather as well as on regional weather. Because of its key role in the offshore cyclogenesis it is important to understand the external forces that create the coastal frontogenesis. During the last two decades several observational, theoretical and numerical studies were carried out to understand the coastal fronts. Bosart (1984) studied the coastal fronts along the Gulf coast of Texas and the coastal fronts along the New England coast of US are investigated by Bosart et al. [9]; Bosart [5]; Marks and Austin [24]; Ballentine [4]; Nielsen [25]; Nielsen and Neilley [26] and along the Carolina Coast By Carson [11]; Bosart [6]; Bosart and Lin [8]; Riordan et al. [29]; Riordan [28]; Doyle and Warner [16]; and Holt and Raman [19]. Two unique processes that are frequently observed along the mid-Atlantic coastal region are due to the presence of the Appalachian mountains, which are located west of the coast, and the Gulf Stream. These processes are the cold-air damming by the Appalachian mountains and transfer of large amounts of sensible and latent heat fluxes from the warm Gulf Stream. The cold-air damming is a process in which the Arctic cold dry air flows northeasterly and is channeled along the Appalachian mountains. The Appalachian mountain acts as a physical barrier to dam the cold and dry air mass to the east, thereby creating a narrow inverted sea level pressure (SLP) ridge.

Some studies suggest that the cold-air damming by the Appalachian mountains may be one of the reasons causing coastal frontogenesis. For example, Bosart et al. [9] and Bosart [5] documented the existence of the narrow inverted SLP ridge in conjunction with the New England coastal frontogenesis, and suggested that the cold air damming by the Northern Appalachian mountains is one of the mechanisms causing frontogenesis. Stauffer and Warner [31] suggested that cold-air damming that contributes to a land-sea temperature contrast in excess of the wintertime climatological value of 2-3C per 100km, may cause the frontogenesis. On the other hand, Ballentine [4], based on numerical experiments, concluded that the presence of the mountain did not affect on the New England frontogenesis. However, it is not clear what role the cold air damming plays in the Carolina coastal frontogenesis.

The Gulf Stream is a warm ocean current observed offshore of the east coast of the United States. The temperature of the Gulf Stream core is about 25C year around and the mean width of the Gulf Stream is roughly 100km and can meander 50km within one week. The temperature difference between the Gulf Stream and the air above can be as large as 20C during a cold air outbreak (Konrad and Colucci, 1989). Some of the highest wintertime energy transfers from the ocean to the atmosphere takes place (Raman and Riordan [27]; Wayland and Raman [32]; Grossman et al. [18]) over the Gulf Stream region of Carolina coast. Sharp horizontal temperature gradients between the coast and the Gulf Stream play a significant role in the frontogenetic processes (Doyle and Warner [16]; Doyle and Warner [17]; Riordan [28]; Cione et al. [14]).

A triple-nested version of the mesoscale model of the Naval Research Laboratory/North Carolina State University (NRL/NCSU) is employed to study the mesoscale coastal processes during the coastal front formation of the GALE IOP-2. Use of a nested model provides better lateral boundary conditions for regions of the interest. Three numerical sensitivity experiments are performed to in-



investigate the role of the Gulf Stream and the Appalachian mountains on the mesoscale circulations and convective precipitation along the Carolina coast.

The synoptic setting of the coastal frontogenesis event during the GALE IOP-2 is described in Section 2. A brief description of the triple-nested version of the NRL/NCSU mesoscale model, followed by a description of the model domain and the data set used for this study are given in Section 3. The experiment designs along with the discussion of results are presented in Section 4. Summary and conclusions are given in Section 5.

## 2 REVIEW OF THE SYNOPTIC SITUATION

Following a cold front passage over mid-Atlantic region on 23 January 1986, an intense anticyclone developed over central Canada. During the next 24 hours the anticyclone intensified as it moved towards the coast. By 1200 UTC 25 January 1986, center of the anticyclone was located over Eastern Canada. Surface winds over the Atlantic ocean, offshore of the east coast of the United States, were mostly easterly. The westward moving cold, dry air mass of Arctic origin was modified by the relatively warmer Gulf Stream into a warm and moist air mass. During this time, cold air was trapped by the Appalachian mountains creating an inverted ridge. The inverted SLP ridge is believed to be the result of the wedge of entrenched cold air to the east of the Appalachian Mountains; and the inverted trough was over the Gulf Stream front (Doyle and Warner [16]). The coastal front was rather disorganized at this time. The anticyclone continually propagated eastwards and provided the easterly wind over the Gulf Stream and brought in modified warm and moist air to coastal regions of the Carolinas by 0000 UTC 26 1986. The inverted SLP ridge was still located east of the Appalachian Mountains while the intensity of the inverted ridge became weaker. On the other hand, the inverted SLP trough intensified and the low SLP zone extended to a larger area along the coast. A mesoscale analysis of this synoptic situation is given by Doyle and Warner [16].

## 3 MODEL AND DATA

The numerical model used in this study is a 10-layer version of the NRL/NCSU mesoscale model. The model is based on primitive equations in a terrain following  $\sigma$  ( $= p/p_s$ ) vertical coordinate, where  $p$  is the pressure and  $p_s$  the surface pressure. The finite difference form of the differential equations is second order accuracy on staggered C-grid (Arakawa and Lamb [3]) in horizontal. In the vertical direction, model domain is divided into ten layers of equal thickness in the  $\sigma$  coordinate. The governing equations in flux form are written as,

Momentum Equations:

$$\begin{aligned} \frac{\partial(p_s \dot{\sigma} u)}{\partial t} + \frac{1}{h_x h_y} \left[ \frac{\partial(p_s u h_y u)}{\partial x} + \frac{\partial(p_s v h_x u)}{\partial y} \right] + \frac{\partial(p_s \dot{\sigma} u)}{\partial \sigma} - f p_s v + p_s \frac{u v}{h_x h_y} \frac{\partial h_x}{\partial y} \\ = - \frac{p_s}{h_x} \frac{\partial \phi}{\partial x} - \frac{R T}{h_x} \frac{\partial p_s}{\partial x} + p_s F_u \end{aligned} \quad (1)$$

$$\frac{\partial(p_s \dot{\sigma} v)}{\partial t} + \frac{1}{h_x h_y} \left[ \frac{\partial(p_s u h_y v)}{\partial x} + \frac{\partial(p_s v h_x v)}{\partial y} \right] + \frac{\partial(p_s \dot{\sigma} v)}{\partial \sigma} + f p_s u - p_s \frac{u^2}{h_x h_y} \frac{\partial h_x}{\partial y}$$

$$= -\frac{p_s}{h_y} \frac{\partial \phi}{\partial y} - \frac{RT}{h_y} \frac{\partial p_s}{\partial y} + p_s F_v \quad (2)$$

**Thermodynamic Equation:**

$$\begin{aligned} & \frac{\partial(p_s T)}{\partial t} + \frac{1}{h_x h_y} \left[ \frac{\partial(p_s u h_y T)}{\partial x} + \frac{\partial(p_s v h_x T)}{\partial y} \right] \\ & + \left( \frac{\sigma}{\sigma_0} \right)^\kappa \frac{\partial(p_s \dot{\sigma})}{\partial \sigma} + \frac{RT}{C_p} \tilde{D} - \frac{RT}{C_p} \left( \frac{u}{h_x} \frac{\partial p_s}{\partial x} + \frac{v}{h_y} \frac{\partial p_s}{\partial y} \right) = p_s F_T \end{aligned} \quad (3)$$

**Moisture Continuity Equation:**

$$\frac{\partial(p_s q)}{\partial t} + \frac{1}{h_x h_y} \left[ \frac{\partial(p_s u h_y q)}{\partial x} + \frac{\partial(p_s v h_x q)}{\partial y} \right] + \frac{\partial(p_s \dot{\sigma} q)}{\partial \sigma} = p_s F_q \quad (4)$$

**Hydrostatic Equation:**

$$\frac{\partial \phi}{\partial \sigma} = -\frac{RT}{\sigma} \quad (5)$$

**Mass Continuity Equation:**

$$\frac{\partial(p_s \dot{\sigma})}{\partial \sigma} = \tilde{D} - D \quad (6)$$

**Surface Pressure Tendency Equation:**

$$\frac{\partial p_s}{\partial t} = -\tilde{D} \quad (7)$$

where  $u, v$  are the zonal and meridional components of the wind, respectively,  $T$  the temperature,  $q$  the specific humidity,  $\dot{\sigma}$  the vertical velocity,  $\phi$  the geopotential,  $\theta$  the potential temperature,  $f$  the Coriolis parameter,  $F_q$  the forcing in moisture equation,  $F_T$  the forcing in thermodynamic equation,  $F_u$  the forcing in zonal momentum equation,  $F_v$  the forcing in meridional momentum equation,  $R$  the gas constant for air and  $\kappa = R/C_p$  where  $C_p$  is the specific heat for air at constant pressure. The  $h_x$  and  $h_y$  are map factors and the horizontal divergence  $D$  and  $\tilde{D}$  are given by,

$$D = \frac{1}{h_x h_y} \left[ \frac{\partial(p_s u h_y)}{\partial x} + \frac{\partial(p_s v h_x)}{\partial y} \right] \quad (8)$$

$$\tilde{D} = \int_0^1 D h_x h_y dx dy. \quad (9)$$

Model physics includes dry convective adjustment, latent heat released due to convective and nonconvective precipitation, planetary boundary layer, and internal diffusion. The atmospheric radiative transfer processes are not included in this version due to short integration period of 24 hours.

Convective heating, precipitation, and moistening of the environment are parameterized using the method developed by Kuo [21] and modified by Anthes [1]. The large-scale precipitation occurs when saturation is reached on the resolvable scale. A part of the excess moisture is assumed to precipitate into the lower model layer and to re-evaporate by a factor that depends on the height where the

saturation occurs. The rest of the excess moisture precipitates to the ground. Exchanging of sensible heat, latent heat, and momentum fluxes between the boundary layer air and underlying surface are parameterized, using a generalized similarity theory, in which the drag coefficients are stability dependent (Chang [12]).

Unrealistic lateral boundary conditions are believed to be a major source of error in regional primitive equation models because of the ill-posed mathematical nature of the problem (Anthes [2]). One option to reduce the error in lateral boundary conditions is using the one way nesting technique. The model has three nests, outer nest with coarse resolution, middle nest with a medium resolution, and inner nest with fine resolution. Boundary conditions for the two inner nests are obtained from the immediate coarser nest through interpolation in time and space at every time step. Boundary conditions for the coarser nest are obtained from NMC/RAFS (National Meteorological Center/Regional Analysis and Forecasting System) at synoptic times through interpolation.

Figure 1 illustrates the model domain used in this study: the outer nest covers the North American continent and the adjacent oceans and extends from 40W to 140W and 10N to 70N with a horizontal resolution of 2 longitude (170km at 40N) by 1.5 latitude (166.5km); the middle nest covers the eastern part of the US and extends from 60W to 100W and 23.5N to 50.5N with a horizontal resolution of 2/3 longitude (56.7km at 40N) by 1.5/3 latitude (55.5km). The inner nest covers the Carolinas and the Gulf Stream and extends from 70W to 90W and 32N to 40N with a horizontal resolution of 2/9 longitude (18.9km at 40N) by 1.5/9 latitude (18.5km). With this grid resolution, the integration time step used is 450 seconds on the outer grid, 150 seconds on the middle grid, and 50 seconds on the inner grid.

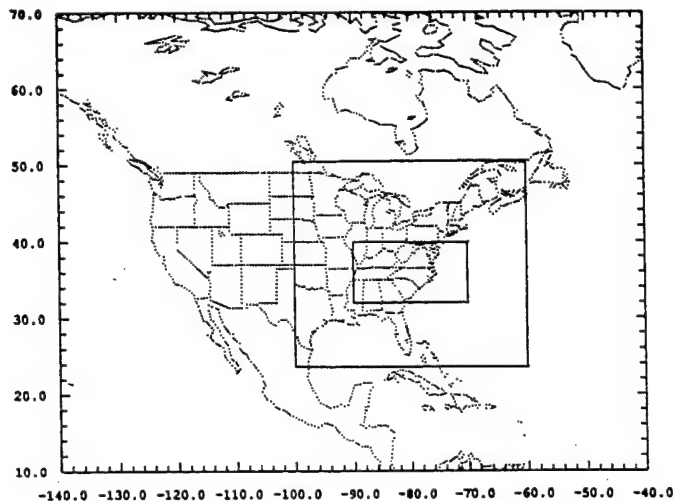
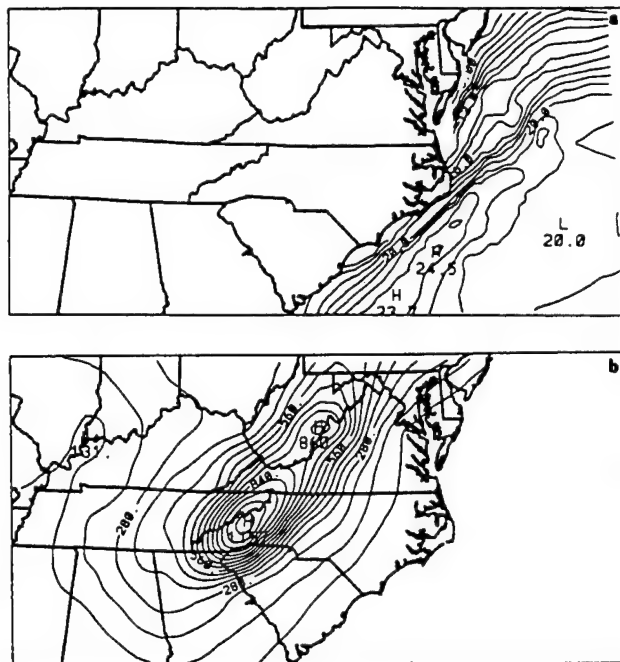
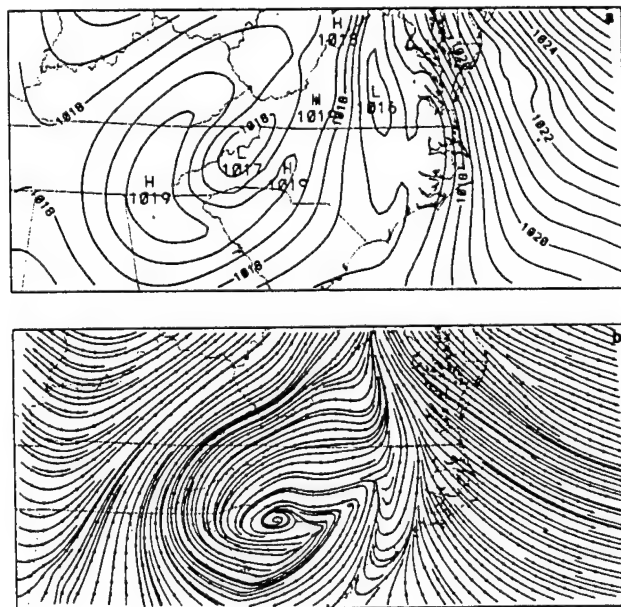


Figure 1. The model domain used in this study.

Since one of the objectives of this study is to examine the importance of the Gulf Stream on the coastal frontogenesis, a high resolution SST data is desired. To represent the Gulf Stream more realistically, the SST analysis of 14km resolution provided by NOAA, taken from the GALE data sets, was interpolated directly to the inner nest. Since the high resolution SST data was available only for the GALE region, the SST data used in both the outer and middle nests were



**Figure 2.** (a) The SST analysis for the inner nest based on 14 km resolution SST provided by NOAA. (b) Terrain height for the inner nest interpolated from the US Navy's 10x10 min data base.



**Figure 3.** 24 h simulation from the EXP1 valid at 0000 UTC 26 January 1986. (a) Sea level pressure. (b) Streamlines at 1000 mb.

obtained from an analysis that merged the weekly mean and the coarse SST observations. Figure 2a shows the SST fields for the inner nest. Sea/ice boundary was derived from the US Navy's climatological sea/ice boundaries for month of

January. The topography data used in the model was directly created by interpolating the US Navy's 10' by 10' data base. Model topography for the inner nest is given in Figure 2b. The Appalachian Mountains can be clearly seen in this figure.

The basic meteorological dataset used for the initial conditions was obtained through horizontal and vertical interpolation from the NMC/RAFS 2.5 degree hemispheric analysis (without enhanced GALE data). The vertical normal mode initialization scheme of Bourke and McGregor [10], as applied by Sashegyi and Madala [30], was then used to reduce the amplitude of spurious gravity wave oscillations that result during the numerical integration of the model. A detailed discussion of the model design, physics, and initialization is given in Madala et al. [23]; Chang et al. [13] and Sashegyi and Madala [30].

#### 4 DISCUSSION OF RESULTS

Main objectives of this study are to understand the impact of the Gulf Stream and the Appalachian mountains on mesoscale circulations along the east coast of the United States. To achieve these objectives three numerical experiments are performed. The first numerical experiment is designed to simulate the coastal frontogenesis and related mesoscale features due to the Appalachian mountains and the Gulf Stream. This is considered the control experiment. Two more experiments were conducted to determine the effect of the Gulf Stream and that of the Appalachian mountains on the coastal frontogenesis. The following is a brief description of the three numerical experiments.

Experiment 1 (EXP1): The purpose of this experiment was to reproduce the coastal frontogenesis event that took place along the Carolina coast during the GALE IOP-2. The external forces are due to both the Gulf Stream and the Appalachian mountains.

Experiment 2 (EXP2): The purpose of this experiment was to investigate the role of the Gulf Stream on the formation of the Carolina coastal frontogenesis. The warm core of the Gulf Stream SST offshore of the Carolinas is about 25C year around. On the other hand, the SST of the shelf water, which is not effected by the Gulf Stream, is about 6C during winter. The Gulf Stream transports a large amount of energy from lower latitudes. Because of the warm SST over the Gulf Stream there is an appreciable amount of turbulent sensible and latent heat fluxes to the atmosphere. If the Gulf Stream did not exist, the SST offshore of the Atlantic coast would be approximately the same as the SST of the shelf water, which was about 6C during the period of the experiment. For simplicity, yet without losing generality, any value of SST larger than 6C is set equal to 6C to eliminate the existence of the Gulf Stream in the model. The impact of the Gulf Stream on coastal mesoscale processes is then examined comparing the results from the EXP2 with the one from the EXP1.

Experiment 3 (EXP3): The purpose of this experiment was to investigate the effects of the Appalachian mountains on the Carolina coastal frontogenesis and associated mesoscale features. An interesting mesoscale feature is the cold air damming east of the Appalachian mountains during the coastal front events. The cold air damming is due to the mechanical blocking of the Appalachian mountains under favorable synoptic conditions. The cold air damming by the Appalachian mountains can create and enhance the lower level atmospheric thermal contrast between land air and oceanic air. However, it is not quite clear how important the cold air damming is in the coastal frontogenesis processes. To

eliminate the mountain, the terrain height is set to zero everywhere in the model domain.

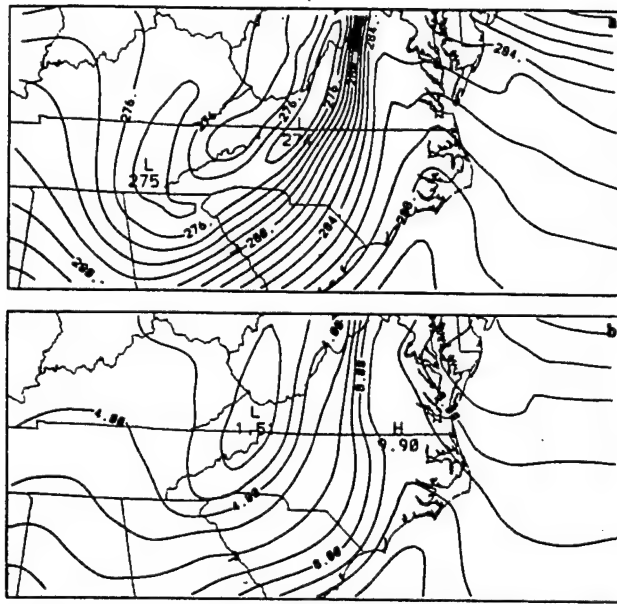


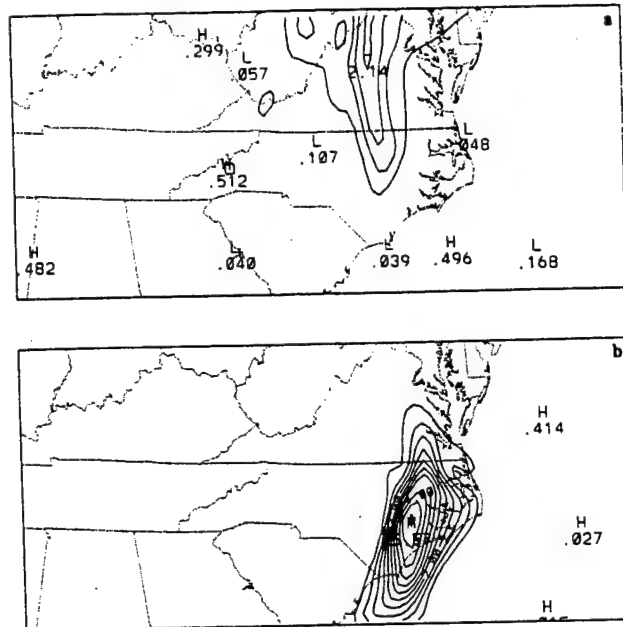
Figure 4. 24 h simulation from the EXP1 valid at 000 UTC 26 January 1986 at 950 mb. (a) Temperature in degree K. (b) Mixing ratio in  $\text{g kg}^{-1}$ .

#### 4.1 EXP1 (Control Experiment)

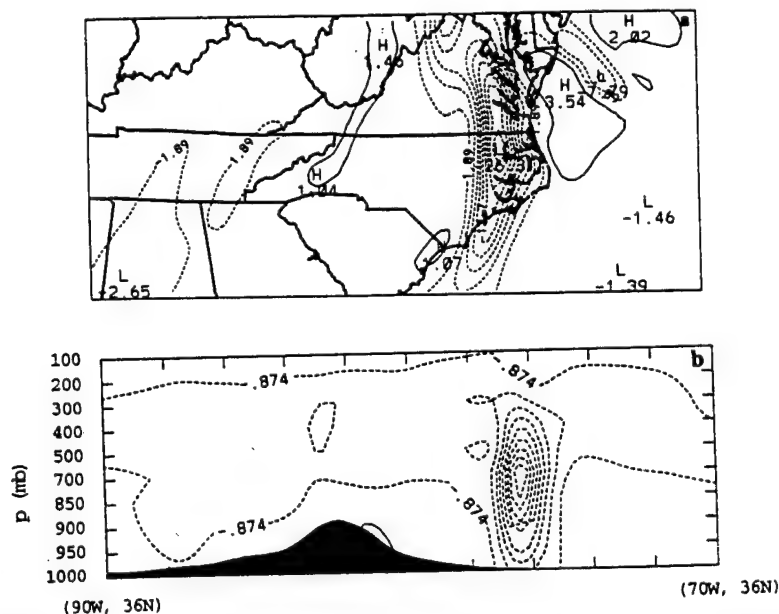
Figure 3a is the simulated 24 h sea level pressure valid at 00Z 26 January 1986. The simulated SLP shows that the pressure values less than 1017 mb covers the eastern part of the Carolinas and Virginia with a mesolow of 1016 mb located at south central Virginia. Surface pressure increases towards the mountain. The simulated SLP reasonably reproduced the observed narrow surface high pressure ridge east of the Appalachian mountains and the inverted trough along the Carolina coast. Figure 3b is the simulated 24h streamline field at 1000 mb valid at 00Z 26 January 1986. The convergence zone along the cyclonic coastal front is well simulated. The model also reproduced the observed northerly wind near the coastal areas of the Carolinas.

Figure 4a is the simulated 24 h temperatures at 950 mb valid at 00Z 26 January 1986. The model simulated the cold air damming by the Appalachian mountains. Low level air flow around the mountain can also be seen. Also seen in Figure 4a is an inverted surface ridge east of the mountain caused by cold air damming. Presence of a warm temperature zone from the Carolina coast to the coastal Virginia coincides with the low pressure zone (Figure 3a). Figure 4b is the simulated mixing ratio at 950 mb valid at 00Z 26 January 1986. Effect of warm air advection by southeasterly wind can be seen along the coastal regions of the Carolinas and Virginia. Mixing ratios in this region are larger than  $9.0 \text{ g kg}^{-1}$ .

Figures 5a and 5b show the accumulated 24 h non-convective and convective precipitation, respectively. The non-convective large scale precipitation, with a



**Figure 5.** 24 h accumulated precipitation from the EXP1. (a) Nonconvective precipitation (in cm). (b) Convective precipitation (in cm).



**Figure 6.** The simulated 24 h vertical velocity (in  $\text{cms}^{-1}$ ) from EXP1 for the inner nest. (a) At 850 mb. (b) East-west cross section at 36N.

maximum value exceeding 2 cm covers most of Virginia. A convective precipitation with a maximum value over 5 cm occurs over the Carolina coast. The simulated 24 h vertical velocity at 850 mb (Figure 6a) shows an upward motion along the Carolina and Virginia coasts, with a maximum vertical velocity of about  $26\text{cms}^{-1}$  over northern North Carolina. However, as can be seen from



Figure 6a the location of the maximum precipitation (Figure 5b) is to the south of the region for two reasons. First, more moist air is available near the coast. Second, frictional convergence near the coast is large. To investigate the vertical structure of the upward motion, an east-west cross section of the simulated 24 h vertical velocity at 36N is shown in Figure 6b. The center of the upward motion is located at 700 mb and has a magnitude of  $28 \text{ cm s}^{-1}$ . The vertical motion is narrow near the coast and sharply defined. Precipitation occurs as the warm, moist air is lifted over the cold air dome east of the Appalachian mountains.

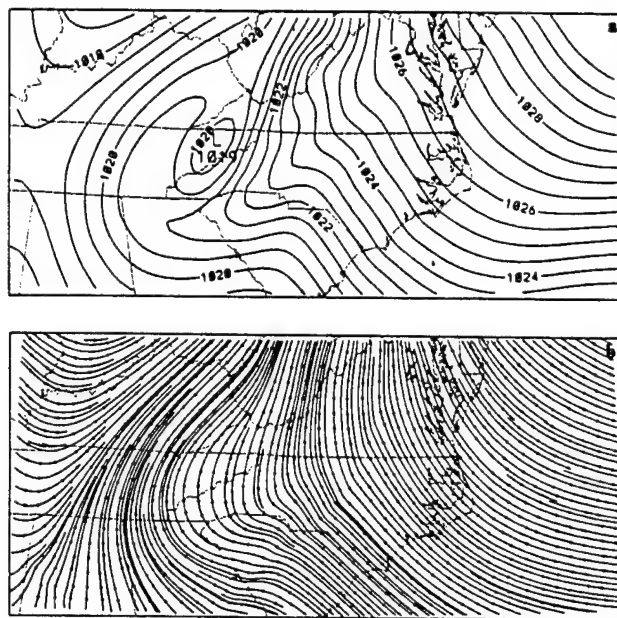


Figure 7. 24 h simulation from the EXP2. (a) Sea level pressure.  
(b) Streamlines at 1000 mb.

#### 4.2 EXP2 (Effect of the Gulf Stream)

Figure 7a presents the simulated 24 h SLP from the EXP2. With the Gulf Stream removed from the model, the coastal front is missing in the simulation although cold air damming by the Appalachian mountains is present. We can see that the SLP distribution over the western half of the model domain to be very similar to the one from the control experiment. However, the SLP distributions along the Carolina coast and the eastern Virginia are quite different from the EXP1 (Figure 3a). The inverted trough along the Carolina coast and the eastern Virginia is absent in the model simulation. The inverted ridge east of the Appalachian mountains has been enhanced significantly (by about 4 mb). An increase in the SLP by about 9 mb is found near the coastal regions as compared to EXP1 (Figure 3a). The increases in SLP are mainly caused by the colder temperature in the simulation. Figure 7b is the simulated 24h streamline field at 1000 mb valid at 00Z 26 January 1986 from the EXP2. Cyclonic coastal front convergence zone is not present in this simulation.

Figures 8a and 8b are the simulated 24h temperatures and the mixing ratios at 950 mb for the EXP2, respectively. Figure 8a shows a much colder air mass over the eastern half of the model domain as compared to the simulation from

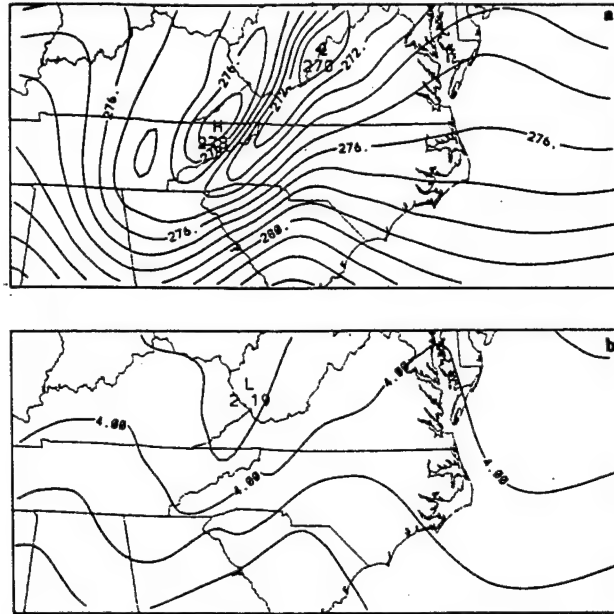


Figure 8. 24 h simulation at 950 mb from the EXP2. (a) Temperature in degree K. (b) Mixing ratio in  $\text{g kg}^{-1}$ .

the EXP1. The air temperature at 950 mb along the Carolina coast and the eastern part of Virginia is about 10C colder as compared to EXP1. It is noticed that the existence of the Gulf Stream not only affects the temperature field, but also influences the moisture field at 950 mb. The mixing ratio differences at 950 mb between the EXP1 and the EXP2 suggest that the air mass at 950 mb (Figure 8b) is about 50% drier over the Carolina coastal region when the Gulf Stream is not present. Because of less latent and sensible heat flux into the atmosphere, the simulated precipitation and its area coverage are greatly reduced in the eastern half of the model domain.

The convective precipitation does not exist in the EXP2 simulation, while the maximum value of non-convective precipitation is reduced by more than 60% as compared to the EXP1. The simulated 24 h vertical velocities at 850 mb are shown in Figure 9a. The magnitudes of the vertical velocities near the coastal region are much smaller (about  $3 \text{ cm s}^{-1}$ ) as compared to the ones in the EXP1 (Figure 6a). There is an upward motion east of the mountains and a downward motion in west caused by the southeasterly flow over the mountains. In the EXP1, flow over the mountains was absent because of the cold air damming. Figure 9b is an east-west cross section of the simulated 24 h vertical velocities at 36N. Most of the vertical motions are near the mountains. Upward motion near the coast for this case is drastically reduced as compared to the case with the Gulf Stream (EXP1). Because of the reduction in moisture availability in the lower atmosphere and weaker upward motions, convective precipitation is totally absent in the EXP2.

#### 4.3 EXP3 (Effect of the Appalachian mountains)

Figure 10a shows the simulated 24 h SLP from the EXP3 valid at 00Z 26 January 1986. The model predicted a much broader ridge over the mountain region and a broader trough over the coastal region as compared to EXP1.

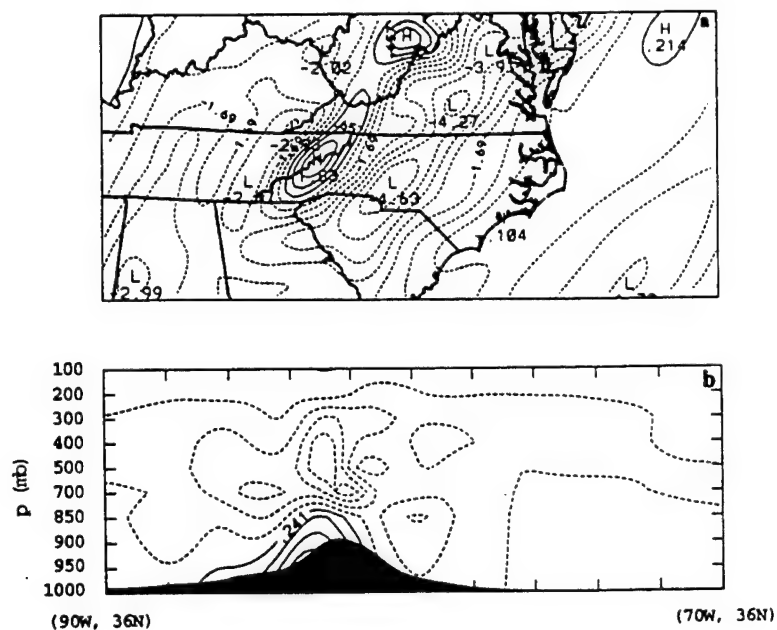


**Figure 9.** The simulated 24 h vertical velocity (in  $\text{cms}^{-1}$ ) from the EXP2. (a) At 850 mb. (b) East-west cross section at 36N.

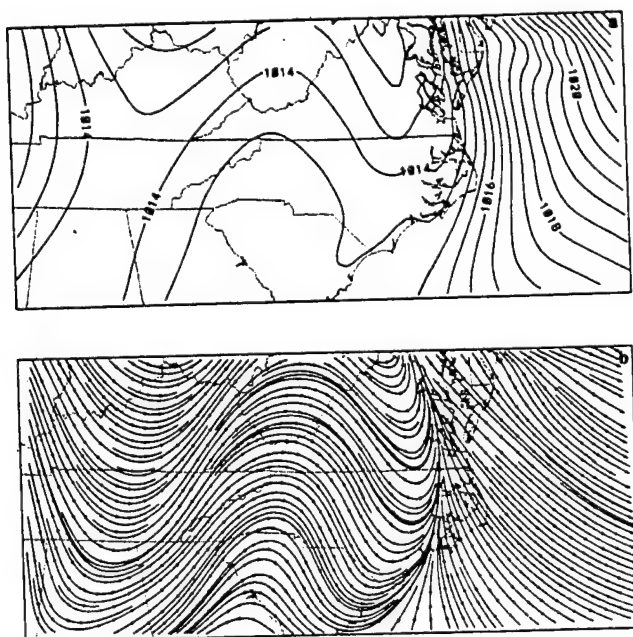


**Figure 10.** 24 h simulation from the EXP3. (a) Sea level pressure. (b) Streamlines at 1000 mb.

Figure 10b is the simulated 24 h streamlines at 1000 mb. The streamlines display a cyclonic convergence along the coastal areas and a coastal front is present. Figure 11a shows the simulated 24 h temperature at 950 mb from EXP3. Without the topography, the cold air damming does not exist. This is reflected by the absence of the cold air belt east of the Appalachian mountains. The warm air modified by the Gulf Stream is able to move more inland without the mountains. A closer examination of the temperature distribution between the EXP1 and EXP3 at 950 mb reveals a warmer temperature of more than  $4^{\circ}\text{C}$  inland for the EXP3. This difference occurs in the region where the Appalachian mountains were present. Negligible temperature difference occurred over the coastal regions. Figure 11b is the simulated 24 h moisture field at 950 mb for EXP3. The moisture distribution in Figure 11b displays a pattern similar to EXP1 (Figure 4b). However, without the topography, the moist air is able to penetrate further inland, but the moisture gradient inland is weaker. The weaker horizontal temperature and moisture gradients caused a broader and weaker coastal front. Consequently the model predicted a weaker but broader precipitation along the front.

The 24 h accumulated convective precipitation is shown in Figure 12. The convective precipitation is over much broader area, which now covers eastern parts of both North Carolina and Virginia. In EXP1 convective precipitation was mainly over the Carolina coast. For EXP3, with the mountain removed the maximum convective precipitation has decreased by about 40%. The results show a weaker non-convective large scale precipitation pattern as well. The simulated 24 h vertical velocity at 850 mb (Figure 13a) indicates upward motion along the Carolina and Virginia coast similar to the EXP1. However, the maximum value of the vertical velocity is now only  $22\text{ cm s}^{-1}$  and is located over the Virginia coast. To examine the vertical structure of the upward motion, an east-west cross section of the simulated 24 h vertical velocity at  $36^{\circ}\text{N}$  was analyzed and is shown in Figure 13b. The center of the vertical motion with a value of about  $15\text{ cm s}^{-1}$  is located at 850 mb and is much broader and weaker as compared to the one in EXP1 (Figure 6b). Without the mountains, cold air damming is absent and the uplifts of the air parcels are weaker. In addition, the cold air damming provided a sharp temperature contrast near the coast in the EXP1. With a broader and weaker vertical motion, the simulated convective precipitation covered a larger area with the maximum value reduced by about 40% as compared to the EXP1.

The most important effect of the Appalachian mountains is to block the cold air on the east side. This cold air damming plays a significant role in forming the observed inverted ridge east of the Appalachian mountains. The inclusion of the Appalachian mountains allows the model to simulate a stronger horizontal temperature and moisture gradient, which then leads to more realistic precipitation forecast.

## 5 SUMMARY AND CONCLUSIONS

Three numerical experiments were conducted to understand the role of the Gulf Stream thermal forcing and the cold air damming due to the Appalachian mountains on coastal frontogenesis. The model used in this study is a triple nested version of the NRL/NCSU mesoscale numerical model based on primitive equations. The model resolutions are approximately 180, 60 and 20 km for the outer, middle, and inner nests, respectively. A vertical normal mode initialization procedure was employed to get the initial data for each of the three

experiments.

The model reasonably simulated the observed cold air damming, inverted ridge east of the Appalachian mountains, inverted trough along the Carolina coast, and the Carolina coastal frontogenesis. The Gulf Stream is found to play a significant role in coastal frontogenesis. The Gulf Stream enhances the low level horizontal temperature and moisture gradients. Presence of the Gulf Stream is found to be important in producing the precipitation along the Carolina coast. Without the Gulf Stream, the coastal front is not simulated. As a consequence, the convective precipitation is totally absent and nonconvective precipitation is greatly reduced. The Appalachian mountains play a secondary role in forming the coastal front.

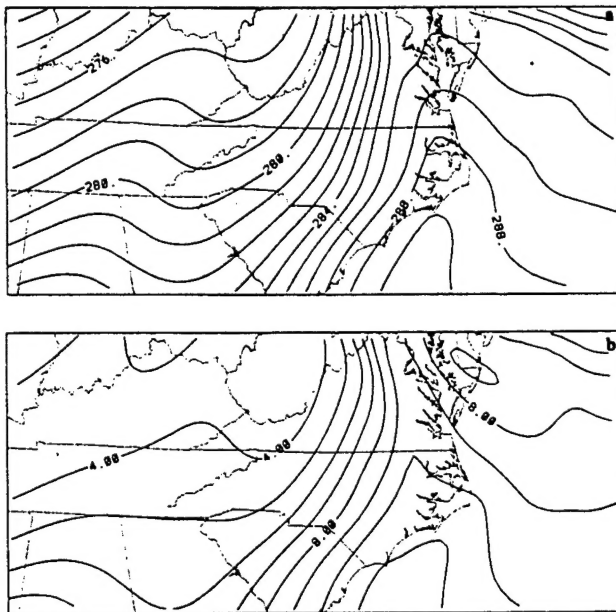
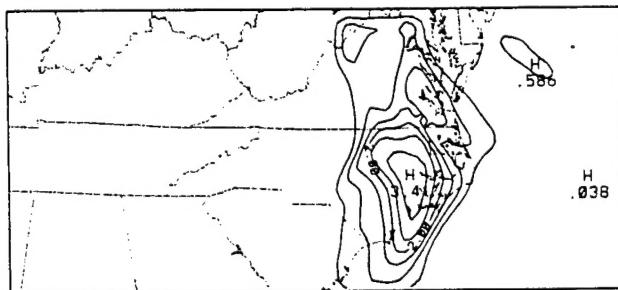


Figure 11. 24 h simulation at 950 mb from the EXP3. (a) Temperature in degree K. (b) Mixing ratio in  $\text{g kg}^{-1}$ .



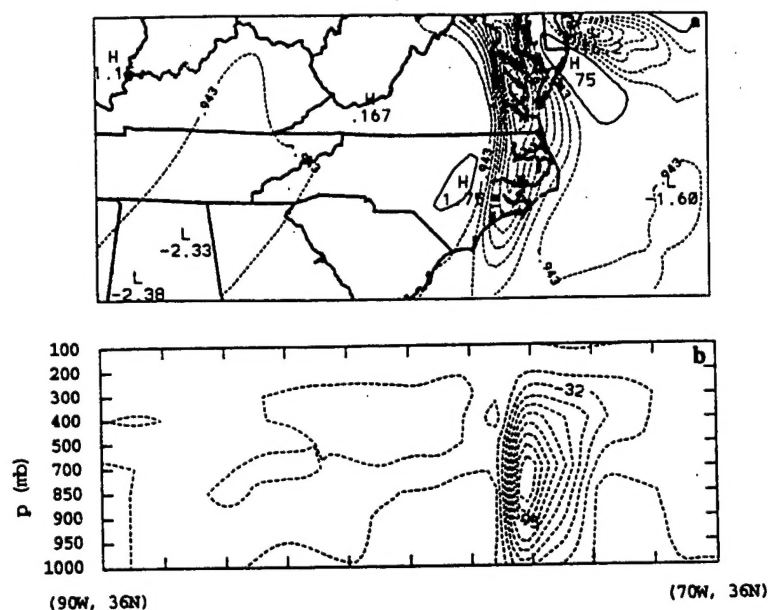


Figure 13. Simulated 24 h vertical velocity (in  $\text{m s}^{-1}$ ) from EXP3. (a) At 850 mb. (b) East-west cross section at 36N.

The mountains are responsible for the observed cold air damming and they also prevent the penetration of moist air further inland. Without the mountains, the simulated coastal front is broader and weaker. As a consequence, the convective precipitation covered a broader area and the maximum value of precipitation decreased by 40%.

### References

- [1] Anthes, R.A. (1977) A cumulus parameterization scheme utilizing a one-dimensional cloud model. *Mon. Wea. Rev.* 105, 270-286.
- [2] Anthes, R.A. (1983) Review regional models of the atmosphere in middle latitudes. *Mon. Wea. Rev.* 111, 1306-1335.
- [3] Arakawa, A. and Lamb, V.R. (1977) Computational design of the basic dynamical processes of the UCLA general circulation model. *Methods in Computational Physics*, 17, General Circulation Models of the Atmosphere, J. Chang, Ed., Academic Press, New York, 173-265.
- [4] Ballentine, R.J. (1980) A numerical investigation of New England coastal frontogenesis. *Mon. Wea. Rev.* 108, 1479-1497.
- [5] Bosart, L.F. (1975) New England coastal frontogenesis. *Quart. J. Roy. Meteor. Soc.* 101, 957-978.
- [6] Bosart, L.F. (1981) The Presidents' Day snowstorm of 18-19 February 1979: A subsynoptic-scale event. *Mon. Wea. Rev.* 109, 1542-1566.
- [7] Bosart, L.F. (1984) The Texas coastal rainstorm of 17-21 September 1979: An example of synoptic-mesoscale interaction. *Mon. Wea. Rev.* 112, 1108-1133.
- [8] Bosart, L.F. and Lin, S.C. (1984) A diagnostic analysis of the Presidents' Day storm of February 1979. *Mon. Wea. Rev.* 112, 2148-2177.
- [9] Bosart, L.F., Vaudo, C.J. and Helsdon, J.H., Jr. (1972) Coastal frontogenesis. *J. Appl. Meteor.* 11, 1236-1258.
- [10] Bourke, W. and McGregor, J.L. (1983) A nonlinear vertical mode initialization scheme

- for a limited area prediction model. *Mon. Wea. Rev.* **111**, 2285-2297.
- [11] Carson, R.B. (1950) The Gulf Stream front: a cause of stratus on the lower Atlantic coast. *Mon. Wea. Rev.* **78**, 91-101.
- [12] Chang, S.W. (1981) Test of a planetary boundary-layer parameterization based on a generalized similarity theory in tropical cyclone models. *Mon. Wea. Rev.* **109**, 843-853.
- [13] Chang, S.W., Brehme, K., Madala, R. and Sashegyi, K. (1983) A numerical study of the East Coast snowstorm of 10-12 February 1983. *Mon. Wea. Rev.* **111**, 1768-1777.
- [14] Cione, J., Raman, S. and Pietrafesa, L.J. (1993) The effect of Gulf Stream induced baroclinicity on U.S. east coast winter cyclones. *Mon. Wea. Rev.* **121**, 421-430.
- [15] Colucci, S.J. (1976) Winter cyclone frequency over the eastern United States and adjacent western Atlantic, 1964-1973. *Bull. Amer. Meteor. Soc.* **57**, 548-553.
- [16] Doyle, J.D. and Warner, T.T. (1990) Mesoscale coastal processes during GALE IOP 2. *Mon. Wea. Rev.* **118**, 283-308.
- [17] Doyle, J.D. and Warner, T.T. (1993) The impact of the sea surface temperature resolution on mesoscale coastal processes during GALE IOP 2. *Mon. Wea. Rev.* **121**, 313-334.
- [18] Grossman, R.L. and Betts, A.K. (1990) Air-sea interaction during an extreme cold air outbreak from the eastern coast of the United States. *Mon. Wea. Rev.* **118**, 324-342.
- [19] Holt, T.R. and Raman, S. (1992) Three-dimensional mean and turbulence structure of a coastal front influenced by the Gulf Stream, Monthly. *Mon. Wea. Rev.* **120**, 17-39.
- [20] Hoskins, B.J., McIntyre, M.E. and Robertson, A.W. (1985) On the use and significance of isentropic potential vorticity maps. *Quart. J. Roy. Meteor. Soc.* **111**, 877-946.
- [21] Kuo, H.-L. (1974) Further studies of the influence of cumulus convection on large-scale flow. *J. Atmos. Sci.* **31**, 1232-1240.
- [22] Konrad, C.E., II and Colucci, S.J. (1989) An examination of extreme cold air outbreaks over eastern North American. *Mon. Wea. Rev.* **117**, 2687-2700.
- [23] Madala, R. V., Chang, S.W., Mohanty, U.C., Madan, S.C., Paliwal, R.K., Sarin, V.B., Holt, T. and Raman, S. (1987) Description of the Naval Research Laboratory Limited Area Dynamical Weather Prediction Model. NRL Memorandum Report 5992, Naval Research Laboratory, Washington, D. C., 131 pp.
- [24] Marks, F.D., Jr. and Austin, P.M. (1979) Effects of the New England coastal front on the distribution of precipitation. *Mon. Wea. Rev.* **107**, 53-67.
- [25] Nielsen, J.W. (1989) The formation of New England coastal fronts. *Mon. Wea. Rev.* **117**, 1380-1401.
- [26] Nielsen, J.W. and Neilley, P.P. (1990) The vertical structure of New England coastal fronts. *Mon. Wea. Rev.* **118**, 1793-1807.
- [27] Raman, S. and Riordan, A.J. (1988) The Genesis of Atlantic Lows Experiment: The planetary-boundary-layer subprogram of GALE. *Bull. Amer. Meteor. Soc.* **69**, 161-172.
- [28] Riordan, A.J. (1990) Examination of the mesoscale features of the GALE coastal front of 24-25 January 1986. *Mon. Wea. Rev.* **118**, 258-282.
- [29] Riordan, A.J., SethuRaman, S., Davis, J.M. and Viessman, S. (1985) Measurements in the marine boundary layer near a coastal front. *Geophys. Res. Lett.* **12**, 681-684.
- [30] Sashegyi, K.D., and Madala, R.V. (1990) Tests of initialization procedures with the NRL limited area numerical weather prediction model. NRL Memorandum Report 6648, Washington, D. C. 88 pp.
- [31] Stauffer, D.R. and Warner, T.M. (1987) A numerical study of Appalachian cold-air damming and coastal frontogenesis. *Mon. Wea. Rev.* **115**, 799-821.
- [32] Wayland, R. and Raman, S. (1989) Mean and turbulent structure of a baroclinic marine boundary layer during the 28 January 1986 cold-air outbreak (GALE 86). *Boundary-Layer Meteorol.* **48**, 227-254.
- [33] Whittaker, L. M. and Horn, L.H. (1981) Geographical and seasonal distribution of North American cyclogenesis, 1958-1977. *Mon. Wea. Rev.* **109**, 2312-2322.



# DISTRIBUTION STATEMENT AUTHORIZATION RECORD

Title: ATMOSPHERIC FORECASTING

Authorizing Official: Dr John Hornstein

Agency: NRL

Ph. No. 2027670766

☐

Internet Document: URL: \_\_\_\_\_  
(DTIC-OCA Use Only)

Distribution Statement: (Authorized by the source above.)

☒

A: Approved for public release, distribution unlimited.

☐

B: U. S. Government agencies only. (Fill in reason and date applied). Other requests shall be referred to (Insert controlling office).

☐

C: U. S. Government agencies and their contractors. (Fill in reason and date applied). Other requests shall be referred to (Insert controlling office).

☐

D: DoD and DoD contractors only. (Fill in reason and date applied). Other requests shall be referred to (Insert controlling office).

☐

E: DoD components only. (Fill in reason and date applied). Other requests shall be referred to (Insert controlling office).

☐

F: Further dissemination only as directed by (Insert controlling DoD office and date), or higher authority.

☐

X: U. S. Government agencies and private individuals or enterprises eligible to obtain export-controlled technical data in accordance with DoD Directive 5230.25.

NOTES: \_\_\_\_\_

\_\_\_\_\_  
\_\_\_\_\_  
\_\_\_\_\_

Norm WATSON  
DTIC Point of Contact

11/14/00  
Date